frontiers | Research Topics

Fine-grained sedimentary rocks: sedimentary processes, diagenesis, geochemistry and their relationship with critical geological events

Edited by
Yifan Li, Zhiyang Li, Jianguo Zhang, Zhen Qiu, George Kontakiotis and Junwen Peng

Coordinated by
Youwei Wang

Published in
Frontiers in Earth Science

ISSN 1664-8714
ISBN 978-2-8325-6439-4
DOI 10.3389/978-2-8325-6439-4

Generative AI statement
Any alternative text (Alt text) provided alongside figures in the articles in this ebook has been generated by Frontiers with the support of artificial intelligence and reasonable efforts have been made to ensure accuracy, including review by the authors wherever possible. If you identify any issues, please contact us.

About Frontiers

Frontiers is more than just an open access publisher of scholarly articles: it is a pioneering approach to the world of academia, radically improving the way scholarly research is managed. The grand vision of Frontiers is a world where all people have an equal opportunity to seek, share and generate knowledge. Frontiers provides immediate and permanent online open access to all its publications, but this alone is not enough to realize our grand goals.

Frontiers journal series

The Frontiers journal series is a multi-tier and interdisciplinary set of open-access, online journals, promising a paradigm shift from the current review, selection and dissemination processes in academic publishing. All Frontiers journals are driven by researchers for researchers; therefore, they constitute a service to the scholarly community. At the same time, the *Frontiers journal series* operates on a revolutionary invention, the tiered publishing system, initially addressing specific communities of scholars, and gradually climbing up to broader public understanding, thus serving the interests of the lay society, too.

Dedication to quality

Each Frontiers article is a landmark of the highest quality, thanks to genuinely collaborative interactions between authors and review editors, who include some of the world's best academicians. Research must be certified by peers before entering a stream of knowledge that may eventually reach the public - and shape society; therefore, Frontiers only applies the most rigorous and unbiased reviews. Frontiers revolutionizes research publishing by freely delivering the most outstanding research, evaluated with no bias from both the academic and social point of view. By applying the most advanced information technologies, Frontiers is catapulting scholarly publishing into a new generation.

What are Frontiers Research Topics?

Frontiers Research Topics are very popular trademarks of the *Frontiers journals series*: they are collections of at least ten articles, all centered on a particular subject. With their unique mix of varied contributions from Original Research to Review Articles, Frontiers Research Topics unify the most influential researchers, the latest key findings and historical advances in a hot research area.

Find out more on how to host your own Frontiers Research Topic or contribute to one as an author by contacting the Frontiers editorial office: frontiersin.org/about/contact

Fine-grained sedimentary rocks: sedimentary processes, diagenesis, geochemistry and their relationship with critical geological events

Topic editors

Yifan Li — China University of Geosciences, China
Zhiyang Li — Texas A&M International University, United States
Jianguo Zhang — China University of Geosciences, China
Zhen Qiu — Research Institute of Petroleum Exploration and Development (RIPED), China
George Kontakiotis — National and Kapodistrian University of Athens, Greece
Junwen Peng — University of Oklahoma, United States

Topic coordinator

Youwei Wang — University of Virginia, United States

Citation

Li, Y., Li, Z., Zhang, J., Qiu, Z., Kontakiotis, G., Peng, J., Wang, Y., eds. (2025). *Fine-grained sedimentary rocks: sedimentary processes, diagenesis, geochemistry and their relationship with critical geological events*. Lausanne: Frontiers Media SA. doi: 10.3389/978-2-8325-6439-4

Table of contents

frontiers | Frontiers in Earth Science

TYPE Editorial
PUBLISHED 22 May 2025
DOI 10.3389/feart.2025.1625168

OPEN ACCESS

EDITED AND REVIEWED BY
Valerio Acocella,
Roma Tre University, Italy

*CORRESPONDENCE
Yifan Li,
liyifan@cugb.edu.cn

RECEIVED 08 May 2025
ACCEPTED 13 May 2025
PUBLISHED 22 May 2025

CITATION
Li Y, Li Z, Zhang J, Qiu Z, Kontakiotis G, Peng J and Wang Y (2025) Editorial: Fine-grained sedimentary rocks: sedimentary processes, diagenesis, geochemistry and their relationship with critical geological events. *Front. Earth Sci.* 13:1625168.
doi: 10.3389/feart.2025.1625168

Editorial: Fine-grained sedimentary rocks: sedimentary processes, diagenesis, geochemistry and their relationship with critical geological events

Yifan Li[1]*, Zhiyang Li[2], Jianguo Zhang[1], Zhen Qiu[3], George Kontakiotis[4], Junwen Peng[5] and Youwei Wang[6]

[1]School of Energy and Resources, China University of Geosciences, Beijing, China, [2]School of Engineering, Texas A&M International University, Laredo, TX, United States, [3]Research Institute of Petroleum Exploration and Development (RIPED), PetroChina, Beijing, China, [4]Department of Historical Geology and Paleontology, Faculty of Geology and Geoenvironment, School of Earth Sciences, National and Kapodistrian University of Athens, Athens, Greece, [5]Oklahoma Geological Survey, University of Oklahoma, Norman, OK, United States, [6]Department of Environmental Sciences, University of Virginia, Charlottesville, VA, United States

KEYWORDS

sedimentary process, sedimentary geochemistry, diagenenesis, shales and mudstones, unconventional reservoir, geological event

Editorial on the Research Topic
Fine-grained sedimentary rocks: sedimentary processes, diagenesis, geochemistry and their relationship with critical geological events

Fine-grained sedimentary rocks are increasingly studied for their complex depositional processes, high organic content, reservoir potential, metal enrichment, and geochemical records of paleoenvironments (Ettensohn et al., 1987; Wignall, 1994; Stow et al., 2001; Aplin et al., 2011; Shahzad et al., 2024). Once seen as homogeneous suspension-settled deposits, flume experiments and sedimentological studies have revealed that they can form under high-energy conditions, influenced by floods, storms, and bottom currents (Schieber et al., 2007; Bohacs et al., 2014; Macquaker et al., 2014; Li et al., 2022; Mehmood et al., 2023). Additionally, finegrained sedimentary rocks may receive sediments of various origins and can be characterized by a complex composition comprising clay minerals, quartz, carbonates, feldspars, sulfides, biogenic debris, and organic matter (Taylor and Macquaker, 2002; Macquaker and Adams, 2003; Milliken, 2014; Camp et al., 2015). Diagenesis in these rocks is governed by mass-balance, fluid transport, and organic-inorganic interactions (Morad et al., 2000; Cobbold et al., 2013; Liang et al., 2018). Geochemical proxies link their formation to major tectonic and environmental events, including rifting, glaciation, volcanism, anoxia, mass

extinctions, and hydrothermal activity (Algeo et al., 2012; Trabucho-Alexandre et al., 2012; Li et al., 2015; Qiu et al., 2022; Shen et al., 2025; Derkowski et al., 2013). These insights are vital to sedimentary and diagenetic theory—especially unconventional petroleum sedimentology (Qiu et al., 2020; Zou et al., 2022)—and to understanding Earth's sphere-system evolution.

This Research Topic comprises ten papers presenting advances in the study of fine-grained sedimentary rocks from three perspectives: depositional processes, diagenetic mechanisms, and geochemical characteristics. Rocks focused in this volume encompass both marine and continental mudstones and shales, spanning strata from the Cambrian to the Eocene, and therefore are broadly representative. Through these case studies, we aim to further enrich the theoretical framework surrounding fine-grained sedimentary rocks.

Sedimentary processes

Wen et al. investigated the Beipiao Formation in western Liaoning, Northeast China, and identified lithofacies formed under the influence of volcanic activities and sediment-gravity flows. Three depositional environments—shallow lake, semi-deep/deep lacustrine, and fan delta—were defined, with basin evolution transitioning from fan delta to deep lake and back, interbedded with volcanic deposits. Volcanism enhanced nutrient supply and organic matter preservation, while gravity flows transported plant fragments to deep lakes, leading to the enrichment of Type III kerogen.

Feng and Zhang analyzed the ShangGanchaigou Formation in the western Qaidam Basin, Northwest China, and identified seven architectural elements (distributary channels, bars, algal mounds, etc.) and three facies belts (proximal delta front, middle isolated lobes, distal algalmarl complexes). Short-term base-level cycles were documented as the dominant factor producing frequent facies variations. Reservoir connectivity was documented to decrease lakeward, revealing challenges in predicting heterogeneous reservoirs.

Diagenesis

Zhang et al. examined coevolution of minerals in lacustrine mudstones from Bohai Bay Basin, East China. Fibrous calcite/ankerite precipitated in primary laminar fractures during peak organic-acid release, with elements supplied by early carbonate dissolution and smectite–illite transformation. Clay alteration led to the formation of microcrystalline quartz, feldspar dissolution, and the increase in pH allowed authigenic albite to form. Authigenic carbonates and colloidal pyrite regulated pore-fluid chemistry, while variations in organic matter governed pore pressure, acid levels, and diagenetic pathways.

Yuan et al. studied tight sandstones of the Jurassic Lianggaoshan Formation in the eastern Sichuan Basin, Southwest China, and identified various facies associated with subaqueous distributary channels and mouth bars. Strong compaction/cementation led to reduction of porosity, while chlorite coatings and weak dissolution preserved pores. Five diagenetic facies were classified, with Type III (chlorite-coating) and IV (weak dissolution) in coarse-grained channels showing high AC, low GR/DEN/RT as optimal reservoirs.

Lin et al. studied analcime formation in Middle Permian reservoirs in the Jinan Sag, Junggar Basin, Northwest China. Analcime was originated from early alkaline hydrolysis of volcanic debris under specific conditions, forming low-silica, Al-rich, Na-poor varieties. Cementation reduced primary porosity, but acidic fluids from oil/gas charging dissolved analcime, generating secondary pores via albitization. Reservoir quality was enhanced by formation of intragranular pores through dissolution of analcime, feldspar or lithic fragments.

Guo et al. investigated glutenite compaction using a self-designed diagenetic simulation system, addressing the lack of quantitative studies on complex rock fabrics. Experiments revealed segmented logarithmic relationships between porosity and depth during mechanical compaction, with larger grains aiding in pore preservation. A 30% sand content in gravel formed stable secondary structures optimizing pressure-bearing capacity, while high heterobase content reduced primary pores.

Ge et al. examined Niutitang shale gas across four palaeouplifts in the Sichuan Basin, Southwest China, showing that structural preservation, thermal maturation, and sedimentary subfacies control enrichment and that thrust-nappe lower plates and deepwater trough facies were recognized as prime exploration targets.

Geochemistry

Lu et al. investigated Qiongzhusi Formation shale from three wells in southern Sichuan Basin, Southwest China, by analyses of lithofacies, mineralogy, TOC, trace elements, and isotopes. They defined two depositional end-members in a fault-controlled, moderately restricted setting: (1) organic-rich black shale formed under anoxic-suboxic conditions during periods of low chemical weathering, cold-arid climate, and high productivity; and (2) organic-lean grey shale deposited under suboxic-oxic conditions during periods of similarly low weathering intensity and aridity but reduced productivity.

Gao et al. analyzed fine-grained floodplain deposits in the Greater Green River Basin, southwestern Wyoming, United States of America. They used paleosol morphology, bulk organic $\delta^{13}C$, leaf-wax $\delta^{13}C$ and δD, and CIA-K–derived MAP to reconstruct LPEE continental hydroclimate. They identified the PETM by a ~4‰–5‰ negative carbon isotope excursion and a 30‰–50‰ leaf wax n-alkanes δ Dn-alk increase. Paleosols indicate generally humid–warm conditions with transient drying during the PETM, with pCO_2 of 600–900 ppm reconstructed through the integration of δ^{13}Corg with carbonate $\delta^{13}C$.

Wang et al. reconciled Qingshankou Formation mud/silt stratigraphy in the southern Songliao Basin, Northwest China, by linking gamma/density logs to astronomical cycles, and developed a high-resolution, isochronous framework. They showed that tectonics and orbital climate paced rhythmic sand–mud progradation and proposed a "synchronous heterotopy" lake-delta

model with overfilling strata lagging eccentricity peaks, whereas balanced - filling strata coinciding with them.

Author contributions

YL: Writing – original draft, Writing – review and editing. ZL: Writing – original draft, Writing – review and editing. JZ: Writing – review and editing. ZQ: Writing – review and editing. GK: Writing – review and editing. JP: Writing – review and editing. YW: Writing – review and editing.

Funding

The author(s) declare that financial support was received for the research and/or publication of this article. This work was supported by the National Natural Science Foundation of China (Grants 42272173, U24B6001), and the National Key Research and Development Program of China (Grant Nos. 2023YFF0804300, 2023YFF0804302).

Conflict of interest

Author ZQ was employed by Petrochina.

The remaining authors declare that the research was conducted in the absence of any commercial or financial relationships that could be construed as a potential conflict of interest.

Generative AI statement

The author(s) declare that no Generative AI was used in the creation of this manuscript.

Publisher's note

References

Algeo, T. J., Morford, J., and Cruse, A. (2012). New applications of trace metals as proxies in marine paleoenvironments. *Chem. Geol.*, 306: 160–164. doi:10.1016/j.chemgeo.2012.03.009

Aplin, A. C., and Macquaker, J. H. S. (2011). Mudstone diversity: origin and implications for source, seal, and reservoir properties in petroleum systems. *AAPG Bull.* 95 (12), 2031–2059.

Bohacs, K. M., Lazar, O. R., and Demko, T. M. (2014). Parasequence types in shelfal mudstone strata—Quantitative observations of lithofacies and stacking patterns, and conceptual link to modern depositional regimes. *Geology*. 42 (2), 131–134. doi:10.1130/g35089.1

Camp, J., Roberts, M., Maclachlan, C., Wallace, E., Hermanson, L., Brookshaw, A., et al. (2015). Seasonal forecasting of tropical storms using the Met Office GloSea5 seasonal forecast system. *Q. J. R. Meteorological Soc.* 141 (691), 2206–2219. doi:10.1002/qj.2516

Cobbold, P. R., Zanella, A., Rodrigues, N., and Løseth, H. (2013). Bedding-parallel fibrous veins (beef and cone-in-cone): Worldwide occurrence and possible significance in terms of fluid overpressure, hydrocarbon generation and mineralization. *Mar. Petroleum Geol.* 43, 1–20. doi:10.1016/j.marpetgeo.2013.01.010

Derkowski, A., Bristow, T. F., Wampler, J. M., Środoń, J., Marynowski, L., Elliott, W. C., et al. (2013). Hydrothermal alteration of the Ediacaran Doushantuo Formation in the Yangtze Gorges area (South China). *Geochimica Cosmochimica Acta*. 107, 279–298. doi:10.1016/j.gca.2013.01.015

Ettensohn, F. R. (1987). Rates of relative plate motion during the Acadian orogeny based on the spatial distribution of black shales. *J. Geol.* 95 (4), 572–582.

Li, Y., Fan, T., Zhang, J., Zhang, J., Wei, X., Hu, X., et al. (2015). Geochemical changes in the Early Cambrian interval of the Yangtze Platform, South China: Implications for hydrothermal influences and paleocean redox conditions. *J. Asian Earth Sci.* 109, 100–123. doi:10.1016/j.jseaes.2015.05.003

Li, Z., and Schieber, J. (2022). Correlative conformity or subtle unconformity? The distal expression of a sequence boundary in the upper cretaceous mancos shale, Henry mountains region, Utah, USA. *J. Sediment. Res.* 92 (7), 635–657.

Liang, C., Wu, J., Jiang, Z., Cao, Y., and Song, G. (2018). Sedimentary environmental controls on petrology and organic matter accumulation in the upper fourth member of the Shahejie Formation (Paleogene, Dongying depression, Bohai Bay Basin, China). *Int. J. Coal Geol.* 186, 1–13. doi:10.1016/j.coal.2017.11.016

Macquaker, J. H. S., and Adams, A. E. (2003). Maximizing information from fine-grained sedimentary rocks: An inclusive nomenclature for mudstones. *J. Sediment. Res.*, 73(5): 735–744.

Macquaker, J. H., Taylor, K. G., Keller, M., and Polya, D. (2014). Compositional controls on early diagenetic pathways in fine-grained sedimentary rocks: Implications for predicting unconventional reservoir attributes of mudstones. *AAPG Bull.* 98 (3), 587–603. doi:10.1306/08201311176

Mehmood, M., Naseem, A. A., Saleem, M., Rehman, Ju, Kontakiotis, G., Janjuhah, H. T., et al. (2023). Sedimentary Facies, Architectural Elements, and Depositional Environments of the Maastrichtian Pab Formation in the Rakhi Gorge, Eastern Sulaiman Ranges, Pakistan. *J. Mar. Sci. Eng.* 11, 726. doi:10.3390/jmse11040726

Milliken, K. (2014). A compositional classification for grain assemblages in fine-grained sediments and sedimentary rocks. *J. Sediment. Res.* 84 (12), 1185–1199. doi:10.2110/jsr.2014.92

Morad, S., Ketzer, J. M., and De Ros, L. F. (2000). Spatial and temporal distribution of diagenetic alterations in siliciclastic rocks: implications for mass transfer in sedimentary basins. *Sedimentology* 47, 95–120. doi:10.1046/j.1365-3091.2000.00007.x

Qiu, Z., and Zou, C. (2020). Controlling factors on the formation and distribution of "sweet-spot areas" of marine gas shales in South China and a preliminary discussion on unconventional petroleum sedimentology. *J. Asian Earth Sci.* 194, 103989.

Qiu, Z., Zou, C., Mills, B. J., Xiong, Y., Tao, H., Lu, B., et al. (2022). A nutrient control on expanded anoxia and global cooling during the Late Ordovician mass extinction. *Commun. Earth and Environ.* 3 (1), 82. doi:10.1038/s43247-022-00412-x

Schieber, J., Southard, J., and Thaisen, K. (2007). Accretion of mudstone beds from migrating floccule ripples. *Science* 318 (5857), 1760–1763. doi:10.1126/science.1147001

Shahzad, A., Kontakiotis, G., Adatte, T., Ahmed, K. S., Riaz, M. T., Janjuhah, H. T., et al. (2024). Multi-Elemental Chemostratigraphy, Sequence Development, Depositional History, and Environmental Importance of Early Eocene Red Beds (Kuldana Formation) in NW Himalayas, Pakistan. *J. Earth Sci.* 35, 349–375. doi:10.1007/s12583-023-1860-6

Shen, B., Lang, X., Wang, R., Liu, Y., Zhang, S., Huang, T., et al. (2025). Resolving the Snowball Earth conundrum: the role of marine dissolved organic carbon pool. *Bull. Sci.*, doi:10.1016/j.scib.2025.03.056

Stow, D. A. V., Huc, A. Y., and Bertrand, P. (2001). Depositional processes of black shales in deep water. *Mar. Petroleum Geol.* 18 (4), 491–498. doi:10.1016/s0264-8172(01)00012-5

Taylor, K. G., and Macquaker, J. H. S. (2002). "Early diagenetic pyrite morphology in a mudstone-dominated succession," in *The lower Jurassic Cleveland Ironstone formation, eastern England*.

Trabucho-Alexandre, J., Hay, W. W., and De Boer, P. L. (2012). Phanerozoic environments of black shale deposition and the Wilson Cycle. *Solid earth*. 3 (1), 29–42. doi:10.5194/se-3-29-2012

Wignall, P. B. (1994). *Black shales*. Clarendon Press.

Zou, C., Qiu, Z., Zhang, J., Li, Z., Wei, H., Liu, B., et al. (2022). Unconventional petroleum sedimentology: Unconventional Petroleum Sedimentology: A Key to Understanding Unconventional Hydrocarbon Accumulation key to understanding unconventional hydrocarbon accumulation. *Engineering* 18, 62–78. doi:10.1016/j.eng.2022.06.016

frontiers | Frontiers in Earth Science

TYPE Original Research
PUBLISHED 04 July 2024
DOI 10.3389/feart.2024.1433517

OPEN ACCESS

EDITED BY
Jianguo Zhang,
China University of Geosciences, China

REVIEWED BY
Changyu Fan,
Northwest University, China
Laixing Cai,
Chengdu University of Technology, China

*CORRESPONDENCE
Daoshen Wang,
wangdaoshen1996@163.com

RECEIVED 16 May 2024
ACCEPTED 11 June 2024
PUBLISHED 04 July 2024

CITATION
Guo H, Wang D, Shan X, Peng B, Zou Z, Wu J and Li K (2024), Preservation of intergranular pore in deep clastic reservoirs by rock fabric based on compaction physics simulation experiments.
Front. Earth Sci. 12:1433517.
doi: 10.3389/feart.2024.1433517

Preservation of intergranular pore in deep clastic reservoirs by rock fabric based on compaction physics simulation experiments

Huajun Guo[1], Daoshen Wang[2]*, Xiang Shan[1], Bo Peng[1], Zhiwen Zou[1], Jin Wu[1] and Ke Li[2]

[1]Petrochina Hangzhou Research Institute of Geology, Hangzhou, China, [2]National Key Laboratory of Deep Oil and Gas, China University of Petroleum (East China), Qingdao, China

Diagenetic physical simulation is a reliable means to study patterns of pore evolution and variations of physical properties, however, the current compaction model is mostly based on sandstone, and there is a lack of quantitative compaction and porosity reduction studies for more complex rock fabrics. In order to simulate the continuous change of intergranular porosity in the reservoir under compaction during the diagenesis of buried sedimentary strata, a self-designed diagenesis simulation experimental system was adopted. Using different modern sediment samples, the simulation experiment of mechanical compaction of glutenite was carried out. The experiment shows that during the process of mechanical compaction of glutenite, the change of porosity with depth is segmented, and there is a good logarithmic relationship between depth and porosity in the process of diagenetic compaction. The larger the grain size in the reservoir rock, the better the pore preservation capacity; When the sand particles fill the pores among gravel, stable secondary support structure formed by gravel and sand grades can effectively take over the bearing pressure, and when the sand-grade particle content is about 30%, the pressure-bearing capacity is the strongest; Intergranular heterobase filling is greater in samples with high heterobase content, high heterobasic content is not favourable to the preservation of primary pores. This study provides favorable experimental support for the preservation mechanism of deep clastic reservoir pores, and has important theoretical and practical significance for oil and gas exploration in the study area. The use of simulation experiment provides a useful idea for the evaluation and prediction of reservoirs and the search for favorable reservoir development zones in the future.

KEYWORDS

compaction physics simulation, clastic reservoirs, rock fabric, intergranular pore, compaction

1 Introduction

The abundant oil and gas resources contained in the gravel reservoirs in the deep field have attracted much attention, showing great succession potential for the next step in energy development and deployment, and gradually becoming an important source of oil and gas reserves and production (Pang X. J. et al, 2020; Li et al., 2020). Reservoir quality is one of the key factors constraining oil and gas exploration in deep

reservoirs (Taylor et al., 2010; Sun et al., 2013; Wang, 2020), mechanical compaction is an important cause of pore permeability reduction in glutenite reservoirs, controlling both the preservation of intergranular pore and the evolution of physical properties (Carvalho and Ros, 2015; Yuan et al., 2017; Pang X. et al, 2020; Li et al., 2021). As the systematic study of reservoir diagenesis is becoming more and more mature, qualitative descriptions and semi-quantitative analyses of mechanical compaction can no longer provide favourable theoretical support for reservoir pore retention mechanisms. Diagenetic physical simulation has emerged as an innovative experimental method for simulating diagenesis indoors, by establishing a compaction model with compaction physical simulation experimental data and setting up temperature, pressure and fluid property conditions in line with the geological situation, it studies pore evolution patterns and physical property variations of reservoir caused by compaction.

In recent years, scholars have introduced simulation experiments of compaction to study the multiple factors affecting compaction and the dynamic response mechanism. The factors affecting sandstone compaction can be categorised into internal factors such as mineral composition, filler, grain size and sortability, and external factors such as pressure, temperature, fluid and time. Liu et al. found that the pore penetration changes in the compaction simulation process have obvious segmentation, and have good linear and exponential relationship with bearing pressure, respectively (Liu et al., 2006). In terms of experimental studies of compaction for endogenous factors such as rock fabric, Fawad and Bjørlykke found that the evolution of reservoir porosity vary with different grain sizes and mineralogical compositions, and that coarser sands with a high content of clasts are more susceptible to compaction than finer quartz-rich sands (Chuhan et al., 2002; Chuhan et al., 2003; Bjørlykke, 2014). Cao et al. and Ji et al. analysed the variation patterns of porosity and permeability in sandstone reservoirs with different grain sizes and sorting under pure compaction conditions, and found that the two showed a good positive correlation with physical properties (Cao et al., 2011; Ji et al., 2017). Gao et al. found that there is a significant negative correlation between matrix content and porosity through the simulation of compaction of sandstone, and the rate of porosity attenuation is larger in sandstone with high matrix content (Gao et al., 2015). In addition, the quantitative impact of the above external factors on the simulation of compaction evolution has also been elaborated. You et al. applied physical simulation experiments to analyse the pore evolution characteristics in the setting of different temperature and pressure fields, and clarified that the protection of primary pores by overpressure is the most constructive role in reservoirs in the setting of high temperature overpressure and strong overpressure (You et al., 2019). Gao et al. carried out physical simulation experiments on the mechanism of the role of overpressure on the physical properties of deep reservoirs, and found that the reduction value of the remaining primary pores by mechanical compaction under overpressure is only one-half of that under hydrostatic pressure, and that overpressure can effectively inhibit the role of mechanical compaction, so that a large number of intergranular primary pores can be preserved (Gao et al., 2023). Hou et al. investigated the varying rules of porosity and permeability of sandstone reservoirs under different ground temperature conditions and different burial ways under compaction by physical simulation, and found that the ground temperature and pore permeability parameters were all in a logarithmic negative correlation, whereas the burial time was in a logarithmic relationship with the pore permeability parameters (Hou et al., 2017).

The deep glutenite of Fukang Sag in Junggar Basin have a large potential of oil and gas resources (He et al., 2021), the stratigraphy of the Upper Urho Formation in this area has a large span of burial depth, and vertical burial compaction dominates, which facilitates comparative studies in the vertical direction, and provides a good example for the study of mechanical compaction response of deep glutenite. With the continuous updating of the petrogenetic physics simulation experimental device, high temperature and high pressure and even ultra-high temperature and ultra-high pressure experimental equipment have been developed successively, which provide the necessary experimental conditions for the study of deep physical and chemical diagenesis. However, most of the current compaction models are based on sandstones, and there is a lack of quantitative compaction and pore reduction studies for glutenite, which are more complex in rock fabric. Previous studies have found that glutenite is more resistant to compaction than sandstone (Xie et al., 2018; Liu et al., 2020), and that particle morphology, grain size and arrangement can have a significant effect on mechanical compaction (De Cola et al., 2018). The structure of gravel is different from that of pure sandstone. If a skeleton is built between gravel particles, it can play a supporting role, and the gravel skeleton can withstand the pressure during the compaction process, which can resist the destruction of sandy debris pores by mechanical compaction (Wei et al., 2015; Mahmic et al., 2018; Kang et al., 2019; Yue, 2019). Therefore, this paper takes the deep Permian glutenite reservoir in Fukang Sag of Junggar Basin as an example, applies the compaction physics simulation experiment to investigate the physical evolution patterns in the process of mechanical compaction of deep glutenite, quantitatively analyses the preservation of intergranular pores by rock fabric, with a goal of providing guidance for the evaluation and prediction of the deep gravel reservoirs and searching for favourable reservoir development zones.

2 Experimental setup and experimental procedure

The experiment adopts the compaction physics simulation experiment system independently designed and developed by the National Key Laboratory of Deep Oil and Gas (China University of Petroleum (East China)), which is able to complete the compaction simulation experiments with the maximum temperature of 500 °C, the maximum static rock pressure of 300 MPa, and the maximum fluid pressure of 100 MPa. It is the experimental device that can simulate the higher temperature and pressure in China, which can meet the high temperature and high pressure environment of deep- and ultra-deep strata under the actual geological conditions. It can simulate the diagenesis and pore evolution process of the reservoir under different temperature, pressure and fluid medium conditions.

The system device includes axial pressure monitoring equipment, flow pressure monitoring equipment, heating furnace and temperature control device, temperature monitoring

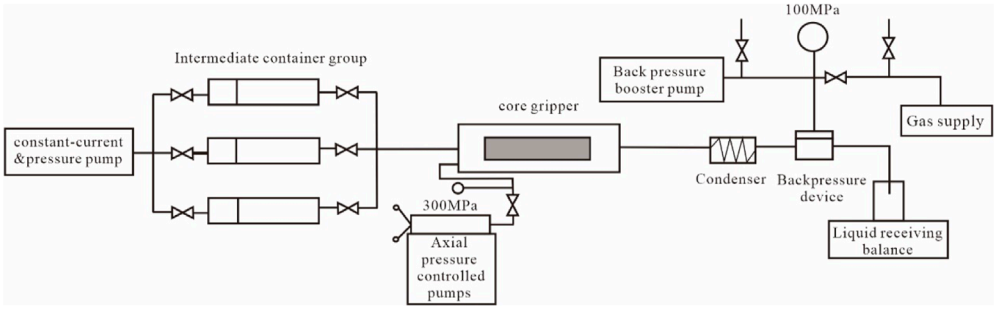

FIGURE 1
Schematic diagram of compaction physical simulation experiment device (modified from Zhou et al., 2011).

equipment, automatic control system and other components. During the experimental process, the configured experimental samples were put into the sample tubes in the reactor, and the warming and pressurisation experiments were carried out under the set temperature and static rock pressure. The overlying formation pressure is simulated by the axial pressure, the pore fluid pressure is regulated by the backpressure booster pump, the constant flow pressure is slowly increased by the constant flow pressure pump to fill the fluid and make it slowly flow through the samples, the strata temperature is simulated by the heater and the temperature control device on the core gripper of the reactor, and the compaction displacement is recorded by the high-precision precision displacement sensors on the two ends of the core gripper (Figure 1).

3 Design of experiments

3.1 Experimental samples and experimental parameters

The samples used in this experiment were modern sediments taken from the surface layers of the sedimentary areas of Golden Beach and Silver Beach in Qingdao, Liansan Island, and Lingshan Island. The compaction physics simulation experiments were carried out by means of artificial natural sampling, and the composition of the experimental samples was referred to the actual clastic group distribution ratio of the deep Permian sandstone and conglomerate reservoir cores in Fukang Sag. The rock type of the reservoir is dominated by clastic sand (conglomerate), and the distribution of quartz content in the grains ranges from 2% to 12%, with an average of 7.5%; the distribution of feldspar content ranges from 3% to 17%, with an average of 8.4%; the distribution of clastic content ranges from 67% to 93%, with an average of 84.1%. In view of this, the seashore glutenite of Qingdao, which is close to the source of this area, was selected as the physical simulation source sample for the experiment, taking 10% quartz particles content, 10% feldspar particles content and 80% rock debris particles content. The source samples were sieved into different particle size groups by sieve analysis and rounded into sub-angular and sub-rounded samples. Accordingly, artificial samples under the corresponding experimental conditions were prepared for physical modelling.

The Junggar Basin is a typical low-temperature cold basin in the west (Cao et al., 2022), and the Fukang Sag is located in the southeastern part of the central depression of the Junggar Basin, the Upper Urho Formation develops a thick layer-scale glutenite reservoir, with the depth of burial ranging from 4,500 to 6,000 m. According to the actual geological situation of the basin, the strata density of 2.5 g/cm^3, the ground temperature gradient of 2.4 °C/hm. The present formation water of Upper Urho Formation in Fukang Sag is $CaCl_2$ type. The density of strata water of 1.01 g/cm^3, and the pressure coefficient under the normal compaction condition are set to be 1.0. Combining the above parameters and setting the temperature and pressure conditions of each depth, the simulated maximum burial depth of the study area is set to be 7,000 m (Table 1).

3.2 Experimental control group

The rock structure of glutenite reservoir of the Upper Urho Formation in the Fukang Sag is complex, with low maturity of composition and structure, and the fraction of clastic particles is dominated by plastic clasts, with an average content of more than 80%, and the average content of quartz, feldspar and other rigid particles is less than 10%, with a wide range of particle size, poor sorting as a whole, and the gravel particles are filled with both sand-scale particles and muddy matrix. Based on the actual geological analysis of the study area, there is little variation in the mineralogical components of the rock, and there is a difference between sand and mud in the support structure and fill material characteristic of the glutenite. Therefore, three sets of variables, grain size, sand content and mud matrix content, were selected and introduced into the compaction physics simulation experiment to investigate the effect of each single factor on the preservation of intergranular porosity in glutenite reservoirs. The experiment was divided into a total of 11 control groups, of which 4 were grain size controls, four were sand content controls, and three were mud matrix tcontent controls, and were analysed and

TABLE 1 Experimental design depth and temperature, pressure parameters.

Depth/m	Static rock pressure/MPa	Skeleton pressure/MPa	Fluid pressure/MPa	Strata temperature/°C
0	0	0	0	25.0
500	12.25	7.30	4.95	37.0
1,000	24.50	14.60	9.90	49.0
1,500	36.75	21.90	14.85	61.0
2000	49.00	29.20	19.80	73.0
2,500	61.25	36.51	24.75	85.0
3,000	73.50	43.81	29.69	97.0
3,500	85.75	51.11	34.64	109.0
4,000	98.00	58.41	39.59	121.0
4,500	110.25	65.71	44.54	133.0
5,000	122.50	73.01	49.49	145.0
5,500	134.75	80.31	54.44	157.0
6,000	147.00	87.61	59.39	169.0
6,500	159.25	94.91	64.34	181.0
7,000	171.50	102.21	69.29	193.0

TABLE 2 Experimental control group design.

Control group	Number	Grain size/mm	Substrate type	Filler content/%
Grain size	1	0.25~0.5	/	0
	2	0.5~1.0	/	0
	3	2.0~3.0	/	0
	4	3.0~4.0	/	0
Sand content	5	0.5~3.0	Fine sand	20
	6	0.5~3.0	Fine sand	30
	7	0.5~3.0	Fine sand	40
	8	0.5~3.0	Fine sand	50
Mud matrix content	9	2.0~3.0	Mud matrix	5
	10	2.0~3.0	Mud matrix	10
	11	2.0~3.0	Mud matrix	15

compared within the groups (Table 2). After the physical simulation experiments, the compacted samples were removed after natural cooling to room temperature and pressure unloading to atmospheric pressure (Figure 2) for subsequent cast thin section preparation and microscopic observation.

4 Experimental data recording and processing

During the experiment, the computer monitors and records the changes in temperature, pressure, fluid flow rate, compaction

FIGURE 2
Sample effect diagram before and after compaction physical simulation experiment **(A)** Compacted samples with 10% sand content; **(B)** Compacted samples with 20% sand content; **(C)** Compacted samples with 30% sand content.

displacement and other relevant experimental conditions and parameters. When the corresponding depth point reached and the pressure was confirmed to be stable, the data were collected to gather and analyse the results at different depths. The calculation method of porosity during the simulation experiment is as follows (Formulas 1–4) (Cao et al., 2011):

$$S_0 = \pi \cdot r^2 \tag{1}$$

$$V_0 = L_0 \cdot S_0 \tag{2}$$

$$V_\phi = \mathrm{V}_0 - \mathrm{V}_\mathrm{g} \tag{3}$$

$$\phi_0 = V_\phi / V_0 \cdot 100\% \tag{4}$$

where r is the radius of the sample cross-section, cm; L_0 is the length of the sample, cm; S_0 is the cross-sectional area of the sample, cm^2; V_0 is the original volume of the sample, cm^3; V_ϕ is the original volume of the pore, cm^3; V_g is the volume of the skeleton of the sample, cm^3; ϕ_0 is the original porosity.

After measuring its original volume, the samples were dried and then the skeleton volume was measured by the drainage method to find the original porosity ϕ_0.

From the recorded compaction displacements, the volume of the rock sample at each depth point during compaction can be derived (Formula 5):

$$V = S_0 \cdot (L_0 - L_1) \tag{5}$$

where L_1 is the experimentally recorded compaction displacement, cm; V is the volume of the rock sample at each point during compaction, cm^3.

During the experiment, it is assumed that the volume of the skeleton remains essentially constant. Then there is (Formula 6):

$$V_0 - V_\phi = V - V \cdot \phi \tag{6}$$

where ϕ is the porosity at each depth point during compaction.

5 Analysis of experimental results

(1) Preservation of intergranular pores by different grain sizes

By preparing and observing cast thin sections of the compacted samples, it is possible to qualitatively describe the degree of compaction hole reduction and the mode of compaction deformation during the simulated experiments. It is worth noting that, in the cast thin sections obtained from the compaction experiments, the particles were found to be loose under microscopic observation, partly due to the outward expansion of the samples after the release of the compaction, and partly due to the lack of systematic diagenesis in the physical simulation experiments, but the microscopic observation can still obtain more effective information on the contact relationship between the particles, the arrangement characteristics, and the fracture information of the compression under force. It was found that the sandstone particles with smaller grain size were adjusted by sliding, rotation, displacement and other positional adjustments, and the particles were rearranged, presenting certain directional arrangement characteristics, and the rupture degree of the particles was smaller. For gravel particles with larger grain size, positional adjustment occurs, the arrangement tends to stabilise, the particles tend to contact the long axis more closely, and the particle skeleton reaches the compressive limit of the rupture phenomenon is more obvious (Figure 3).

The results of physical simulation experiments on mechanical compaction of samples with different grain sizes show that the porosity evolution has a segmented characteristic (Figure 4). In the early stage of mechanical compaction, with the increase of pressure, the debris particles slide, misalign and rotate, rearranging and adjusting their positions so as to reach the state of compact accumulation, i.e., the rapid compaction stage; after this stage, the debris particles reach a stable stacking state, and with the increase of pressure, the degree of compact stacking increases and the porosity decreases slowly, this is the slow compaction stage. Meanwhile, it was found that with the gradual increase of the sample grain size, the stage of rapid change gradually became shorter, and it was analysed that the gravel scale formed the support structure faster than the sand scale particles, and the adjustment of particles in the later stage was smaller, the reservoir was more resistant to pressure. In addition, based on the results of physical simulation experiments, the relationship between porosity and depth of the four groups of samples was obtained by fitting curves, and the results showed

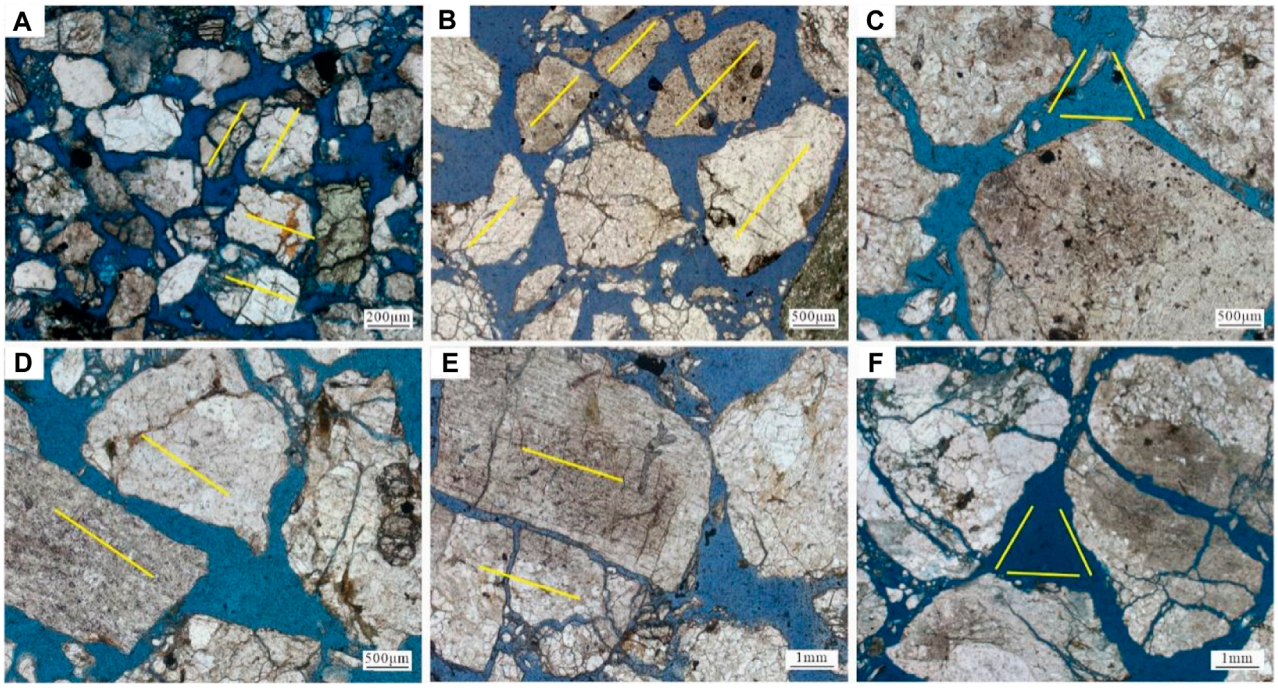

FIGURE 3
Compaction characteristics of samples with different grain size **(A)** Sample with grain size 0.25–0.5 mm, partially orientated arrangement of particles (–); **(B)** Sample with grain size 0.5–1.0 mm, obvious orientated arrangement of particles (–); **(C)** Sample with grain size 2.0–3.0 mm, particles supported, low degree of rupture (–); **(D)** Sample with grain size 2.0–3.0 mm, particles orientated arrangement (–); **(E)** Sample with grain size 3.0–4.0 mm, particles orientated and tightly arranged (–); **(F)** Sample with grain size 3.0–4.0 mm, particles supported, visible rupture (–).

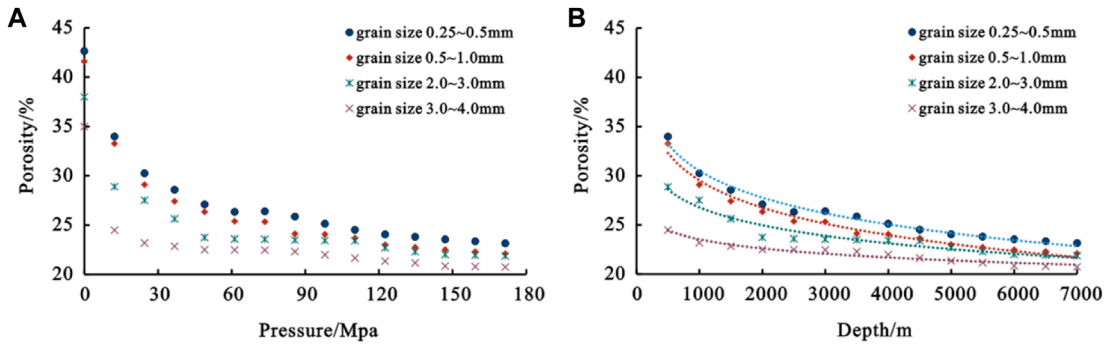

FIGURE 4
Physical simulation experiment results of mechanical compaction of samples with different grain size **(A)** Porosity-pressure correlation; **(B)** Porosity-depth correlation.

that porosity and depth were basically in a logarithmic relationship (Table 3).

Through the quantitative analysis of the test data, in the rapid compaction stage, the rate of pore reduction was 11.8%/km for samples with grain sizes of 0.25–0.5 mm, 11.5%/km for samples with grain sizes of 0.5–1.0 mm, 10.5%/km for samples with grain sizes of 2.0–3.0 mm, 11.2%/km for samples with grain sizes of 3.0–4.0 mm, it shows that the rate of pore reduction is larger for samples with smaller grain size in this stage. During the slow compaction stage, the rate of pore reduction was 1.16%/km for samples with grain sizes of 0.25–0.5 mm, 1.17%/km for samples with grain sizes of 0.5–1.0 mm, 0.94%/km for samples with grain sizes of 2.0–3.0 mm, and 0.68%/km for samples with grain sizes of 3.0–4.0 mm (Figure 5). Therefore, the preservation of pore space by grain size is mainly in the slow-change compaction stage. It was analysed that, with the increase of burial depth and overlying pressure, the finer-grained samples have less force per unit area, and their overlying pressure is mainly used to squeeze the pore space, while the coarser-grained samples have more force per unit area, and the support structure formed earlier carries part of the pressure and reduces part of the

10.3389/feart.2024.1433517

TABLE 3 The fitting results of porosity and depth of samples with different particle sizes.

Number	Grain size/mm	Fitting curve	Correlation coefficient R^2
1	0.25~0.5	y = −3.93ln(x) + 57.678	0.985
2	0.5~1.0	y = −4.01ln(x) + 57.211	0.983
3	2.0~3.0	y = −2.63ln(x) + 44.947	0.942
4	3.0~4.0	y = −1.33ln(x) + 32.75	0.943

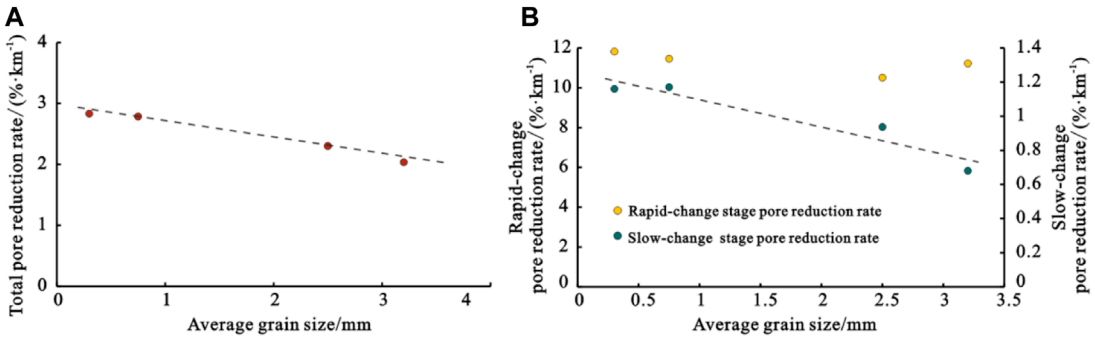

FIGURE 5
Mechanical compaction pore reduction characteristics of samples with different grain size.

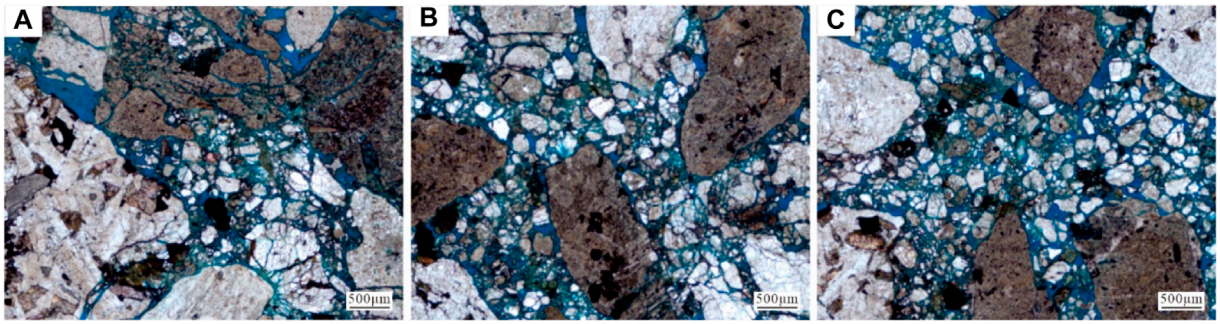

FIGURE 6
Compaction characteristics of samples with different sand content **(A)** Samples with 20% sand content (–); **(B)** Samples with 30% sand content (–); **(C)** Samples with 50% sand content (–).

force to squeeze the pore space. Therefore, the coarser grain size samples have better pore preservation ability.

(2) Preservation of intergranular pores by different sand contents

Microscopic observation revealed that with the increase of sand content, the sand-scale particles gradually occupied the intergranular pore space, and the gravel-scale particles gradually transitioned from point contact to floating, while the long-axis contact of the particles gradually weakened (Figure 6). By analysing the pore evolution of the compaction simulation with different sand contents, the porosity evolution with depth was also segmented (Figure 7), and the results of the fitted curves yielded a logarithmic relationship between porosity and depth for samples with different sand contents (Table 4).

During the fast compaction stage, the samples show similar trends in porosity evolution and insignificant differences in pore reduction. After entering the slow compaction stage, with the increase of overburden pressure, the evolution process of the samples began to show a non-monotonic pattern, i.e., the pore reduction rate showed a tendency of decreasing and then increasing with the increase of sand-scale particle content. Further quantitative analysis of the test data showed that in the fast compaction stage, the rate of pore reduction was 8.15%/km for samples of 20% sand content, 8.44%/km for samples of 30% sand content, 7.94%/km for

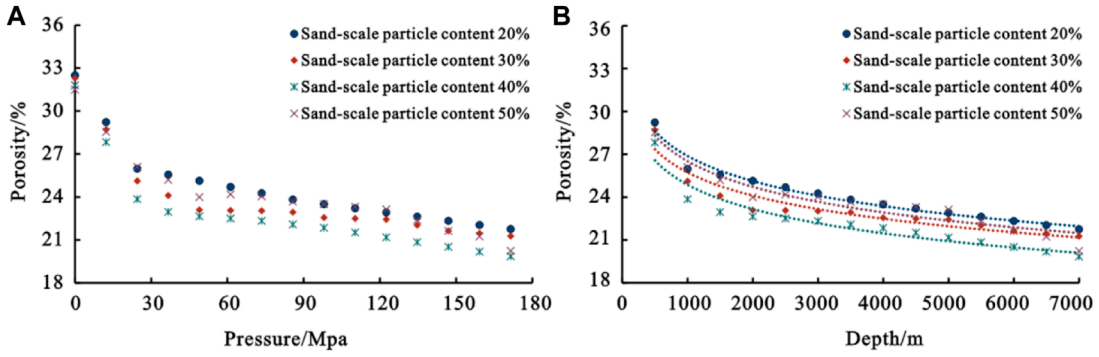

FIGURE 7
Physical simulation experiment results of mechanical compaction of samples with different sand content. **(A)** Porosity-pressure correlation; **(B)** Porosity-depth correlation.

TABLE 4 The fitting results of porosity and depth of samples with different sand content.

Number	Sand-scale particle content (%)	Fitting curve	Correlation coefficient R^2
5	20	y = −2.53ln(x) + 44.322	0.972
6	30	y = −2.58ln(x) + 44.365	0.922
7	40	y = −2.35ln(x) + 41.873	0.905
8	50	y = −2.45ln(x) + 41.824	0.917

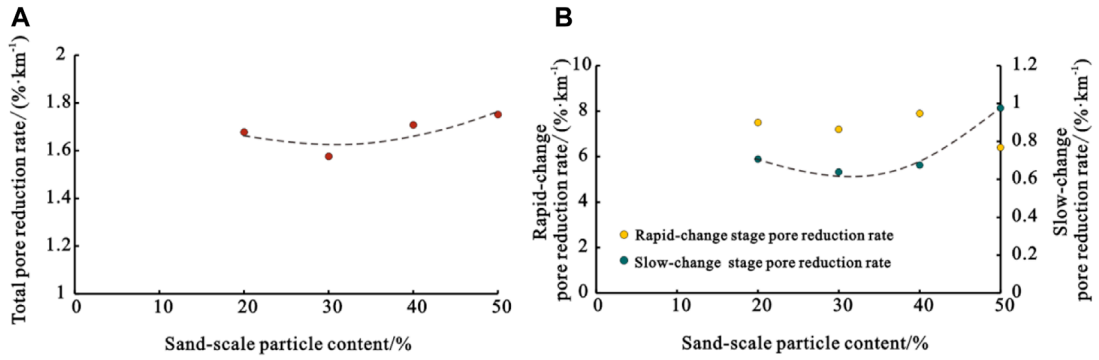

FIGURE 8
Mechanical compaction pore reduction characteristics of samples with different sand content **(A)** Characteristics of total pore reduction rate for samples with different sand content; **(B)** Characteristics of different stages of pore reduction rate for samples with different sand content.

samples of 40% sand content, and 6.75%/km for samples of 50% sand content. During the slow compaction stage, the rate of pore reduction was 0.68%/km for samples of 20% sand content, 0.55%/km for samples of 30% sand content, 0.67%/km for 40% samples of sand content, and 0.97%/km for samples of 50% sand content, which shows that the pore preservation effect of the samples with different sand contents is mainly reflected in this stage (Figure 8).

It was analysed that in the rapid compaction stage, when the position of particles of different grain sizes was adjusted and rearranged, the finer particles were forced to squeeze and fill in the pore space formed by the arrangement of coarse particles, resulting in a rapid loss of porosity. However, after entering the slow compaction stage, the particles have a stable stacking state, and compaction further increases the tightness of the particles and the degree of compaction. At this time, the content of sand particles is not enough to completely fill the pore between gravel particles, the pressure increase will be further extrusion caused by the loss of the pore, and when the sand particle content exceeds the limit of filling the pore between gravel particles, the gravel particles show incomplete contact, which makes it difficult to form a stable mechanical structure between the gravel particles, and the pressure increase will be turned to extrusion of sand particles caused by the

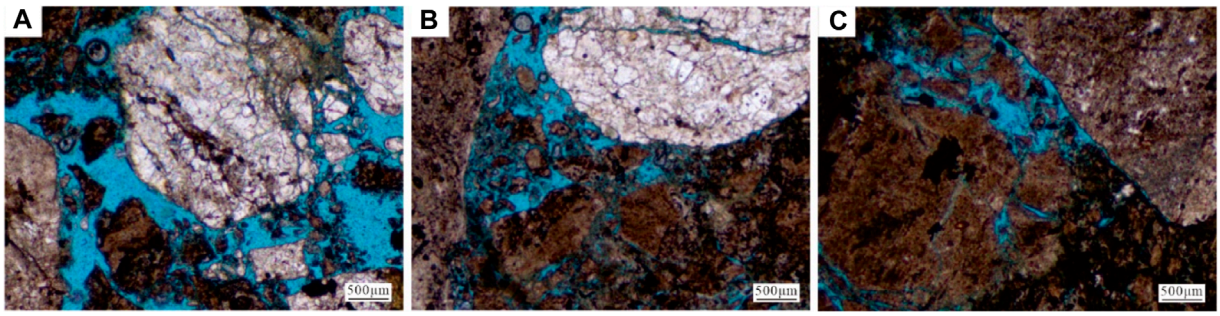

FIGURE 9
Characteristics of samples with different mud content **(A)** Samples with 5% mud content (–); **(B)** Samples with 10% mud content (–); **(C)** Samples with 15% mud content (–).

TABLE 5 The fitting results of porosity and depth of samples with different mud matrix content.

Number	Mud matrix content (%)	Fitting curve	Correlation coefficient R^2
9	5	y = −2.23ln(x) + 45.53	0.977
10	10	y = −2.47ln(x) + 45.433	0.965
11	15	y = −2.34ln(x) + 41.573	0.906

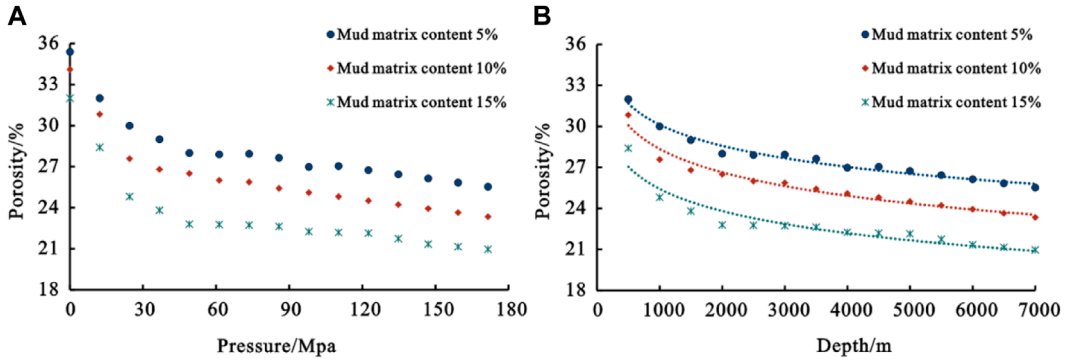

FIGURE 10
Physical simulation experiment results of mechanical compaction of samples with different mud matrix content. **(A)** Porosity-pressure correlation; **(B)** Porosity-depth correlation.

loss of the pore. Therefore, only when the sand-scale particles can just fill the pore between gravel-scale particles, the external gravel bridges the pressure, and the internal sand particles take over the pressure, which makes the best preservation of the intergranular pore space. It was found by the experiment that when the sand particles can just fill the pore space between gravels, the content of sand particles is about 30%.

(3) Preservation of intergranular pores by different mud matrix contents

Through microscopic observation, it was found that the particles of the sample with matrix content of 5% were mainly in point contact, with only a small amount of line contact. With the gradual increase of compaction effect, the particles tend to be tight contact with each other, and a small number of micro-cracks begin to appear on the surface of the particles. For loose gravel particles with 10% matrix, the intergranular space was filled with matrix, and the intergranular pore was further reduced. Loose gravel grade particles with 15% matrix radicals, the contact degree of the particles is increasing, the position between the particles is adjusted, and the matrix radicals are squeezed and filled into the remaining intergranular pore, which makes the pore decrease significantly and the intergranular pore reduce (Figure 9).

By analysing the pore evolution of the compaction simulation for different mud contents, the porosity evolution with depth is also segmented, and the results of the fitted curves yielded a

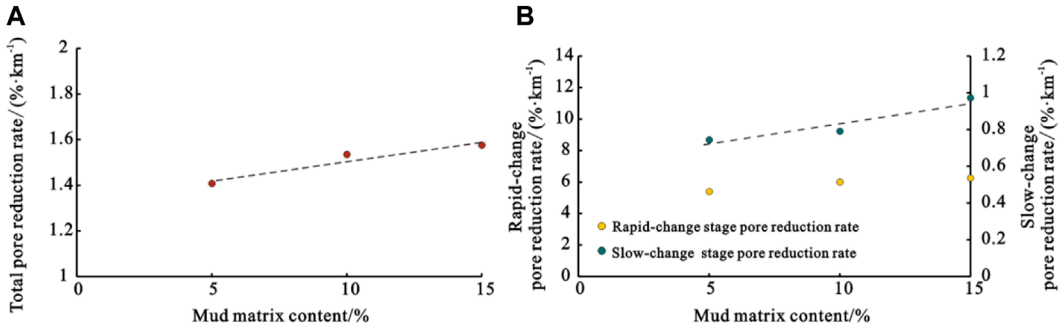

FIGURE 11
Mechanical compaction pore reduction characteristics of samples with different mud contents **(A)** Characteristics of total pore reduction rate of samples with different mud contents; **(B)** Characteristics of different stages of pore reduction rate of samples with different mud contents.

logarithmic relationship between porosity and depth for the samples with different clay contents (Table 5). In addition, it was found that the rate of pore reduction gradually increases with the increase of matrix content (Figure 10).

In the fast compaction stage, the rate of pore reduction was 5.4%/km for samples with 5% mud content, 6.0%/km for samples with 10% mud content, and 6.3%/km for samples with 15% mud content. In the slow compaction stage, the rate of pore reduction was 0.74%/km for samples with 5% mud content, 0.79%/km for samples with 10% mud content, 0.97%/km for samples with 15% mud content (Figure 11).

It is analysed that at the early stage of compaction, different contents of mud matrix were forced to squeeze into the intergranular pore, resulting in a reduction of porosity, and with the increase of overburden pressure, the samples with higher matrix content had greater intergranular matrix filling degree, resulting in a greater reduction of porosity. It shows that high matrix content will occupy intergranular pore, especially for gravel close to the source and easy to receive a large number of source area deposits, usually the storage space is not developed, and the preservation of intergranular pore is poor.

6 Conclusion

(1) In the process of mechanical compaction of glutenite, the change of porosity with depth is segmented, i.e., the fast-change phase in the early stage of compaction and the slow-change phase in the later stage. The depth of the boundary between the fast-change and slow-change phases is about 1,000 m.
(2) Regression fitting using the slow-change phase data revealed a good logarithmic relationship between depth and porosity during diagenesis compaction, with correlation coefficients of 0.90 or higher for the data fitting results of the 11 sets of experiments.
(3) In the case of only experiencing mechanical compaction, the coarser the grain size of the sample particles, the smaller the rate of compaction pore reduction during compaction, the more pores are eventually preserved, and the preservation of pores by the grain size is mainly reflected in the stage of slow-change compaction.
(4) When the sand particles fill the pore space between gravels, the stable secondary support structure formed by gravel-scale and sand-scale can effectively take over the pressure, and when the content of sand particles is about 30%, the pressure-bearing capacity is the strongest. The preservation effect of sand particles on pore is mainly reflected in the slow-change compaction stage.
(5) Samples with high mud matrix content have low initial porosity and greater intergranular matrix filling, and samples with high mud matrix content have a greater rate of pore reduction throughout all stages of the compaction process, so high matrix content is not conducive to the preservation of intergranular pores.

Data availability statement

The original contributions presented in the study are included in the article/Supplementary material, further inquiries can be directed to the corresponding author.

Author contributions

HG: Writing–review and editing. DW: Writing–original draft. XS: Writing–review and editing. BP: Writing–review and editing. ZZ: Writing–review and editing. JW: Writing–review and editing. KL: Writing–review and editing.

Funding

The author(s) declare that financial support was received for the research, authorship, and/or publication of this article. PetroChina

Key Research Program on Deep Petroleum System in the Tarim Basin (No. ZD 2019-183-001-003).

Conflict of interest

The authors declare that the research was conducted in the absence of any commercial or financial relationships that could be construed as a potential conflict of interest.

Publisher's note

References

Bjørlykke, K. (2014). Relationships between depositional environments, burial history and rock properties. Some principal aspects of diagenetic process in sedimentary basins. *Sediment. Geol.* 301, 1–14. doi:10.1016/j.sedgeo.2013.12.002

Cao, Y. C., Xi, K. L., Wang, J., Yuan, G. H., and Yang, T. (2011). Preliminary study on diagenetic simulation experiment of mechanical compaction and physical property evolution of sandstone. *Geoscience* 25, 1152–1158. (in Chinese). doi:10.3969/j.issn.1000-8527.2011.06.014

Cao, Y. C., Yuan, G. H., Yang, H. J., Wang, Y. Z., Liu, K. Y., Zan, N. M., et al. (2022). Current situation of oil and gas exploration and research progress of the origin of high-quality reservoirs in deep-ultra-deep clastic reservoirs of petroliferous basins. *Acta Petrol. Sin.* 43, 112–140. (in Chinese). doi:10.7623/syxb202201010

Carvalho, A. D. S. G., and Ros, L. F. D. (2015). Diagenesis of aptian sandstones and conglomerates of the campos basin. *J. Petrol. Sci. Eng.* 125, 189–200. doi:10.1016/j.petrol.2014.11.019

Chuhan, F. A., Kjeldstad, A., Bjørlykke, K., and Høeg, K. (2002). Porosity loss in sand by grain crushing—experimental evidence and relevance to reservoir quality. *Mar. Petrol. Geol.* 19, 39–53. doi:10.1016/S0264-8172(01)00049-6

Chuhan, F. A., Kjeldstad, A., Bjørlykke, K., and Høeg, K. (2003). Experimental compression of loose sands: relevance to porosity reduction during burial in sedimentary basins. *Can. Geotech. J.* 40, 995–1011. doi:10.1139/t03-050

De Cola, F., Pellegrino, A., Glößner, C., Penumadu, D., and Petrinic, N. (2018). Effect of particle morphology, compaction, and confinement on the high strain rate behavior of sand. *Exp. Mech.* 58, 223–242. doi:10.1007/s11340-017-0331-x

Gao, Z. Y., Cui, J. G., Fan, X. R., Feng, J. R., and Shi, Y. X. (2023). The mechanism of abnormal fluid pressure on the physical properties of deep reservoirs: a case study of the Jurassic Toutunhe Formation in the southern margin of Junggar Basin. *Petrol. explor. Dev.* 50, 1221–1232. (in Chinese). doi:10.11698/PED.20230030

He, H. Q., Zhi, D. M., Tang, Y., Liu, C. W., Chen, H., Guo, X. G., et al. (2021). A great discovery of well kangtan 1 in the Fukang Sag in the Junggar Basin and its significance. *China Petrol. Explor* 26, 1–11. (in Chinese). doi:10.3969/j.issn.1672-7703.2021.02.001

Hou, G. F., Ji, Y. L., Wu, H., Li, L. L., Wang, Y. S., and Wang, W. (2017). Quantitative characterization on the influence factors of porosity and permeability characteristics of clastic reservoirs by physical experiment simulation. *Geol. Sci. Technol. Inf.* 36, 153–159. (in Chinese). doi:10.19509/j.cnki.dzkq.2017.0419

Ji, Y. L., Wu, H., Wang, Y. S., Zhou, Y., Wang, W., Hou, G. F., et al. (2017). Applying physical simulation to study the physical property evolution in clastic reservoirs: a case from the paleogene shahejie Formation in the shengli oil zone, bohai bay basin. *Geol. J. China Univ.* 23, 657–669. (in Chinese). doi:10.16108/j.issn1006-7493.2017042

Kang, X., Hu, W., Cao, J., Wu, H., Xiang, B., and Wang, J. (2019). Controls on reservoir quality in fan-deltaic conglomerates: insight from the lower triassic baikouquan formation, Junggar Basin, China. *Mar. Petrol. Geol.* 103, 55–75. doi:10.1016/j.marpetgeo.2019.02.004

Li, M. Q., Zhang, L. Q., Li, Z. H., Zhang, L., Mao, L. X., and Xu, X. T. (2021). Diagenetic facies division and logging identification of tight sandstone in the lower conglomerate member of Lower Jurassic Ahe Formation in Tarim Basin: case study of Yiqikelike area in Kuqa Depression. *Nat. Gas. Geosci.* 32, 1559–1570. (in Chinese). doi:10.11764/j.issn.1672-1926.2021.03.001

Li, Y., Xue, Z. J., Cheng, Z., Jiang, H. J., and Wang, R. Y. (2020). Progress and development directions of deep oil and gas exploration and development in China. *China Petrol. Explor* 25, 45–57. (in Chinese). doi:10.3969/j.issn.1672-7703.2020.01.005

Liu, B., Yang, Y., Li, J., Chi, Y., Li, J., and Fu, X. (2020). Stress sensitivity of tight reservoirs and its effect on oil saturation: a case study of Lower Cretaceous tight clastic reservoirs in the Hailar Basin, Northeast China. *J. Petrol. Sci. Eng.* 184, 106484. doi:10.1016/j.petrol.2019.106484

Liu, G. Y., Liu, Y., and Zhang, L. P. (2006). Experimental study on the effects of compaction on the properties of sandstone reservoir. *J. Xi'an Shiyou Univ. Nat. Sci.* 21, 24–28. (in Chinese). doi:10.3969/j.issn.1673-064X.2006.04.006

Mahmic, O., Dypvik, H., and Hammer, E. (2018). Diagenetic influence on reservoir quality evolution, examples from Triassic conglomerates/arenites in the Edvard Grieg field, Norwegian North Sea. *Mar. Petrol. Geol.* 93, 247–271. doi:10.1016/j.marpetgeo.2018.03.006

Pang, X., Jia, C., Zhang, K., Li, M., Wang, Y., Peng, J., et al. (2020b). The dead line for oil and gas and implication for fossil resource prediction. *Earth Syst. Sci. Data* 12, 577–590. doi:10.5194/essd-12-577-2020

Pang, X. J., Niu, C. M., Du, X. F., Wang, Q. B., and Dai, L. M. (2020a). Quantitative characterization of sandstone reservoir difference between member 1 and member 2 of shahejie Formation in northeastern margin of shijiutuo uplift, bohai sea. *Acta Petrol. Sin.* 41, 1073–1088. (in Chinese). doi:10.7623/syxb202009004

Sun, L. D., Zou, C. N., Zhu, R. K., Zhang, Y. H., Zhang, S. C., Zhang, B. M., et al. (2013). Formation, distribution and potential of deep hydrocarbon resources in China. *Petrol. explor. Dev.* 40, 687–695. (in Chinese). doi:10.1016/s1876-3804(13)60093-2

Taylor, T. R., Giles, M. R., Hathon, L. A., Diggs, T. N., Braunsdorf, N. R., Birbiglia, G. V., et al. (2010). Sandstone diagenesis and reservoir quality prediction: models, myths, and reality. *AAPG Bull.* 94, 1093–1132. doi:10.1306/04211009123

Wang, B. (2020). *Study on formation mechanism and seismic prediction method of deep sandy conglomerate dessert reservoir in Mahu area, Junggar Basin. [dissertation]*. Chengdu: Chengdu University of Technology. (in Chinese).

Wei, W., Zhu, X., Tan, M., Xue, M., Guo, D., Su, H., et al. (2015). Diagenetic and porosity evolution of conglomerate sandstones in bayingebi formation of the lower cretaceous, chagan Sag, China-Mongolia frontier area. *Mar. Petrol. Geol.* 66, 998–1012. doi:10.1016/j.marpetgeo.2015.08.011

Xie, Y. H., Zhang, G. C., Shen, P., Liu, L. F., and Huang, S. B. (2018). Formation conditions and exploration direction of large gas field in Bozhong Sag, Bohai Bay Basin. *Acta Petrol. Sin.* 39, 1199–1210. (in Chinese). doi:10.7623/syxb201811001

You, L., Qu, X. Y., Zhong, J., Li, C., Wu, S. J., Gao, Y., et al. (2019). Physical simulation experiments on pore evolution in high-temperature and overpressure reservoirs. *Nat. Gas. Ind.* 39, 21–30. (in Chinese). doi:10.3787/j.issn.1000-0976.2019.07.003

Yuan, G., Cao, Y., Qiu, L., and Chen, Z. (2017). Genetic mechanism of high-quality reservoirs in Permian tight fan delta conglomerates at the northwestern margin of the Junggar Basin, northwestern China. *AAPG Bull.* 101, 1995–2019. doi:10.1306/02071715214

Yue, Z. Q. (2019). *Diagenetic characteristics of sand conglomerate in Mahu Depression, Junggar Basin and its influence on reservoir*. Xi'an: Northwest University. [master's thesis] (in Chinese).

Zhuo, X. Z., Zhang, L. Y., Chen, X. S., Zhang, J. J., Yang, J. L., and Li, Y. C. (2015). Influence of the argillaceous matrix on pore evolution model of the deep reservoir in well kun-2, qaidam basin. *Geol. Rev.* 61, 1447–1457. (in Chinese). doi:10.16509/j.georeview.2015.06.021

frontiers | Frontiers in Earth Science

TYPE Original Research
PUBLISHED 17 July 2024
DOI 10.3389/feart.2024.1416594

OPEN ACCESS

EDITED BY
Jianguo Zhang,
China University of Geosciences, China

REVIEWED BY
Mabrouk Sami,
United Arab Emirates University, United Arab Emirates
Qinghai Xu,
Yangtze University, China

*CORRESPONDENCE
Xiaohong Liu,
liuxiaohong_swpu@163.com

RECEIVED 12 April 2024
ACCEPTED 18 June 2024
PUBLISHED 17 July 2024

CITATION
Lin T, Wang W, Ma Q, Kang J, Yang R and Liu X (2024), Formation mechanism and implication of analcime in the sandstone reservoirs of the Permian Jingjingzigou formation in the Jinan sag, southern Junggar basin, NW China. *Front. Earth Sci.* 12:1416594. doi: 10.3389/feart.2024.1416594

Formation mechanism and implication of analcime in the sandstone reservoirs of the Permian Jingjingzigou formation in the Jinan sag, southern Junggar basin, NW China

Tong Lin[1], Weiwei Wang[2,3], Qiang Ma[4], Jilun Kang[4], Runze Yang[1] and Xiaohong Liu[2]*

[1]Research Institute of Petroleum Exploration and Development, PetroChina, Beijing, China, [2]School of Geoscience and Technology, Southwest Petroleum University, Chengdu, China, [3]Sinopec Henan Oil-field Company, Nanyang, China, [4]Research Institute of Exploration and Development, Tuha Oilfield Company, PetroChina, Hami, China

Analcime plays a significant role in sandstone reservoirs as an authigenic diagenetic mineral in the Junggar Basin (northwestern China). However, the origin and controls on the reservoirs have received remarkably little attention. This study investigates the formation mechanism of analcime in the Middle Permian strata in the Jinan sag (southern Junggar Basin) through petrography and geochemistry. The results show that analcime is formed through early alkaline hydrolysis of volcanic materials under specific temperature and pressure conditions. The reservoir rocks primarily consist of various lithic sandstones, including volcanic debris such as basalt, andesite, and tuff. Analcime is characterized as rich in aluminium and poor in sodium, classified as low-silica analcime with a low Si-Al ratio (1.98–2.38). Furthermore, various other diagenetic minerals, such as glauconite, chlorite, albite, and calcite have been identified. The primary reservoir space chiefly consists of intragranular dissolved pores of analcime, while secondary pores are formed by intragranular pores of feldspar and lithic, along with some remaining intergranular pores. Cementation of analcime during early diagenesis changes primary pore structures and reduces reservoir properties. The low-silica analcime dissolves due to acidic pore fluids associated with three stages of oil and gas charging, transforming into albite and creating numerous secondary pores, thereby enhancing reservoir quality.

KEYWORDS

Northwestern China, Junggar basin, Permian, sandstone reservoir, analcime, secondary pore, diagenetic evolution

1 Introduction

Zeolite Minerals significantly impact on oil and gas reservoirs (Iijima, 2001). During the diagenetic evolution process, diagenesis involving the precipitation, dissolution, and transformation of authigenic zeolite minerals, directly affects the pore evolution

of sandstone reservoirs, therefore influencing reservoir performance (Sun et al., 2014; Zhu et al., 2020). Analcime as a common type of zeolite minerals, pervasively occurs in oil and gas bearing basins such as central Australia (English, 2001), northwestern Argentina (Campo et al., 2007), Canada (Gall and Hyde, 2010), Turkey (Varol, 2020), western and eastern China (Lin et al., 2017; Fang et al., 2020).

Despite the causes and formation environments of analcime have been studied, but the results are controversial. Renaut (1993) summarized four formation mechanisms of authigenic analcime in sandstone: 1) alteration of volcanic glass and zeolite precursors; 2) formation from a gel; 3) direct precipitation of interstitial pore fluid or lake water; and 4) reactions of saline, alkali pore water with detrital silicates (e.g., clay and plagioclase). Sheppard and Hay (2001) and Langella et al. (2001) systematically discussed the occurrence, formation conditions and genetic characteristics of authigenic analcime, suggest water chemistry, temperature and pressure composed influenced the formation. Guo et al. (2022) proposed that the lower the concentration ratio of hydrogen ions to alkali metal ions in the formation water, the more conducive it is to the formation of zeolite minerals. In addition, the pH value of the pore water may control the types of zeolites formed: neutral to moderate pH values are conducive to the formation of zeolite with a high Si/Al ratio, while aluminium-rich zeolite (e.g., analcime) is more likely to be formed at a high pH value (Jin and Boles, 1993; Neuhoff, 2002). The larger the silica-to-alumina ratio of zeolite minerals, the stronger the acid resistance; otherwise, the acid resistance is low and zeolite minerals are easily dissolved by it.

Partly scholars suggested that the precipitation and filling of zeolite minerals have a destructive effect on the original pore structure in the early stage, leading to a reduction in primary pores and a decrease in reservoir performance (Taylor and Surdam, 1981; Noh and Boles, 1993; Utada, 2001). However, the presence of analcime cement can also enhance the strength of the reservoir structure, improve its resistance to compaction, and inhibit compaction-induced reduction in porosity. Additionally, the analcime cement can indirectly provide a material basis for later acidic fluids (e.g., organic acids) to cause dissolution (Schmidt and McDonald, 1979; Dutton and Loucks, 2010; Fu et al., 2010; Yuan et al., 2015). Weibel et al. (2019) indicated that thermogenic degradation of early zeolite cementation can create deep-buried sandstone reservoirs with abnormally high porosity and permeability levels. In the middle diagenetic stage, the analcime cement formed in the early stage can undergo widespread dissolution, resulting in the formation of secondary pores, enhanced porosity and permeability, and ultimately improved reservoir quality (Zhu et al., 2011; Meng et al., 2013; Sun et al., 2014).

Terrigenous clastic rock reservoirs are the primary oil and gas reservoirs in western China (Jia, et al., 2016; Zheng, et al., 2019). For instance, in the Junggar Basin (northwest China), clastic reservoirs hold almost all proven oil reserves and over half of the natural gas reserves. High-quality secondary reservoirs of clastic rocks, characterized by intergranular dissolution pores, are closely linked to the cementation of authigenic zeolite minerals (Zhu et al., 2011; Wang et al., 2022; Gao et al., 2023). Various researchers have investigated the formation mechanism of zeolite-based high-quality secondary reservoirs in China's oil- and gas-bearing basins and discussed the reservoir distribution (Zhang, 1985; Han et al., 2007; Li et al., 2014; Sun et al., 2014; Li et al., 2019; Yuan et al., 2020; Zhu et al., 2020; Li et al., 2022). Zhu et al. (2020) provided a review of the occurrence, composition, and origin of analcime sourced from Permian to Paleogene sedimentary rocks in nonmarine petroleum basins in China. The review indicates that the formation of natural analcime is influenced by factors such as the of parent material composition, temperature during crystallization, chemical properties of fluid, and thermodynamic characteristics of the geological environment. Particularly, the Junggar Basin has developed high-quality secondary reservoirs related to analcime cementation facies (Zhu et al., 2020). Diagenetic analcime, found in forms like pyroclastic sandstone and conglomerate intergranular cement, is the most common type of analcime. Analcime is speculated to form during the burial stage of diagenesis through the alteration of minerals such as volcanic glass, clay, or zeolite precursors. It often occurs together with other authigenic zeolites, carbonates, clay minerals and albite, and plays a significant role in controlling the reservoirs quality (Tang et al., 1997a; Tang et al., 1997b; Zhu et al., 2011).

It was identified through exploration in the new Permian Jingjingzigou Formation in the Jinan Sag (NW China, Junggar Basin). The Jinan Sag, along with high-yield oil and gas, presents a total exploration potential of 100 million tons (Liang et al., 2021). Preliminary research shows that analcime is the most common zeolite mineral in the Permian Jingjingzigou Formation, with paragenetic minerals including chlorite, carbonate, and albite. However, the zeolite-related diagenesis and its impacts on reservoir development have not been thoroughly studied. This study utilizes various methods such as cast thin sections, scanning electron microscopy (SEM), whole rock-clay mineral X-ray diffraction, electron probe, and fluid inclusion analyses to examine the development characteristics and related diagenesis of analcime in the Permian Jingjingzigou Formation reservoirs in the Jinan Sag. The primary objectives of this study are to determine the origins of analcime and to assess the impact on reservoirs.

2 Geological setting

The Junggar Basin is one of the main oil and gas-bearing basins in Northwest China. It is an extremely superimposed basin formed by the superposition and composite of several prototype basins with different properties, and it has a complicated evolutionary history. Multiple sets of primary rock-reservoir-caprock assemblages have developed in the basin with very rich hydrocarbon resources. Since the Permian period, the Junggar Block has been in the development and reformation stages of intraplate basins, and it has experienced a complex evolutionary history featuring the early differentiation of uplifts and depressions, the formation of unified basins, and the superposition of later foreland basins (Zhang and Zhang, 2006).

Located in the southern margin of the Junggar Basin, the Jinan Sag is a recently discovered Permian fault depression with an NW-SE direction half-graben structure, similar to the Jimsar Sag. The Jinan Sag is a small sedimentary sag recently discovered in the footwall of the Fukang fault zone's eastern segment in the Junggar Basin's south margin. The Jinan Sag adjoins the Guxi uplift to the east and the Santai uplift to the west; it is bounded to the north by the Jinan uplift, it faces the Jimsar Sag and it is adjacent to the hanging wall of the eastern segment of the Fukang fault zone to the south. The

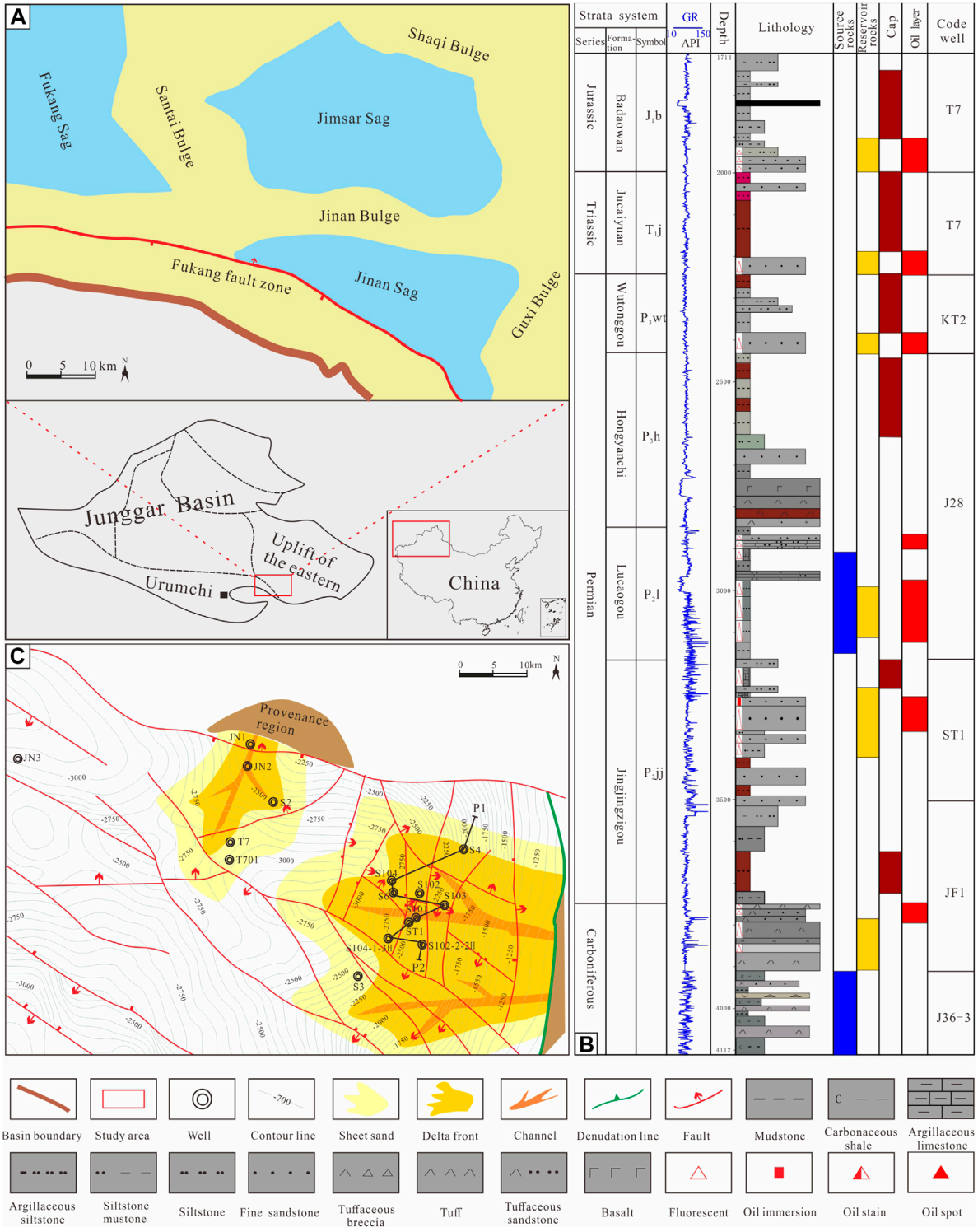

FIGURE 1
Structure location **(A)**, stratigraphic column **(B)** and sandstone distribution **(C)** of the Permian Jingjingzigou Formation in the Jinan Sag.

Jinan Sag has experienced the superposition and transformation of multiphase tectonic movements, such as the Hercynian, Indosinian, Yanshanian, and Himalaya; faults have developed in the sag with obvious thickness in the east and thinness in the west (Wu et al., 2013; Liang et al., 2021) (Figure 1A).

The middle and upper Permian wells in the Jinan Sag have developed from the bottom upwards, including the Jingjingzigou Formation (P_2jj), the Lucaogou Formation (P_2l), the Hongyanchi Formation (P_2h), and the Wutonggou Formation (P_3wt) (Figure 1B). The Jingjingzigou Formation is the primary clastic rock reservoir

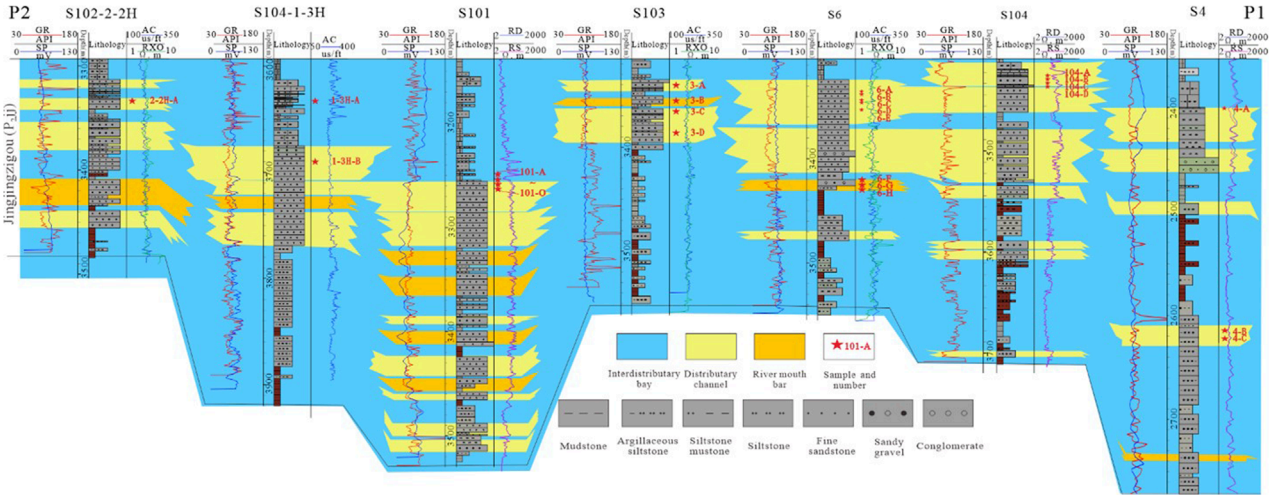

FIGURE 2
Profile of sedimentary facies of the Permian Jingjingzigou Formation in the Jinan Sag. (Line P1-P2 is shown in Figure 1B).

in the Jinan Sag, while the Lucaogou Formation serves as a shale reservoir and is in a conformity contact with the overlying Lucaogou Formation. The upper member features thick sandstone and a high sandstone-stratum ratio, whereas the lower member consists mainly of interbedded red mudstone and grey fine-siltstone. The Lucaogou Formation is characterized by a predominance of continuous thick grey-black mud shale, serving as high-quality hydrocarbon source rocks and effective regional caprocks. The geological setting of Jinan Sag is influenced by the provenance area of the Guxi uplift, resulting in the development of an east-west delta plain facies–delta front facies–shallow lacustrine sedimentary system (Figure 1C). In general, the Jingjingzigou Formation of the Permian is a widely distributed far-source new bed-generating and old bed-storing accumulation lithological reservoir, featuring a favorable source rock–reservoir–caprock configuration (Li et al., 2023). The sandstones are main deposited in delta environment, and the distributary channel and river mouth bar are favorable sedimentary facies for the development of sand bodies (Figure 2).

3 Samples and methods

Based on core observations and descriptions, thin sections (30 samples) were cast from seven drilled wells (S101, S102-2-2H, S103, S104, S104-1-3H, S4 and S6) for observation and quantitative statistics. For mored detailed descript the petrography and highlight difference of reservoirs which bearing analcime, we preferred choose samples of high porosity sandstones, and consider the siltstones with high porosity and relative dense sandstones.The experimental instrument used was an Olympus BX53M reflected polarizing microscope. The thin sections were cast with blue epoxy resin to identify rock pores, stained with alizarin red + potassium ferricyanide mixture to differentiate authigenic carbonate minerals qualitatively, and the thin section porosity, pore size, and pore distribution were measured (12 samples) using Tiger 3000P polarizing image processing software. The fluid-inclusion measurement (10 samples) of Goldstein and Reynolds (1994) was employed for experimentation at Southwest Petroleum University, which involved the use of a Linkam THMSG600 system. Scanning electron microscopy observations (5 samples) were conducted on pore development in the reservoirs and the paragenetic assemblage of authigenic minerals, while electron probe analysis (5 samples) was completed with 60 points on authigenic minerals, such as clays, zeolites, and carbonates in reservoir pores. Both scanning electron microscopy and electron probe analyses were carried out at the State Key Laboratory of Oil and Gas Reservoir Geology and Exploitation, Southwest Petroleum University. For scanning electron microscopy, the specimens were made into block samples and sprayed with gold on their surfaces, while for electron probe analysis, the specimens were ground into polished thin sections and sprayed with carbon on their surfaces. The experimental instruments included an FEI Quanta 650 FEG field emission scanning electron microscope (configured with Qemscan software for minerals recognition) and JXA-8230 electron probe analyzer. The electron probe created spectra after testing the contents of nine common elements in carbonate minerals. The accuracy of spectrum analysis exceeded 1% (major element content >5%) and 5% (minor element content 1%–5%); it could automatically identify elements above 0.1 wt%, and the detection limit was 0.01 wt%. The State Key Laboratory of Oil and Gas Reservoir Geology and Development Engineering conducted an analysis of 20 samples using X-ray diffraction on both whole-rock and clay minerals. The analysis was performed with an X'Pert PRO analyzer, where the detection criterion was set to a maximum current of 60 mA and a pressure of 60 kV. The temperature range was maintained at 23–30°C, while the humidity level was kept above 70% to ensure accurate results.

4 Results

4.1 Reservoir characteristics

Observations and statistics of the cast thin sections show that the reservoir rocks in the study area are mainly lithic sandstone,

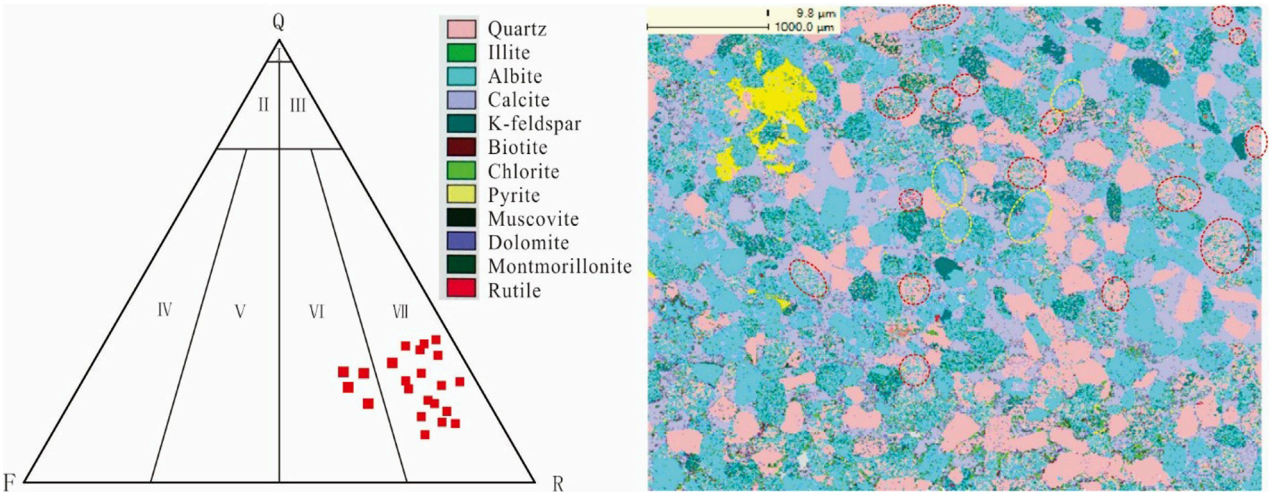

FIGURE 3
Ternary diagram of rock classification (Left) and distribution of the mineral components (Right) of the Jingjingzigou Formation. I- quartz sandstone; II- feldspar-quartz sandstone; III- lithic quartz sandstone; IV- feldspar sandstone; V- lithic feldspar sandstone; VI- feldspar lithic sandstone; and VII- lithic sandstone cement. Q-quartz, F-feldspar, R-rock fragments. Detrital compositions are mainly composed of quartz, feldspar and debris. A large amount of calcite cement was found at Well S104, 3440.16 m.

with a small amount of feldspar lithic sandstone in some wells (Figure 3 left). The general content of debris is between 55% and 70%, and the types include extrusive rock debris, such as basalt, andesite, and tuff, a small amount of sedimentary rock debris, such as siltstone and mudstone, and metamorphic rocks, such as quartzite and phyllite. The plastic debris is significantly transformed into pseudo matrix. The quartz is mainly monocrystalline quartz, with a small amount of polycrystalline quartz, and the secondary enlargement of quartz does not occur. The plagioclase is mainly intermediate acid plagioclase with developed polysynthetic twin, and the potassium feldspar is mainly orthoclase and striated feldspar, with the surface generally kaolinized. The results of whole-rock X-ray diffraction analysis show that the quartz content in the rocks is between 23.8% and 33.3% (Table 1), which is consistent with the detrital quartz content obtained from microscopic thin section statistics, indicating that quartz mainly occurs in the form of detrital quartz and is rarely seen in debris. The potassium feldspar content in the rocks is between 2.7% and 4.8%, and the plagioclase content reaches 46.3%–64.5%. The Qemscan images and statistical results show that, in addition to the single-crystal quartz in the rocks, a small amount of fine-grained quartz is observed in the chert and siltstone debris (red circle in Figure 3 right). The plagioclase is mainly composed of albite feldspar with a relatively small content of potassium feldspar; the phenomena of calcite replacing the potassium feldspar in the striped feldspar and retaining albite stripes can be found (yellow circle in Figure 3 right). The particle size analysis shows that the mean value of the debris particle size is between 0.1 mm and 0.6 mm; the median particle size is 0.18–0.27 mm, and the average particle size is 0.16–0.24 mm. The sorting index (σ_1) is 1.61–1.89, indicating that the sample is fine-medium sandstone with poor sorting. The roundness of particle size is mainly subangular, which is generally supported by grains, with the main line contact between grains and local point contact (Figures 3, 4).

4.2 Mineral characteristics of analcime

Based on the observations of cast thin sections, scanning electron microscopy, electron probe, and X-ray diffraction analyses, authigenic mineral analcime is commonly present in the reservoirs of the Jingjingzigou Formation. In particular, analcime is known to fill intergranular pores with varying degrees of dissolution (Figures 4A–F; Figures 5A–G). Within these pores, analcime may either dissolve, creating a harbor-like structure, while coexisting with albite, or exhibit a complete/hollow equiaxed granular form, occasionally wrapped by calcite minerals. The particle size of analcime ranges from 20 μm to 60 μm, with a maximum size of 100 μm, and a content exceeding 15% (Figures 4A–F; Figures 4A–G). Quantitative electron probe analysis indicates that analcime has an average SiO_2 content of 58.16% (above the standard value of 54.58%), Al_2O_3 concentrations ranging mainly between 23.46% and 24.30% (slightly above the standard value of 23.16%), and an average Na_2O content of 11.12% (considerably below the standard of 13.5%) (Table 2). The calculated average Si/Al ratio of analcime in the study area is 2.14, with values ranging from 1.98 to 2.38, indicating it is a low-silica analcime (Table 2).

4.3 Minerals paragenetic with analcime

In the study area, the reservoirs within the Jingjingzigou Formation commonly contain paragenetic minerals such as analcime, along with clay minerals, albite, calcite, and other minerals. Dissolution processes vary across different areas, leading to transformations where analcime can convert to albite or be replaced by calcite or other minerals (Figures 4A–F; Figures 5A–G). Therefore, analyzing these paragenetic minerals can elucidate the mineral paragenetic sequence, providing a basis for investigating the genetic mechanism of analcime.

TABLE 1 Mineral composition of the Permian Jingjingzigou Formation in the Jinan Sag (%).

Sample ID	Depth (m)	Wells	Clay mineral (%)	Felsic minerals (%)			Carbonate minerals (%)	Zeolite minerals (%)	Clay mineral (%)			Smectite (%)
			Total	Q	K-F	P	Cal	Anl	Sme	Ill	C/S	C/S
101-B	3254.73	S101	4	31	4	45	5	9	4	3	93	38
101-D	3255.52	S101	4	35	4	45	4	7	4	2	94	34
101-F	3256.44	S101	2	40	4	37	9	7	3	4	93	41
101-G	3257.66	S101	3	32	4	43	10	8	4	2	94	38
101-H	3258.30	S101	5	38	0	45	4	8	7	2	91	38
101-I	3259.67	S101	4	41	4	40	2	9	3	5	92	49
101-K	3261.06	S101	4	34	4	48	3	7	3	2	95	45
101-M	3262.17	S101	2	33	4	40	13	8	4	4	92	41
101-O	3263.12	S101	4	35	4	39	11	7	2	5	93	38

Abbreviation: Q, quartz; K-f, K-feldspar; P, plagioclase; Cal, Calcite; Anl, Analcime; Sme, Smectite; Ill, Illite; C/S, Mixed layer Chlorite/Smectite.

Firstly, authigenic albite has been developed in the study area, mainly appearing as lath-shaped crystals filling intergranular pores under the microscope, showing a negative low protrusion. The highest interference colour is off-white in the first order (Figures 4A,B,G–I). When observed under the scanning electron microscope, albite is primarily seen in plate-shaped forms occupying intergranular or analcime dissolution pores, displaying a good euhedral degree (Figure 5). Electron probe analysis reveals that albite mainly consists of Ab, ranging from 98.98% to 99.61%, with only trace amounts of potassium feldspar (Or) and anorthite (An) components present.

In addition, chlorite is mainly distributed along the margins of the pores (encapsulated debris grains) in the form of a film-like pore liner cement with varying degrees of development (Figures 4A,F). In the intergranular dissolution pores of some well sections, the chlorite film is obviously separated from the clastic grains and exists as pore fillings (Figures 4G, 5B,F), indicating that it undergoes a certain degree of corrosion after formation. X-ray diffraction results of clay minerals show that the total amount of clay minerals is between 5.2% and 6.4%, with chlorite accounting for 55.4%–60%, and the mixed chlorite/smectite layer (C/S%) accounting for 37.5%–42.6%. The ratio of smectite (S%) in the chlorite/smectite mixed layer (C/S %) is 40% (Table 1).

Besides, calcite is relatively abundant in some intervals. Based on the staining of the cast thin sections, calcite can be categorized into three types: calcite, ferroan calcite, and ferrocalcite. Calcite appears mainly as microcrystalline grains filling the analcime dissolution pores or as continuous crystals. The mixed solution turns red when intergranular pores are filled; ferroan calcite and ferrocalcite mainly fill the intergranular pores and partial corrosion pores in the shape of continuous crystals, with the mixed solutions stained purple and blue, respectively (Figures 4D–H). It is imperative to acknowledge that the time of calcite formation and the subsequent dissolution during the later phases of diagenesis play a vital role in their influence on the reservoir. According to the quantitative analysis results of the electron probe, it is evident that calcite can be classified into three distinct stages. During these stages, there is a noticeable and consistent increase in the MnO content. In contrast, the FeO content is lowest during the first stage, while the SrO content is highest in the third stage (Figures 6A,B). It can be inferred that calcite undergoes partial dissolution during the first two stages, indicating an earlier formation time. Furthermore, ferrocalcite, the most recent cement, exhibits less dissolution (Figures 5D–H).

Based on the occurrence and paragenetic mineral characteristics of analcime minerals, four paragenetic evolution sequences related to analcime diagenetic minerals can be summarized as follows: ① chlorite → analcime → ferroan calcite (minor quantity). This sequence is mainly observed in Well S101 and Well S4. ② chlorite → analcime → calcite → ferroan calcite → ferrocalcite. This sequence is predominantly found in Wells S101, S104, and S104-1–3H. ③ chlorite → analcime → albite → ferroan calcite (minor quantity). This sequence is mainly identified in Well S101. ④ chlorite → albite → (sphene) → calcite (minor quantity). This sequence is primarily noted in Wells S6 and S102-2-2H. In the above sequences, when the chlorite film has a low development level and the clastic grains are not completely wrapped, small amounts of secondary authigenic quartz enlargement and authigenic feldspar can form on the edges of quartz and feldspar grains (Figures 4G,Q).

4.4 Fluid inclusions

Fluid inclusion analysis is mostly used as an effective tool to investigate the formation condition of analcimes. 10

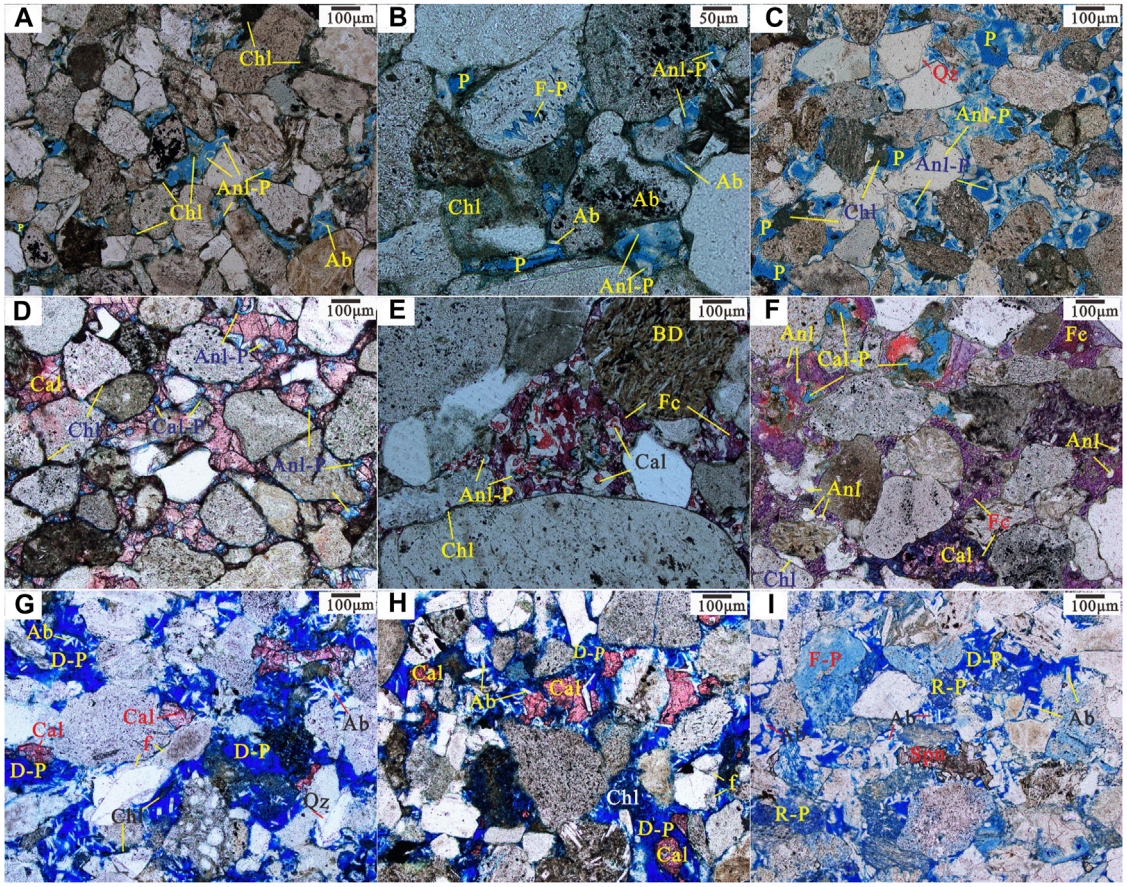

FIGURE 4
Microscopic images of petrography and reservoir space. **(A)** Lithic sandstone, chlorite encapsulated clastic grains, partially filled intergranular pores, developed intergranular analcime dissolution pores, occasional authigenic albite feldspar in the dissolution pores, and additional observed residual intergranular pores (Well S101, 3255.07 m, single polarized light). **(B)** Lithic sandstone, chlorite encapsulated clastic grains, partially filled intergranular pores, developed intergranular analcime dissolution pores, authigenic albite feldspar in the dissolution pores, and a small amount of residual intergranular pores (Well S101, 3262.52 m, single polarized light). **(C)** Feldspar lithic sandstone, weak chlorite film development, locally enriched chlorite, a large amount of filled intergranular analcime, developed analcime dissolution pores, and a small amount of residual intergranular pores (Well S4, 2399.59 m, single polarized light). **(D)** Detritus sandstone, chlorite film-calcite sequentially filled intergranular pores, complete chlorite film, developed analcime dissolution pores, calcite-filled intergranular pores in continuous crystals, and local weak corrosion (Well S104-1-3H, 3478.20 m, single polarized light). **(E)** Detritus sandstone, typical basalt debris, chlorite film developed on grain edge, intergranular pores filled with analcime, dissolution pores partially filled by calcite (red) and residual intergranular pores filled with ferrocalcite (purple-red) (Well S101, 3043.58 m, single polarized light). **(F)** Lithic sandstone, sequentially filled intergranular pores with chlorite-calcite (red)-ferroan calcite (purple-red)-ferrocalcite (blue-purple), intact analcime crystal form, and partially corroded calcite forming secondary dissolution pores (Well S104, 3440.16 m, single polarized light). **(G)** Lithic sandstone, strong dissolution, chlorite film detached from the clastic grains and locally enriched, intergranular pores filled with authigenic albite and partially calcite, calcite-encapsulated albite feldspar, and local phenomenon of authigenic feldspar (Well S102-2-2H, 3334.30 m, single polarized light). **(H)** Lithic sandstone, intensive corrosion, locally enriched chlorite, intergranular pores filled with authigenic albite and partially calcite, calcite-encapsulated albite, and local authigenic feldspar (Well S6, 3343.15 m, single polarized light). **(I)** Feldspar lithic sandstone, strong corrosion, various developed corrosion pores, undeveloped chlorite, and intergranular pores filled with authigenic albite and partially wrapped in authigenic sphene (Well S6, 3421.50 m, single polarized light). Cal: calcite; Fc: ferrocalcite; Chl: chlorite; Ab: albite; (F): feldspar; Spn: sphene; Anl: analcime; Anl-P: analcime dissolution pores; Cal-P: calcite dissolution pores; FP: feldspar dissolution pores; RP: debris dissolution pores; D-P: intergranular dissolution pores; and P: residual intergranular pores; BD: basalt debris; Qz: quartz.

fluid-inclusion analyses of the analcimes in Well S101 are measured (Table 3; Figures 7A,B). The fluid inclusions from analcimes have homogenization temperatures ranging from 78.5°C to 85.1°C, with a comparatively low average of 81.9°C (Figure 7C). The ice melting temperatures ranging from −1.3 to −0.8°C, with an average of −1.1°C. The salinities of the primary fluid inclusions with an average of approximately 1.82 wt% (Figure 7D).

5 Discussion

5.1 Origin of analcime and paragenetic minerals

The types of fragments in the Jingjingzigou sandstones in the Jinan Sag varied. The fragment components were mainly intermediate–basic volcanic rocks. Moreover, there were

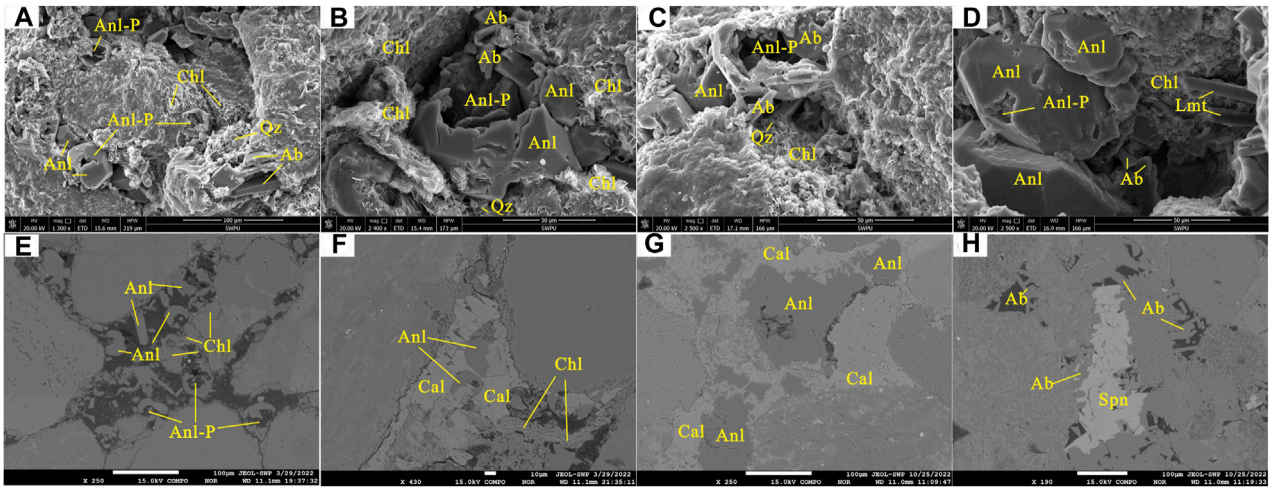

FIGURE 5
Characteristics of analcime and paragenetic minerals under Scanning electron microscopy (SEM) **(A–D)** and Backscattered electron (BSE) **(E–H)**. **(A)** Chlorite encapsulates clastic grains and fills the pores in a plate-like morphology. Equiaxed granular analcime occupies the intergranular pores and undergoes a certain degree of dissolution. Plate-like albite is observed filling the intergranular pores. Authigenic quartz particles are situated between chlorite crystals (Well S101, 3255.07 m, SEM). **(B)** The chlorite film is partially detached from the clastic particles. Analcime is locally dissolved. Dissolution pores are filled with plate-like albite. Authigenic quartz particles are sporadically detected between the chlorite crystals (Well S101, 3255.07 m, SEM). **(C)** Chlorite encases clastic grains. Analcime is evidently dissolved and appears hollow. Plate-like albite is present in the dissolved pores. Authigenic quartz particles are intermittently found between the chlorite crystals (Well S101, 3262.52 m, SEM). **(D)** The chlorite crystal structure is poorly developed. The intergranular analcime is subject to localized dissolution. The intergranular dissolution pores are filled with albite, as exhibited in laumontite (Well S101, 3262.52 m, SEM). **(E)** Significant corrosion of chlorite film and analcime is observed. Intergranular pores are evident (Well S101, 3043.58 m, backscattered electron (BSE)). **(F)** The chlorite is corroded and detached from the detrital grains. The analcime dissolves into a harbor shape and is enveloped by calcite (Well S101, 3261.40 m, BSE). **(G)** Analcime corrosion is not readily apparent. The intergranular pores are filled with encapsulated calcite (Well S6, 3421.50 m, BSE). **(H)** The intergranular dissolution pores are filled with authigenic albite and partially enclosed by authigenic sphene (Well S104-1-3H, 3692.00 m, BSE). Cal: calcite; Chl: chlorite; Ab: albite; Spn: sphene; Anl: analcime; Lmt: laumontite; Qz-quartz; and Anl-p: dissolution pores of analcime.

sedimentary tuff layers with smectite contents greater than 90% in some well intervals (Figure 8A). Between these layers, a large amount of analcime mineral was replaced by calcite, and euhedral dolomite grew coaxially along the bioclasts (Figure 8B). The analcime content in the sandstone above this layer could reach 15%, suggesting that the formation of zeolite minerals was closely related to the genesis of volcanic materials. Based on the mineral assemblage paragenetic associated with analcime, the diagenetic environment of the Jingjingzigou Formation rocks should be a freshwater–brackish water environment (Ji, 2016). The glauconite clastic mineral was commonly found in the sandstone reservoir and appeared emerald green under the microscope (Figure 8C). Glauconite of nonmarine origin is generally considered to be formed under weakly alkaline conditions, with a pH value of 7–8, and its formation is closely related to biological and biochemical processes. Based on the previous understanding of the sedimentary environment of the area, a comprehensive analysis revealed that the glauconite in the Jingjingzigou Formation could be the product of the gradual salinization of the lacustrine, weakly alkaline water medium and the weakening of hydrodynamic conditions during the epidiagenetic stage (Xing et al., 1982; Li et al., 1996).

Moreover, the results of fluid inclusions indicate that analcime were formed in relatively low temperature and brackish water environments (Figure 7D). In terms of results chemical composition, the analcime was slightly rich in aluminium and poor in sodium. The Si/Al ratios fell within the typical range for analcime of lacustrine origin (Si/Al ratio between 1.95 and 2.80). This indicates that the analcime was formed through the interaction of moderate volcanic substances and alkaline water, with the containing low level of SiO_2 activity (Han et al., 2007; Karakaya et al., 2013; Zhu et al., 2020).

Based on the 1) analcime mainly filling the intergranular pores, 2) resulting in a significant weakening of the sandstone compaction (Figure 4C), and 3) the relatively low temperature and salinity of fluid inclusions, it can be concluded that analcime is a product of the early diagenetic stage. During this stage, the volcanic substances present in large amounts in the rocks were hydrolysed by the formation water, releasing large amounts of sodium, aluminium, and silicon ions. This process increased the pH and salinity of the solution, leading to the formation of analcime under appropriate temperature and pressure conditions. Additionally, the precipitation of calcium ions facilitated the subsequent precipitation of calcite (Zhu et al., 2011). In addition to analcime, there were euhedral columnar minerals that were entirely replaced by calcite. Some intervals showed a symbiosis relationship between analcime and intact crystals filling the intergranular pores (Figure 8B). It is possible that a zeolite mineral formed without the influence of obvious acidic fluids during diagenetic evolution and was completely replaced by calcite. Under the scanning electron microscope, laumontite was observed to be paragenetic with analcime, though it was not completely replaced in certain intervals (Figure 5D).

TABLE 2 Electron microprobe analysis of analcime, albite and sphene (unit: wt%).

Sample ID	Wells	Depth (m)	Elemental composition (wt%)											Si/Al	Mineral
			Na_2O	MgO	K_2O	CaO	TiO_2	SiO_2	Al_2O_3	FeO	MnO	Cr_2O_3	Total		
101-A	S101	3043.58	13.110	0.028	0.000	0.376	0.000	56.049	24.005	0.001	0.010	0.003	93.582	1.98	Analcime
101-A	S101	3043.58	11.470	0.000	0.010	0.292	0.000	58.278	23.790	0.034	0.001	0.000	93.875	2.08	Analcime
101-A	S101	3043.58	11.276	0.004	0.018	0.212	0.017	57.916	23.496	0.050	0.000	0.010	92.999	2.09	Analcime
101-A	S101	3043.58	10.580	0.000	0.015	0.207	0.034	59.413	23.276	0.008	0.009	0.008	93.550	2.17	Analcime
101-L	S101	3261.40	12.481	0.000	0.031	0.012	0.000	56.371	23.106	0.073	0.000	0.000	92.074	2.07	Analcime
101-L	S101	3261.40	10.679	0.000	0.023	0.023	0.029	58.142	24.296	0.114	0.018	0.012	93.336	2.03	Analcime
101-L	S101	3261.40	11.185	0.000	0.026	0.005	0.000	56.831	23.359	0.144	0.014	0.000	91.564	2.06	Analcime
101-L	S101	3261.40	10.463	0.001	0.030	0.000	0.000	58.763	22.842	0.077	0.008	0.000	92.184	2.18	Analcime
101-L	S101	3261.40	10.623	0.012	0.000	0.034	0.014	58.533	23.248	0.155	0.002	0.000	92.621	2.14	Analcime
101-L	S101	3261.40	9.759	0.019	0.026	0.003	0.000	59.390	23.152	0.123	0.010	0.000	92.482	2.18	Analcime
101-L	S101	3261.40	9.582	0.013	0.004	0.031	0.000	59.086	23.511	0.118	0.010	0.000	92.355	2.13	Analcime
1-3H-A	S104-1–3H	3692.00	11.659	0.000	0.044	0.076	0.011	58.382	21.826	0.039	0.000	0.019	92.056	2.27	Analcime
1-3H-A	S104-1–3H	3692.00	11.050	0.019	0.071	0.058	0.016	59.198	21.125	0.010	0.000	0.003	91.550	2.38	Analcime
1-3H-A	S104-1–3H	3692.00	11.750	0.008	0.067	0.048	0.013	57.884	21.698	0.020	0.011	0.006	91.505	2.26	Analcime
101-L	S101	3261.40	11.823	0.012	0.037	0.039	0.000	69.023	19.902	0.033	0.000	0.014	100.883	99.61	Albite
101-L	S101	3261.40	11.663	0.025	0.149	0.041	0.005	68.536	20.188	0.155	0.006	0.000	100.768	98.98	Albite
101-L	S101	3261.40	11.946	0.014	0.054	0.049	0.036	68.939	19.984	0.094	0.000	0.023	101.139	99.48	Albite
6-F	S6	3421.50	11.875	0.008	0.080	0.066	0.004	69.873	19.595	0.006	0.000	0.000	101.507	99.26	Albite
6-F	S6	3421.50	11.678	0.025	0.037	0.128	0.009	69.648	19.729	0.009	0.003	0.004	101.270	99.19	Albite
6-F	S6	3421.50	0.030	0.021	0.001	28.656	32.294	31.077	5.090	0.552	0.005	0.029	97.755	—	Sphene
6-F	S6	3421.50	0.058	0.019	0.011	28.835	31.418	31.024	5.292	0.540	0.000	0.000	97.197	—	Sphene

10.3389/feart.2024.1416594

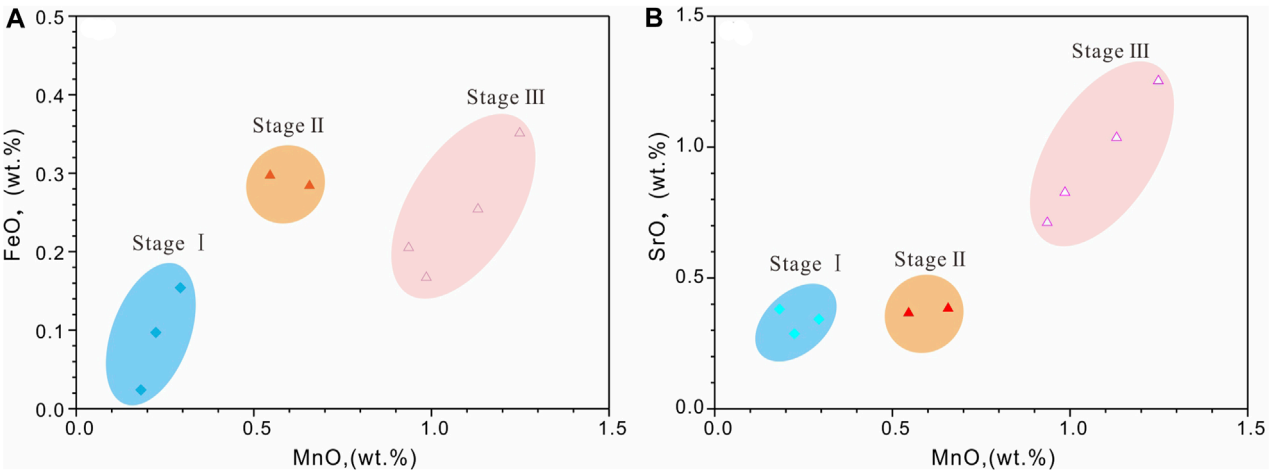

FIGURE 6
Relationship of between MnO-FeO content **(A)** and MnO-SrO content **(B)** the stage division of calcite.

TABLE 3 Analytical data: Fluid inclusion homogenization temperatures (Th), ice temperatures (Tm) and salinity of the Permian Jingjingzigou Formation.

Well name	Formation	Depth (m)	Sample ID	Lithology	FI type	Th aq (°C)	Tm aq (°C)	Sal (wt%)
S101	P_2jj	3043.58	S101FI-A	Anl	Pr	85.1	−0.8	1.40
S101	P_2jj	3255.07	S101FI-C	Anl	Pr	81.8	−1.3	2.24
S101	P_2jj	3261.40	S101FI-L	Anl	Pr	80.2	−1.2	2.07
S101	P_2jj	3261.40	S101FI-L	Anl	Pr	82.3	−1.2	2.07
S101	P_2jj	3261.40	S101FI-L	Anl	Pr	83.0	−1.0	1.74
S101	P_2jj	3261.40	S101FI-L	Anl	Pr	81.9	−1.1	1.91
S101	P_2jj	3261.40	S101FI-L	Anl	Pr	80.5	−1.3	2.07
S101	P_2jj	3261.40	S101FI-L	Anl	Pr	78.5	−1.0	1.74
S101	P_2jj	3262.52	S101FI-N	Anl	Pr	82.3	−0.9	1.57
S101	P_2jj	3262.52	S101FI-N	Anl	Pr	83.4	−0.8	1.40

Th aq, homogenization temperatures of aqueous inclusions; Tm aq, ice melting temperatures of the aqueous inclusions; Sal (wt%), salinity computed from NaCl-H_2O, system; Pr, primary; Anl, analcime.

During the diagenesis process, albite was mainly formed in the following manners (Yang et al., 2003; Zhu et al., 2011): 1) Albitization related to replacement. As the burial depth increased, the temperature and pressure also increased, leading to ion exchange between pore water and clastic substances. 2) Authigenic albite associated with the dissolution of feldspar grains. In the early stage of diagenesis, sodium ions released by the dissolution of feldspar clastic grains reached saturation levels, causing them to grow and adhere to the feldspar clastic grains, forming secondary enlarged edges. Later, as diagenesis intensified, the feldspar clastic grains further dissolved, resulting in the formation of albite. 3) During the alteration process of zeolite, under the influence of chemical factors in the formation water, the SiO_2 activity significantly increased, leading to the replacement of analcime by albite under specific conditions of temperature, pressure, and burial depth conditions (Fathy et al., 2023). In the reservoirs of the Jingjingzigou Formation in the study area, albite was produced as metasomatized plagioclase clastic grains, secondary enlargement edges, or analcime-filled dissolution pores, and authigenic albite was linked to feldspar particle dissolution. The albite filling the intergranular pores in Well S101 and other wells was paragenetic with analcime, originating mainly from the diagenetic transformation of analcime. The albite in Well S6 and other wells, not paragenetic with analcime but authigenic sphene, could be influenced by various factors. Sphene is a diagenetic product of the middle and late diagenetic stages in a freshwater to brackish water environment (Ji, 2016), and its occurrence significantly predates the precipitation of ferrocalcite in this well, indicating an earlier diagenetic period product. Earlier studies revealed that SiO_2-rich hydrothermal fluid activity during the Late Jurassic–Early Cretaceous (middle Yanshanian)

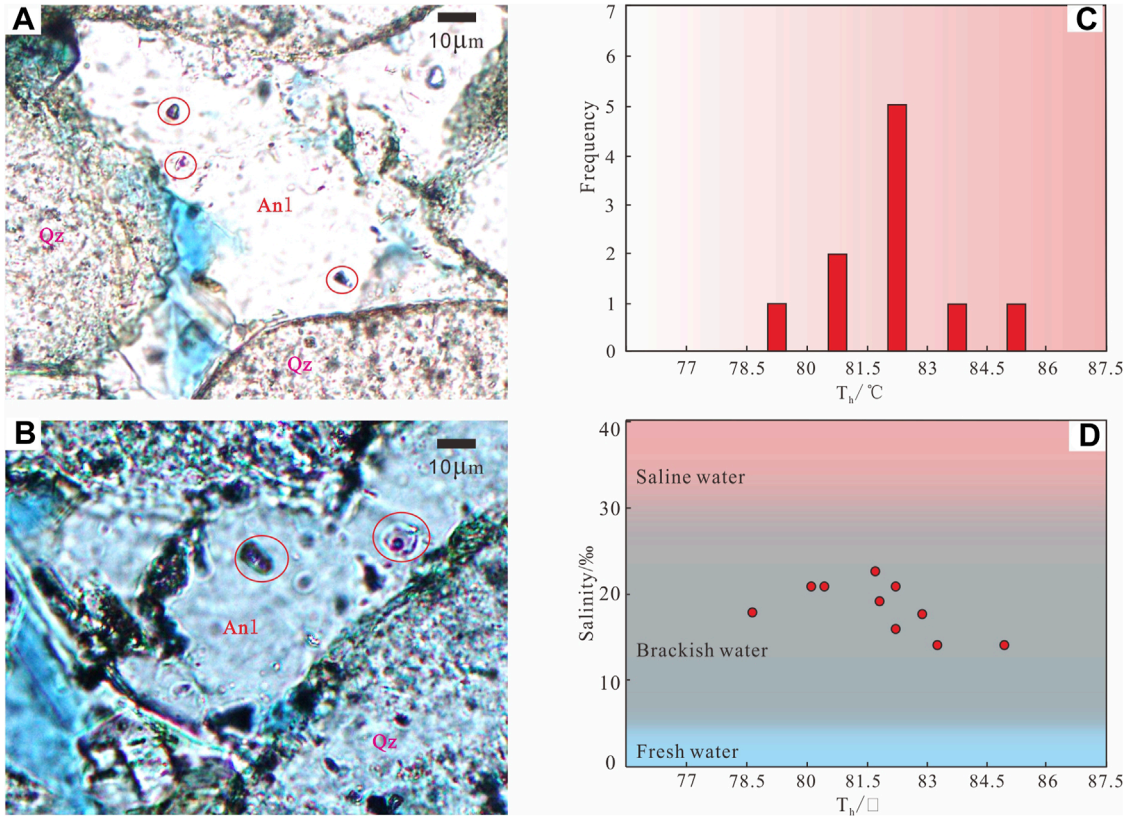

FIGURE 7
Characteristics of fluid inclusion in analcime of the Permian Jingjingzigou Formation in the Jinan Sag. **(A)** and **(B)** are photographs of fluid-inclusion in analcime cement. **(C)** Histogram of fluid-inclusion homogenization temperature (Th). **(D)** Crossplots of fluid inclusion homogenization temperature against salinity for analcime cement. The red circle are typical fluid inclusions. Anl: analcime; Qz: quartz.

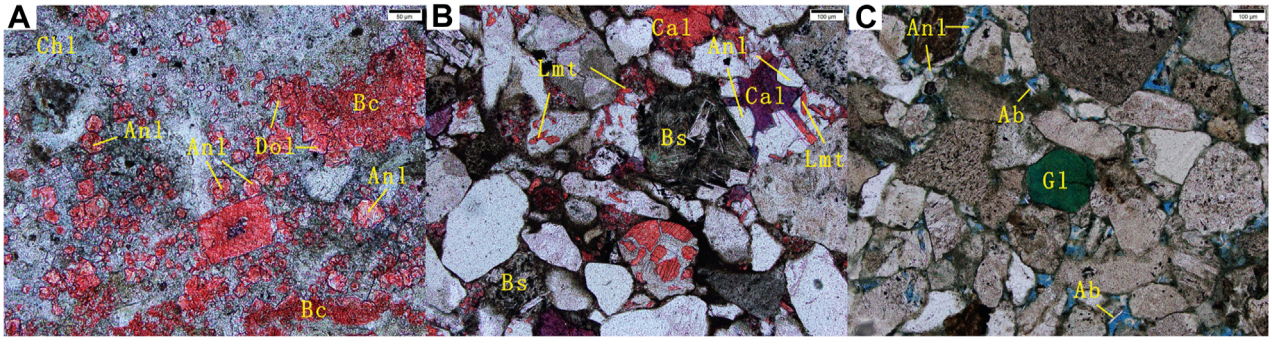

FIGURE 8
Other minerals associated with analcime formation in the study area. **(A)** Granular analcime was replaced by calcite and dolomite along the bioclastic edge developed in the tuffite (Well S4, 3221.33 m). **(B)** The intergranular filling of analcime did not undergo significant corrosion. Columnar mineral crystals (laumontite) were replaced by calcite, and the residual pores were filled with ferroan calcite (Well S104, 3435.90 m). **(C)** Emerald green glauconite spherules were found in lithic sandstone, and crescent-shaped analcime and lath-shaped analcimes were dissolved in the intergranular pores filled with albite (Well S101, 3261.40 m) (red in ab is alizarin red staining, blue in c is epoxidized resin). Chl: chlorite; Anl: analcime; BD: basalt debris; Dol: dolomite; Ab: albite; Cal: calcite; Fc: ferrocalcite; Lmt: laumontite; Glt: Glauconite.

induced the precipitation of albite and hydrothermal sphene in the secondary pores of the carboniferous pyroclastic rocks in the Kelamei area in the hinterland of the basin, leading to improved reservoir performance. The sphene from neighboring areas of the Jinan area and the Kelamei area exhibited similar composition characteristics (Table 2) and was found concurrently with albite

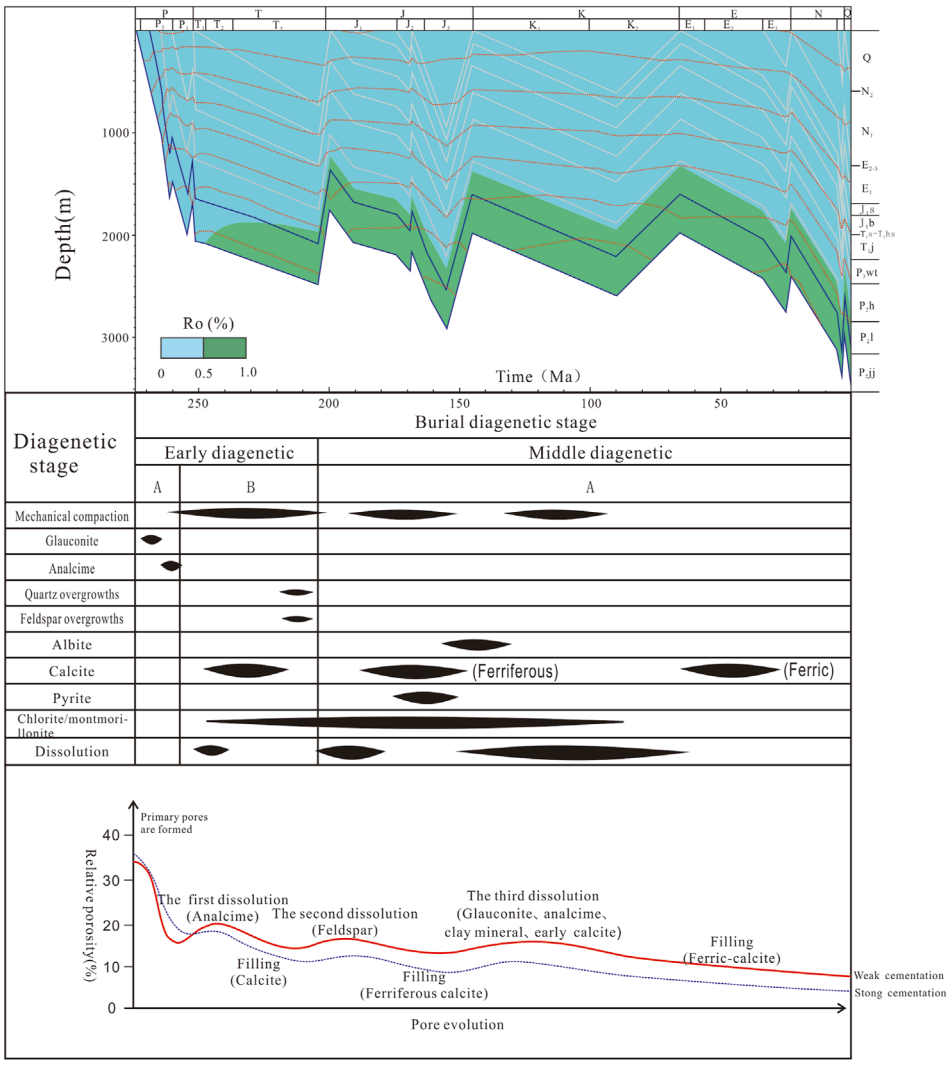

FIGURE 9
Burial diagenesis and pore evolution diagram of the Jingjingzigou Formation in the well S101.

in intergranular pores, potentially affected by higher temperatures, SiO_2-rich thermal fluid activity, and hydrocarbon charging during this period (Liu et al., 2022a, 2022b).

5.2 Burial diagenetic evolution sequence related to analcime

The burial thermal evolution history restoration results indicated that during the middle Permian, despite the overall subsidence of the Zhundong area, the southern Jinan area experienced minimal subsidence, preventing the hydrocarbon source rocks from reaching the hydrocarbon generating threshold (Figure 9). In the Early and Middle Jurassic, following a significant tectonic uplift in the Indosinian period at the end of the Late Triassic, the strata in the southern Jilin area continued to subside, leading the hydrocarbon source rocks to advance to the low mature–mature stage. Despite the subsequent uplift during the Yanshanian and Himalayan periods, resulting in substantial uplift of the hanging wall of the Fukang fault zone, the hydrocarbon source rocks remained stagnant during hydrocarbon formation. Conversely, the Jinan Sag was within the buried zone of the footwall of the fault zone, allowing the hydrocarbon source rocks to stay deeply buried and evolve to the mature stage during the Cenozoic. The Jingjingzigou Formation underwent three periods of oil accumulation during the middle and late Permian, middle and late Jurassic, and the late Neogene. The first accumulation phase occurred due to the lateral long-distance migration of mature crude oil from the neighboring Bogda rift (which includes the hanging wall of the Fukang fault zone). Towards the end of reservoir formation, crude oil generated by the hydrocarbon source rocks in the Jinan Sag collected towards the eastern and northern high points (Li et al., 2023).

Based on the characteristics of sandstone pore development and the relationship between mineral paragenesis assemblage, the Jingjingzigou Formation in the study area went through three stages of calcite filling after early chlorite and analcime

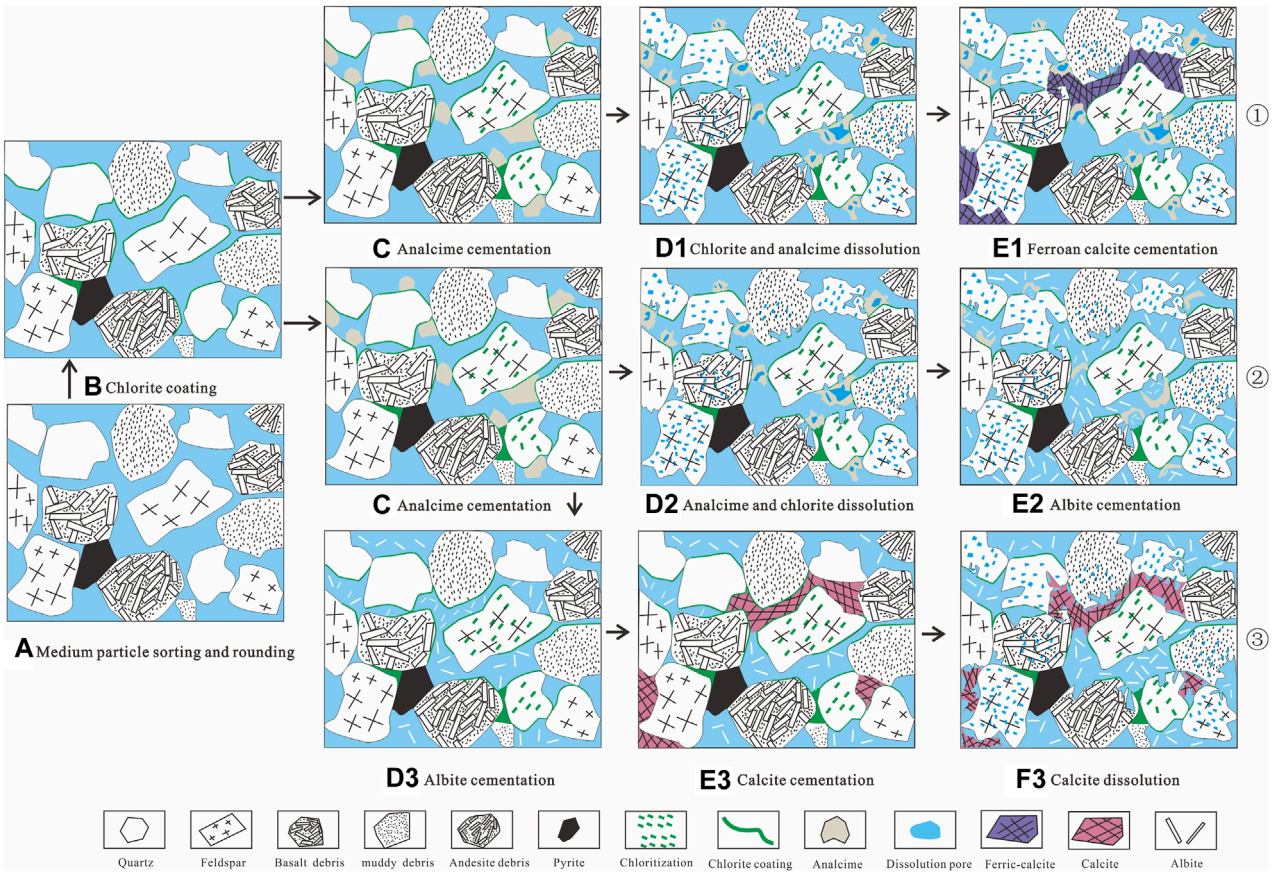

FIGURE 10
Diagram of the high-quality reservoir formation related with analcime in the study area. Three typical diagenetic evolution processes (①②③) are proposed.

mineral cementation. Additionally, it underwent at least three stages of dissolution of diagenetic minerals to varying degrees: 1) dissolution of chlorite and analcime; 2) initial dissolution of calcite; and 3) secondary dissolution of calcite. The first stage of dissolution occurred during the immature stage of hydrocarbon source rocks and could be linked to the early phase of hydrocarbon charge through lateral long-distance migration. The third stage of dissolution was observed in sections where calcite had not developed, characterized by significant corrosion of clastic feldspar, debris, and early chlorite and analcime cement, accompanied by the precipitation of authigenic albite minerals. Based on the fabrics of sandstone, pore types, degree of clay mineral evolution, and relationship between mineral paragenesis, in addition to burial thermal evolution history and hydrocarbon charging history, the diagenetic stages of the Jingjingzigou Formation reservoirs in the study area could be classified as middle diagenesis stage A (Figure 9).

5.3 Impact of analcime related diagenesis on reservoir quality

In summary, during the epidiagenetic stage, the formation of the chlorite film partially hindered the compaction and pressure solution processes. This film also preserved some primary intergranular pores, and reduced the occurrence of secondary quartz enlargement (Surdam et al., 1989; Worden et al., 2020). In the early stage of diagenesis, the precipitation and filling of analcime disrupted the primary pore structure of the sandstone, resulting in a decrease in reservoir porosity. In the middle and late stages of diagenesis, low-silicon analcime readily dissolved in organic acids or acidic pore fluids, transforming into albite. The secondary pores formed by the dissolution or transformation of analcime significantly enhanced the physical properties. The filling of calcite, which formed slightly later than the third stage of dissolution, greatly reduced porosity. Early calcite dissolution could enhance reservoir performance to some extent, but the degree of corrosion was generally not significant, and the improvement effect on the reservoir was not significant either. As a result, the pore formation and evolution of the Jingjingzigou Formation reservoirs in the study area have been determined, as illustrated in Figure 10. The formation of high-quality reservoirs related to analcime can be attributed to three crucial diagenetic processes: 1) moderate dissolution (Figure 10①), 2) relatively intense dissolution (Figure 10②), and 3) intense dissolution (Figure 10③).

Chlorite was the earliest cement formed in the reservoir, and its cementation preserved part of the primary pore space (Figures 10A,B). Subsequently, the precipitation of analcime caused

a reduction of pore (Figure 10C). The release of mature organic acids from hydrocarbon source rocks led to partial dissolution of analcime, but some pores subsequently being filled with ferroan calcite, resulting in moderate dissolution (Figures 10D1, E1). In contrast, areas with partially intensive dissolution experienced extensive dissolution of analcime followed by burial. Under appropriate temperature and pressure conditions, authigenic albite formed, leading to relatively intense dissolution (Figure 10C, D2, E2). Furthermore, in certain wells, reservoirs were clearly influenced by deep hydrothermal fluids and organic acids associated with the second stage of hydrocarbon charging. The dissolution of analcime and precipitation of albite occurred nearly simultaneously. Moreover, the analcime was completely dissolved, and the intergranular space was primarily composed of authigenic albite. Subsequently, some pores were filled with ferroan calcite, and the pores further dissolved under the influence of acidic fluids in the later stage, resulting in intense dissolution (Figures 10D3, E3, F3).

In comparison to other petroliferous basins rich in analcime worldwide, whether unconventional shale oil/gas of fine-grained sediments (Eocene Green River Formation in North America) or tight sandstone reservoir (western and eastern China) (Wang et al., 2022), porosity is mainly proportional to analcime content. However, it is important to know that the formation of high-quality reservoir is closely related to analcime, heavily influenced by factors such as volcanism, sedimentary environment, and diagenetic stage configuration. Furthermore, the development of dissolution pores within analcime has a certain degree of zoning. It is necessary to consider the limitations of being controlled laterally by sedimentary facies and provenances, and vertically by deep-buried diagenesis.

6 Conclusion

(1) The sandstone reservoirs of the Permian Jingjingzigou Formation in the Jinan sag (Junggar Basin, northwest China) primarily consist of lithic sandstone. The dominant debris present in these reservoirs is intermediate to basic extrusive rock. Analcime, clay, albite, and calcite are commonly found in these reservoirs, exhibiting differential dissolution. They either transform into albite or are replaced by other minerals. The main types of pores observed are intragranular dissolution pores of analcime.

(2) Analcime is characterized by its high aluminium content, low sodium content, and low Si/Al ratio. It forms during the early diagenetic stage when there is a significant presence of volcanic material in the rocks. This formation occurs under the influence of alkaline formation water, along with suitable temperature and pressure conditions. During the early diagenetic stage, analcime precipitates and fills the intergranular pores, which can result in damage to the structure of the primary pore and a reduction in porosity. The middle diagenetic stage is characterized by the formation of secondary pores through the dissolution of chlorite, analcime, and certain carbonate minerals. This process enhances the reservoir properties.

(3) In sandstone reservoirs with abnormally developed secondary pores at the similar sedimentary environments, it is essential for identify whether the presence of early analcime cement. Besides, to effectively distinguish the controlled factors requires combination of the mineral paragenesis relationship and experiments, it is helpful for quantitatively assess the effects of analcime precipitation-dissolution of deep clastic reservoirs during burial stage.

Data availability statement

The original contributions presented in the study are included in the article/Supplementary Material, further inquiries can be directed to the corresponding author.

Author contributions

TL: Conceptualization, Methodology, Writing–original draft. WW: Formal Analysis, Investigation, Writing–review and editing. QM: Data curation, Software, Writing–review and editing. JK: Software, Writing–review and editing. RY: Software, Writing–review and editing. XL: Data curation, Supervision, Validation, Writing–review and editing.

Funding

The author(s) declare that financial support was received for the research, authorship, and/or publication of this article. This work was supported by the Enterprise Innovation and Development Joint Fund National Natural Science Foundation of China (U22B6002); and The Xinjiang Uygur Autonomous Region "Tianshan Talents" Scientific and Technological Innovation Leading Talents Support Project (2022TSYCLJ0070); and the Scientific Research and Technology Development Project of China National Petroleum Corporation (2023YQX10109).

Conflict of interest

Authors TL and RY were employed by the PetroChina. Author WW was employed by the Sinopec Henan Oil-field Company. Authors QM and JK were employed by the Tuha Oilfield Company, PetroChina.

The remaining author declares that the research was conducted in the absence of any commercial or financial relationships that could be construed as a potential conflict of interest.

Publisher's note

References

Campo, M. D., Papa, C. D., Jiménez-Millán, J., and Nieto, F. (2007). Clay mineral assemblages and analcime formation in a Palaeogene fluvial-lacustrine sequence (MaízGordo Formation Palaeogen) from northwestern Argentina. *Sediment. Geol.* 201 (1-2), 56–74. doi:10.1016/j.sedgeo.2007.04.007

Dutton, S. P., and Loucks, R. G. (2010). Reprint of: diagenetic controls on evolution of porosity and permeability in lower Tertiary Wilcox sandstones from shallow to ultradeep (200–6700 m) burial. Gulf of Mexico Basin, USA. *Mar. Pet. Geol.* 27 (1), 1775–1787. doi:10.1016/j.marpetgeo.2009.12.010

English, P. M. (2001). Formation of analcime and moganite at Lake Lewis, central Australia: significance of groundwater evolution in diagenesis. *Sediment. Geol.* 143 (3), 219–244. doi:10.1016/S0037-0738(01)00063-X

Fang, R., Dai, Z. Y., Chen, Z. J., Shan, J. F., Jin, K., and Zhang, Y. F. (2020). Characteristics and genesis of analcites in different occurrence states: a case study of the fourth member of Shahejie Formation in the Leijia area of the Western Liaohe Depression. *Acta mineralogica sinica*. 40 (6), 734–764. doi:10.16461/j.cnki.1000-4734.2020.40.155

Fathy, D., Abart, R., Wangreich, N., Gier, S., Ahmed, M., and Sami, M. (2023). Late campanian climatic-continental weathering assessment and its influence on source rocks deposition in southern tethys, Egypt. *Minerals* 13 (2), 160. doi:10.3390/min13020160

Fu, G. M., Dong, M. C., Zhang, Z. S., et al. (2010). Formation process and distribution of laumontite in Yanchang 3 reservoir of Fuxian exploration area in north Shaanxi province and the controls of the high-quality reservoirs. *Earth Sci. J. China Univ. Geosci.* 35 (1), 107–114. doi:10.3799/dqkx.2010.011e

Gall, Q., and Hyde, R. (2010). Analcime in lake and lake-margin sediments of the carboniferous Rocky Brook Formation, western newfoundland, Canada. *Sedimentology* 36 (5), 875–887. doi:10.1111/j.1365-3091.1989.tb01751.x

Gao, C., Meng, S., Zhang, J., Wang, J., and Sun, Y. (2023). Effects of cementation on physical properties of clastic rock-originated weathering crust reservoirs in the Kexia region, Junggar Basin, NW China. *Energy Geoscience* 4 (1), 74–82. doi:10.1016/j.engeos.2022.08.006

Guo, H., Ji, B. Q., Yang, S., Wang, R., Zhang, S. C., Li, J. S., et al. (2022). Formation of zeolite cement in Permian sandy conglomerate reservoir in the circumMahu sag, Junggar Basin and its petroleum geological significance. *Acta Pet. Sin.* 43 (03), 341–354. doi:10.7623/syxb202203002

Han, S. H., Yu, H. Z., Si, C. S., Chen, S. H., Chen, N. G., and Yu, L. (2007). Corrosion of analcite in reservoir of Junggar Basin. *Acta Pet. Sin.* (3), 51–54+62. doi:10.7623/syxb200703010

Sheppard, R. A., and Hay, R. L. (2001). Occurrence of zeolites in sedimentary rocks: an overview. *Rev. Mineral. Geochem.* 45 (1), 217–234. doi:10.2138/rmg.2001.45.6

Iijima, A. (2001). 12. Zeolites in petroleum and natural gas reservoirs. *Rev. Mineral. Geochem.*, 347–402. doi:10.1515/9781501509117-014

Ji, Y. L. (2016). *Oil and gas reservoir Geology*. China University of Petroleum Press, 64–72.

Jia, C. Z., Pang, X. Q., and Jiang, F. J. (2016). Research status and development directions of hydrocarbon resources in China. *Petroleum Sci. Bull.* 1 (01), 2–23. doi:10.3969/j.issn.2096-1693.2016.01.001

Jin, H. N., and Boles, J. R. (1993). Origin of zeolite cements in the Miocene sandstones, north tejon oil fields, California. *J. Sediment. Res.* 63 (2), 248–260. doi:10.1306/D4267AD2-2B26-11D7-8648000102C1865D

Karakaya, N., Muazzez, C. K., and Temel, A. (2013). Mineralogical and chemical properties and the origin of two types of analcime in SW Ankara, Turkey. *Clays Clay Minerals* 61 (3), 231–257. doi:10.1346/CCMN.2013.0610306

Langella, A., Cappelletti, P., and Gennaro, R. D. (2001). Zeolites in closed hydrologic systems. *Rev. Mineral. Geochem.* 45 (1), 235–260. doi:10.2138/rmg.2001.45.7

Li, J., Zhang, W. J., Xiang, B. L., He, D., Yang, S. C., Wang, J., et al. (2022). Characteristics of dissolved pores and dissolution mechanism of zeolite-rich reservoirs in the Wuerhe Formation in Mahu area, Junggar Basin. *Energy Explor. Exploitation* 40 (1), 421–441. doi:10.1177/01445987211028732

Li, J. S., Fu, L., Zhang, J. L., Chen, J., Niu, B., and Zhang, S. C. (2019). Diagenesis and secondary pore evolution of Middle and Upper Permian clastic rocks in Wu-Xia area, Junggar Basin. *Lithol. Reserv.* 31 (6), 54–66. doi:10.12108/yxyqc.20190606

Li, J. Z., Chen, X., Yang, R. Z., Lin, T., Yang, F., Ma, Q., et al. (2023). Petroleum geology and sub-source hydrocarbon accumulation of Permian reservoirs in Jinan Sag, eastern Junggar Basin, NW China. *Petroleum Explor. Dev.* 50 (3), 558–572. doi:10.1016/s1876-3804(23)60410-0

Li, Z. H., Qiu, L. W., Shi, Z., Tang, Y., Kong, Y. H., and Zhu, S. B. (2014). Diagenesis of zeolite minerals and its significance for hydrocarbon accumulation in the second member of Jiamuhe formation of Zhongguai area, Junggar Basin. *J. China Univ. Petroleum*. 38 (01), 1–7. doi:10.3969/jissn.1673-5005.2014.01.001

Liang, S. J., Luo, Q. S., Kang, J. L., Li, F. L., Ma, Q., Wang, X. C., et al. (2021). Breakthrough and significance of risk exploration in well satan 1 in jinan sag, Junggar Basin. *China Pet. Explor.* 26 (4), 72–83. doi:10.3969/j.issn.1672-7703.2021.04.00

Lin, P. X., Lin, C. M., Yao, Y., Wang, B. J., Li, L., Zhang, X., et al. (2017). Characteristics and causes of analcime distributed in dolostone of the Member 3 of Paleogene Shahejie Formation in Beitang sag, Bohai Bay Basin. *Journal of Palaeogeography* 19 (2), 241–256. doi:10.7605/gdlxb.2017.02.019

Liu, X. H., Wang, W. W., Feng, M. Y., Zhuo, Y. Q., and Yue, H. H. (2022a). Hydrothermal process and duration of carboniferous altered tuff reservoir in well dixi 14 area of kelameili gas field (Junggar Basin), NW China. *Earth Sci.* 47 (5), 1694–1710. doi:10.3799/dqkx.2021.188

Liu, X. H., Zhuo, Y. Q., Feng, M. Y., Zhang, B. J., Xia, M. L., and Wang, X. Z. (2022b). Constrains of eruption environment and hydrothermal fluid on the Permian pyroclastic reservoirs in the Sichuan Basin, SW China. *Petroleum* 8, 17–30. doi:10.1016/j.petlm.2021.03.005

Meng, Y. L., Liang, H. T., Wei, W., et al. (2013). Thermodynamic calculations of the laumontite dissolution and prediction of secondary porosity zones: a case study of horizon of Xujiaweizi fault depression. *Acta Sedimentol. Sin.* 31 (3), 509–515. doi:10.1016/j.petlm.2021.03.005

Neuhoff, P. S. (2002). Natural zeolites: occurrence, properties, applications. *Am. Mineralogist* 45 (11-12), 1737–1738.

Noh, J. H., and Boles, J. R. (1993). Origin of zeolite cements in the Miocene sandstones, North Tejon oil f-ields, California. Sediment. *Res* 63 (2), 248–260. doi:10.1306/d4267ad2-2b26-11d7.8648000102c1865d

Renaut, R. W. (1993). Zeolitic diagenesis of late Quaternary fluviolacustrine sediments and associated calcrete formation in the Lake Bogoria Basin, Kenya Rift Valley. *Sedimentology* 40 (2), 271–301. doi:10.1111/j.1365-3091.1993.tb01764.x

Schmidt, V., and McDonald, D. A. (1979). The role of secondary porosity in the course of sandstone diagenesis. *SPEM Spec. Publ.* 26, 175–207. doi:10.2110/pec.79.26.0175

Sun, Y. S., Liu, X. N., Zhang, Y. Q., Dong, W. K., Xu, Y. L., Shi, G. X., et al. (2014). Analcite cementation facies and forming mechanism of high-quality secondary clastic rock reservoirs in western China. *J. Paleogeogr.* 16 (04), 517–526. doi:10.7605/gdlxb.2014.04.042

Surdam, R. S., Crossey, L. J., Hangen, E. S., and Heasler, H. P. (1989). Organic-inorganic interaction and sandstone diagenisis. *AAPG Bull.* 73 (1), 1–23. doi:10.1306/703C9AD7-1707-11D7-8645000102C1865D

Tang, Z. H., John, P., and Fred, J. L. (1997a). Diagenesis and reservoir potential of Permian-Triassic fluvial/lacustrine sandstones in the southern Junggar basin, Northwestern China. *AAPG Bull.* 81 (11), 1843–1865. doi:10.1306/3B05C64A-172A-11D7-8645000102C1865D

Tang, Z. H., John, P., and Fred, J. L. (1997b). Diagenesis of analcime-bearing reservoir sandstones: the upper permian pingdiquan formation, Junggar Basin, Northwest China. *Sediment. Res.* 67 (3), 486–498. doi:10.1306/D42685A4-2B26-11D7-8648000102C1865D

Taylor, M. W., and Surdam, R. C. (1981). Zeolite reactions in the tuffaceous sediments at Teels marsh, Nevada. *Clay Clay Min.* 29, 341–352. doi:10.1346/ccmn.1981.0290504

Utada, M. (2001). Zeolites in burial diagenesis and low-grade metamorphic rocks. *Rev. Mineral. Geochem.* 45 (1), 277–304. doi:10.2138/rmg.2001.45.9

Varol, E. (2020). Interpretation of the origin of analcimes with mineralogical, microtextural, and geochemical investigations:a case study from Aktepe region (NE of Kalecik, Ankara,Central Anatolia, Turkey). *Arabian J. Geosciences* 13 (10), 343–410. doi:10.1007/s12517-020-05315-9

Wang, J. R., Liang, C., Cao, Y. C., and Tian, Y. (2022). Occurrence, genesis, and significance of analcime in fine-grained sedimentary rocks. *Geofluids* 2022 (2), 1–17. doi:10.1155/2022/3633047

Weibel, R., Olivarius, M., Jakobsen, F. C., Whitehouse, M., Larsen, M., Midtgard, H., et al. (2019). Thermogenetic degradation of early zeolite cement: an important process for generating anomalously high porosity and permeability in deeply buried sandstone reservoirs? *Mar. Petroleum Geol.* 103, 620–645. doi:10.1016/j.marpetgeo.2019.02.006

Worden, R. H., Utley, J. E., Butcher, A. R., Griffiths, L. J., Wooldridge, L. J., and Lawan, A. Y. (2020). Improved imaging and analysis of chlorite in reservoirs and modern day analogues: new insights for reservoir quality and provenance. *Geol. Soc. Lond. Spec. Publ.* 484 (1), 189–204. doi:10.1144/SP484.10

Wu, J. J., You, L. P., and Yang, H. S. (2013). Structural evolution and hydrocarbon accumulation of Fukang fault zone in Junggar Basin. *Xinjiang Pet. Geol.* 34 (1), 36–40. doi:10.11743/ogg20180506

Xing, S. Q., Xiao, Z. S., and Zhang, S. G. (1982). Mineralogical characteristic of glauconite and conditions of its formation in the Taikang inlet, Songliao Basin. *Acta Mineral. Sin.* (01), 52–58+85.

Yang, G. H., Zhuo, S. G., Niu, B., and E, J. J. (2003). Albitization of detrital feldspar in cretaceous sandstones from the songliao basin. *Geol. Rev.* 49 (03), 155–161+228. doi:10.16509/j.georeview.2003.02.007

Yuan, G. H., Cao, Y. C., Gluyas, J., Li, X., Xi, K., Wang, Y., et al. (2015). Feldspar dissolution, authigenic clays, and quartz cements in open and closed

sandstone geochemical systems during diagenesis: typical examples from two sags in Bohai Bay Basin, East China. *AAPG Bull.* 99 (11), 2121–2154. doi:10.1306/07101514004

Yuan, Z., Li, W. H., Yuan, H. L., and Guo, Y. Q. (2020). Pore evolution characteristic of sandstone reservoir with laumontite cement and its influence on reservoir properties: chang10_1, reservoir of Yanchang Formation in Southeast of Ordos Basin. *Chin. J. Geol.* 55 (3), 767–781. doi:10.12017/dzkx.2020.047

Zhang, P. H. (1985). Precipitation of zeolite and pore evaluation of coarse clastic rock reservoir in permian from karamay. *Xinjiang Pet. Geol.* (2), 30–47.

Zhang, Y. Q., and Zhang, N. F. (2006). Oil/gas enrichment of large superimposed basin in Junggar Basin. *China Pet. Explor.* (1), 59–6478.

Zheng, M., Li, J. Z., Wu, X. Z., Wang, S. J., Guo, Q. L., Chen, X. M., et al. (2019). Potential of oil and natural gas resources of main hydrocarbon bearing basins and Key exploration fields in China. *Earth Sci.* 44 (3), 833–847. doi:10.3799/dqkx.2019.957

Zhu, S. F., Cui, H., Jia, Y., Zhu, X. M., Tong, H., and Ma, L. C. (2020). Occurrence, composition, and origin of analcime in sedimentary rocks of non-marine petroliferous basins in China. *Mar. Petroleum Geol.* 113, 104164–104216. doi:10.1016/j.marpetgeo.2019.104164

Zhu, S. F., Zhu, X. M., Wang, X. L., and Liu, Z. Y. (2011). Zeolite diagenesis and its control on petroleum reservoir quality of Permian in northwestern margin of Junggar Basin, China. *China Sci. China Earth Sci.* 41 (11), 1602–1612. doi:10.1007/s11430-011-4314-y

frontiers | Frontiers in Earth Science

TYPE Original Research
PUBLISHED 14 August 2024
DOI 10.3389/feart.2024.1441548

OPEN ACCESS

EDITED BY
Jianguo Zhang,
China University of Geosciences, China

REVIEWED BY
Chao Liang,
China University of Petroleum (East China), China
Qiqi Lyu,
Yangtze University, China

*CORRESPONDENCE
Laixing Cai,
qingxin717717@126.com

RECEIVED 31 May 2024
ACCEPTED 05 July 2024
PUBLISHED 14 August 2024

CITATION
Yuan C, Guo W, Cai L, Zeng Y, Zhang Z, Liu Y and Yang T (2024), Sedimentological and diagenetic facies of tight sandstones in lacustrine delta-front: A case study of the Jurassic Lianggaoshan Formation, eastern Sichuan Basin.
Front. Earth Sci. 12:1441548.
doi: 10.3389/feart.2024.1441548

Sedimentological and diagenetic facies of tight sandstones in lacustrine delta-front: A case study of the Jurassic Lianggaoshan Formation, eastern Sichuan Basin

Chengfang Yuan[1], Weixue Guo[1], Laixing Cai[1,2]*, Yangjing Zeng[3], Zhenkai Zhang[4], Yinglin Liu[1] and Tian Yang[1,2]

[1]Institute of Sedimentary Geology, Chengdu University of Technology, Chengdu, China, [2]State Key Laboratory of Oil and Gas Reservoir Geology and Exploitation, Chengdu University of Technology, Chengdu, China, [3]No. 5 Oil Production Plant, PetroChina Changqing Oilfield Company, Gaoling, China, [4]Shanxi Satellite Application Center for Natural Resources, Shanxi Institute of Geological Survey, Xi'an, China

In this study, taking the Jurassic Lianggaoshan Formation (J_1l) tight sandstones in the eastern Sichuan Basin as an example, the types and well-logging responses of main sedimentological and diagenetic facies in the lacustrine delta-front are investigated based on summarizing the sedimentary characteristics and reservoir properties. Subsequently, further validation and application are conducted in the study area through machine learning. Research results show that the J_1l lacustrine delta-front in the eastern Sichuan Basin mainly develops subaqueous distributary channels and mouth bar sand bodies, exhibiting typical densification reservoirs, with porosity and permeability distributed between 0.48% and 11.24% (av. 3.87%) and 0.0003–0.653 × 10^{-3} μm^2 (av. 0.026 × 10^{-3} μm^2), respectively. Strong compaction and strong cementation are the primary factors leading to densification, whereas chlorite coatings and weak dissolution play constructive roles in preserving some primary pores, creating a small amount of dissolution pores, and enhancing permeability. In terms of manifestation, the pore-throat content with a radius greater than 0.006 μm governs the reservoir quality. Furthermore, five types of diagenetic facies are identified in the J_1l subaqueous distributary channels and mouth bars: strong compaction facies (Type I), strong cementation facies (Type II), chlorite-coating and intergranular pore facies (Type III), weak dissolution and intragranular pore facies (Type IV), and medium compaction and cementation facies (Type V). Overall, the thick and coarse-grained subaqueous distributary channels can be considered as the preferred exploration targets for tight oil and gas, with type III and type IV diagenetic facies being the most favorable reservoirs, characterized by well-logging responses of high AC and low GR, DEN, and RT. Based on the fine division of sedimentological and diagenetic facies, establishing well-logging interpretation models and

then employing machine learning to achieve sweet spot reservoir prediction can provide valuable insights for tight oil and gas exploration in regions lacking core data.

KEYWORDS

sedimentological and diagenetic facies, well-logging response, machine learning method, tight sandstone, Lianggaoshan Formation, eastern Sichuan Basin

1 Introduction

Since the beginning of the 21st century, the petroleum industry worldwide has extended from conventional to unconventional fields, with the United States and China leading the development of unconventional hydrocarbon (Law and Curtis, 2002; Stephen, 2006; Külaots et al., 2010; Soeder, 2018; Zhu et al., 2019) and gradually forming the "symbiotic enrichment theory" of conventional–unconventional oil and gas (Zou et al., 2013; Yang et al., 2021; Jia et al., 2023). Currently, the recoverable resources of tight oil and gas account for approximately 40% and 45% of China's recoverable oil and natural gas resources, respectively (Sun et al., 2019; Zou et al., 2022). Compared to the nascent shale oil and gas and slowly developing coalbed methane, tight sandstones have emerged as a focus area for energy replacement in China, especially in the basins such as Ordos, Sichuan, Songliao, and Bohai Bay that have achieved remarkable exploration achievements (Jia et al., 2018; Dai et al., 2021; Guo et al., 2022; Wang et al., 2023). As a crucial carrier for hydrocarbon migration and accumulation, tight sandstones consistently stand at the forefront and core of reservoir geological research; that is, the central objective of seeking oil–gas accumulation zones is to locate the reservoir sweet spots.

In the absence of tectonic activity, reservoir quality is jointly influenced by the original sedimentary environment and later diagenetic reconstruction, exhibiting a pattern of "facies control" (Haile et al., 2018; Yang et al., 2021; Alam et al., 2022; Kra et al., 2022). Sedimentary processes control the spatial distribution of sand bodies, and the original reservoir properties are determined through rock composition and texture characteristics, such as initial mineral composition, particle size, and sorting (Khalifa and Morad, 2015; Bahrehvar et al., 2021; Lai et al., 2023). After entering the burial environment, the sediments not only undergo continuous mechanical compaction but also pass through a series of water–rock reactions to modify the material and pore distribution, ultimately forming the current reservoir characteristics, known as diagenetic facies. Moreover, there is a spatiotemporal correlation between diagenetic facies and sedimentary facies, which means that there is certain regularity in the distribution of diagenetic facies within sand bodies (Henares et al., 2014; Zhang et al., 2014; Wang et al., 2017).

Early diagenetic facies were proposed as an important approach to solve the diagenesis and heterogeneity in carbonate reservoirs (Packham and Keith, 1960; Railsback, 1984). Later, it was continuously supplemented and developed in research on sandstone reservoirs, but a unified concept and division scheme have not yet been formed. Railsback (1984) regarded diagenetic facies as rock masses or geological units with different diagenetic textures, and after being introduced into China, this concept was extended to a comprehensive representation of diagenetic environments and products, encompassing the sum of petrological, geochemical, and petrophysical characteristics (Chen and Liu, 1994). To date, many scholars emphasize that diagenetic facies are physical manifestations reflecting the diagenetic environment (Carvalho et al., 1995; Dill et al., 2005; Zheng et al., 2007; Zou et al., 2008; 2013; Lai et al., 2018). This includes the aforementioned diagenetic products as well as the intensity of diagenetic events revealed by them, including comprehensive characteristics such as rock particles, cement types, petrofabrics, pores, and fractures (Zou et al., 2008; He et al., 2011). Moreover, due to differences in classification criteria, there is no convention for naming diagenetic facies. Factors such as reservoir lithology, porosity and permeability, pore type, diagenetic event, and the intensity and combination of diagenesis are all involved in this context (Cao et al., 2015; Mou et al., 2016; Lai et al., 2019; Fang, 2020; Wu et al., 2020; Li et al., 2022). However, the common understanding is that the diagenetic facies, based on revealing the current characteristics and genesis of reservoirs, summarize the regional diagenetic evolution patterns (Cui et al., 2017; Liu et al., 2018; Lai et al., 2019; Li et al., 2020). Well-logging data record multiple information such as mineral composition, lithological combination, pore structure, porosity, and permeability in rocks, with outstanding characteristics of good vertical continuity, high resolution, and low economic cost, providing a scientific basis for identifying diagenetic facies in sections lacking core samples (Lai et al., 2020; Wu et al., 2020; Li et al., 2022; Zhao et al., 2022). The widely used methods based on well-logging data include cross-plot, spider chart, mathematical analyses (Fisher discriminant analysis and factor analysis), and neural network algorithms (probabilistic neural network and BP neural network) (Lai et al., 2018; 2019; Li et al., 2022; Zhao et al., 2022; Zheng et al., 2022).

The tight sandstones of Lower Jurassic Lianggaoshan Formation (J_1l) have become a new exploration focus in the Sichuan Basin, owing to its shallow burial and low exploration costs (Zhang, 2021; Zhang and Yang, 2022; Cheng et al., 2023a). Previous studies have indicated that the geological resources of the J_1l tight gas in the eastern Sichuan Basin reach 2.0×10^8t, and abundant hydrocarbon shows, including industrial oil and gas flows, have been discovered in over 50 wells (Zou et al., 2018; Zhang, 2021; Yi et al., 2022). In view of the heterogeneity of the reservoir of the J_1l tight sandstones, containing differences in porosity and permeability, pore–throat structure, and diagenesis, this study investigates the joint control of sedimentological and diagenetic facies on reservoir quality. This not only contributes to understanding the mechanisms and processes of reservoir densification but also accurately serves as the optimization of exploration targets.

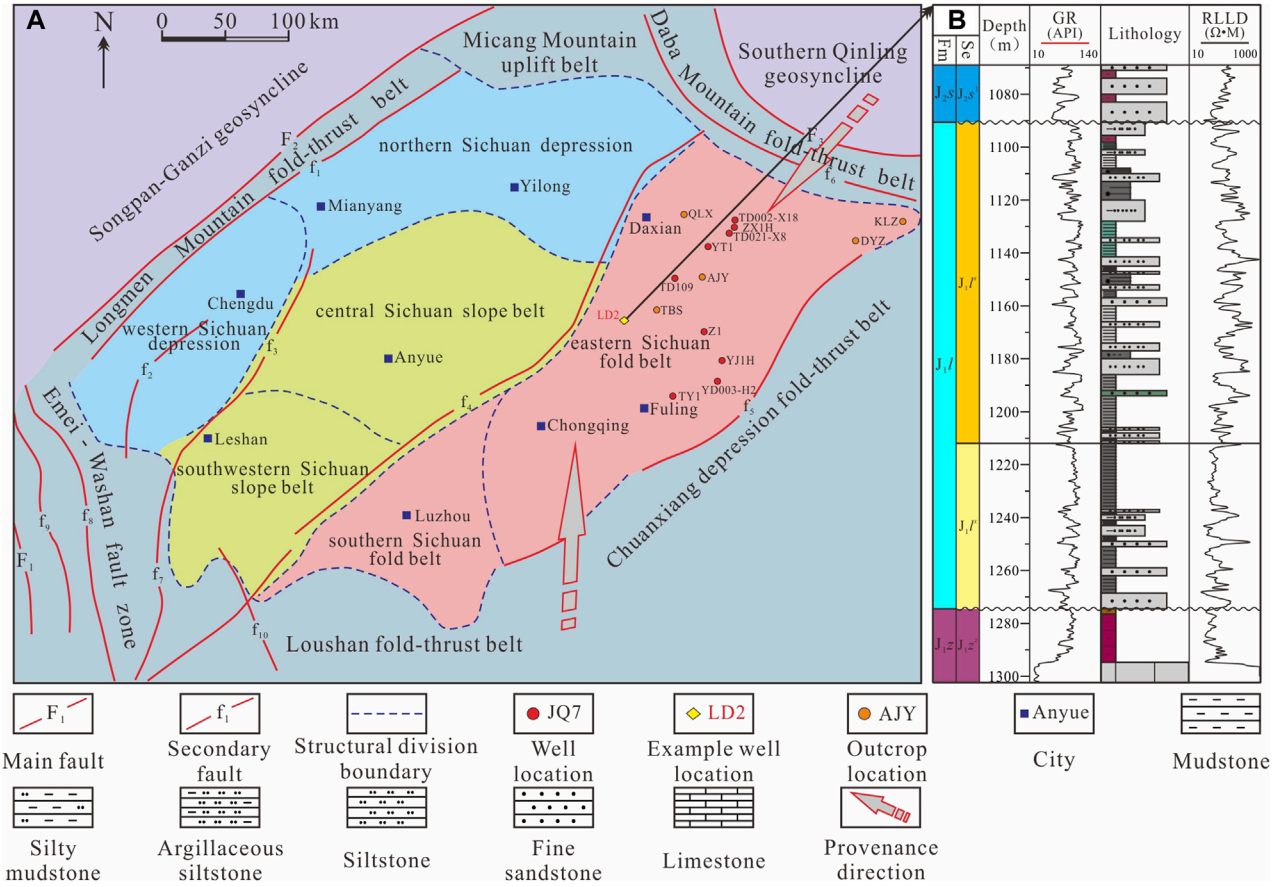

FIGURE 1
Structural divisions of the Sichuan Basin **(A)** and the J_1l stratigraphic characteristics in well LD2, eastern Sichuan Basin **(B)**. F_1, Anninghe fault; F_2, Longmen Mountain fault; F_3, Chengkou fault; f_1, Pengguan fault; f_2, Xiongpo fault; f_3, Longquan Mountain fault; f_4, Huaying Mountain fault; f_5, Qiyue Mountain fault; f_6, Wanyuan fault; f_7, Emei–Washan fault; f_8, Hanyuan fault; f_9, Puxiong river fault; f_{10}, Yadu-Mashan fault.

2 Regional geological background

The Sichuan Basin is located in the northwest of the Yangtze Plate and is a large superimposed basin based on rigid granite, with abundant marine and continental petroleum resources (Korsch et al., 1991; Yokoyama et al., 2001; Wang CY. et al., 2022; He, 2022). The periphery of the basin is surrounded by the Longmen Mountain fold–thrust belt, Micang Mountain uplift belt, Daba Mountain fold–thrust belt, Chuanxiang depression fold–thrust belt, Loushan fold–thrust belt, Emei–Washan fault zone (Zhao et al., 2012; Wang et al., 2020; Huang et al., 2023; Kane et al., 2023). In addition, the interior of the basin is divided into six secondary structural units: western Sichuan depression, northern Sichuan depression, central Sichuan slope belt, southwestern Sichuan slope belt, southern Sichuan fold belt, and eastern Sichuan fold belt (Zhu et al., 2018; Wang XJ. et al., 2022; Figure 1A). Among them, the eastern Sichuan fold belt is separated from the central Sichuan slope belt by the Huaying Mountain fault, bordering the Daba Mountain fold–thrust belt in the north and the South China fold system in the southeast (Figure 1A).

Under the tectonic setting of compressional orogeny following the Indosinian Movement (Şengör, 1985; Xu et al., 2012), the Micang Mountain and Daba Mountain in the northeast margin of the basin rapidly uplifted in the early Jurassic and transported a large amount of terrigenous clastics into the basin as the main provenance areas (Li et al., 2018; Meng et al., 2022; Cheng et al., 2023b). Additionally, the secondary provenance area known as the Xuefeng uplift is developed in the southeastern part of the basin (Zheng et al., 2019; Cheng et al., 2023b). Against the backdrop of multiple transitions from shallow to semi-deep lake depositional environments, the Jurassic system in the eastern Sichuan Basin is successively developed from the bottom to top as follows: the Ziliujing Formation (J_1z), Lianggaoshan Formation (J_1l), and Shaximiao Formation (J_2s), with widespread delta sedimentary facies in J_1l (Wang ZC. et al., 2022; Yi et al., 2022; Cheng et al., 2023a; Yu et al., 2023). Under the comprehensive control of factors such as paleoclimate change, lake-level fluctuation, and ancient source supply, the mudstones of the prodelta and semi-deep lake are vertically superimposed with the sandstones of delta front, forming a favorable configuration of hydrocarbon source rocks and reservoirs (Figure 1B).

3 Samples and testing methods

3.1 Sample collection

Based on the core observation of six wells (TD021-X8, TD109, YT1, YD003-H2, ZX1H, and YJ1H) in the eastern Sichuan Basin, this study additionally supplemented five outcrops to summarize the sedimentary characteristics, namely, QLX (107°44′37″E, 31°11′49″N), TBS (107°31′32″E, 30°36′1″N), AJY (107°52′20″E, 30°47′52.2″N), DYZ (109°1′31.2″E, 30°59′44.4″N), and KLZ (109°28′49.2″E, 31°5′41.5″N) profiles (Figure 1A). All the samples were taken from intact block rocks on the core and outcrop, and all the samples were sandstone, except mudstone for major and trace elements. A total of 605 samples were tested at the State Key Laboratory of Oil and Gas Reservoir Geology and Exploitation (Chengdu University of Technology), including 63 casting thin sections, 173 particle-size analyses, 174 X-ray diffraction (XRD) analyses, 14 whole-rock major and trace elements, 10 scanning electron microscopic (SEM) observations, 16 high-pressure mercury injection (HPMI) analyses, and 155 porosity and permeability testing.

3.2 Testing methods

3.2.1 Analyses of minerals and rocks

According to the rock thin-section preparation standard SY/T 5913-2021 of China's petroleum and gas industry, rock samples were polished to a thickness of approximately 0.03 mm and stained with a mixed solution of alizarin Red S and potassium ferrocyanide to prepare casting thin sections. The mineral composition and structure of rocks were then observed using a Zeiss AxToScope.A1ApoL polarizing microscope. XRD testing requires first grinding the dried sample to a particle size smaller than 200 mesh and later obtaining the spectrum using a D/Max-2500 X-ray diffractometer, with specific testing conditions of 1° emission slit, 0.3 mm receiving slit, 2°/min scanning speed, and 0.02° sampling width. In response to the fine-grained rocks in the study area, particle size analyses were conducted in accordance with the standard of SY/T 5434-2018, using an APA2000 laser particle size analyzer as the testing instrument. In addition, the major element determination was carried out using an Axios PW4400 X-ray fluorescence spectrometer, and the trace elements were conducted using a Thermo XSERIES 2 inductively coupled plasma mass spectrometry (ICP-MS), both with an analysis accuracy of ±5%.

3.2.2 Analyses of reservoir characteristics

The porosity and permeability related to reservoir evaluation were tested following the core analysis practices of the standard SY/T 5913-2006, using instruments such as the UltraPore-200 A helium porosimeter and ULTRA-PERM^{TM}200 permeameter, respectively. SEM testing was performed under an FEG 450 scanning electron microscope to identify mineral types and pore morphology, with the standard of GB/T 18295-2001. The minimum pore radius measured using the AutoPore IV 9505 mercury porosimeter can reach 5 nm, which is suitable for characterizing the pore–throat structure of tight sandstones (Cai et al., 2019; Zhang et al., 2019).

4 Results

4.1 Sedimentary characteristics

4.1.1 Marks of sedimentary facies identification

Rock colors: in the eastern Sichuan Basin, the J_1l cores and outcrops display a rich variety of rock colors, including reduced colors such as black, grayish black, and dark gray, as well as reddish brown, grayish green, and grayish white formed in oxidizing conditions (Figures 2A–C). Meanwhile, the color of mudstones changes regularly, from grayish black and dark gray in the J_1l^x segment to gray, grayish green, and reddish brown in the J_1l^s segment (Figure 1B), indicating that the J_1l water body is shifting from deep to shallow and frequent small-scale lake transgression and regression cycles.

Petrology characteristics: the content of the argillaceous matrix in the J_1l sandstones ranges from 2% to 9%, with an average value of about 6%, making it an arenite. Thin sections show that the particle sizes are relatively fine, distributed in the range of 0.06–0.25 mm, and the rocks exhibit a particle-supported texture, with moderate sorting and a sub-rounded to hypo-edge angle in roundness (Figure 2D). The main types of sandstones are feldspathic litharenite and lithic arkose (Figure 2E). Among them, the content distribution ranges of quartz, feldspar, and rock debris are 52.53%–66.22%, 13.40%–26.46%, and 17.35%–29.29%, with the average contents of 56.50%, 22.42%, and 21.08%, respectively. Furthermore, in terms of rock debris types, sedimentary rock is predominant, with a relative content of 47.67%, followed by metamorphic rock, with a relative content of 44.96% (Figure 2F).

XRD testing of the core and AJY outcrop samples further revealed the mineral characteristics of "high content of quartz and feldspar, as well as low content of calcite and dolomite." In sandstones, the quartz content generally ranges from 26.3% to 88.4% (av. 52.98%), and the contents of plagioclase and K-feldspar account for 0.7%–38.4% (av. 21.79%) and 1.4%–23.2% (av. 6.38%), respectively. Correspondingly, the average contents of calcite and dolomite are only 2.2% and 0.59%, respectively (Table 1). The content of clay minerals is distributed between 8.3% and 36.1%, with an average value of 18.03%. Combined with the lower content of the argillaceous matrix, it reflects a stronger cementation of clay minerals in the later diagenetic stage. Kaolinite is commonly developed in clay minerals, with a content range of 6.4%–47.0% and an average content range of 20.41%. Chlorite and illite are quite similar, with average contents of 16.4% and 15.0%, respectively. In addition, minerals such as siderite, pyrite, and anhydrite are rare, and their contents generally do not exceed 1.4% (Table 1).

Sedimentary structures: in the J_1l sandstones, bedding structures characterized by abundant trough cross-bedding (Figure 3A) and parallel bedding (Figure 3B) reflect strong hydrodynamic conditions. Additionally, wedge-shaped cross-bedding (Figure 3C), wavy bedding (Figure 3D), and flaser bedding (Figure 3E) can also be observed, revealing the hydrodynamic forces of waves and tides. Oblique bedding in fine sandstones is interbedded with the horizontal bedding in mudstones (Figure 3F), indicating the alternating variations in sediment dynamics. As the river energy gradually weakens, fine-grained sediments such as siltstones and argillaceous siltstones form wave-ripple bedding and climbing ripple bedding under the repeated wave erosion

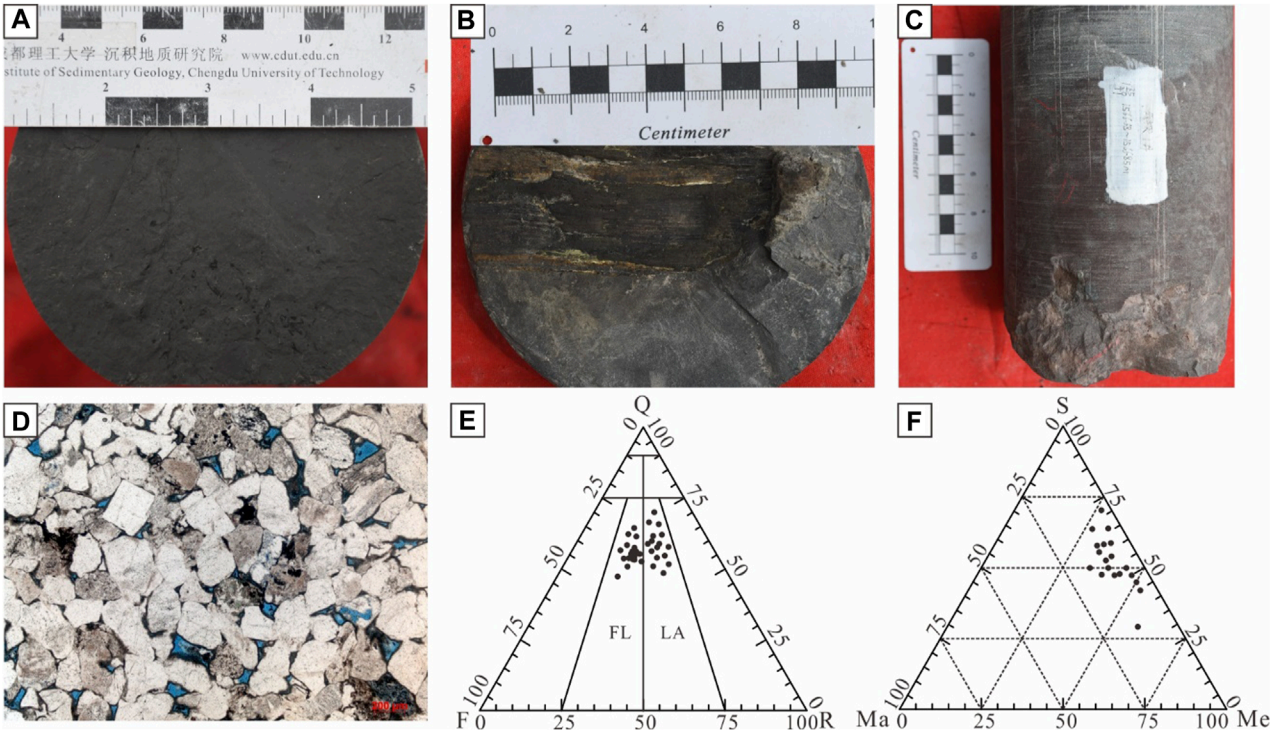

FIGURE 2
Petrology characteristics of the J_1l tight sandstones in the eastern Sichuan Basin. **(A)** Well ZX1H, 1891.4 m, J_1l^x segment, grayish black mudstone; **(B)** well TD109, 1328.9 m, J_1l^s segment, gray mudstone; **(C)** well YT1, 1566.8 m, J_1l^s segment, grayish green and reddish brown silty mudstone; **(D)** well ZX1H, 1817.36 m, J_1l^s segment, fine sandstone with a moderate sorting and hypo-edge angle in roundness; **(E)** triangular diagram for the classification of sandstones (Q, quartz; F, feldspar; R, rock debris; FL, feldspathic litharenite; and LA, lithic arkose); and **(F)** triangular diagram for the classification of rock debris (S, sedimentary rock; Ma, magmatic rock; and Me, metamorphic rock).

(Figure 3G), often accompanied by reverse grading. Due to the erosion of the overlying sandstone into the underlying mudstone, a bottom surface of scour is formed (Figure 3H), which usually indicates the presence of strong hydrodynamic channel deposition. Additionally, flame structure, ball–pillow structure, and convolute bedding are also common deformation structures near the sand–mud contact surface (Figures 3I, J). Fossils and bioglyphs are developed in the study area, such as Muschel sandstone (Figure 3K), shell mudstone (Figure 3L), bioturbation structure (Figure 3M), and phytoclast (Figure 3N), which further confirm the sedimentary background of shallower water and nearby provenance.

4.1.2 Sedimentary environments

Geochemical methods are widely used in the restoration and reconstruction of sedimentary environments. For example, the values of Sr/Cu, Rb/Sr, K_2O/Al_2O_3, and paleoclimate index C are considered as effective indicators for discussing paleoclimate (Beckmann et al., 2005; Moradia et al., 2016; Cai et al., 2023). The ratio of metal elements such as V, Cr, Co, and Ni can be used to distinguish paleo-redox conditions, and parameters like Sr/Ba and Rb/K are employed to characterize the paleosalinity of water bodies (Jones and Manning, 1994; Wei and Thomas, 2020). In addition, the relative contents of elements Al and Ti are applied to analyze the input intensity of terrigenous clastics (Greber and Dauphas, 2019; Han et al., 2022).

In the J_1l^x segment, K_2O/Al_2O_3 values are all below 0.2, with a maximum value of 0.188, indicating an overall warm and humid paleoclimate. The paleoclimate index C values are relatively large, especially for the lower three samples, all of which exceed 0.80 with an average value of 1.02, further confirming this conclusion. The test results of the J_1l^s 11 rock samples show that the distribution range of K_2O/Al_2O_3 values slightly increases to 0.165–0.270, with an average value of 0.205, and the paleoclimate index C values decrease to 0.59–0.86, with an average value of 0.76, both revealing the development of a semi-humid to semi-arid climate. Overall, the paleoclimate transitioned from warm and humid to later semi-humid conditions. After experiencing a short-term dry heat fluctuation, the characteristics of drought and heat are obvious in the early stage of J_2S (Figure 4).

According to the V/Cr parameter boundary proposed by Jones and Manning (1994), the J_1l sedimentary water body can be divided into two stages: hypoxic environment and oxygen-rich environment (Figure 4). In the J_1l^x segment, except for the bottom sample with a V/Cr value of 1.25, the V/Cr values of the other samples range from 1.56 to 4.63, with an average of 2.37, indicating a typical reducing environment. In the later stage, the V/Cr values of the J_1l^s samples significantly decrease to the range of 1.50–2.29, with an average value of 1.73, reflecting the transition of the water body from hypoxia to relatively oxygen enrichment. The variation trend of Ni/Co values is similar to that of V/Cr values, which also reveals the difference in the oxygen content of the water, but all the Ni/Co values

TABLE 1 XRD test results of the J_1l tight sandstones in the eastern Sichuan Basin.

Sample no.	Depth (m)	Relative content of ordinary non-clay mineral (%)								Relative content of clay mineral (%)					
		Quartz	K-feldspar	Plagioclas	Calcite	Dolomite	Siderite	Pyrite	Anhydrite	Total content	Kaolinite	Chlorite	Illite	I/S	C/S
AJY04	54.5	88.4	—	0.7	2.6	—	—	—	—	8.3	21.9	23.7	19.4	20.5	14.5
AJY12	113.5	51.7	2.9	21.3	1.9	0.1	0.4	—	—	21.7	47.0	6.6	19.7	15.0	11.7
AJY18	196.4	60.9	1.4	16.9	0.2	0.2	—	—	—	20.4	24.4	7.9	16.6	14.6	36.5
AJY23	223.0	59.3	5.0	25.1	0.2	1.4	—	—	—	9.0	6.4	11.9	8.6	1.8	71.3
AJY26	232.0	32.4	23.2	31.2	0.3	—	—	—	1.2	11.7	11.4	14.5	15.7	11.8	46.6
AJY28	242.5	35.9	10.1	36.7	0.2	—	0.4	—	1.4	15.3	12.0	18.3	11.3	12.8	45.6
AJY49	405.5	44.5	1.8	36.7	0.2	—	—	0.3	—	16.5	19.8	32.1	13.9	21.3	12.9
YJ1H01	2010.0	40.5	—	16.5	6.9		—	—	—	36.1	—	—	—	—	—
YJ1H02	2034.0	42.0	—	17.2	11.7	0.5	—	—	—	28.6	—	—	—	—	—
ZX1H01	1764.8	58.2	9.9	21.9	1.1	0.4	—	—	—	8.5	—	—	—	—	—
ZX1H02	1766.2	26.3	3.9	38.4	—	—	—	—	—	31.4	—	—	—	—	—
ZX1H03	1767.7	61.7	3.0	22.2	0.3	—	—	—	—	12.8	—	—	—	—	—
ZX1H04	1769.2	48.1	3.4	31.1	0.8	0.6	—	—	—	16.0	—	—	—	—	—
ZX1H05	1770.9	63.6	4.5	14.7	—	—	—	—	—	17.2	—	—	—	—	—
ZX1H06	1775.6	51.3	2.2	15.0	1.4	—	—	—	—	30.1	—	—	—	—	—
ZX1H07	1777.1	59.2	1.7	11.8	—	—	—	—	—	27.3	—	—	—	—	—
ZX1H08	1817.2	60.9	8.3	17.4	0.5	—	—	—	—	12.9	—	—	—	—	—
ZX1H09	1818.3	54.9	4.2	25.9	1.6	0.7	—	—	—	12.7	—	—	—	—	—
ZX1H10	1820.9	61.7	2.7	17.3	0.9	0.5	—	—	—	16.9	—	—	—	—	—
ZX1H11	1823.3	50.2	3.3	28.3	3.1	—	—	—	—	15.1	—	—	—	—	—
ZX1H12	1824.3	57.8	4.0	21.7	0.9	0.7	1.3	—	—	13.6	—	—	—	—	—

(Continued on the following page)

10.3389/feart.2024.1441548

TABLE 1 (*Continued*) XRD test results of the J_1l tight sandstones in the eastern Sichuan Basin.

Sample no.	Depth (m)	Relative content of ordinary non-clay mineral (%)									Relative content of clay mineral (%)					
		Quartz	K-feldspar	Plagioclase	Calcite	Dolomite	Siderite	Pyrite	Anhydrite	Total content	Kaolinite	Chlorite	Illite	I/S	C/S
ZX1H13	1825.5	45.0	13.4	23.2	0.6	—	—	—	—	17.8	—	—	—	—	—
ZX1H14	1826.9	35.3	18.6	23.1	—	0.8	—	—	—	22.2	—	—	—	—	—
ZX1H15	1895.5	59.5	—	15.9	7.6	—	—	—	—	17.0	—	—	—	—	—
ZX1H16	1897.5	66.6	—	16.2	3.2	—	—	—	—	14.0	—	—	—	—	—
ZX1H17	1907.5	61.8	—	20.3	2.3	—	—	—	—	15.6	—	—	—	—	—

are smaller than the previous boundary of 5.00 between poor and rich oxygen. On the one hand, this implies that the oxygen content in the study area is relatively low but still insufficient to be clearly defined as hypoxic conditions. On the other hand, this may reflect certain differences in the sedimentary response of continental and marine basins.

The paleosalinity can also be divided into two evolutionary stages: the J_1l^x segment characterized by salt water and the J_1l^s segment characterized by brackish water (Figure 4). The Sr/Ba value of the sample in the 6th sub-layer is relatively low, at 0.327, and then rapidly increases to 2.24 in the 21st sub-layer. Contrary to it, the Rb/K value gradually decreases from 0.007 at the bottom to 0.001, providing further confirmation of the brackish water environment. Form the J_1l^s period to the early J_2s stage, the distribution range of Sr/Ba values is 0.078–0.372, with an average value of 0.157, and the Rb/K values range from 0.004 to 0.007, with an average value of 0.005. Two types of parameters indicate that the water salinity decreased, with brackish water being the main component.

Under the warm and humid paleoclimate background of the early J_1l Formation, the Si/Al and Ti/Al values in the J_1l^x segment decreased significantly, which indicates relatively weak input intensity of terrigenous clastics, dropping from 3.176 to 0.063 in the 9th layer to 3.092 and 0.046 in the 21st layer, respectively. Controlled by the overall lake regression in the J_1l^s segment, the sand bodies show significant progradation characteristics. The Si/Al and Ti/Al values of the J_1l^s samples are distributed in the ranges of 2.703–3.365 and 0.037–0.052, with average values of 3.118 and 0.048, respectively, which are slightly higher than those in the J_1l^x segment (Figure 4).

4.2 Reservoir qualities

4.2.1 Porosity and permeability

A total of 155 measured data of the J_1l sandstones reveal that the porosity (Φ) and permeability (K) range from 0.48% to 11.24% and from 0.0003×10^{-3} μm^2 to 0.653×10^{-3} μm^2, with average values of 3.87% and 0.026×10^{-3} μm^2. Among them, the samples with porosity less than 6% account for 71.0% and the samples with permeability less than 0.05×10^{-3} μm^2 account for 91% (Figure 5A), indicating typical tight and ultra-tight sandstone reservoirs. In addition, there is a significant positive correlation between porosity and permeability as a whole, and there are two types of abnormal cases. Type A is characterized by low porosity with relatively high permeability, which may be due to the presence of micro-fractures enhancing the reservoir's permeability. Type B is characterized by relatively high porosity with low permeability, suggesting that the reservoir space may be dominated by primary pores (Figure 5A). Excluding the two types of abnormal data, the positive correlation coefficient of the remaining porosity and permeability data is about 0.0428.

4.2.2 Pore-throat structures

Consistent with low porosity, reservoir spaces of the J_1l sandstones are generally underdeveloped, primarily comprising original intergranular pores, secondary dissolution pores, and a few micro-fractures (Zhang et al., 2022; Yu et al., 2023). The micron

10.3389/feart.2024.1441548

FIGURE 3
Sedimentary structures of the J_1l tight sandstones in the eastern Sichuan Basin. **(A)** Well YD003-H2, 2104.3 m, J_1l^S segment, trough cross-bedding; **(B)** KLZ outcrop, J_1l^S segment, parallel bedding; **(C)** KLZ outcrop, J_1l^S segment, wedge-shaped cross bedding; **(D)** KLZ outcrop, J_1l^S segment, wavy bedding; **(E)** well YT1, 2167.3 m, J_1l^S segment, flaser bedding; **(F)** TBS outcrop, J_1l^X segment, oblique bedding and horizontal bedding; **(G)** well ZX1H, 1909.3 m, wave-ripple bedding; **(H)** well TD021-X8, 1800.62 m, J_1l^S segment, bottom surface of scour; **(I)** well TD109, 1330.9 m, ball–pillow structure; **(J)** well TD109, 1331.1 m, convolute bedding; **(K)** KLZ outcrop, J_1l^X segment, Muschel sandstone; **(L)** well ZX1H, 1896.9 m, J_1l^X segment, shell mudstone; **(M)** well YT1, 2152.3 m, J_1l^S segment; and **(N)** well YT1, 2152.3 m, J_1l^S segment, phytoclast.

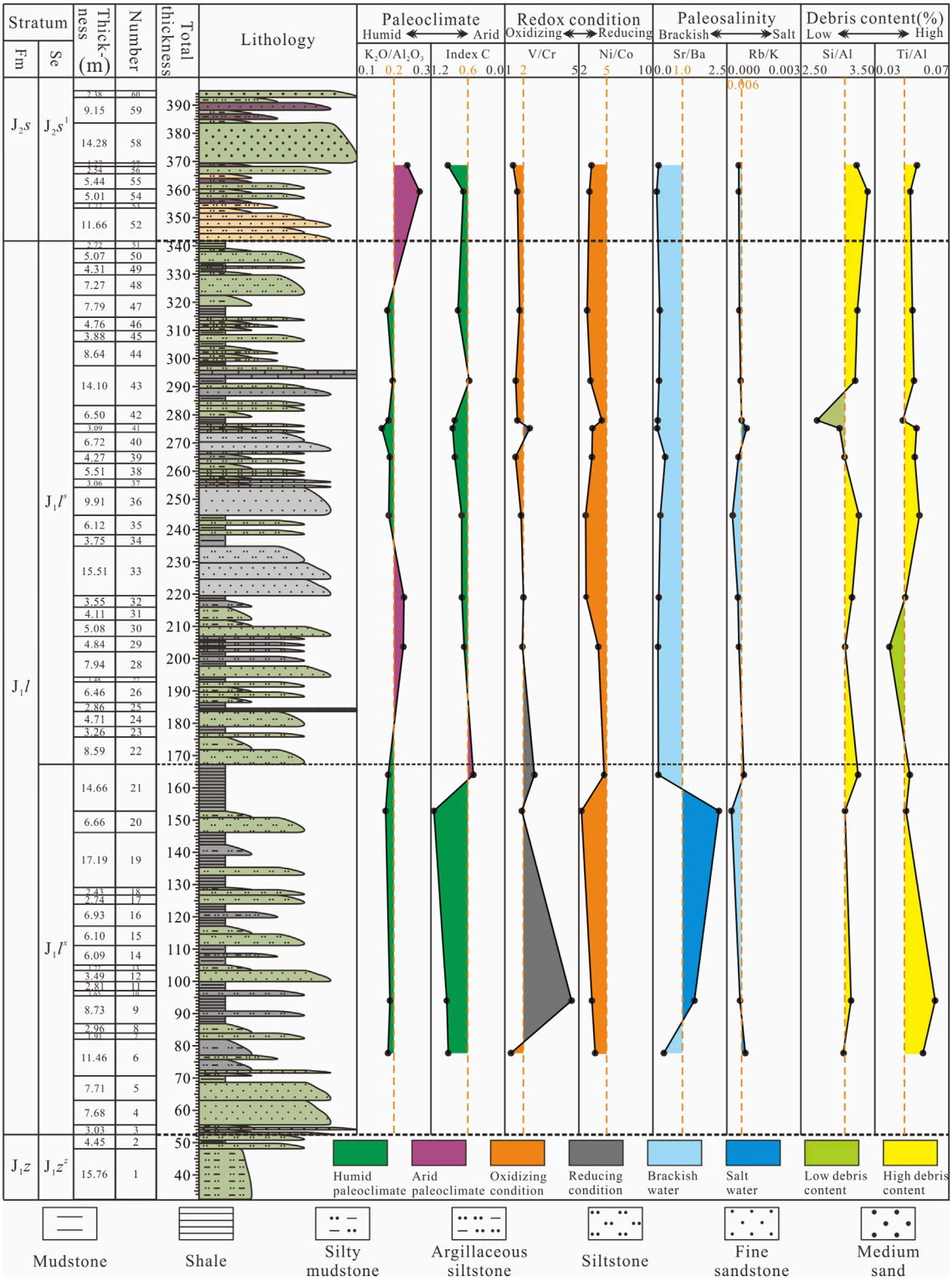

FIGURE 4
Geochemical profile and depositional environment of J_1l in AJY outcrop, eastern Sichuan Basin.

pores are connected by nanoscale throats, and the maximum pore-throat radius is 1.085 μm. The mean values of pore-throat radii are distributed in the range of 0.011–0.09 μm, and the median values range from 0.007 to 0.163 μm (Figure 5B). Meanwhile, the sorting coefficient and homogeneity coefficient of pore-throat structures are concentrated within the ranges of 0.99–2.27 and 0.22–0.31, with

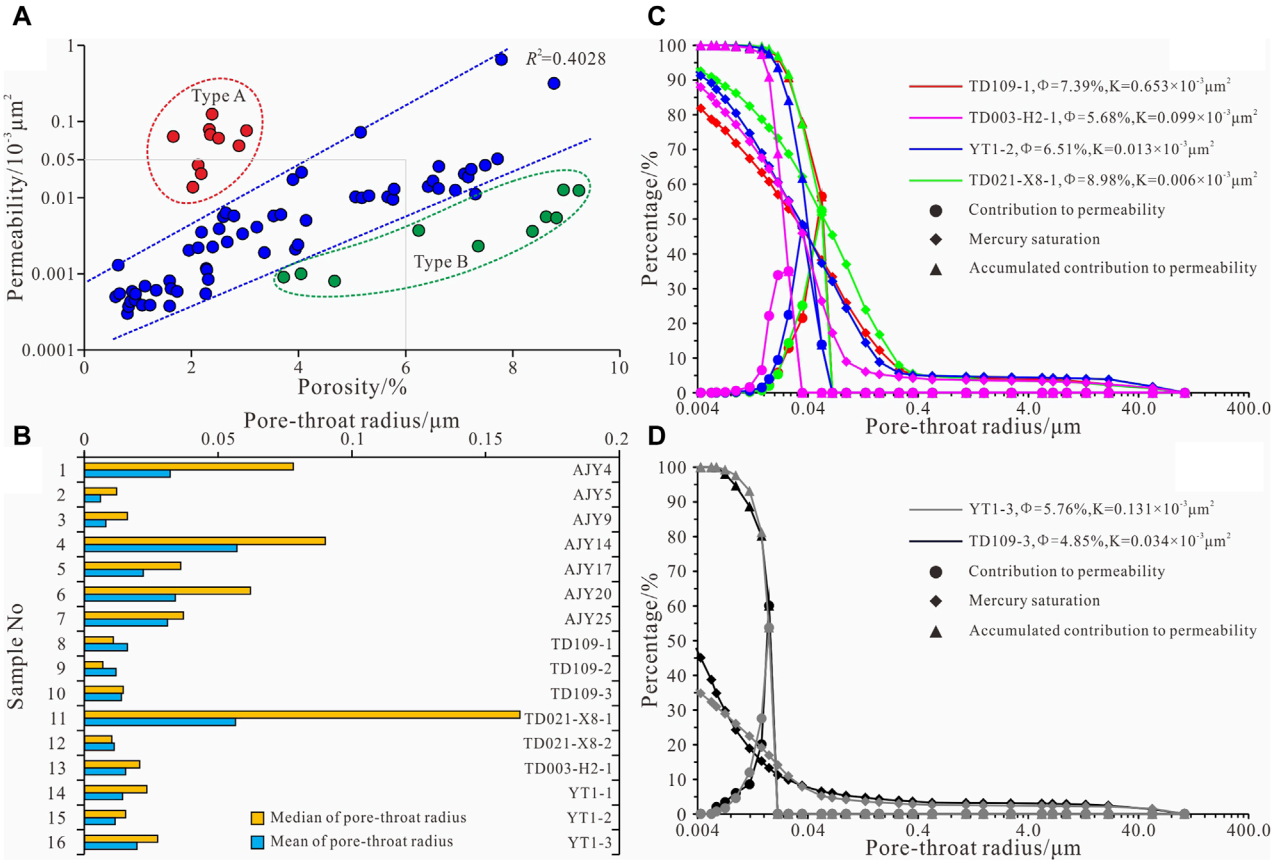

FIGURE 5
Reservoir properties and pore-throat structures of the J_1l tight sandstones in the eastern Sichuan Basin. **(A)** Distribution characteristics of porosity and permeability; **(B)** distribution characteristics of pore-throat radius; **(C)** pore-throat structures of relatively favorable reservoirs; and **(D)** pore-throat structures of relatively poor reservoir.

average values of 1.67 and 0.25, respectively, indicating that the pores and throats are not only tiny but also poorly sorted and highly heterogeneous. Comparing the samples with significant differences in mercury saturation, it is found that the oil saturation of tight sandstones is positively correlated with porosity and permeability but fundamentally depends on the maximum throat radius. For example, in Figures 5C, D, the samples with a mercury saturation of 83.7%–93.9% exhibit pore-throat radii ranging from 0.006 to 0.053 μm, whereas radii of the samples with a mercury saturation of 36.5%–49.4% are significantly reduced to 0.006–0.018 μm. However, the common feature is that the permeability of all samples is mainly contributed by the larger pore-throats. In contrast, the pore-throats with smaller radii may accumulate relatively large volumes but limited contribution to permeability.

5 Discussions

5.1 Sedimentological and diagenetic facies

5.1.1 Types and characteristics of sedimentary micro-facies in lacustrine delta-front

Under the continuous debris supply from the two provenance systems in the northeastern and southeastern Sichuan Basin (Yi et al., 2022; Cheng et al., 2023a; 2023b; Figure 1), sand bodies of the delta-front sub-facies are widely distributed in the study area, and the sedimentary micro-facies such as subaqueous distributary channels (SDC), mouth bars (MB), and sheet sands (SS) can be identified (Figure 6).

As the framework of the delta-front, the subaqueous distributary channels mainly deposit fine sandstones and siltstones, with obvious normal-graded bedding and bottom surface of scour (Figures 3H, 6). Vertically, the superposition of multiple channels creates a thick composite sand body, whose thickness and scale are controlled by the intensity and duration of flowing water, presenting a box-shaped or bell-shaped well-logging curve (Figure 6). On the plane, the channels extend far, and trough cross-bedding, wedge-shaped cross-bedding, and parallel bedding are often developed in the sand bodies, with common deformation structures (Figure 3).

After the fine-grained debris carried by the river enters the lake, it accumulates at the estuaries and forms mouth bars as the flow velocity decreases. The thickness of a single sand body is approximately 0.3–2.0 m, with reverse grading and swash bedding as typical identification marks (Figures 3G, 6). At the same time, bioturbation structures and shell layers can also be observed (Figure 3K), and the well-logging curve is generally funnel shaped (Figure 6). The sheet sand has the

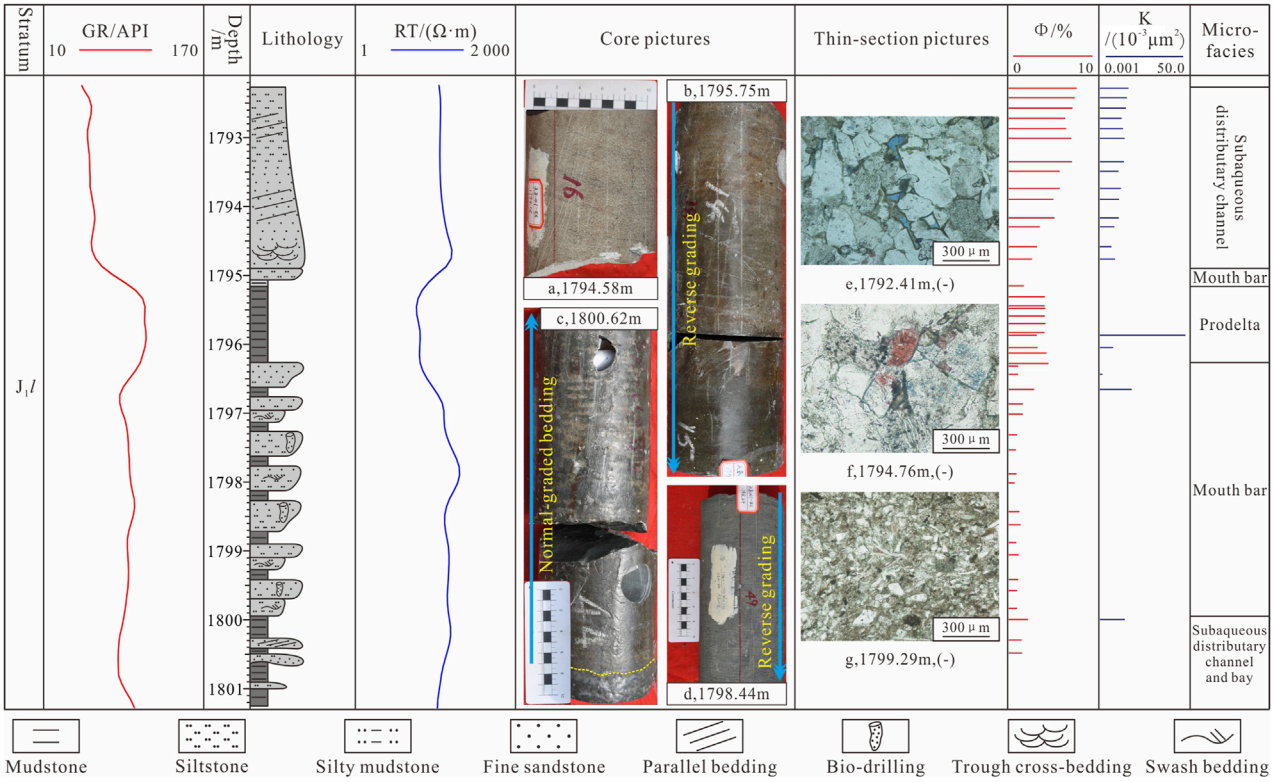

FIGURE 6
Sedimentary facies profile of the J_1l tight sandstones in well TD021-X8 in the eastern Sichuan Basin. Pic. a. 1794.58 m, trough cross-bedding; Pic. b. 1795.75 m, reverse grading; Pic. c. 1800.62 m, bottom surface of scour and normal-graded bedding; Pic. d. 1798.44 m, reverse grading; Pic. e. 1792.41 m, original intergranular pores; Pic. f. 1794.76 m, secondary dissolution pores; and Pic. g. 1799.29 m, argillaceous siltstone under strong compaction.

same structure as the mouth bars, with extensive cross-bedding but few biological fossils.

5.1.2 Types and characteristics of diagenetic facies in lacustrine delta-front

There are various types and multiple stages of diagenesis in the study area, and compaction and carbonate cementation are the most prominent and destructive to the reservoir quality. Although chlorite coatings and dissolution processes have increased the porosity and permeability to some extent, their effects are not significant. The relatively finer particles and higher content of the argillaceous matrix lead to strong compaction of the rock, with the particles exhibiting an overall linear contact relationship (Figure 7A), and the mica and debris particles are deformed due to compression (Figure 7B). After staining, calcite cement appears red under the microscope, filling intergranular pores and secondary dissolution pores (Figures 7C, D). It is found that the lowest and highest temperatures of fluid inclusions in calcite cement are 57.9° and 125°, respectively (Liu AQ. et al., 2023; Figure 7E), with the majority occurring in the late stages and often within the sand bodies near mudstones. The siliceous cementation event also occurs in two stages, and the thickest enlarged edge with a thickness of 1 mm mainly fills intergranular pores (Figure 7F). The chlorite coatings are usually formed before siliceous cementation and can even be considered one of the earliest diagenetic events, coexisting with intergranular pores (Figure 7G). This may be because the chlorite coatings resist a certain degree of compaction and pressolution (Ehrenberg, 1993; Bloch et al., 2002; Huang et al., 2021) and also hinder the contact between particles and pore fluids (Cho and Fawcett, 1986; Ehrenberg, 1993; Worden et al., 2020). However, the abundant intercrystalline pores in clay minerals may not completely prevent the exchange of matter and energy between pore fluids and particle surfaces. For instance, the feldspar wrapped in chlorite coatings can also undergo dissolution (Figure 7H), as can the siliceous nodules growing on chlorite flakes (Figure 7I).

Based on the reference of particle contact relationship and strength (Formula 1; Mou et al., 2017), pore-throat structure, and plane porosity, the three parameters, namely, the apparent compaction rate, apparent cementation rate, and apparent dissolution rate, are calculated according to Formulas 2–5 (Beard and Weyl, 1973; Yang et al., 2014; Lai et al., 2018; 2023; Liu HK. et al., 2023). Furthermore, the compaction, cementation, and dissolution are classified into three levels: strong, medium, and weak (Table 2).

$$\text{Contact Intensity(CI)} = \frac{1a + 1.5ab + 2b + 3c + 4d}{a + ab + b + c + d}, \quad (1)$$

where “a” represents the number of samples with point contact particles, “b” represents the number of samples with point-line contact particles, “c” represents the number of samples with

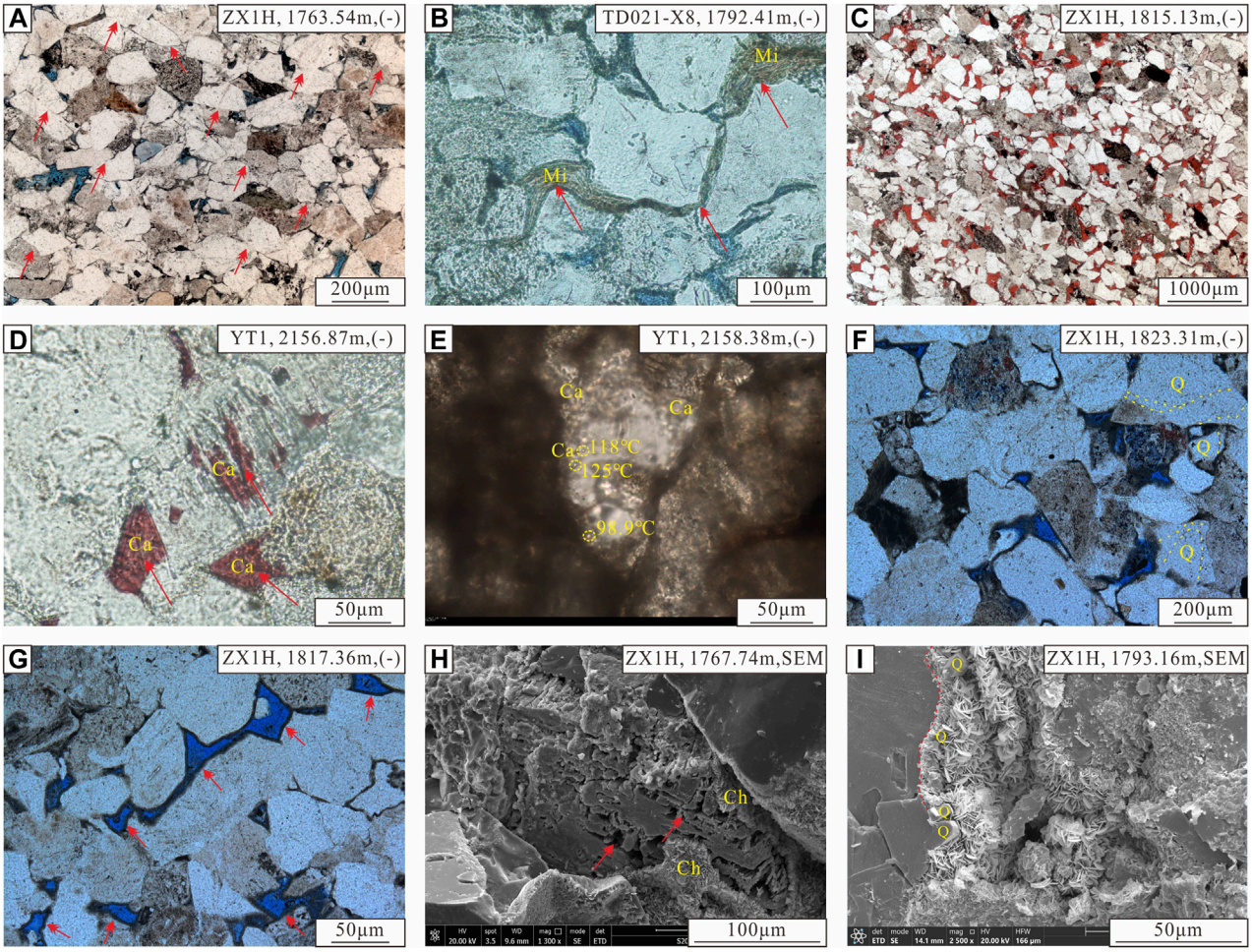

FIGURE 7
Diagenetic characteristics of the J_1l tight sandstones in the eastern Sichuan Basin. **(A)** Well ZX1H, 1763.54 m, J_1l^5 segment, linear and concavo–convex contact relationship between particles; **(B)** well TD021-X8, 1792.41 m, J_1l^5 segment, mica deformation under compression; **(C)** well ZX1H, 1815.13 m, J_1l^5 segment, strong calcite cementation; **(D)** well YT1, 2156.87 m, J_1l^5 segment, calcite cement-filled dissolution pores; **(E)** well YT1, 2,158.38 m, J_1l^5 segment, fluid inclusion temperature of calcite cement; **(F)** well ZX1H, 1823.31 m, J_1l^5 segment, two stages of siliceous cementation; **(G)** well ZX1H, 1817.36 m, J_1l^5 segment, chlorite coatings associated with intergranular pores; **(H)** well ZX1H, 1767.74 m, J_1l^5 segment, feldspar dissolution wrapped in chlorite coatings; and **(I)** well ZX1H, 1793.16 m, J_1l^5 segment, siliceous nodules growing on chlorite flakes.

TABLE 2 Classification criteria for diagenetic intensity of the J_1l tight sandstones in the eastern Sichuan Basin [modified from Yang et al. (2014), Peng et al. (2016), and Liu et al. (2023)].

Diagenetic intensity	Compaction			Cementation		Dissolution	
	R_{co} (%)	CI	Particle contact relationship	R_{ce} (%)	Cementation type	R_d (%)	Pore type
Strong	≥70	≥2.5	Linear and concavo–convex contact	≥70	Basal and porous cementation	≥60	Intragranular dissolution pores Interparticle dissolution pores Mold pores
Medium	30–70	1.5–2.5	Point-line contact	30–70	Contact cementation	30–60	Small-diameter dissolution pores
Weak	≤30	≤1.5	Point contact	≤30	Mosaic cementation	≤30	Scattered dissolution pores

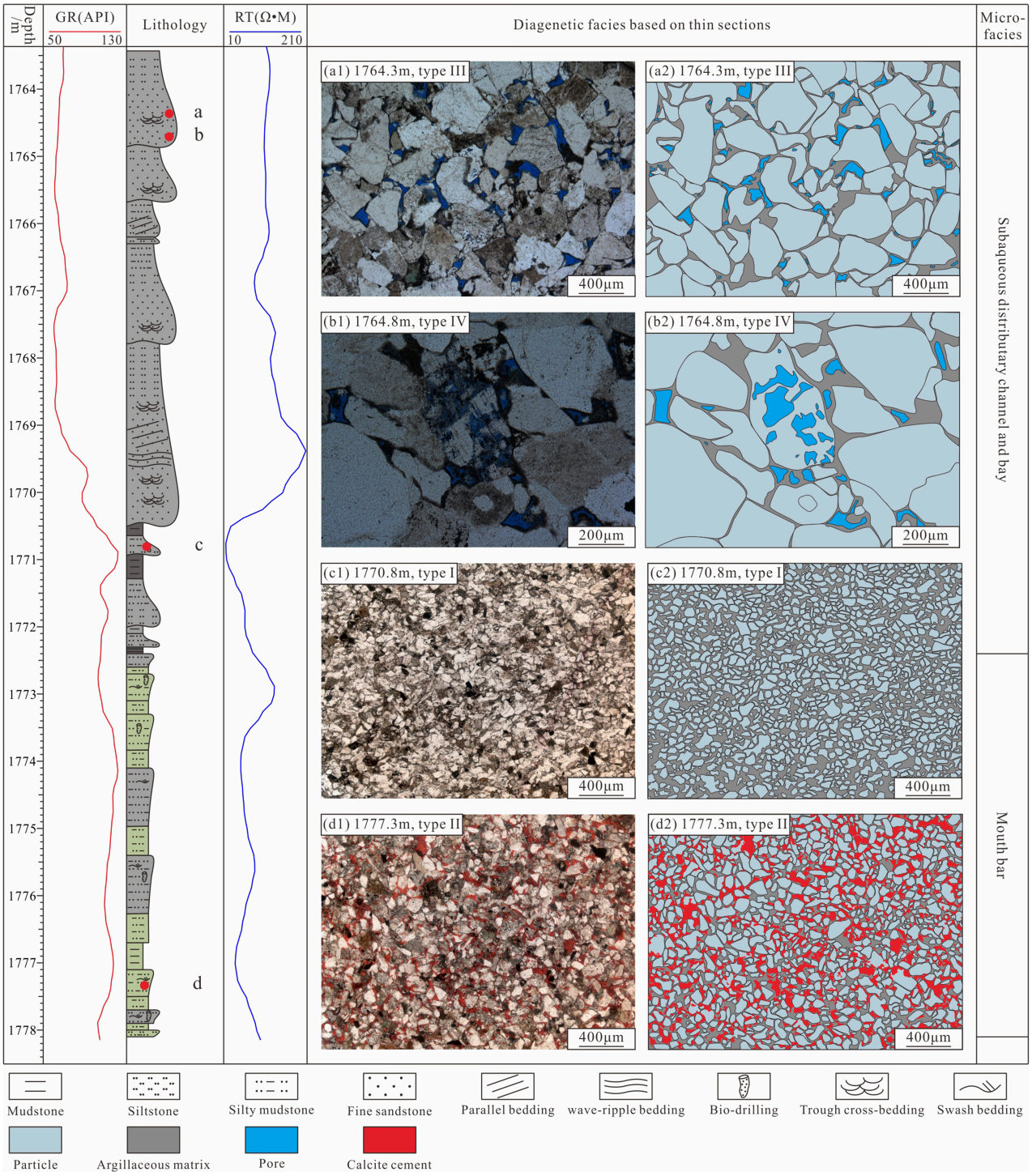

FIGURE 8
Sedimentological and diagenetic facies of the J_1l tight sandstones in Well ZX1H, eastern Sichuan Basin. Type I, strong compaction facies; type II, strong cementation facies; type III, chlorite-coating and intergranular pore facies; and type IV, weak dissolution and intragranular facies.

concavo–convex contact particles, and "d" represents the number of samples with stylolite contact particles.

$$\Phi_o = 20.91 + \frac{22.9}{S_0}, \tag{2}$$

$$R_{co} = \frac{\Phi_o - \Phi_r - V_c - V_m}{\Phi_0} \times 100\%, \tag{3}$$

$$R_{ce} = \frac{V_c}{V_c + \Phi_r} \times 100\%, \tag{4}$$

TABLE 3 Identification standards for sedimentological and diagenetic facies of the J_1l tight sandstones in the eastern Sichuan Basin.

Diagenetic facies		Sedimentary micro-facies	Lithology	Thin-section characteristic				Φ (%)	Well-logging response				
				R_{co} (%)	R_{ce} (%)	R_d (%)	P_d (%)		GR (API)	AC (μs/m)	RT (Ω•m)	DEN (g/cm^3)	CNL (%)
I	Strong compaction facies	MB and SS	Siltstone and argillaceous siltstone	78.6(12) 73.2-85.4	19.6(12) 14.6-26.8	0	0	1.42(12) 0.51-3.06	100.9(12) 63.6-116.8	64.8(12) 60.0-68.5	101.1(12) 55.4-260.8	2.65(12) 2.49-2.69	17.4(12) 10.8-22.4
II	Strong cementation facies	MB, SS, and edge of SDC	Various sandstones	37.6(9) 31.3-52.5	72.3(9) 67.5-78.7	0	0	1.84(9) 0.53-4.12	104.7(9) 97.1-114.5	64.1(9) 58.4-68.6	445.4(9) 59.6-1420.7	2.65(9) 2.63-2.70	14.5(9) 8.0-21.3
III	Chlorite-coating and intergranular pore facies	Middle of SDC and top of MB	Fine sandstone and siltstone	47.2(12) 27.8-59.3	13.8(12) 9.3-17.2	15.4(12) 13.2-17.6	31.8(12) 27.5-39.7	5.95(12) 1.74-7.97	68.3(12) 55.0-79.6	68.7(12) 60.1-80.8	76.2(12) 18.3-117.6	2.52(12) 2.43-2.60	15.4(12) 9.5-24.5
IV	Weak dissolution and intragranular pore facies	Middle of SDC and top of MB	Fine sandstone and siltstone	51.8(9) 39.2-76.3	23.4(9) 14.6-31.4	26.9(9) 16.5-28.8	57.4(9) 47.2-63.9	7.05(9) 5.53-8.35	68.2(9) 60.6-74.7	67.2(9) 64.0-70.4	92.8(9) 66.6-132.1	2.51(9) 2.44-2.61	16.3(9) 6.0-27.7
V	Medium compaction and cementation facies	Top and bottom of SDC	Fine sandstone and siltstone	56.7(21) 17.3-66.4	42.1(21) 30.7-54.8	9.5(21) 8.1-12.4	24.7(21) 18.8-29.5	3.75(21) 1.96-7.40	82.7(21) 65.5-100.6	65.0(21) 61.2-69.8	122.1(21) 38.1-335.3	2.59(21) 2.48-2.73	15.4(21) 6.4-34.3

Data in Table 3 can be expressed as $\frac{\text{Average value (Sample quantity)}}{\text{Minimum value–Maximum value}}$.

10.3389/feart.2024.1441548

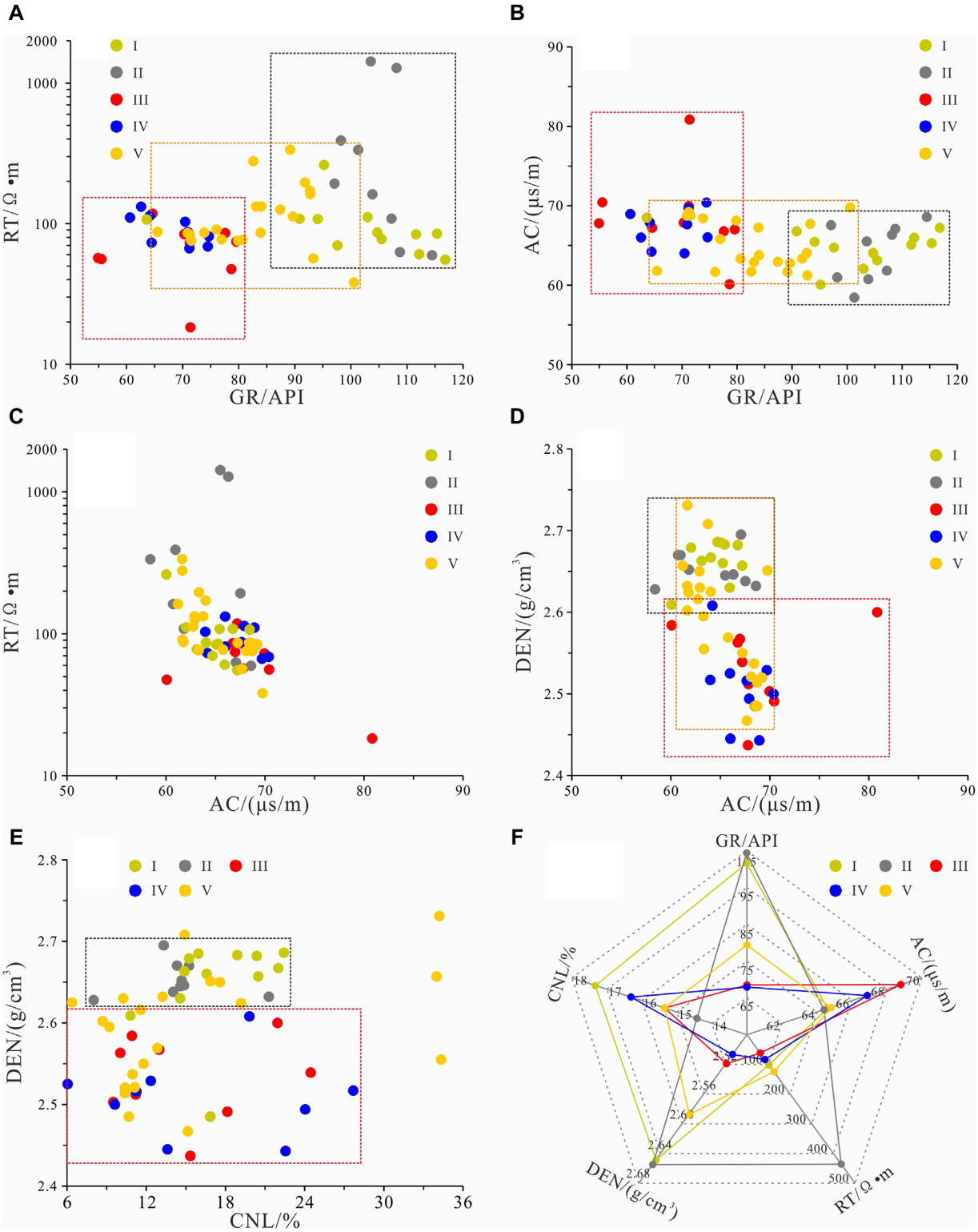

FIGURE 9
Well-logging parameter crossplots of the J_1l diagenetic facies in the eastern Sichuan Basin. I: Strong compaction facies; II: Strong cementation facies; III: Chlorite coating and intergranular pore facies; IV: Weak dissolution and intragranular facies; V: Medium compaction and cementation facies. **(A)**: The Interaction diagram between GR and RT; **(B)**: The Interaction diagram between GR and AC; **(C)**: The Interaction diagram between AC and RT; **(D)**: The Interaction diagram between AC and DEN; **(E)**: The Interaction diagram between CNL and DEN; **(F)**: The radar chart among GR, AC, RT, DEN, CNL.

$$R_d = \frac{P_d}{P_a} \times 100\%, \quad (5)$$

where Φ_o and Φ_r indicate the original porosity and current residual intergranular porosity, respectively, the unit is %; S_o is the sorting coefficient, dimensionless; R_{co}, R_{ce}, and R_d represent the apparent compaction rate, apparent cementation rate, and apparent dissolution rate, respectively, all in percentage (%); V_c and V_m refer to the volume fractions of diagenetic cements and micropores in the argillaceous matrix, %; and P_d and P_a stand for the plane porosity of secondary dissolution pores, all pores in percentage (%). These parameters are estimated through quantitative statistics of casting thin sections under the microscope.

Based on the sedimentary micro-facies and anatomy of sand bodies, and considering the relative intensities of various diagenesis and predominant types of micro-pores, a composite nomenclature is adopted in this study, using "sedimentary micro-facies (sand body parts) + typical diagenetic events + predominant pore types." Five diagenetic facies, including strong compaction facies (type I), strong cementation facies (type II), chlorite-coating and intergranular pore facies (type III), weak dissolution and intragranular facies (type IV), and medium compaction and cementation facies (type V) have been identified (Figure 8; Table 3). Metasomatism is common, but its impact on reservoir quality is limited, so no further discussion will be conducted here.

In well ZX1H, the strong compaction facies (type I) and strong cementation facies (type II) are mainly distributed in MB and SS with the finer particle size and higher content of the argillaceous matrix, as well as along the edges of SDC, which are characterized by the high R_{co} value of 73.2%–85.4% (av. 78.6%) and the R_{ce} value of 67.5%–78.7% (av. 72.3%), respectively. Simultaneously, there is almost no secondary dissolution, and R_d and P_d values are close to zero (Figure 8; Table 3). The chlorite-coating facies and weak dissolution facies improve the reservoir quality by protecting the primary intergranular pores or increasing the secondary intragranular pores (Figure 8), with the average porosities of 5.95 and 7.05 significantly higher than 1.42 and 1.84 of type I and type II diagenetic facies (Table 3). The R_{co} and R_{ce} parameters indicate that both of them are characterized by moderate compaction and weak cementation diagenesis, whereas R_d and P_d reveal varying degrees of dissolution (Table 3). It is clear that type III and type IV diagenetic facies in the middle of SDC and the top of MB are indicators for finding favorable reservoirs in the study area (Figure 8). The medium compaction and cementation facies (type V) are common in siltstones and fine sandstones at the top and bottom of SDC, resulting in porosity ranging from 1.96% to 7.40%, with an average value of 3.75% (Table 3).

5.2 Well-logging responses of sedimentological and diagenetic facies

When the matrix minerals of rocks, that is, the sedimentary facies, are essentially determined, the differences in diagenetic characteristics, pore structures, and physical properties of various diagenetic facies lead to their different responses on well-logging data. On the basis of deep repositioning of core samples and standardization of well-logging curves, the longitudinal continuous identification of diagenetic facies can be achieved by summarizing the well-logging response patterns of different diagenetic facies (Peng et al., 2016; Lai Jet al., 2018; Liu AQ. et al., 2023). Natural gamma (GR) ray well logging can reflect the sedimentary environment and lithology, and density (DEN), interval transit time (AC), and neutron porosity (CNL) well logging are intuitive displays of reservoir physical properties, whereas resistivity well logging can indirectly reflect the pore structures of reservoirs (Cao et al., 2015; Huang et al., 2022). Therefore, according to the correlation among GR, AC, RT, DEN, CNL, and diagenetic facies, well-logging identification standards for diagenetic facies have been established (Figure 9; Table 3).

First, by intersecting GR with RT and AC, respectively, the constructive type III and type IV diagenetic facies can be clearly distinguished from the destructive type I and type II diagenetic facies, whereas the transitional type V intersects with both of them (Figures 9A, B). Affected by strong compaction and relatively high content of argillaceous matrix, type I diagenetic facies is characterized by high amplitude GR in the range of 63.6–116.8 API (av. 100.9 API) and medium amplitude RT in the range of 55.4–260.8 Ω•m (av. 101.1 Ω•m) (Table 3). After being strongly cemented by calcite, the reservoir porosity decreases, and the rock density increases, resulting in "three high and two low" well-logging responses of type II diagenetic facies, that is, high RT (59.6–1420.7 Ω•m, av. 445.4 Ω•m), high DEN (2.63–2.70 g/cm^3, av. 2.65 g/cm^3), high GR (97.1–114.5 API, av. 104.7 API), low CNL (8.0%–21.3%, av. 14.5%), and low AC (58.4–68.6 μs/m, av. 64.1 μs/m) (Figures 9A–E; Table 3). On the contrary, the development of chlorite coatings is beneficial for maintaining porosity, as evidenced in well-logging data by low GR (55.0–79.6 API, av. 68.3 API), low RT (18.3–117.6 Ω•m, av. 76.2 Ω•m), low DEN (2.43–2.60 g/cm^3, av. 2.52 g/cm^3), and relatively high AC (60.1–80.8 μs/m, av. 68.7 μs/m), along with moderate CNL (9.5%–24.5%, av. 15.4%) as typical features (Figures 9A–E; Table 3). The well-logging responses of type IV diagenetic facies are essentially consistent with these, with only slight increases in RT and CNL, ranging from 66.6 Ω•m to 132.1 Ω•m (av. 92.8 Ω•m) and 6.0% to 27.7% (av. 16.3%), respectively (Table 3). The radar chart indicates that as favorable tight sandstone reservoirs, type III and type IV diagenetic facies can be identified by high AC and low GR, DEN, and RT, whereas the ineffective exploration targets of type I and type II diagenetic facies exhibit high GR, DEN, CNL, and RT (Figure 9F).

5.3 Machine learning method of sedimentological and diagenetic facies and its application

Machine learning can efficiently process large-scale geological data, including geophysical data and chemical properties of rock samples. In the processing, machine learning fully excavates well-logging information, automatically selects key parameter features related to sedimentological and diagenetic facies, and accelerates data decision-making behaviors, reducing subjectivity

TABLE 4 Machine learning models and prediction results of the J_1l diagenetic facies in the eastern Sichuan Basin.

Sample no.	AC (μs/m)	CAL (cm)	CNL (%)	DEN (g/cm^3)	GR (API)	RT (Ω•m)	RXO (Ω•m)	Label	
0	65.559	9.169	11.572	2.664	103.105	54.534	50.788	Type I	Strong compaction facies
1	66.381	9.820	13.498	2.604	124.422	39.383	36.643	Type I	Strong compaction facies
2	67.803	10.021	16.844	2.565	127.910	30.057	27.748	Type V	Medium compaction and cementation facies
3	67.629	9.849	24.650	2.541	120.058	23.508	21.481	Type III	Chlorite-coating and intergranular pore facies
4	67.205	9.708	25.402	2.543	111.427	24.251	22.053	Type IV	Weak dissolution and intragranular pore facies
…	…	…	…	…	…	…	…	…	…
9,806	67.778	9.493	14.675	2.396	82.379	20.178	21.717	Type II	Strong cementation facies
9,807	67.780	9.149	14.675	2.307	80.447	20.195	21.698	Type II	Strong cementation facies
9,808	67.809	7.805	14.583	2.256	78.224	20.261	21.729	Type III	Chlorite-coating and intergranular pore facies
9,809	67.780	6.788	14.824	2.238	79.169	20.390	21.849	Type III	Chlorite-coating and intergranular pore facies
9,810	67.787	6.310	14.751	2.246	82.098	20.397	21.918	Type III	Chlorite-coating and intergranular pore facies

and human errors (Zheng et al., 2021; Antariksa et al., 2022; Zhao et al., 2022; Gu et al., 2023; Hansen et al., 2023). The common prediction models include decision tree algorithm, random forest algorithm, and Bayesian algorithm (Zheng et al., 2021; Antariksa et al., 2022; Hansen et al., 2023). For the identification of diagenetic facies in logging, probabilistic neural network is used, and the simulated classification surface is close to the surface under the Bayesian optimal criterion.

On the basis of the mentioned sedimentological and diagenetic facies and their well-logging responses, CAL and RXO well-logging data are added to the well-logging database after standardization, serving as the input data for machine learning. In order to enhance the model's generalization ability, 70% of the data are randomly extracted as the training samples (Table 4). During the training process, the remaining 30% data are used as the validation dataset to test the recognition results of different well-logging combinations. As shown in Figure 10, five of the six thin sections from well TD021-X8 match the expected values, and the overall accuracy of the training results is around 75%, indicating that the training results are relatively reliable. The diagenetic facies of type III and type IV are mostly developed in the middle of thick subaqueous distributary channels (Figure 10), making them the preferred exploration targets for favorable reservoirs in lacustrine delta-front tight sandstones.

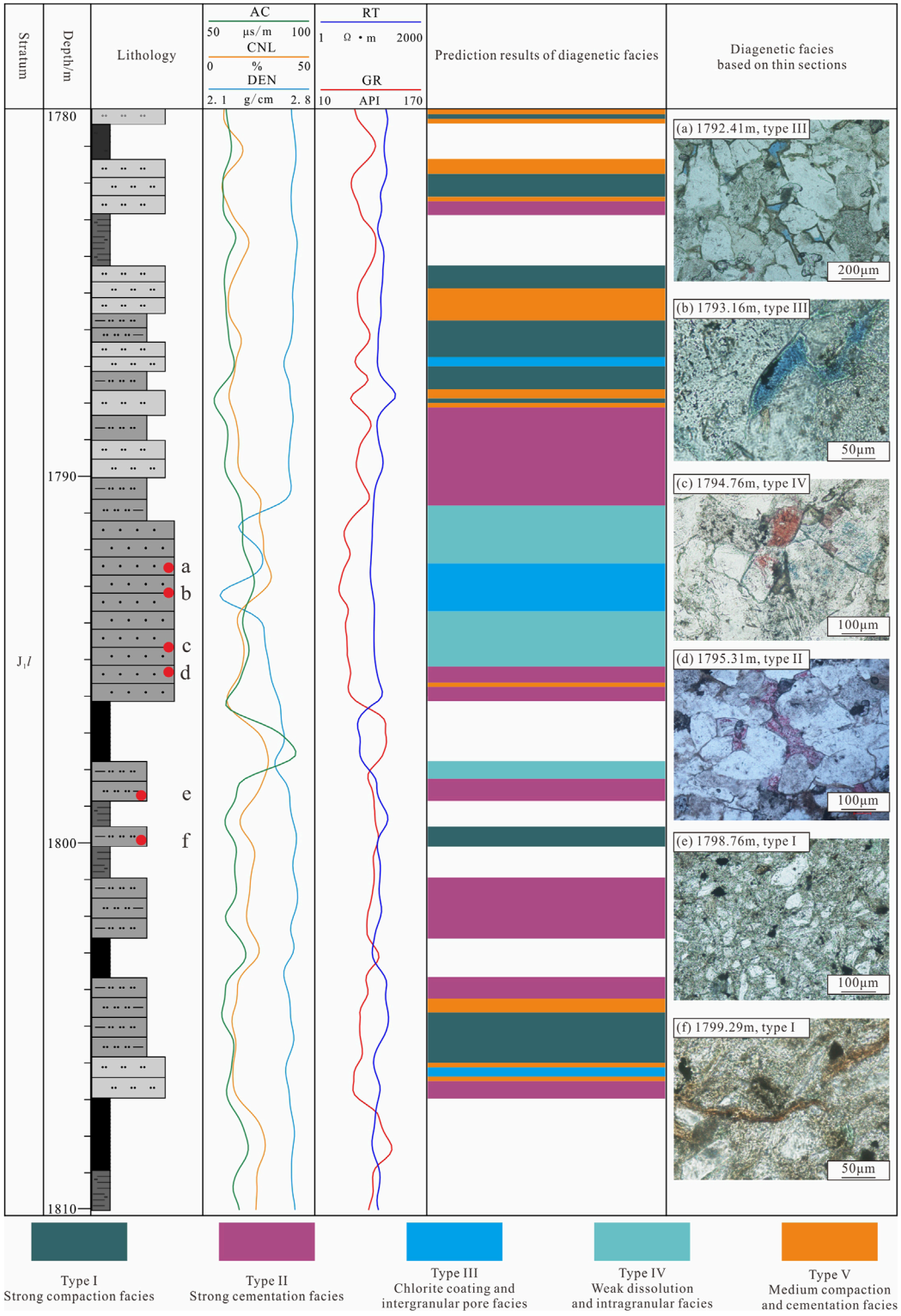

FIGURE 10
Machine learning results of the J_1l diagenetic facies in well TD021-X8, eastern Sichuan Basin.

6 Conclusion

Taking the J_1l delta-front tight sandstones in the eastern Sichuan Basin as a case, the types, characteristics, and well-logging responses of the main sedimentological and diagenetic facies were analyzed in detail, and the understanding was further applied to petroleum exploration by means of the machine learning method. The main conclusions are as follows.

(1) Under the warm and humid paleoclimate and lake transgression and regression cycles, J_1l develops lacustrine delta-front sub-facies, which are mainly characterized by subaqueous distributary channels and mouth bars.
(2) The J_1l sandstones exhibit typical dense features, with porosity and permeability in the range of 0.48%–11.24% (av. 3.87%) and 0.0003×10^{-3} μm^2–0.653×10^{-3} μm^2 (av. 0.026×10^{-3}μm^2), respectively, and the reservoir quality largely depends on the pore–throat content with radii greater than 0.006 μm. Strong compaction and cementation are the major diagenetic events leading to densification, whereas chlorite coatings and weak dissolution, as constructive diagenetic processes, retain some primary pores and increase a few dissolution pores.
(3) According to the types and development degree of sedimentary micro-facies, diagenesis, and pore–throats, five sedimentological and diagenetic facies have been identified in the J_1l tight sandstones, namely, strong compaction facies of MB and SS (type I); strong cementation facies of MB, SS, and the edge of SDC (type II); chlorite-coating and intergranular pore facies in the middle of SDC and the top of MB (type III); weak dissolution and intragranular facies in the middle of SDC and the top of MB (type IV); and medium compaction and cementation facies at the top and bottom of SDC (type V).
(4) The sedimentological and diagenetic facies of type III and type IV are favorable tight sandstone reservoirs in lacustrine delta-front, characterized by high AC and low GR, DEN, and RT in well logging. On the basis of the sedimentological and diagenetic facies and their well-logging responses, CAL and RXO well-logging data are added to the well-logging database after standardization, serving as the input data for machine learning. In addition, the training results are relatively reliable. The thick-layer, coarse-grained subaqueous distributary channels, in which the diagenetic facies of type III and type IV are mostly developed, have been identified as the primary exploration targets for tight hydrocarbon reservoirs.

Data availability statement

The original contributions presented in the study are included in the article material; further inquiries can be directed to the corresponding author.

Author contributions

CY: data curation, investigation, software, and writing–original draft. WG: data curation, investigation, methodology, software, and writing–original draft. LC: conceptualization, funding acquisition, resources, supervision, validation, visualization, writing–original draft, writing–review and editing, data curation, and methodology. YZ: formal analysis, funding acquisition, project administration, supervision, validation, and writing–review and editing. ZZ: formal analysis, funding acquisition, project administration, resources, validation, and writing–review and editing. YL: methodology, software, supervision, validation, and writing–original draft. TY: conceptualization, methodology, supervision, validation, and writing–review and editing.

Funding

The authors declare that financial support was received for the research, authorship, and/or publication of this article. This work was co-supported by the National Natural Science Foundation of China (Nos 41906188 and 42372139) and the Science and Technology Program of Sichuan Province (Nos 2022NSFSC0990 and 2023NSFSC1986).

Acknowledgments

The authors would like to appreciate PetroChina Southwest Oil and Gas Field Company for providing rock samples and partial testing data.

Conflict of interest

Author YZ was employed by PetroChina Changqing Oilfield Company.

The remaining authors declare that the research was conducted in the absence of any commercial or financial relationships that could be construed as a potential conflict of interest.

Publisher's note

References

Alam, K., Abdullatif, O., El-Husseiny, A., and Babalola, L. (2022). Depositional and diagenetic controls on reservoir heterogeneity and quality of the Bhuban formation, Neogene Surma Group, Srikail Gas Field, Bengal Basin, Bangladesh. *J. Asian Earth Sci.* 223. doi:10.1016/j.10.1016/J.JSEAES.2021.104985

Antariksa, G., Muammar, R., and Lee, J. (2022). Performance evaluation of machine learning-based classification with rock-physics analysis of geological lithofacies in Tarakan Basin, Indonesia. *J. Petroleum Sci. Eng.* 208, 109250. doi:10.1016/j.petrol.2021.109250

Bahrehvar, M., Mehrabi, H., Akbarzadeh, S., and Rahimpour-Bonab, H. (2021). Depositional and diagenetic controls on reservoir quality of the uppermost Jurassic-Lower Cretaceous sequences in the Persian Gulf; a focus on J–K boundary. *J. Petroleum Sci. Eng.* 201, 108512. doi:10.1016/j.petrol.2021.108512

Beard, D. C., and Weyl, P. K. (1973). Influence of texture on porosity and permeability of unconsolidated sand. *AAPG Bull.* 57 (2), 349–369. doi:10.1306/819a4272-16c5-11d7-8645000102c1865d

Beckmann, B., Flögel, S., Hofmann, P., Schulz, M., and Wagner, T. (2005). Orbital forcing of cretaceous river discharge in tropical africa and ocean response. *Nature* 437, 241–244. doi:10.1038/nature03976

Bloch, S., Lander, R. H., and Bonnell, L. (2002). Anomalously high porosity and permeability in deeply buried sandstone reservoirs: origin and predictability. *AAPG Bull.* 86 (2), 301–328. doi:10.1306/61eedabc-173e-11d7-8645000102c1865d

Cai, L. X., Guo, X. W., Zhang, X. H., Zeng, Z., Xiao, G., Pang, Y., et al. (2019). Pore-throat structures of the permian longtan formation tight sandstones in the South yellow sea basin, China: a case study from borehole CSDP-2. *J. Petroleum Sci. Eng.* 186, 106733. doi:10.1016/j.petrol.2019.106733

Cai, L. X., Zhang, X. H., Guo, X. W., Gao, X. H., Pang, Y. M., and Zhu, X. Q. (2023). Formation mechanisms and geological significance of the lower triassic fine-grained mixed sedimentary rocks in the central uplift of the South yellow sea basin, eastern China. *J. Asian Earth Sci.* 247, 105609. doi:10.1016/j.jseaes.2023.105609

Cao, Y. C., Xi, K. L., Zhao, X. Z., Jin, F. M., Zhou, L., Su, R., et al. (2015). Reservoir diagenetic facies and its logging identification of Es4s in Langgu sag. *J. Central South Univ. Sci. Technol.* 46 (11), 4183–4194. (in Chinese with English abstract).

Carvalho, M. V. F., De Ros, L. F., and Gomes, N. S. (1995). Carbonate cementation patterns and diagenetic reservoir facies in the Campos Basin Cretaceous turbidites, offshore eastern Brazil. *Mar. Petroleum Geol.* 12 (7), 741–758. doi:10.1016/0264-8172(95)93599-y

Chen, Y. H., and Liu, Y. (1994). Diagenetic facies — a new approach to the prediction of reservoir rocks. *Exp. Pet. Geol.* 16 (3), 274–281. (in Chinese with English abstract).

Cheng, D. W., Zhang, Z. J., Hong, H. T., Zhang, S., Qin, C., Yuan, X., et al. (2023a). Sequence structure, sedimentary evolution and their controlling factors of the jurassic Lianggaoshan Formation in the east Sichuan Basin, SW China. *Petroleum Explor. Dev.* 50 (2), 293–305. doi:10.1016/s1876-3804(23)60388-x

Cheng, D. W., Zhang, Z. J., Hong, H. T., Zhang, S., Qin, C., Yuan, X., et al. (2023b). Sequence structure, sedimentary evolution and their controlling factors of the jurassic Lianggaoshan Formation in the east Sichuan Basin, SW China. *Petroleum Explor. Dev.* 50, 293–305. doi:10.1016/s1876-3804(23)60388-x

Cho, M. S., and Fawcett, J. J. (1986). Morphologies and growth mechanisms of synthetic mg-chlorite and cordierite. *Am. Mineralogist* 71 (1-2), 78–84.

Cui, Y. F., Wang, G. W., Jones, S. J., Zhou, Z., Ran, Y., Lai, J., et al. (2017). Prediction of diagenetic facies using well logs — a case study from the upper Triassic Yanchang Formation, Ordos Basin, China. *Mar. Petroleum Geol.* 81, 50–65. doi:10.1016/j.marpetgeo.2017.01.001

Dai, J. X., Ni, Y. Y., Liu, Q. Y., Wu, X., Gong, D., Hong, F., et al. (2021). Sichuan super gas basin in southwest China. *Petroleum Explor. Dev.* 48 (6), 1251–1259. doi:10.1016/s1876-3804(21)60284-7

Dill, H. G., Khishigsuren, S., Melcher, F., Bulgamaa, J., Bolorma, K., Botz, R., et al. (2005). Facies-related diagenetic alteration in lacustrine-deltaic red beds of the paleogene ergeliin zoo formation (erdene sum area, S. Gobi, Mongolia). *Sediment. Geol.* 181, 1–24. doi:10.1016/j.sedgeo.2005.06.007

Ehrenberg, S. N. (1993). Preservation of anomalously high porosity in deeply buried sandstones by grain-coating chlorite: examples from the Norwegian continental shelf. *AAPG Bull.* 77 (7), 1260–1286. doi:10.1306/bdff8e5c-1718-11d7-8645000102c1865d

Fang, W. X. (2020). Classification and types of diagenetic lithofacies systems in the sedimentary basin. *Geol. Bull. China* 39 (11), 1692–1714. (in Chinese with English abstract).

Greber, N. D., and Dauphas, N. (2019). *The chemistry of fine-grained terrigenous sediments reveals a chemically evolved Paleoarchean emerged crust*, 255, 247–264.

Gu, Y. F., Li, Y., Yang, Y. S., Xiao, B., Zhang, D., and Bao, Z. (2023). Classification pattern of lacustrine carbonate diagenetic facies and logging-based data-driven prediction via a generalized and robust ensemble learning: a demonstration of pre-salt profile, santos basin. *Geoenergy Sci. Eng.* 223, 211543. doi:10.1016/j.geoen.2023.211543

Guo, J. Y., Qi, X. N., Hou, L. H., Hao, A., Zeng, X., Lin, S., et al. (2022). Origin and accumulation models of ultra-low permeability-tight sandstone (gravel) gas in Bohai Bay Basin, China. *J. Nat. Gas Geoscience* 7, 211–223. doi:10.1016/j.jnggs.2022.08.002

Haile, B. G., Klausen, T. G., Czarniecka, U., Xi, K., Jahren, J., Hellevang, H., et al. (2017). How are diagenesis and reservoir quality linked to depositional facies? A deltaic succession, Edgeøya, Svalbard. *Mar. Pet. Geol.* 92, 519–546. doi:10.1016/j.marpetgeo.2017.11.019

Han, Z., Hu, X. M., Hu, Z. Y., Jenkyns, H. C., and Su, T. (2022). Geochemical evidence from the Kioto Carbonate Platform (Tibet) reveals enhanced terrigenous input and deoxygenation during the early Toarcian. *Glob. Planet. Change* 215, 103887. doi:10.1016/j.gloplacha.2022.103887

Hansen, H. N., Haile, B. G., Müller, R., and Jahren, J. (2023). New direction for regional reservoir quality prediction using machine learning - example from the Stø Formation, SW Barents Sea, Norway. *J. Petroleum Sci. Eng.* 220, 111149. doi:10.1016/j.petrol.2022.111149

He, D. F. (2022). Multi-cycle superimposed sedimentary basins in China: formation, evolution, geologic framework and hydrocarbon occurrence. *Earth Sci. Front. (in Chinese with English abstract)* 29 (6), 24–59. doi:10.13745/j.esf.sf.2022.8.1

He, Z., Shi, J. A., Tang, Y., Ding, C., and Zhang, S. C. (2011). Characteristics of diagenesis and diagenetic facies of permian clastic reservoir in northwest margin of junggar basin. *Acta Sedimentologica Sinica (in Chinese with English abstract)* 29 (6), 1069–1078. doi:10.14027/j.cnki.cjxb.2011.06.003

Henares, S., Caracciolo, L., Cultrone, G., Fernández, J., and Viseras, C. (2014). The role of diagenesis and depositional facies on pore system evolution in a Triassic outcrop analogue (SE Spain). *Marine and Petroleum Geology* 51, 136–151. doi:10.1016/j.marpetgeo.2013.12.004

Huang, H. Y., He, D. F., Li, Y. Q., and Zhang, C. (2023). Provenance and paleogeography of the Early Paleozoic basin in the northern Yangtze Block: constraints from detrital zircon U-Pb-Hf data. *Gondwana Research* 125, 210–228. doi:10.1016/j.gr.2023.08.011

Huang, L. S., Yan, J. P., Liu, M. J., Zhang, Z., Ye, S. J., Zhang, F., et al. (2022). Diagenetic facies logging identification and application of deep tight sandstone gas reservoir: a case study of the third member of Xujiahe formation in Dayi area of western Sichuan depression. *Journal of China University of Mining & Technology* 51 (1), 107–123. (in Chinese with English abstract). doi:10.13247/j.cnki.jcumt.001325

Huang, X., Duan, D. P., Liu, B. B., Li, B. Y., Ding, F., Wang, W., et al. (2021). Origin mechanism of chlorite and its impact on reservoir properties in Huagang Formation, Xihua Depression. *Journal of Jilin University* 51 (3), 669–679. (Earth Science Edition) (in Chinese with English abstract). doi:10.13278/j.cnki.jjuese.20200149

Jia, C. Z., Pang, X. Q., and Song, Y. (2023). Whole petroleum system and ordered distribution pattern of conventional and unconventional oil and gas reservoirs. *Petroleum Science* 20, 1–19. doi:10.1016/j.petsci.2022.12.012

Jia, C. Z., Zou, C. N., Yang, Z., Zhu, R., Chen, Z., Zhang, B., et al. (2018). Significant progress of continental petroleum geological theory in basins of Central and Western China. *Petroleum Exploration and Development* 45 (4), 573–588. doi:10.1016/s1876-3804(18)30064-8

Jones, B., and Manning, D. A. C. (1994). Comparison of geochemical indices used for the interpretation of palaeoredox conditions in ancient mudstones. *Chemical Geology* 111, 111–129. doi:10.1016/0009-2541(94)90085-x

Kane, O. I., Hu, M. Y., Cai, Q. S., Deng, Q., Yang, W., and Zuo, M. (2023). Sedimentary facies, lithofacies paleogeography, and an evaluation of the Ordovician sequences in the Sichuan Basin, southwest China. *Marine and Petroleum Geology* 149, 106096. doi:10.1016/j.marpetgeo.2023.106096

Khalifa, M. A., and Morad, S. (2015). Impact of depositional facies on the distribution of diagenetic alterations in the Devonian shoreface sandstone reservoirs, Southern Ghadamis Basin, Libya. *Sedimentary Geology* 329, 62–80. doi:10.1016/j.sedgeo.2015.09.003

Korsch, R. J., Mai, H. Z., Sun, Z. C., and Gorter, J. (1991). The Sichuan Basin, southwest China: a late proterozoic (sinian) petroleum province. *Precambrian Research* 54, 45–63. doi:10.1016/0301-9268(91)90068-l

Kra, K., Qiu, L. W., Yang, Y. Q., Yang, B. L., Ahmed, K. S., Camara, M., et al. (2022). Sedimentological and diagenetic impacts on sublacustrine fan sandy conglomerates reservoir quality: An example of the Paleogene Shahejie Formation (Es4s Member) in the Dongying Depression, Bohai Bay Basin (East China). *Sediment. Geol.* 427. doi:10.1016/J.SEDGEO.2021.106047

Külaots, I., Goldfarb, J. L., and Suuberg, E. M. (2010). Characterization of Chinese, American and Estonian oil shale semicokes and their sorptive potential. *Fuel* 89, 3300–3306. doi:10.1016/j.fuel.2010.05.025

Lai, J., Fan, X. C., Pang, X. J., Zhang, X., Xiao, C., Zhao, X., et al. (2019). Correlating diagenetic facies with well logs (conventional and image) in sandstones: the Eocene-Oligocene Suweiyi Formation in Dina 2 Gasfield, Kuqa depression of China. *Journal of Petroleum Science and Engineering* 174, 617–636. doi:10.1016/j.petrol.2018.11.061

Lai, J., Fan, X. C., Liu, B. C., Pang, X. J., Zhu, S. F., Xie, W. B., et al. (2020). Qualitative and quantitative prediction of diagenetic facies via well logs. *Mar. Pet. Geol.* 120, 104486. doi:10.1016/j.marpetgeo.2020.104486

Lai, J., Wang, G. W., Wang, S., Cao, J., Li, M., Pang, X., et al. (2018). Review of diagenetic facies in tight sandstones: diagenesis, diagenetic minerals, and prediction via well logs. *Earth-Science Reviews* 185, 234–258. doi:10.1016/j.earscirev.2018.06.009

Lai, J., Xiao, L., Zhao, X., Zhao, F., Li, Y. H., Zhu, S. F., et al. (2023). Genesis and logging evaluation of deep to ultra-deep high-quality clastic reservoirs: a case study of the Cretaceous Bashijiqike Formation in Kuqa depression. *Acta Petrolei Sinica (in Chinese with English abstract)* 44 (4), 612–625.

Law, B. E., and Curtis, J. B. (2002). Introduction to unconventional petroleum systems. *American Association of Petroleum Geologists Bulletin* 86 (11), 1851–1852. doi:10.1306/61eedda0-173e-11d7-8645000102c1865d

Li, S. M., Han, R. B., Du, Y. J., Liu, P., and Bie, H. (2020). Quantitative characterization of diagenetic reservoir facies of the Karamay alluvial fan in the Junggar Basin, western China. *Journal of Petroleum Science and Engineering* 188, 106921. doi:10.1016/j.petrol.2020.106921

Li, Y. Q., He, D. F., Li, D., Lu, R., Fan, C., Sun, Y., et al. (2018). Sedimentary provenance constraints on the jurassic to cretaceous paleogeography of Sichuan Basin, SW China. *Gondwana Research* 60, 15–33. doi:10.1016/j.gr.2018.03.015

Li, Z. H., Zhang, L. Q., Yuan, W. F., Chen, X., and Li, M. (2022). Logging identification for diagenetic facies of tight sandstone reservoirs: a case study in the lower jurassic ahe formation, kuqa depression of tarim basin. *Marine and Petroleum Geology* 139, 105601. doi:10.1016/j.marpetgeo.2022.105601

Liu, A. Q., Tian, J. C., Chen, S. C., Yi, J. Z., Zhang, S. M., Luo, X., et al. (2023a). Characteristics and controlling factors of Jurassic Lianggaoshan Formation tight sandstone reservoirs in the eastern Sichuan Basin. *Mineralogy and Petrology (in Chinese with English abstract)* 43 (1), 144–155. doi:10.19719/j.cnki.1001-6872.2023.01.12

Liu, H. K., Ai, Y., Wang, G. W., Chen, K. J., Cai, D. Y., Cao, J. T., et al. (2023b). Quantitative well logging evaluation of diagenetic facies of deep and ultra deep tight sandstone reservoirs: a case study of Bozi-Dabei area in Kuqa Depression. *Bulletin of Geological Science and Technology (in Chinese with English abstract)* 42 (1), 299–310. doi:10.19509/j.cnki.dzkq.2022.0256

Liu, Y. F., Hu, W. X., Cao, J., Wang, X., Tang, Q., Wu, H., et al. (2018). Diagenetic constraints on the heterogeneity of tight sandstone reservoirs: a case study on the Upper Triassic Xujiahe Formation in the Sichuan Basin, southwest China. *Marine and Petroleum Geology* 92, 650–669. doi:10.1016/j.marpetgeo.2017.11.027

Meng, L. F., Chen, W., Shen, T., and Cai, J. (2022). A study on the provenance of early to late Triassic clastic rocks from the northwestern Sichuan Basin, southwestern China: constraints on the early Mesozoic tectonic evolution of the western Yangtze Block. *Frontiers in Earth Science* 10, 940301. doi:10.3389/feart.2022.940301

Moradia, A. V., Sarı, A., and Akkayaa, P. (2016). Geochemistry of the miocene oil shale (hançili formation) in the çankırı-çorum basin, Central Turkey: implications for paleoclimate conditions, source–area weathering, provenance and tectonic setting. *Sedimentary Geology* 341, 289–303. doi:10.1016/j.sedgeo.2016.05.002

Mou, C. L., Wang, X. P., Wang, Q. Y., and Wang, Y. C. (2016). The recognition of diagenetic facies on the case from the reservoir in He8 section of Shihezi Formation, East II part of Sulige gas field, Qrdos Basin. *Acta Sedimentologica Sinica (in Chinese with English abstract)* 34 (2), 346–355. doi:10.14027/j.cnki.cjxb.2016.02.013

Mou, W. W., Wang, Q., Tian, B., He, L. W., and Hu, Z. J. (2017). The diagenetic facies logging response characteristics of medium-deep reservoirs in the north slope of Baiyun Sag, Pearl River Mouth Basin. *Natural Gas Geoscience (in Chinese with English abstract)* 28 (10), 1601–1612.

Packham, G. H., and Keith, A. W. C. (1960). The principle of diagenetic facies and some of its implications. *The Journal of Geology* 68 (4), 392–407. doi:10.1086/626673

Peng, J., Wu, H. M., Han, H. D., Yang, S. J., Zhang, H. B., and Liu, L. (2016). Study on diagenetic facies of the Donghetang tight sandstone reservoirs in Bachu area. *Oil & Gas Geology (in Chinese with English abstract)* 37 (2), 245–255.

Railsback, L. B. (1984). Carbonate diagenetic facies in the upper pennsylvanian dennis formation in Iowa, Missouri, and Kansas. *Journal of Sedimentary Research* 54 (3), 986–999. doi:10.1306/212f8549-2b24-11d7-8648000102c1865d

Şengör, A. M. C. (1985). Geology: east asian tectonic collage. *Nature* 318, 16–17. doi:10.1038/318016a0

Soeder, D. J. (2018). The successful development of gas and oil resources from shales in North America. *Journal of Petroleum Science and Engineering* 163, 399–420. doi:10.1016/j.petrol.2017.12.084

Stephen, A. H. (2006). Tight gas sands. *SPE Journal* 58 (6), 86–93. doi:10.2118/103356-jpt

Sun, L. D., Zou, C. N., Jia, A. L., Wei, Y., Zhu, R., Wu, S., et al. (2019). Development characteristics and orientation of tight oil and gas in China. *Petroleum Exploration and Development* 46 (6), 1073–1087. doi:10.1016/s1876-3804(19)60264-8

Wang, C. Y., Chang, J., Li, N., Hong, H. T., Li, Y. N., Wang, X. J., et al. (2022a). Paleo-water-depth reconstruction of early Jurassic lakes in the eastern Sichuan Basin. *Acta Sedimentologica Sinica*. (in Chinese with English abstract). doi:10.14027/j.issn.1000-0550.2022.036

Wang, J., Cao, Y. C., Liu, K. Y., Liu, J., and Kashif, M. (2017). Identification of sedimentary-diagenetic facies and reservoir porosity and permeability prediction: an example from the Eocene beach-bar sandstone in the Dongying Depression, China. *Marine and Petroleum Geology* 82, 69–84. doi:10.1016/j.marpetgeo.2017.02.004

Wang, X. J., Hong, H. T., Wu, C. J., Liu, M., Guan, X., Chen, S. L., et al. (2022b). Characteristics and formation mechanisms of tight sandstone reservoirs in Jurassic Shaximiao Formation, central of Sichuan Basin. *Journal of Jilin University (Earth Science Edition)* 52 (4), 1037–1051. (in Chinese with English abstract). doi:10.13278/j.cnki.jjuese.20210247

Wang, Z. C., Jiang, H., Chen, Z. Y., Liu, J., Ma, K., Li, W., et al. (2020). Tectonic paleogeography of Late Sinian and its significances for petroleum exploration in the middle-upper Yangtze region, South China. *Petroleum Exploration and Development* 47 (5), 946–961. doi:10.1016/s1876-3804(20)60108-2

Wang, Z. C., Shi, Y. Z., Wen, L., Jiang, H., Jiang, Q., Huang, S., et al. (2022c). Exploring the potential of oil and gas resources in Sichuan Basin with super basin thinking. *Petroleum Exploration and Development* 49 (5), 977–990. doi:10.1016/s1876-3804(22)60326-4

Wang, Z. Y., Zhou, N. W., Lu, S. F., Liu, Y., Lin, L., Liu, Y., et al. (2023). Generation, accumulation, and distribution of Upper Paleozoic tight sandstone gas in the northeastern margin of the Ordos Basin. *Marine and Petroleum Geology* 156, 106463. doi:10.1016/j.marpetgeo.2023.106463

Wei, W., and Thomas, J. A. (2020). Elemental proxies for paleosalinity analysis of ancient shales and mudrocks. *Geochimica et Cosmochimica Acta* 287, 341–366. doi:10.1016/j.gca.2019.06.034

Worden, R. H., Griffiths, J., Wooldridge, L. J., Utley, J., Lawan, A., Muhammed, D., et al. (2020). Chlorite in sandstones. *Earth-Science Reviews* 204, 103105. doi:10.1016/j.earscirev.2020.103105

Wu, D., Liu, S. B., Chen, H. D., Lin, L., Yu, Y., Xu, C., et al. (2020). Investigation and prediction of diagenetic facies using well logs in tight gas reservoirs: evidences from the Xu-2 member in the Xinchang structural belt of the western Sichuan Basin, western China. *Journal of Petroleum Science and Engineering* 192, 107326. doi:10.1016/j.petrol.2020.107326

Xu, Z. Q., Yang, J. S., Li, H. Q., Wang, R. R., Cai, Z. H., et al. (2012). Indosinian collision-orogenic system of Chinese continent and its orogenic mechanism. *Acta Petrologica Sinica (in Chinese with English abstract)* 28 (6), 1697–1709.

Yang, L., Fan, A. P., Yang, R. C., Sun, Y. P., and Lenhardt, N. (2021). Sedimentary facies control on sandstone reservoir properties: A case study from the permian Shanxi Formation in the southern Ordos basin, central China. *Mar. Pet. Geol.* 129, 105083. doi:10.1016/J.MARPETGEO.2021.105083

Yang, N., Wang, G. W., Li, C. L., et al. (2014). Reservoir diagenetic facies of Bashijiqike Formation in Dabei gas field compartmentalization and quantitative evaluation. *Journal of China University of Petroleum* 38 (5), 18–24. (in Chinese with English abstract).

Yang, Z., Zou, C. N., Chen, J. J., Wu, S. T., Pan, S. Y., Ma, F., et al. (2021). Exploring petroleum inside or near the source kitchen": innovations in petroleum geology theory and reflections on hydrocarbon exploration in key fields. *Acta Petrolei Sinica (in Chinese with English abstract)* 42 (10), 1310–1324.

Yi, J. Z., Zhang, S. M., Cai, L. X., Chen, S. C., Luo, X., Yu, J. X., et al. (2022). Strata and sedimentary filling characteristics of the lower jurassic Lianggaoshan Formation and its hydrocarbon exploration in eastern Sichuan Basin. *Journal of Jilin University (Earth Science Edition)* 52 (3), 795–815. (in Chinese with English abstract). doi:10.13278/j.cnki.jjuese.20210429

Yokoyama, M., Liu, Y. Y., Halim, N., and Otofuji, Y. i. (2001). Paleomagnetic study of upper jurassic rocks from the Sichuan Basin: tectonic aspects for the collision between the Yangtze block and the north China block. *Earth and Planetary Science Letters* 193, 273–285. doi:10.1016/s0012-821x(01)00498-8

Yu, X., Yang, Y. X., Zhou, H. H., Luo, B., Luo, L., Luo, X., et al. (2023). Genetic mechanism of tight sandstone reservoir of lacustrine - delta sand-mud interlayer in Lianggaoshan Formation of Jurassic, eastern Sichuan Basin. *Natural Gas Geoscience (in Chinese with English abstract)* 34 (9), 1595–1611.

Zhang, C., Sun, W., Gao, H., Xi, T. D., and He, Q. (2014). Reservoir diagenetic facies and porosity evolution pathways of chang 8 formation in huachi, Ordos basin. *Earth Science (in Chinese with English abstract)* 39 (4), 411–420.

Zhang, D. W. (2021). Development prospect of natural gas industry in the Sichuan Basin in the next decade. *Natural Gas Industry (in Chinese with English abstract)* 41 (8), 34–45.

Zhang, D. W., and Yang, Y. (2022). Exploration potential and development direction of continental tight sandstone gas in the Sichuan Basin. *Natural Gas Industry (in Chinese with English abstract)* 42 (1), 1–11.

Zhang, F., Jiang, Z. X., Sun, W., Li, Y., Zhang, X., Zhu, L., et al. (2019). A multiscale comprehensive study on pore structure of tight sandstone reservoir realized by nuclear magnetic resonance, high pressure mercury injection and constant-rate mercury injection penetration test. *Marine and Petroleum Geology* 109, 208–222. doi:10.1016/j.marpetgeo.2019.06.019

Zhang, L. Q., Li, J. J., Wang, W., Li, C. Y., Zhang, Y. J., Jiang, S., et al. (2022). Diagenetic facies characteristics and quantitative prediction via wireline logs based on machine learning: a case of Lianggaoshan tight sandstone, fuling area, Southeastern Sichuan Basin, Southwest China. *Frontiers in Earth Science* 10, 1018442. doi:10.3389/feart.2022.1018442

Zhao, C. J., Jiang, Y. L., and Wang, L. J. (2022). Data-driven diagenetic facies classification and well-logging identification based on machine learning methods: a case study on Xujiahe tight sandstone in Sichuan Basin. *Journal of Petroleum Science and Engineering* 217, 110798. doi:10.1016/j.petrol.2022.110798

Zhao, Z. J., Zhou, H., Chen, X., Liu, Y. H., Zhang, Y. B., Liu, Y. E., et al. (2012). Sequence lithofacies paleogeography and favorable exploration zones of the Permian in Sichuan Basin and adjacent areas, China. *Acta Petrolei Sinica (in Chinese with English abstract)* 33 (S2), 35–51.

Zheng, C., Xu, C. H., Brix, M. R., and Zhou, Z. (2019). Evolution and provenance of the Xuefeng intracontinental tectonic system in South China: constraints from detrital zircon fission track thermochronology. *Journal of Asian Earth Sciences* 176, 264–273. doi:10.1016/j.jseaes.2019.02.012

Zheng, D. Y., Hou, M. C., Chen, A. Q., Zhong, H., Qi, Z., Ren, Q., et al. (2022). Application of machine learning in the identification of fluvial-lacustrine lithofacies from well logs: a case study from Sichuan Basin, China. *Journal of Petroleum Science and Engineering* 215, 110610. doi:10.1016/j.petrol.2022.110610

Zheng, D. Y., Wu, S. X., and Hou, M. C. (2021). Fully connected deep network: an improved method to predict TOC of shale reservoirs from well logs. *Marine and Petroleum Geology* 132, 105205. doi:10.1016/j.marpetgeo.2021.105205

Zheng, R. C., Geng, W., Zhou, G., Han, Y. L., Wang, H. H., and Wen, H. G. (2007). Diagenesis and diagenetic facies of chang 6 sandstone of yanchang formation in baibao area, Ordos basin. *Lithologic Reservoirs (in Chinese with English abstract)* 19 (2), 1–8.

Zhu, H., Yang, G., Yuan, B. G., Ying, D. L., Dai, X., Zhou, H. F., et al. (2018). Geological conditions, resource potential and exploration direction of conventional gas in Sichuan Basin. *Natural Gas Geoscience (in Chinese with English abstract)* 29 (10), 1475–1485.

Zhu, R. K., Zou, C. N., Mao, Z. G., Yang, H., Hui, X., Wu, S., et al. (2019). Characteristics and distribution of continental tight oil in China. *Journal of Asian Earth Sciences* 178, 37–51. doi:10.1016/j.jseaes.2018.07.020

Zou, C. N., Tao, S. Z., Zhou, H., Zhang, X. x., He, D. b., Zhou, C. m., et al. (2008). Genesis, classification, and evaluation method of diagenetic facies. *Petroleum Exploration and Development* 35 (5), 526–540. doi:10.1016/s1876-3804(09)60086-0

Zou, C. N., Yang, Z., Dong, D. Z., Zhao, Q., Chen, Z. H., Feng, Y. L., et al. (2022). Formation, distribution and prospect of unconventional hydrocarbons in source rock strata in China. *Earth Science (in Chinese with English abstract)* 47 (5), 1517–1533.

Zou, C. N., Zhang, G. S., Yang, Z., Tao, S., Hou, L., Zhu, R., et al. (2013). Concepts, characteristics, potential and technology of unconventional hydrocarbons: on unconventional petroleum geology. *Petroleum Exploration and Development* 40 (4), 413–428. doi:10.1016/s1876-3804(13)60053-1

Zou, J., Le, Y., Jin, T., Li, X. Q., Li, X. S., and Wei, T. Q. (2018). Genesis and sweet spot prediction of Jurassic tight sandstone reservoir in central Sichuan Basin. *Xinjiang Petroleum Geology (in Chinese with English abstract)* 39 (5), 555–560.

frontiers | Frontiers in Earth Science

TYPE Original Research
PUBLISHED 14 October 2024
DOI 10.3389/feart.2024.1437205

OPEN ACCESS

EDITED BY
Yifan Li,
China University of Geosciences, China

REVIEWED BY
Jiawang Ge,
Southwest Petroleum University, China
Sarp Karakaya,
Chevron, United States
Shuyuan Shi,
Research Institute of Petroleum Exploration and Development (RIPED), China

*CORRESPONDENCE
Feng Wenjie,
fwj1017@yangtzeu.edu.cn

RECEIVED 23 May 2024
ACCEPTED 25 September 2024
PUBLISHED 14 October 2024

CITATION
Wenjie F and Ye Z (2024) Sedimentary characteristics and reservoir architecture of a lacustrine mixed carbonate/siliciclastic system: the lower member of the ShangGanchaigou Formation, Neogene, in the western Qaidam Basin, China.
Front. Earth Sci. 12:1437205.
doi: 10.3389/feart.2024.1437205

Sedimentary characteristics and reservoir architecture of a lacustrine mixed carbonate/siliciclastic system: the lower member of the ShangGanchaigou Formation, Neogene, in the western Qaidam Basin, China

Feng Wenjie* and Zhang Ye

School of Geosciences, Yangtze University, Wuhan, China

Lacustrine mixed carbonate/siliciclastic sediment is an important type of oil and gas reservoir with significant potential. Although previous studies have investigated the sedimentary characteristics of the mixed depositional system in numerous oil and gas-bearing basins worldwide, a detailed sedimentary architecture model is still lacking for guiding reservoir characterization at the hydrocarbon reservoir scale. In this paper, a typical lacustrine mixed carbonate/siliciclastic sedimentary system, preserved in the lower member of the ShangGanchaigou Formation, Neogene, in the western Qaidam Basin, Western China, was deeply investigated based on well logging data from 640 wells, 438 m of cores from 3 core wells, and outcrop studies. The results demonstrate that 1) seven types of architecture elements, namely, distributary channel, channel mouth bar, distal bar, sheet-like sand, shallow water mud, algal mound, and marl flat characterized by different lithofacies associations, were recognized based on core and well logging data. 2) The lacustrine mixed carbonate/siliciclastic depositional system can be divided into three facies belts. Along the lakeward direction, the proximal facies belt is dominated by delta front deposits and characterized by gradually downstream bifurcating distributary channels and associated lateral amalgamated delta lobes. The middle facies belt is characterized by isolated and small-scale delta lobes and inter-lobe deposits, including sheet-like sand, small-scale algal mounds, and marl flats, and the distal facies belt is a combination of large-scale algal mounds and marl flats. 3) Within a depression, short-term base-level cycles controlled the facies belt transition, and the proximal, middle, and distal facies belts formed under relatively low, middle, and high base-level conditions, respectively. 4) The scale and connectivity of reservoirs gradually decreased from the proximal to the distal belt.

KEYWORDS

mixed siliciclastic, carbonate sediments, sedimentary architecture, sedimentary model, Qaidam Basin, base-level cycle

1 Introduction

The mixed carbonate/siliciclastic depositional systems are widely distributed in marine and terrestrial environments (Dolan, 1989; Xu et al., 2019; Li Y et al., 2021; Karakaya et al., 2022; Lebrec et al., 2023). There are four types of mixing of clastic and carbonate sediments: punctuated mixing, facies mixing, *in situ* mixing, and source mixing (Mount, 1984). In the mixed depositional system, gravel-to-sandy deposits and permeable carbonate deposits formed large-scale reservoirs, while muddy and impermeable carbonate deposits formed stable and effective cap rock. Therefore, the mixed depositional systems can form large-scale oil and gas traps with good potential for oil and gas resources (Dolan, 1989; Chen et al., 2015; Zhao, 2015; Wei et al., 2021; Wu et al., 2022; Cui et al., 2023; Mutti et al., 2023; Kjøll et al., 2024; Karakaya et al., 2024). In the past decades, a marine mixed carbonate/siliciclastic sedimentary system was deeply investigated based on modern and ancient sedimentary records (Mount, 1984; Mount, 1985; Dolan, 1989; Lee and Kim, 1992; Lebrec et al., 2023). However, the lacustrine mixed carbonate/siliciclastic depositional systems were poorly understood due to the development conditions and limited preserved sedimentary records (Feng et al., 2013; Li Y et al., 2021; Li Q et al., 2021; Chen et al., 2022; Wu et al., 2022).

In recent years, lacustrine mixed carbonate/siliciclastic depositional records were widely observed along the margin of terrestrial depression basins such as the Bohai Bay Basin, Junggar Basin, and Qaidam Basin in China and the Williston Basin in North America (Palermo et al., 2008; Li et al., 2009; Meng et al., 2009; Feng et al., 2013; Zhao, 2015; Gao et al., 2018). Facies mixing resulting from facies belt transitions and *in situ* mixing caused by the activity of algal biota and clastic sediment deposition are the primary mixing types in depressions (Feng et al., 2013; Gierlowski-Kordesch et al., 2014; Chen et al., 2015; Du et al., 2020). Sedimentary characteristics and the diversity of lacustrine mixed carbonate/siliciclastic depositional systems were investigated in numerous studies. Basin-scale sedimentary models were found in large-scale oil and gas-bearing basins worldwide (Feng et al., 2011a; Feng et al., 2011b; Wu et al., 2019; Ye et al., 2019; Fu et al., 2020; Wang J et al., 2020; Wang Q et al., 2020). However, the detailed sedimentary characteristics and depositional model focus on the hydrocarbon reservoir scale are poorly understood. A detailed sedimentary architecture model for subsurface reservoir characterization is urgently needed.

In this paper, we deeply investigated the sedimentary characteristics and sedimentary architecture of the lacustrine mixed carbonate/siliciclastic system preserved in the lower member of the ShangGanchaigou Formation, Neogene, in the western Qaidam Basin. Lithofacies were identified from core data, and lithofacies associations were further recognized for classifying sedimentary architecture elements. A 3D outcrop model and an orthophoto projection image were produced utilizing a drone. Spatial patterns and the evolution of the lacustrine mixed carbonate/siliciclastic system in the target interval were detailed. A detailed and reliable sedimentary architecture model of a lacustrine mixed carbonate/siliciclastic system was established based on the compressive analysis of subsurface reservoir data and outcrop data.

2 Geological settings

The Qaidam Basin is a large-scale oil and gas-bearing basin located north of the Qinghai–Tibet Plateau, Western China (Figure 1). It is a Mesozoic and Cenozoic continental basin (Feng et al., 2013). The study area includes a subsurface oil and gas reservoir and an outcrop. The subsurface reservoir within the Huatugou Oilfield and the outcrop in the Ganchaigou area are distributed in the western part of the Qaidam Basin. The target interval of the study is the facies mixing types of mixed deposits and the VI and VII oil zones of the lower member of the ShangGanchaigou Formation, Neogene (Figure 2). There is slight compositional mixing, but it is atypical. During the early Neogene, the Qaidam Basin was a depression characterized by shallow lacustrine deposition (Zhang et al., 2004; Wu et al., 2019). The western Altun Mountains and the western Qimantag Mountain supplied adequate clastic sediments, and the sediments were transported from the end of the west of the basin to the depression (Figure 1).

During the sedimentation of the target interval, the paleoclimate is arid (Zhang et al., 2004; Chen et al., 2004; Li et al., 2009; Wang et al., 2012). The fossil assemblage identified from the cores is Eucypris–Youshashania–Hemicyprinotus, indicating shallow and semi-saline–saline water at the margin of the depression (Li et al., 2020). During the deposition of the target interval, the average paleo-salinity was 1.27%, and the maximum paleo-salinity was 2.66% (Chen et al., 2015). The arid paleo-climate, high salinity, and shallow water provided favorable carbonate production conditions (Chen et al., 2015; Chen et al., 2022; Li et al., 2020). The target interval is approximately 150 m thick and can be divided into 41 single-layer units. Three middle-term base-level cycles (MSC1–MSC3) and nine short-term base-level cycles (SSC1–SSC9) were recognized based on well logging and core data (Figure 2). According to previous research, the study area is located at the transformation zone between the upstream deltas and lakeward algal mound (AM)–marl flats (MFs) (Zhang et al., 2004).

3 Results

3.1 Lithofacies, lithofacies associations, and interpretations

3.1.1 Core lithofacies

Based on lithological characteristics, sediment structures, and rock colors, seven lithofacies were observed from 438 m of the core of three core wells, as shown in Figure 1C. Typical core images and thin-section images are shown in Figure 3.

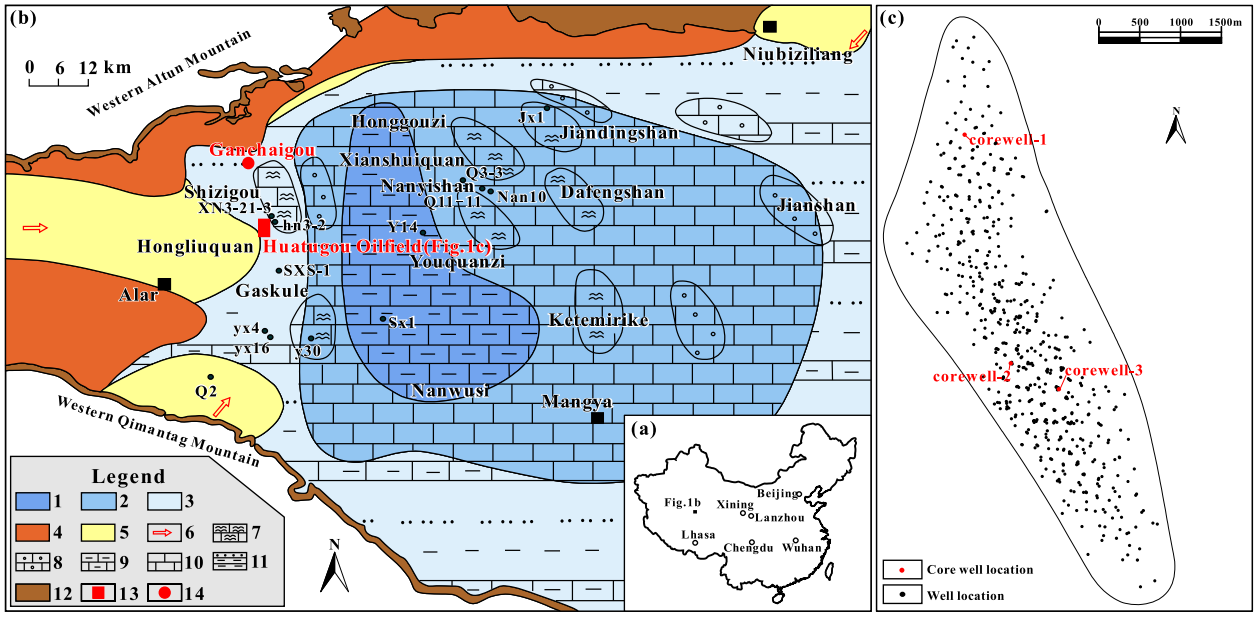

FIGURE 1
(A) Location of the western Qaidam Basin; **(B)** distribution of the upper Ganchaigou Formation sedimentary system in the western Qaidam Basin [modified based on the study by Zhang et al. (2004)]; and **(C)** well location distribution in the Huatugou Oilfield. 1) Semi-deep lacustrine deposits, 2) shallow lacustrine deposits, 3) shore deposits, 4) degradation terrace, 5) alluvial fan to delta, 6) source, 7) algal mounds and marl flats, 8) oolitic beach, 9) marl, 10) limestone flat, 11) sandy and marl flats, 12) mountains, 13) subsurface study area, and 14) outcrop location.

3.1.1.1 Facies 1—massive bedding gravel–coarse sandstone

Facies 1 (F1) is characterized by poorly sorted gravel clastic, fine–coarse sand, and muddy sediments. The proportion of gravel debris is 5%–30%, with particle diameters ranging from 2 mm to 25 mm, usually consisting of brown or gray metamorphic debris (Figure 3A). Mud pebble was observed in a low ratio of F1 (Figure 3B), which reveals the existence of reworking and short-distance redeposition of pre-existing muddy sediment. Predominant sedimentary structures of F1 are massive bedding, with occasional occurrences of trough cross-bedding. F1 is formed under the action of strong tractional flows, and its thickness is approximately 0.5~5.0 m. The commonly observed upward-fining trend indicates that F1 belongs to channel deposits. In order to track and measure the scale of the lithofacies unit, well correlation sections with a well spacing of 20~100 m are built and analyzed. The lateral tracking of the F1 unit in the subsurface reservoir shows a width of approximately 100–200 m.

3.1.1.2 Facies 2—massive bedding medium sandstone

Facies 2 (F2) is characterized by well-sorted medium sand. Muddy sediment content is relatively low (Figure 3C). The main sedimentary structure is massive bedding. Due to low compaction and cementation, the details of sedimentary structures are difficult to observe. The thickness of an F2 unit is approximately 0.2~1.0 m. Usually, several F2 units are vertically stacked to form large-scale sand layers with a thickness of 2.0–8.0 m. According to core observation and well logging data analysis, F2 is generally distributed within channel or channel mouth bar (CMB) deposits. Occasionally, there are mud interlayers between two F2 units. The lateral tracking results of subsurface reservoirs show that the width of F2 units can reach several hundred meters.

3.1.1.3 Facies 3—massive bedding fine sandstone

Facies 3 (F3) is characterized by well-sorted, fine sand (Figure 3D). Muddy sediment content is slightly higher than that in F2. Massive bedding is recognized from cores, indicating that F3 is formed in relatively open waters near the channel mouth and unaffected by waves. The thickness of an F3 unit is generally below 0.5 m, and the unit is separated by consistently distributed mudstone in the vertical direction. In subsurface reservoirs, F3 units are mainly distributed along the edge of F2.

3.1.1.4 Facies 4—interbedded siltstone–mudstone with deformed bedding, wavy bedding, and a bioturbation structure

Facies 4 (F4) is characterized by interbedded siltstone and mudstone (Figures 3E, F). The thickness of a siltstone or mudstone layer is approximately 0.5–5 cm. Alternating changes in siltstone and mudstone indicate the frequent hydrodynamic variations in the area far from the channel mouth. Wavy bedding is formed by the force of waves in open waters (Figure 3E). Suspended sediments, including mud and silt, are alternately deposited with the change in upstream channel systems and lake currents. Due to the shallow water depth, burrow pores with varied directions reworked the siltstone and mudstone (Figure 3F). Mudstone in F4 is usually red, demonstrating that the water depth is very shallow and the water level fluctuates frequently.

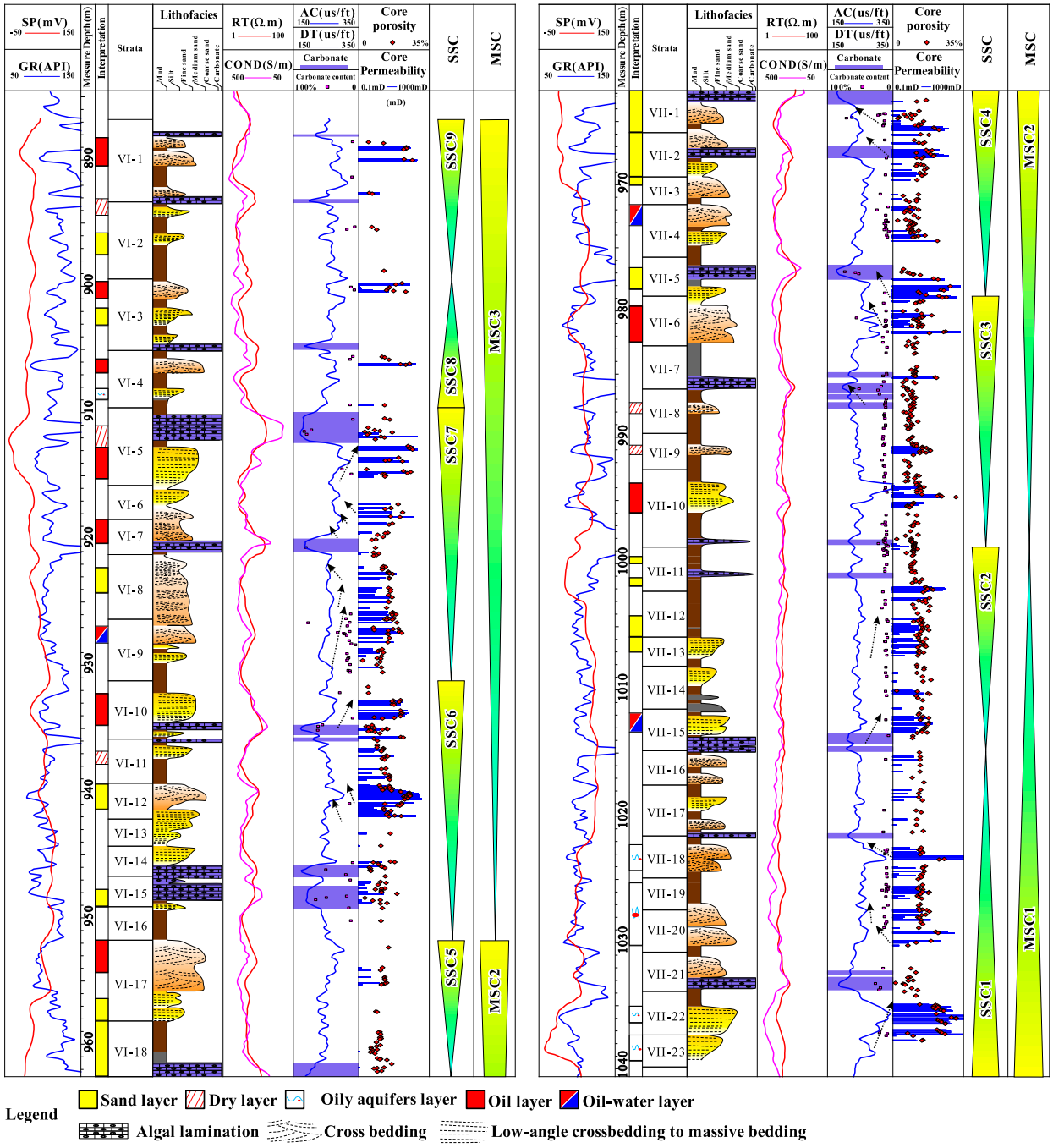

FIGURE 2
Stratigraphic column for VI–VII oil groups in the ShangGanchaigou Formation, Huatugou Oilfield. The interpretations of sedimentary characteristics and base-level cycles are based on continuous core data and well logging data. The core well is corewell-2, as shown in Figure 1C.

3.1.1.5 Facies 5—mudstone with horizontal bedding and muddy pebbles

Facies 5 (F5) is characterized by dark mudstone with horizontal bedding, which is formed under static water (Figure 3G). Floating mud pebbles and fine gravel clastic are recognized in a low ratio of F5 units (Figure 3H), indicating the presence of storm events (Chen et al., 2022). Compared to F4, F5 is formed in a deeper lake area, significantly further away from the channel mouth.

3.1.1.6 Facies 6—stromatolitic algal limestone

Facies 6 (F6) is characterized by stromatolitic algal limestone, and typical stromatolite pillars are observed on cores (Figures 3I, J, L). Thin-section observations suggest that

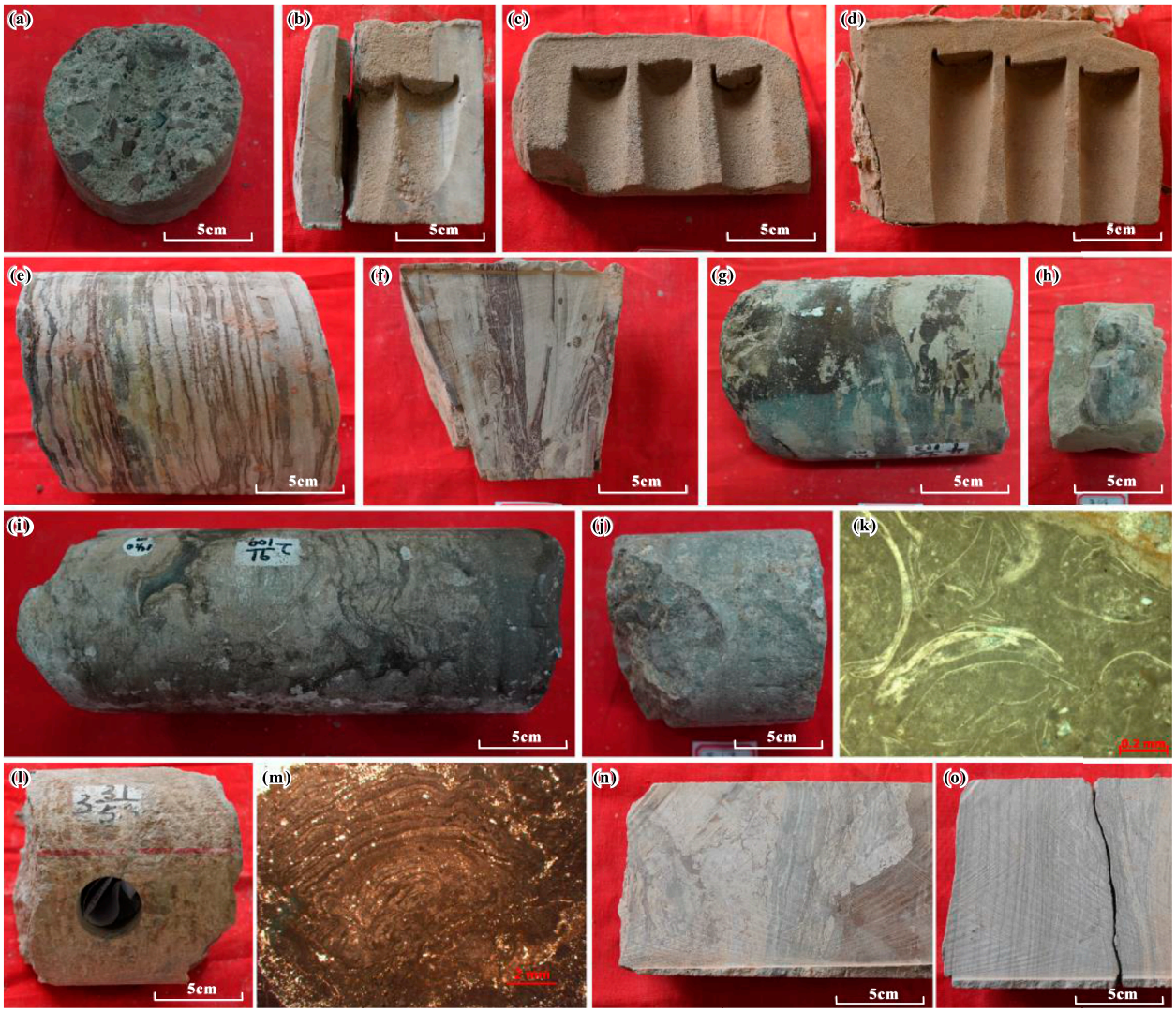

FIGURE 3
Typical core images and microscopic pictures of the mixed sedimentary record. **(A)** Core from corewell-1 with massive bedding of gravel–coarse sandstone and a core depth of 1,394.15 m. **(B)** Core from corewell-2 with massive bedding of gravel–coarse sandstone and a core depth of 968.05 m. **(C)** Core from corewell-2 with massive bedding of medium sandstone and a core depth of 1,033.21 m. **(D)** Core from corewell-2 with massive bedding of fine sandstone and a core depth of 931.53 m. **(E)** Core from corewell-3 with interbedded siltstone–mudstone with deformed bedding, wavy bedding, and a bioturbation structure and a core depth of 986.39 m. **(F)** Core from corewell-3 with interbedded siltstone–mudstone with deformed bedding, wavy bedding, and a bioturbation structure and a core depth of 1,009.25 m. **(G)** Core form corewell-2 with mudstone with horizontal bedding and muddy pebbles and a core depth of 1,417.11 m. **(H)** Core form corewell-2 with mudstone with horizontal bedding and muddy pebbles and a core depth of 1,418.72 m. **(I)** Core from corewell-1 with stromatolitic algal limestone and a core depth of 1,389.72 m. **(J)** Core from corewell-1 with stromatolitic algal limestone and a core depth of 1,375.39 m. **(K)** Core from corewell-1 with stromatolitic algal limestone and a core depth of 1,375.43 m. **(L)** Core from corewell-3 with stromatolitic algal limestone and a core depth of 961.45 m. **(M)** Core from corewell-1 with stromatolitic algal limestone and a core depth of 1,537.83 m. **(N)** Core from corewell-2 with marl with horizontal bedding and deformed bedding and a core depth of 902.35 m. **(O)** Core from corewell-2 with marl with horizontal bedding and deformed bedding and a core depth of 903.42 m. Locations of the three core wells are given in Figure 1C.

bioclasts, mud, and carbonate sediment filled the spaces between stromatolite pillars (Figure 3K). In some thin sections, growth laminae within the stromatolites are also discernible (Figure 3M). The thickness of an F6 unit ranges from 0.5 to 5.0 m, and the width of F6 can reach hundreds of meters in subsurface reservoirs. In some instances, carbonate sediments within F6 units have undergone dissolution, leading to the formation of larger-scale pores, thereby becoming high-quality reservoirs.

3.1.1.7 Facies 7—marl with horizontal bedding and deformed bedding

Facies 7 (F7) is characterized by horizontal-bedding marl and deformed bedding (Figure 3N, O). During marl formation, hydrodynamic forces were weak, and the water depth was significantly deeper than that of F6, resulting predominantly in horizontal bedding. Most marls are subject to varying degrees of deformation due to compaction effects and/or storm-related activity, giving rise to the coexistence of deformed and horizontal bedding.

TABLE 1 Typical well logging patterns, lithologies, sedimentary structures, and sedimentary rhythm of the facies belts and microfacies in the mixed sedimentary system. The yellow intervals are the recognized elements.

Facies belt	Delta front					Prodelta	
Architecture element	Distributary channel	Channel mouth bar	Distal bar	Sheet-like sand	Shallow-water mud	Algal mound	Marl flat
Typical well logging pattern	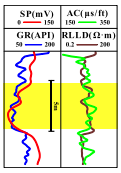	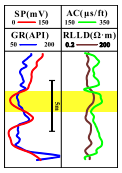	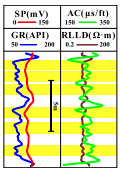	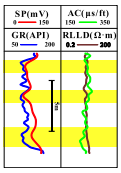	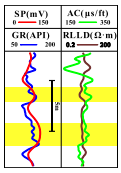	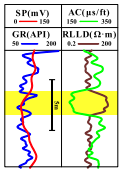	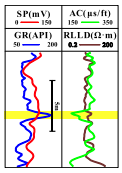
Lithology	Gravel, pebbled sandstone, and coarse–medium sandstone	Coarse–fine sandstone	Fine sandstone and muddy siltstone	Muddy siltstone	Mudstone	Algal limestone	Marl
Lithofacies associations	F1 + F2	F2 + F3 + F4	F3 + F4	F4	F5	F6	F7
Sedimentary structure	Massive bedding, parallel bedding, and scour and filling	Massive bedding and low-angle cross-bedding	Massive bedding, wavy bedding, and bioturbation structure	Wavy bedding, horizontal bedding, and bioturbation structure	Massive bedding, horizontal bedding, and bioturbation structure	Algal-laminated	Horizontal bedding and deformation
Sedimentary rhythm	Positive, homogeneous	Negative	Negative	Negative, homogeneous	Homogeneous	-	-
Thickness (m)	2.0–5.0	2.0–5.0	0.5–2.0	0.2–0.5	-	0.5–5.0	0.2–0.5

3.1.2 Lithofacies associations and architecture elements

To characterize the sedimentary architecture of the target interval, the lithofacies associations and corresponding architecture elements were recognized based on well logging patterns, lithofacies associations, and sedimentary rhythms (Table 1). The well logging patterns consist of spontaneous potential (SP), gamma ray (GR), acoustic (AC), deep induction resistivity (RILD) curves, and yellow interpreted elements. The patterns were built based on core description and core-well logging correlation analysis. The sedimentary characterization observed in core and subsurface reservoir data shows that the lacustrine mixed carbonate/siliciclastic system was composited by clastic sediments of the braided river delta and carbonate sediments of the algal mound and marl flat deposits. Seven architecture elements distributed from the delta front to the prodelta were recognized.

3.1.2.1 Distributary channel

Distributary channels (DCs) distribute from the delta plain to the delta front, transporting clastic sediments to the downstream areas. Due to the strong hydrodynamic force of channelized flow, the coarsest sediments (F1) are deposited at the bottom of active channels. As the river continues to evolve, its water flow tends to decrease, leading to a gradual decrease in the sediment particle size and the formation of relatively fine sediment (F2). Therefore, the DC units observed from well logs are characterized by a positive to homogeneous rhythm (Table 1). From the bottom to the top, the lithofacies type transforms from F1 to F2, and the gradually increasing GR presents the upward fining trend of the particle size. Due to the downstream bifurcation of the channel system, the scale of channels decreased along the flow direction.

3.1.2.2 Channel mouth bar

The channel mouth bar is formed by the continuous feeding of distributary channels and the deposition of upward coarsening sediments with their progradation. In subsurface reservoirs, CMBs are distributed along or ahead of DCs to form DC-CMB lobes. F4, F3, and F2 form a typical CMB from the bottom to the top, respectively (Table 1). Therefore, a CMB can be recognized by upward decreasing GR and the negative rhythm of the particle size from well logs. Controlled by the complex variations in DCs, the vertical lithofacies association may be repeating, inter-overlapping to form a thick CMB unit.

3.1.2.3 Distal bar

A distal bar (DB) is formed along the outer edge of CMBs. Due to its deposition area being remote from channel mouths, the hydrodynamic force is relatively weak, resulting in sediments primarily comprising fine-grained suspended matter, such as fine sand, silt, and clay. A DB is composed of F4 units at the bottom and F3 units at the top (Table 1). Several muddy interlayers appear between the lithofacies units in the vertical direction. A DB exhibits a distinct negative rhythm characterized by gradually decreasing GR values from bottom to top. Still, it further reveals multiple thin, negative-rhythm layers separated by muddy interlayers (Table 1).

3.1.2.4 Sheet-like sand

Sheet-like sand (SS) is formed in the open waters far from channel mouths, primarily composed of suspended sediments such as silt and clay, and characterized by relatively thin thickness. Sheet-like sand deposits are typically prone to reshaping by lake waves during deposition and subsequent periods, forming randomly dispersed, isolated, thin laminae of sand bodies. The predominant lithofacies type in such deposits is F4 (Table 1). Similar to DBs, sheet-like sand units are often separated by intervals of mudstone, which effectively isolate F4 units in the vertical direction. A slight negative rhythm indicated by gradually decreasing GR values from bottom to top is the typical identification mark (Table 1).

3.1.2.5 Shallow water mud

Shallow water mud (SWM) is characterized by pure mudstone formed in still waters within the distal part of the delta front. Massive or horizontal bedding mudstone is re-worked by bioturbation (Table 1). A high GR value indicates a higher mud content than that of the other architectural elements.

3.1.2.6 Algal mound

Algal mounds formed in the clean and shallow water area in the prodelta are characterized by mound-shaped, thick-bedded algal limestone. The main lithofacies is F6. The formation of algal mounds primarily results from the accumulation of carbonate sediments produced by algal growth, mixed with bioclasts and clay, typically forming isolated, mound-shaped structures offshore. Their characteristic log response patterns include acoustic impedance (AC) values significantly lower than those of both shales and sandstones, GR readings similar to those of mudstones, and a slight negative anomaly observable in the SP (Table 1).

3.1.2.7 Marl flat

In contrast to algal mounds, a marl flat (MF) develops in settings with higher carbonate productivity and is primarily composed of layers of mud, along with carbonate (including limy and dolomitic) deposits, stacked in thin interbeds (Table 1). The main lithofacies type of MF is F7. They are predominantly found along the margins of algal mounds and in the distal parts of the prodelta. The MF units are significantly thinner and wider than the AM units. Owing to their high content of both clay and carbonate, their logging responses are characterized by GR values significantly higher than those of shales, AC values notably lower than those of shales, and SP readings close to the baseline (Table 1).

3.2 Sedimentary characteristics of the Ganchaigou outcrop

In order to investigate the spatial patterns of the mixed carbonate/siliciclastic system, a virtual 3D outcrop model was built, and a high-resolution orthographic image that vertically sliced the exposed stratum of the Ganchaigou outcrop was further created (Figure 4A). As illustrated in Figure 4A, we perform an orthographic projection on highly inclined outcrops to obtain images that reveal the true characteristics of geological stratification sections. The stratigraphic interface and boundary of algal and muddy limestone were recognized and traced on the outcrop image (Figure 4A).

The results show that the thickness of each stratum unit is constant in at least a 1,500-m-wide section. Thin algal limestone and marl layers exist within stratum units and form an interlayered pattern with the clastic rock (Figure 4A). Typical sedimentary characteristics of the outcrop are given in Figures 4B–E. Marl layers typically occur as nearly evenly thick–thin beds interbedded within clastic rock layers, with thicknesses of 0.2–0.5 m and widths extending from hundreds of meters to several kilometers (Figure 4C). Algal limestone exhibits prominent mound-like structures, typically with a flat base and a domed top, varying in thickness from 0.5 to 5.0 m, while the width of algal mound units spans from tens to hundreds of meters (Figures 4C–D). Clastic rock layers belong to deltaic deposits and typically progress upward from mudstones, through silty mudstones, to fine–coarse-grained sandstones (Figure 4F).

According to the observation of the outcrop, deltaic deposits are the predominant component of the target interval, accounting for over 80%, while algal mount and marl flat contents are relatively minor, generally occurring between accretions at the lower to middle part of channel mouth bar deposits (Figure 4B). Carbonate deposits mostly coexist with the mudstone deposited far away from deltas. The frequent transformation from clastic to carbonate deposits demonstrated that the sedimentary environment changed rapidly under arid climate conditions.

3.3 Spatial patterns of the mixed carbonate/siliciclastic depositional system

The architecture elements were distinguished from well logging data based on the identification of lithofacies associations. The spatial patterns of the mixed carbonate/siliciclastic depositional system were discovered, and three representative facies belts were characterized (Figure 5).

3.3.1 Proximal facies belt

The proximal facies belt is characterized by a multi-level branching distributary channel network and the associated channel mouth bars and distal bars (Figure 5A). A typical facies map presented in Figure 5A showed that three deltas coexist, and the average width of a delta ranges from hundreds of meters to several kilometers (Figure 5A). The widely developed distributary channel, channel mouth bar, and distal bar units within the proximal part of the delta front amalgamated laterally, forming extensive interconnected reservoirs (Figures 5A, 6). The proximal facies belt is dominated by deltas, and carbonate deposition is found only in restricted shallow-water areas between distributary channels, primarily as thin layers of marl, which are of limited extent (Figure 5A).

3.3.2 Middle facies belt

The middle facies belt is characterized by smaller deltas and larger-scale carbonate deposits than that of the proximal facies belt (Figure 5B). Deltas are isolated, and distributary channels exhibit a higher curvature with fewer bifurcations in general. The thickness and width of delta deposits are significantly smaller than that of the proximal facies belt (Figure 6). Marl layers exist between deltas and coexist with shallow-water mudstone. In this belt, algal

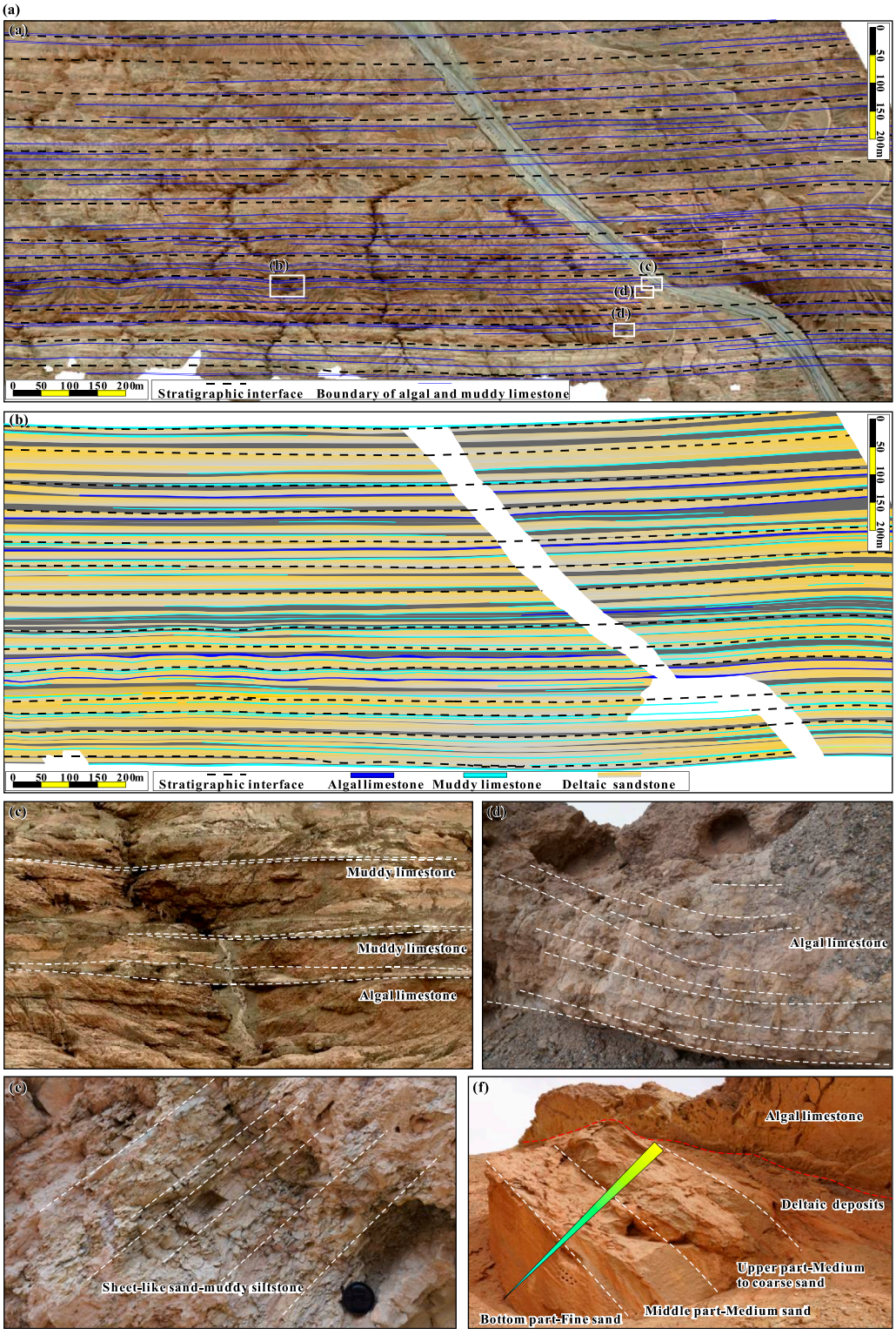

FIGURE 4
Orthorectified aerial image and sedimentary facies analysis of the Upper Ganchaigou Formation in the Ganchaigou outcrop area. **(A)** Orthorectified aerial image. **(B)** Facies interpretation of the outcrop **(C–F)**. Typical deposits of the outcrop.

mound elements are distributed very sparingly in the broader areas between deltas, and sheet-like sand occasionally develops in the lakeward area (Figure 5B).

3.3.3 Distal facies belt

The distal facies belt is characterized by very limited delta deposits and large-scale algal mounds, marl flats, and sheet-like sand

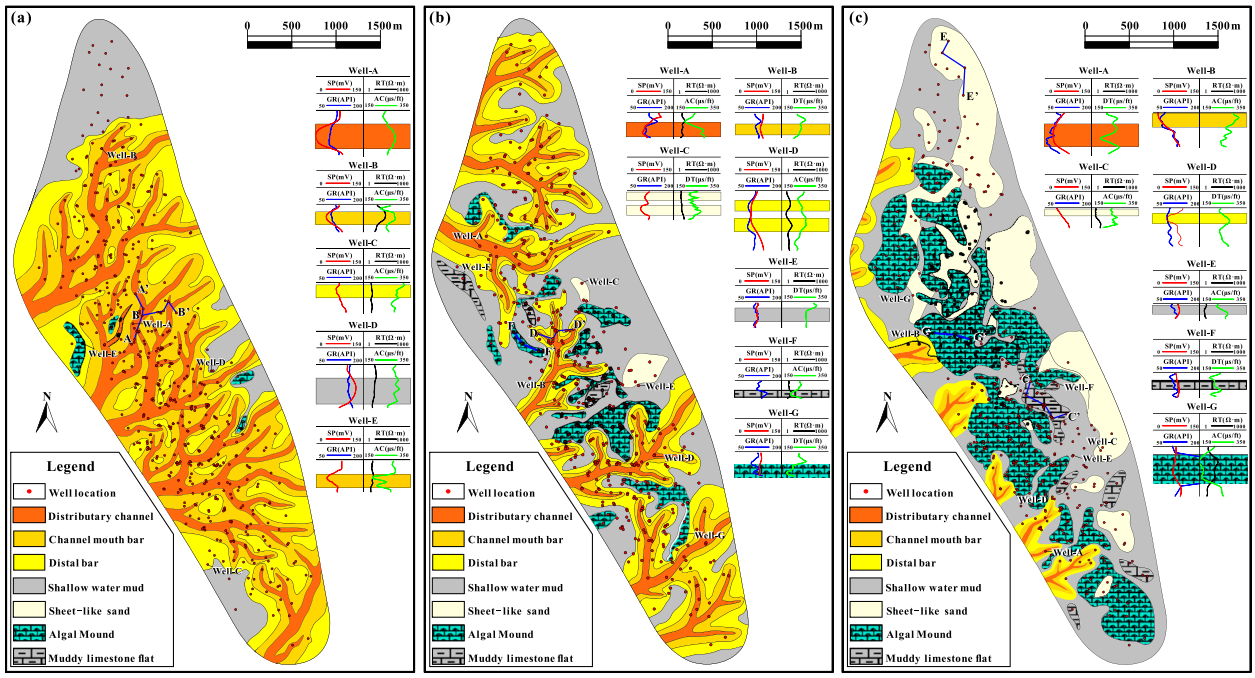

FIGURE 5
Spatial patterns of the mixed carbonate/siliciclastic depositional system. **(A)** Proximal facies belt, strata VI-17 in Figure 2. **(B)** Middle facies belt, strata VII-21 in Figure 2. **(C)** Distal facies belt, strata VII-5 in Figure 2.

layers (Figure 5B). This belt is located within the open waters in the prodelta, with sheet-like sand generally distributed in the lower part of the stratum unit with mudstone. Meanwhile, algal mound units are mainly distributed at the lower to middle part of the stratum unit (Figure 6). A marl flat usually develops around or between two algal mounds. The facies map and sections show that the distal facies belt is stacked by interlayered sheet-like sand, algal mounds, and marl flat units (Figures 5, 6).

4 Discussion

4.1 Sedimentary model of a lacustrine mixed carbonate/siliciclastic system

In this paper, a lacustrine mixed carbonate/siliciclastic system was discovered based on data from subsurface reservoirs and outcrops. Core lithology revealed that the mixing type of the target interval is mainly facies mixing. Compared to the marine mixed carbonate/siliciclastic system (Mutti et al., 2023; Kjøll et al., 2024), the production of carbonate deposits at the margin of the depression is limited due to the unstable salinity and clastic sediment transportation driven by changing climate. Therefore, only limited *in situ* mixing occurred (Wu et al., 2019; Wu et al., 2022; Chen et al., 2022). In the past 20 years, extensive research has discovered the sedimentary model of the lacustrine mixed carbonate/siliciclastic depositional system along the margin of depressions (Chen et al., 2004; Zhang et al., 2004; Dong et al., 2007; Li et al., 2009; Meng et al., 2009; Feng et al., 2011a; Feng et al., 2011b; Wang et al., 2012; Wang J et al., 2020; Wei et al., 2021; Liu et al., 2021; Wu et al., 2022; Cui et al., 2023). However, the detailed sedimentary architecture and sedimentary model of the mixed deposits for subsurface reservoir characterization still need to be explored.

Within the lacustrine mixed sedimentary system, three sedimentary facies belts with significant spatial pattern variations are recognized (Figure 5). Along the lakeward direction, the mixed sedimentary system can be divided into three facies belts, namely, the proximal facies belt, dominated by the delta front; the middle facies belt, characterized by the delta front and small-scale carbonate deposits; and the distal facies belt consisting of algal mounds and marl flats (Figure 7).

Large-scale delta-front deposits characterize the proximal facies belt. Distributary channels gradually bifurcate along the lakeward direction, creating an intricate channel network. Channel mouth bars developed with the lakeward extension of bifurcating channels, forming delta lobes composed of distributary channel–channel mouth bar–distal bars, and these lobes amalgamated to form a large-scale, widely distributed, and interconnected clastic rock reservoir. Due to the arid climate, the activity of deltas is driven by flood events. As a result, carbonate deposits occasionally developed within the restricted waters between the lateral combinations during inter-flood periods (Figure 7).

The middle facies belt covered the transitional area between the delta front and prodelta. Only a few distributary channels extended into the area and formed small-scale and isolated delta lobes. Sheet-like sand, algal mounds, and marl flats developed within the area between two delta lobes. In this belt, carbonate deposits also formed during the inter-flood periods. In general,

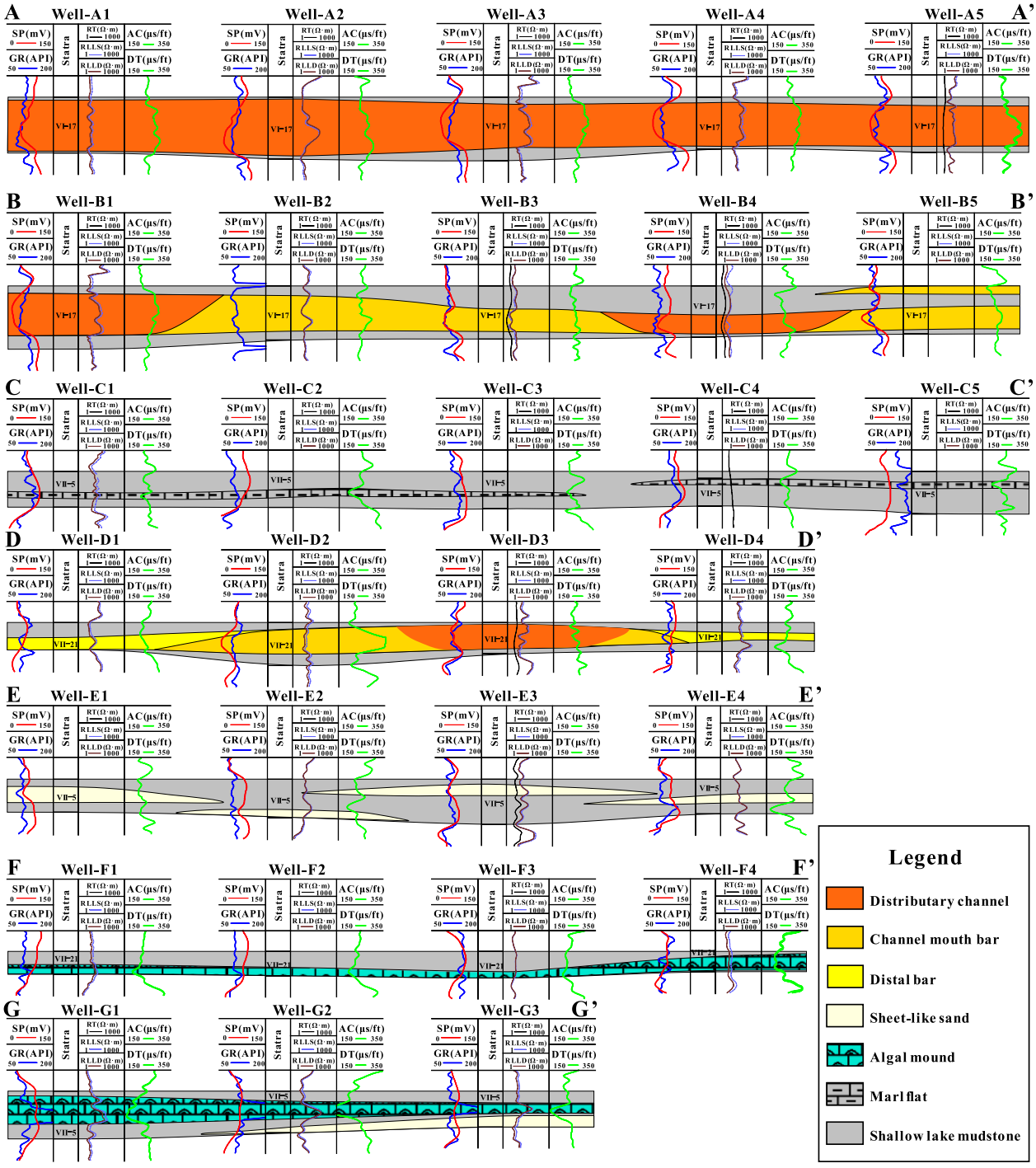

FIGURE 6
Typical sedimentary architecture sections. Locations of **(AA',BB')** are given in Figure 5A, locations of **(CC',EE', GG')** are given in Figure 5C, and locations of **(DD',FF')** are given in Figure 5B.

the algal mounds developed after the abandonment of the upstream deltas.

The distal facies belt forms within prodelta areas and is characterized by large-scale algal mounds and marl flats (Figure 7). Due to the area being far away from the upstream deltas, clastic deposits are mainly suspended, transported clay and silt. Alga-generated carbonate sediments mixed with bioclasts and clay deposits to form algal mounds and marl flats. As the algal mounds and mar flats are thin-layered, multiple layers are vertically stacked to form interlayered mudstone, sheet-like sand, algal mounds, and marl flats.

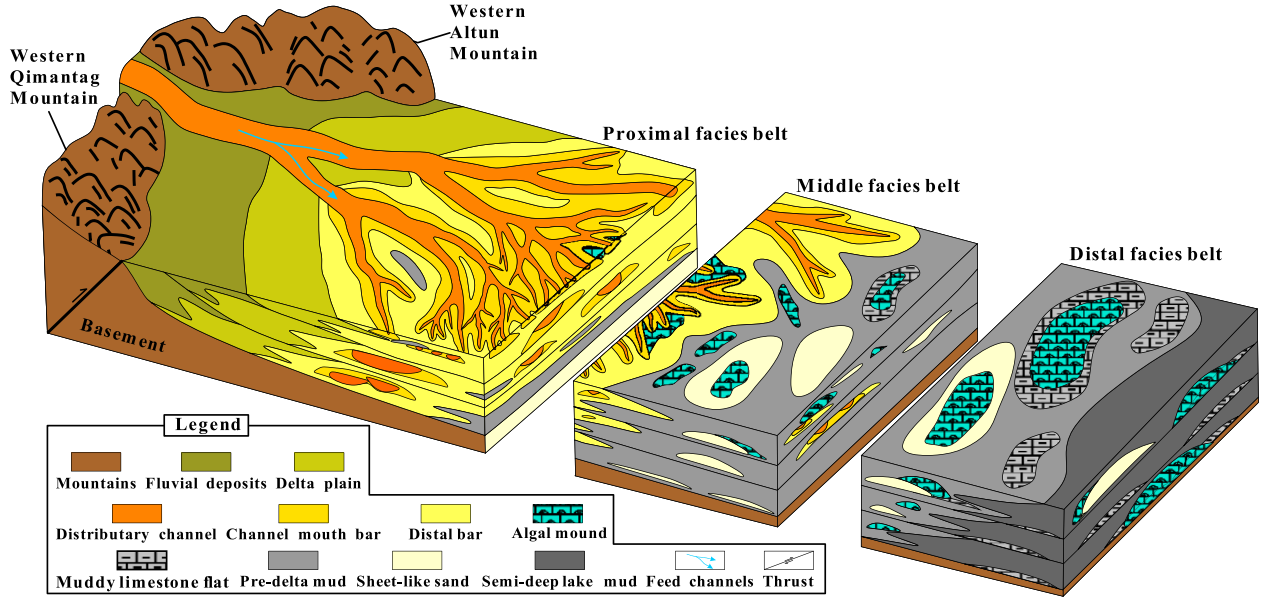

FIGURE 7
Sedimentary model of the lacustrine mixed carbonate/siliciclastic depositional system.

In the mixed system, the main mixing type is facies mixing. There is slight compositional mixing, but it is atypical. Therefore, the deltaic reservoir within the mixed system is highly qualified (Fang, 2010). Some of the algal mounds that have undergone large-area dissolution can be regarded as reservoirs with good potential, and undissolved algal mounds and marl flats generally have extremely low permeability and can be treated as barriers to subsurface fluid flow (Chen et al., 2004).

4.2 Base-level fluctuations drive facies belt transition.

The base-level cycle is a comprehensive reflection of factors such as tectonic activity and climate change and a key factor driving the evolution of sedimentary systems in shallow-water areas in the lacustrine environment (Wu et al., 2019; Chen et al., 2022; Mutti et al., 2023). In a depression, due to the low intensity of tectonic activity (Wu et al., 2019; Wu et al., 2022), the paleoclimate is the dominant factor affecting the base-level cycles (Wu et al., 2019). A short-term base-level cycle is the dominant factor controlling the facies belt transformation within the study area. Three typical stratum units are taken as examples and explained below.

The distal facies belt appears at the stage of the rise-to-fall transformation of two adjacent short-term base-level cycles (Figure 2), and arid climate and relatively deep water are conducive to algae flourishing and the production of carbonate and algal mounds (Ye et al., 2019). As a result, marl flats are the dominant architectural elements in the distal facies belt (Figure 5C).

The middle facies belt is formed during the middle stage of a short-term base-level cycle (Figure 2). The water depth is generally shallower than that in the initial stage, and the production of carbonate decreases, resulting in the mixing of the terminal part of deltas. Algal mounds and marl flats are produced on a smaller scale (Figure 5B).

The proximal facies belt is formed at the stage of the fall-to-rise transformation of two adjacent short-term base-level cycles (Figure 2). The very limited accommodation space and relatively shallow water hinder carbonate production (Ye et al., 2019) while enhancing the development of deltas (Figure 5A).

With the transformation of facies belts within a short-term–sub-short-term base-level cycle, a mixing of carbonate and siliciclastic layers in the vertical and downstream directions occurs (Figure 4).

5 Conclusion

This paper focuses on the discovery of the sedimentary characteristics, spatial patterns, and architecture of a lacustrine mixed carbonate/siliciclastic system at the margin of a depression based on outcrop and subsurface reservoir data.

Seven types of lithofacies, including clastic and carbonate deposits, were identified based on core data. Core data, well logging data, and outcrop data were used to establish a classification of sedimentary architecture elements distributed along the lakeward direction. Seven types of sedimentary architecture elements were identified from well data, and the spatial distribution and patterns were characterized for each single-layer unit.

The sedimentary system can be divided into three facies belts along the lakeward direction. The proximal facies belt is characterized by large-scale, widely distributed, and interconnected delta-front deposits, which are composed of lakeward bifurcating distributary channels and corresponding delta lobes. The middle facies belt is characterized by relatively small-scale isolated distributed delta lobes, sheet-like sand, and limited carbonate

deposits. The distal facies belt is dominated by algal mounds and surrounding marl flats.

Within the study area, the development of facies belts in different single-layer units is closely related to the short-term base-level cycles. The proximal and distal facies belts are formed during the fall-to-rise and rise-to-fall transformation of two adjacent short-term base-level cycles, respectively. The middle facies belt is formed during the middle stage of a short-term base-level cycle. At the margin of the depression, a short-term base-level cycle dominated the facies belt transformation during the formation of the target interval, resulting in the inter-layered vertical stacking of the three facies belts. According to the established sedimentary model, the scale, connection, and quality of reservoirs gradually decreased from the proximal to the distal facies belt.

Data availability statement

The original contributions presented in the study are included in the article/Supplementary Material; further inquiries can be directed to the corresponding author.

Author contributions

FW: conceptualization, data curation, formal analysis, funding acquisition, investigation, methodology, project administration, resources, software, supervision, validation, visualization, writing–original draft, and writing–review and editing. ZY: data curation, formal analysis, funding acquisition, resources, software, validation, visualization, and writing–original draft.

Funding

The author(s) declare that financial support was received for the research, authorship, and/or publication of this article. This research was funded by the National Natural Science Foundation of China with grant numbers 41802123 and 42130813.

Conflict of interest

The authors declare that the research was conducted in the absence of any commercial or financial relationships that could be construed as a potential conflict of interest.

Publisher's note

References

Chen, Z., Shou, J., Wang, S., and Meng, S. (2004). Tertiary lake algal limestone oil and gas reservoirs in the western part of Qaidam Basin and exploration potential. *China Pet. Explor.* 9, 59–66.

Chen, N. G., Wang, Y. Q., Xu, F., Yang, T. Y., and Xia, Z. Y. (2015). Palaeosalinity characteristics and its sedimentary response to the Cenozoic salt-water lacustrine deposition in Qaidam Basin. *J. Palaeogeogr.* 17, 371–380. doi:10.7605/gdlxb.2015.03.31

Chen, Y., Xia, X. M., Zhao, J., Cui, J., Qiao, B. H., Zhao, D. S., et al. (2022). Sedimentary characteristics and formation mechanisms of Neogene algal limestone in Western Qaidam Basin. *Acta Sedimentol. Sin.* 40, 1323–1334. doi:10.14027/j.issn.1000-0550.2021.056

Cui, H., Zhu, S., Liang, C., Ma, W., Tong, H., and Shi, Z. (2023). Facies association analysis of a Toarcian siliciclastic-carbonate lacustrine system, Sichuan Basin, China. *Palaeogeogr. Palaeoclimatol. Palaeoecol.* 631, 111841. doi:10.1016/j.palaeo.2023.111841

Dolan, J. F. (1989). Eustatic and tectonic controls on deposition of hybrid siliciclastic/carbonate basinal cycles: discussion with examples. *AAPG Bull.* 73, 1233–1246. doi:10.1306/44b4aa0f-170a-11d7-8645000102c1865d

Dong, G., Chen, H., He, Y., Qing, Z., and Luo, J. (2007). Some problems on the study of the mixed siliciclastic carbonate sediments. *Adv. Earth Sci.* 22, 931. doi:10.11867/j.issn.1001-8166.2007.09.0931

Du, X. F., Xu, C. G., Zhu, H. T., Xie, X. N., Zhu, X. M., Liu, K. Y., et al. (2020). Research advances of mixed siliciclastic and carbonate sediments in continental rift basins. *Earth Sci.* 45, 3509–3526. doi:10.3799/dqkx.2020.251

Fang, S. Y. (2010). *Study on the technology of improving secondary oil recovery effect-taking Huatugou Oilfield in the west of Qaidam Basin as an Example*. Chengdu: Chengdu University of Technology. PhD dissertation.

Feng, J. L., Cao, J., Hu, K., Chen, Y., Yang, S. Y., Liu, Y. T., et al. (2011a). Forming mechanism of middle-deep mixed rock reservoir in the Qaidam basin. *Acta Petrol. Sin.* 27, 2461–2472.

Feng, J. L., Hu, K., Cao, J., Chen, Y., Wang, L. G., Zhang, Y., et al. (2011b). A review on mixed rocks of terrigenous clastics and carbonates and their petroleum-gas geological significance. *Geol. J. China Univ.* 17, 297. doi:10.16108/j.issn1006-7493.2011.02.016

Feng, J. L., Cao, J., Hu, K., Peng, X. Q., Chen, Y., Wang, Y. F., et al. (2013). Dissolution and its impacts on reservoir formation in moderately to deeply buried strata of mixed siliciclastic–carbonate sediments, northwestern Qaidam Basin, northwest China. *Mar. Petroleum Geol.* 39, 124–137. doi:10.1016/j.marpetgeo.2012.09.002

Fu, X., Du, X. F., Guan, D. Y., Wang, Q. M., and Ye, M. S. (2020). Depositional system, plane distribution and exploration significance of fan delta mixed siliciclastic-carbonate sediments in lacustrine basin: an example of Member 1-2 of Shahejie Formation in offshore Bohai Bay, Eastern China. *Earth Sci.* 45, 3706–3720. doi:10.3799/dqkx.2020.173

Gao, G., Yang, S. R., and Qu, T. (2018). Research status of mixing sediments and their relationship with petroleum enrichment. *Geol. Sci. Technol. Inf.* 37, 82–88. doi:10.19509/j.cnki.dzkq.2018.0610

Gierlowski-Kordesch, E., Finkelstein, D. B., Truchan Holland, J. J., and Kallini, K. D. (2014). Carbonate lake deposits associated with distal siliciclastic perennial-river systems. *J. Sediment. Res.* 83, 1114–1129. doi:10.2110/jsr.2013.81

Karakaya, S., Ogiesoba, O. C., and Olariu, C. (2022). Lateral lithology heterogeneity due to autogenic processes in mixed carbonate and siliciclastic deposits of Cisco Group, the Eastern Shelf of the Permian Basin. *King Cty. north-central Texas[C]//SEG Int. Expo. Annu. Meet. SEG*. D011S023R004. doi:10.1190/image2022-3751846.1

Karakaya, S., Ogiesoba, O. C., Olariu, C., and Bhattacharya, S. (2024). Generating 3D lithology probability volumes using poststack inversion, probabilistic neural networks, and Bayesian classification—a case study from the mixed carbonate and siliciclastic deposits of the Cisco Group of the Eastern Shelf of the Permian Basin, north-central Texas. *Geophysics* 89 (2), B131–B146. doi:10.1190/geo2023-0157.1

Kjøll, H. J., Midtkandal, I., Planke, S., Millett, J., Manton, B., and Anderskouv, K. (2024). The interplay between siliciclastic and carbonate depositional systems: maastrichtian to Danian basin-floor sediments of the MID-Norwegian Møre Basin. *Basin Res.* 36, e12827. doi:10.1111/bre.12827

Lebrec, U., Lang, S. C., Paumard, V., O'Leary, M. J., Yokoyama, Y., Hacker, J., et al. (2023). Discovery of holocene ooid shoals in a siliciclastic delta, de grey river, north west shelf, Australia. *Geology* 51, 366–371. doi:10.1130/g50840.1

Lee, Y. I., and Kim, J. C. (1992). Storm-influenced siliciclastic and carbonate ramp deposits, the lower ordovician dumugol formation, South Korea. *Sedimentology* 39, 951–969. doi:10.1111/j.1365-3091.1992.tb01990.x

Li, Y., Gou, Y., Cao, Z., and Sun, X. (2009). Identification of algal limestone reservoir with logging in Yuexi area, Qaidam basin. *J. Southwest Petroleum Univ. Sci. and Technol. Ed.* 31, 56.

Li, T., Huang, Z., Feng, Y., Chen, X., Ma, Q., Liu, B., et al. (2020). Reservoir characteristics and evaluation of fluid mobility in organic-rich mixed siliciclastic-carbonate sediments: a case study of the lacustrine Qiketai Formation in Shengbei Sag, Turpan-Hami Basin, Northwest China. *J. Petroleum Sci. Eng.* 185, 106667. doi:10.1016/j.petrol.2019.106667

Li, Q. Q., Bao, Z. D., Xiao, Y. X., Chen, J. Y., Li, Z. C., Wang, Z. J., et al. (2021). Research advances and prospect of mixed deposition. *Acta Sedimentol. Sin.* 39, 153–167. doi:10.14027/j.issn.1000-0550.2020.140

Li, Y., Huang, W., and Jiu, B. (2021). Factors that controlled deposition of lacustrine, mixed siliciclastic-carbonate sediments in the upper fourth member of the Eocene Shahejie Formation in the Zhanhua Sag, East China. *J. Paleolimnol.* 66, 55–70. doi:10.1007/s10933-021-00185-x

Liu, Z. G., Zhang, Y. S., Song, G. Y., Li, S. M., Long, G. H., Zhao, J., et al. (2021). Mixed carbonate rocks lithofacies features and reservoirs controlling mechanisms in a saline lacustrine basin in Yingxi area, Qaidam Basin, NW China. *Petroleum Explor. Dev.* 48, 80–94. doi:10.1016/s1876-3804(21)60006-x

Meng, Z., Feng, B., and Wang, G. (2009). Sedimentation of mixed bioclastic shallows of steep slope zone in Gubei Depression. *Petroleum Geol. Eng.* 23, 9–11.

Mount, J. F. (1984). Mixing of siliciclastic and carbonate sediments in shallow shelf environments. *Geology* 12, 432–435. doi:10.1130/0091-7613(1984)12<432:mosacs>2.0.co;2

Mount, J. (1985). Mixed siliciclastic and carbonate sediments: a proposed first-order textural and compositional classification. *Sedimentology* 32, 435–442. doi:10.1111/j.1365-3091.1985.tb00522.x

Mutti, M., Vallati, M., Tomás, S., Galli, C., Bahniuk Rumbelsperger, A. M., Maerz, S., et al. (2023). Constraining depositional evolution and reservoir compartmentalization in a mixed carbonate-siliciclastic lacustrine system: the Yacoraite formation, Salta Group, NW Argentina. *Mar. Petroleum Geol.* 149, 106049. doi:10.1016/j.marpetgeo.2022.106049

Palermo, D., Aigner, T., Geluk, M., Poeppelreiter, M., and Pipping, K. (2008). Reservoir potential of a lacustrine mixed carbonate/siliciclastic gas reservoir: the Lower Triassic Rogenstein in The Netherlands. *J. Petroleum Geol.* 31, 61–96. doi:10.1111/j.1747-5457.2008.00407.x

Wang, Y. Q., Gong, Q. S., Xia, Z. Y., and Xiong, S. Y. (2012). Provenance analysis of oligocene sediments in western Qaidam Basin. *Geol. China* 39, 426–435.

Wang, J., Zhang, D., Yang, S., Li, X., Shi, Y., Cui, J., et al. (2020). Sedimentary characteristics and genesis of the salt lake with the upper member of the Lower Ganchaigou Formation from Yingxi sag, Qaidam basin. *Mar. Petroleum Geol.* 111, 135–155. doi:10.1016/j.marpetgeo.2019.08.006

Wang, Q. M., Du, X. F., and Wan, L. W. (2020). Characteristics of mixed sedimentary development and main control factors in lower third member of shahejie formation of southern slope belt of laizhouwan sag, Bohai sea. *Earth Sci.* 45, 3645–3662. doi:10.3799/dqkx.2020.187

Wei, X., Li, Z., Ma, Y., Li, Y., Hu, J., Liu, K., et al. (2021). Sedimentology and sequence stratigraphy of the mixed clastic-carbonate deposits in the Late Paleozoic icehouse period: a case study from the northern Qaidam Basin. *China Geol.* 4, 1–13. doi:10.31035/cg2021068

Wu, Y. Y., Lü, J. L., and Fang, X. (2019). Analysis of favorable facies belts in reservoir of lacustrine carbonate rocks-hybrid sediments: case study of Paleogene in Qaidam Basin. *Nat. Gas. Geosci.* 30, 1150–1157. doi:10.11764/j.issn.1672-1926.2019.05.019

Wu, H., Liu, H., Wang, L., Gui, L., Yang, C., and Wang, L. (2022). Mixed carbonate-siliciclastic reservoir characterization and hydrocarbon accumulation process of the Ganchaigou area in the western Qaidam Basin, Tibet Plateau. *Carbonates Evaporites* 37, 26. doi:10.1007/s13146-022-00769-2

Xu, W., Du, X. F., Huang, X. B., Song, Z., and Li, Z. (2019). Research Advances and Critical Issues of "mixed siliciclastic and carbonate sediments". *Acta Sedimentol. Sin.* 37, 225–238. doi:10.14027/j.issn.1000-0550.2018.152

Ye, M., Xie, X., Xu, C., Du, X., Du, X., and Song, Z. (2019). Sedimentary features and their controls in a mixed siliciclastic–carbonate system in a shallow lake area: an example from the BZ-X block in the Huanghekou Sag, Bohai Bay Basin, Eastern China. *Geol. J.* 54, 2016–2033. doi:10.1002/gj.3275

Zhang, M., Yin, C. M., Shou, J. F., Chen, Z. L., and Zhang, Y. Z. (2004). Sedimentary facies of carbonate rocks of the paleogene and Neogene in western Qaidam Basin. *J. Palaeogeogr.* 6, 391–400.

Zhao, F. (2015). Identification of Neogene mixed lacustrine carbonate in western Qaidam basin. *Carbonates Evaporites* 30, 281–285. doi:10.1007/s13146-014-0210-9

frontiers | Frontiers in Earth Science

TYPE Original Research
PUBLISHED 12 November 2024
DOI 10.3389/feart.2024.1472206

OPEN ACCESS

EDITED BY
Jianguo Zhang,
China University of Geosciences, China

REVIEWED BY
Yiquan Ma,
Chengdu University of Technology, China
Rui Zhang,
Peking University, China

*CORRESPONDENCE
Yu Sun,
sunyu_hc@163.com

RECEIVED 29 July 2024
ACCEPTED 29 October 2024
PUBLISHED 12 November 2024

CITATION
Wang X, Sun Y, Yu L, Tang Z, Yan B and Liu R (2024) High-resolution cyclic framework for the Songliao Basin in northeastern China, and its implications for sedimentation and organic matter enrichment.
Front. Earth Sci. 12:1472206.
doi: 10.3389/feart.2024.1472206

High-resolution cyclic framework for the Songliao Basin in northeastern China, and its implications for sedimentation and organic matter enrichment

Xinrui Wang[1], Yu Sun[1]*, Limin Yu[2], Zhenxing Tang[2], Baiquan Yan[3] and Ruhao Liu[4]

[1]School of Earth Science, Northeast Petroleum University, Daqing, Heilongjiang, China, [2]PetroChina Jilin Oilfield Company, Songyuan, Jilin, China, [3]Sanya Offshore Oil and Gas Research Institute, Northeast Petroleum University, Sanya, Hainan, China, [4]Institute of Unconventional Oil and Gas Development, Chongqing University of Science and Technology, Chongqing, China

The study of fine-grained sedimentation has consistently concentrated on investigating the mechanisms and principles governing the enrichment of organic matter. However, the lack of unified stratigraphic framework has always existed as fine-grained sedimentation covers two distinct grain-size grades, namely, mud and silt, which has impeded the progress of subsequent production research. This study exemplified this issue by analyzing the first member of the Qingshankou Formation in the southern Songliao Basin. We established reconstructed gamma and density curves that mitigated filter noise interference, integrated high-resolution sequence results with astronomical cycle divisions, and created a high-frequency isochronous stratigraphic framework for clastic fine-grained sedimentation by leveraging the weak sensitivity of sandstone density curves and the robust stability in eccentricity cycle extraction. This approach addresses the inconsistencies in stratigraphic division methodologies and mismatched outcomes stemming from the use varying techniques to delineate mud and silt components within clastic fine-grained sedimentary sequences. Furthermore, it elucidates how tectonic-scale variations in sediment supply coupled with potential accommodation changes dictate macroscopic stacking patterns within strata, whereas climate fluctuations on orbital time scales govern sand-mud progradation degrees within these layers, culminating in periodic rhythmic characteristics characterized by vertical sand-mud interbedding. A model for stratigraphic development pertaining to lake delta systems constrained by a "synchronous heterotopy" paradigm is proposed for the southern Songliao Basin. The organic matter enrichment pattern aligns with its filling dynamics, indicating an "overfilling" type developmental pattern at lower strata levels where organic material predominantly originates from terrestrial plant debris external to the basin; this material accumulates primarily within silty zones along layers—with areas exhibiting heightened enrichment values slightly lagging behind short-eccentric maxima positions. In contrast, under an upper

"balanced filling" type developmental framework, sources of organic matter are derived both internally and externally relative to the basin—exhibiting substantial heterogeneity—and regions marked by elevated organic matter concentrations are directly associated with locations identified as short-eccentric maxima.

KEYWORDS

astronomical cycle, high-resolution sequence, Qingshankou Formation, Songliao Basin, organic matter enrichment

1 Introduction

The importance of studying fine-grained sedimentary patterns and the accumulation of organic matter (OM) has been highlighted in the exploration of unconventional reservoirs of shale oil and gas. Fine-grained sediments, with particle sizes smaller than 62 μm, are particularly sensitive to minor climatic changes, and exhibit complex lithological, structural, and compositional characteristics that involve a highly heterogeneous OM content (Wang X. R. et al., 2023). The OM within shales significantly influences their potential for hydrocarbon generation as well as the type of reservoir space, reservoir capacity, and the presence of hydrocarbons (Olga et al., 2023; Wang Y. C. et al., 2023; Wang et al., 2022a; Dong et al., 2022; Yu et al., 2020). Therefore, comprehensively understanding the mechanisms and patterns of OM accumulation is crucial for examining fine-grained sedimentary rocks. Two primary hypotheses for OM accumulation are currently in vogue: the model of primary productivity and the preservation model (Calvert and Pedersen, 1993; Tyson, 2005; Bechtel et al., 2012; Jia et al., 2013a). The former emphasizes the influence of OM sources and the strength of primary productivity on OM accumulation, while the latter provides a clearer explanation of the subsequent conditions for OM preservation, such as salinity and redox conditions. Researchers believe that these two models may be jointly applicable to specific sedimentary environments. This suggests that the formation and preservation of OM are complex processes that are influenced by such factors as the terrigenous clastic input and the sedimentary environment (Pan et al., 2021; Song et al., 2016).

Numerous studies have shown that fine-grained lacustrine sediments are more sensitive to changes in the sedimentary environment, paleoclimate, and redox conditions than fine-grained marine sediments. Lacustrine sediments can provide high-resolution records of the terrestrial paleoenvironment. The Songliao Basin in China is a typical basin of the Mesozoic lacustrine revolution (Cohen, 2003), and contains complete and continuous records of the inland environmental climate in the Cretaceous. The Qingshankou and Nenjiang Formations are major source rocks for the Upper Cretaceous in the Songliao Basin, and a considerable amount of research has been devoted to examining their OM characteristics and mechanisms of OM enrichment (Jia et al., 2013a; Jia et al., 2013b). It is widely accepted that marine transgressions during a global rise in sea level (OAE3) led to OM enrichment in the Nenjiang Formation (Liu et al., 2021; Xu et al., 2019; Liu et al., 2022; Cao et al., 2016; Zhang et al., 2020; Zhang et al., 2021). However, debate persists regarding the mechanisms of OM enrichment in the Qingshankou Formation. This is because the southern Songliao Basin is influenced by many factors, including the paleoclimate, lake transgression events, and anoxic events. Many types of fine-grained sedimentary rocks have formed in the first member of the Qingshankou Formation, which has a high heterogeneity (Ma et al., 2022). The terrigenous clastic input near the edge of the lake basin in particular has caused the trend of OM enrichment in the area to be influenced by multiple factors, in contrast to the trend of OM enrichment in the deep-lake area in the northern Songliao Basin. Researchers have used wavelet spectral analysis to identify the astronomical cycles of lacustrine mudstones of the Qingshankou Formation, used this to establish a coupling relationship between the evolution of the sedimentary environment and vertical OM enrichment, and have examined astronomical-scale cycles that drive OM enrichment. Some scholars have analyzed geochemical elements from well GY1, and proposed that a 405 ka long eccentricity controls the cycles of OM enrichment in the Qingshankou Formation (Feng et al., 2023). When the eccentricity is near its maximum, the corresponding sedimentary cycle is in an organic-rich interval. Huang compiled high-resolution datasets of the total organic carbon (TOC) and stable carbon isotope (13Corg) contents of SK1 to investigate its processes of organic carbon burial, and reported a robust cyclicity of TOC of approximately 173,000 years (Huang et al., 2023). The ~173 ka obliquity-related forcing signal was amplified by the internal climatic feedback of the carbon cycle under different geographic and climatic conditions, and led to periodic OM enrichment. However, most such research has focused on vertical variations in the organic matter in single-core wells in the central part of the lake basin, such that a continuous lateral comparison and evolutionary analysis are lacking. A consensus on the periodicity of OM enrichment also remains elusive (Liu et al., 2022; Wang X. R. et al., 2023; Xu et al., 2015; Zhang et al., 2022; Liu et al., 2021; Wang M. et al., 2023; Liu et al., 2021; Wang H. R. et al., 2023).

The area of hydrocarbon exploration in the first member of the Qingshankou Formation (referred to hereinafter as the "First Member") in the southern Songliao Basin is located at the terminus of a deltaic depositional system. When analyzing the mechanisms of OM enrichment, it is important to integrate the near-source terrigenous clastic influences within a shallow lake with the sand-rich environment. A unified model of this is lacking because researchers have investigated OM contents in different locations without using a common temporal framework. A coherent, high-frequency, sequential stratigraphic framework that can cover the area from the sand-rich lake margin to the mud-rich center of the lake is needed to this end.

The conventional clastic strata along the margin of the basin and the mudstone strata at the center of the lake are often discussed

separately in currently used high-frequency sequential stratigraphic divisions of the Qingshankou Formation in the southern Songliao Basin. Traditional and high-resolution sequential stratigraphy are still used for dividing clastic strata, while cyclic stratigraphy is applied to mudstone layers at the center of the lake by using astronomical rhythms (Wu et al., 2009), and T-R (Cheng et al., 2003) and GPR sequences (Du et al., 2016) are used to restore the characteristics of depositional rhythm of mudstone to construct its spatio-temporal order. Both high-resolution sequences and astronomical Milankovitch cycles play a vital role in establishing the framework for fine-grained lacustrine sedimentary strata. Despite their interconnections, however, differences in their foci of research, scales, and emphases prevent a clear correlation between them.

High-resolution sequential stratigraphy is significantly influenced by subjective human decisions (Cross, 1994), and identifying the data surfaces in mud-rich areas is challenging. Although astronomical cycles offer a higher resolution, they are suitable only for analyzing continuously deposited and tectonically stable mudstone strata. Astronomical noise, such as that owing to autocyclic processes, obscures the clear identification of the cycles in sand-rich areas. Thus, the high-resolution sequential stratigraphic results for the margins of terrestrial lakes and mud-rich lake centers cannot be integrated, and this leads to a "segmented, blocky, and methodological" characteristic in a basin-wide sequential framework of analysis (Sun et al., 2017; Wu et al., 2009; Zhang et al., 2019).

Both astronomical cycles and high-resolution sequential stratigraphy fundamentally describe the repetitiveness of the strata, and represent branches of cyclostratigraphy at different scales (Zheng et al., 2001; Wang et al., 2018). In light of this, we use the floating astronomical timescale of the Songliao Basin as a reference to combine these cyclostratigraphic methods based on Milankovitch's theory such that this yields the advantages of high-resolution sequential stratigraphy. We then compare the characteristics of sequential development of deep-water mud-rich zones and shallow-water sand-rich zones within fine-grained sedimentary systems. Following this, we construct the corresponding relationship between astronomical cycles (long eccentricity, short eccentricity, obliquity, and precession cycles) in the mud-rich center of the lake basin and the base-level cyclic hierarchies (fourth to seventh order) in the shallow-water sand-rich margins.

This study bridges the gap between the results of high-resolution sequential stratigraphy of the margins of the lake basin, and those of the division of the astronomical cycles of the lake center to establish a high-frequency sequential stratigraphic framework that is constrained by astronomical cycles. This framework restores the ordered spatio-temporal relationships of the complex strata, and can be used to identify the pattern of evolution of the depositional sequence along the margins of continental rift lake basins. Based on this, we use the tectonic and orbital timescales in conjunction with the differences in OM characteristics to extract the important factors controlling OM enrichment. We also establish a model of OM enrichment in fine-grained sediments under strong terrigenous clastic influences.

2 Geological setting

2.1 Tectonics and sedimentation

The Songliao Basin is a large-scale Mesozoic–Cenozoic petroleum-bearing continental sedimentary basin in northeastern China, with a dual structural feature of an initial fault-induced depression followed by a superimposed depression in the NNE direction (Feng et al., 2010). The foundation of the basin consists of Carboniferous–Permian metamorphic rocks and granite, while the sedimentary cover includes Jurassic, Cretaceous, Paleogene, Neogene, and Quaternary deposits (Figure 1C). Based on the properties of the basement rocks and the regional geological characteristics of the caprock, the structural layers of the depression in the Songliao Basin can be divided into six first-order structural units, which are believed to control the distribution of reservoirs for oil, natural gas, shale gas, and oil sands (Figures 1A, C). The central depression has long been the sedimentary and subsidence-related center of the Songliao Basin, and almost all of its strata are well developed. The thickness of the Cretaceous stratum exceeds 6500 m, and it contains two kinds of high-quality rocks that are the source of hydrocarbons: First Member and the Second Member of the Nenjiang Formation (Liu et al., 2019).

The Songliao Lake Basin underwent significant subsidence and expansion, and developed a water inlet system during the development of the Qingshankou Formation, especially in the early stages of formation of the Qingshankou section when the rate of expansion of the water surface was the highest. Analyses of the stratigraphy and the thickness of the mudstone layer show that the depositional center of the depression extends along Qijia, Gulong, Daan, Changling to Lishu, and Sanshao to Dewei (Sun, 2010). The rate of subsidence of the sedimentary system in the lake basin extension is greater than the rate of sedimentation, and has led to a landward retreat of the background (Wang et al., 2007; Wang et al., 2009) such that only the Tongyu–Baokang sedimentary system remains intact. Its depositional end is the shale area of the southern Songliao Basin (Wang M. et al., 2023; Li et al., 2020). Unlike the shale oil-rich Qijia–Gulong Sag in the north of the Songliao Basin, where dark mudstone and shale that are rich in organic matter are deposited in deep and semi-deep lake facies, the organic-rich shale in the south is located in the outer front surfaces of the delta (shallow lake facies) of the Daqingzijing area, which is more severely affected by terrigenous debris (Figure 1B).

2.2 Sequential stratigraphy

The Cretaceous system, featuring a continental clastic rock mixed with a sedimentary formation of oil shale (Figure 2A), was the main sedimentary stratum during the depression of the Songliao Basin. It can be divided into upper and lower series, consisting of nine formations and 27 lithological sections. The period considered here pertained to the First Member of the Upper Cretaceous (hereinafter referred to as Qn1). This period featured a rapid expansion of the lake basin during the early stage of the overall depression of the Songliao Basin. The basin

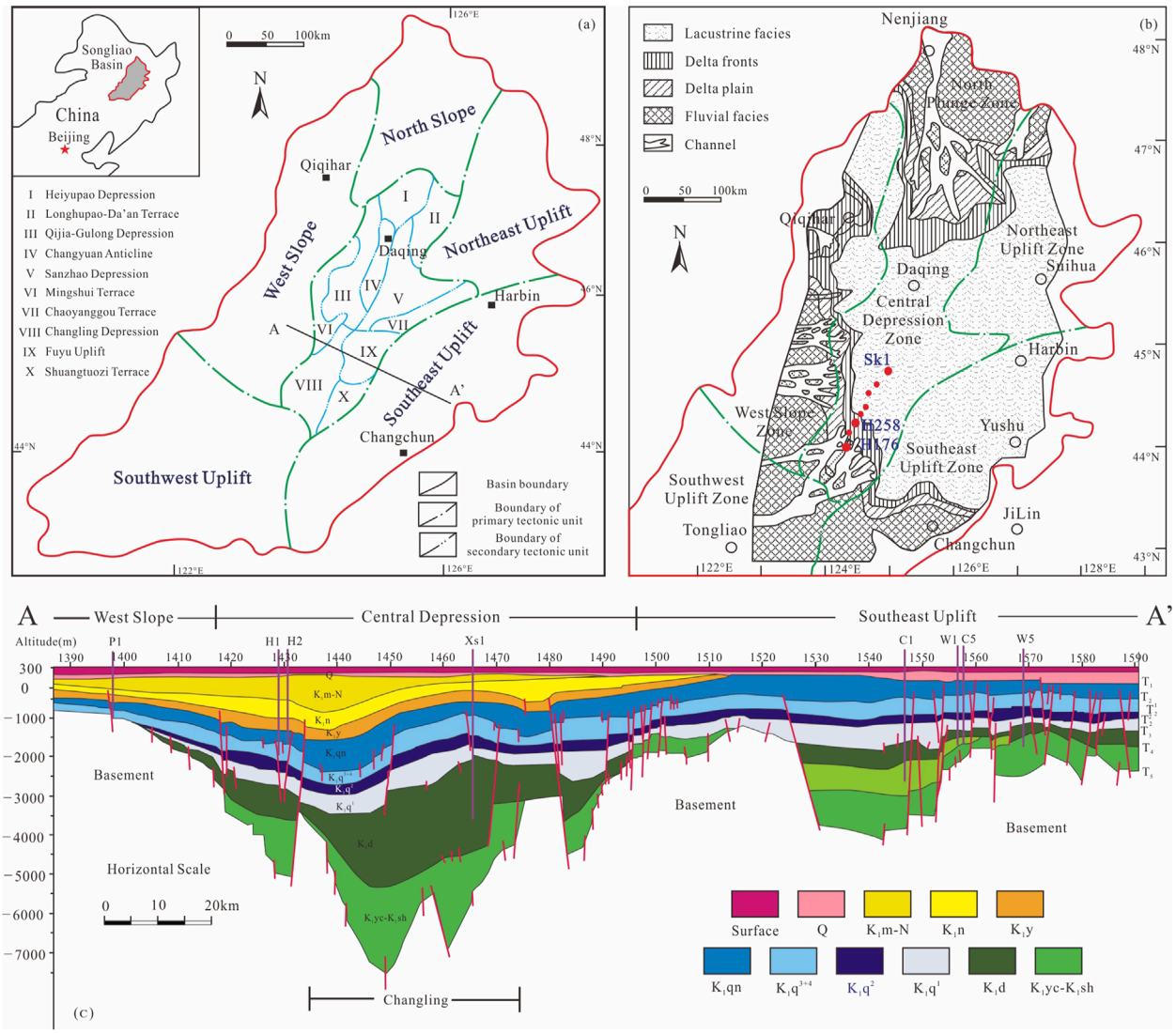

FIGURE 1
Tectonic position and comprehensive stratigraphic map of the study area in the southern part of the Songliao Basin (Liu et al., 2023; Wu et al., 2009). **(A)** Location map of the Sanzhao depression and tectonic units of the Songliao Basin. The black line (AA') shows the location of the stratigraphic profile (Figure 1C) of the Songliao Basin. **(B)** The locations of the study area and important wells considered in this study. **(C)** Stratigraphic section across the central part of the Songliao Basin, showing its structure.

was dominated by delta and lake sedimentary systems, and its lithology involved greyish-green, dark mudstone, and a dark-gray siltstone interbedding, while the bottom often featured dark mudstone.

Wu et al. have continually sought to calibrate the astronomical age of the Qingshankou Formation in the Songliao Basin since 2009 (Wu et al., 2009). They used information acquired from well SK1 to determine the presence of an astronomically driven Milankovitch sequence within the Qingshankou Formation. They also established the floating astronomical scale (ATS) by combining radioisotope ages and paleomagnetic analyses (Figure 2B). They concluded that the three sets of oil shale and black shale deposits at the bottom of the First Member in the Songliao Basin can be attributed to the first anoxic event of the lake basin (LAE1). This event corresponded to the Late Cretaceous Cenomanian–Late Turonian–Early Oceanic anoxic event (OAE2) (Demaison and Moore, 1980), which constrained the timeframe of development of the Qingshankou Formation such that its absolute geological age was determined to be 91.341 Ma. It was located in the lower 20 m of LAE1—at the junction of the sandstone and mudstone between the fourth and first members of the Qingshankou Formation, and the underlying Quantou Formation (Wu et al., 2009; Wu et al., 2013; Wu et al., 2014; Wu et al., 2022).

However, when analyzing sedimentary and tectonic evolution as well as oil shales, the First Member in the Songliao Basin is usually considered to be the boundary between the Quantou Formation and the Qingshankou Formation, with the oil shale at the bottom of the First Member designated as the boundary between them (Liu et al., 2019). Owing to the large deposition

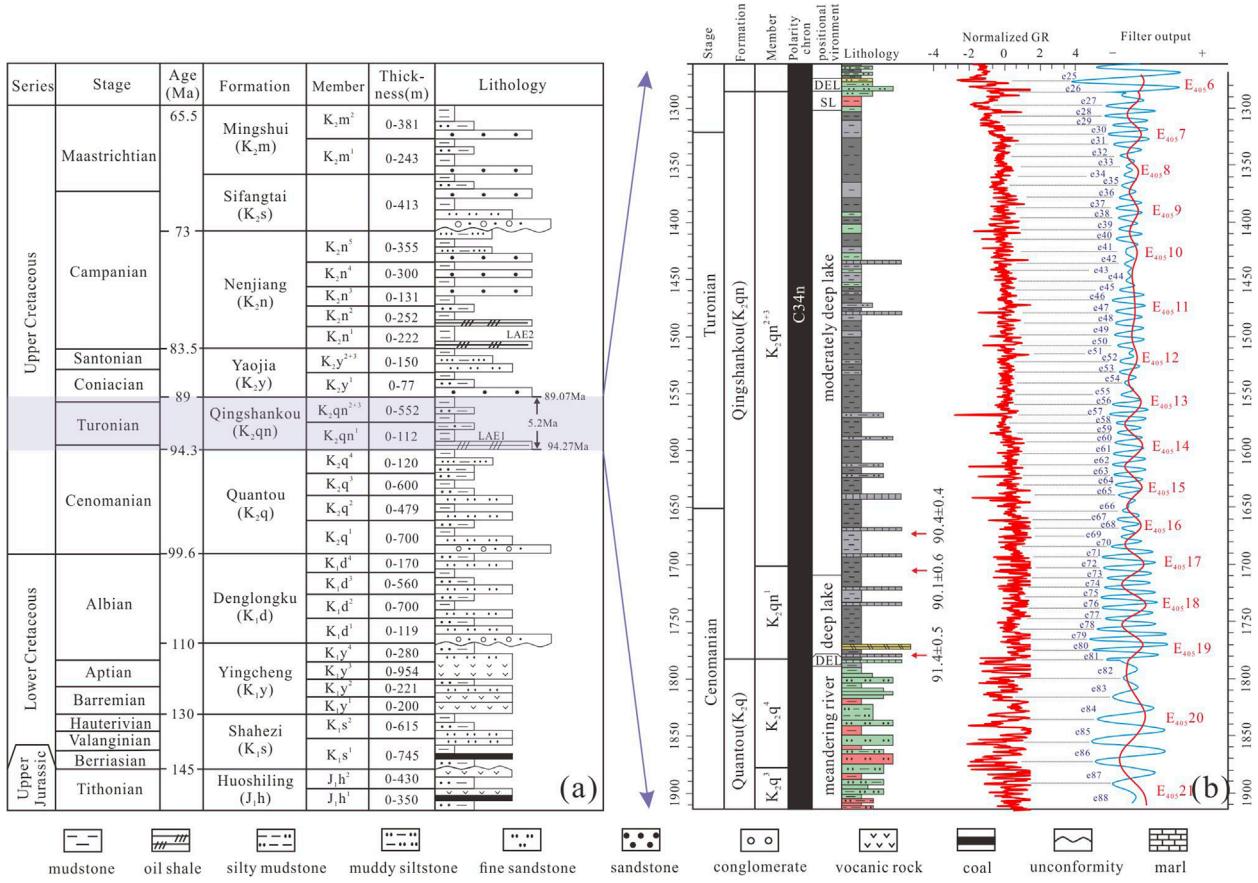

FIGURE 2
Extent of the target layer, and characteristics of the lithology and the astronomical cycle (Modified by Wu et al., 2009; Wu et al., 2013). **(A)** Comprehensive stratigraphic characteristics of the Cretaceous system in the Songliao Basin. **(B)** Compilation of key data showing the stratigraphy, polarity chron, paleoenvironments, lithology, SIMS U–Pb zircon ages, and cyclostratigraphic interpretation of the SK-Is borehole in the SLB. "e" (blue) and "E" (red) represent 100 ka short and 405 ka long eccentricity cycles, respectively. The interpreted 100 ka and 405 ka eccentricity cycles were extracted by using Gaussian bandpass filters. Filter passband for 405 ka eccentricity cycles: K_2qn—0.0261 ± 0.005 cycles/m. Filter passband for 100 ka eccentricity cycles: K_2qn—0.113 ± 0.025 cycles/m.

in sand-rich areas along the edge of the basin, it is difficult to distinguish between the bottom of the Qingshankou Formation and the sandstone of the underlying Quantou Formation (Xu et al., 2019b). For the sake of convenience, we follow past research and set this boundary at the bottom of the First Member, i.e., the bottom of the first set of oil shales corresponding to the bottom of event 2023 of LAE1 (OAE2). This boundary is useful for the subsequent analysis of sedimentation and patterns of OM enrichment.

3 Methods and dataset

3.1 Data selection

Starting from well SK1 in the deep lake region of the Qingshankou Formation in the southern Songliao Basin, our research extended southward toward the delta front of the Daqingzijing area, passing through areas with wells such as Xinbei, Miaoxi, and Qian'an. The total number of wells exceeded 4,000, including conventional logging sequences such as GR, AC, DEN, and R, and unconventional logging sequences like imaging logs and elemental logs. Based on the characteristics of stratigraphic development, we chose wells near the lake area (SK1, NEN8, XIN342, XIN328, RANG32, QIAN189) and those in the deltaic sedimentary region along the margin of the lake basin (QIANSHENG11, HEI258, HEI197, CHANGSHEN107) to analyze the astronomical cycle (as shown in Figure 1). We plotted complete curves of the natural gamma ray (GR), spontaneous potential (AC), density (DEN), and resistivity (R) of all wells in the Qingshankou Formation. We also considered seven cored wells and analyzed over 120 core samples to examine their lithological and mineral compositions as well as their OM characteristics. Wells SK1 and HEI258, which were located in the deep-lake mud-rich area and the sand-rich area along the margin of the lake basin, respectively, were highly comparable and have been well documented. These were thus important for the analysis of the astronomical cycle provided in this study.

3.2 Sequential stratigraphic analysis

Variations in Earth's orbital parameters cause changes in the amount of solar radiation received per unit area by its surface. These changes in the solar radiation can alter patterns of atmospheric circulation, causing latitudinal shifts in climate zones, and resulting in changes in the atmospheric temperature, ocean circulation, and precipitation. Changes in climate in turn influence glacial activity, the flow of rivers, and the strength of wind to further impact the processes of weathering, transport, and deposition. Changes in solar radiation also influence the influx of nutrients into lakes, evaporation from them, and processes of marine and lacustrine circulation. All these interrelated factors ultimately control the formation of sedimentary products, which are expressed in strata as rhythmic or cyclic variations in the lithology, facies, or geochemical parameters to form stratigraphic cycles that are consistent with astronomical orbital cycles.

Elements of the Milankovitch cycle can be used to establish high-frequency sequential stratigraphic frameworks for fine-grained sediments (Milankovitch, 1941). Astronomical cycles based on Milankovitch's theory include cycles with long eccentricity, short eccentricity, obliquity, and precession. By establishing a correspondence between the astronomical cycles and base-level cycles, the temporal properties of the former can be used to constrain the latter, such that this can reduce the influence of subjectivity and human bias on the division of base-level cycles.

Compared with previously reported extractions of astronomical cycles in the context of fine-grained sediments, the lacustrine sediments of the First Member encounter challenges in terms of astronomical tuning owing to frequent terrigenous clastic inputs. Regions with deep lakes exhibit clear boundaries of the astronomical cycle, such as well SK1 (Wu et al., 2013). However, closer proximity to the source of the sediment in shallow lakes and outer front areas increases noise during astronomical tuning. Conventional methods of data preprocessing, such as detrending, fail to eliminate this noise, and it requires techniques for the targeted reconstruction of the curves of astronomical tuning.

3.3 Methods of time series analysis

We conducted experiments on cyclic analysis by using Acycle V2.4.1 in the MATLAB platform.

3.3.1 Data selection

Before conducting cyclostratigraphic analysis, we needed to choose suitable proxy indicators for the paleoclimate. The gamma ray (GR) curve preserves the primary signals related to climate change, Moreover, the paleoclimate reflected by the GR curve is not influenced by such factors as sedimentary hiatus and diagenesis (Kemp, 2011; Hilgen et al., 2015). High GR values indicate warm and humid conditions owing to the greater input of clay minerals, and organic matter from enhanced chemical weathering and precipitation. Conversely, low GR values indicate cold and dry conditions owing to greater physical weathering and reduced vegetation, which lead to a decreased input of clay and an increased input of inorganic carbonates. Traditional studies have primarily used the GR curve to examine the astronomical cycle (Li et al., 2019; Boulila et al., 2021; Li et al., 2016; Xu et al., 2019a; Li et al., 2018). However, frequent interactions with the terrigenous clastic input increases noise in the astronomical tuning of continental depositional environments, and conventional methods of data preprocessing like detrending cannot eliminate this noise. To accurately extract astronomical cycles from data on fine-grained sediments in areas with shallow lakes, the obtained curves need to be reprocessed to weaken the noise from terrigenous inputs. Researchers have used the curves of density to extract astronomical cycles in past work. We combined the curves of density, which have a low sensitivity to radioactivity, and weak responses to sand and mud, with the GR curve to analyze the astronomical cycle in shallow-lake areas.

3.3.2 Curve fusion

We subjected logging data from the shallow-lake region of K_2qn^1 to a sensitivity analysis. The GR curve is sensitive to lithological changes, and thus can be used to clearly identify lithological variations like thin layers of sand (Hesselbo, 1996). By contrast, the DEN (density) curve has a wide zone of transition that can be used to identify sand and mud. An analysis of the correlation between these curves shows that the GR curve has a larger difference in amplitude between lithologies, particularly between sandstone and mudstone, while the DEN curve has a larger difference in amplitude for mudstone and a smaller difference for sandstone. Therefore, noise from the auto-cycles can be weakened by reconstructing the GR curve based on trends of the curve of density such that it features the strengths of both kinds of curves. This method retains the stability of the curve of density in reflecting sand–mud transitions, while preserving the detailed characteristics of the GR curve for sections of mudstone. The main steps are as follows: 1) Normalize the curves of sand and mud. 2) Determine the threshold of sandstone-related anomalies in the GR curve and calculate its index. 3) Separate high and low frequencies in the curve of density to obtain the differences in high- and low-frequency amplitudes. 4) Calibrate the amplitude of the curve of the anomaly index by using the differences in high- and low-frequency amplitudes of the curve of density. 5) Reconstruct the characteristic GR curve Equations 1–3:

$$GRS = ((GR\text{-}GRmin(sand)/(GRmax(mud)\text{-}GRmin(sand))/G \quad (1)$$

$$DENS = ((GRS\text{-}GRSmin)/(GRSmax\text{-}GRSmin) + 1) * C \quad (2)$$

$$GRR = DENF + B + DENS \quad (3)$$

where GRS is the anomaly index, GR represents natural gamma rays, GRmin(sand) and GRmax(mud) are the natural gamma ray values for stable sandstone and mudstone, respectively, G is the threshold of the anomaly for sandstone, DENS is the amplitude-normalized anomaly index of the density, GRSmax and GRSmin are the maximum and minimum values of the index of anomaly in sandstone, respectively, C is the original difference in the high-/low-frequency amplitudes of density, GRR is the reconstructed curve, DENF is the low-frequency curve of density, and B is an empirical coefficient (ranging from zero to one). Its value is chosen to ensure that the reconstructed GR reflects the original trend, and it uses the curve of density to weaken anomalies close to the values for

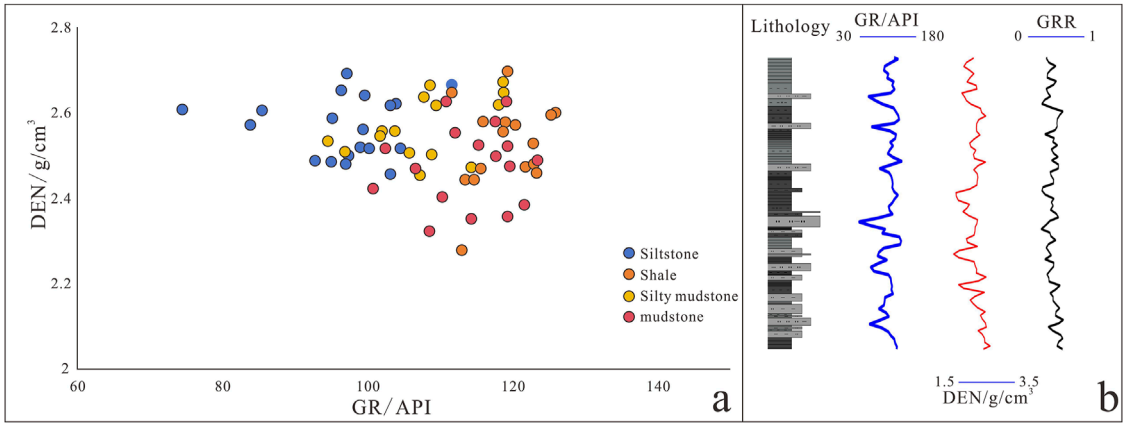

FIGURE 3
Reconstruction of the GR and DEN curves. **(A)** The GR curve is highly precise in identifying sandy bodies with different lithologies, with a numerical range greater than that of the DEN curve. The DEN curve is less sensitive to lithological changes than the GR curve. **(B)** The reconstructed GRR curve retains the characteristics of the original GR curve while using features of the DEN curve to reduce variations in the amplitude caused by frequent sand–mud interbedding.

stable sandstone. The reconstructed GRR curve weakens anomalies in the GR brought about by the development of sand bodies in the foreground (Figure 3).

3.3.3 Data preprocessing

Raw data contain environmental noise that can affect the accuracy of the subsequent experimental results. Therefore, we preprocessed the data before analyzing the cycles:

1) We used the "Sort/Unique/Delete-empty" package to remove outliers that deviated from the normal range of fluctuations, duplicates at the same depth, and empty values.
2) We used the "Interpolation" package to perform linear interpolation and ensure that the data were equidistant.
3) We used the "Detrending" package by using the LOWESS method to eliminate the long-term suppression of high-frequency signals.

3.3.4 Cycle analysis

Spectral Analysis: We applied the multi-taper method along with the robust AR red noise model confidence test to extract significant peaks with a confidence level of >90%. The graph of the spectrum showed the distribution of signal power within the spectral range, with the *x*-axis representing the frequency (its inverse represented the corresponding cycle thickness) and the *y*-axis representing the relative amplitude of the target frequency.

Sliding-window Spectral Analysis: We used the fast Fourier transform (FFT) to obtain the spectra of evolution in the depth domain. This provided a visual representation of changes in the rate of sedimentation along the vertical axis while identifying potential interruptions in sedimentation.

Filtering: We extracted specific mixed and overlapping stratigraphic signals by using the filtering operation. We applied the high-pass operation of the Gaussian filter to set the center frequency and filter bandwidth, and used them to extract potential signals of the target orbital.

3.3.5 Wavelet analysis

The continuous wavelet transform is used for wavelet analysis. Wavelengths with a high power and relative continuity in the spectrum are the main features of the continuous wavelet transform. Wavelet analysis is a time–frequency method of analysis that can localize the signal in the time and frequency domains. It can extract local features of the signal, including changes in its frequency and energy. We used wavelet analysis to identify the dominant cycles in the formation.

3.3.6 Modeling sedimentary noise

Sedimentary noise can be modeled to analyze the dynamics of the signal-to-noise ratio in proxy data on the climate (Li et al., 2018). It is a powerful tool for reconstructing the levels of both seas and lakes in marginal marine and lacustrine paleoenvironments. The DYNOT model is designed to measure noise in data on the climate and proxies of water depth (Wang et al., 2020), such as those in the GR signals in this study. It is based on establishing the ratio of variance in the signal that is unrelated to orbital forcing (i.e., noise) to the total variance in the dataset. All modeled sedimentary noise presented here was computed by using DYNOT functions in Acycle v2.4.1 (Li et al., 2019). All the periodograms, and the steps of the AM and F-test were also executed by using Acycle v2.4.1.

4 Results

4.1 Sequential stratigraphic analysis

4.1.1 Tectonic timescale: high-resolution sequential stratigraphic framework

Sedimentary systems are primarily driven at the tectonic timescale (usually greater than 1 Ma) by interactions among the Earth's spheres (Houston, 2004; Cross, 1194). The balance between the climate-driven supply of sediment and the space

to accommodate it at this scale, which is controlled by tectonic subsidence and lake-level fluctuations, is the key factor influencing the characteristics of the sequence as well as the types of internal sediments, their patterns of distribution, and evolutionary characteristics (Carroll and Bohacs, 1999). High-resolution sequential stratigraphy is commonly used to analyze sedimentary systems at this scale.

In light of past research (Wang, 2022b), we used the high-resolution sequential stratigraphy of the sand-rich area on the margin of the lake basin to divide the strata into one long-term base-level cycle (LSC1), four mid-term cycles (MSC1–MSC4 from bottom to top), and 16 short-term cycles (SSC1–SSC16 from bottom to top). The short-term base-level cycles were of four types: asymmetric up-deepening cycle (A), asymmetric "up-shallowing" cycle (B), symmetric cycle (C1), and incomplete symmetric cycle (C2). The positions of spatial development, types of internal sediments, and characteristics of different cycles varied.

We obtained several insights by analyzing the patterns of vertical variations in the ratio of the space to accommodate the sediment (A) to its supply (S), based on the characteristics of internal development of sand bodies within distinct cyclic structural patterns (Figure 4). The mid-term base-level cycles in the First Member exhibited a pronounced dichotomy. During the MSC1–2 depositional periods in the lower section, the long-term base level rose steadily and gradually, and manifested as the vertical periodic superposition of multiple short-term cycles of types A, C1, and C2. At this time, the transition from $A/S < 1$ to $A/S > 1$ suggests that the rate of sediment supply at the base—near the main flowline—exceeded the potential rate of growth of the space to accommodate it, and led to the superimposition of sand bodies that was represented by sparse type-A features. As the lake level rose, the space for accommodation expanded, and the supply of sediment became insufficient to fill this space. Consequently, the capability of incision of the river weakened while lateral erosion intensified, leading to a transition in the process of deposition from progradation to aggradation. The sedimentary record of the rising hemicycle within this type of mid-term base-level cycle remained intact. The base was characterized by weak erosion, or abrupt lithological transitions between sandstone and mudstone, with internal muddy and silty laminae common between them. Conversely, the upper MSC3–4 section was dominated by descending hemicycles, corresponding to the decline of the long-term base level, and comprised short-term base-level cycles of types B and C2. Cycles of types B, C2, and A were observed along the margins of the lake basin and near the main flowline. As the space for accommodation consistently exceeded the flux in the supply of the sediment ($A/S > 1$) in this period, a state of under-compensated to weakly compensated deposition emerged to form vertically composite, inversely rhythmic sedimentary sequences that were characterized by aggradational–retrogradational patterns.

4.1.2 Orbital timescale: stratigraphic framework of astronomical cycle

We used the standard modeling scheme developed by Laskar et al. to extract the theoretical cyclic curves of eccentricity and cyclic variations in the slope during 85–95 Ma in the Cretaceous, as a benchmark for determining the astronomical cycle (Laskar et al., 2011). We analyzed the spectra of multiple wells, with SK1 as the starting point, along the direction from the center of the lake basin toward the shallow-water area. We considered the horizontal coordinates of the multi-frequency spectrogram as the cyclotomic frequency of the depth sequence, obtained the frequency of the dominant cyclotomic cycle with a confidence of higher than 95%, and compared it with the theoretical orbital period. The frequencies were 0.0206 cycle/m, 0.0887 cycle/m, and 0.211 cycle/m. The ratio of the inverse was 10.41:2.37:1, which is very close to the ratio of 10.8:2.67:1 at 405 ka (long eccentricity), 100 ka (short eccentricity), and 37.5 ka (slope) for the Earth's orbital parameters. We analyzed six typical wells in the near-deepwater area (SK1, N8, X342, X328, R32, and Q189), and found that all of them followed the sequence of Miskovic rotation (Table 1; Figure 5).

A set of high-confidence frequencies, with an average of about 0.02341 cycles/m, and a cycle thickness of 41.4 m were identified in the astronomical cycle based on the GR curve, and conformed to the characteristics of the 405 ka long eccentricity cycle. Moreover, the characteristics of variations in the curve corresponding to the maxima and minima of this cycle were consistent with those of well SK1 in the deep-lake area. This indicates that the long eccentricity with a longer cycle persisted in the shallow-lake area, and controlled the long cyclic interface of the First Member in the deep-lake and outer front areas. The confidence of each cycle within the range of the short eccentricity cycle was complex. There were two distinct high-confidence cycles of 90.1 ka and 81.1 ka that deviated significantly from the short eccentricity cycle in the deep-lake area. If the short eccentricity was extracted according to different ranges of depth, the number of extracted short eccentricities in the upper long eccentricity center E2 was not significantly different from that in the deep-lake area, while the number of short eccentricity cycles in the lower long eccentricity E1 significantly increased. The reconstructed curve of GRR was able to more accurately extract the astronomical cycles in the shallow-lake area, which is consistent with the results for well SK1 in the deep-lake area (Figure 6).

The astronomical cycles extracted based on the GR curve, from well SK1 in the deep-lake area to the edge of the lake basin, showed approximately 1.8 cycles of the 405 ka long eccentricity, seven cycles of the 100 ka short eccentricity, and 21 cycles of 37.5 ka obliquity. These cycles could still be identified in well R30 along the edge of the basin, and matched those of well SK1 (Figure 7). The consistency of the astronomical cycles weakened from south to north toward the edge of the lake basin. Owing to filtered noise from terrigenous clastic inputs, the GRR curves derived from the fusion of the GR and DEN curves were used to extract the astronomical cycles in the marginal front area. This method was also used to successfully identify stable cycles of 1.8 for the 405 ka long eccentricity and seven for the 100 ka short eccentricity. Therefore, stable eccentricity cycles could be extracted by using both the basic GR curve and the reconstructed GRR curve.

4.1.3 Integration of sequential stratigraphic frameworks

To integrate astronomical cyclic stratigraphy with high-resolution sequential stratigraphy, a matching relationship needed to be established between these frameworks. The accuracy of extraction of the astronomical cycles gradually decreased from

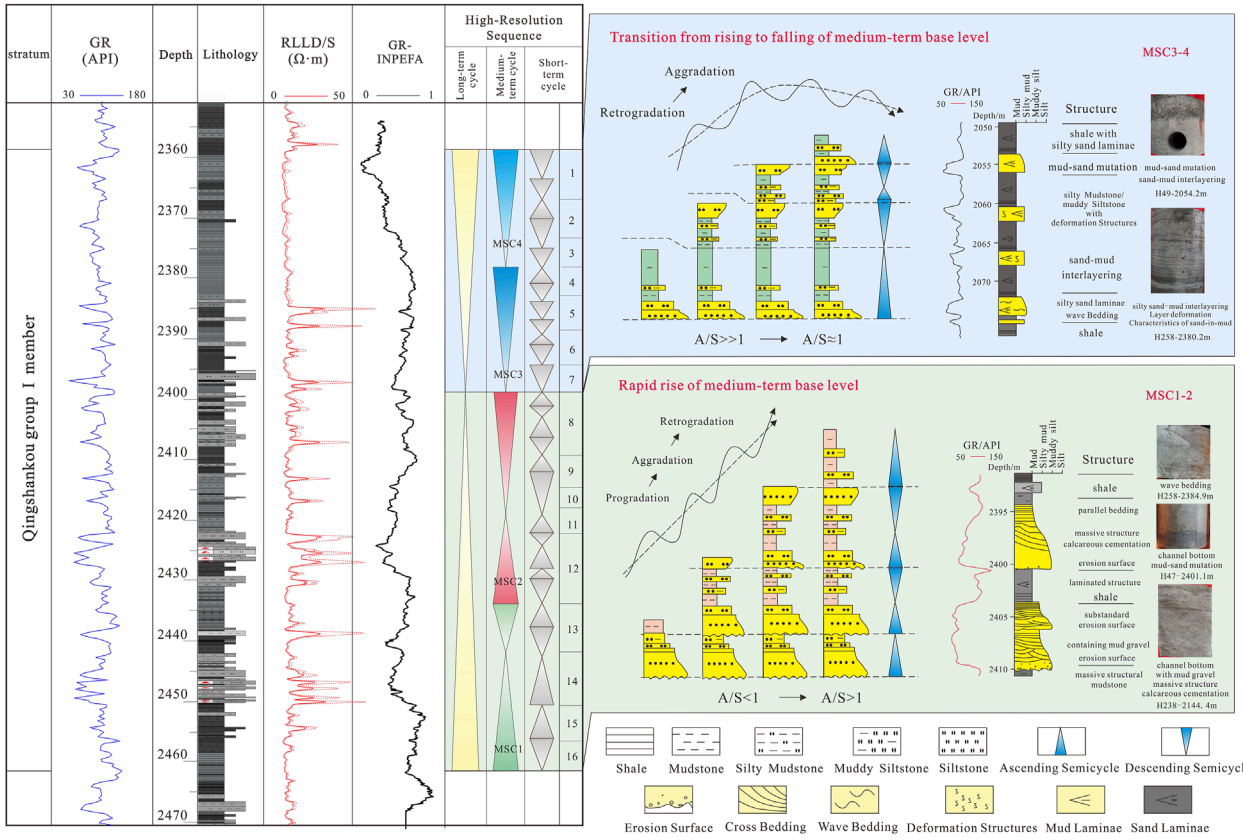

FIGURE 4
Scheme of mid-term base-level cycles in K_2qn^1 and their patterns of stratigraphic stacking, with the depositional characteristics obtained from well Hei 258. The long-term base level in the study area exhibited a complete transgressive–regressive cycle with a distinct bipartite nature. The long-term base level in the lower part rose steadily, and the rate of sediment supply exceeded the rate of growth of the potential accommodation for it, resulting in retrogradational and aggradational stacking patterns. The cycles were primarily asymmetric, and were dominated by either rising or falling phases that constituted the mid-term and short-term base-level cycles of this period, respectively. The upper part corresponded to the transition from rising to falling long-term base level. During this time, the space for accommodation was large but the supply of the sediment was insufficient to fill it, resulting in underfilled to weakly compensated depositional conditions. This led to the formation of multiple, vertically compounded mid-term and short-term base-level cycles with aggradational–retrogradational stacking patterns in an anti-thetic manner.

well SK1 toward the shallow lake. Astronomical cycles could be extracted from sandy areas in the shallow lake by sacrificing the precision of vertical resolution of the GR curve and reducing noise arising due to the development of the sand body. The high-resolution sequences were distinguishable at the edge of the lake basin, but it became challenging to identify them at the center of the basin, which featured reduced development of sand. We integrated the two methods by using data on wells close to the zones of overlapping confidence as bridges. This process involved assigning temporal significance to the high-resolution sequential stratigraphic framework and structural characteristics to the framework of astronomical cycles.

A comparison of the high-resolution sequences in sandy areas with the stratigraphy of the astronomical cycles in muddy areas revealed some correspondence as well as differences between them. We identified three long eccentricity maxima of 405 ka in the first section, with four long eccentricity cycles between them. These cycles were controlled by the climate and tectonics, and represented secondary lake transgression–regression cycles that reflected changes in the climate, temperature, and intensity of terrigenous clastic input.

We identified eight maxima of 100 ka short eccentricity and 14 cycles in the first section, where this was correlated with the sediment facies and trends of mineral composition. Moreover, we identified 22 maxima of 37.5 ka obliquity cycles that formed 42 obliquity cycles. The mid-term cycles in the high-resolution sequences corresponded well with the long eccentricity cycles, while the short-term cycles differed due to over-differentiation between sand and mud in the high-resolution sequential division. This led to the breakdown of the symmetrical cycles into asymmetrical ones. We established a more comprehensive process of lake transgression–regression by constraining the lower sandy zone with the astronomical cycles. Our observations showed that neither the failure of high-resolution sequence stratigraphy owing to unrecognizable base-level characteristics in mudstone, nor the failure of the astronomical cycles owing to sedimentary noise caused by spin-back was sudden. There was a superimposed zone of confidence between them. The integration of the results of these

TABLE 1 Frequency of deep-cycle sequences *versus* the astronomical cycles of orbits.

Well ID	Frequency/(cycle/m)	Cycle thickness/m	Ratio	Periodic ratio of theoretical orbit	Period of theoretical orbital/ka
SK1	0.02026	49.3583	10.41	10.8	405
	0.0887	11.2739	2.37	2.67	100
	0.211	4.7393	1	1	37.5
Nen8	0.0221	45.2488	10.97	10.8	405
	0.101	9.9009	2.40	2.67	100
	0.2425	4.1237	1	1	37.5
Xin342	0.0245	40.8163	10.30	10.8	405
	0.098	10.2040	2.57	2.67	100
	0.2525	3.9603	1	1	37.5
Xin328	0.0267	37.4531	10.63	10.8	405
	0.12	8.33333	2.36	2.67	100
	0.284	3.52112	1	1	37.5
Rang32	0.0189	52.9100	10.845	10.8	405
	0.081	12.3456	2.53	2.67	100
	0.205	4.8780	1	1	37.5
Qian189	0.0224	44.6428	10.40	10.8	405
	0.0954	10.4821	2.44	2.67	100
	0.233	4.29184	1	1	37.5

two sets of stratigraphic divisions in the confidence zone solved the problem of constructing the stratigraphic framework of clastic fine-grained sedimentary rocks that are significantly influenced by land-borne debris (Figure 8).

4.2 Characteristics of tectonic and orbital timescales

The fundamental concept of continental sequential stratigraphy is that the geometry and lithology of the stratigraphic units are controlled by four major factors: tectonic subsidence (which dictates the space to accommodate sediment deposition), lake-level changes (which control the stratigraphy and patterns of the facies), paleoclimate (which influences the types of sediment), and sediment supply (which governs sediment fill and paleodepth). Moreover, sudden marine transgressions and volcanic activities may impact these units. Climatic conditions mainly influence the types of sediment, while tectonic subsidence and sediment supply collectively control the internal composition and morphology of the sequences.

4.2.1 Analysis of environmental evolution at tectonic timescales

4.2.1.1 Characteristics of restoration of accommodation space for sediment (parameter A)

The characteristics of the space to accommodate the sediment were primarily influenced by the paleotopography and paleodepth, with a minor change in the overall paleoslope (0.013°). The space for accommodation (A) was mainly controlled by lake-level fluctuations while the rate of sedimentation reflected the supply of the sediment (S). The characteristics of environmental evolution at the orbital timescale indicate that the paleoclimate became increasingly humid during the K_2qn^1, leading to deeper lakes. The results of the DYNOT model showed that the lake levels were relatively low during MSC1–2, began to rise after MSC3, and peaked during MSC4. Therefore, changes in the space for accommodation (A) around the Daqingzi well during K_2qn^1 were mainly related to changes in the depth of the lake (Figure 9).

4.2.1.2 Restoration of sediment supply (parameter S)

The supply of sediment was jointly controlled by the depositional environment, temperature, and climate. The characteristics of

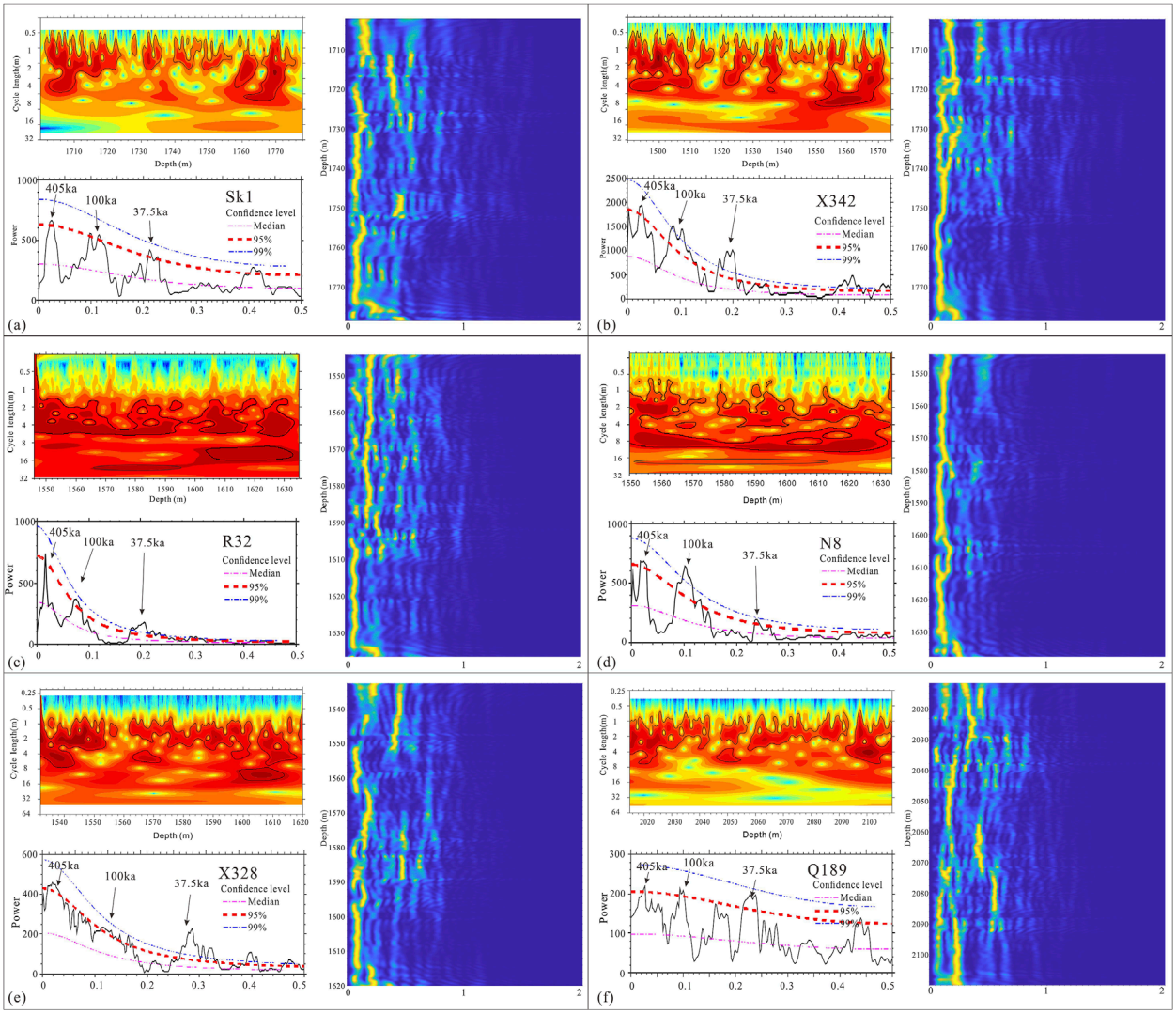

FIGURE 5
The 2π MTM (multi-taper method) power spectra, wavelet scalograms, and evolutionary spectrum of GR logging data from the First Member. Data on six wells in the mud-rich area are shown as examples (SK1, R32, X328, X342, N8, Q189). We show the spectra of the wavelet power and frequency of each well. The purple curve "Median" represents the smoothed and fitted red-noise spectrum. The blue and red curves represent 99% and 95% confidence levels, respectively. The shaded contours in the wavelet scalograms are normalized linear variances, with blue representing low spectral power and red representing high spectral power.

environmental evolution at the orbital timescale revealed that the depositional environment, as reflected by tests of the elemental and grain sizes (Figure 10), was generally reductive during K_2qn^1, with increasing reductiveness and humidity from bottom to top. The rate of sedimentation reflected the sediment supply (S), was high during MSC1 and MSC2, and gradually decreased upward.

In summary, the K_2qn^1 exhibited a dichotomy at the tectonic timescale: There was a gradual increase in the space for the sediment and a gradual decrease in the rate of sedimentation from bottom to top, with frequent internal fluctuations. The lower MSC1 and MSC2 periods featured higher sedimentation rates and smaller spaces to accommodate the sediment, thus exhibiting the characteristics of transitional filling, while the upper MSC3 and MSC4 periods had the opposite trend, with characteristics of balanced filling.

4.2.2 Analysis of environmental evolution on orbital timescale

High-frequency fluctuations in the depths of lakes on an orbital timescale are largely controlled by the climate. The configuration of the Earth's orbital parameters influences the distribution and intensity of the solar radiation received by it, and leads to periodic climatic fluctuations over millennial to million-year timescales. This in turn directly or indirectly influences the Earth's surface system, and leaves its traces in sediments. Milankovitch cycles incorporate sedimentary environments and tectonic changes within the framework of the astronomical rhythm of the Earth's orbital parameters, particularly in highly continuous lacustrine and marine strata. They can accurately illustrate information on climate change within a given basin on an orbital timescale.

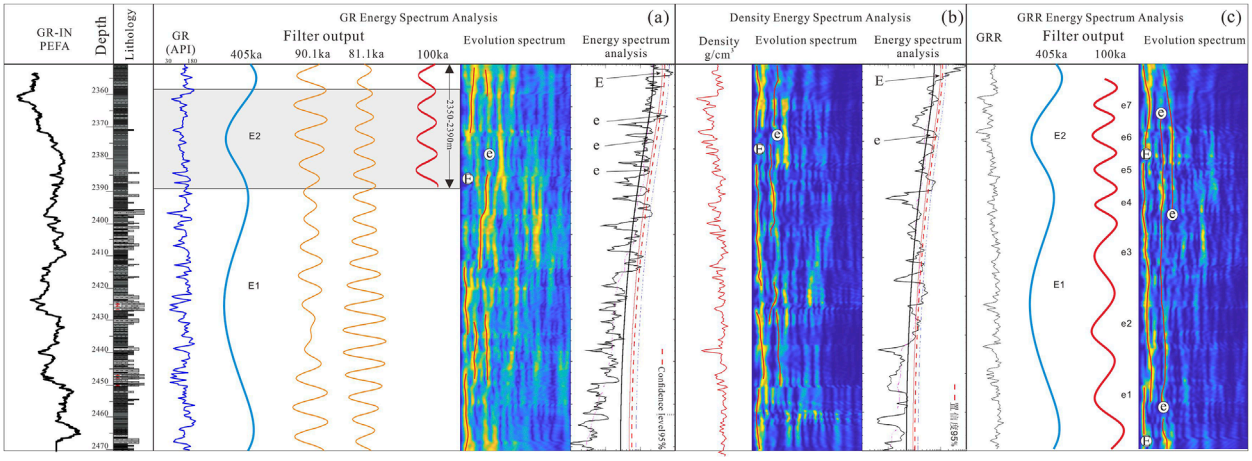

FIGURE 6
Extraction of the astronomical cycles for shallow-lake areas. **(A)** Spectral analysis of the astronomical cycle based on the GR curve. **(B)** Spectral analysis of the astronomical cycle based on the density curve. **(C)** Spectral analysis of the astronomical cycle based on the reconstructed GRR curve. Its characteristics were consistent with those of well SK1 in the deep-lake area.

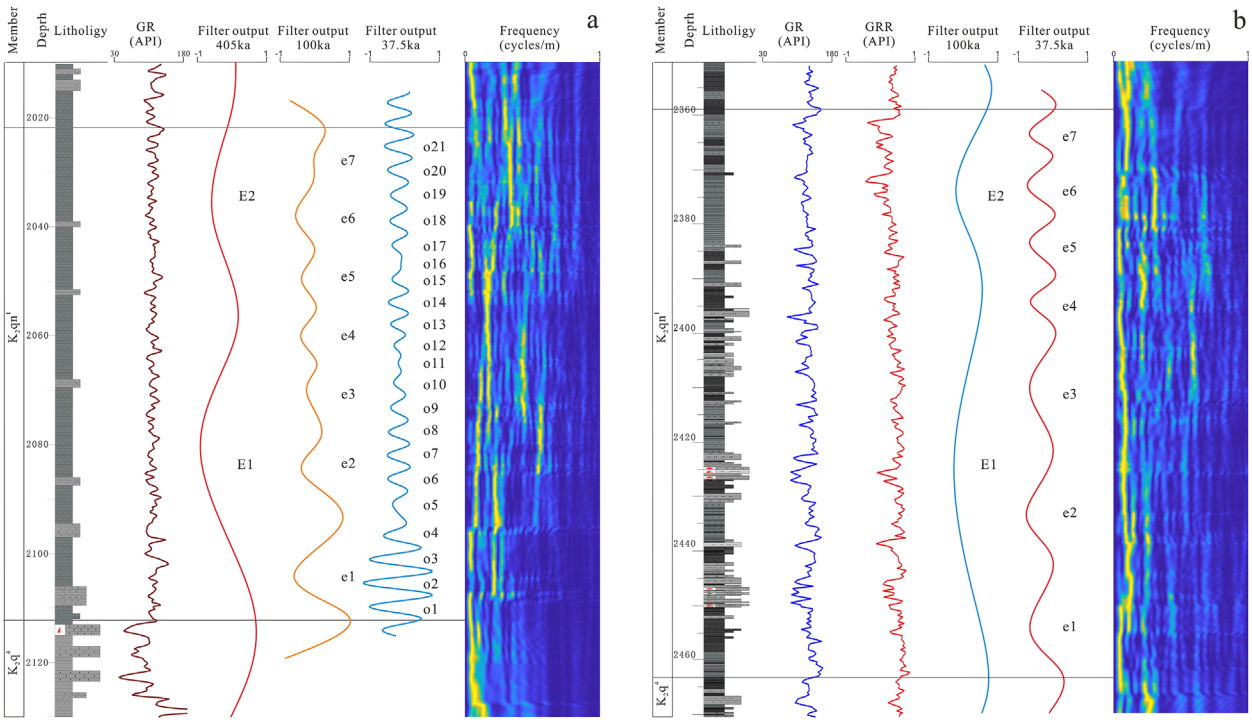

FIGURE 7
Composite stratigraphic column for the extraction of astronomical cycles. **(A)** Well R30: We identified 1.8 long eccentricity cycles, seven short eccentricity cycles, and 21 obliquity cycles in the First Member. Filter passband for 405 ka eccentricity cycles: K_2qn^1—0.0202 ± 0.007 cycles/m. Filter passband for 100 ka eccentricity cycles: K_2qn^1—0.0876 ± 0.021 cycles/m. **(B)** Well Hei 258: The GRR curve identified 1.8 long eccentricity cycles and seven short eccentricity cycles. Filter passband for 405 ka eccentricity cycles: K_2qn^1—0.0217 ± 0.006 cycles/m. Filter passband for 100 ka eccentricity cycles: K_2qn^1—0.087 ± 0.029 cycles/m.

We used sequences of the Milankovitch cycle as a framework, and used it to comprehensively analyze changes in the geochemical parameters based on data on elemental logging. The results showed a significant bipartite sedimentary environment in section K_2qn^1, which was divided at 2396 m (Couch, 1971; Roy and Roser, 2013). The sedimentary noise reflected a continuous rise in the lake level and a gradual deepening of the water body, with a slower change in its depth in the lower part and multiple oscillations in it as well. When the 2396-m boundary was crossed, the rate of rise in the lake level increased significantly and it became

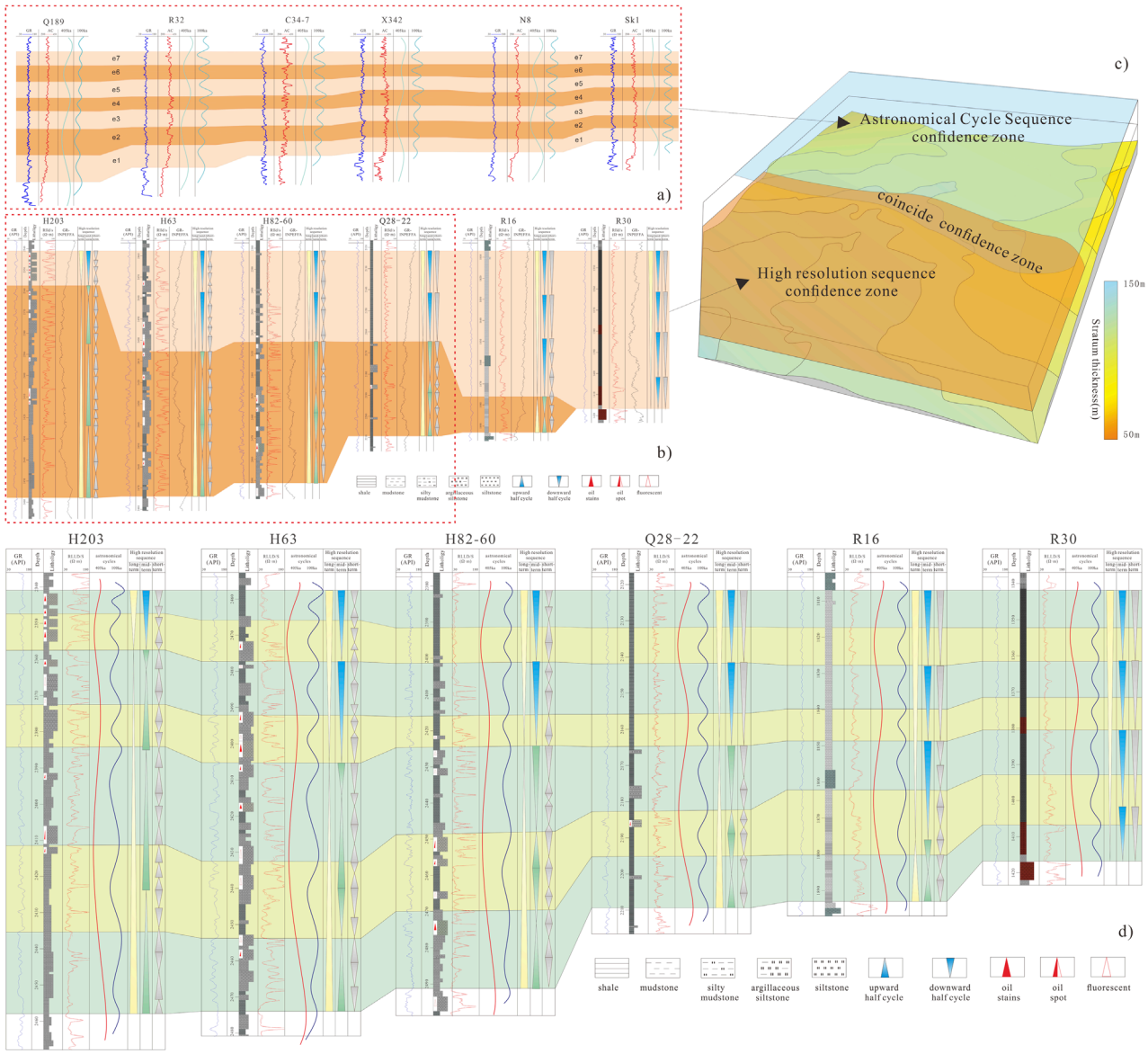

FIGURE 8
Comparison of the range of confidence and results of division between the sequence of astronomical cycles and the high-resolution sequence. **(A)** From well SK1 to well Q189, the stratigraphic framework of astronomical cycles comprised approximately 1.8 complete long eccentricity cycles and seven complete short eccentricity cycles, exhibiting good stability. The confidence interval was primarily located in the southern region. **(B)** From well H203 along the margin of the lake basin to well R30, the resolution of the framework for high-resolution sequential stratigraphy gradually decreased, with poor precision in areas around wells R16 and R30, and the confidence interval was situated in the southern region. **(C)** When the distributions of the confidence intervals of the frameworks for high-resolution sequential stratigraphy and the astronomical cycle-based stratigraphy are combined, the overlapping areas form the integrated confidence interval. The high-resolution sequential and astronomical cyclic stratigraphic frameworks can be fused and extended based on the integrated confidence interval. This enables the formation of stratigraphic frameworks at both scales. **(D)** The high-frequency sequential framework of the margin of the lake basin under astronomical constraints.

considerably deeper. The contents of Mg/Ca, Ca/(Ca+Fe), Th/U, and (Al+Fe)/(Ca+Mg) all exhibited similar characteristics. The lower part of the body of water was mainly shallow and semi-deep, with a semi-arid to semi-humid climate, weakly reducing to weakly oxidizing environment, and oscillatory deepening of the body of water accompanied by the periodic input of terrestrial material. The lake was deeper above the boundary, and was dominated by deep-water deposition with a low rate of sedimentation, increased salinity of water, a relatively humid climate, and enhanced conditions for reduction.

4.3 Characteristics of organic matter

Based on the results of the astronomical cycles as well as the sequential stratigraphy of mud-rich and sand-rich areas, we matched the

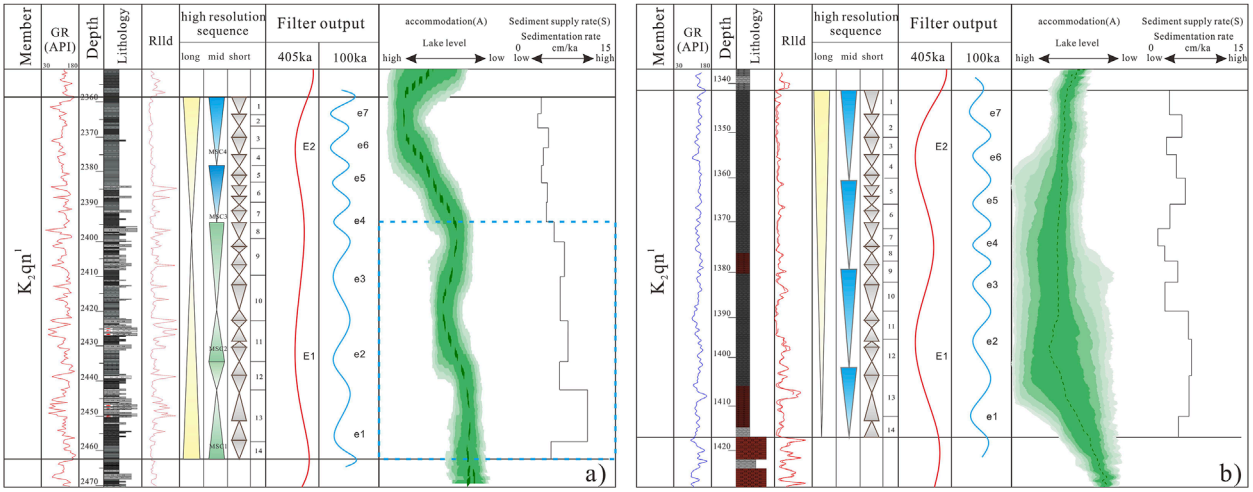

FIGURE 9
Composite columnar sections at the tectonic timescale. **(A)** Well H258 in the sand-rich region. **(B)** Well R30 in the mud-rich region. Curves of the depth of the lake obtained by the DYNOT model indicate an increase in its depth from bottom to top. Correspondingly, the curves of the rate of sedimentation suggest a decreasing sediment supply from bottom to top. The DYNOT models were estimated by using a running window of 405 ka, while the confidence levels were estimated by using Monte Carlo analysis over 5,000 iterations.

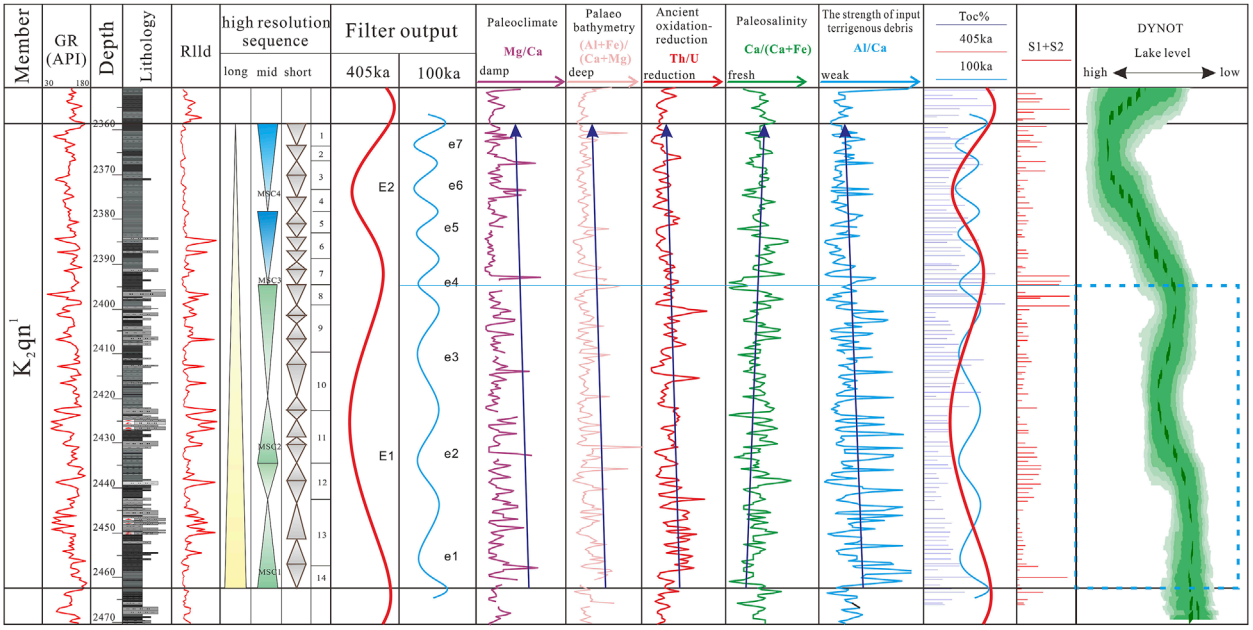

FIGURE 10
Vertical variations in the geochemical parameters, organic matter content, and sedimentary noise for well Hei 258 at the astronomical cycle scale. Its geochemical parameters and sedimentary noise exhibited significant differences above and below the 2396-m boundary. The lower section was characterized by shallow to semi-deep water bodies, a semi-arid to semi-humid climate, and a weakly reductive to weakly oxidizing environment. The depth of water gradually increased with periodic oscillations and the episodic input of terrigenous material. The lake was significantly deeper above the boundary, and was dominated by deep-water deposition with a low rate of sedimentation, increased salinity, a relatively humid climate, and enhanced conditions for reduction. This reflects the clear bipartite nature of the depositional environment of K_2qn^1.

curves of the astronomical cycles with models of the total organic carbon (TOC), geochemical elements, and sedimentary noise to reconstruct environmental changes on an astronomical scale. Consider well HEI258 in the shallow-water area as an example. This stratum contained approximately four long eccentricity cycles and 14 short eccentricity cycles. The latter were well correlated with the characteristics of variations in the TOC. Seven high-TOC zones primarily developed in the First Member (K_2qn^1), which aligns well with the maxima of the 100 ka short eccentricity cycles. This suggests that the patterns of enrichment of organic matter, whether at the center or the margin of the

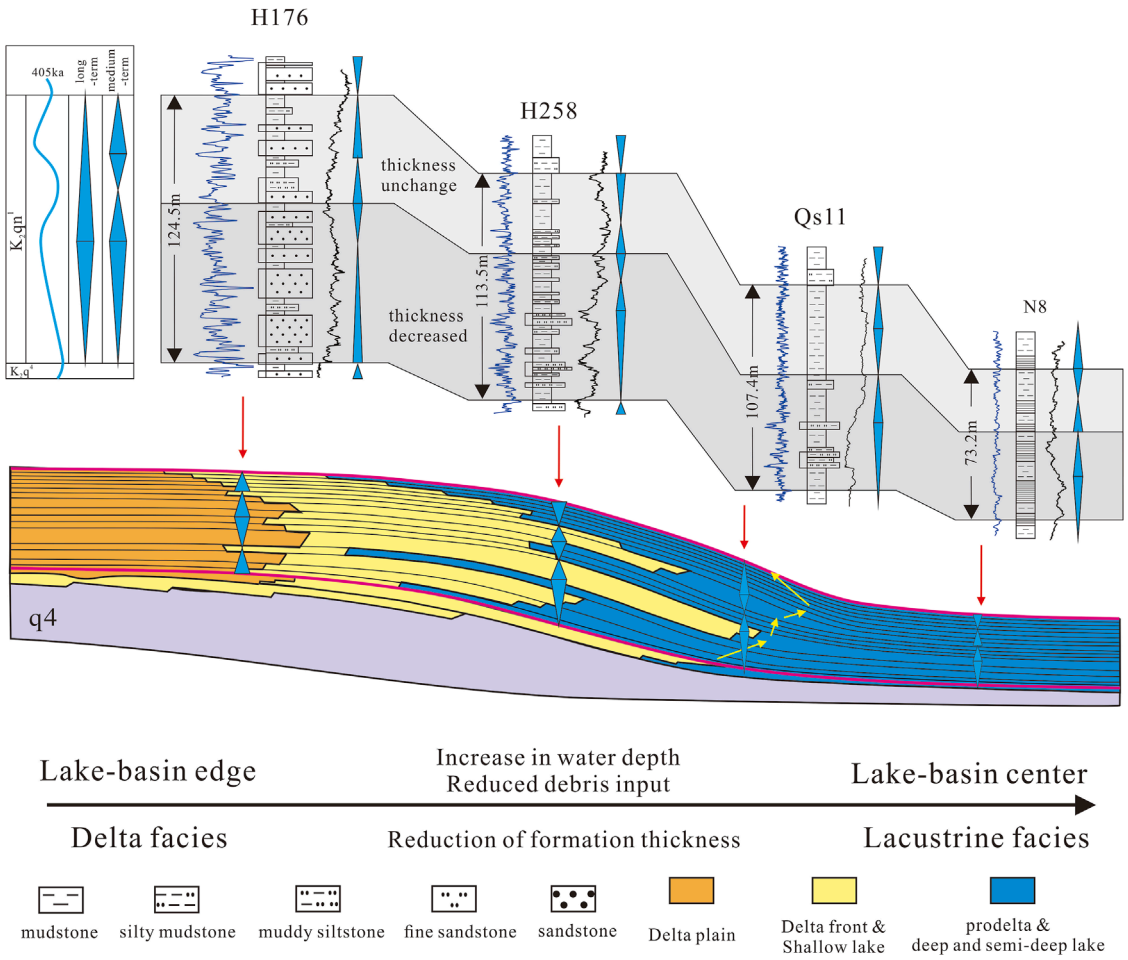

FIGURE 11
Profile of the stratigraphic framework of the deep-water, sand-rich area in the First Member. Wells QS11 and N8 were located along the edge of a shallow lake, where the sand bodies were not developed, and astronomical cycles of 405 ka, 100 ka, and 37.5 ka were observed. Wells Qs11 and H258 were situated along the edge of the delta front near the shallow lake. We unified the frameworks of high-resolution sequential stratigraphy and astronomical cycle stratigraphy by integrating them. The thickness of the upper mud-rich strata remained constant from the sand-rich area to the mud-rich area, while the thickness of the cyclic strata in the lower sand-rich deposits increased due to differences between the rates of sedimentation of sand and mud, which obscured the astronomical signals. This method accurately restored the characteristics of astronomical signals in sand-rich areas.

lake basin, were controlled by the astronomical cycles, although these patterns varied at the vertical level (Figure 10).

The enrichment of organic matter was constrained by primary productivity and subsequent conditions of preservation, which were closely related to the types and patterns of the deposited sediments. We can better reconstruct the original patterns of organic matter accumulation by analyzing sedimentary environments on the same scale as the changes in organic matter enrichment.

5 Discussion

5.1 Models of stratigraphic development and patterns of basin filling

The sedimentation of modern lakes illustrates that the relationship between the supply of sediment and water (mostly climatic), and changes in the potential space to accommodate the sediment (mostly climatic) in each lake controlled its sedimentary characteristics, distribution, and patterns. Our analysis of the types of sediments, their spatial distribution, and evolutionary characteristics based on our model of stratigraphic development confirmed that a delta system for lakes had developed in the southern Songliao Basin, with a gentle slope that was constrained by patterns of "synchronous heterotopy." The supply of the sediment in the model decreased progressively from the land toward the lake basin, the rate of sedimentation decreased, and geomorphologically controlled changes in the space to accommodate the sediment. This led to the general trend of thinning strata toward the center of the lake basin (Figure 11).

The model of stratigraphic development represented the characteristics of sedimentary filling of the basin as well. We used it with the aforementioned characteristics of the tectonic and orbital timescales to conclude that the lake in the study area had undergone two main processes of evolution: an early

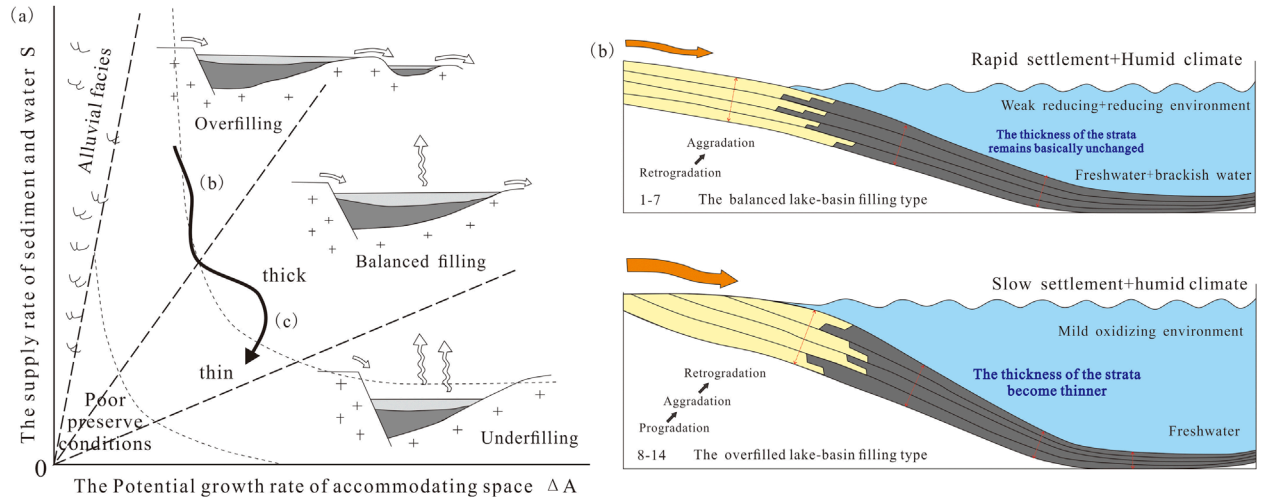

FIGURE 12
Patterns of stratigraphic stacking and sedimentary models from the margin of the basin to its center in the Daqingzi well. **(A)** Patterns of stratigraphic stacking (Carroll and Bohacs, 1999). **(B)** Sedimentary models. A lacustrine delta system developed in the study area that was constrained by a pattern of synchronous heterotopy under a gentle slope. The stratigraphic model was influenced by changes in the space to accommodate the sediment, resulting in progressively thinner strata from the land toward the lake basin. Based on its patterns of stratigraphic stacking, the model can be divided into a lower/shallow-water "overfilled" sedimentary model and an upper/deep-water "balanced filling" sedimentary model. The rates of supply of the sediment and water consistently exceeded the potential space to accommodate them in the "overfilled" sedimentary model. The periodicity (more oscillatory) and progradation of the strata were mainly controlled by the periodic supply of terrigenous clastics. By contrast, the "balanced filling" model featured rates of supply of the sediment and water that were roughly balanced over the span of development of the sequence. The strata exhibited aggradational–retrogradational characteristics, with a periodicity that was consistent with astronomically driven features.

pattern of excessive basin filling followed by a later, more "balanced filling" pattern.

"Overfilled" sedimentary model: There was an abundant supply of sediment in this model, which led to the development of distributary channels in shallow-water deltas. The large influx of terrigenous clastics led to the formation of progradational stratigraphic features (Figure 12). Internal bioclastic material mainly originated from terrestrial input, while other bodies of freshwater carbonates had not developed. They occur when the rates of supply of the sediment and water consistently exceed the potential space to accommodate them. Climatically driven fluctuations in the lake level were minimal, and the periodic increase in terrigenous clastic input owing to the humid climate controlled the oscillatory pattern of sedimentation (Figure 13).

"Balanced filling" sedimentary model: The supply of the sediment was lower in this model, resulting in a deeper lake in which the terrigenous clastic input was less influential, and the stratigraphy exhibited aggradational–retrogradational characteristics (Figure 12). Sedimentation was primarily influenced by fluctuations in the groundwater level due to the chemistry of the water, its temperature, and chemical stratification, and led to the local formation of interbed clastics and carbonates. This occurs when the rates of supply of the sediment and water are balanced with the space to accommodate them over the span of development of the sequence. The inflow of water was sufficient to periodically fill the space, but was not always in equilibrium with it. Hence, astronomically driven characteristics were more pronounced, and climatically driven fluctuations in the lake level led to common periodic sedimentary features in the model (Figure 13).

5.2 Organic matter enrichment under astronomical cycle

The cyclicity of fine-grained lacustrine sedimentary environments and the parameters of the organic matter revealed stratigraphic cyclicity, with a high correlation between the distribution of shale lithofacies and cycles of organic matter enrichment. The average TOC and the highest S1+S2 values of the mudstone layers were always high at the transgressive–regressive positions of transition within the stratigraphic cycles, corresponding to high values of short eccentricity cycles within the astronomical cycles. These were the most favorable facies for the exploration of shale oil. It is evident from the above that organic matter, whether at the edge or the center of the basin, was periodically enriched with a 100 ka limit. This periodicity fitted well at the center of the lake basin but exhibited a lag, with the high-TOC zones vertically positioned in the latter half of the 100 ka (short eccentricity) maximum.

Figures 9, 10 show the clear bipartite nature of the K_2qn^1 in the study area. The rates of supply of the sediment and water, and the rate of increase in the space to accommodate the sediment were roughly balanced over the span of sequential development in the upper part of the deep-water area, exhibiting features that were highly driven by the astronomical cycles. This model of the "balanced filling" of the lake basins was the best combination for the production, preservation, and dilution of organic matter in the basin. The periodic stratification induced by astronomically driven climatic changes provided favorable conditions for its periodic deposition and preservation. OM enrichment was most likely to occur at the transition from a fall in the base level to a rise in it, i.e., at the

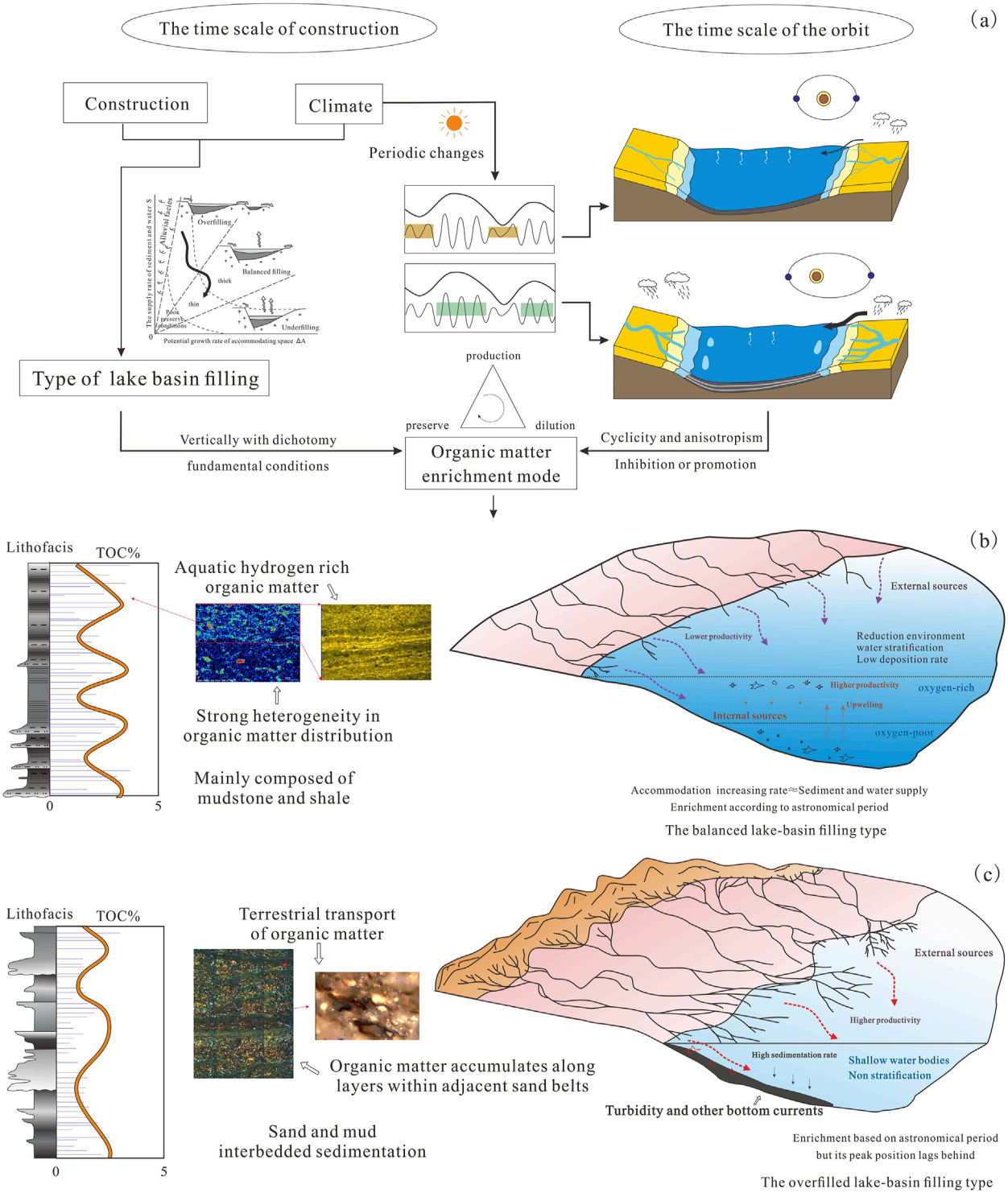

FIGURE 13
Models of the differential enrichment of organic matter from the margin of the lake basin to its center in the Daqingzi well area. The two models differed in the sources of organic matter, mechanisms of its enrichment, and conditions of water during deposition, resulting in different characteristics of enrichment at the astronomical scale. **(A)** The bipartite pattern of filling of the basin arose from varying rates of sediment supply and the space to accommodate it at the tectonic scale. Moreover, the distinct climatic characteristics at the maximum eccentricity at the orbital timescale influenced the patterns of organic matter enrichment. **(B)** The "balanced filling" model of organic matter enrichment of the lake basin in the deep part of the lake shows that the organic matter originated from both within and outside the basin, and exhibited strong heterogeneity. The zones of high enrichment in organic matter aligned with the maxima of short eccentricity. **(C)** The "overfilled" model of organic matter enrichment in the lake basin in the shallow-water area of the lake shows that the organic matter mainly originated from terrestrial plant debris outside the basin. The layers in the siltstone bands featured abundant organic matter, with the zones of high enrichment slightly lagging behind the maxima of short eccentricity.

maximum short eccentricity, matching the 97 ka cycle of deposition of organic matter.

By contrast, the peaks of organic matter along the edges of the sand-rich basin did not strictly correspond to the 100 ka short eccentricity cycles, and exhibited a lag. The model of "overfilled lake basins" featured sound aquatic production and abundant input from terrestrial plants. The main challenges to the concentration of organic matter were its preservation and dilution. The control of density stratification by solutes was unlikely to develop under continuously open hydrological conditions, and required the temperature-influenced stratification of water for the effective preservation of organic matter. Dilution was common owing to the strong riverine influence, and led to a lagged enrichment of the organic matter above the flooding surface, and in the latter part of the maximum of short eccentricity. Moreover, the curves of sedimentary noise reflected an overall transgressive trend in the K_2qn^1. The top of the sand-rich area also began to exhibit the "balanced filling" patterns of organic matter enrichment owing to increased lake depth and reduced terrigenous clastic energy.

6 Conclusion

In this study, we combined the results of astronomical cycle-based and high-resolution stratigraphic delineation to construct a stratigraphic framework of fine-grained, high-frequency sedimentary sequences in a lake, as constrained by the astronomical cycle in the mud-rich zone at the center of the basin and the sand-rich zone along its edge. Our analyses of the sedimentary environment and noise, recovery of the lacustrine level, and geochemical parameters confirmed that the pattern of stratigraphic development of the lake delta system in the study area was constrained according to the model of the "contemporaneous heterogeneous phase," with a gradual decrease in the rate and supply of sediment to the lake basin, a significant change in the geomorphologically controlled space to accommodate it, and the gradual thinning of the stratigraphic layers. This pattern of stratigraphic development controlled the patterns of deposition and distribution of shale that was rich in organic matter.

The cyclic nature of the fine-grained sedimentation of the lake basin revealed the hierarchical nature of the sequence, and the sedimentary strata in the First Member were clearly dichotomous. The features of the lower, early strata suggest that the depositional environment was a low-salinity, weakly oxidized one with relatively shallow water, a strong input of terrestrial debris, and rapid vertical changes in the geochemical parameters. This suggests that the environment fluctuated considerably at this time. By contrast, the water body was significantly deeper, the salinity slightly higher, the reductive nature of the environment was enhanced, the climate shifted from semi-humid to warm and humid, and the input of terrestrial detritus was significantly reduced during the period of deposition of the upper, late sedimentary strata. The difference between the space to accommodate the sediment and the input of terrestrial detritus formed the distinct depositional patterns of the First Member, i.e., the "overfilled" depositional pattern in the lower part of the formation and the "equilibrium" pattern of deposition.

The pattern of fine-grained sedimentation had an important influence on organic matter enrichment, the balanced lake-basin filling type organic matter enrichment pattern in the deep-water area of the lake, at this time, the source of organic matter inside and outside of the basin, non-homogeneous and strong, organic matter enrichment of the high value of the area and the location of the maximum value of the short eccentricity is the same. The organic matter mainly originated from terrestrial plant debris outside the basin, according to the model of the "overfilled" pattern of organic matter enrichment of the lake basin. It filled the silt zone along the layer, the OM content of which slightly lagged behind the position of the extremum of the short eccentricity.

Data availability statement

The original contributions presented in the study are included in the article/supplementary material, further inquiries can be directed to the corresponding author.

Author contributions

XW: Writing–original draft, Writing–review and editing. YS: Writing–review and editing. LY: Writing–review and editing. ZT: Writing–review and editing. BY: Writing–review and editing. RL: Writing–original draft, Writing–review and editing.

Funding

The author(s) declare that financial support was received for the research, authorship, and/or publication of this article. This research was funded by the Heilongjiang Provincial Natural Science Foundation of China (No. ZD2023D002) and Project of Sanya Yazhou Bay Science and Technology City (No. SCKJ-JYRC-2022-09).

Conflict of interest

Authors LY and ZT were employed by PetroChina Jilin Oilfield Company.

The remaining authors declare that the research was conducted in the absence of any commercial or financial relationships that could be construed as a potential conflict of interest.

Publisher's note

References

Bechtel, A., Jia, J. L., Strobl, S. A. I., Sachsenhofer, R. F., Püttmann, W., Gratzer, R., et al. (2012). Palaeo-environmental conditions during deposition of the Upper Cretaceous oil shale sequences in the Songliao Basin (NE China): implications from geochemical analysis. *Org. Geochem.* 46, 76–95. doi:10.1016/j.orggeochem.2012.02.003

Boulila, S., Dupont-Nivet, G., Galbrun, B., Bauer, H., and Chteauneuf, J. J. (2021). *Age and driving mechanisms of the Eocene-Oligocene Transition from astronomical tuning of a lacustrine record (Rennes Basin, France)*. Copernicus GmbH. doi:10.5194/cp-2021-46

Calvert, S. E., and Pedersen, T. F. (1993). Geochemistry of recent oxic and anoxic marine sediments: implications for the geological record. *Mar. Geol.* 113 (1-2), 67–88. doi:10.1016/0025-3227(93)90150-t

Cao, H. S., Kaufman, A. J., Shan, X. L., Cui, H., and Zhang, G. J. (2016). Sulfur isotope constraints on marine transgression in the lacustrine Upper Cretaceous Songliao Basin, northeastern China. *Palaeogeogr. Palaeoclimatol. Palaeoecol.* 451, 152–163. doi:10.1016/j.palaeo.2016.02.041

Carroll, A. R., and Bohacs, K. M. (1999). Stratigraphic classification of ancient lakes: balancing tectonic and climatic controls. *Geology* 27, 99–102. doi:10.1130/0091-7613(1999)027<0099:scoalb>2.3.co;2

Cheng, X. L., Zhou, X. J., and Guo, J. H. (2003). Study on the sequence stratigraphy of T-R cycles and subtle oil pools in the Dongpu Depression. *Petroleum Geol. and Exp.* (S1), 548–552+556.

Cohen, A. S. (2003). *Paleolimnology: the history and evolution of lake systems*. Oxford University Press.

Couch, E. L. (1971). Calculation of paleosalinities from boron and clay mineral data. *AAPG Bull.* 55 (10), 1829–1837. doi:10.1306/819a3dac-16c5-11d7-8645000102c1865d

Cross, T. A. (1994). High-resolution stratigraphic correlation from the perspective of baselevelcycles and sediment accommodation, in *Proceeding of northwestern European sequence stratigraphy congress*, 105–123.

Demaison, G. J., and Moore, G. T. (1980). Anoxic environments and oil source bed genesis. *Org. Geochem.* 64. doi:10.1306/2f91945e-16ce-11d7-8645000102c1865d

Dong, M. Z., Gong, H. J., Sang, Q., Zhao, X. Y., and Zhu, C. F. (2022). Review of CO2-kerogen interaction and its effects on enhanced oil recovery and carbon sequestration in shale oil reservoirs. *Resour. Chem. Mater.* 1 (1), 93–113. ISSN 2772-4433. doi:10.1016/j.recm.2022.01.006

Du, X. B., Liu, H., Liu, H. M., Lu, Y. C., Wang, Y., Hao, X. F., et al. (2016). Methods of sequence stratigraphy in the fine-grained sediments: a case from the upper fourth sub-member and the lower third sub-member of the shahejie Formation in well fanye 1 of dongying depression. *Bull. Geol. Sci. Technol.* 35 (04), 1–11.

Feng, L. Y., Zhang, J. G., Jiang, Z. X., Li, C. S., and Bai, Y. F. (2023). High-precision sedimentary cycle framework and organic matter enrichment response of Qinghsankou Formation in Songliao Basin. *Acta Pet. Sin.* 44 (02), 299–311. doi:10.7623/syxb202302006

Feng, Z. Q., Jia, C. Z., Xie, X. N., Zhang, S., Feng, Z. H., and Cross, T. A. (2010). Tectonostratigraphic units and stratigraphic sequences of the nonmarine Songliao basin, northeast China. *Basin Res.* 22 (1), 79–95. doi:10.1111/j.1365-2117.2009.00445.x

Hesselbo, S. P. (1996). "Spectral gamma-ray logs in relation to clay mineralogy and sequence stratigraphy," in *Cenozoic of the Atlantic margin*. offshore New Jersey.

Hilgen, F. J., Hinnov, L. A., Abdul Aziz, H., Abels, H. A., Batenburg, S., Bosmans, J. H. C., et al. (2015). Stratigraphic continuity and fragmentary sedimentation: the success of cyclostratigraphy as part of integrated stratigraphy. *.Geol. Soc.* 404, 157–197. doi:10.1144/sp404.12

Houston, J. (2004). High-resolution sequence stratigraphy as a tool in hydrogeological exploration in the Atacam a Desert. *Q. J. Eng. Geol. Hydrogeology* 37 (1), 7–17. doi:10.1144/1470-9236/03-013

Huang, H., Gao, Y., Ma, C., Jones, M. M., Wang, C., Ibarra, D. E., et al. (2023). Organic carbon burial is paced by a~173-ka obliquity cycle in the middle to high latitudes. *Sci. Adv.* 7 (28), eabf9489. [2023-07-05]. doi:10.1126/sciadv.abf9489

Jia, J. L., Bechtel, A., Liu, Z. J., Strobl, S. A. I., Sun, P. C., and Sachsenhofer, R. F. (2013b). Oil shale Formation in the upper cretaceous Nenjiang Formation of the Songliao Basin (NE China): implications from organic and inorganic geochemical analyses. *Int. J. Coal Geol.* 113 (Complete), 11–26. doi:10.1016/j.coal.2013.03.004

Jia, J. L., Liu, Z. J., Bechtel, A., Susanne, A. I. S., and Sun, P. (2013a). Tectonic and climate control of oil shale deposition in the upper cretaceous Qingshankou Formation (Songliao Basin, NE China). *Int. J. Earth Sci.* 102 (6), 1717–1734. doi:10.1007/s00531-013-0903-7

Kemp, D. B. (2011). Shallow-water records of astronomical forcing and the eccentricity paradox. *Geology* 39 (5), 491–494. doi:10.1130/g31878.1

Laskar, J., Fienga, A., Gastineau, M., and Manche, H. (2011). La2010: a new orbital solution for the long-term motion of the earth. *Astronomy and Astrophysics* 532 (2), A89–A785. doi:10.1051/0004-6361/201116836

Li, M. S., Hinnov, L. A., Huang, C. J., and Ogg, J. G. (2018). Sedimentary noise and sea levels linked to land-ocean water exchange and obliquity forcing. *Nat. Commun.* 9 (1), 1004. doi:10.1038/s41467-018-03454-y

Li, M. S., Huang, C. J., Ogg, J., Zhang, Y., Hinnov, L. A., Wu, H. C., et al. (2019). Paleoclimate proxies for cyclostratigraphy: comparative analysis using a Lower Triassic marine section in South China. *Earth-Science Rev.* 189, 125–146. doi:10.1016/j.earscirev.2019.01.011

Li, M. S., Ogg, J., Zhang, Y., Huang, C. J., Hinnov, L., Chen, Z. Q., et al. (2016). Astronomical tuning of the end-permian extinction and the early triassic epoch of south China and Germany. *Earth and Planet. Sci. Lett.* 441, 10–25. doi:10.1016/j.epsl.2016.02.017

Li, Q. Z., Chen, J. L., Zou, H., Wang, C. S., Meng, Q. A., Liu, H. L., et al. (2020). Mesozoic–cenozoic tectonic evolution and dynamics of the Songliao Basin, NE asia: implications for the closure of the paleo-asian ocean and mongol-okhotsk ocean and subduction of the paleo-pacific ocean. *Earth-Science Rev.* 218, 103471. doi:10.1016/j.earscirev.2020.103471

Liu, B., Sun, J. H., Zhang, Y. Q., He, J. L., Fu, X. F., Yang, L., et al. (2021). Reservoir space and enrichment model of shale oil in the first member of Cretaceous Qingshankou Formation in the Changling Sag, southern Songliao Basin, NE China. *Petroleum Explor. Dev.* 48 (3), 608–624. doi:10.1016/s1876-3804(21)60049-6

Liu, B., Wang, H., Fu, X., Bai, Y., Bai, L. H., Jia, M. C., et al. (2019). Lithofacies and depositional setting of a highly prospective lacustrine shale oil succession from the Upper Cretaceous Qingshankou Formation in the Gulong sag, northern Songliao Basin, northeast China. *AAPG Bull.* (2), 103. doi:10.1306/08031817416

Liu, Q. Y., Shi, J. Y., Jin, Z. J., Liu, Q., Huang, Z. K., and Zhang, R. (2019). Quantitative classification of high-frequency sequences in fine-grained lacustrine sedimentary rocks based on Milankovitch theory. *Oil&Gas Geol.* 40 (06), 1205–1214.

Liu, R. H., Sun, Y., Wang, X. R., Yan, B. Q., Yu, L. M., and Li, Z. (2023). Production capacity variations of horizontal wells in tight reservoirs controlled by the structural characteristics of composite sand bodies: fuyu Formation in the qian'an area of the Songliao Basin as an example. *Processes* 11, 1824. doi:10.3390/pr11061824

Liu, W., Liu, M., Yang, T., Liu, X., Them, T. R., Wang, K., et al. (2022). Organic matter accumulations in the santonian-campanian (upper cretaceous) lacustrine Nenjiang shale (K2n) in the Songliao Basin, NE China: terrestrial responses to OAE3? *Int. J. Coal Geol.* 260, 104069. doi:10.1016/j.coal.2022.104069

Ma, Y., Sun, Y. H., Feng, J. L., Liu, Y., and Yin, C. H. (2022). Study on differential enrichment mechanisms of organic matter in a typical lithofacies fine-grained sag, Songliao Basin. *Acta Sedimentol. Sin.*, 1–21. [2024-09-13]. doi:10.14027/j.issn.1000-0550.2023.037

Milankovitch, M. (1941). *Kanon der Erdbestrahlung und seine Anwendung auf das Eiszeitenproblem*. Academic Serbe, 133.

Olga, O., Grzegorz, M., Marek, S., Filipek, A., Więcław, D., Perotta, I. D., et al. (2023). Spatial distribution of micro- and nanoporosity in Oligocene Menilite and Cretaceous Lgota mudstones (Outer Carpathians): organic porosity development as a key to understanding unconventional hydrocarbon reservoirs. *Mar. Petroleum Geol.* 148 (2023), 106028. ISSN 0264-8172. doi:10.1016/j.marpetgeo.2022.106028

Pan, S. Q., Zou, C. N., Li, Y., Jing, Z. H., Liu, E. T., Yuan, M., et al. (2021). Major biological events and fossil energy formation: on the development of energy science under the earth system framework. *Petroleum Explor. Dev.* 48 (3), 581–594. doi:10.1016/s1876-3804(21)60047-2

Roy, D. K., and Roser, B. P. (2013). Climatic control on the composition of carboniferous–permian gondwana sediments, khalaspir basin, Bangladesh. *Gondwana Res.* 23 (3), 1163–1171. doi:10.1016/j.gr.2012.07.006

Song, Y., Liu, Z., Meng, Q., Xu, J., Sun, P. C., Cheng, L. J., et al. (2016). Multiple controlling factors of the enrichment of organic matter in the upper cretaceous oil shale sequences of the Songliao Basin, NE China: implications from geochemical analyses. *Oil Shale* 33 (2), 142. doi:10.3176/oil.2016.2.04

Sun, S., Liu, H., Cao, Y., Zhang, S., Wang, Y., and Yang, W. (2017). Milankovitch cycle of lacustrine deepwater fine-grained sedimentary rocks and its significance to shale oil: a case study of the upper Es4 member of well NY1 in Dongying sag. *J. China Univ. Min. and Technol.* 46 (04), 846–858. doi:10.13247/j.cnki.jcumt.000638

Sun, Y. (2010). "A study on high-resolution sequence stratigraphy and rule of hydro-carbon accumulations of lithologic reservoirs in meandering river delta ——example of fuyu oil layer in the liangjingdong-mutounan area," in *Northeast petroleum university*.

Tyson, R. V. (2005). The "productivity versus preservation" controversy: cause, flaws, and resolution.

Wang, C. S., Huang, Y. J., and Zhao, X. X. (2009). Unlocking a Cretaceous geologic and geophysical puzzle: scientific drilling of Songliao Basin in northeast China. *Lead. Edge* 28, 340–344. doi:10.1190/1.3104081

Wang, H. R., Guo, Y. J., Huang, Y. M., Yu, C. Q., Huo, Z. P., Li, X. L., et al. (2023d). Morphologies, patterns, and filling architectures at the confluence zones of the cretaceous shallow-water delta in the Songliao Basin, NE China. *J. Asian Earth Sci.* 254, 105758–109120. doi:10.1016/j.jseaes.2023.105758

Wang, K., Ma, L., and Taylor, K. G. (2022a). Nanoscale geochemical heterogeneity of organic matter in thermally-mature shales: an AFM-IR study. *Fuel* 310, 122278. doi:10.1016/j.fuel.2021.122278

Wang, L., Zhang, R., Hua, G. L., and Zhang, L. (2018). On stratigraphy from spatial and temporal perspectives: review and interpretation. *Acta Sedimentol. Sin.* 36 (06), 1059–1074. doi:10.14027/j.issn.1000-0550.2018.091

Wang, M., Chen, H. H., Huang, C. J., Kemp, D. B., Xu, T. W., Zhang, H. G., et al. (2020). Astronomical forcing and sedimentary noise modeling of lake-level changes in the paleogene dongpu depression of north China. *Earth Planet. Sci. Lett.* 535, 116116. doi:10.1016/j.epsl.2020.116116

Wang, M., Zhang, Y. C., Li, J. B., Ma, R., Wang, X., Li, Y., et al. (2023c). Thermal and nonthermal effect of microwave irradiation on the pore microstructure and hydrocarbon generation of organic matter in shale. *Mar. Petroleum Geol.* 150, 106151. doi:10.1016/j.marpetgeo.2023.106151

Wang, P. J., Xie, X. A., Frank, M., Ren, Y. G., Zhu, D. F., and Sun, X. M. (2007). The cretaceous Songliao Basin: volcanogenic succession, sedimentary sequence and tectonic evolution, NE China. *Acta Geol. Sin.* 81, 1002–1011. doi:10.1111/j.1755-6724.2007.tb01022.x

Wang, W. X. (2022b). Study on sandbody distribution in sequence stratigraphic framework of the first member of Qingshankou Formation in Hei258 block, Songliao Basin. *Northeast Pet. Univ.*

Wang, X. R., Sun, Y., Liu, R. H., and Li, Z. (2023a). Research progress into fine-grained sedimentary rock characteristics and formation in a continental lake basin. *Acta Sedimentol. Sin.* 41 (2), 349–377. doi:10.14027/j.issn.1000-0550.2021.117

Wang, Y. C., Li, P. P., Feng, Z. H., Shao, H. M., Jia, Z. W., Xia, Y. Q., et al. (2023b). Geochemical characteristics of shales from the first member of Qingshankou Formation in Gulong Sag, Songliao Basin, China: implication for mechanism of organic matter enrichment. *Mar. Petroleum Geol.* 150, 106142. ISSN 0264-8172. doi:10.1016/j.marpetgeo.2023.106142

Wu, H. C., Hinnov, L. A., Zhang, S. H., Jiang, G. Q., Yang, T. S., Li, H. Y., et al. (2022). Continental geological evidence for solar system chaotic behavior in the late cretaceous. *GSA Bull.* 135 (3-4), 712–724. doi:10.1130/b36340.1

Wu, H. C., Zhang, S. H., Hinnov, L. A., Jiang, G. Q., Yang, T. S., Li, H. Y., et al. (2014). Cyclostratigraphy and orbital tuning of the terrestrial upper santonian–lower danian in Songliao Basin, northeastern China. *Earth Planet. Sci. Lett.* 407 (407), 82–95. doi:10.1016/j.epsl.2014.09.038

Wu, H. C., Zhang, S. H., Jiang, G. Q., Hinnov, L. A., Yang, T. S., Li, H. Y., et al. (2013). Astrochronology of the early turonian–early campanian terrestrial succession in the Songliao Basin, northeastern China and its implication for long-period behavior of the solar system. *Palaeogeogr. Palaeoclimatol. Palaeoecol.* 385, 55–70. doi:10.1016/j.palaeo.2012.09.004

Wu, H. C., Zhang, S. H., Jiang, G. Q., and Huang, Q. H. (2009). The floating astronomical time scale for the terrestrial Late Cretaceous Qingshankou Formation from the Songliao Basin of Northeast China and its stratigraphic and paleoclimate implications. *Earth Planet. Sci. Lett.* 278 (3-4), 308–323. doi:10.1016/j.epsl.2008.12.016

Xu, J. J., Liu, Z. J., Bechtel, A., Meng, Q. T., Sun, P. C., Jia, J. L., et al. (2015). Basin evolution and oil shale deposition during Upper Cretaceous in the Songliao Basin (NE China): implications from sequence stratigraphy and geochemistry. *Int. J. Coal Geol.* 149, 9–23. doi:10.1016/j.coal.2015.07.005

Xu, J. J., Liu, Z. J., Bechtel, A., Sachsenhofer, R. F., Jia, J. L., Meng, Q. T., et al. (2019a). Organic matter accumulation in the upper cretaceous Qingshankou and Nenjiang formations, Songliao Basin (NE China): implications from high-resolution geochemical analysis. *Mar. Petroleum Geol.* 102, 187–201. doi:10.1016/j.marpetgeo.2018.12.037

Xu, K., Chen, H. H., Huang, C. J., Ogg, J. G., Zhu, J. X., Lin, S. Q., et al. (2019b). Astronomical time scale of the Paleogene lacustrine paleoclimate record from the Nanxiang Basin, central China. *Palaeogeogr. Palaeoclimatol. Palaeoecol.* 532, 109253. doi:10.1016/j.palaeo.2019.109253

Yu, F. N., Sun, P. C., Zhao, K. G., Ma, L., and Tian, X. M. (2020). Experimental constraints on the evolution of organic matter in oil shales during heating: implications for enhanced *in situ* oil recovery from oil shales. *Fuel.* 261, 116412–116412.14. doi:10.1016/j.fuel.2019.116412

Zhang, P. L., David, M., Hu, F., Nikolaos, K., Reinhard, S., Liu, Z. J., et al. (2021). Porosity evolution in organic matter-rich shales (Qingshankou Fm.; Songliao Basin, NE China): implications for shale oil retention. *Mar. Petroleum Geol.* 130 (1), 105139. doi:10.1016/j.marpetgeo.2021.105139

Zhang, P. L., Misch, D., Meng, Q. T., Sachsenhofer, R. F., Liu, Z. J., Jia, J. L., et al. (2022). Lateral changes of organic matter preservation in the lacustrine Qingshankou Formation (Cretaceous Songliao Basin, NE China): evidence for basin segmentation. *Int. J. Coal Geol.* 254, 103984. ISSN 0166-5162. doi:10.1016/j.coal.2022.103984

Zhang, P. L., Xu, Y. B., Meng, Q. T., Liu, Z. J., Zhang, J. Q., Shen, L., et al. (2020). Sequence stratigraphy and geochemistry of oil shale deposits in the upper cretaceous Qingshankou Formation of the Songliao Basin, NE China: implications for the geological optimization of *in situ* oil shale conversion processing. *Energies* 13, 2964. doi:10.3390/en13112964

Zhang, R., Jin, Z. J., Liu, Q. Y., Li, P., Huang, Z. K., Shi, J. Y., et al. (2019). Astronomical constraints on deposition of the middle triassic chang 7 lacustrine shales in the ordos basin, Central China. *Palaeogeogr. Palaeoclimatol. Palaeoecol.* 528, 87–98. doi:10.1016/j.palaeo.2019.04.030

Zheng, R. C., Peng, J., and Wu, C. R. (2001). Grade division of base-level cycles of terrigenous basin and its implications. *Acta Sedimentol. Sin.* 19 (02), 7.

frontiers | Frontiers in Earth Science

TYPE Original Research
PUBLISHED 04 December 2024
DOI 10.3389/feart.2024.1507359

OPEN ACCESS

EDITED BY
Junwen Peng,
University of Oklahoma, United States

REVIEWED BY
Ling Guo,
Northwest University, China
Haibo Jia,
Shandong University of Science and Technology, China

*CORRESPONDENCE
Jie Xu,
jiexu@cugb.edu.cn

RECEIVED 07 October 2024
ACCEPTED 20 November 2024
PUBLISHED 04 December 2024

CITATION
Wen J, Xu J, Jiang Z, Liu T, Meng J, Zhang J, Wei S, Shen Z, Li Y and Zhang X (2024) A volcanic and gravity flow controlled fine-grained organic rich deposits of the lower Jurassic Beipiao formation in the Western Liaoning, northeast China. *Front. Earth Sci.* 12:1507359. doi: 10.3389/feart.2024.1507359

A volcanic and gravity flow controlled fine-grained organic rich deposits of the lower Jurassic Beipiao formation in the Western Liaoning, northeast China

Jiucun Wen[1,2,3], Jie Xu[1,2,3]*, Zaixing Jiang[4], Tong Liu[4], Jiayi Meng[4], Jiazhi Zhang[4], Siyuan Wei[4], Zhihan Shen[4], Yongfei Li[5,6] and Xi Zhang[7]

[1]School of Ocean Sciences, China University of Geosciences (Beijing), Beijing, China, [2]Key Laboratory of Polar Geology and Marine Mineral Resources, China University of Geosciences (Beijing), Beijing, China, [3]Hainan institute of China University of Geosciences (Beijing), China University of Geosciences (Beijing), Sanya, Hainan, China, [4]School of Energy Resources, China University of Geosciences (Beijing), Beijing, China, [5]Shenyang Geological Survey Center, China Geological Survey, Shenyang, China, [6]Observation and Research Station of Mesozoic Stratigraphic System in western Liaoning, China Geological Survey, Shenyang, China, [7]SINOPEC Northeast Oil & Gas Branch, Exploration and Development Research Institute, Changchun, China

Introduction: The Lower Jurassic Beipiao Formation in the western Liaoning of northeast China represents a significant case study for understanding the interplay between volcanic activity, sedimentary processes, and organic matter enrichment.

Methods: This study aims to investigate the lithofacies, depositional environments, and hydrocarbon potential of the Beipiao Formation, using core, outcrop, thin-section, and geochemical data.

Results: Thirteen lithofacies types were identified, which reflect a complex depositional history influenced by volcanic processes and gravity flows. The sedimentary facies analysis revealed three key depositional environments: shallow lake, semi-deep to deep lacustrine, and fan delta. The basin evolution suggests a transition from fan delta deposits to deep lake deposits and then back to fan delta, with volcanic and gravity flow deposits interbedded. Volcanic activity not only provided nutrient-rich environments conducive to biological productivity but also helped create conditions favorable for organic matter preservation. The earthquake, flooding or stormed events induced gravity flow, which favored plant fragments dispersal to the deep-lake and formed type III kerogen in the deep-lake developed area.

Discussion: These findings suggest that the Jurassic Beipiao Formation in western Liaoning Province, exhibit significant hydrocarbon potential. This challenges previous assumptions regarding the dominance of shallow water environments and limited exploration prospects within the Yanshan Orogenic Belt. Furthermore, this study highlights the crucial role of volcanic activity and gravity flow in organic matter enrichment, transportation, and preservation

within a volcanic-rift basin, with potential applicability to similar basins worldwide.

KEYWORDS

Beipiao formation, gravity flow, volcanic process, black shale, organic matter

1 Introduction

Volcanic eruptions release substantial amounts of material and energy, significantly impacting the atmosphere, hydrosphere, and biosphere. Recently, an increasing number of oil- and gas-bearing black mudstones have been found to originate closely in relation to volcanic activity (Zhou et al., 1989; Wang et al., 2013; Aarnes et al., 2010; Felipe et al., 2007; Aarnes et al., 2015). Numerous studies indicate that since the Cambrian, organic carbon burial and the formation of shale oil and gas in multiple marine basins are often associated with global or regional high-frequency volcanic activities (e.g., Trabucho-Alexandre et al., 2012; Abrajevitch et al., 2014; Lee et al., 2018; Lu et al., 2020). Extensive oil and gas explorations in China have also discovered abundant shale oil and gas resources associated to some extent with volcanic-hydrothermal activities. Examples include the Permian Lucaogou Formation in the Malang Depression of the Santanghu Basin (Wang et al., 2013; Jiao et al., 2021; Fan, 2004), the Upper Triassic Yanchang Formation in the Ordos Basin (Zou et al., 2019; Yuan et al., 2019), the Permian Lucaogou Formation in the Jimusar Depression of the Junggar Basin (Qu et al., 2019a), and the Ordovician–Silurian Wufeng–Longmaxi Formation in the southern Yangtze region (Qiu et al., 2018; Du et al., 2022).

Observations of outcrops and cores in the Chang 7 Member of the Ordos Basin reveal that organic-rich shale layers are interbedded with multiple tuff layers, ranging from millimeters to centimeters in thickness. Statistical analyses show that an increased number of sedimentary tuff layers correlates with greater source rock thickness and higher total organic carbon (TOC) values (Zhang R. et al., 2017). Lu et al. (2022) suggested that volcanic ash induces reducing conditions and promotes the deposition of pyrite layers, which favor the preservation of organic matter in shale. Therefore, strong links exist between volcanic activity and organic matter enrichment in black shale.

In this study, we investigate the Lower Jurassic Beipiao Formation in the Western Liaoning to examine the influence of depositional processes and volcanic activity on organic enrichment in black shale. Despite earlier beliefs that the Mesozoic basins of the Yanshan orogenic belt lacked significant hydrocarbon potential due to predominant shallow-water deposits and severely eroded reservoirs (Wu et al., 2004; Jia et al., 2019a; Dou et al., 2020), recent findings have challenged this perspective. The discovery of shale oil in the Cretaceous Xiguayuan Formation of the Luanping Basin in 2020 (Well Luantan-1) overturned the traditional view that Mesozoic strata in this region are barren of oil, emphasizing the role of volcanic activity in hydrocarbon generation and preservation (Yuan et al., 2020).

Similarly, the western Liaoning, part of the Yanshan tectonic belt, has its Mesozoic tectonic and sedimentary evolution strongly influenced by the Yanshanian movement and related volcanism. Recent hydrocarbon shows in the Lower Jurassic Beipiao Formation within the Beipiao-Jinyang Basin in the western Liaoning suggest significant exploration potential (Chen et al., 2013; Sun S. L. et al., 2019; Li and Chen, 2014; Zhang et al., 2015). Observations indicate that, contrary to previous beliefs of a purely shallow-water coal-bearing environment, the Beipiao Formation also contains deep-water lacustrine deposits, including black mudstones with gravity flow characteristics and volcaniclastic sediments (Zhang et al., 2016). Volcanic activity during the deposition of the Beipiao Formation may have played a crucial role in organic matter enrichment and hydrocarbon accumulation.

Therefore, this study aims to reevaluate the influence of depositional processes and volcanic activity on organic enrichment in the Lower Jurassic Beipiao Formation of the Western Liaoning. By systematically analyzing lithofacies and sedimentary environments based on core samples, outcrop profiles, thin-section and geochemical data, we seek to provide theoretical support for selecting favorable zones and guiding future exploration efforts.

2 Geological background

The Western Liaoning, located in the eastern part of the Yanshan orogenic belt, contain several Mesozoic lacustrine basins, including Beipiao Basin, Jinyang Basin, Jianchang-Kazuo Basin and Chaoyang Basin (Figure 1). It is bounded to the northwest by the nearly east-west-trending axial uplift known as the Inner Mongolia Axis, to the south by the Shanghaiguan Platform Arch, and to the east by the Beizhen Uplift, which separates it from the North China Rift (Yan et al., 2003; Wang et al., 2001). Since the end of the Middle Triassic, influenced by the Indosinian and Yanshanian orogenies, the region's folds and faults predominantly trend northeast, forming a structural pattern of alternating basement uplifts—composed of Archean to Paleozoic rocks—and Mesozoic to Cenozoic basins (Figure 1) (Zhen et al., 2016; Lin, 2019; Liu, 2019). Since the Jurassic, the Yanshan Orogeny has been the dominant geological force shaping basin structure, sedimentary filling, and paleontological evolution in northeast China. The Yanshan Orogeny is generally divided into three major stages: a strong compressional stage (175–136 Ma), a primary extensional stage (135–90 Ma), and a weak compression-deformation stage (~80 Ma) (Dong et al., 2018). The Beipiao Formation formed during the first stage of strong regional compression and developed between two significant pulses of volcanic activity, as evidenced by the widespread volcanic rocks of the underlying Xinglonggou Formation and the overlying Tiaojishan Formation (Figure 2). During the Late Jurassic, volcanic eruptions of the Yixian Formation induced strong compressional torsion within the basin, leading to the formation of the Nantianmen Fault Zone. This fault zone exposed Middle to Late Proterozoic and Paleozoic carbonates, as well as Mesozoic volcanic rocks, effectively

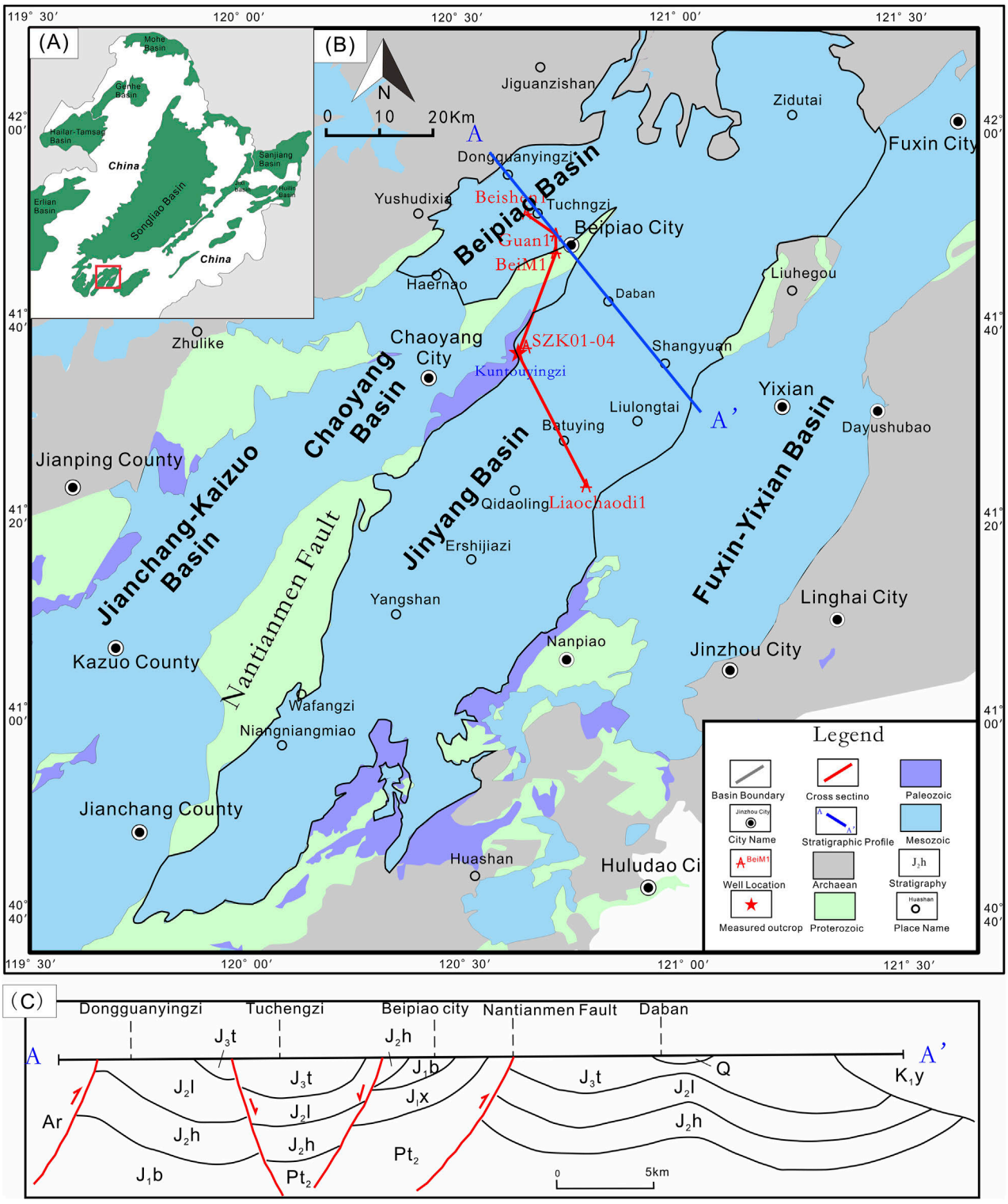

FIGURE 1
Overview of the study area. **(A)** The Mesozoic basin distribution in the Western Liaoning (modified after Deng et al., 2022); **(B)** Cross section A-A1(From Yang et al., 2003); **(C)** A-A' Stratigraphic profile.

dividing the large basin present during the deposition of the Lower Jurassic Beipiao Formation into the current Beipiao and Jinyang basins (Yan et al., 2003; Wang et al., 2001; Zhou and Zhao, 1999).

Prior to the Late Triassic, the region underwent basin basement evolution. The basin variably exposes Archean Jianping and Fuping groups; Mesoproterozoic and Neoproterozoic Changcheng, Jixian,

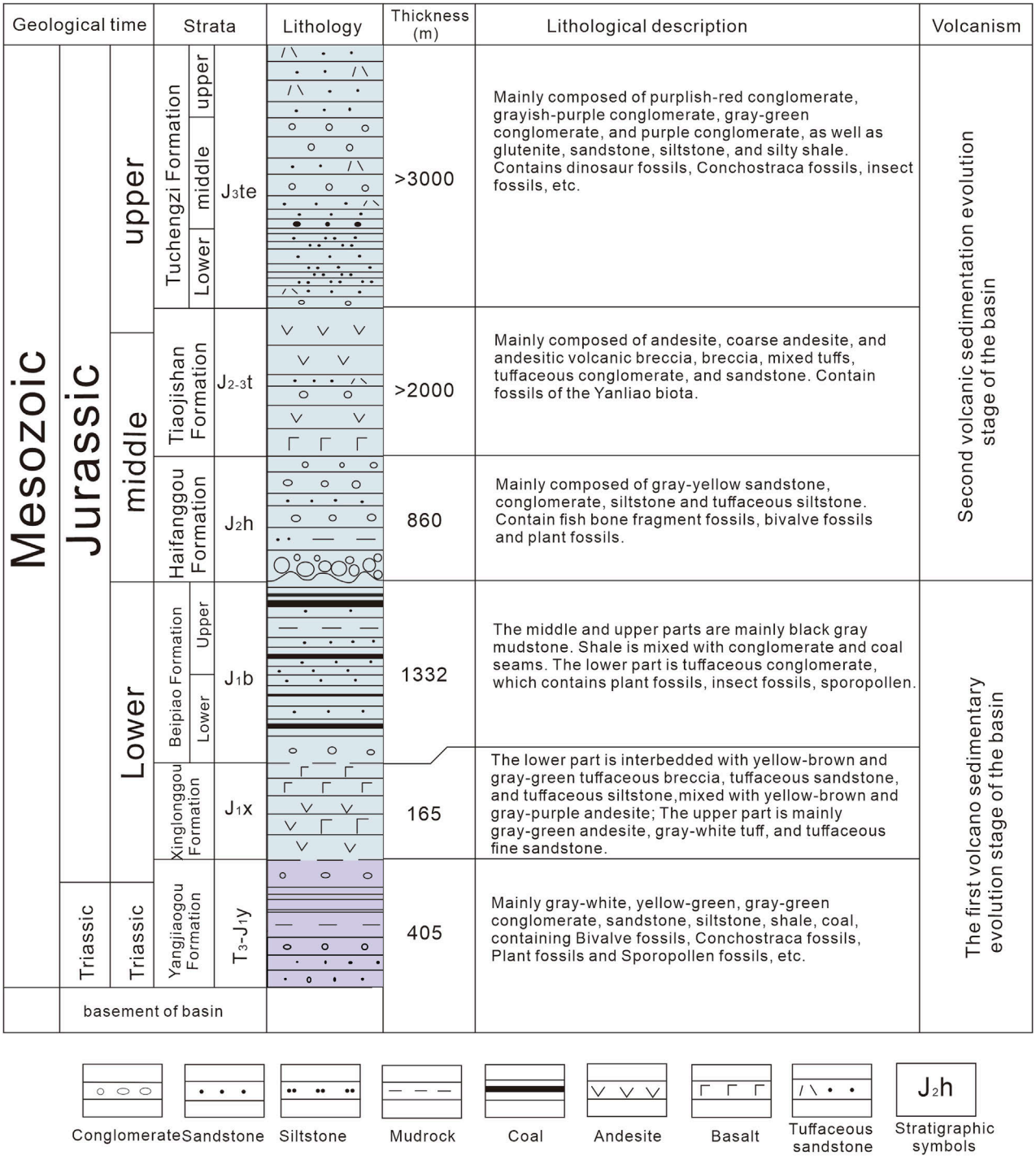

FIGURE 2
Comprehensive stratigraphic column of the mesozoic in the western liaoning (modified after Yan et al., 2002; Yan et al., 2003).

and Qingbaikou systems; and Paleozoic Cambrian, Ordovician, Carboniferous, Permian, and Lower to Middle Triassic strata. Since the end of the Middle Triassic, the area experienced intense tectono-magmatic reactivation under an overall compressive stress regime, undergoing two complete volcanic-sedimentary cycles. This led to the development of a northeast to north–northeast-trending structural pattern of alternating basins and ranges. Extensive Mesozoic volcanic-sedimentary sequences were deposited within the basin, with the Jurassic strata being particularly well developed. From bottom to top, these include the Xinglonggou Formation, Beipiao Formation, Haifanggou Formation, Lanqi Formation, and Tuchengzi Formation (Figure 2) (Yan et al., 2002; 2003).

The focus of this study is the Jurassic Beipiao Formation. Following the volcanic eruptions of the Xinglonggou Formation,

the Beipiao-Jinyang Basin underwent differential subsidence and further expansion, experiencing a significant lacustrine transgression. This event led to the deposition of lacustrine sediments characterized mainly by lake systems accompanied by volcanic sedimentary features (Zhen et al., 2016).

Previous studies have considered the Beipiao Formation in western Liaoning as a set of coal-bearing strata, suggesting an overall shallow-water environment (He et al., 2006; Wang, 2011). However, some researchers have observed gray-black sandstone, mudstone, and shale in core samples, indicating that in addition to shallow-water environments, the Beipiao Formation also contains deep-water deposits, mainly lacustrine facies ranging from marshes to shore-shallow lakes and semi-deep lakes, albeit with a relatively limited extent (Fan, 2004; Zhen et al., 2016). They proposed that during the Early Jurassic, multiple lake basins existed in the Beipiao-Jinyang Basin, with strong separation between them. As research progressed, other scholars suggested that during the deposition of the Beipiao Formation in the Early Jurassic, the basin was a large lacustrine basin. The currently existing Nantianmen Fault Zone was only a latent fault within the basin before the end of the Early Jurassic. Since the Middle Jurassic, influenced by the Yanshanian movement, the Nantianmen Fault Zone gradually became active and developed into a significant uplift that divided the basin.

3 Dataset and methodology

This study utilizes data from three wells Bei M1, Beican 1, and Guan one in the Beipiao Basin; five wells LiaochaoD one and SZK01-04, as well as a long Kuntouyingzi outcrop section in the Jinyang Basin. The Kuntouyingzi outcrop, a long and well-exposed section in the basin center, provides a relatively complete stratigraphic record for this study. The LiaochaoD one well, located near the basin margin, was selected to represent the marginal depositional facies in the study area, while all other wells are situated in the basin center, reflecting the depositional facies in basin center. Integrating these data enables a comprehensive understanding of the lithology and depositional history of the Beipiao Formation across the study area. The primary focus is on the upper member of the Beipiao Formation, which predominantly consists of volcanic lava, volcanic breccia, tuff, thick mudstone, sandstone, and conglomerate. The thickness of this interval can exceed 800 m in the subsidence centers.

In this work we first classify the major lithofacies of the Beipiao Formation in the study area and then analyze the sedimentary processes and facies based on the lithofacies description. To elucidate the lithofacies types and sedimentary facies characteristics of the upper member of the Beipiao Formation in the Beipiao-Jinyang Basin, the following research methods were employed. (1) Core Observation and Description: Detailed descriptions of cores from the target interval of the Beipiao Formation were conducted. This included recording and analyzing typical sedimentary structures, photographing cores, and sampling for thin-section preparation. (2) Field Measured Section Analysis: The Kuntouyingzi outcrop section was investigated and measured in the field. Samples were collected for thin-section analysis. (3) Microscopic Thin-Section Observation: Thin sections were examined under an optical microscope to finely identify and classify the lithologies of the Beipiao Formation in the study area. We then examine the geochemical features of the black shale, e.g., the total organic carbon (TOC) and kerogen type, to explore the relationship between volcanic activity and depositional processes and the enrichment of organic matter in the black shale.

4 Lithofacies

Lithofacies (LF) are rocks or rock assemblages formed within a specific depositional environment, encompassing both the paleogeographic conditions of environment and the lithological characteristics of the sediments, which are fundamental blocks to interpret the sedimentary environment (Jiang et al., 2022a; Feng, 2022). Based on core observation, microscopic identification and assessment of volcanic clastic material input, terrigenous material input, and endogenous material (Liu et al., 2022; Jiang et al., 2022b; Ren, 2012), we have classified the lithofacies types of the Beipiao Formation in the Beipiao-Jinyang Basin into 13 categories (Table 1). The volcanic-related lithofacies classification follows the system proposed by Sun et al. (2001), which divides volcanic rocks into three main categories: pyroclastic lithofacies (volcanic clasts >90%), sedimentary pyroclastic clastic lithofacies (volcanic clasts 50%–90%), and pyroclastic sedimentary lithofacies (volcanic clasts 10%–50%). These lithofacies can be further subdivided into several subcategories based on grain size (e.g., coarse-grained: 0.1–2 mm; medium-grained: 0.01–0.1 mm; fine-grained: <0.01 mm), sedimentary structures (e.g., cross-bedding or planar bedding), lamination and grading (e.g., normal or inverse grading). Among these, volcanic clastic materials are various fragments formed during volcanic activity, collectively referred to as pyroclastics. The cement can be substances formed from the decomposition of volcanic ash or may be partially lava or terrestrial matrix.

4.1 Volcanic lava (LF1)

Rhyolite and basalt were primarily found in well SZK02, where volcanic lava deposits are relatively proximal to the volcanic crater. The volcanic lava is quite thin, indicating low volcanic activity intensity. The volcanic lava discovered mainly includes rhyolite and basalt. Rhyolite (Figures 3A–C) has a resorbed porphyritic texture, with the matrix exhibiting a felsitic texture composed of small felsic minerals and glass. Phenocrysts show resorbed edges and contain some pseudomorphs of primary crystals, as well as relicts and felsitic structures. The basalt (Figures 3D–F) in core samples appears gray-green, with a hyalopilitic texture. The matrix consists of early-crystallized pyroxene, which appears crystalline under crossed polarized light, with numerous feldspar grains present in the matrix. Phenocrysts show zoning textures.

4.2 Volcanic breccia (LF2)

Volcanic breccia is widely distributed, especially evident between 29.6 and 58.9 m in well SZK03 and 29–54 m in well SZK04. The volcanic breccia fragments are sub-angular, poorly sorted,

TABLE 1 Lithofacies classification of the beipiao formation in the beipiao-jinyang basin.

No.	Lithofacies	Formation mechanism	Depositional environment
1	Volcanic Lava	Magma effusion	Volcanic crater
2	Volcanic Breccia	Volcanic debris flow	Near volcanic crater
3	Medium- to Coarse-grained Tuff	Medium to coarse volcanic density flow	Volcanic slope
4	Massive Fine-grained Tuff	Fine volcanic ash density flow	Semi-deep lake to deep lake
5	Laminated Fine-grained Tuff	Fine volcanic ash buoyant flow	Semi-deep lake to deep lake
6	Massive Tuffaceous Mudstone/Sedimentary Tuff	Fine volcanic ash density flow, mud gravity flow	Lake
7	Imbricated Conglomerate	Debris flow	Fan delta
8	Massive (Tuffaceous) Sandstone	Rapid deposition; sandy debris flow	Fan delta front, shallow lake, semi-deep lake
9	Massive Mudstone	Deep-water deposition	Deep lake
10	Normal Graded (Tuffaceous) Sandstone	Sandy turbidity flow, Ta segment; density flow	Semi-deep lake
11	Parallel-Laminated (Tuffaceous) Sandstone	Sandy turbidity flow, Tb segment	Semi-deep lake
12	Cross-Laminated (Tuffaceous) Sandstone	Sandy turbidity flow, Tc segment	Semi-deep lake
13	Deformed Sand-Mudstone	Slumping	Semi-deep lake

and matrix-supported. The matrix consists of medium-to fine-grained tuff (Figure 3G). The volcanic breccia contains relatively small clastic particles, and the multiple depositional phases of volcanic breccia are interbedded with extensive black mudstone, indicating a distal deep-water depositional environment from the volcanic crater.

4.3 Medium to coarse-grained tuff (LF3)

Medium to coarse-grained tuff occurs in wells SZK02-04 and is deposited on volcanic slopes. Thin-section analysis reveals poorly sorted, sub-angular clastic grains with a clast-supported structure. The clasts are angular felsic crystal fragments, glass shards, and volcanic rock fragments, with feldspar grains often altered to carbonate particles. The interstitial material is tuffaceous, and there is an erosional contact with the underlying stratified sedimentary tuff (Figures 3H, I).

4.4 Massive fine-grained tuff (LF4)

Massive fine-grained tuff is widely developed in the study area, with tuffaceous content exceeding 50%. The massive tuff appears as massive gray-white material (Figure 4A). Under the microscope, crystal and glass shards are observed within a tuffaceous matrix, showing a matrix-supported structure. The crystal fragments are sub-angular to angular, poorly sorted, and small lenticular bodies are present, indicating turbulent water conditions during deposition (Figure 4F).

4.5 Laminated Fine-Grained Tuff (LF5)

Laminations usually consist of tuffaceous mudstone or sedimentary tuff interbedded with tuffaceous mudstone (Figures 4B, G). Within the laminated tuff, tuffaceous mudstone or sedimentary tuff forms mud clasts, showing weak basal scouring characteristics. The laminations exhibit gradual transitions between layers and are relatively rare in the study area.

4.6 Massive tuffaceous mudstone/sedimentary tuff (LF6)

The tuffaceous mudstone contains more than 50% mudstone or limestone components and is widely developed in the Kuntouyingzi area of the study region. The cores mostly exhibit a massive structure, and microscopic analysis reveals a complex composition including clay, carbonate grains, and tuffaceous material, with quartz crystal shards commonly present (Figure 4I). Under crossed polarized light, quartz grains show polycrystalline characteristics. Sedimentary tuff is characterized by high tuffaceous (>50%) content mixed with clay and carbonate grains, whereas tuffaceous mudstone has relatively lower tuffaceous content (<50%) and abundant crystal and glass shards (Figure 4H).

Pyroclastic rocks are well-developed in this region. Research indicates that the rapid burial of volcanic fine-grained materials is favorable for the preservation of organic matter (Liu et al., 2022). Volcanic activity plays an important role in the enrichment of organic matter (Lu et al., 2021), and the deep-sourced hydrothermal materials provided by volcanic processes are

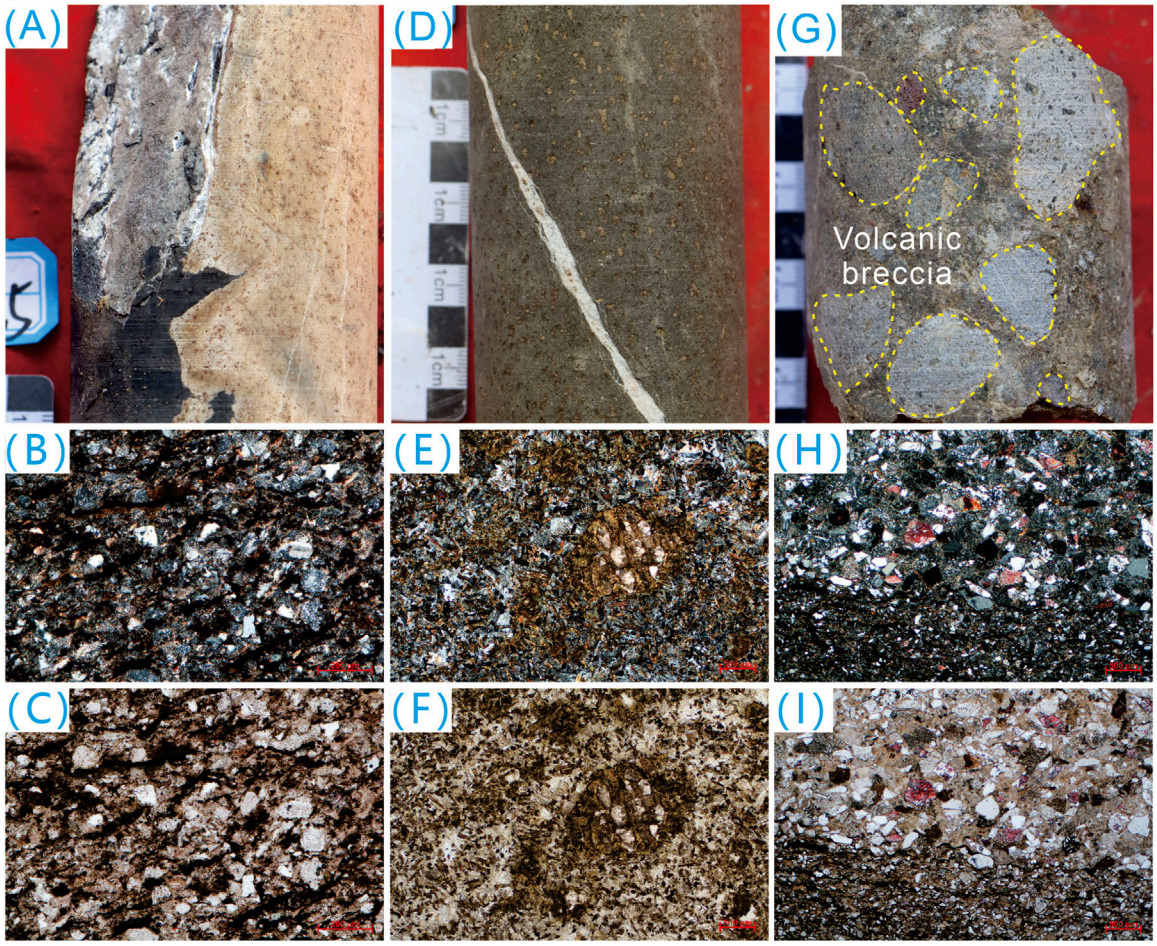

FIGURE 3
Features of Volcanic Lava, Volcanic Breccia, and Medium to Coarse-Grained Tuff. **(A)** Volcanic Lava - Rhyolite core, well SZK02, depth 296.05 m; **(B, C)** Rhyolite thin section under crossed polarized light and plane polarized light, well SZK02, depth 296.05 m; **(D)** Volcanic Lava - Basalt, well SZK03, depth 65.9 m; **(E, F)** Basalt thin section under crossed polarized light and plane polarized light, well SZK03, depth 65.9 m; **(G)** Volcanic Breccia core, well SZK03, depth 39.40 m **(H, I)** Medium to Coarse-Grained Tuff thin section under crossed polarized light and plane polarized light, well SZK02, depth 122.5 m.

crucial for hydrocarbon generation and reservoir improvement (Ren, 2012). The interbedding of organic-rich laminated mudstone and tuff, along with interlayer fractures, facilitates the migration of oil and gas. The presence of fine volcanic material positively impacts organic matter enrichment, hydrocarbon generation, and the conditions for oil and gas accumulation (Liu et al., 2022).

4.7 Imbricated conglomerate (LF7)

The imbricated conglomerate is mainly developed at well LiaochaoD one on the southeastern margin, belonging to marginal facies deposits. The clast diameters are mostly between 3–15 cm, poorly sorted, clast-supported, with clasts arranged in an imbricated fashion. The matrix is minor, gray to gray-white, but mostly reddish or red-brown (Figure 4C). The conglomerate composition is complex, indicating rapid fan delta deposition.

4.8 Massive tuffaceous sandstone (LF8)

Massive sandstone is developed at the top and bottom of the Beipiao Formation in the study area. The massive sandstone primarily consists of sandy material with a clastic (tuffaceous) structure and variegated fabric. The volcanic material typically results from pyroclastic deposits falling into a lacustrine basin, mixed with mud, gravel, and other sediments, and undergoing cementation and lithification. In the shallow drilled SZK01-04 cores, “mudstone rip-up clasts” or mudstone fragments with directional orientation can be seen (Figure 4D). In the Kuntouyingzi outcrop section, massive tuffaceous sandstone is observed (Figures 4L, M). Thin-section analysis shows fine-grained lithic sandstone with a clast-supported structure, where the clasts are mainly andesite or basalt rock fragments along with quartz grains. The quartz grains range from rounded to angular, suggesting a mix of terrigenous quartz and volcanic quartz crystals. The interstitial material is tuffaceous and carbonate (Figures 4J, K).

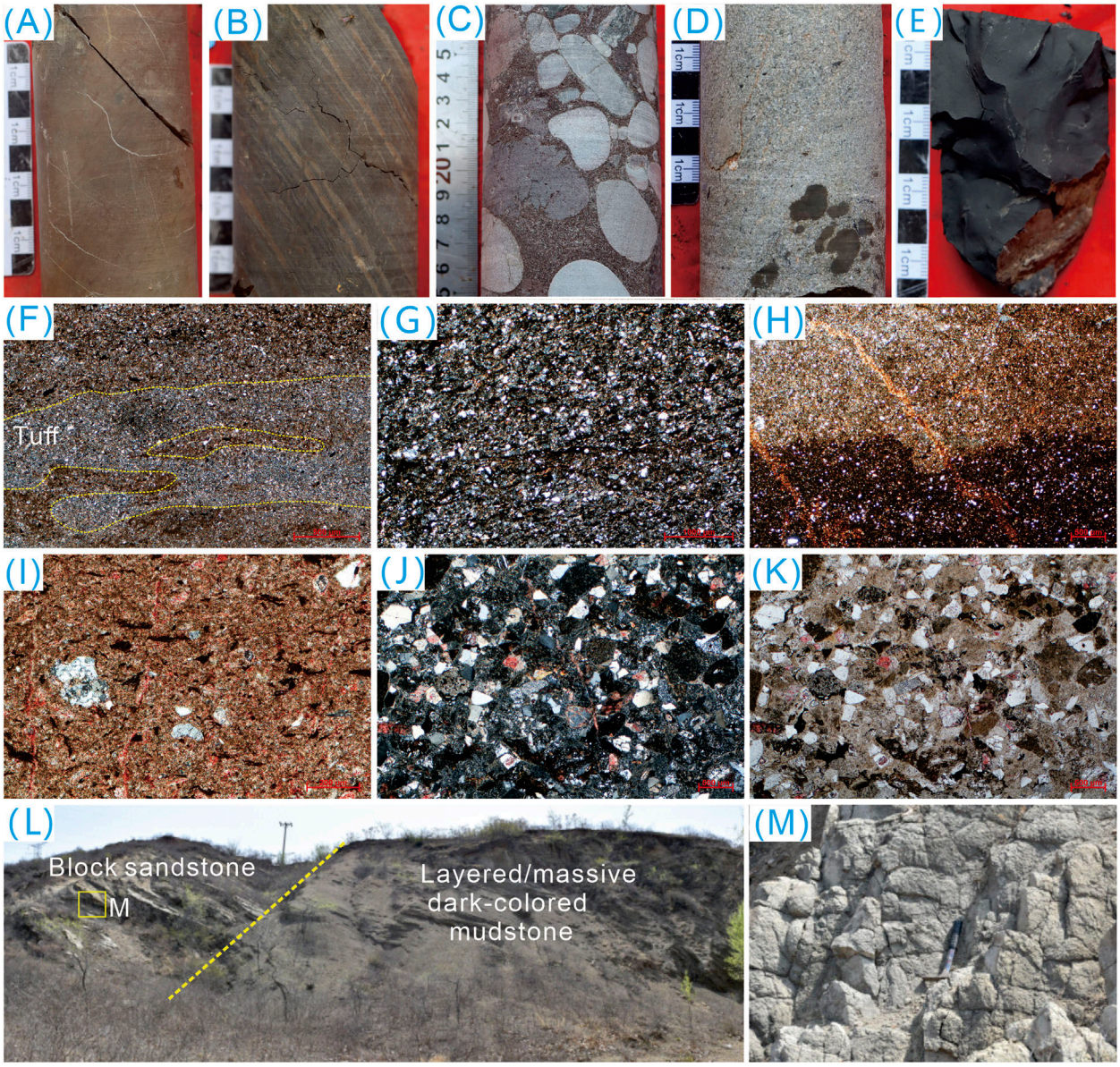

FIGURE 4
Features of Stratified/Massive/Striated Tuff, Stratified/Massive Tuffaceous Mudstone, and Conglomerate. **(A)** Massive Fine-Grained Tuff Core Photo, well SZK03, depth 57.02 m. **(B)** Laminated Fine-Grained Tuff, well SZK03, depth 39.05 m. **(C)** Conglomerate, well LiaochaoD 1, depth 857.6 m. **(D)** Massive Sandstone (with Mud Clasts), well SZK02, depth 131.5 m. **(E)** Black massive Mudstone, well SZK02, depth 222.85 m. **(F)** Laminated Fine-Grained Tuff, well SZK03, depth 39.05 m. **(G)** Glass Shard-Containing Tuff, thin section under crossed polarized light, well SZK02, depth 296.5 m. **(H)** Sedimentary Tuff/Tuffaceous Mudstone, thin section under crossed polarized light, well SZK02, depth 222.85 m. **(I)** Sedimentary Tuff, thin section under plane and crossed polarized light, well SZK03, depth 57.02 m **(J, K)** Massive (Tuffaceous) Sandstone, thin section under plane and crossed polarized light, well SZK02, depth 121.05 m. **(L)** Massive Sandstone and Bedded/Massive Mudstone, Kuntouyingzi outcrop. **(M)** Massive Sandstone, Kuntouyingzi outcrop.

4.9 Massive black mudstone/shale (LF9)

In the middle part of the Beipiao Formation in the Beipiao-Jinyang Basin, there is a substantial thick sequence of dark black mudstone. In the core samples, it appears as black and massive (Figure 4E), while in the Kuntouyingzi outcrop it is observed as bedded/massive black mudstone or shale (Figure 4L). The Beipiao Formation contains considerable thickness of black mudstone and shale, which can serve as a main hydrocarbon source rock.

4.10 Normal graded tuffaceous sandstone (LF10), parallel-laminated tuffaceous sandstone (LF11), cross-laminated tuffaceous sandstone (LF12)

These three lithofacies belong to the Ta, Tb, and Tc divisions of the Bouma sequence and are typically observed individually. In well SZK02, from 136.00 to 193.00 m, these features are evident. The Ta unit is represented by normal graded sandstone with mud clasts,

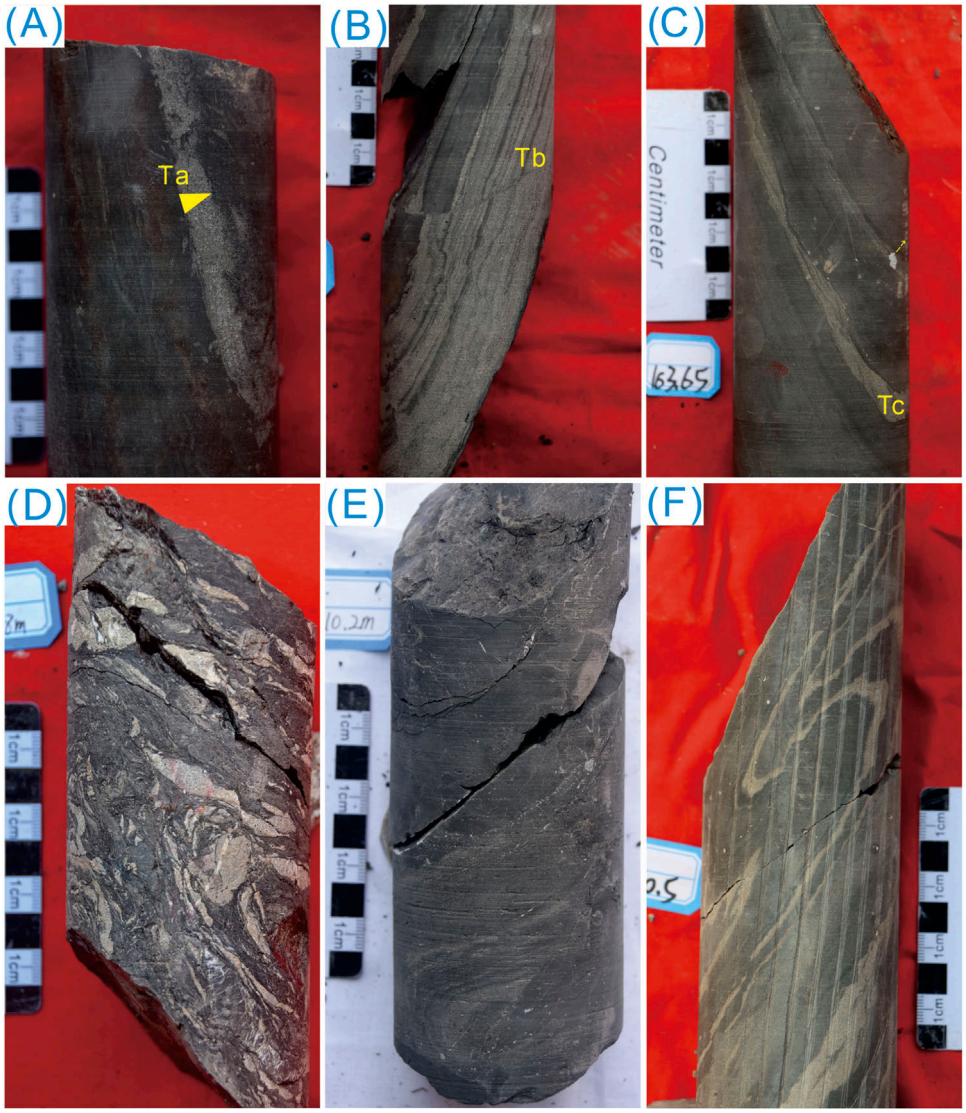

FIGURE 5
Characteristics of Normal Graded/Parallel-Laminated/Sand Grain Cross-Laminated (Tuffaceous) Sandstone and Deformed Sand-Mudstone. **(A)** Massive Tuffaceous Sandstone, well SZK02, depth 173.10 m. Ta-Turbidite Bouma sequence A; **(B)** Parallel-Laminated Tuffaceous Sandstone, well SZK02, depth 158.6 m. Tb- Turbidite Bouma sequence **(B, C)** Massive Tuffaceous Sandstone/Tuffaceous Mudstone, well SZK02, depth 163.65 m. Tc- Turbidite Bouma sequence **(C, D)** Slump Fold, well SZK02, depth 112.8 m. **(E)** Slump Fold, well SZK02, depth 210.2 m. **(F)** Slump Fold, well SZK02, depth 280.4 m. Please note the high dip angle of bedding in wells SZ01-SZK04 is not the depositional dip, instead it is caused by the titling of the strata due to the uplift.

erosional structures, load casts, and flame structures at the base of the layer (Figure 5A). The Tb unit consists of parallel-laminated sandstone (Figure 5B), while the Tc unit is characterized by siltstone with small ripples and deformation layers (Figure 5C), indicating gravity flow deposition in a deep-water environment with turbulent conditions.

4.11 Deformed Sandstone and mudstone (LF13)

Deformed sandstone and mudstone formed by slumping is widely developed in the deep-water area of the Beipiao-Jinyang Basin (Figures 5D, E). These rocks exhibit slump folding structures, reflecting the rapid depositional process of gravity flows. In well SZK02, slump-related sandstone and mudstones are developed, with sandy masses enveloped in mudstone (Figure 5E) and deformed lenticular sand bodies (Figure 5F). The mudstone is black to dark gray, indicating a deep to semi-deep lacustrine depositional environment at that time.

The 13 lithofacies classifications are building blocks that are then used to interpret sedimentary facies. Different facies combination can represent different sedimentary process and environment.

5 Sedimentary facies and environment

Based on field outcrops, core observations, lithofacies classification, and thin-section analysis, the depositional facies interpretation for the Beipiao Formation in the Beipiao-Jinyang Basin has been established. The study area is primarily characterized by fan delta facies, and lacustrine deposits, with subfacies including a shallow lacustrine subfacies between the fair-weather wave base and storm wave base, and a semi-deep to deep lacustrine subfacies below the storm wave base.

The shallow lacustrine subfacies include microfacies of fine-grained shallow lake deposits. The semi-deep to deep lacustrine subfacies consist of microfacies of fine-grained semi-deep to deep lake deposits, gravity flow deposits, and volcaniclastic deposits. On the southeastern margin of the basin, fan deltas are well developed, mainly characterized by braided channel deposits of fan delta plain and fan delta front.

5.1 Shallow lake

5.1.1 Fine-grained shallow lake deposits microfacies

The lithology of fine-grained shallow lake deposits mainly includes mudstone (LF6), silt-bearing mudstone, and siltstone, typically dark gray in color. Bioturbation features are visible (Figures 6A, B), with thin siltstone layers often present. The mudstone may have been deposited under slack water conditions during fair weather, while the thin sandy layers (Figure 6C) have diverse origins, primarily resulting from the reworking of delta-derived sediments by wave action.

5.2 Semi-deep to deep lacustrine subfacies

5.2.1 Tempestite microfacies

Core observations from the wells in the Beipiao-Jinyang Basin indicate the presence of storm deposits within the Beipiao Formation. These deposits are characterized by siltstone, silty sandstone, and fine sandstone, with few muddy siltstone containing mud clasts. The deposits commonly display an inverse-to-normal grading sequence or a normal grading similar to Bouma sequences. The mudstone is gray-green to dark gray, suggesting a reducing environment. Typical storm-related structures include hummocky cross-stratification (Figures 6D, E), mudstone rip-up clasts, and gutter casts (Figure 6F), as well as wavy bedding (Figure 6G) and lenticular bedding (Figure 6I). Deformation features such as load casts and fold deformations are also present (Figure 6F). Massive sandstone indicative of rapid deposition is also observed, along with bioturbation features (Figure 5H).

5.2.2 Deep-water gravity flow microfacies

This study uses a classification scheme for sediment gravity flows based on sedimentary processes and rheology proposed by previous researchers' work (Pan, et al., 2017; Zavala and Pan, 2018). Core observations reveal that the gravity flow deposits in the Beipiao Formation of the Beipiao-Jinyang Basin include slumping deposits, sandy debris flows, and turbidites, with sandy debris flows and turbidites being the most common.

The sandy debris flow deposits in the Beipiao Formation mainly consist of siltstone, massive fine-grained sandstone (LF8), and muddy siltstone, with occasional conglomerates. Slumping deposits, originating from thin interbedded siltstone and mudstone, exhibit thin sandstone layers that form convoluted and faulted structures called sand pillows (LF13). The interiors of sand pillows display inclined "S"-shaped convoluted laminations, or the pillows themselves may fold into horizontal or inclined "S"-shaped irregular sand bodies, with some forming slump folds (Figures 7A–C). Sandy debris flow deposits in the region often contain poorly sorted shell fragments. Other sedimentary structures observed in sandy debris flow deposits include groove casts, gutter casts, load casts, liquefaction cones, subaqueous dikes, and escape structures. These deposits are found in wells SZK01-04 (Figures 7D–H).

Turbidite deposits are also widespread in the Beipiao Formation, typically with sand bodies less than 1 m thick, and often even less than 0.1 m, indicating frequent turbidite events (LF11 and 12). The turbidite lithology mainly consists of siltstone, fine sandstone, and muddy siltstone, with occasional conglomerates. Turbidite deposits are characterized by graded bedding (LF10) (Figure 7I), with the tops of graded beds showing small-scale parallel laminations (LF11) (Figure 7L), cross-laminations (LF12), and ripple cross-laminations (generally less than 10 cm thick) (Figure 7J). Groove casts and gutter casts are commonly found at the base, and liquefaction features are often seen within the deposits (Figures 7E, K).

5.2.3 Pyroclastic microfacies

Core and thin-section observations from the Guan one well (depth 400–550 m) in the Beipiao Basin reveal that the Beipiao Formation contains significant amounts of pyroclastic material. These contemporaneous volcanic clasts (lithic fragments, crystal shards, and glass shards) were transported by air or water into the lake basin, where they were deposited and consolidated. The deposits primarily consist of tuffaceous siltstone and thin tuff layers, ranging from centimeters to micrometers in thickness (Figure 8A). The tuffaceous siltstone displays characteristics of volcanic density currents (Figure 8B). Thin layers of tuff, often in micrometer scale, are typically in abrupt contact with dark mudstone or oil shale, indicating a deep-water stagnant depositional environment (Figures 8C, D). The tuff layers contain abundant volcanic glass but relatively few crystal shards, and they exhibit horizontal and massive bedding structures (Figure 8E).

In wells SZK01-04, several layers of volcanic breccia were found. These breccias are characterized by composite volcanic clasts within a matrix-supported tuff. The tuff is rich in crystal fragments, while the clasts are sub-angular to angular. The clast sizes vary from a few millimeters to several centimeters, with the most developed layers observed in well SZK04, suggesting strong volcanic influence in proximity to the volcanic source.

5.2.4 Semi-deep to deep lacustrine fine-grained sedimentary microfacies

The semi-deep to deep lacustrine fine-grained microfacies is extensively developed and represents the primary depositional facies type of the Beipiao Formation in the Beipiao-Jinyang

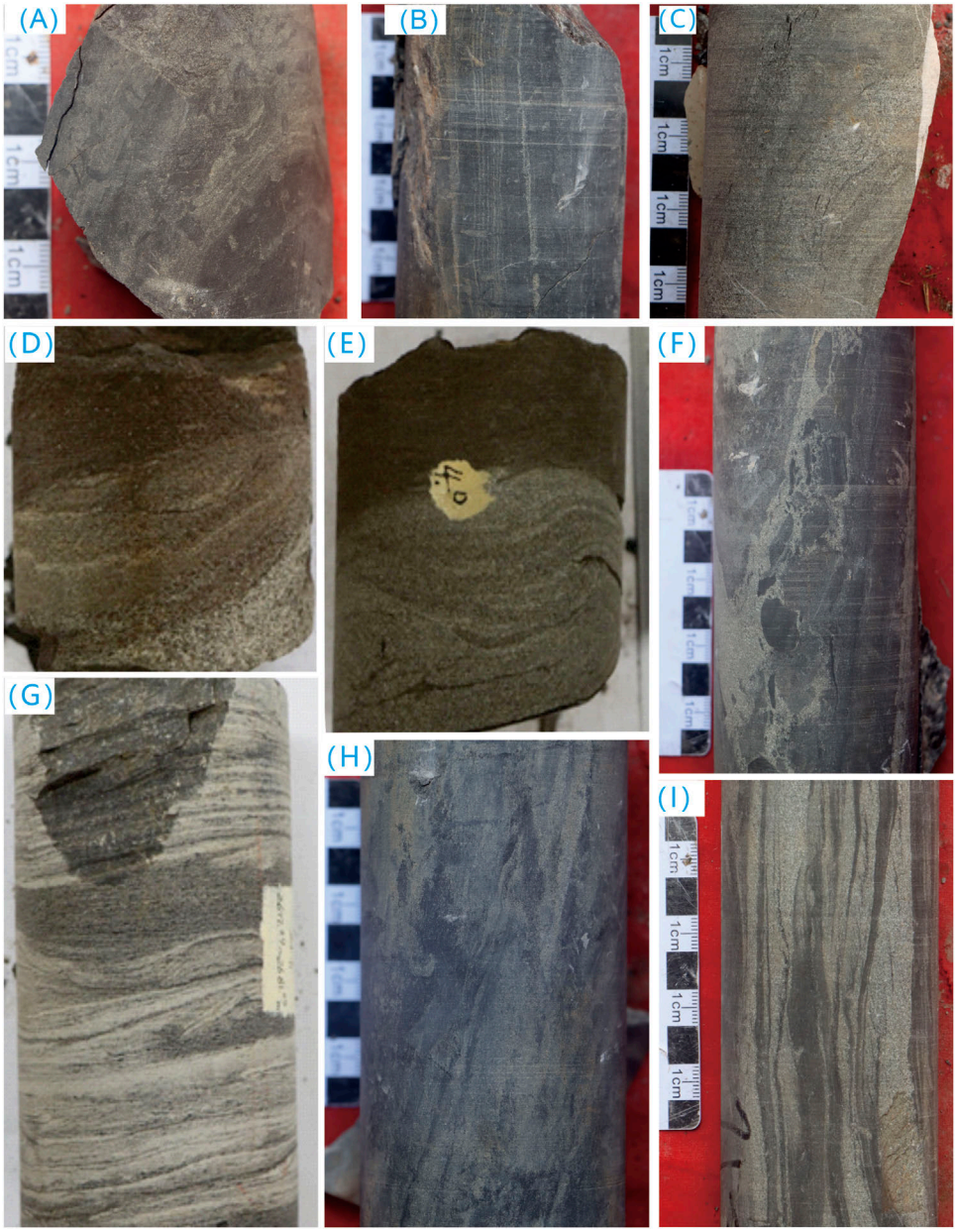

FIGURE 6
Typical Facies characteristics of Storm s and Shallow Lake Fine-Grained deposits. **(A)** Mudstone with thin siltstone layers, extensive bioturbation with visible burrows, well SZK 03, depth 155.20 m. **(B)** Mudstone with millimeter-scale thin siltstone layers, visible bioturbation, well SZK 03, depth 231.80 m. **(C)** Muddy siltstone, well SZK04, depth 79.55 m. **(D)** Storm truncation structure, trough cross-stratification, well Guan 1, depth 399.8 m. **(E)** Deformation and truncation structure, well Guan 1, depth 426.2 m. **(F)** Basal scour with retained mud clasts arranged in a v shape, well SZK 03, depth 254.2 m. **(G)** Hummocky cross-stratification in microcrystalline limestone, well Beican 1, depth 2,677.4 m. **(H)** Bioturbation structure, well Szk03, depth 259.90 m. **(I)** Wavy bedding, well SZK03, depth 212.5 m.

Basin. The lithology of these deposits is dominated by mudstone or, which appears dark gray to black and mostly occurs as massive deposits (LF4, 5, six and 9; Table 1) (Figure 8F). Laminated black mudstone and shale deposits are both observed in outcrop section and core (Figure 8G), and the accumulated thickness is significant, indicating a deep-water semi-deep to deep lacustrine environment. In the Beipiao-Jinyang Basin center, the total mudstone thickness can exceed several hundred meters.

5.3 Fan delta

The fan delta facies is primarily observed in well LiaochaoD 1. In this location, the lithology of the Beipiao Formation consists mainly of extensive conglomerate beds interbedded with medium to coarse-grained sandstone containing lithic feldspar. Some layers are cemented with tuffaceous material, and no typical Beipiao Formation fine-grained shale strata are observed, indicating the development of the fan delta.

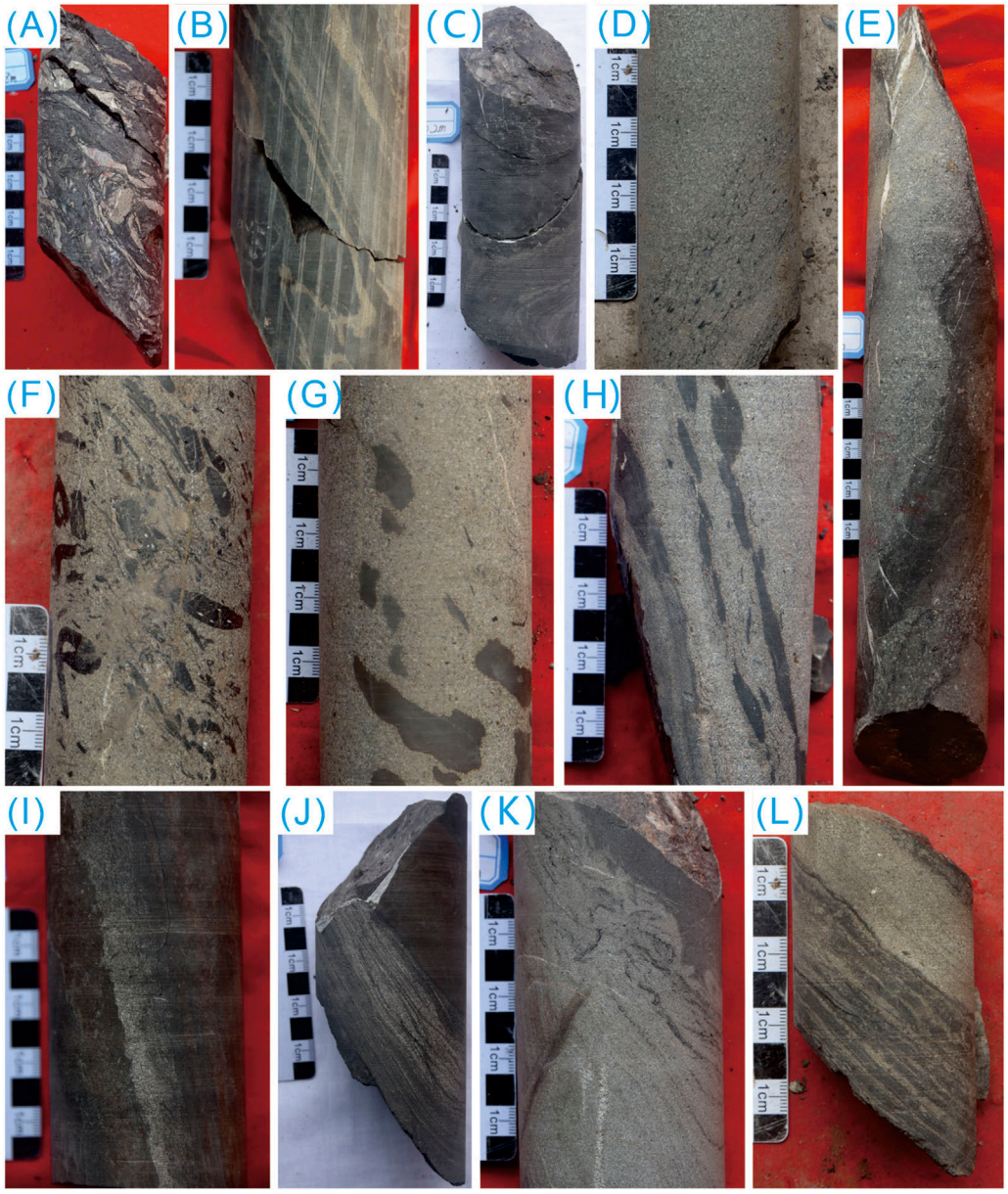

FIGURE 7
Typical characteristics of deep-water gravity flow sedimentary microfacies. **(A–C)** Slumping Deposits, Slump Structures, well SZK02. **(D)** Sandy Debris Flow Deposit, Massive Sandstone with Millimeter-Scale Mudstone Clasts, well SZK01, depth 252.8 m. **(E)** Turbidite Ta Unit, well SZK02, depth 197 m. **(F)** Sandy Debris Flow Deposit, Chaotically Distributed Mud Clasts, well SZK01, depth 252.18 m. **(G)** Sandy Debris Flow Deposit, Chaotically Distributed Mudstone Fragments, well SZK02, depth 303.37 m. **(H)** Sandy Debris Flow Deposit, Mud Clasts Aligned Along Bedding, well SZK02, depth 129.6 m. **(I)** Turbidite Ta Unit, well SZK02, depth 173.1 m. **(J)** Turbidite Tc Unit, Sand Laminations, well SZK02, depth 211.3 m. **(K)** Turbidite Ta-Tb Unit, Basal Load Cast with Liquefaction Features, well SZK02, depth 170.4 m. **(L)** Turbidite Tb Unit, Parallel Laminations, well SZK01, depth 254.95 m.

The braided channel of the fan delta plain exhibits imbricated gravel deposits and massive conglomerates (Figure 9A). In some areas, the gravels display an oriented arrangement (Figures 9B, C), and at the contact between gravel and sand, a clear scour-and-fill structure is observed, indicating erosional contacts (Figure 9D). Due to strong hydrodynamics, the matrix is mainly composed of medium-grained sandstone rather than mudstone. The conglomerates are dispersed within the sandy matrix, indicating rapid deposition. Furthermore, the varied grain sizes of the conglomerates and poor sorting suggest a quick unloading of sediments. The braided channel of the fan delta front is characterized by sandy deposits with cross-bedding, and no mudstone or siltstone is present.

The fan delta deposits can also be observed on the Kuntouyingzi outcrop when the lake level low and the fan delta can prograded into the center of the lacustrine basin. It is mainly characterized by thick and massive conglomerate and sandstone on the outcrop (Figure 10).

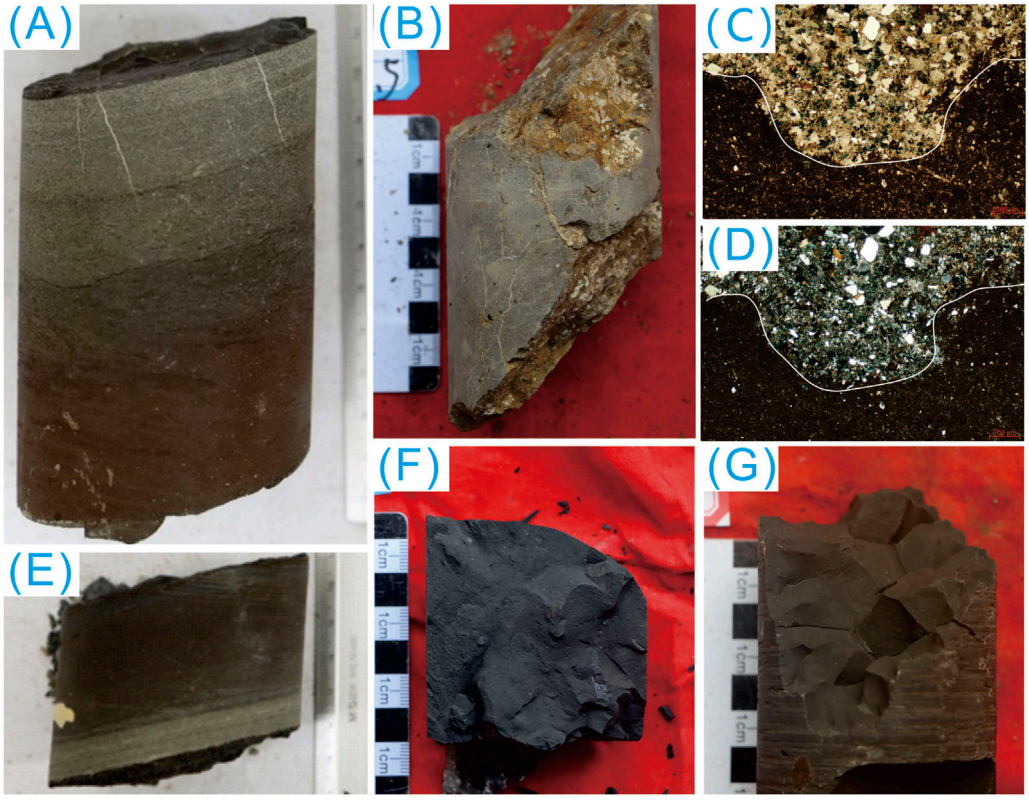

FIGURE 8
Pyroclastic sediments and semi-deep-deep lake fine-grained sedimentary characteristics. **(A)** Massive Tuff, well Guan 1, depth 424.1 m. **(B)** Massive-Bedded Tuff, well SZK04, depth 35.50 m **(C, D)** Volcanic Lithic Fragments, Groove Casts (under plane and crossed polarized light), well Guan 1, depth 464 m. **(E)** Massive Mudstone and Parallel-Laminated Tuff, well Guan 1, depth 418.3 m. **(F)** Dark Gray Massive Mudstone, well SZK02, depth 253.15 m. **(G)** Dark Gray Massive Mudstone, well SZK03, depth 344.8 m.

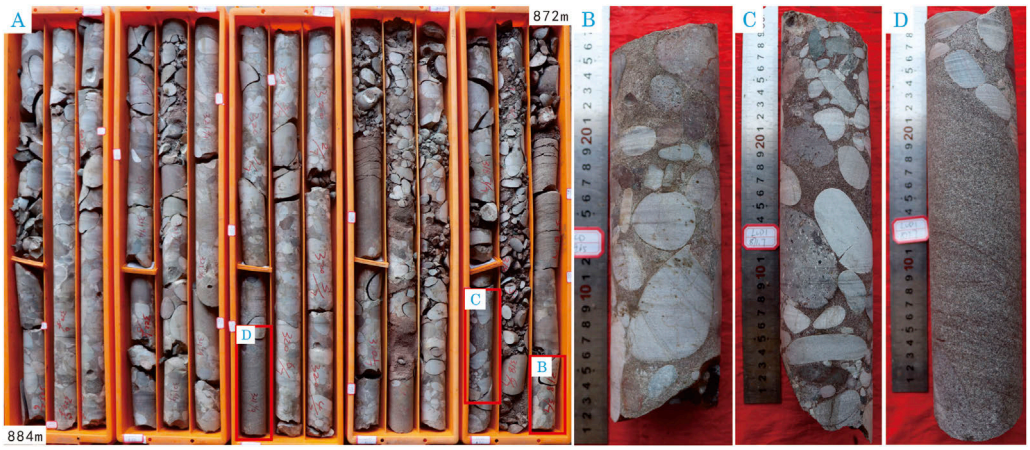

FIGURE 9
Typical characteristics of fan delta sedimentary facies. **(A)** Core Box Photo, red box indicates red-brown sandstone, well LiaochaoD 1, depth 884–872 m. **(B)** Conglomerate with grain size 2–10 cm, well LiaochaoD 1, depth 869.65 m. **(C)** Conglomerate with oriented arrangement of gravel, well LiaochaoD 1, depth 871.7 m. **(D)** Red-brown sandstone with developed scour surfaces and cross-bedding, well LiaochaoD 1, depth 877.7 m.

5.4 Vertical sedimentary facies evolution

Based on lithofacies and sedimentary facies analysis, the sedimentary environment of the Jurassic Beipiao Formation can be interpreted from its basal to upper sections (Figure 10). The Kuntouyingzi outcrop offers a continuous and well-exposed view of the Beipiao Formation, including its unconformable contact with the underlying Neoproterozoic Wumishan Formation dolomite (Figure 10A). Although portions of the basal and upper sections of the Beipiao Formation are missing at

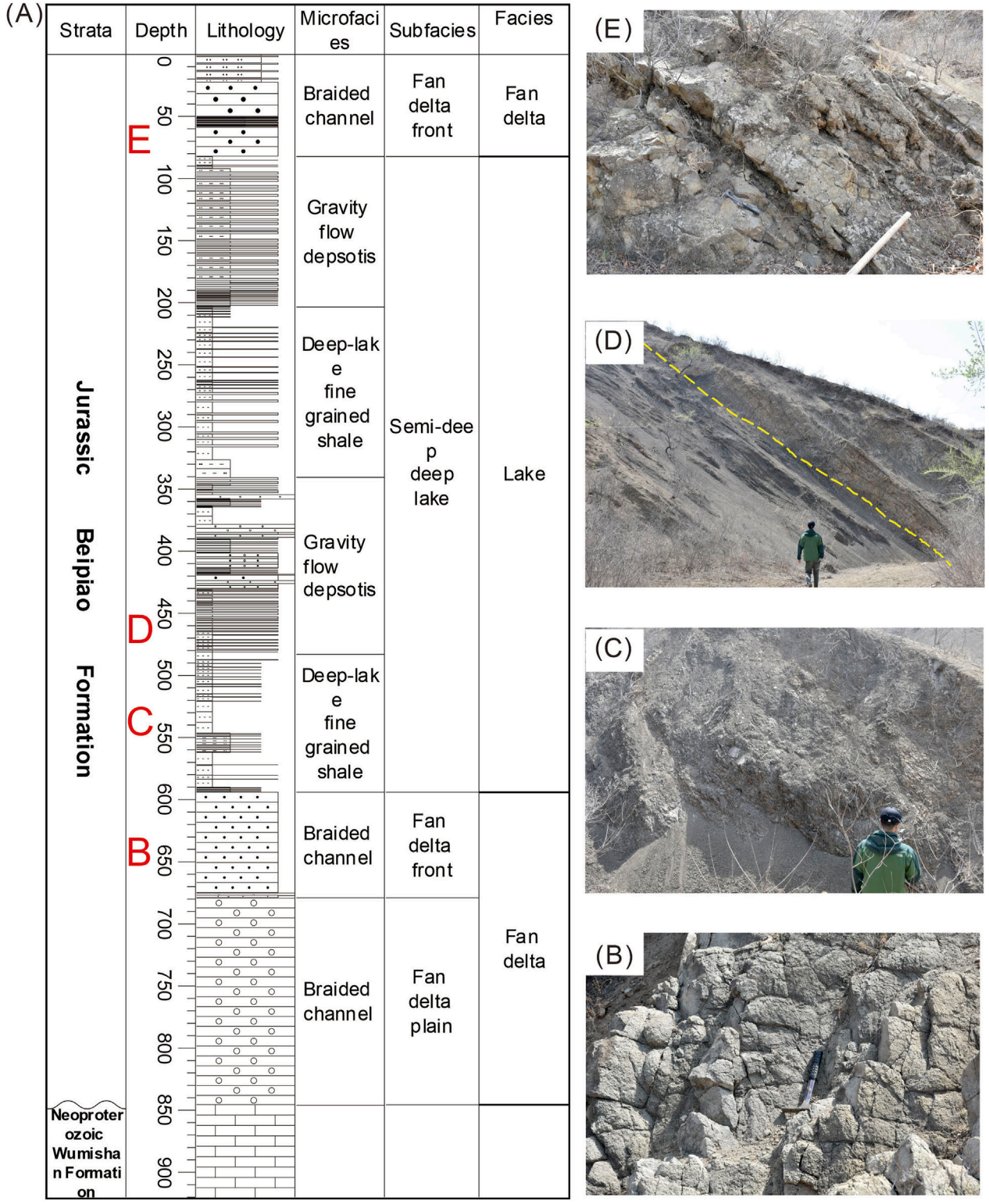

FIGURE 10
(A) The sedimentary facies and environment evolution from basal to top of the Beipiao Formation, Kuntouyingzi outcrop. **(B–E)** is the photo location.

this location, the approximately 900-m-thick exposed outcrop effectively represents the sedimentary characteristics of the formation.

The lower part of the Beipiao Formation is dominated by massive conglomerates and thick to medium-grained sandstones, indicative of a fan delta depositional environment (Figure 10B). The

fan delta facies is commonly developed along the basin margin. Well Liaochaodi one is located on the eastern basin margin and shows a continuous and long interval of conglomerate, indicating strong hydrodynamics. The high dipping angle of conglomerates indicates they are deposited in a steep slope, likely suggesting a depositional environment of fan delta near the sediment source. Due to its proximity to the basin, the Well Liaochaodi one is dominated by fan delta facies in the whole Beipiao Formation. The middle section of Kuntouyingzi outcrop is primarily composed of thick shale, interbedded with thin sandstone or pyroclastic deposits, characteristic of deep-water fine-grained sediments and gravity flow deposits (Figures 10C, D). Such fine-grained lithologies characterized by thick shale or turbidite Bouma sequence are also common in wells SZK01-04 (see Figure 1 for location; Figures 6–8). During this period, the lake expanded, reaching its maximum depth. The upper part of the Beipiao Formation transitions back to coarse-grained sandy deposits, reflecting the progradation of the fan delta into the lake (Figure 10E). These lithological changes represent a complete sequence cycle: an initial low lake level followed by transgression, culminating in a stable highstand lake level.

The facies evolution aligns with regional geological history. Previous studies indicate that the Beipiao Formation is influenced by the Yanshan orogenic event (Sun QS. et al., 2019). Following the volcanic eruption of the Xinglonggou Formation, the basin began to rift, leading to the deposition of relatively coarse-grained fan and alluvial delta facies. As rifting continued, the basin area expanded, and lake depth increased, favoring the development of deep-lake environments. Subsequently, as basin extension slowed, deltaic facies began to prograde into the basin center, which corresponds to the coarse-grained deposits in the upper part of the Beipiao Formation. Later, the basin was filled by another pulse of volcanic activity, resulting in the formation of Haifanggou-Tiaojishan pyroclastic deposits (Wang, 1993; Sun S. L. et al., 2019).

5.5 Sedimentary facies spatial distribution characteristics

Based on the lithofacies and sedimentary facies analyses, as well as the thickness map of the Beipiao Formation in the study area (Figure 11), a spatial facies distribution can be obtained. During the deposition of the Beipiao Formation in the Beipiao-Jinyang Basin, alluvial fan and fan delta deposits developed in the eastern and southern parts of the basin. These deposits, characterized by limited sandbody extension and distribution (Figure 12), were the primary sources of terrigenous clastic input, with well LiaochaoD one serving as the key representative. In the eastern parts of Batuying and Ershijiazi towns, shore-shallow lake and storm deposits are primarily developed. The shore-shallow lake deposits cover a relatively small area and are generally distributed in a northeast-southwest elongated pattern.

In the northwest part of the basin, west of Jinlingsi and Yangshanzhen, semi-deep to deep lacustrine deposits are extensively developed. Volcanic deposits are frequently observed in the Kuntouyingzi area, represented by wells SZK01-04 and Bei M1. Along the northern margin of the Beipiao Basin, small nearshore subaqueous fans have developed, which also evolved into semi-deep to deep lacustrine deposits, with wells Guan one and Beican one serving as representative wells in this region.

In general, the Beipiao Formation in the study area is characterized by fan delta deposits at the basin margin and widespread deep-lake environments in the basin center, with fan delta fronts and shallow lakes developed in between. The deep-lake facies are predominantly found in the middle part of the Beipiao Formation, while the lower and upper parts are dominated by fan delta and braided delta deposits.

6 Geochemical characteristics of source rocks

A total of 209 data samples were collected for this study, including 170 drilling core samples and 39 field outcrop samples. The data mainly includes five organic geochemical analyses, such as total organic carbon (TOC) and pyrolysis. Of the samples, 200 are from the Jinyang Basin and nine are from the Beipiao Basin. The samples were taken from wells SZK01, SZK02, SZK03, and Guan 1, as well as outcrops at Xiaogangou, Wolong, Dajingou, Shimen Gou, Dongkuntouyingzi, Shimen Gou Village, and Nanyao Village.

6.1 Organic matter abundance

Organic matter abundance is the material basis for evaluating source rocks, and commonly used indicators for assessing the organic matter abundance in source rocks include total organic carbon (TOC%), chloroform "A," total hydrocarbons (HC), and pyrolysis hydrocarbon potential (S1+S2). Analysis of these indicators reveals variability in organic matter abundance across different wells and outcrops. Well SZK02 has the highest organic matter abundance, followed by well SZK03 and the Shimen Gou outcrop in Changbaoyingzi Township. The Wolong, Nanpiao Yanjialing, and Diaojiagou outcrops in Batuyingzi Township exhibit the lowest values, with average indicator values far below the average for the Jinyang Basin.

The TOC content of core and field-measured outcrop samples ranges from 0.16% to 14.2%, with an average of 1.89% (Figure 13A). Only five samples have a TOC content below 0.4%; two samples fall between 0.4% and 0.6%; 32 samples are between 0.6% and 1.0%; 86 samples, accounting for 46%, are between 1.0% and 2.0%; and 62 samples, accounting for 33.15%, have TOC values greater than 2.0%. These results indicate that the mudstone in the Beipiao Formation generally represents moderate to good source rock, with very few poor or non-source rock samples.

The chloroform "A" content in core samples ranges from 0.0030% to 0.3072%, with an average of 0.0846% (Figure 13B). Seven samples have a chloroform "A" content below 0.015%; 30.52% of the samples are between 0.015% and 0.050%; 34.42% are between 0.050% and 0.100%; 25.32% are between 0.100% and 0.200%; and eight samples have values greater than 0.200%. These indicators consistently suggest that the Beipiao Formation source rocks are mainly moderate to good in terms of organic matter abundance.

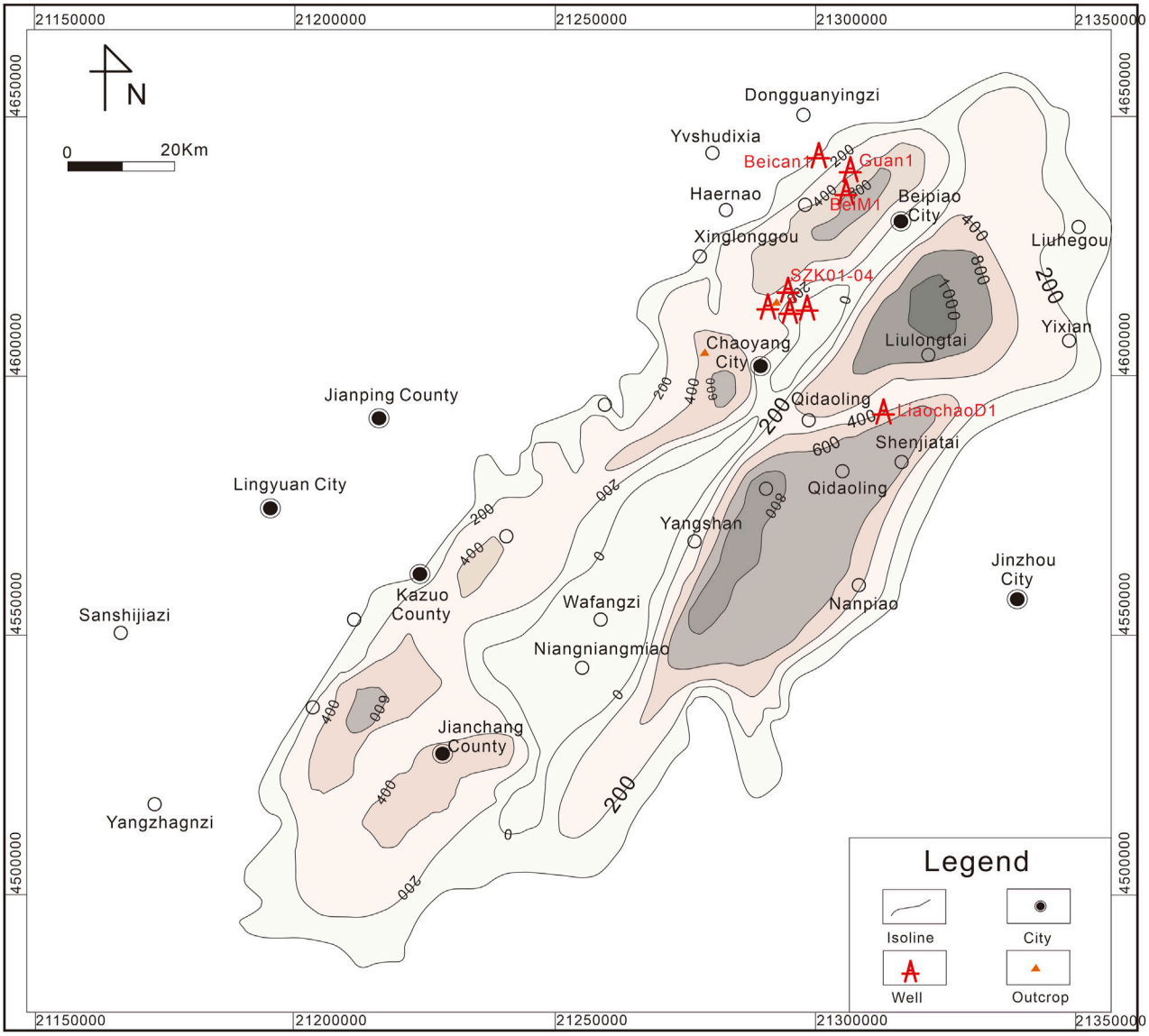

FIGURE 11
Strata thickness map of the Beipiao Formation in the Western Liaoning.

6.2 Organic matter types of source rocks

The organic matter type of the Beipiao Formation source rocks in the study area was analyzed using the pyrolysis parameters IH (hydrogen index) and IO (oxygen index). In the organic matter type identification diagram (Figure 13D), most of the sample points fall in the Type II region, with only a few in the Type III region. Therefore, it is concluded that the organic matter in the Beipiao Formation source rocks is predominantly Type II, which leans toward humic-sapropelic. This indicates that the hydrocarbon precursors mainly originated from lower aquatic organisms and higher plants, with a greater contribution from higher plants.

The cross-plot of HI *versus* Tmax for the Beipiao Formation source rock kerogen (Figure 13D) suggests that it generally belongs to a mixed organic matter type, making it challenging to accurately identify. This also indicates that the Beipiao Formation source rocks are in a high to over-mature stage. It can be observed that the kerogen from wells SZK02 and SZK03 has reached an over-mature stage, making its type difficult to distinguish. The kerogen in field outcrops is primarily of Type II2, while the kerogen in well Guan one mainly falls between Type II1-II2 and Type II2.

6.3 Organic matter maturity

Comparing the Wolong and Kuntouyingzi sections, although both have relatively high residual organic carbon, the Wolong section shows extremely low hydrocarbon potential (S1+S2). The vitrinite reflectance (Ro) measurements (Figure 13F) indicate that the samples from the Wolong section generally have Ro values greater than 1.5%, with higher values found closer to the diorite

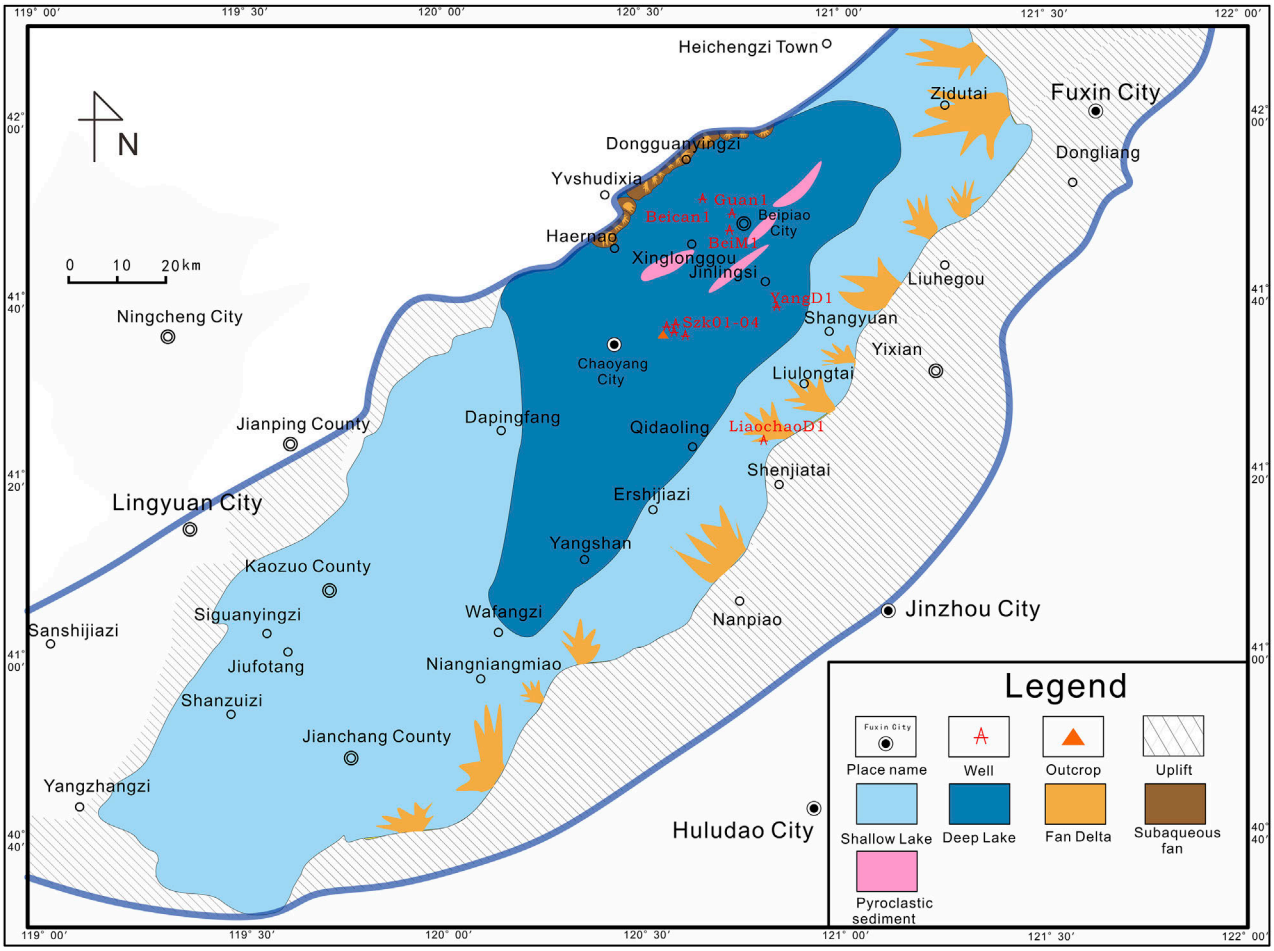

FIGURE 12
Spatial sedimentary facies distribution in the lower jurassic beipiao formation of the beipiao-jinyang basin, western liaoning.

porphyry dike, reflecting thermal alteration of the source rock by the intrusive body.

Based on organic matter abundance and distribution data, as well as Tmax distribution (Figure 13E) and the cross-plot of Production Index (PI) *versus* Tmax (Figure 13C), it is observed that Tmax is positively correlated with vitrinite reflectance (Ro). Typically, Tmax greater than 435°C is considered indicative of a mature stage, whereas Tmax below 435°C indicates an immature stage. For the Beipiao-Jinyang Basin samples, most of the Tmax values fall within the range of 445°C–480°C, indicating a mature stage. The PI *versus* Tmax cross-plot shows that the thick mud-shale layers in wells SZK01-04, located at the center of the basin, are in the later stage of the oil-generation peak and have reached a high maturity to over-mature stage suitable for gas generation. In contrast, shallower areas closer to the basin margins are currently in the oil-generation stage.

It can be concluded that the Lower Jurassic Beipiao Formation in the Jinyang-Beipiao Basin has potential source rocks that are at the mature stage and have reached the oil-generation peak. Although the sample data are from outcrop-controlled areas influenced by faulting and thrust structures, which are unfavorable for hydrocarbon preservation, recent seismic exploration results indicate that beneath the large volcanic clastic rock coverage of the Yixian and Tiaojishan Formations on the eastern side of the basin, there are still substantial deposits of the Beipiao Formation. The hydrocarbon source rocks in these regions are well-developed, showing similar or even better characteristics compared to the existing data, and the two regions are interconnected.

7 Discussion

7.1 Depositional environment

Previous studies have considered the Beipiao Formation in western Liaoning as a set of coal-bearing strata, suggesting an overall shallow-water environment (He et al., 2006; Wang, 2011). However, some researchers have observed gray-black sandstone, mudstone, and shale in core samples, indicating that in addition to shallow-water environments, the Beipiao Formation also contains certain deep-water deposits, mainly lacustrine facies ranging from marshes to shore-shallow lakes and semi-deep lakes, albeit with a relatively limited extent (Fan, 2004; Zhen et al., 2016). They proposed that

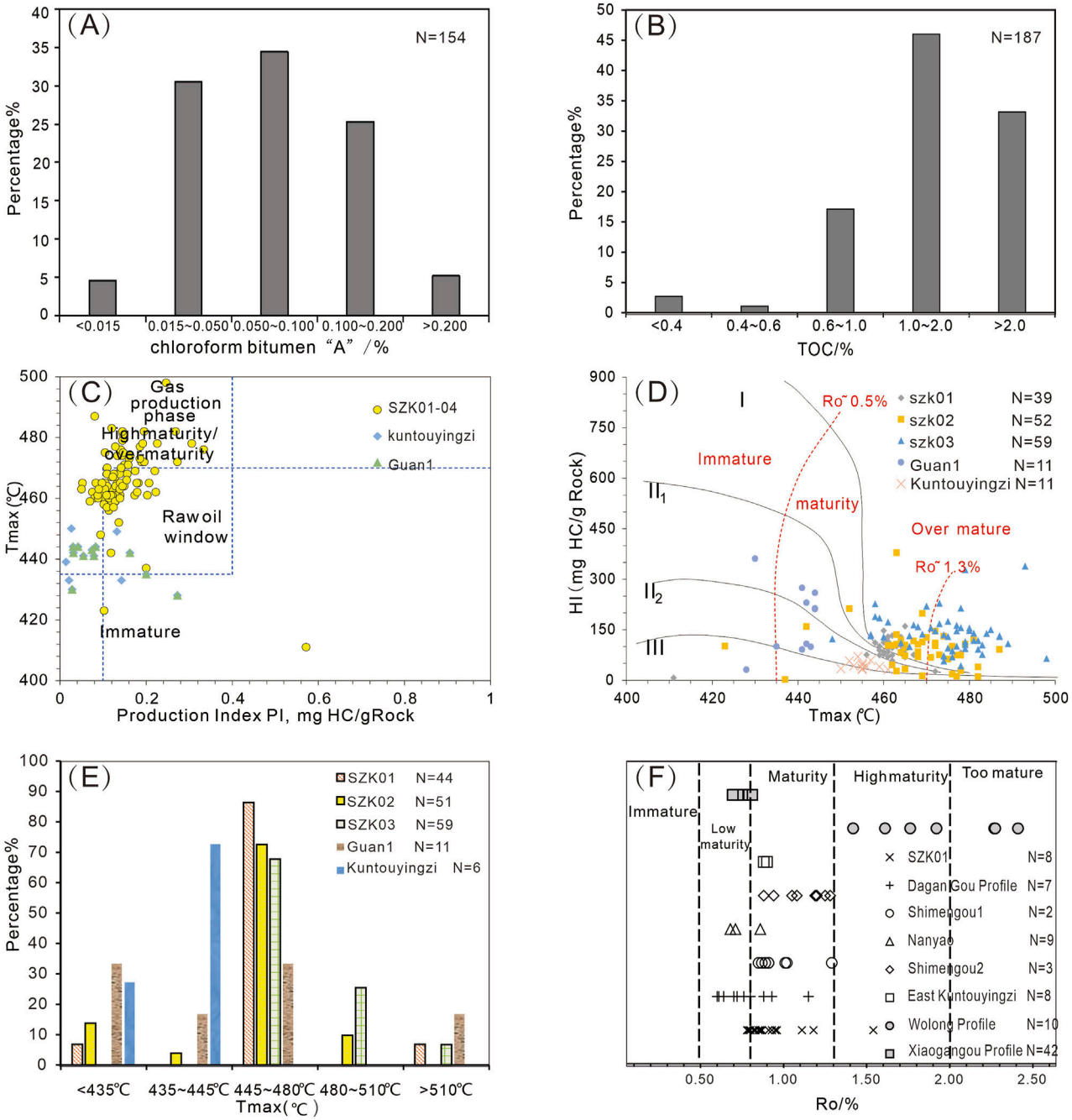

FIGURE 13
Geochemical features of the source rocks of the Beipiao Formation in the Western Liaoning. **(A, B)** Histogram of Organic Matter Abundance; **(C)** Cross plot of the PI and Tmax; **(D)** Organic matter types and source rock maturity; **(E)** Kerogen maturity based on Tmax data; **(F)** Distribution map of vitrinite reflectance (R_0). Some of the organic data was collected from published articles (Sun QS. et al., 2019; Zhen et al., 2016; He et al., 2006; Zhang et al., 2017a; Sun et al., 2017a; Fan, 2004).

during the Early Jurassic, multiple lake basins existed in the Beipiao-Jinyang Basin, with strong separation between them. As research progressed, other scholars suggested that during the deposition of the Beipiao Formation in the Early Jurassic, the basin was a large lacustrine basin. The currently existing Nantianmen Fault Zone was only a latent fault within the basin before the end of the Early Jurassic. Since the Middle Jurassic, influenced by the Yanshanian movement, the Nantianmen Fault Zone gradually became active and developed into a significant uplift that divided the basin.

In this study, wells from the Beipiao Basin (wells Bei M1, Guan1, and BeiCan 1) and the Jinyang Basin (wells SZK01, SZK02, SZK03, and SZK04) are characterized by thick black mudstones in the middle of the Beipiao Formation, indicating a semi-deep to deep lake environment. The storm deposits observed on cores also

indicate a relative deep lake level that below the storm wave base. The abundant gravity flow deposits in the middle part of the Beipiao Formation further support a deep-water environment. Additionally, the Kuntouyingzi outcrop contains approximately 300 m of thick black shale interbedded with thin gravity flow deposits, suggesting a deep-water setting. Regional strata thickness mapping (Lee et al., 2018) shows extensive Beipiao strata distribution in western Liaoning (Figure 11), verifying that the Jinyang, Beipiao, and Jianchang-Kazuo Basins (locations shown in Figure 1) were part of a single large basin during the depositional period of the Beipiao Formation.

Overall, drilling data and outcrop observations in the basin center, along with the strata thickness map, indicate the presence of a widely developed deep-water environment in the middle Beipiao Formation across western Liaoning. The only exception is the LiaochaoD one well, located at the basin margin, which displays conglomerate and coarse-grained deposits indicative of fan delta deposition (Figure 9). These findings provide additional evidence that the Jurassic Beipiao Formation in western Liaoning was deposited in a large, deep-water basin. More importantly, these findings suggest that the organic-rich black shale development has been largely underestimated. Continued exploration has also led to the discovery of hydrocarbon shows in shallow wells SZK01-04 in the Jinyang Basin (Li et al., 2014; Zhang et al., 2015; Zhang T. et al., 2017). Core samples revealed extensive black mudstone deposits with gravity flow characteristics and the presence of volcaniclastic deposits, highlighting significant discrepancies in rock types and sedimentary facies compared to previous understandings.

The widespread presence of storm deposits and gravity flow deposits helps explain the occurrence of type III kerogen in the deep-lake fine-grained sediments (Figure 13D). Plant fragments from the deltas, which are the source of type III kerogen, could have been transported by gravity flows triggered by sediment overloading, storm disturbances or earthquakes. Given the common volcanic activity during the Yanshan Orogeny, seismic events could have frequently induced delta failure, transporting plant fragments to deep-water settings. The Beipiao Formation is formed during the Yanshan orogenic event with intensive faulting activity (Sun QS. et al., 2019), which may induce the frequency of earthquakes in the study area. Additionally, hyperpycnal flow could serve as an alternative mechanism, carrying plants and coal fragments into the deep-water basin. The warm and hot climate in the Early Jurassic may also favor the flooding event. From another perspective, the storm wave and gravity flow may also introduce the oxygen into the deep lake basin, reducing the preservation potential of organic matter. However, the relatively high TOC of Beipiao black shale suggests that such sedimentary processes have limited influences on organic matter preservation.

Based on these findings, we propose the following: (1) The Western Liaoning region was a single large lacustrine basin during the depositional period of the Beipiao Formation, rather than consisting of several smaller basins. The uplifts that later divided the Liao Depression were the result of activity along the Nantianmen Fault after the Beipiao Formation was deposited, as supported by several previous studies (Liu and Li, 1997). (2) A widely developed deep lake formed during the deposition of the middle Beipiao Formation, indicating that the development of organic shale has been underestimated, revealing substantial hydrocarbon potential in the study area. (3) Gravity flow, whether caused by delta sediment failure due to sediment overloading, storm disturbances or seismic activity, or by hyperpycnal flow, contributed additional organic material to the black shale of the Beipiao Formation. (4) Clastics from volcanic activity were transported into the deep-water environment by rivers, hyperpycnal flow, or volcanic ash hypopycnal flow, contributing additional sediments. The volcanic processes will be discussed in the following section. Based on these observations and interpretations, we developed a depositional model summarizing the depositional processes from the basin margin to the deep-water basin (Figure 14). The earthquake, flooding induced by heavy raining, storm disturbance and volcanic activity have triggered the sediment failure and density flow that contribute abundant plant fragments (type III kerogen) to the deep-lake basin.

7.2 Volcanic process

As previously mentioned, volcanic lava, volcanic breccia, and massive tuff are extensively developed in the study area, indicating that the region has undergone significant volcanic activity. Based on the identification and classification of lithofacies in cores, combined with field lithofacies distribution and sedimentary facies classification, the volcanic processes in the study area can be categorized into three types: volcanic breccia deposits, volcanic hyperpycnal flow deposits, and volcanic ash buoyant flow deposits. Below is an analysis of these volcanic processes and their genesis.

7.2.1 Volcanic breccia deposits

In well SZK03, clear evidence of volcanic breccia can be seen, distributed within thick mudstone units. The volcanic breccia fragments are sub-angular, poorly sorted, and matrix-supported, with a fine-grained tuff matrix, indicating deep-water clastic flow deposits influenced by volcanic activity and located relatively far from the volcanic crater. Pyroclasitc flow deposits are high-density clastic flows consisting of volcanic debris ejected during eruptions, which flow along low-lying areas near the volcanic crater under a subaqueous medium, mix with local deposits, and cool and compact to form rock. Volcanic breccia results from fallout of coarse clastic fragments after a volcanic eruption, deposited locally with a short transport distance. Coarse volcanic debris flows can easily incorporate the underlying fine-grained tuff during transport, and due to the influence of water flow, underwater volcanic breccia typically has finer grain sizes and better rounding compared to land-based volcanic debris.

7.2.2 Hyperpycnal flow deposits

Broadly speaking, hyperpycnal flows occur when two fluids of similar but slightly different densities mix, resulting in relative movement due to the density difference under suitable environmental conditions. In this study, hyperpycnal flows are primarily composed of volcanic products like fine volcanic dust, which sink into the surface water, creating a density difference between the surface water and the bottom water near the volcanic crater. Under suitable conditions, this leads to the formation of hyperpycnal flow deposits.

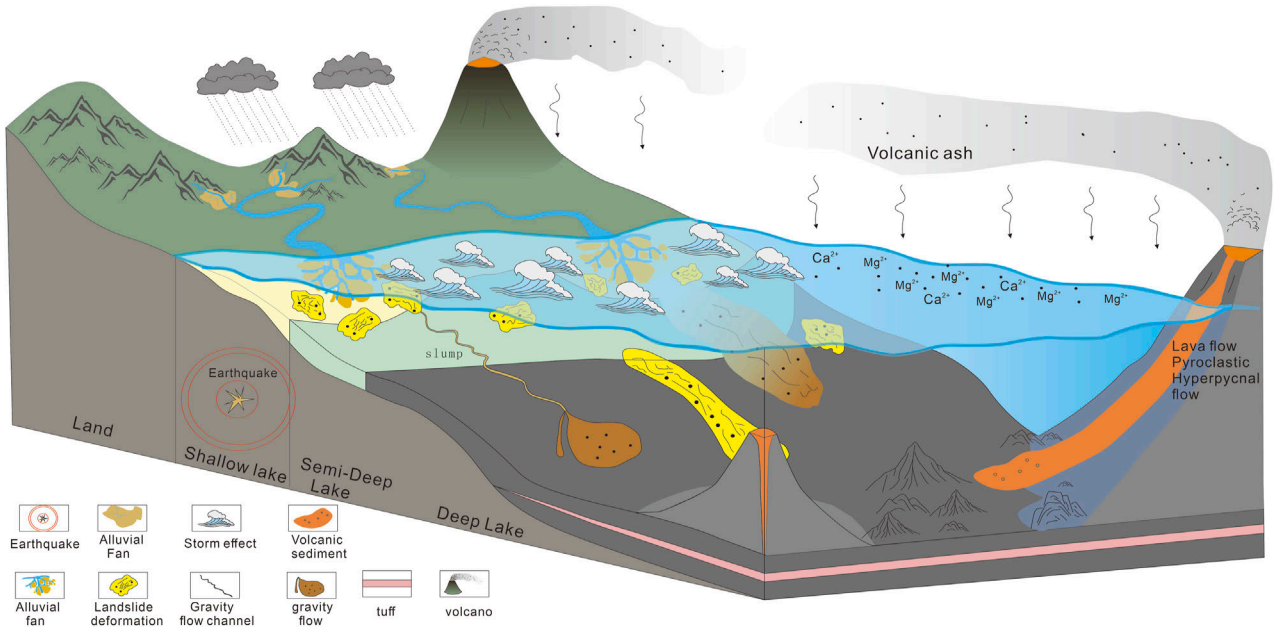

FIGURE 14
Depositional pattern of the Beipiao Formation in the Western Liaoning, Northeast China.

Several types of tuffs are developed in the study area, including massive fine-grained tuff, laminated tuff, massive tuff, and medium to coarse-grained tuff. The medium to coarse-grained tuff was transported along volcanic slopes by hyperpycnal flows and rapidly deposited in the lake basin, forming massive structures with angular volcanic clasts at the base, which are generally poorly sorted and poorly rounded. Medium to coarse-grained volcaniclastic hyperpycnal flows show abrupt contact with the underlying gray-black tuffaceous mudstone. Another portion of medium to coarse volcanic debris was deposited in a semi-consolidated state on volcanic slopes or breaks, and under the influence of volcanic activity, earthquakes, or storms, it lost stability and moved downslope, resulting in slumping deformation. Massive fine-grained tuff traveled longer distances than medium to coarse volcanic debris, reaching further from the volcanic crater, thus having relatively finer grain sizes. The overall color is gray, with a massive structure, lacking other bedding or grading structures. Its genesis may be related to volcanic eruptions involving highly viscous fine volcanic ash that moved along volcanic slopes through hyperpycnal flows and was rapidly deposited.

7.2.3 Volcanic ash hypopycnal flow deposits

In a broad sense, hypopycnal flows refer to the movement of two fluids of similar but slightly different densities, with the less dense fluid on top known as a hypopycnal flow. In this study, volcanic ash hypopycnal flow deposits are formed when hot magma comes into contact with cooler lake water, generating large amounts of steam and releasing significant energy, resulting in intense fragmentation. The fine-grained components formed during this fragmentation float upwards due to buoyancy. During this process, the fluid is gradually diluted by the lake water, and its density decreases until it matches that of the surrounding water, at which point the volcanic ash separates from the fluid and slowly settles in suspension. As the energy of the volcanic ash hyperpycnal flow diminishes, hypopycnal flows continue transporting the volcanic ash at the water surface over long distances into the deep lake area, resulting in finer material. In the study area, fine volcanic ash often co-deposits with terrigenous muddy material and carbonate, forming laminated tuffaceous mudstone and tuffaceous carbonate.

The input of terrigenous material into the lake, combined with the effects of hypopycnal volcanic ash flows and the slow suspension deposition of volcanic fine particles, resulted in the development of laminated tuffaceous mudstone and laminated tuffaceous carbonate in the study area. Microscopic examination of laminated tuffaceous mudstone reveals alternating dark muddy laminae and bright tuffaceous laminae. Areas with a higher proportion of dark laminae indicate a volcanic quiescence period, with a lower supply of volcanic glass shards, dominated by terrigenous muddy material. Areas with a higher proportion of bright laminae indicate active volcanic periods with abundant volcanic glass shards. The alternating pattern of bright and dark laminae is the result of alternating deposition of hypopycnal volcanic ash and terrigenous mud in a suspended state in the lake environment, possibly linked to the pulse-like nature of volcanic eruptions.

7.2.4 Volcanic process and organic enrichment in shales

Many previous studies found that the toxic effects of volcanic ash eruptions can lead to massive biological extinction. Additionally, volcanic materials coming into contact with lake water during eruptions can cause acidification of the water, resulting in large-scale mortality of organisms due to the unfavorable conditions.

This leads to rapid burial and deposition of abundant hydrocarbon precursors, forming thick sequences of high-quality source rocks, which provide the necessary conditions for hydrocarbon generation in the study area (Wang et al., 2013; Kamo et al., 2003; Schoene et al., 2015).

On the other hand, nutrients transported by volcanic ash may promote biological prosperity (Zhou et al., 1989; Duggen et al., 2007; Langmann et al., 2010; Olgun et al., 2013; Wang et al., 2013; Wu et al., 2018; Qu et al., 2019b; Guo et al., 2021). When volcanic gas particles (containing acids and water-soluble metal salts) adsorbed on the surface of volcanic ash dissolve in water, they release large amounts of nutrients and trace metals, which can increase the primary productivity of seawater, leading to massive reproduction of algae, bacteria, and other organisms (Frogner et al., 2001). The iron content in volcanic ash promotes chlorophyll synthesis and photosynthesis (Coale et al., 1996; Geider, 1999) and enhances nutrient bioavailability (Coale et al., 1996; Takeda, 1998), which facilitates phytoplankton blooms (Yao et al., 2010). Furthermore, the hot climate resulting from volcanic eruptions can create a reducing environment in stagnant, isolated bodies of water. Tuffaceous material supplies ions such as Ca^{2+} and Mg^{2+}, increasing the salinity of lake water and creating stratification, which maintains a stable reducing environment at the calm lake bottom, thereby favoring the preservation of organic matter (Qu et al., 2019a).

In this study, we found that the organic rich shale is commonly associated with the massive or fine-grained tuff, tuffaceous siltstone and mudstone (lithofacies 4, five and 6; Table 1 and Figure 4). The black shale shows a relatively high TOC which might be related to the nutrients provided by volcanic activity. We observed widely developed gravity flow, which may introduce oxygen to deepwater and is not favorable to preserve organic matters. However, the volcanic eruptions provide large amounts of clasts into the lake and induce the stratification of the lake, which could help create a reducing environment and favor the preservation of the organic matter. Therefore, we think that the volcanic activity had increased the productivity of the organic matter in the shallow water and help create a reducing environment to preserve the organic matter, which final lead to the high TOC of the black shale in the Jurassic Beipiao Formation.

As a less-explored basin, many aspects of volcanic activity, depositional processes, and the development of organic-rich black shales remain poorly understood. Future research and additional data will be crucial for advancing our knowledge in this area. For instance, petrographic analyses, element analyses mf shales or isotopic studies on kerogen types could help determine the origin of organic matter and clarify the hydrodynamic processes that transport it, particularly in the basin center, where organic matter is most concentrated.

Although more data gained will increase our understanding the organic matter enrichment and fine-grained black shale depositional mechanisms, our current findings are consistent with several studies conducted in the Yanshan orogenic belt region. For example, Zhang et al. (2021) investigated the Cretaceous Jiufotang Formation in the Luanping Basin, located within the Yanshan orogenic belt, and suggested that volcanic activity and a warm climate were the primary factors driving the deposition of thick organic-rich black shales (with an average organic content of 1.39% and Ro values ranging from 0.84% to 1.21%), which exhibit significant hydrocarbon potential in volcanic-rift basins. Similarly, studies in the Cretaceous Jiufotang Formation of the Chaoyang Basin in western Liaoning, adjacent to our study area, indicate that volcanic activity, gravity flow, hydrothermal intrusion, and microbial activity have all played crucial roles in the production and preservation of organic matter (Li et al., 2020; Zhang et al., 2024). Comparable phenomena have also been observed in the Jiufotang Formation of the Fuxin Basin, where sediment supply, hydrothermal intrusion, and gravity flow have shaped both the basin structure and the black shale deposits (Jia et al., 2021). These studies highlight that volcanic activity and gravity flow are common geological processes in volcanic-rift basins of the Northeastern Yanshan orogenic belt, promoting the development of deep-lake, organic-rich black shale deposits and indicating significant, yet often overlooked, hydrocarbon potential.

8 Conclusions

This study presents a detailed analysis of the Beipiao Formation in the Beipiao-Jinyang Basin of the western Liaoning province, northeast China, focusing on the lithofacies, sedimentary facies, and the influence of volcanic and depositional processes on hydrocarbon potential. The lithofacies types were identified and classified into 13 categories, including volcanic breccia, tuff, and sedimentary structures indicative of gravity and density flow processes. These lithofacies highlight the significant role that both volcanic and gravity-driven depositional processes played in shaping the basin's stratigraphy.

The basin's evolution transitioned from fan delta to lacustrine environments, with volcanic activity playing a key role in organic matter enrichment. Middle to deep lacustrine deposits, associated with volcanic events, created favorable conditions for preserving organic-rich shales, highlighting the potential for hydrocarbon accumulation.

Geochemical analyses indicate that the organic matter is primarily Type II kerogen, derived from higher plants and aquatic organisms, with moderate to good hydrocarbon potential. The organic matter is at its oil-generation peak in areas with slightly shallower water depths and thinner strata (e.g., well Guan 1). In areas of the basin center (e.g., wells SZK01-04), the organic matter reaches high to over-mature stages, which are more suitable for gas generation.

The interplay between volcanic activity and lacustrine processes led to high-quality source rocks, suggesting significant hydrocarbon potential in the Beipiao Formation, particularly in the deeper lacustrine and volcaniclastic facies. The analysis presented in this work regarding the influence of volcanic activity and gravity flow on organic enrichment, transportation, and preservation can also serve as a valuable reference for investigating other volcanic-lacustrine basins that have developed under comparable geological conditions.

Future exploration should focus on these areas, e.g., areas adjacent to wells SZK01-04 located where deep lake and organic rich shale are developed, to unlock the basin's hydrocarbon resources. Furthermore, this study demonstrates the significant

hydrocarbon potential within this underexplored area, suggesting that similar potential resources may be found in other Jurassic basins formed under comparable tectonic settings in northeast China.

Data availability statement

The raw data supporting the conclusions of this article will be made available by the authors, without undue reservation.

Ethics statement

Written informed consent was obtained from the individual(s) for the publication of any potentially identifiable images or data included in this article.

Author contributions

JW: Writing–original draft, Writing–review and editing. JX: Writing–original draft, Writing–review and editing. ZJ: Conceptualization, Methodology, Resources, Writing–review and editing. TL: Conceptualization, Investigation, Writing–original draft, Writing–review and editing. JM: Conceptualization, Data curation, Writing–review and editing. JZ: Conceptualization, Data curation, Writing–review and editing. SW: Investigation, Writing–review and editing. ZS: Investigation, Methodology, Writing–review and editing. YL: Conceptualization, Investigation, Methodology, Resources, Writing–review and editing. XZ: Investigation, Writing–review and editing.

Funding

The author(s) declare that financial support was received for the research, authorship, and/or publication of this article. This work is supported by China National Natural Science Foundation of China (No. 41902108). This work is also supported by Hainan Institute of China University of Geosciences, Beijing (No. HNPY-202401) and the Chinese "111" project (B20011).

Conflict of interest

Author XZ was employed by SINOPEC Northeast Oil & Gas Branch, Exploration and Development Research Institute.

The remaining authors declare that the research was conducted in the absence of any commercial or financial relationships that could be construed as a potential conflict of interest.

Generative AI statement

The author(s) declare that no Generative AI was used in the creation of this manuscript.

Publisher's note

References

Aarnes, I., Planke, S., Trulsvik, M., and Svensen, H. (2015). Contact metamorphism and thermogenic gas generation in the Vøring and Møre basins, offshore Norway, during the Paleocene-Eocene thermal maximum. *J. Geol. Soc.* 172 (5), 588–598. doi:10.1144/jgs2014-098

Aarnes, I., Svensen, H., Connolly, J. A. D., and Podladchikov, Y. Y. (2010). How contact metamorphism can trigger global climate changes: modeling gas generation around igneous sills in sedimentary basins. *Geochimica Cosmochimica Acta* 74 (24), 7179–7195. doi:10.1016/j.gca.2010.09.011

Abrajevitch, A., Andrew, P. R., and Kazuto, K. (2014). Volcanic iron fertilization of primary productivity at kerguelen plateau, southern ocean, through the middle miocene climate transition. *Palaeogeogr. Palaeoclimatol. Palaeoecol.* 410, 1–13. doi:10.1016/j.palaeo.2014.05.028

Chen, S. W., Ding, Q. H., Zheng, Y. J., Li, Y. F., Zhang, J., Wang, J., et al. (2013). New areas and series of strata on the periphery of Songliao Basin: the progress and recognition based on foundational geological survey for oil and gas resources. *Geol. Bull. China* 32 (8), 1147–1158. doi:10.3969/j.issn.1671-2552.2013.08.002

Coale, K. H., Steve, E. F., Gordon, R. M., Johnson, K. S., and Barber, R. T. (1996). Control of community growth and export production by upwelled iron in the equatorial Pacific Ocean. *Nature* 379, 621–624. doi:10.1038/379621a0

Dong, S., Zhang, Y., Li, H., Shi, W., Xue, H., Li, J., et al. (2018). The yanshan orogeny and late mesozoic multi-plate convergence in east asia—commemorating 90th years of the "yanshan Orogeny". *Sci. China Earth Sci.* 61, 1888–1909. doi:10.1007/s11430-017-9297-y

Dou, L. X., Hou, J. G., Song, S. H., Zhang, L., Liu, Y., Sun, S., et al. (2020). Sedimentary characteristics of hyperpycnites in a shallow lacustrine environment: a case study from the lower cretaceous Xiguayuan Formation, Luanping Basin, northeast China. *Geol. J.* 55 (5), 3344–3360. doi:10.1002/gj.3599

Du, X. B., Jia, J. X., Zhao, K., Lu, Y. C., Tan, C., Lu, Y. B., et al. (2022). Development characteristics of deep-time volcanic ash layers and its influence on deposition of organic-rich shale across Ordovician—silurian transition in Yangtze area, south China. *Zhongnan Daxue Xuebao (Ziran Kexue Ban)/Journal Central South Univ. Sci. Technol.* 53 (9), 3509–3521. doi:10.11817/j.issn.1672-7207.2022.09.017

Duggen, S., Croot, P., Schacht, U., and Hoffmann, L. (2007). Subduction zone volcanic ash can fertilize the surface ocean and stimulate phytoplankton growth: evidence from biogeochemical experiments and satellite data. *Geophys. Res. Lett.* 34 (1). doi:10.1029/2006gl027522

Fan, T. G., Xu, X. F., Fan, L., Feng, Y. Q., Liu, W. H., Liu, J. T., et al. (2021). Geological characteristics and exploration prospect of shale oil in permian Lucaogou Formation, Santanghu Basin. *China Pet. Explor.* 26 (4), 125–136. doi:10.3969/j.issn.1672-7703.2021.04.010

Fan, X. J. (2004). *The analysis and evaluation of petroleum geological condition in jinlingsi-yangshan basin*. Liaoning: Liaoning University of Technology.

Felipe, R., Hector, J. V., and Roger, B. (2007). "Hydrocarbon generation, migration, and accumulation related to igneous intrusions: an atypical petroleum system from the Neuquen Basin of Argentina," in *SPE 10th Latin American and caribbean petroleum engineering conference, X LACPEC 07*.

Feng, Z. Z. (2022). Some new thoughts on definitions of terms of sedimentary facies: based on Miall's paper (1985). *J. Palaeogeogr. Chin. Ed.* 24 (2), 183–190. doi:10.7605/gdlxb.2022.02.027

Frogner, P., Gislason, S. R., and Niels, O. (2001). Fertilizing potential of volcanic ash in ocean surface water. *Geology* 29 (6), 487–490. doi:10.1130/0091-7613(2001)029<0487:fpovai>2.0.co;2

Geider, R. J. (1999). Biological oceanography: complex lessons of iron uptake. *Nature* 400 (6747), 815–816. doi:10.1038/23582

Guo, Y., Nishizawa, T., Sakagami, N., Fujimura, R., Kamijo, T., and Ohta, H. (2021). Root bacteriome of a pioneer grass Miscanthus condensatus along restored vegetation on recent Miyake-jima volcanic deposits. *Rhizosphere* 19, 100422. doi:10.1016/j.rhisph.2021.100422

He, B., Fu, Q. P., and Zhang, Y. M. (2006). *Beipiao group hydrocarbon material distribution and organic matter abundance of Jinlingsi—yangshan basin in western part of Liaoning*. Liaoning: Journal of Liaoning Technical University, 24–27.

Jia, J., Wu, Y., Miao, C., Fu, C., Xie, W., Qin, J., et al. (2021). Tectonic controls on the sedimentation and thermal history of supra-detachment basins: a case study of the early cretaceous Fuxin basin, NE China. *Tectonics* 40, e2020TC006535. doi:10.1029/2020TC006535

Jia, L. Q., Wang, L., Wang, G. H., Lei, S., and Wu, X. (2019a). Petrogenesis of the Late Triassic shoshonitic Shadegai pluton from the northern North China Craton: implications for crust-mantle interaction and post-collisional extension. *Geosci. Front.* 10 (2), 595–610. doi:10.1016/j.gsf.2018.08.002

Jia, L. Q., Wang, L., Wang, G. H., Lei, S., and Wu, X. (2019b). Petrogenesis of the Late Triassic shoshonitic Shadegai pluton from the northern North China Craton: implications for crust-mantle interaction and post-collisional extension. *Geosci. Front.* 10 (2), 595–610. doi:10.1016/j.gsf.2018.08.002

Jiang, Z. X., and Chen, D. Z. (2021). *Sedimentology*. Beijing: China Petroleum Publishing House.

Jiang, Z. X., Wang, Y. Z., Wang, L., Kong, X. S., Yang, Y. Q., Zhang, J. G., et al. (2022a). Review on provenance, transport-sedimentation dynamics and multi-source hydrocarbon sweet spots of continental fine-grained sedimentary rocks. *Oil and Gas Geol.* 43 (5), 1039–1048. doi:10.11743/ogg20220503

Jiang, Z. X., Zhang, Y. F., and Yuan, X. D. (2022b). Formation conditions and exploration discoveries of Mesozoic oil and gas in Luanping Basin, Yanshan tectonic belt. *Acta Pet. Sin.* 43 (2), 167–179. doi:10.7623/syxb202202001

Jiao, X., Liu, Y. Q., Zhou, D. W., Li, H., Meng, Z. Y., Zhao, M. R., et al. (2021). Progress on coupling relationship between volcanic and hydrothermal-originated sediments and hydrocarbon generation in lacustrine source rocks. *J. Palaeogeogr. Chin. Ed.* 23 (4), 789–809. doi:10.7605/gdlxb.2021.04.040

Kamo, S. L., Czamanske, G. K., Amelin, Y., Fedorenko, V. A., Davis, D., and Trofimov, V. (2003). Rapid eruption of Siberian flood volcanic rocks and evidence for coincidence with the Permian-Triassic boundary and mass extinction at 251 Ma. *Earth Planet. Sci. Lett.* 214 (1-2), 75–91. doi:10.1016/s0012-821x(03)00347-9

Langmann, B., Zakšek, K., Hort, M., and Duggen, S. (2010). Volcanic ash as fertiliser for the surface ocean. *Atmos. Chem. and Phys.* 10 (8), 3891–3899. doi:10.5194/acp-10-3891-2010

Lee, C. A., Jiang, H. H., Ronay, E., Minisini, D., Stiles, J., and Neal, M. (2018). Volcanic ash as a driver of enhanced organic carbon burial in the Cretaceous. *Sci. Rep.* 8 (1), 4197. doi:10.1038/s41598-018-22576-3

Li, L., Liu, Z. J., Sun, P. C., Li, Y., and George, S. C. (2020). Sedimentary basin evolution, gravity flows, volcanism, and their impacts on the formation of the Lower Cretaceous oil shales in the Chaoyang Basin, northeastern China. *Mar. Petroleum Geol.* 119, 104472. doi:10.1016/j.marpetgeo.2020.104472

Li, Y. F., and Chen, S. W. (2014). New discoveries in oil and gas resources survey at Jiling Temple - yangshan Basin in Liaoxi region. *Geol. Bull. China* 33 (9), 1463–1464. doi:10.3969/j.issn.1671-2552.2014.09.023

Lin, C. F. (2019). *Jurassic tectono-sedimentary evolution history of the western Yanshan fold-thrust belt, North China, and its tectonic implication*. Beijing: China University of Geosciences.

Liu, H. (2019). *Analysis and evaluation of mesozoic intermountain basins groups in western liaoning and its peripheral areas*. Beijing: China University of Geosciences.

Liu, J. J., and Li, Y. H. (1997). Nantianmen Fault in the west liaoning province and its relationship with the development of Beipiao Formation. *Liaoning Geol.* (2), 91–98.

Liu, X. N., Jiang, Z. X., Yuan, X. D., Chen, C., and Wang, C. (2022). Influence of the Cretaceous fine-grained volcanic materials on shale oil/gas, Luanping Basin. *Oil and Gas Geol.* 43 (2), 390–406. doi:10.11743/ogg20220212

Lu, X. Z., Shen, J., Guo, W., and Feng, Q. (2021). Influence of mercury geochemistry and volcanism on the enrichment of organic matter near the Ordovician-Silurian transition in the Middle and Upper Yangtze. *Editor. Comm. Earth Science-Journal China Univ. Geosciences* 46 (7), 2329–2340. doi:10.3799/dqkx.2020.258

Lu, Y. B., Hao, F., Lu, Y. C., Yan, D. T., Xu, S., Shu, Z. G., et al. (2020). Lithofacies and depositional mechanisms of the Wufeng-Longmaxi organic-rich shales in the upper Yangtze area, south China. *AAPG Bull.* 104 (1), 97–129. doi:10.1306/04301918099

Lu, Y. B., Hao, F., Shen, J., Lu, Y. C., Song, H. Y., Wang, Y. C., et al. (2022). High-resolution volcanism-induced oceanic environmental change and its impact on organic matter accumulation in the Late Ordovician Upper Yangtze Sea. *Mar. Petroleum Geol.* 136, 105482. doi:10.1016/j.marpetgeo.2021.105482

Olgun, N., Duggen, S., Andronico, D., Kutterolf, S., Croot, P. L., Giammanco, S., et al. (2013). Possible impacts of volcanic ash emissions of Mount Etna on the primary productivity in the oligotrophic Mediterranean Sea: results from nutrient-release experiments in seawater. *Mar. Chem.* 152, 32–42. doi:10.1016/j.marchem.2013.04.004

Pan, S. X., Liu, H. Q., Zavala, C., Liu, C., Liang, S., Zhang, Q., et al. (2017). Sublacustrine hyperpycnal channel-fan system in a large depression basin: a case study of Nen 1 Member, Cretaceous Nenjiang Formation in the Songliao Basin, NE China. *Petroleum Explor. Dev.* 44 (6), 911–922. doi:10.1016/s1876-3804(17)30103-9

Qiu, Z., Zou, C. N., Li, X. Z., Wang, H. Y., Dong, D. Z., Lu, B., et al. (2018). Discussion on the contribution of graptolite to organic enrichment and reservoir of gas shale: a case study of the Wufeng-Longmaxi Formations in South China. *Nat. Gas. Geosci.* 29 (5), 606–615. doi:10.11764/j.issin.1672-1926.2018.04.005

Qu, C. S., Qiu, L. W., Cao, Y. C., Yang, Y. Q., and Yu, K. H. (2019b). Sedimentary environment and the controlling factors of organic-rich rocks in the Lucaogou Formation of the jimusar sag, Junggar Basin, NW China. *Petroleum Sci.* 16 (4), 763–775. doi:10.1007/s12182-019-0353-3

Qu, C. S., Qiu, L. W., Yang, Y. Q., Yu, K. H., Tang, L., and Wan, M. (2019a). Environmental response of the permian volcanism in Lucaogou Formation in jimsar sag, Junggar Basin, northwest China. *Seismol. Geol.* 41 (3), 789–802. doi:10.3969/j.issn.0253-4967.2019.03.016

Ren, Y. (2012). *The study of yingcheng formation volcanism influence on hydrocarbon source rock in songtiao basin*. Jilin: Jilin University.

Schoene, B., Samperton, K. M., Eddy, M. P., Keller, G., Adatte, T., Bowring, S. A., et al. (2015). U-Pb geochronology of the Deccan Traps and relation to the end-Cretaceous mass extinction. *Science* 347 (6218), 182–184. doi:10.1126/science.aaa0118

Sun, Q. S., Xiao, F., Gao, X. Y., Zong, W., Li, Y., Zhang, J., et al. (2019b). A new discovery of Mesoproterozoic erathem oil and oil-source correlation in the Niuyingzi area of western Liaoning Province, NE China. *Mar. Petroleum Geol.* 110, 606–620. doi:10.1016/j.marpetgeo.2019.07.048

Sun, S. L., Zhang, T., Liu, M., Li, Y. F., Chen, S. W., Zhang, J., et al. (2019a). Sedimentary environment and genesis of source rocks of Beipiao Formation in Jinyang Basin, western liaoning. *J. Northeast Petroleum Univ.* 43 (6), 1–12. doi:10.3969/j.issn.2095-4107.2019.06.001

Sun, S. P., Liu, Y. S., Zhong, R., Bai, Z. D., Li, J. Z., Wei, H. Q., et al. (2001). Classification of pyroclastic rocks and trend of volcanic sedimentology: a review. *Acta Petrologica Mineralogica* 20 (3), 313~317. doi:10.3969/j.issn.1000-6524.2001.03.014

Takeda, S. (1998). Influence of iron availability on nutrient consumption ratio of diatoms in oceanic waters. *Nature* 393 (6687), 774–777. doi:10.1038/31674

Trabucho-Alexandre, J., Hay, P. L. B., and de Boer, P. L. (2012). Phanerozoic environments of black shale deposition and the Wilson Cycle. *Solid earth* 3 (1), 29–42. doi:10.5194/se-3-29-2012

Wang, G. H., Zhang, C. H., Wang, G. S., and Wu, Z. W. (2001). Tectonic framework of western liaoning province and its evolution during mesozoic. *J. Graduate Sch.* (1), 1–7. doi:10.3969/j.issn.1000-8527.2001.01.001

Wang, H. Z. (1993). *A course in Earth history*. Beijing: Geological Publishing House, 295–298.

Wang, J. (2011). *Tectonic evolution of mesozoic volcanic basins in western liaoning and northern hebei*. Beijing: China University of Petroleum.

Wang, S. R., Song, D. F., and He, D. F. (2013). The enrichment effect of organic materials by volcanic ash in sediments of the Santanghu Basin and the evolutionary pattern of tuffaceous source rocks. *Acta Pet. Sin.* (6), 1077–1087. doi:10.7623/syxb201306006

Wu, G., Li, Z. T., and Wang, W. W. (2004). Geochemical characteristics of the Middle Jurassic volcanic rocks from Haifanggou Formation in western Liaoning area and geological significance. *Acta Petrologica Mineralogica* 23 (2), 97–108. doi:10.3969/j.issn.1000-6524.2004.02.001

Wu, L. Y., Lu, Y. C., Jiang, S., Liu, X., and He, G. (2018). Effects of volcanic activities in ordovician wufeng–silurian longmaxi period on organic-rich shale in the upper Yangtze area, south China. *Petroleum Explor. Dev.* 45 (5), 862–872. doi:10.1016/s1876-3804(18)30089-2

Yan, Y., Lin, G., and Li, Z. A. (2002). Characteristics of the jurassic filling sequence and the indication of tectonic evolution of Beipiao Basin, western liaoning. *J. Stratigr.* (2), 151–155. doi:10.3969/j.issn.0253-4959.2002.02.014

Yan, Y., Lin, G., Li, Z. A., He, S. J., and Xv, Z. Y. (2003). Detrital composition of mesozoic sandstone and its implication for provenance and tectonic evolution of Beipiao (Jin-Yang) basin, western liaoning province. *Acta Sedimentol. Sin.* (3), 441–447. doi:10.14027/j.cnki.cjxb.2003.012

Yao, B., Xi, B. D., Hu, C. M., Ding, J. T., Zhang, J. T., Xv, Q. G., et al. (2010). A review of iron limitation on the growth and competition of phytoplankton. *Ecol. Environ. Sci.* (2), 459–465. doi:10.3969/j.issn.1674-5906.2010.02.039

Yuan, W., Liu, G. D., Xu, L. M., and Niu, X. B. (2019). Main controlling factors for organic matter enrichment in Chang 7 member of the Yanchang Formation, Ordos Basin. *Oil Gas Geol.* 40 (2), 326–334. doi:10.11743/ogg20190211

Yuan, X. D., Jiang, Z. X., Zhang, Y. F., and Jiang, H. F. (2020). Characteristics of the Cretaceous continental shale oil reservoirs in Luanping Basin. *Acta Pet. Sin.* 41, 1197–1208. doi:10.7623/syxb202010004

Zavala, C., and Pan, S. X. (2018). Hyperpycnal flows and hyperpycnites: origin and distinctive characteristics. *Lithol. Reserv.* 30 (1), 1–18. doi:10.3969/j.issn.1673-8926.2018.01.001

Zhang, J. Z., Jiang, Z. X., Xu, J., Wei, S. Y., Song, L. Z., Liu, T., et al. (2024) *Volcanic sedimentation of cretaceous Jiufotang Formation in the Chaoyang Basin and its impact on organic matter enrichment*, 3, 284–297.

Zhang, K., Li, Y. F., Tang, Y. J., Gao, X. Y., Sun, S., Zhou, T. S., et al. (2015). Characteristics of biomarker compounds in oil sands of the Beipiao Formation, liaoxi Jinyang Basin — a case study of well SZK02. *Geol. Rev.* 61 (S1), 198–199.

Zhang, L. S., Xie, M. Z., Zhang, S. S., Zhang, X. S., Shang, H. T., Li, X. H., et al. (2016). Rediscussion on geologic age and regional correlation about Beipiao Formation in western liaoning. *Geol. Rev.* 62 (6), 1392–1402. doi:10.16509/j.georeview.2016.06.003

Zhang, R., Jiang, T., Tian, Y., Xie, S. C., Zhou, L., Li, Q., et al. (2017a). Volcanic ash stimulates growth of marine autotrophic and heterotrophic microorganisms. *Geology* 45 (8), 679–682. doi:10.1130/G38833.1

Zhang, T., Li, Y. F., Sun, S. L., Gao, X. Y., Zhou, T. S., Sun, P., et al. (2017b). Saturated hydrocarbon geochemical characteristics of the oil sand from YD1 well in Jinyang Basin and its significance for oil and gas exploration. *Geol. Bull. China* 36 (4), 582–590. doi:10.3969/j.issn.1671-2552.2017.04.012

Zhang, Y. F., Yuan, X. D., Wang, M., Ge, P., Huo, Y., Xu, J., et al. (2021). Discovery of lacustrine shale deposits in the Yanshan Orogenic Belt, China: implications for hydrocarbon exploration. *Geosci. Front.* 12 (6), 332–359. doi:10.1016/j.gsf.2021.101256

Zhen, Z., Li, Y. F., Gao, X. Y., Sun, S. L., and Zhou, T. S. (2016). Characteristics of sedimentary facies and organic matter of lower jurassic Beipiao Formation of well SZK01 in Jinyang Basin. *Glob. Geol.* (1), 207–215. doi:10.3969/j.issn.1004-5589.2016.01.021

Zhou, L. D., and Zhao, M. P. (1999). Study on evolution history of the fault zone on the west edge of Jinlingsi-Yangshan Basin in West Liaoning. *Liaoning Geol.* (4), 11–16.

Zhou, Z. Y., Sheng, G. Y., and Min, Y. S. (1989). A primary study of tuffaceous source rock by organic geochemistry. *Acta Sedimentol. Sin.* 7 (3), 3–9.

Zou, C. N., Guo, Q. L., Yang, Z., Wu, S., Chen, N., Lin, S., et al. (2019). Resource potential and core area prediction of lacustrine tight oil: the Triassic Yanchang Formation in Ordos Basin, China. *AAPG Bull.* 103 (6), 1493–1523. doi:10.1306/11211816511

frontiers | Frontiers in Earth Science

TYPE Original Research
PUBLISHED 19 February 2025
DOI 10.3389/feart.2025.1447949

OPEN ACCESS

EDITED BY
George Kontakiotis,
National and Kapodistrian University of Athens, Greece

REVIEWED BY
Ping Gao,
China University of Geosciences, China
Xiaoxue Liu,
Shandong University of Science and Technology, China

*CORRESPONDENCE
Mingna Ge,
610144368@qq.com

RECEIVED 12 June 2024
ACCEPTED 27 January 2025
PUBLISHED 19 February 2025

CITATION
Ge M, Bao S, Wang Y, Li H, Wang T and Liang H (2025) Difference analysis of shale gas-bearing property —a case study of the shale within lower Cambrian Niutitang Formation on the margin of palaeouplift. *Front. Earth Sci.* 13:1447949. doi: 10.3389/feart.2025.1447949

Difference analysis of shale gas-bearing property —a case study of the shale within lower Cambrian Niutitang Formation on the margin of palaeouplift

Mingna Ge[1,2]*, Shujing Bao[1], Yufang Wang[1], Haohan Li[1], Ting Wang[1] and Hongbo Liang[3]

[1]School of Energy and Resources, China University of Geosciences, Beijing, China, [2]Oil and Gas Survey, China Geological Survey, Beijing, China, [3]PetroChina Research Institute of Petroleum Exploration and Development, Beijing, China

Introduction: Shale gas has become an important field for increasing oil and gas reserves and production in China. The breakthrough of Cambrian shale gas in Sichuan Basin provides guidance for the exploration of shale gas in southern China. However, the Niutitang Formation shale on the periphery of Sichuan Basin exhibits multiple depositional subfacies and complex structural styles, and the factors of gas diversity are not clear.

Methods: By the methods of organic geochemistry experiment, reservoir physical property test and gas content test, combined with the hydrocarbon generation history and structural evolution history data, the gas content difference is analyzed of Hannan palaeouplift, Shennongjia palaeouplift, Huangling palaeouplift and Xuefengshan palaeouplift.

Results: The organic matter type of Niutitang Formation shale is mainly type I, the average organic carbon content is 1.50%–3.56%, the average R_o is 2.37%–3.90%, the brittle minerals are mainly quartz that the content is 28%–53%, and the average porosity is 0.51%–3.34%. The pores contain organic pores, inorganic pores and micro-fractures, and the fractures are mostly filled with calcite. Gas content 0.13m^3/t–4.19m^3/t. Through comparative analysis of main controlling factors affecting gas content of shale, the causes of gas diversity of Niutitang Formation shale are identified.

Discussion: (1) the differences in preservation conditions caused by structural strength, fracture development degree and the coupling relationship with tectonic fractures are the key factors restricting the gas content of shale. (2) Early deep burial time, long deep burial time and fast deep burial are the key factors that cause the difference of thermal evolution degree of shale. (3) The difference of hydrocarbon generation potential caused by sedimentary subfacies in the same facies zone is an important factor restricting the gas generation capacity of shale. (4) The areas with the lower Plate of thrust nappe, the degree of thermal evolution is less than 3.0%, and the deepwater facies of trough are favorable directions for further exploration. This study will provides reference

significance for shale gas exploration of Cambrian Niutitang Formation in the complex structural area periphery of Sichuan Basin in south China.

KEYWORDS

gas diversity, controlling factors, periphery of palaeouplift, shale gas, Niutitang Formation, lower Cambrian

1 Introduction

The shale gas revolution in the United States has made the United States the largest natural gas producer in the world (Hammes and Frbourg, 2012). Commercial production of major shale gas reservoirs from Barnett to Marcellus (Abouelresh and Slatt, 2012; Bruner et al., 2015), successfully reversed the situation of US natural gas imports to exports, while changing the world's energy market land-scape. China's shale gas has experienced nearly 20 years of exploration and has entered the substantial commercial development stage. The increase in production is mainly concentrated in the Wufeng-Longmaxi Formation, Sichuan Basin (He et al., 2016). In the background of carbon peak and carbon neutrality, it is urgent to increase the exploration and development of shale gas in new areas, new formations, new types and new fields (He et al., 2021a). Previous studies have shown that the periphery of palaeouplift has low thermal evolution and relatively stable structural characteristics, which is an important target area for the investigation of Cambrian shale gas in southern China (Bao et al., 2018). The predecessors established a new shale gas enrichment model in the slope belt of palaeouplift margin, which is "favorable facies zone is the foundation, organic matter content is the guarantee, basement uplift and evolution is the key," and guided the breakthrough of shale gas exploration. The Well EYY1HF in Huangling Uplift (Li et al., 2019; Zhang et al., 2020) and Well SNY1 in Hannan Uplift, achieving breakthrough in low-pressure shale gas reservoir. However, Well GDD1, HY1 and HD 1 in Xuefeng Uplift, Well EHD1 in Shenlongjia Palaeouplift and Well SNY1 in Hannan Palaeouplift only found oil and gas shows without shale industrial gas flow (Xie et al., 2014), demonstrating the gas diversity of Niutitang formation on the periphery of palaeouplift in the outer area of Sichuan Basin. Significant variations in hydrocarbon generation conditions, thermal evolution levels, and structural preservation conditions exist across different structural locations. These differences have resulted in considerable variability in gas content. The main controlling factors for the differential enrichment of shale gas in the Niutitang Formation on the periphery of the paleo-uplift remain unclear.

In this study, taking four typical wells around the palaeouplift as analysis objects, based on the analysis of shale gas geological conditions, the research focuses on discussing the influencing factors and main controlling factors that affect the gas content of shale gas, in order to find favorable areas for Niutitang shale gas exploration in the outer area of Sichuan Basin and serve new oil and gas prospecting breakthrough.

2 Geological setting and sampling sections

The Cambrian shales in south China generally have a high degree of thermal evolution, and the study area is located in the eastern and northern margins of Sichuan Basin, from north to south are respectively Hannan Palaeouplift, Shenlongjia Palaeouplift, Huangling Palaeouplift and Xuefengshan Palaeouplift. The paleouplift experienced tectonic uplift in the Paleozoic, and its rigid basement structure was stable, which was conducive to shale gas preservation. For the southern Cambrian, the paleouplift has early uplifting time and short deep burial time, and the thermal evolution of the Cambrian shale is lower than that of other regions.

Seven wells on the periphery of four ancient uplifts were selected as the research objects, including Well 1 and Well 2 on the southern margin of Hannan Ancient Uplift, Well 3 on the western margin of Shenlongjia Ancient Uplift, Well 4 on the southwest margin of Huangling Ancient Uplift and Well 5 on the southeast margin of Huangling Ancient Uplift, Well 6 and Well 7 on the southwest margin of Xuefengshan Ancient Uplift (Figure 1).

3 Samples and analytical methods

3.1 Samples

In this study, data were collected from 7 wells in the paleouplift, including 35 samples from Well 1, 25 samples from Well 2, 18 samples from Well 3, 120 samples from Well 4, 50 samples from Well 5, 49 samples from Well 6, and 12 samples from Well 7. Detail information of studied wells are listed in Table 1.

3.2 Experimental methods

In this study, seven wells were selected to carry out organic geochemical experiments, such as TOC, Asphalt reflectance, organic matter types, etc. Reservoir physical properties, such as rock and mineral composition, porosity, permeability, pore type, fracture development, etc. Gas content testing experiments, such as field Desorption gas content measurement, gas component analysis, isothermal adsorption, etc. In addition, the well logging data, hydrocarbon generation history and structural evolution history in the study area were studied.

The experiments of organic geochemistry and reservoir physical properties were determined by the Geochemical

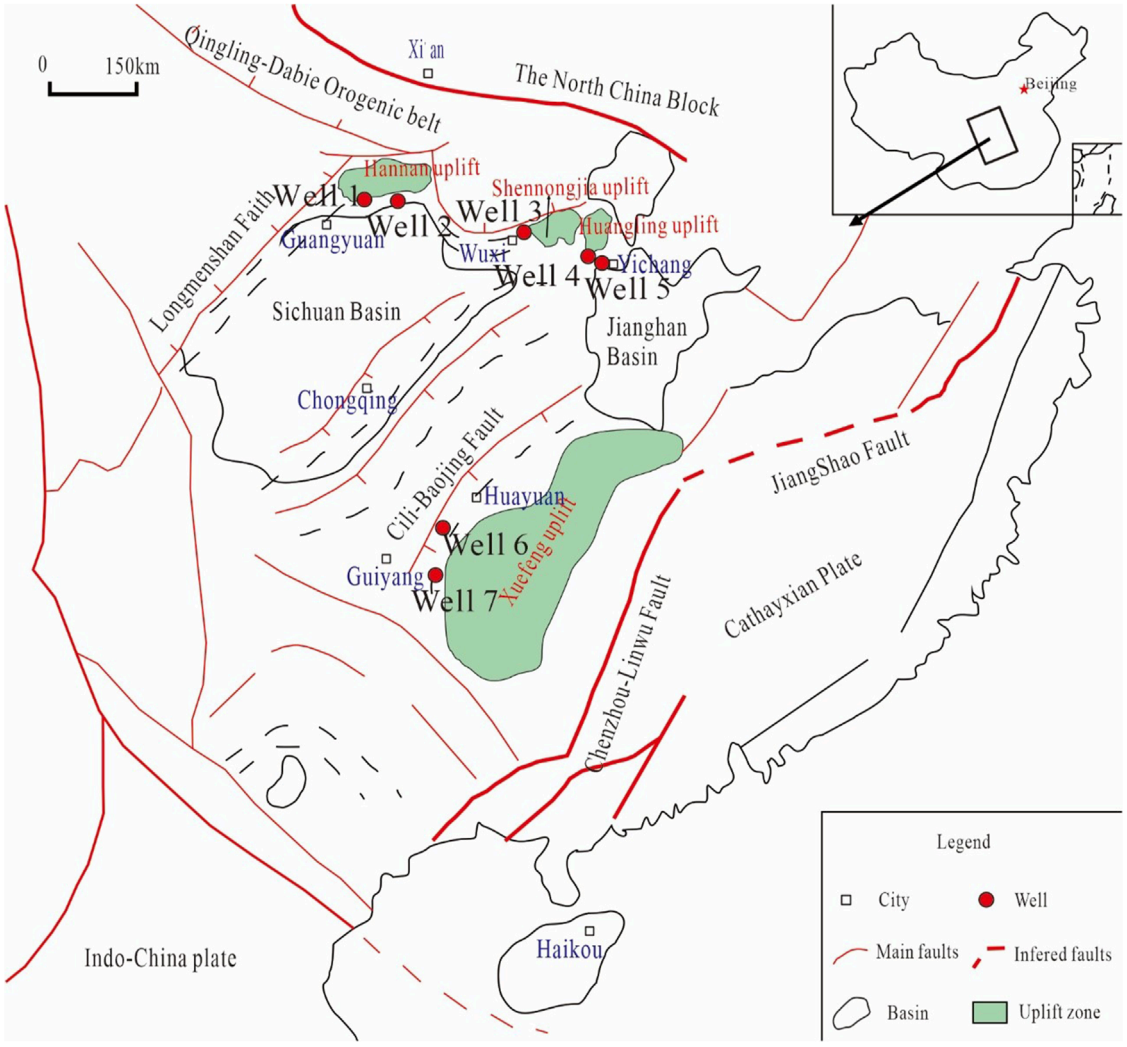

FIGURE 1
Study area and drilling structure location. Well 1 and 2 belong to the periphery of Hannan Palaeohigh, Well 3 belong to the periphery of Shennongjia Palaeohigh, Well 4 and 5 belong to the periphery of Huangling Palaeohigh, and Well 6 and 7 belong to the periphery of Xuefeng Palaeohigh.

Laboratory of Yangtze University. The porosity and permeability were tested by two methods: overburden porous test and mercury injection test. It should be noted that the sample comes from the ancient formation of Niutitang Formation, the sample does not contain vitrinite, and the Ro cannot be measured by conventional vitrinite reflectance. The asphalt reflectance of these samples is measured and converted to R_o. The gas content and gas composition were determined by YSQ-IV analytical analyzer, which was independently developed. During the measuring process, continuous drainage gas collection method was applied to collect gas samples and analyze gas composition. The desorption gas and residual gas were directly measured by this method, and the total gas content was finally calculated by combining with the simulation of lost gas.

4 Results

4.1 Organic geochemical characteristics

The research area consists of seven wells that are deposited in the continental shelf to slope facies. The dominant organic matter type is Type I, with high organic carbon content. These wells are located on the periphery of an ancient uplift. According to the theory "Reservoir control at the margin of paleo-uplift" (Zhai et al., 2017), Compared with southeast Chongqing area and West Hunan and Hubei area, the degree of thermal evolution in the study area is relatively low, which is the main consideration for drilling.

The kerogen type of shale in Well 1 is type I, and the organic carbon content is 0.52%–3.02%, with an average of 1.50%. TOC of

10.3389/feart.2025.1447949

TABLE 1 Information of 7 wells.

Well number	Geographical position	Tectonic position	Well type	Formation	Depth m	Start drilling formation	Completed formation	Hydrocarbon indication
1	Nanzheng, Shaanxi	Between Hannan Uplift and Micang Mountain uplift	Parameter well	Niutitang Formation	2,150-2,380	Permian	Nanhuan (Nantuo Formation)	Gas showing
2	Zhenba, Shaanxi	Southeastern margin of Micang Mountain uplift	Survey well	Niutitang Formation	1,670-1750	Silurian	Sinian (Dengying Formation)	gas show strong
3	Shennongjia, Hubei	Northern wing of Shennongjia complex anticline	Survey well	Niutitang Formation	1,454-1852	Silurian	Sinian (Dengying Formation)	No gas show
4	Changyang, Hubei	South margin of Huangling uplift	Parameter well	Niutitang Formation	2,600-3,069	Cambrian	Nanhuan (Nantuo Formation)	Industrial gas flow
5	Dianjun, Hubei Province	South margin of Huangling uplift	Parameter well	Niutitang Formation	1787-1871	Cretaceous	Nanhuan (Nantuo Formation)	Industrial gas flow
6	Huangping, Guizhou	Southwest margin of Xuefeng uplift	Survey well	Niutitang Formation	1,286-1,406	Cambrian	Nanhuan (Nantuo Formation)	Gas showing
7	Danzhai, Guizhou	Southwest margin of Xuefeng uplift	Survey well	Niutitang Formation	960-1,070	Cambrian	Sinian (Doushantuo Formation)	Gas showing

shale with high gas content in middle and lower section can reach more than 2.0%. The value of R_o range from 2.48% to 4.36%, with an average of 3.0%, which is in the stage of over-mature evolution. The main organic matter types of shale in Well 2 are type I and type II_1 (Xu et al., 2019). TOC content of 31 core samples from Well 2 ranges from 0.88% to 8.61%, with an average value of 3.37%. The shale with TOC >2% has a thickness of 78m, and the maturity of 34 samples ranges from 2.04% to 3.14%, with an average value of 2.66%, and is in the over-mature evolution stage.

The TOC of shale in Well 3 is between 0.49% and 4.14%, with an average of 1.96%, The R_o is between 3.02% and 3.25%, which has entered the mature evolution stage, and the maceral of kerogen is dominated by sapropelic amorphous type. TOC of shale in Well 4 ranges from 0.04% to 3.88%, with an average of 2.01%, and the lower section of the second segment of Niutitang Formation with a better gas content ranges from 0.68% to 3.88%, with an average of 2.44%. The R_o is between 2.0% and 2.77%, which entered the mature to overmature stage. The TOC of shale in Well 5 ranges from 0.43% to 10.45%, with an average of 2.62%. The maceral of kerogen is mainly sapropelic amorphous type, The kerogen type of shale is type I, R_o ranges from 2.06% to 2.66%, with an average of 2.29%, which is in the stage of over-mature evolution.

The abundance of organic matter in Niutitang Formation in the South Guizhou Depression is generally high (Teng et al., 2008). The TOC of shale in Well 6 ranges from 0.60% to 8.89%, with an average of 3.55%. R_o ranges from 1.43% to 2.81%, with an average of 2.37%, which is in the early stage of maturation and overmaturity. The main kerogen is type I. In addition, 30 stable carbon isotope experiments of kerogen show that δ13C‰ ranges from −29.2‰ to −34.7‰ that the kerogen style is type I. The organic matter type of shale in Well 7 is mainly type I, the TOC is 0.25%–8.72%, with an average of 3.56%. The R_o value of upper and lower shale strata is high, the distribution range is 3.26%–4.4%, with an average of 3.90%, and it is in the late over-mature - metamorphic stage, especially after the bottom 997 m, R_o is greater than 4.00% which is in the metamorphic stage (Table 2).

4.2 Reservoir property

The brittle mineral content of core samples from Well 1 ranges from 52.7% to 74.1%, mainly quartz. The main clay minerals are chlorite, kaolinite, illite and montmorillonite. The measured porosity ranges from 0.02% to 5.17%, with an average value of 2.01% by Overburden pore permeability test. The porosity was 1.7%–2.78%, with an average value of 2.15% by mercury injection experiment. The permeability ranges from 0.00053 mD to 0.0041 mD, with an average value of 0.0008 mD, which belongs to the low porosity ultra-low permeability reservoir. The pores can be divided into three categories: mineral matrix pores, organic matter pores and micro-fractures, among which micro-fractures are mainly marginal cracks between organic matter and inorganic minerals, with a slit width of 0.5μm–8.6 μm (Wang et al., 2014). The brittle mineral content of shale in Well 2 ranges from 40.6% to 64.8%, with an average of 53.6%, among which quartz content is the highest, ranging from 47% to 25.6%, with an average content of 37.16%. The pore types are mainly mineral dissolution pores, intercrystalline pores of pyrite are occasionally found, and organic pores are few. Microfractures are abundant, and the seam width is 0.5 μm–8.6 μm (Wang et al., 2014).

The brittle mineral content of shale in Well 3 is the highest 74%, and the average is 50%. The porosity is 1.45%–8.04%, with an average of 3.33%, and the permeability is 0.0005 mD −0.004 mD, with an average of 0.0015 mD. The pore types include intergranular pores, intra granular pores, organic pores, solution pores, mold holes and micro-fractures. The fractures are mainly high Angle fractures with large dip Angle and low density. Some fractures have crossover phenomenon and are mostly filled with calcite.

There are differences in mineral composition among different formations of the shale of Niutitang Formation in Well 4. The lower section of the second segment of Niutitang Formation, which has the high gas content and organic matter abundance. It is dominated by quartz with an average content of 37%, followed by carbonate rock, clay (illite and chlorite), the average content of 19%, the pyrite content is relatively high, up to 3% on average. Other segment are dominated by calcite. The porosity ranges from 2.01% to 3.61%, with an average value of 2.88%. Permeability ranges from 0.00031 mD to 0.00078 mD, with an average of 0.00054mD. The pores are rich in organic matter, followed by the solution pores and micro-fractures, belonging to the low porosity and ultra-low permeability reservoir. A total of 34 filling cracks and 66 open cracks were picked up from the electrical imaging data. The dip Angle ranges from 20.3° to 89.7°, and the inclination is mainly south. The fracture trajectory is clear, indicating that the fracture has good connectivity and ductility (Liu et al., 2019) (Figure 2).

The brittle mineral content of Well 5 is high, ranging from 45% to 75%, shale gas-bearing interval from 1788 m to 1872 m, in which the content of carbonate and clay minerals is higher in the shale from 1788 m to 1832 m, and the content of quartz minerals is lower. The mineral content in the smaller depth section changes greatly, and the material composition is obviously heterogeneous. The content of quartz and clay minerals is high and the content of carbonate minerals is low in the shale of 1 832 m −1 872 m, and the mineral content changes relatively little in the shale of small depth, and the rock mineral composition is relatively stable. The reservoir space is divided into three types: inorganic pore, organic pore and microfracture. Microfractures are mainly layered fractures inside clay minerals, which have good extensibility and connectivity, and can optimize the transformation of pore system (Lee et al., 2003).

The brittle mineral content of Well 6 rangs from 37% to 68%, with an average of 51%. The quartz content is 28%–53%, with an average of 37.8%. The average porosity and permeability of shale are 0.51% and 0.001mD respectively. The microcosmic reservoir space is dominated by matrix pores, followed by organic pores. Pyrite is common and a few residual pores can be found. The fractures are mainly manifested as tensile cracks and slip cracks. Affected by the detachment structure, it is mainly filled with calcite veins. The above two groups of fractures have the characteristics of multi-phase, staggered with each other, and local grid shape.

The content of quartz minerals of shale in Well 7 is 35.1%–51.8%, with an average of 43.5%. The brittle mineral is conducive to the later fracturing. The upper section of Niutitang Formation has an average porosity of 2.00%, which corresponds to high gas content. The reservoir space is dominated by inorganic mineral matrix pores, with micro-fractures and organic pores are few. Micropores are connected with microfractures, forming a complex network of pores

10.3389/feart.2025.1447949

TABLE 2 Basic geological parameters of 7 wells.

Well number	Fault/ structure	Lithology	Thickness/m	TOC/%	R_0/%	Gas content m^3/t	Brittle mineral/%	Porosity/%	Permeability/mD	Fracture
1	Less/weak deformation	Black carbonaceous shale	103.5	0.52–3.02/1.5	2.48–4.36/3.0	0.2–4.4	52.7–74.1	0.02–5.17/2.01	0.00053–0.0041/0.0008	rich
2	Less/weak deformation	Dark grey siliceous carbonaceous shale interspersed with carbonaceous siltstone	90	0.88–8.61/3.37	2.04–3.14/2.66	0.77–3.39	40.6–64.8/53.6	—	—	rich
3	Many/strong structure	Gray-black calcareous silty mudstone interbedded with argillaceous limestone	397.86	0.49–4.14/1.96	3.02–3.25	0.0002–0.13/0.032	20-74/50	1.45–8.04/3.33	0.0005–0.004/0.0015	are mostly filled
4	Less/Structural stability	Shale, mixed with argillaceous limestone and argillaceous siltstone	468.5	0.04–3.88/2.01	2.0–2.77	0.26–4.48	55-75	2.01–3.61/2.88	0.00031–0.00078/0.00054	rich
5	Less/Structural stability and simple	Gray-black gray shale with dark gray argillaceous limestone	86	0.43–10.45/2.62	2.06–2.66/2.29	0.58–5.48	45-75	1.48–2.5	—	rich
6	Many/Strong structure	Black carbonaceous shale	119.95	0.60–8.89/3.55	1.43–2.81/2.37	0.09–1.31/0.42	37–68/51	0.2–1.8/0.51	0.0001–0.01/0.001	Slip fracture
7	Many/Strong structure	Black carbonaceous mudstone	105	0. 25-8.72/3.55	3.26–4.4	0.06–1.97	35.1–51.8/43.5	0.65–1.21	0.001–0.012	are mostly filled

Note: "/" represents the average value.

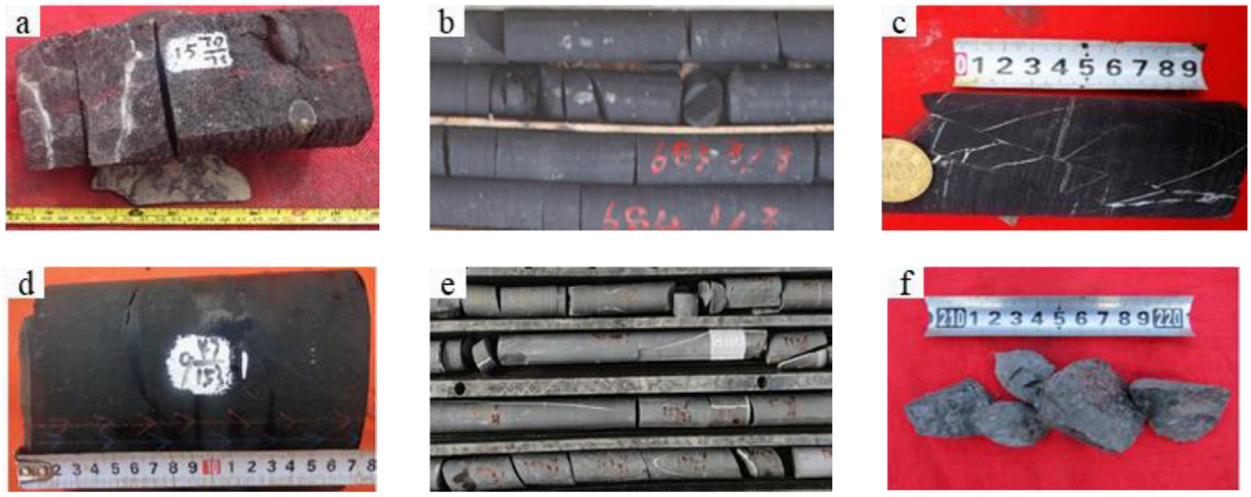

FIGURE 2
Core fractures of Niutitang Formation in different drilling wells. **(A)** Core fracture of Niutitang Formation in Well 1, along with bedding fracture, are partially filled; **(B)** The core fracture of Niutitang Formation in Well 2, along with the bedding joint, is not filled; **(C)** The cracks of Niutitang Formation in Well 3 are filled with calcite, and the filling degree is high; **(D)** The core crack of Niutitang Formation in Well 4 is open and not filled; **(E)** Niutitang Formation of Well 6 has high Angle shear fracture and high filling degree; **(F)** Core fracture of Niutitang Formation, Well 7, Slip cracks, core breakage.

and fractures with good connectivity (Diaz et al., 2013). More high-angle fractures are often filled with quartz, calcite, pyrite and other minerals, and the filling degree is relatively high.

4.3 Gas-bearing

The total hydrocarbon of Niuitang Formation in Well 1 is the highest at 2,201.00m–2271.00m and 2,353.00m–2387.00m, accounting for 4.28%. The Desorption gas content is 0.20 m^3/t –4.50 m^3/t, in which the gas content is greater than 2.00 m^3/t between 2,150 m and 2380m. The total gas content of Well 2 is 0.77 m^3/t –3.39 m^3/t, showing high gas content. The gas content increases gradually with the depth.

The overall gas content of Well 3 is low, and the maximum gas content is 0.13 m^3/t in the 1,156.62m–1852.76m. At the top of Niutitang Formation 1,454 m - 1591m, a gas anomaly occurred, with a maximum total hydrocarbon value of 3.65%.

The Desorption gas content of Well 4 is 0.13 m^3/t- 2.16 m^3/t, and the total gas content is 0.26 m^3/t- 4.48 m^3/t, among which 2,980 m - 3055m has a higher gas content with an average of 2.30 m^3/t. The core bubbles violently in water immersion test, and the gas ignition is flammable. The gas content of Well 5 is 0.58 m^3/t - 5.48 m^3/t. Among them, the gas content of the well depth of 1837 m - 1872m is greater than 2.00 m^3/t, and the average is 2.78 m^3/t; the gas content of the well depth of 1854 m - 1872m is greater than 3.00 m^3/t, and the average is as high as 3.80 m^3/t.

The Desorption gas content in Well 6 ranges from 0.09 m^3/t to 1.11 m^3/t, with an average value of 0.42 m^3/t. The gas content of Niutitang Formation in Well 7 ranges from 0.06 m^3/t - 1.97 m^3/t, with an average of 0.32 m^3/t. There are two high gas content segments in the middle and upper section. The first segment is 957 m - 975m with calcareous carbonaceous shale and the maximum gas content is 1.10 m^3/t. Second, in the 1005m–1013m segment, gas penetration occurred at the wellhead during drilling, and the maximum gas content was 1.97 m^3/t. The gas logging showed a high gas anomaly with a maximum value of 7.92% (Figure 3).

5 Discussion

5.1 Hydrocarbon control by sedimentation

Favorable sedimentary facies zones control the hydrocarbon generation capacity of source rocks, are the material basis of shale gas enrichment, and are closely related to gas-bearing properties. From the successful development examples and experiences of shale gas in Wufeng-Longmaxi Formation in China (Guo, 2014), it can be seen that deep-water facies deposits such as deep-water shelf are one of the most important theories in the "ternary enrichment model" theory of shale gas (Guo and Zhang, 2014). The favorable facies zone model of the Carboniferous platform basin-lower slope facies in the south of Guizhou and the middle of Guangxi has guided the shale gas investigation.

5.1.1 Sedimentary characteristics

The sedimentary environment determines the material basis of shale gas formation (Qiu et al., 2022), The division scheme of sedimentary environment of Niutitang Formation in the four palaeouplifts in the study area can be divided into two categories: The first type is classified as shelf facies, which can be subdivided into two subfacies: deep shelf and shallow shelf, which is adopted by most scholars. The second category is divided into rifting trough facies, which can be subdivided into aulacogen basin and slope subfacies (Zhai et al., 2017).

In general, southern Shaanxi belongs to passive continental margin deposits on the northern margin of the Upper Yangtze Block. According to the first classification scheme, the Niutitang Formation

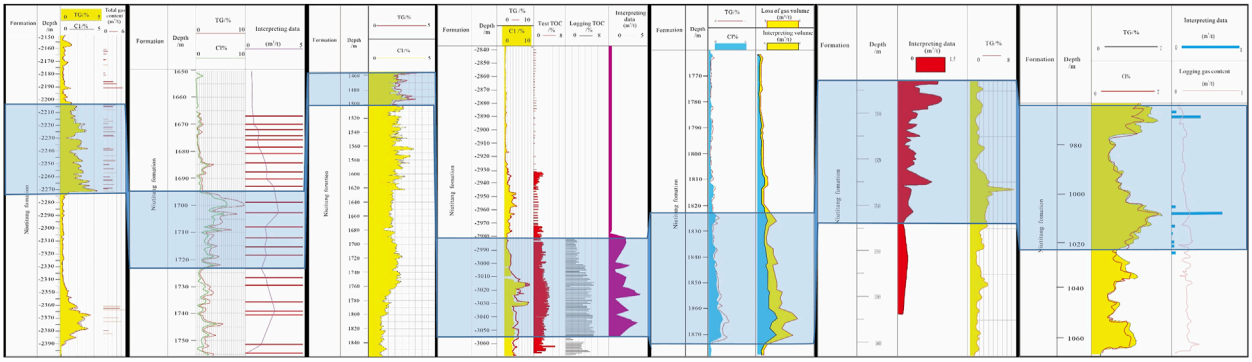

FIGURE 3
Gas content column of 7 wells (High gas content intervals are represented in the blue line). (High gas content intervals are represented in the blue line).

of Well 1 and Well 2 in southern Shaanxi is mainly shallow shelf sedimentary subfacies, and the high-quality shale segment is deep shelf subfacies. The better gas-bearing of the two wells is the middle and lower section of Niutitang Formation, and the lithology is dark gray carbonaceous shale, silty shale, silty carbonaceous shale with carbonaceous siltstone and marl.

The Niutitang Formation in Shennongjia area is mainly composed of sedimentary shelf facies and slope facies, among which shelf facies can be further divided into deep water shelf subfacies and shallow water shelf subfacies, and slope facies can be divided into slope foot subfacies (Xie et al., 2017). The Niutitang Formation can be divided into the first, second and third members from the bottom up, corresponding to deep shelf subfacies, shallow shelf subfacies and slope foot subfacies respectively. The first segment of Niutitang Formation with better gas-bearing is characterized by deep grayish-black calc-carbonaceous mudstone, black calc-carbonaceous mudstone, argillaceous siltstone lamination, rich pyrite nodules and pyrite bands.

Tectonic evolution controls the distribution of sedimentary facies zones in Yi-chang area of western Hubei. In the early Cambrian, influenced by the large-scale transgression of the Yangtze River, the sediments in this area were successively com-posed of tidal flat facies, shallow water facies and deep shelf facies from northeast to southwest (Zhang et al., 2023). Both Well 4 and 5 are deepwater shelf facies, and the former has deeper water. The second segment of Niutitang Formation, lithology of which is gray-black and black carbonaceous shale, is a deep water shelf deposit.

The paleogeothermal environment of Niuitang Formation in the Qiannan Depression has low water temperature and dark anoxic deposits, and the organic matter is well preserved. The sedimentary environment of Well 6 and 7 is deep shelf - subdeep sea basin deposition. The second member of Niutitang Formation with good gas-bearing capacity is gray-black mudstone, mixed with gray argillaceous limestone, containing pyrite nodules or bands. A complete trilobite fossil was found in Niutitang Formation in Well 6.

According to the second category, Well 1 is the slope subfacies, and Well 2 is the aulacogen basin facies of the rift trough, the Well 3 is rifted trough basin subfacies, Well 4 is aulacogen basin subfacies, Well 5 is slope subfacies, and Well 6 is aulacogen basin, and Well 7 is deep shelf deposition (Figure 4).

5.1.2 The relationship between sedimentary subphase and gas-bearing

The Niutitang Formation in the study area has the characteristics of multi-stage hydrocarbon generation of organic matter. The results show that the Niutitang Formation generally has the high organic matter abundance. However, the influence of organic matter abundance is usually ignored when analyzing the influencing factors of shale gas content in the Niutitang Formation. According to the analysis of sedimentary facies of 7 wells, all of them belong to rifting trough facies. However, in the case of similar thermal evolution degree and structural preservation conditions, although Hannan palaeouplift and Huangling palaeouplift belong to the same sedimentary zone - West Hubei Trough, due to different sedimentary subfacies, the hydrocarbon generation capacity of shale is affected, and thus the gas content of shale is affected (Figure 5). Although Well 1, 2 and 4 are all located in the same large rifting trough, and the R_o of the key factor for the Niutitang Formation is generally less than 3.00%, different sedimentary subfacies lead to differences in their gas-bearing properties. Well 2 and 4 are subfacies of rifting trough basin, while Well 1 is subfacies of rifting trough slope. The sedimentary environment is different, which leads to the lower hydrocarbon generation potential of shale in Well 1 than that in Well 2 and 4, resulting in the difference of gas content. In addition, the stable gas flow of 21 × 10^4 m^3/d in Well Shanzhenye 1 in Zhenba area, which is adjacent to Well 2, also confirms the controlling effect of sedimentary subfacies relative gas content.

5.2 Thermal evolution degree control zone

5.2.1 Differential tectonic subsidence affects the degree of thermal evolution

Although the seven wells are located in the periphery of the outer palaeouplift of Sichuan Basin, the differences of thermal evolution degree and hydrocarbon generation are caused by different tectonic subsidence in different regions. Compared with Huangling Palaeouplift and Xuefeng Palaeouplift, R_o in Wells 4 and 5 is generally lower than 3.00%, while the minimum of R_o in 7 wells are higher than 3.00%. The main reasons are as follows:

First, the deep burial time is late, the deep burial time is short, the thermal evolution degree is low, and it is in the best

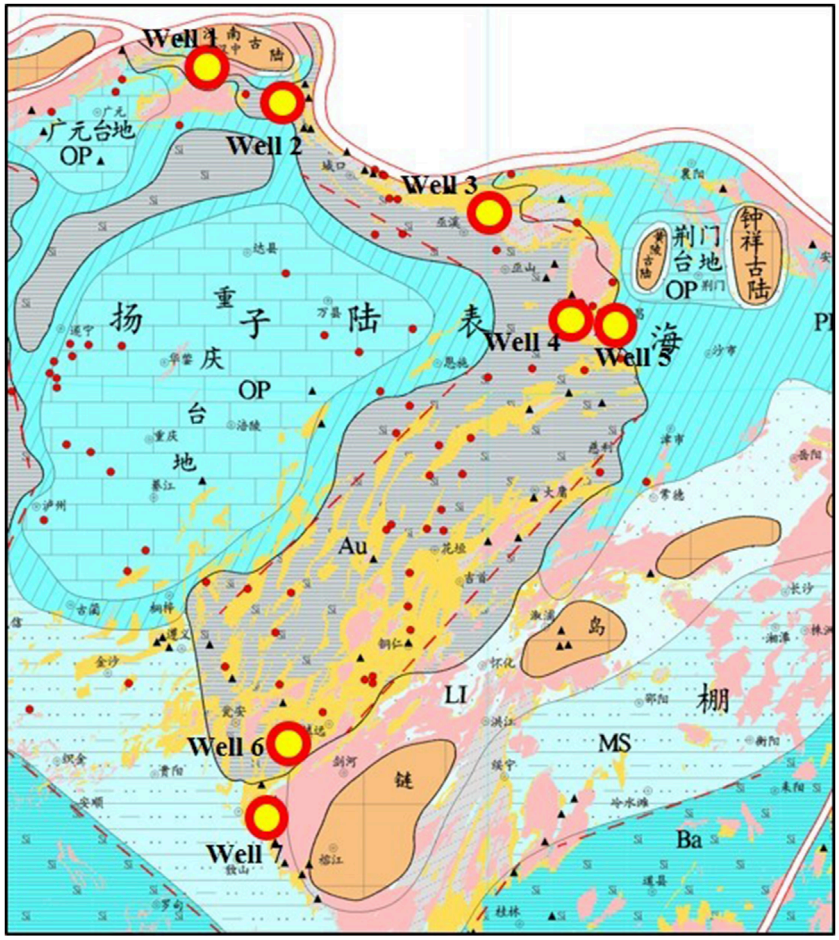

FIGURE 4
Sedimentary facies of Niutitang Formation in the study area (modified by Zhai Gangyi).

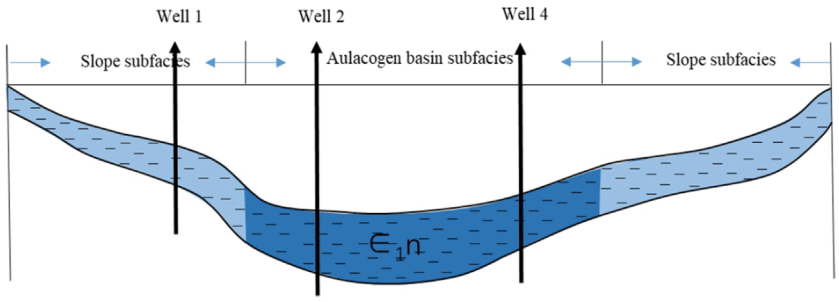

FIGURE 5
Schematic diagram in the Aulacogen basin sedimentary subfacies of Niutitang formation.

gas generation period, which is beneficial to gas enrichment. The Niutitang Formation shale of Huangling Uplift entered the oil-generating stage in the middle Silurian, entered the thermal cracking condensate oil-gas stage at the end of Permian, and remained relatively stable until the middle Triassic. At present, the shale R_o of Niutitang Formation in Well 4 and Well 5 is 2.26%–2.77%, and the latter is smaller with an average of 2.29%, which is in the best gas window range. From the end of Permian to the beginning of Triassic, it experienced rapid subsidence, and was in the deep burial period (>3500m) in the late Jurassic (before Yanshan uplift), with a deep burial time of about 85Ma (Figure 6). The hydrocarbon generation time of Niutitang Formation in Well 7 was early. The Niujutang Formation was buried rapidly after deposition, and entered the hydrocarbon generation threshold in the early Middle Cambrian

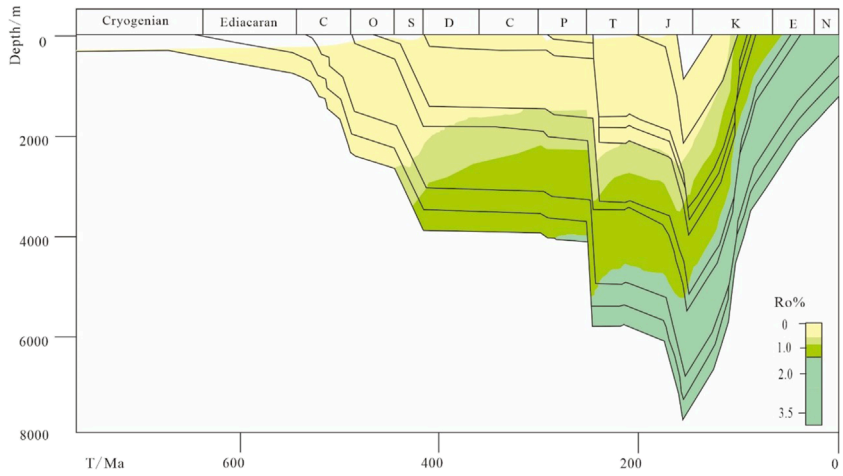

FIGURE 6
History of sedimentary burial in Huangling palaeouplift

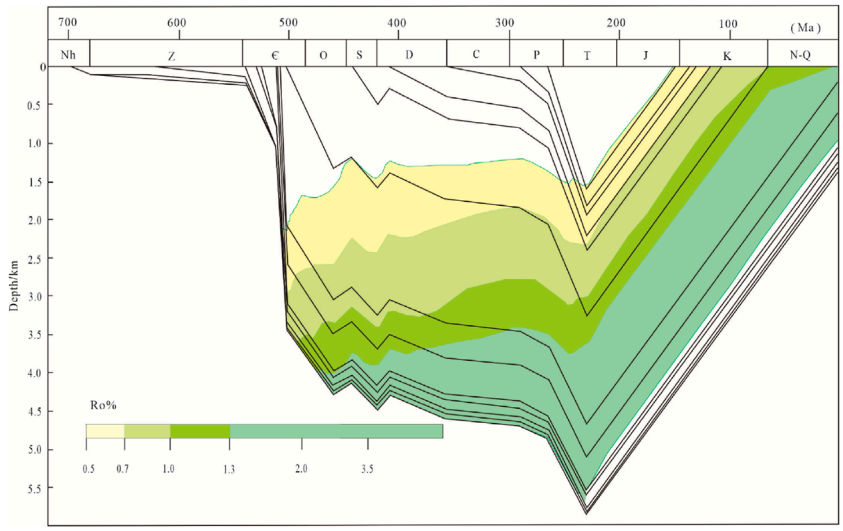

FIGURE 7
History of sedimentary burial in Xuefeng palaeouplift

(about 508 Ma), the burial depth exceeded 3,500 m in the Late Cambrian, reached the late oil-generation and early gas generation stage until the early Middle Triassic (before the Indo uplift), and was in the continuous deep gas burial stage with the maximum burial depth exceeding 5700m and the hydrocarbon generation time exceeding 270Ma. Deep burial time (>3500 m) exceeds 250Ma (Figure 7). The southern margin of Huangling Uplift is generally shorter than that of Niutitang Formation on the western margin of Xuefeng uplift (Nie et al., 2021) and the deep burial time is later, resulting in a lower degree of thermal evolution and still in the optimal gas generation stage, which is more conducive to shale gas enrichment.

Second, hydrothermal intrusion along the fault may lead to an increase in the degree of thermal evolution. The comparison of R_o between Doushantuo Formation and Niutitang Formation in Well 7 shows that the R_o of Doushantuo Formation is 3.32%–3.59%, but it is significantly lower than the lower part of Niutitang Formation. It is believed that the small fault drilled at the bottom of Niutitang may locally warm the shale in Niutitang, resulting in abnormal maturity, while the Doushantuo shale is normal geothermal warming, which is lower than the maturity of the lower part of Niutitang Formation. The main reasons are as follows: ① the first segment of Niutitang Formation consists of gray-black thin-layer siliceous rocks, phosphorus-bearing siliceous rocks and phosphorite nodules with thickness of 2 m–15 m. This phosphorus may be related to the volcano, and there may be volcanic hydrothermal intrusion, which increases the temperature of Niutitang Formation. (2) The fault was drilled at the bottom of Niuitang Formation, which penetrated the Dengying Formation, and hydrothermal minerals such as barite, fluorite and quartz were found in the cracks. From this point

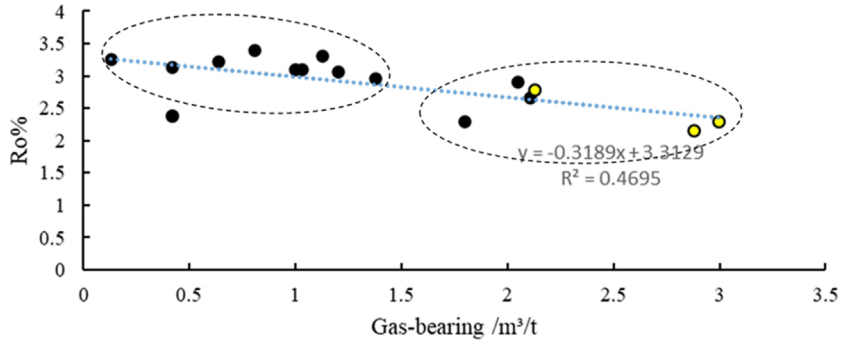

FIGURE 8
Relationship between Ro and gas content.

of view, the thermal migration of Dengying Formation along the fault probably affected the temperature of Niutitang Formation and accelerated the thermal evolution of organic matter.

5.2.2 Correlation between R_o and gas content

On the basis of the study of 7 wells, 9 wells in the adjacent area are investigated and analyzed comprehensively (Figure 8). Based on the relationship between R_o and gas content of 16 wells, it is found that: 1) the correlation between R_o and gas content is weak and linear, and the correlation coefficient is 0.47. 2). the value of R_o can qualitatively reflect the size of the gas content. ① As can be seen from the figure, there are 8 data with R_o higher than 3.00%, and the R_o value is 3.06%–3.40%, with an average of 3.20%. The gas content is 0.13 m^3/t - 1.20m^3/t, the average is 0.75 m^3/t, and the gas content of 50% data is less than 1.00 m^3/t. ② There were 7 datas whose R_o value was less than or equal to 3.00%, with a value of 2.15%–2.95% and an average of 2.57%. The gas content is 1.38 m^3/t - 3.00m^3/t, with an average of 2.19 m^3/t, and the gas content of 71% data is greater than 2.00 m^3/t. The average R_o of the three wells obtained shale gas flow is 2.40%, and the gas content is 2.13 m^3/t - 3.00m^3/t, with an average of 2.67 m^3/t. Therefore, the degree of thermal evolution is the key factor affecting gas content. The R_o of well 6 is 2.37% and the gas content is low. The reason is that the gas content of well 6 is not only affected by R_o, but also restricted by other factors.

5.3 Preservation controls the reservoir

5.3.1 Major faults characteristics

Fracture is closely related to shale gas-bearing and mainly controls the preservation conditions of shale gas. Faults can be used not only as a migration pathway of shale gas to cause gas loss and damage shale gas preservation (Gao et al., 2014), but also as a shale gas sealing formation to prevent gas loss and facilitate shale gas enrichment (Hu et al., 2014). It can even be used as a release pathway of tectonic energy to control the integrity of the formation. Therefore, by analyzing the fractures and their properties of different research objects, the influence of fractures on shale gas preservation can be comprehensively judged.

The fault structure of Qinling region in southern Shaanxi is complex, and in addition to some regional plate edge faults and intraplate faults, there are also buried faults (Zhang et al., 2004). Under the influence of late Indosinian and Yanshanian strong uplift, the Micangshan tectonic belt is a forward-spreading structure from north to south caused by the superposition of two thrust nappe structures in different directions. From the initial underwater uplift, it rose to land after the Indochina movement. Among them, Well 1 is mainly affected by the Yangpingguan-Yangxian fault in the near east-west direction, while Well 2 is surrounded by the Dachimba-Zhenba fault in the near east-west direction and the Sishang-Xiaoyangba fault in the north-west-southeast direction (Chen et al., 2018).

There is a regional fault-Yangriwan Fault on the western margin of Shennongjia (He et al., 2021b). And Well 3 is located about 1 km to the south of the fault. Several fracture zones and a buried fault were found during drilling. The core of the dark shale section has different degrees of fractures and is partially or completely filled with calcite.

There are fault structures of different periods, different scales and different directions in western Hubei, which form regular network. Some important faults constitute the division boundary of the secondary tectonic units, and have obvious control over the regional structural styles, and are also of great significance to the preservation of shale gas. Well 4 and 5 are located on the Yichang slope, with the Wuduhe fault in the southeast, which breaks into the core of the uplift and serves as the boundary of the stable region of the southern Yichang slope belt together with the Tianyangping fault (Figure 9).

The eastern part of the Qiannan Depression is bounded by the Tonren-Sandu fault and the Xuedeng Uplift (Bai et al., 2010). The southeast part is bounded by the Libo Fault and the Guizhong Depression. The southwest part is bounded by the Ziyun-Luodian-Nandan -Du 'an fault and the Luodian Fault depression; the northwest part is bounded by the Guiyang-Zhenyuan fault and the Qianzhong Uplift, and the plane is a triangle that is wide in north and narrow in south. It mainly presents three groups of fault systems with different scales in the NNE - near SN, NW, NEE - near EW direction (Peng et al., 2019).

5.3.2 The relationship between structural preservation and gas-bearing

Well 4 and 5 are located in the bottom of thrust nappe, with relatively stable, simple structure and few faults, which is conducive to the preservation of shale gas. The Niuitang Formation of Well 1 is deformed by long-term compression, with deep gully, broken

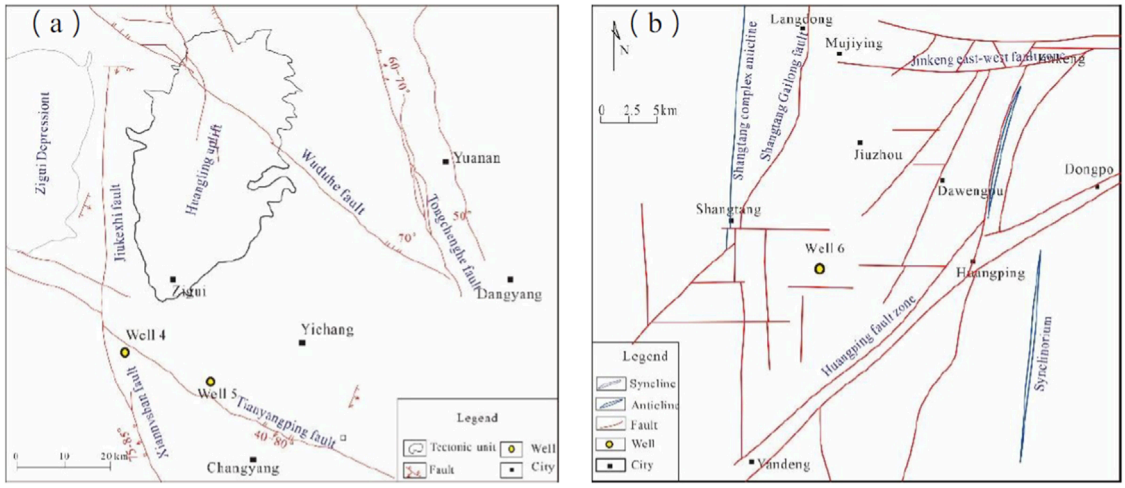

FIGURE 9
Distribution of major faults. **(A)** periphery of Huangling Uplift. **(B)** periphery of Xuefeng Uplift.

terrain and strong dynamic geological action, which is not conducive to shale gas preservation. Well 4 is located about 1 km south of the major fault, encountered several fracture zones and a buried fault during drilling. The core of the dark shale section has varying degrees of fractures, and is partially or completely filled with calcite. The mirror scratches can be seen in the core of the two wells 1824.06m–1824.12m, which indicates that the tectonic movement in this area is relatively intense, which is not conducive to the preservation of shale gas.

Although Well 6 and Well 7 are located in the Qiannan Depression, Well 7 is located in the Danzhai area, which is far from the fault position, the formation of Niuitang Formation is stable, and the degree of structural deformation is relatively weak (Dan et al., 2023). However, there are three regional large faults around Well 6, and a number of secondary small faults develop near the well. Due to the relatively staggered formation, the low-grade tension-torsion fault develops in the direction of 65° NW, making the Huangping fault zone more complicated and damaging the preservation conditions (Ge et al., 2018; 2020), resulting in slightly lower gas content in Well 6 than Well 7. In addition, there are many faults in the south Guizhou Depression with multi-stage and complex structure, and the gas components can reflect the destructive effect of faults on the gas content of shale. The nitrogen content of Well 7 is 30%, while the nitrogen content of Well 6 is 50%–79%, indicating that the gas may contains atmospheric components. Considering that the gas-bearing formation is connected with the atmosphere through fracture, the enrichment of shale gas is destroyed. The higher atmospheric content in Well 6 also confirms that the gas reservoir is more destructive and has relatively lower gas content.

In addition, the fracture is favorable to the gas content of shale gas. The Niutitang Formation, where Well 4 and 5 are located, is located in the footwall of thrust nappe and has a stable structure. It plays an effective role in releasing stress during multi-stage structural transformation, thus protecting the upper overlying Sinian, Cambrian, Upper Ordovician and Lower Silurian shales from being strongly damaged on the rigid base. From the perspective of integrity and stability of source rock development, fracture has a favorable influence on shale enrichment.

5.4 Differential enrichment of shale gas in the periphery of palaeouplift

Through these studies, the differential enrichment mechanism of shale gas on the periphery of palaeouplift is summarized:

(1) Variations in hydrocarbon generation potential within the same facies zone are significantly influenced by depositional subfacies. The main reason that the gas content of Well 1 is lower than that of Well 2 is that the former is slope facies of rifting trough and the latter is deep water facies of rifting trough basin. The difference of hydrocarbon generation potential caused by sedimentary subfacies in the same facies zone is an important factor restricting the gas content of shale.

(2) The difference in the degree of thermal evolution caused by the beginning time, time span and rate of deep burial is the key factor restricting the gas bearing of shale. The rigid basement on the periphery of the ancient uplift has the effect of "heat insulation and preservation", which makes the thermal evolution degree of the periphery generally low, and most of them have not entered the graphitization stage. Due to the impact of tectonic evolution and hydrothermal intrusion, significant variations in the thermal maturity of organic matter exist across different structural units. The degree of thermal evolution is moderate, and it is in the best gas generation period, which is conducive to the enrichment of shale gas.

(3) The structural preservation conditions are the key factors affecting the enrichment of shale gas. The paleouplift peripheral areas are characterized by high structural stability, weak deformation, and undeveloped faults and fractures, which provide favorable conditions for the enrichment and preservation of shale gas. This stable structural environment can effectively prevent gas from escaping through faults or

fractures, enhance the sealing of the cap layer, and reduce the risk of compression and failure of the reservoir, thereby maintaining the pore structure and adsorption capacity of the reservoir. In addition, structural stability helps to maintain a moderate geothermal gradient and avoid the adverse effects of too high or too low thermal evolution on shale gas generation and preservation. In summary, the structural features of the periphery of the palaeouplift promote the enrichment and long-term preservation of shale gas by reducing gas escape, protecting reservoir physical properties and optimizing thermal evolution conditions.

6 Conclusion

(1) Hydrocarbon control by sedimentation. Sedimentary facies zones determine the paleoproductivity of shale deposits and the redox conditions of water bodies, which in turn control the enrichment of organic matter and lead to differences in hydrocarbon generation potential. In the Cambrian system surrounding the paleouplift, various sedimentary types are observed. Among these, the rifting trough subfacies exhibit superior organic matter enrichment conditions compared to the rifting trough slope subfacies, providing a favorable material basis for shale gas accumulation.

(2) Thermal evolution degree control zone. The rigid basement on the periphery of the ancient uplift has the effect of "heat insulation and preservation," which makes the thermal evolution degree of the periphery generally low, and most of them have not entered the graphitization stage. However, the differences in the thermal evolution degree of the Niutitang shale on the periphery of different ancient uplift due to the deep burial starting time, deep burial time span and deep burial rate are the key factors restricting the gas content of the shale.

(3) Preservation control the reservoir. The tectonic deformation around the paleouplift was weak, the rigid basement of granite formed in the early stage weakened the tectonic failure. The tructural stability is beneficial to maintain a moderate geothermal gradient and avoid the adverse effects of too high or too low thermal evolution on shale gas generation and preservation. The difference in preservation conditions caused by the structural strength, fracture development degree and the coupling relationship with tectonic fractures is the key factor restricting the gas-bearing of shale.

(4) The geological conditions of shale gas enrichment at the periphery of palaeouplift, favorable preservation conditions such as lower plate of thrust nappe, the moderate thermal evolution degree and deep water facies area of trough are favorable directions for further exploration.

Data availability statement

The original contributions presented in the study are included in the article/supplementary material, further inquiries can be directed to the corresponding author.

Author contributions

MG: Conceptualization, Investigation, Methodology, Writing–original draft, Writing–review and editing, Data curation, Formal Analysis. SB: Writing–review and editing. YW: Writing–review and editing. HaL: Writing–review and editing. TW: Writing–review and editing. HoL: Writing–review and editing.

Funding

The author(s) declare that financial support was received for the research, authorship, and/or publication of this article. This work was supported by the National Natural Science Foundation of China (42130803) and the Geological Survey Project (DD20230257).

Acknowledgments

We sincerely thank Prof. Zhai for his sedimentary facies figures that greatly improved the manuscript.

Conflict of interest

Author HL was employed by PetroChina Research Institute of Petroleum Exploration and Development.

The remaining authors declare that the research was conducted in the absence of any commercial or financial relationships that could be construed as a potential conflict of interest.

Publisher's note

References

Abouelresh, M. O., and Slatt, R. M. (2012). Lithofacies and sequence stratigraphy of the Barnett shale in EastCentral fort worth basin, Texas. *AAPG Bull.* 96, 1–22. doi:10.1306/04261110116

Bai, Y.-S., Xiong, C.-Y., Wang, C.-S., Li, X.-B., Liu, A., and Zhang, M. (2010). Tectonic evolution of north area of xuefengshan uplift and its relation to marine hydrocarbon formation. *Geol. Mineral Resour. South China* 96, 68–75.

Bao, S.-J., Zhai, G.-Y., Zhou, Z., Yu, S.-F., Chen, K., Wang, Y.-F., et al. (2018). The evolution of the Huangling uplift and its control on the accumulation and preservation of shale gas. *China Geol.* 1, 346–353. doi:10.31035/cg2018052

Bruner, K. R., Walker-Milani, M., and Smosna, R. (2015). Lithofacies of the Devonian Marcellus Shale In the Eastern Appalachian Basin, U.S.A. *U.S. A. J. Sediment. Res.* 85, 937–954. doi:10.2110/jsr.2015.62

Chen, X.-L., Zhai, G.-Y., Bao, S.-J., Pang, F., Wang, J.-Z., and Tong, C.-C. (2018). Shale gas accumulation and gas-bearing properties of Niutitang formation in well Zhendi 1, Zhenba region of southern Shaanxi province. *China Min. Mag.* 27, 101–106. doi:10.12075/Qissn.1004-4051.2018.S1.079

Dan, Y., Yan, J.-F., Bao, S.-J., Lang, B., Ma, L., Nie, G.-Q., et al. (2023). Discovery of Sinian-Cambrian multi-tier shale gas in Guidandi-1 well of southwest margin of Xuefeng uplift. *Geol. China* 50, 291–292. doi:10.12029/gc20201216004

Diaz, H. G., Lewis, R., Miller, C., and Fuentes, C. C. (2013). *Evaluating the impact of mineralogy on reservoir quality and completion quality of organic shale plays*. Salt Lake City, USA: AAPG Rocky Mountain Section Meeting.

Gao, J., He, S., He, Z.-L., Zhou, Y., and Zhao, M.-L. (2014). Genesis of Calcite Vein and Its Implication to Petroleum Preservation in Jingshan Region, Mid-Yangtze. *Oile&Gas Geol.* 35, 33–41. doi:10.11743/ogg20140105

Ge, M.-N., Bao, S.-J., He, W., Chen, X.-L., Lin, T., and Chen, K. (2018). The discovery of shale gas in Lower Cambrian marine shale gas at Huangdi-1 Well in Huangping region of northern Guizhou. *Geol. China* 45, 851–852. doi:10.12029/gc20180414

Ge, M.-N., Chen, K., Chen, X.-L., Wang, C., and Bao, S.-J. (2020). The influence factors of gas-bearing and geological characteristics of Niutitang Formation shale in the southern margin of Xuefeng Mountain ancient uplift: A case of Well Huangdi 1. *Geol. China* 3, 533–544. doi:10.31035/cg2020072

Guo, T.-L., and Zhang, H.-R. (2014). Formation and enrichment mode of Jiaoshiba shale gas field,Sichuan Basin. *Petroleum Explor. Dev.* 41, 31–40. doi:10.1016/s1876-3804(14)60003-3

Guo, X.-S. (2014). Rules of Two-Factor Enrichiment for Marine Shale Gas in Southern China—Understanding from the Longmaxi Formation Shale Gas in Sichuan Basin and Its Surrounding Area. *Acta Geol. Sin.* 88, 1209–1218. doi:10.19762/j.cnki.dizhixuebao.2014.07.001

Hammes, U., and Frbourg, G. (2012). Haynesville and Bossier mudrocks: a facies and sequence stratigraphic investigation, East Texas and Louisiana,USA. *Mar. Petroleum Geol.* 31, 8–26. doi:10.1016/j.marpetgeo.2011.10.001

He, W., Chen, Y., Lei, Y.-Y., Qian, C., Chen, K., Lin, T., et al. (2021b). Analyses of the relationship between lithology and shale gas accumulation for the Wufeng Formation to Longmaxi Formation in the west of Hubei Province:A case study of the Erhongdi 1 well. *J. China Coal Soc.* 46, 1014–1023. doi:10.13225/j.cnki.jccs.2019.1559

He, Z.-L., Nie, H.-K., Li, S.-J., Liu, G.-X., Ding, J.-H., Bian, R.-K., et al. (2021a). Differential occurrence of shale gas in the Permian Longtan Formation of Upper Yangtze region constrained by plate tectonics in the Tethyan domain. *Oil and Gas Geol.* 42, 1–15. doi:10.1743/ogg20210101

He, Z.-L., Nie, H.-K., and Zhang, Y.-Y. (2016). Analysis of themain controlling factors of shale gas enrichment in the Ordovician Wufeng Formation and Silurian Longmaxi Formation in Sichuan Basin and its peripheral areas. *Earth Sci. Front.* 23, 8–17. doi:10.13745/j.esf.2016.02.002

Hu, D.-F., Zhang, H.-R., Ni, K., and Yu, G.-C. (2014). Main Controlling Factors for Gas Preservation Conditions of Marine Shales in Southeastern Margins of the Sichuan Basin. *Nat. Gas. Ind.* 34, 17–23. doi:10.3787/J.ISSN.1000-0976.2014.06.003

Lee, S. G., Lee, D. H., Kim, Y., Chae, B. G., and Woo, N. C. (2003). Rare Earth Elements as Indicators of Groundwater Environment Changes in a Fractured Rock System:Evidence from Fracture-Filling Calcite. *Appl. Geochem.* 18, 135–143. doi:10.1016/s0883-2927(02)00071-9

Li, H., Liu, A., Luo, S.-Y., Chen, X.-H., and Chen, L. (2019). Characteristics of the Cambrian Shuijingtuo shale reservoir on Yichang Slope, western Hubei Province: a case study of well EYY 1. *Petroleum Geol. and Exp.* 41, 76–82. doi:10.11781/sysydz201901076

Liu, L., He, S., Zhai, G.-Y., Chen, K., Liu, Z.-X., Wang, Y., et al. (2019). Diagenetic Environment Evolution of Fracture Veins of Shale Core in Second Member of Niutitang Formation in Southern Limb of Huangling Anticline and Its Connection with Shale Gas Preservation. *Earth Sci.* 44, 3583–3597. doi:10.3799/dqkx.2019.142

Nie, G.-Q., Li, X.-P., Dan, Y., Liang, B., Zhang, Q.-Y., Li, J.-R., et al. (2021). Burial and thermal history of mud shale in Niutitang formation of lower Cambrian in southern Guizhou depression:A case study of Guidudi well 1. *Carsologica Sin.* 40, 760–767. doi:10.11932/karst20210503

Peng, Z.-Q., Tian, W., Miao, F.-B., Wang, B.-Z., and Wang, C.-S. (2019). Geological Features and Favorable Area Prediction of Shale Gas in Lower Cambrian Niutitang Formation of Xuefeng Ancient Uplift and Its Periphery. *Earth Sci.* 44, 3512–3528. doi:10.3799/dqkx.2019.956

Qiu, Z., Zou, C.-N., Mills, B.-J.-M., Xiong, Y.-J., Tao, H.-F., Liu, B., et al. (2022). A nutrient control on expanded anoxia and global cooling during the Late Ordovician mass extinction. *Commun. Earth and Environ.* 3, 82–89. doi:10.1038/s43247-022-00412-x

Teng, G.-E., Qin, J.-Z., and Zheng, L.-Y. (2008). Hydrocarbon Potential on Excellent Hydrocarbon Source Rock in Southern Guizhou Depression and Its Spacial-Temporal Distribution. *Acta Geol. Sin.* 82, 366–372.

Wang, Y.-M., Dong, D.-Z., Yang, H., He, L., Wang, S.-Q., Huang, J.-L., et al. (2014). Quantitative characterization of reservoir space in the Lower Silurian Longmaxi Shale, southern Sichuan, China. *Earth Sci.* 57, 313–322. doi:10.1007/s11430-013-4645-y

Xie, X.-N., Hao, F., Lu, Y.-C., He, S., Shi, W.-Z., Jiang, Z.-X., et al. (2017). Differential Enrichment Mechanism and Key Technology of Shale Gas in Complex Areas of South China. *Earth Sci.* 42, 1045–1056.

Xie, Z., Lu, S.-F., Yu, L., Chen, Y.-P., Wang, M., Chen, F.-W., et al. (2014). Assessment of Natural Gas Loss from Mudstone Gas Source Rocks — an Example from Jiumenchong Formation of Huangye 1 Well, Lower Cambrian, Southern Guizhou Sag,China. *Acta Mineral. Sin.* 34, 137–143. doi:10.16461/j.cnki.1000-4734.2014.01.013

Xu, T., Xu, F., Guo, Y.-H., Wang, N., Xie, Q.-Z., and Huang, W. (2019). Organic geochemical characteistics of the Lower Paleozoic shales in Xixiang-Zhenba Area,Southern Shaanxi. *J. Northeast Petroleum Univ.* 43, 59–68. doi:10.3969/j.issn.2095-4107.2019.04.006

Zhai, G.-Y., Bao, S.-J., Wang, Y.-F., Chen, K., Wang, S.-J., Zhou, Z., et al. (2017). Reservoir Accumulation Model at the Edge of Palaeohigh and Significant Discovery of Shale Gas in Yichang Area, Hubei Province. *Acta Geosci. Sin.* 38, 441–447. doi:10.3975/cagsb.2017.04.01

Zhang, G.-W., Dong, Y.-P., Lai, S.-C., Guo, A.-L., Meng, Q.-R., Liu, S.-F., et al. (2003). Mianlue tectonic zone and Mianlue suture zone at the southern margin of the Qinling-Dabie orogenic belt. *Sci. China Earth Sci.* 47, 300–316.

Zhang, J.-F., Zhai, G.-Y., Wang, D.-M., Bao, S.-J., Chen, K., Li, H.-H., et al. (2020). Tectonic evolution of the Huangling dome and its control effect on shale gas preservation in the north margin of the Yangtze Block, South China. *China Geol.* 3, 28–37. doi:10.31035/cg2020025

Zhang, Y., Huang, D.-J., Zhang, L.-L., Wan, C.-H., Luo, H., Shao, D.-Y., et al. (2023). Biogenic silica of the Lower Cambrian Shuijingtuo Formation in Yichang,western Hubei Province-features and influence on shale gas accumulation. *Earth Sci. Front.* 30, 83–100. doi:10.13745/j.esf.sf.2022.5.40

frontiers | Frontiers in Earth Science

TYPE Original Research
PUBLISHED 04 April 2025
DOI 10.3389/feart.2025.1509332

OPEN ACCESS

EDITED BY
Ángel Puga-Bernabéu,
University of Granada, Spain

REVIEWED BY
Luis Gago Duport,
University of Vigo, Spain
Shansi Tian,
Northeast Petroleum University, China
Bo Ran,
Chengdu University of Technology, China
Tong Sun,
Chengdu University of Technology, China

*CORRESPONDENCE
Bin Lu,
lubin0921@163.com
Zhen Qiu,
qiuzhen316@163.com

RECEIVED 10 October 2024
ACCEPTED 20 March 2025
PUBLISHED 04 April 2025

CITATION
Lu B, Hou D-j, Zou C-n, Li X-z, Gao R-s, Wei H-y and Qiu Z (2025) Depositional environment and organic matter enrichment mechanism of the lower cambrian shale in the southern Sichuan Basin.
Front. Earth Sci. 13:1509332.
doi: 10.3389/feart.2025.1509332

Depositional environment and organic matter enrichment mechanism of the lower cambrian shale in the southern Sichuan Basin

Bin Lu[1,2]*, Du-jie Hou[2], Cai-neng Zou[1], Xi-zhe Li[1], Ri-sheng Gao[1], Heng-ye Wei[3] and Zhen Qiu[1]*

[1]Research Institute of Petroleum Exploration and Development, China National Petroleum Corporation, Beijing, China, [2]School of Energy Resources, China University of Geosciences (Beijing), Beijing, China, [3]School of Geoscience and Technology, Southwest Petroleum University, Chengdu, China

The Ediacaran-Cambrian transition was one of the most important periods in Earth's history. Based on the analysis of lithofacies, mineral composition, total organic carbon major and trace elements, we have studied the depositional environment and organic matter enrichment mechanism of Qiongzhusi Formation shale in the southern Sichuan Basin. The results show that V/Cr, Ni/Co, U/Th, Mo-EF and U-EF values suggest stronger reducing conditions in black shale compared to grey shale, with anoxic conditions decreasing from the interior of the faulted-sag to its exterior. Mo-TOC crossplots and U-Mo covariation analyses indicate a moderately restricted environment during the deposition of the Qiongzhusi Formation. Ba/Al and biogenic barium (Ba_{xs}) suggest that the black shale had higher paleoproductivity than grey shale, and the faulted-sag interior higher paleoproductivity compared to that of the slope and outside faulted-sag. The Ti/Al ratio indicates a stable terrigenous input during deposition. The chemical index of alteration (CIA) values in the Qiongzhusi formation range mostly from 50 to 70, indicating low chemical weathering under a cold and arid climate. The Cd/Mo ratio and Co (μg/g) × Mn (%) plot indicate that upwelling had a minor influence in general. Overall, the organic matter enrichment in the Qiongzhusi Formation was primarily controlled by the redox conditions, which were influenced by the Mianyang-Changning faulted-sag. We proposed two depositional models for the Qiongzhusi Formation shale in the southern Sichuan Basin: (1) OM-enriched black shale, deposited under anoxic-suboxic conditions, experiencing low chemical weathering, cold and arid climate and high paleoproductivity; (2) OM-lean grey shale, deposited under suboxic-oxic conditions, with low chemical weathering, a cold and arid climate and low paleoproductivity.

KEYWORDS

sichuan basin, lower cambrian, qiongzhusi formation, shale, deposit ional environment, organic matter enrichment

1 Introduction

The Ediacaran-Cambrian (~540 Ma) transition marks one of the most important periods in Earth's geological history, characterized by significant events such as the "Snowball Earth" and the "Cambrian Explosion". These events triggered profound changes in Earth's paleoclimate and paleoenvironment, setting the stage for major geological and biological transformations (Knoll and Walter, 1992; Kirschvink et al., 1997; Hoffman et al., 1998; Hyde et al., 2000; Guo et al., 2007; Maruyama and Santhosh, 2008; 2014; Payne et al., 2009; Zhang et al., 2014; Jin et al., 2016; Li et al., 2018). During the Early Cambrian, the breakup of the Rodinia supercontinent led to extensive marine transgressions and global sea-level rise. The Sichuan Basin and its surrounding areas were influenced by these two events. During the deposition of the Qiongzhusi Formation in the Early Cambrian, this region was characterized by a semi-restricted to semi-open deep-water shelf environment. This environment remained locally anoxic for extended periods, leading to deposition of organic-rich black shale, predominantly distributed in the Mianyang-Changning faulted-sag in the Sichuan Basin (Huang et al., 2012; Li et al., 2013; Zou et al., 2015). While considerable research has investigated the depositional environment and organic matter (OM) enrichment mechanisms in the Lower Cambrian black shale of the Middle and Upper Yangtze Plate, most studies have primarily focused on provinces such as Hunan, Hubei, Guizhou and Yunnan (Wang et al., 2015; Gao et al., 2016; Zhai et al., 2018; Li et al., 2018; Fang, 2019; Zhao et al., 2020; Fu et al., 2021). In contrast, less attention has been given to the southern Sichuan Basin, particularly regarding the role of the Mianyang-Changning faulted-sag in influencing the depositional environment of Qiongzhusi Formation.

A large quantity of black shale is extensively present in the Sichuan Basin and its surroundings, particularly during the Ordovician-Silurian and the Ediacaran-Cambrian transition. Black shales are important source rocks and reservoirs for hydrocarbons, playing a crucial role in the accumulation and preservation of conventional natural gas and shale gas. In recent years, significant breakthroughs have been made in the exploration of marine shale gas in the Longmaxi Formation in the Sichuan Basin and its periphery. Commercial development of shale gas has been concentrated in large shale gas fields in Changning, Weiyuan, Zhaotong and Fuling, with proven geological reserves exceeding hundreds of billions of cubic meters (Zou et al., 2021). The Qiongzhusi Formation, also known by regional names such as the Niutitang, Shuijingtuo, and Jiulaodong formations, has also emerged as a promising target for shale gas exploration (Dong et al., 2025). Initial breakthroughs suggest that this formation could become the second commercially significant shale gas reservoir in China, following the Longmaxi Formation (He et al., 2024). Therefore, research on the depositional environments and organic matter enrichment of Lower Cambrian black shale in the Sichuan Basin is crucial for guiding shale gas exploration and development in this region.

Given the economic and scientific importance of the Qiongzhusi Formation, understanding the depositional environments and factors controlling organic matter enrichment in the southern Sichuan Basin is crucial for guiding future exploration and development efforts. However, significant discrepancies remain regarding the mechanisms controlling for organic matter enrichment. It has been suggested that factors such as paleoproductivity, depositional environment, sedimentation rate, terrigenous input, sea-level fluctuations, volcanic activity, upwelling currents and hydrothermal processes influence the organic matter enrichment (Demaison and Moore, 1980; Pedersen and Calvert, 1990; Canfield, 1994; Gallego-Torres et al., 2007; Lash et al., 2014). However, the main controlling factor for organic matter (OM) accumulation is still debated, mostly focusing on primary productivity vs redox conditions. Our study tries to figure out this problem *via* the OM enrichment in the Lower Cambrian black shale in the Sichuan Basin. Previous studies have focused on the depositional environments and controlling factors of organic matter enrichment in Lower Cambrian black shale of the Middle and Upper Yangtze Plate, but the influence of Mianyang-Changning faulted-sag have not been discussed (Wang et al., 2015; Gao et al., 2016; Yin et al., 2017; Zhai et al., 2018; Li et al., 2018; Fang, 2019; Zhao et al., 2020; Fu et al., 2021). This paper aims to conduct a comparative study of the Qiongzhusi Formation shale in the intra-faulted-sag, slope and extra-faulted-sag areas of the Mianyang-Changning faulted-sag in the southern Sichuan Basin using geochemical methods. By doing so, the depositional environment and organic matter (OM) enrichment mechanisms of the Qiongzhusi Formation shale in the southern Sichuan Basin could be further elucidated, which is of great significance to understand the distribution of organic-rich black shale.

2 Geological setting

The Yangtze Block evolved from a rift basin to a passive continental margin basin during the Ediacaran-Cambrian transition (Wang and Li, 2003), which could be divided into carbonate platform, transitional belt and slope to deep basin. The sedimentary facies are usually shallow-water carbonate platform facies, transitional facies, and deep water slope and basinal facies from the northwest to southeast (Figure 1) (Chen et al., 2009).

The studied wells are located in the Sichuan Basin, which was situated in the transitional zone between the Gondwana and Laurasia continents, located in the western part of the Upper Yangtze Block and the eastern part of the Qinghai-Tibet Plateau (Figure 1). This area has been influenced by multiple stages of thrusting and nappe from mountain-building events, resulting in typical overlapping basin topography features observed today, surrounded by a complex basin-mountain system (Li et al., 2006; Liu et al., 2011). The Qiongzhusi Formation (~520 Ma) in the Sichuan Basin and its surrounding areas has experienced multiple tectonic movements such as the Tongan, Xingkai Rift, Caledonian, Hercynian, Indosinian, Yanshan and Himalayan Movements. During the late Cambrian, the Tongan Movement caused a regional uplift of the Sichuan Basin, leading to erosion and the formation of incised valleys at the top of the Dengying Formation in the Mianyang-Changning area. The Xingkai Movement resulted in structural inversion, further extending and subsiding the incised valleys, forming the north-south trending Mianyang-Changning faulted-sag (Figure 1). The formation of this faulted-sag created accommodation space for the deposition of the Maidiping and Qiongzhusi formations black shales during the Early Cambrian. The Mianyang-Changning faulted-sag significantly controlled

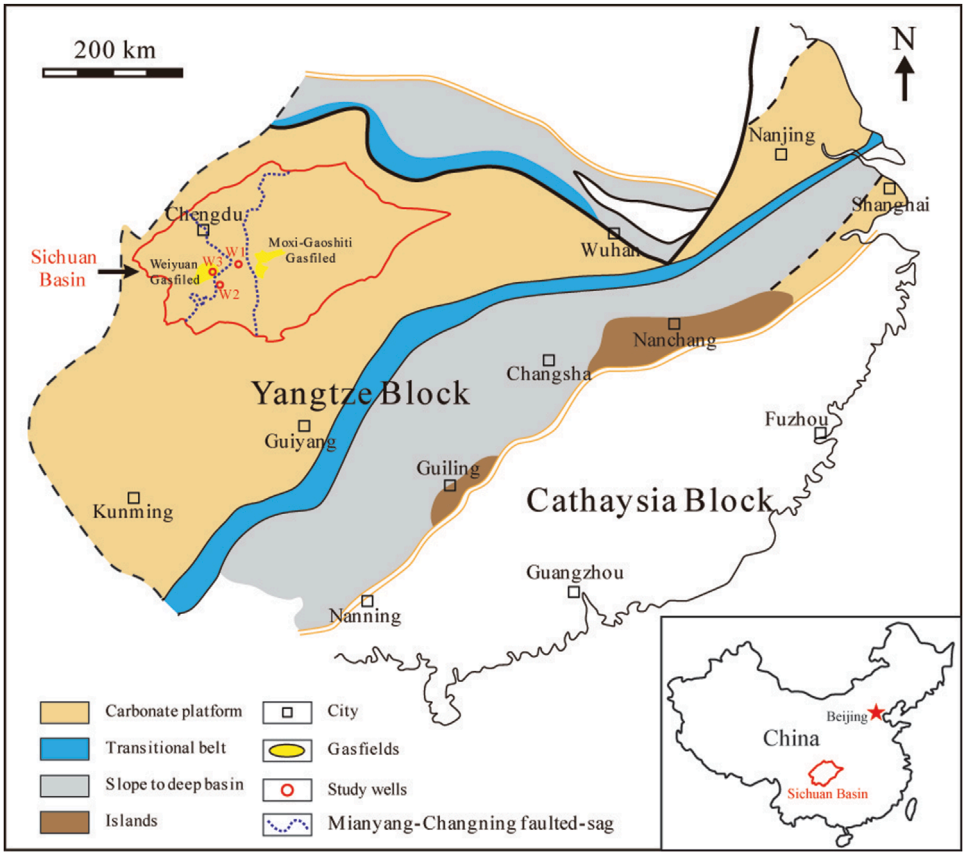

FIGURE 1
Sketch map showing the location of study area and the depositional facies and paleoenvironments of the South China Craton during the early Cambrian (modified from Gao et al., 2016).

the deposition of the Qiongzhusi Formation in the southern Sichuan Basin (Zhong et al., 2013; Wang et al., 2016). In the Sichuan Basin, the Qiongzhusi Formation shale thickens gradually from north to south, ranging from 250 to 600 m. The thickest section is found in the Changning structural zone, reaching up to 650 m. The lowermost black shale of the Qiongzhusi Formation is 60–300 m thick (Huang et al., 2012).

3 Data and methods

This study analyzed a total of 140 fresh drilling core samples from three wells (W1, W2 and W3) in the southern Sichuan Basin, located inside, on slope and outside the Mianyang-Changning faulted-sag, respectively (Figure 1). The Qiongzhusi Formation predominantly comprises black and grey shale. Vertically, it can be classified into six members (M1 through M6, from bottom to top). M1, M3 and M5 are composed of OM-enriched (TOC ≥ 2%) black shale, while members M2, M4 and M6 comprise of OM-lean (TOC < 2%) grey shale (Tables 1 and 2).

The mineral composition, major and trace elements were conducted at the Institute of Geology and Geophysics, Chinese Academy of Sciences. The mineral composition of the shale samples were determined by the X-ray diffraction (XRD) technique (D/Max-IlB, Rigaku Co. Japan). CuKa radiation (35 kV × 30 mA) and a graphic mono-chrometer for diffractedbeams were used. Major element concentrations were determined using AXIOS Minerals made by PANalytical Corporation of Holland, with analytical precision better than 1%. Trace element concentrations were determined using element inductively coupled plasma mass spectrometry (ICP-MS) from FINNIGAN MAT Company, with analytical precision better than 3%.

Enrichment factors (EF) are used to show trace metal concentrations, excluding the effects of dilution by calcium carbonate and organic matter. EF for trace elements relative to upper continental crust (UCC) (McLennan, 2001) were calculated as: $(\text{Element/Al})_{\text{sample}}/(\text{Element/Al})_{\text{UCC}}$. Excess Ba ($Ba_{xs}$) was calculated as an indicator of biogenic barium, using the equation: $Ba_{xs} = Ba_{total} - (Ba/Al)_{detr} \times Al_{sample}$ (Schoepfer et al., 2015).

The CIA can be calculated using the molar ratios of specific substances, according to the following formula:

$$CIA = Al_2O_3/(Al_2O_3 + CaO^* + Na_2O + K_2O) \times 100$$

The term CaO^* refers specifically to the CaO present in silicates. The content of CaO^* is primarily determined using the formula CaO_residual = CaO - P_2O_5 × (10/3). If CaO_residual is less than Na_2O, then CaO^* equals CaO_residual. If CaO_residual is greater than Na_2O, then CaO^* equals Na_2O (Mclennan, 1993). The CIA

TABLE 1 Average mineralogical composition of the Qiongzhusi shale in Lower Cambrian from the wells in Sichuan Basin (%).

Well	Member	Quartz	K-feldspar	Plagioclase	Calcite	Dolomite	Pyrite	Clay minerals
W1	M6	61.86	2.81	15.77	1.96	3.16	4.46	9.97
	M5	52.05	3.75	20.00	2.79	2.55	5.08	13.79
	M4	55.89	2.21	18.70	1.36	2.66	4.08	15.10
	M3	54.77	2.55	14.29	3.33	4.24	3.77	17.04
	M2	44.40	0.95	8.50	6.15	16.60	3.30	20.10
	M1	47.90	1.39	11.37	6.61	5.89	3.55	23.29
	M1~M6	54.79	2.79	16.06	3.13	4.06	4.31	14.85
W2	M6	38.49	11.81	25.21	4.68	4.57	1.58	13.67
	M5	37.73	8.43	28.95	6.94	1.19	2.00	14.76
	M4	38.87	12.88	28.72	5.39	2.37	1.50	10.26
	M3	39.87	2.93	34.93	4.56	1.28	1.00	15.44
	M2	42.59	3.33	36.14	2.72	2.38	0.67	12.16
	M1	38.83	0.00	21.71	8.14	3.97	0.00	27.35
	M1~M6	38.83	7.49	28.67	5.66	2.57	1.37	15.40
W3	M6	35.59	4.58	20.54	5.05	5.10	5.63	23.51
	M5	39.08	4.56	22.16	3.66	4.02	4.28	22.24
	M4	45.38	2.85	22.70	3.08	3.98	2.28	19.75
	M3	30.60	1.10	10.65	6.35	6.30	4.65	40.35
	M2	32.20	1.30	12.10	10.40	6.35	3.90	33.75
	M1	35.30	2.47	14.60	6.60	4.03	4.27	32.73
	M1~M6	37.31	4.00	20.15	4.76	4.65	4.65	24.47

value increases with greater chemical weathering intensity. During diagenesis, clay minerals are susceptible to potassium exchange, which requires assessing the degree of potassium exchange and correcting for it. Because plagioclase (Na and Ca) is more susceptible to weathering than potassium feldspar (K), (Nesbitt and Young, 1982), thus K and CIA need to be corrected. Nesbitt et al. (1996) proposed using an Al_2O_3-CaO + Na_2O-K_2O ternary diagram for this correction to obtain the corrected CIA*, reflecting the adjusted chemical weathering index.

4 Results

4.1 Shale lithofacies

Based on the observation of thin sections, the shale lithofacies of six members are analyzed. The black shales from M1, M3 and M5 have similar lithofacies, showing weakly laminated fine-grained mudstone with a lamina spacing ranging from 0.5 to 2 mm (Figures 2A,C,E), indicating a deep-water depositonnal environment. The grey shales from M2 and M6 show different lithofacies with weakly laminated and laminated mudstone (Figures 2B,D,F), respectively, indicating a shallow-water depositional environment. The grey shale from M4 shows homogeneous mudstone with a particle-size ranging from 20 to 50 um (Figure 2D), but appear as laminated mudstone in M6, with a lamina spacing of 0.1–0.5 mm (Figure 2F). Notably, the mud content of black shale is higher than that of grey shale, while the sand content of grey shale is higher than that of black shale, and the lamina in grey shale are more developed (Figure 2). Due to the shallower water and inceasing terrigenous input during the deposition of grey shale, a lamellar sedimentary structure with interlayers of sand and mud was formed.

TABLE 2 TOC, major element contents and geochemical parameters of the Qiongzhusi shale in Lower Cambrian from the wells in Sichuan Basin.

Sample	Member	TOC (%)	Fe (%)	Al (%)	Mn (%)	Ti (%)	Mo (ug/g)	Ti/Al	V/Cr	Ni/Co	U/Th	Mo-EF	U-EF	Ba_{xs} (ug/g)	Ba/Al	Cd/Mo	Co(ug/×Mn (%)	CIA
W1-1	M6	0.22	3.98	7.72	0.075	0.47	2.87	0.061	1.78	2.71	0.51	1.99	1.62	775	0.017	0.423	1.331	63
W1-2	M6	0.37	3.88	7.40	0.095	0.42	4.65	0.057	2.73	3.78	0.73	3.37	2.50	930	0.019	0.777	1.408	62
W1-3	M6	0.72	4.19	8.04	0.068	0.46	8.78	0.057	3.41	3.80	0.82	5.85	3.30	916	0.018	0.179	1.337	64
W1-4	M6	0.83	4.38	8.02	0.069	0.47	7.01	0.058	1.86	2.85	0.64	4.69	2.45	989	0.019	0.313	1.306	64
W1-5	M6	0.97	4.13	7.35	0.149	0.45	8.75	0.061	2.08	3.50	0.83	6.38	2.97	415	0.012	0.218	2.252	64
W1-6	M6	1.11	4.11	8.02	0.060	0.47	13.99	0.059	2.20	3.62	0.85	9.35	3.30	1,143	0.021	0.055	1.164	64
W1-7	M6	1.85	3.44	7.66	0.073	0.46	24.01	0.060	2.02	3.70	1.61	16.80	5.49	735	0.016	0.046	1.161	63
W1-8	M6	1.02	2.74	5.56	0.154	0.39	12.43	0.071	1.88	4.08	0.76	11.98	3.08	830	0.022	0.025	1.548	53
W1-9	M6	1.36	3.69	7.40	0.055	0.47	13.36	0.064	1.28	3.57	0.83	9.67	3.59	936	0.019	0.060	0.673	58
W1-10	M6	1.52	3.87	7.39	0.060	0.49	17.22	0.066	1.27	3.10	1.16	12.49	4.91	805	0.018	0.047	0.819	58
W1-11	M6	1.64	3.17	7.28	0.042	0.49	16.46	0.067	1.55	4.34	1.11	12.11	3.92	570	0.015	0.225	0.506	58
W1-12	M6	1.45	3.75	7.69	0.052	0.50	14.93	0.065	1.42	3.49	1.10	10.41	4.77	847	0.018	0.062	0.799	60
W1-13	M5	1.53	3.91	7.35	0.047	0.47	16.83	0.064	1.48	3.01	0.96	12.27	3.80	861	0.019	0.031	0.735	59
W1-14	M5	1.90	3.82	7.35	0.048	0.47	27.14	0.064	1.60	4.88	1.39	19.78	5.47	891	0.019	0.088	0.700	59
W1-15	M5	1.46	3.99	7.71	0.047	0.48	26.26	0.062	1.67	4.75	1.17	18.25	5.18	1,092	0.021	0.057	0.773	61
W1-16	M5	1.92	3.96	7.76	0.045	0.47	24.26	0.060	1.61	5.00	1.24	16.75	5.06	1,037	0.020	0.075	0.705	61
W1-17	M5	1.80	3.97	7.69	0.047	0.46	22.75	0.060	1.65	5.04	1.53	15.86	5.70	1,133	0.022	0.035	0.697	62
W1-18	M5	1.86	4.12	7.48	0.089	0.45	26.05	0.061	1.48	3.90	1.47	18.66	6.20	804	0.018	0.035	1.373	61
W1-19	M5	2.63	3.59	7.66	0.038	0.47	42.70	0.062	1.71	5.15	2.53	29.90	9.36	1,031	0.020	0.021	0.619	60
W1-20	M5	1.91	3.82	7.57	0.055	0.49	36.47	0.064	2.44	6.45	2.85	25.84	10.28	199	0.009	0.032	0.870	58
W1-21	M5	2.39	3.37	7.73	0.035	0.52	48.62	0.067	3.35	7.72	3.03	33.69	12.12	1,050	0.020	0.024	0.537	60
W1-22	M5	2.58	3.08	6.63	0.066	0.49	37.68	0.074	2.46	6.19	2.88	30.46	13.41	1,052	0.023	0.026	0.823	54

(Continued on the following page)

10.3389/feart.2025.1509332

TABLE 2 (*Continued*) TOC, major element contents and geochemical parameters of the Qiongzhusi shale in Lower Cambrian from the wells in Sichuan Basin.

Sample	Member	TOC (%)	Fe (%)	Al (%)	Mn (%)	Ti (%)	Mo (ug/g)	Ti/Al	V/Cr	Ni/Co	U/Th	Mo-EF	U-EF	Ba_{xs} (ug/g)	Ba/Al	Cd/Mo	Co(ug/×Mn (%)	CIA
W1-23	M5	4.86	3.66	6.98	0.047	0.53	80.99	0.076	5.79	12.13	4.56	62.16	22.82	997	0.021	0.063	0.704	56
W1-24	M5	3.11	3.58	7.43	0.044	0.53	49.42	0.071	1.20	3.20	1.46	35.66	7.11	965	0.020	0.007	0.782	57
W1-25	M5	1.79	4.22	7.52	0.056	0.51	25.73	0.068	1.21	3.21	0.95	18.33	4.47	1,024	0.020	0.015	0.974	57
W1-26	M5	1.95	4.12	7.84	0.039	0.50	22.53	0.064	1.44	3.90	0.98	15.41	4.09	932	0.019	0.016	0.647	59
W1-27	M4	0.16	2.91	6.22	0.079	0.53	1.32	0.084	1.11	2.63	0.18	1.14	1.07	1,216	0.026	0.188	0.648	48
W1-28	M4	0.28	3.21	6.52	0.062	0.44	1.05	0.067	1.26	3.25	0.21	0.86	0.90	978	0.022	0.167	0.392	50
W1-29	M3	2.20	4.18	6.81	0.074	0.48	36.02	0.071	11.41	6.64	1.65	28.36	7.81	856	0.019	0.045	1.170	57
W1-30	M3	3.39	3.93	6.67	0.043	0.48	54.02	0.071	1.98	6.21	4.19	43.41	20.01	942	0.021	0.018	0.705	56
W1-31	M3	2.35	3.68	6.90	0.072	0.47	26.08	0.069	12.60	7.81	2.05	20.25	9.36	1,049	0.022	0.216	1.039	58
W1-32	M3	2.50	3.45	6.29	0.044	0.44	31.78	0.070	5.98	5.21	2.31	27.06	8.88	939	0.022	0.025	0.940	59
W1-33	M3	2.70	4.85	7.43	0.037	0.52	86.00	0.070	1.72	4.17	2.18	62.06	9.59	425	0.013	0.006	0.908	63
W1-34	M3	2.64	3.63	6.73	0.057	0.43	38.28	0.064	1.48	3.54	2.53	30.47	10.39	1,182	0.024	0.010	0.877	57
W1-35	M3	2.66	3.07	6.91	0.030	0.46	41.38	0.066	15.00	7.43	2.80	32.08	9.80	722	0.017	0.046	0.438	59
W1-36	M3	2.21	2.95	6.65	0.039	0.46	26.31	0.069	5.61	6.47	1.48	21.19	6.25	1,121	0.024	0.043	0.543	58
W1-37	M3	2.82	3.49	6.90	0.045	0.45	28.04	0.065	14.42	7.84	2.46	21.79	8.63	639	0.016	0.220	0.757	60
W1-38	M3	4.47	3.15	6.18	0.051	0.42	43.35	0.068	1.80	5.69	3.16	37.61	14.56	1,328	0.028	0.017	0.769	57
W1-39	M3	4.81	2.91	4.81	0.067	0.33	36.65	0.068	15.87	14.15	4.61	40.82	19.67	1,210	0.032	0.085	0.872	59
W1-40	M3	5.40	2.16	5.68	0.029	0.36	40.88	0.063	1.55	3.77	3.14	38.59	11.85	1736	0.037	0.008	0.354	59
W1-41	M3	4.42	3.23	5.48	0.071	0.36	41.63	0.066	1.96	6.85	3.07	40.68	12.27	1,642	0.037	0.021	1.120	55
W1-42	M2	3.13	2.94	7.60	0.025	0.48	29.52	0.063	1.45	4.80	1.99	20.82	6.52	542	0.014	0.018	0.493	60
W1-43	M2	2.76	2.96	6.98	0.073	0.45	22.31	0.065	1.28	3.28	1.31	17.13	4.79	1,201	0.024	0.036	1.186	56

(Continued on the following page)

10.3389/feart.2025.1509332

TABLE 2 (*Continued*) TOC, major element contents and geochemical parameters of the Qiongzhusi shale in Lower Cambrian from the wells in Sichuan Basin.

Sample	Member	TOC (%)	Fe (%)	Al (%)	Mn (%)	Ti (%)	Mo (ug/g)	Ti/Al	V/Cr	Ni/Co	U/Th	Mo-EF	U-EF	Ba_{xs} (ug/g)	Ba/Al	Cd/Mo	Co(ug/×Mn (%)	CIA
W1-44	M1	4.53	2.62	6.09	0.019	0.35	33.68	0.058	2.26	12.66	2.63	29.62	10.58	1,496	0.031	0.513	0.179	63
W1-45	M1	5.02	1.20	3.51	0.012	0.21	22.38	0.059	4.51	16.31	3.62	34.18	13.72	2,388	0.075	0.422	0.075	60
W1-46	M1	3.17	1.10	4.95	0.023	0.18	37.67	0.037	20.56	19.05	5.40	40.78	22.52	657	0.020	0.324	0.117	64
W1-47	M1	5.09	1.46	3.58	0.024	0.22	30.82	0.063	13.25	18.95	5.27	46.09	24.52	1931	0.061	0.264	0.139	60
W2-1	M6	0.67	4.38	8.90	0.049	0.48	7.93	0.054	2.12	2.80	0.64	4.78	2.27	452	0.012	0.146	1.147	65
W2-2	M6	0.71	4.02	8.33	0.060	0.46	5.65	0.055	2.84	3.28	0.73	3.64	2.48	626	0.014	0.214	1.155	64
W2-3	M6	0.81	4.26	8.41	0.064	0.47	4.69	0.056	2.54	3.78	0.60	2.99	2.03	635	0.014	0.197	1.306	64
W2-4	M6	1.14	4.02	8.37	0.073	0.48	5.11	0.057	2.26	3.18	0.65	3.27	2.39	554	0.013	0.173	1.385	64
W2-5	M6	1.11	4.26	8.97	0.058	0.47	6.41	0.052	1.94	5.43	0.83	3.83	3.22	550	0.013	0.082	1.266	64
W2-6	M6	0.37	2.75	7.19	0.047	0.50	2.42	0.070	1.42	3.79	0.34	1.80	1.54	476	0.013	0.105	0.545	55
W2-7	M6	0.40	3.19	7.75	0.041	0.53	2.91	0.068	1.37	3.01	0.33	2.02	1.51	394	0.012	0.147	0.515	58
W2-8	M6	0.39	2.83	7.47	0.047	0.53	2.79	0.070	1.35	2.95	0.38	2.00	1.69	335	0.011	0.145	0.546	57
W2-9	M6	0.50	3.47	7.76	0.052	0.52	4.42	0.067	1.43	3.22	0.40	3.05	1.65	369	0.012	0.108	0.802	58
W2-10	M6	0.58	3.28	7.84	0.045	0.53	4.69	0.067	1.39	2.72	0.37	3.21	1.58	423	0.012	0.048	0.605	58
W2-11	M6	0.68	3.43	7.75	0.053	0.50	5.39	0.064	1.39	2.84	0.53	3.73	2.04	497	0.013	0.085	0.730	58
W2-12	M6	0.91	3.44	7.61	0.052	0.48	9.12	0.063	1.48	3.61	0.83	6.42	2.97	529	0.014	0.026	0.689	57
W2-13	M5	1.29	3.65	7.92	0.043	0.49	15.38	0.062	1.49	3.51	0.93	10.41	3.57	633	0.015	0.045	0.658	58

(Continued on the following page)

10.3389/feart.2025.1509332

TABLE 2 (*Continued*) TOC, major element contents and geochemical parameters of the Qiongzhusi shale in Lower Cambrian from the wells in Sichuan Basin.

Sample	Member	TOC (%)	Fe (%)	Al (%)	Mn (%)	Ti (%)	Mo (ug/g)	Ti/Al	V/Cr	Ni/Co	U/Th	Mo-EF	U-EF	Ba_{xs} (ug/g)	Ba/Al	Cd/Mo	Co(ug/g) × Mn (%)	CIA
W2-14	M5	1.13	3.60	7.73	0.051	0.47	16.07	0.061	1.58	4.27	0.89	11.14	3.45	730	0.016	0.022	0.773	58
W2-15	M5	1.07	3.54	7.87	0.046	0.50	12.64	0.063	1.56	3.58	0.73	8.61	2.95	695	0.016	0.040	0.748	59
W2-16	M5	1.24	3.66	7.80	0.048	0.51	10.28	0.065	1.52	3.44	0.85	7.07	3.50	708	0.016	0.028	0.789	58
W2-17	M5	1.11	3.72	7.93	0.044	0.49	13.41	0.062	2.37	4.52	1.07	9.06	4.37	714	0.016	0.048	0.750	59
W2-18	M5	1.37	3.09	7.61	0.047	0.49	37.55	0.064	3.45	5.44	1.62	26.44	6.36	764	0.017	0.009	0.646	56
W2-19	M5	2.14	3.82	7.06	0.068	0.53	25.21	0.075	1.53	5.28	1.56	19.12	7.58	600	0.015	0.011	1.133	53
W2-20	M5	2.83	3.60	6.99	0.042	0.50	28.68	0.071	2.61	9.08	1.69	21.98	8.06	549	0.015	0.039	0.618	52
W2-21	M5	1.77	3.01	6.79	0.068	0.51	18.79	0.075	2.16	4.80	1.10	14.83	5.26	403	0.013	0.014	0.833	50
W2-22	M5	2.21	5.55	7.11	0.040	0.48	36.19	0.068	1.27	5.05	1.32	27.28	6.23	460	0.013	0.007	0.615	56
W2-23	M5	1.90	3.82	7.60	0.044	0.52	15.75	0.068	1.27	2.94	0.98	11.11	4.33	442	0.013	0.010	0.693	57
W2-24	M5	1.56	3.97	7.20	0.070	0.51	10.31	0.071	1.21	2.39	0.49	7.68	2.37	485	0.014	0.074	1.161	56
W2-25	M5	1.62	4.05	7.61	0.047	0.50	15.34	0.065	1.35	3.29	0.72	10.81	3.41	493	0.013	0.037	0.854	58
W2-26	M5	1.56	3.54	7.13	0.055	0.51	9.02	0.072	1.39	3.45	0.61	6.78	2.87	461	0.013	0.054	0.823	55
W2-27	M4	1.11	4.18	7.75	0.046	0.55	12.71	0.071	1.43	3.43	0.81	8.79	3.69	400	0.012	0.032	0.865	57
W2-28	M4	0.91	3.96	7.81	0.046	0.51	12.15	0.065	2.39	3.88	0.59	8.34	2.56	456	0.013	0.016	0.857	58
W2-29	M4	0.97	3.91	7.44	0.047	0.51	9.62	0.069	3.24	3.51	0.62	6.93	2.68	461	0.013	0.087	0.854	58
W2-30	M4	1.14	4.74	7.61	0.044	0.50	17.51	0.066	1.36	2.81	0.76	12.33	3.14	388	0.012	0.014	0.872	58
W2-31	M3	1.40	3.80	7.90	0.042	0.50	17.36	0.063	6.84	4.30	1.50	11.78	6.24	365	0.011	0.066	0.693	58
W2-32	M3	1.46	4.12	7.82	0.039	0.52	20.54	0.066	4.68	4.88	1.01	14.07	4.63	490	0.013	0.039	0.722	58
W2-33	M3	0.68	4.05	11.38	0.028	0.52	14.34	0.046	3.76	5.10	0.74	6.75	3.04	933	0.015	0.040	0.429	67

(Continued on the following page)

10.3389/feart.2025.1509332

TABLE 2 (*Continued*) TOC, major element contents and geochemical parameters of the Qiongzhusi shale in Lower Cambrian from the wells in Sichuan Basin.

Sample	Member	TOC (%)	Fe (%)	Al (%)	Mn (%)	Ti (%)	Mo (ug/g)	Ti/Al	V/Cr	Ni/Co	U/Th	Mo-EF	U-EF	Ba_{xs} (ug/g)	Ba/Al	Cd/Mo	Co(ug/ × Mn (%)	CIA
W2-34	M3	1.86	4.60	7.59	0.054	0.50	28.62	0.066	1.50	5.44	1.89	20.20	8.52	535	0.014	0.022	0.978	58
W2-35	M3	2.01	3.92	7.44	0.041	0.49	30.54	0.065	1.34	2.70	0.94	22.01	4.12	540	0.014	0.006	0.751	58
W2-36	M3	3.34	3.81	6.88	0.068	0.46	42.77	0.066	11.57	7.10	2.61	33.30	12.87	687	0.017	0.011	1.219	56
W2-37	M3	3.15	3.67	5.66	0.064	0.41	23.79	0.072	2.13	7.67	1.62	22.53	8.95	695	0.019	0.040	0.967	56
W2-38	M3	3.99	3.61	6.61	0.048	0.40	39.76	0.061	1.53	4.39	2.81	32.23	10.58	712	0.018	0.006	0.781	57
W2-39	M2	0.92	3.12	6.95	0.078	0.46	9.08	0.066	1.21	2.38	0.28	7.00	1.20	721	0.017	0.018	1.339	57
W2-40	M2	0.39	3.79	9.22	0.039	0.50	6.39	0.054	1.71	3.03	0.44	3.71	1.89	683	0.014	0.024	0.778	63
W2-41	M2	0.31	1.43	6.26	0.093	0.37	1.04	0.060	1.29	2.18	0.23	0.89	0.77	729	0.018	0.075	0.634	52
W2-42	M1	2.65	3.09	8.00	0.037	0.44	37.24	0.055	11.21	5.90	2.14	24.94	9.10	799	0.017	0.007	0.704	60
W2-43	M1	2.77	3.42	6.76	0.036	0.39	26.60	0.057	4.78	9.11	2.35	21.10	10.19	905	0.020	0.012	0.666	59
W2-44	M1	3.67	3.09	6.96	0.033	0.40	67.01	0.057	4.28	8.50	3.61	51.58	16.24	952	0.021	0.011	0.591	60
W2-45	M1	3.35	2.69	6.41	0.031	0.36	38.86	0.056	16.36	9.32	2.54	32.50	10.63	1,007	0.023	0.030	0.541	61
W2-46	M1	4.11	2.63	7.01	0.035	0.38	101.36	0.055	1.80	7.63	3.18	77.51	10.59	1,076	0.022	0.043	0.456	60
W3-1	M6	0.51	3.56	7.21	0.051	0.36	11.68	0.050	2.43	3.70	0.98	8.69	3.06	1,019	0.021	0.097	0.850	60
W3-2	M6	0.95	3.94	7.84	0.055	0.39	7.48	0.049	1.95	2.72	0.69	5.11	2.22	1,335	0.024	0.173	0.952	62
W3-3	M6	0.74	4.50	8.15	0.059	0.45	6.24	0.055	2.11	2.60	0.63	4.11	1.96	821	0.017	0.091	1.099	64
W3-4	M6	0.80	4.06	7.87	0.070	0.47	4.67	0.059	3.04	3.57	0.66	3.18	2.31	973	0.019	0.233	1.142	64
W3-5	M6	0.73	4.83	7.53	0.043	0.48	11.26	0.064	3.19	4.29	0.67	8.02	0.90	1,154	0.022	0.220	0.856	59
W3-6	M6	0.69	4.56	8.26	0.063	0.45	4.01	0.054	2.40	3.12	0.38	2.60	1.13	787	0.016	0.052	1.093	65
W3-7	M6	1.25	4.48	8.56	0.055	0.42	6.65	0.049	2.41	4.41	0.67	4.16	2.85	387	0.011	0.107	0.952	65
W3-8	M6	0.64	2.15	5.97	0.073	0.42	3.14	0.070	0.95	4.29	0.56	2.82	2.70	847	0.021	0.292	0.613	51

(Continued on the following page)

10.3389/feart.2025.1509332

TABLE 2 (*Continued*) TOC, major element contents and geochemical parameters of the Qiongzhusi shale in Lower Cambrian from the wells in Sichuan Basin.

Sample	Member	TOC (%)	Fe (%)	Al (%)	Mn (%)	Ti (%)	Mo (ug/g)	Ti/Al	V/Cr	Ni/Co	U/Th	Mo-EF	U-EF	Ba_{xs} (ug/g)	Ba/Al	Cd/Mo	Co(ug/x Mn (%)	CIA
W3-9	M6	1.09	2.91	7.10	0.047	0.47	5.14	0.066	1.36	3.47	0.41	3.88	1.98	508	0.014	0.068	0.465	54
W3-10	M6	0.44	2.77	7.13	0.043	0.50	3.22	0.071	1.16	3.02	0.46	2.42	1.87	447	0.013	0.148	0.493	55
W3-11	M6	0.38	2.84	6.96	0.050	0.47	2.86	0.068	1.27	3.05	0.34	2.20	1.29	1,503	0.028	0.218	0.586	54
W3-12	M6	0.50	2.84	6.35	0.055	0.45	3.71	0.072	1.28	3.03	0.59	3.13	2.20	408	0.013	0.116	0.535	51
W3-13	M6	0.44	3.09	6.79	0.057	0.46	8.51	0.067	4.09	3.48	0.87	6.72	2.78	1,073	0.023	0.252	1.017	55
W3-14	M6	0.36	2.77	6.39	0.060	0.46	3.39	0.071	1.37	3.37	0.42	2.84	2.14	392	0.013	0.194	0.576	54
W3-15	M6	0.58	3.07	7.05	0.055	0.47	4.94	0.067	1.24	3.12	0.41	3.76	1.43	798	0.018	0.095	0.565	55
W3-16	M6	0.50	2.95	6.75	0.054	0.44	3.43	0.065	1.42	2.69	0.47	2.72	1.85	495	0.014	0.123	0.509	53
W3-17	M6	0.76	3.05	6.77	0.051	0.47	5.08	0.069	1.47	3.07	0.57	4.03	2.13	578	0.015	0.112	0.499	54
W3-18	M6	0.45	3.86	7.38	0.068	0.47	14.52	0.064	1.47	3.38	0.77	10.55	1.82	695	0.016	0.017	0.836	58
W3-19	M6	1.01	4.17	7.51	0.052	0.45	14.19	0.060	1.74	2.69	0.78	10.14	2.12	948	0.019	0.017	0.660	59
W3-20	M5	1.26	4.02	7.56	0.050	0.46	21.21	0.061	2.68	4.88	1.59	15.03	2.62	776	0.017	0.011	0.608	59
W3-21	M5	1.60	3.78	7.49	0.041	0.48	36.97	0.064	2.17	4.82	2.10	26.45	4.45	799	0.018	0.013	0.505	58
W3-22	M5	1.41	3.52	7.48	0.046	0.46	17.35	0.062	2.98	5.20	1.16	12.42	1.61	811	0.018	0.010	0.447	58
W3-23	M5	1.72	3.06	6.58	0.044	0.47	21.84	0.072	3.46	6.61	1.55	17.79	3.72	1,401	0.028	0.031	0.133	51
W3-24	M5	3.06	4.09	6.94	0.041	0.49	44.40	0.071	1.47	8.88	2.99	34.27	9.00	673	0.017	0.343	0.635	57
W3-25	M5	2.67	3.16	6.87	0.052	0.48	26.24	0.070	3.35	7.10	1.36	20.47	9.14	759	0.018	0.073	0.634	54
W3-26	M5	2.77	3.40	6.93	0.048	0.48	32.12	0.070	1.99	5.55	1.39	24.84	9.01	655	0.016	0.039	0.757	54
W3-27	M5	3.01	5.51	6.94	0.047	0.45	77.12	0.065	1.09	4.73	4.35	59.57	10.62	667	0.016	0.005	0.699	57
W3-28	M5	3.40	3.54	7.02	0.044	0.49	31.17	0.070	2.61	5.47	1.58	23.80	9.88	516	0.014	0.047	0.757	54
W3-29	M5	2.18	3.94	7.46	0.049	0.49	17.81	0.066	1.28	3.06	3.85	12.80	2.88	651	0.016	0.030	0.816	56

(Continued on the following page)

10.3389/feart.2025.1509332

TABLE 2 (*Continued*) TOC, major element contents and geochemical parameters of the Qiongzhusi shale in Lower Cambrian from the wells in Sichuan Basin.

Sample	Member	TOC (%)	Fe (%)	Al (%)	Mn (%)	Ti (%)	Mo (ug/g)	Ti/Al	V/Cr	Ni/Co	U/Th	Mo-EF	U-EF	Ba_{xs} (ug/g)	Ba/Al	Cd/Mo	Co(ug/g) × Mn (%)	CIA
W3-30	M5	1.62	3.85	7.05	0.059	0.47	13.27	0.066	1.33	2.18	0.55	10.09	0.92	662	0.016	0.011	0.664	56
W3-31	M5	1.61	4.02	7.09	0.059	0.47	11.34	0.067	1.49	3.15	0.58	8.57	1.01	644	0.016	0.010	0.678	54
W3-32	M5	1.60	3.90	7.35	0.049	0.50	12.24	0.068	2.31	4.60	0.67	8.93	3.25	488	0.013	0.033	0.690	55
W3-33	M5	1.34	3.85	6.95	0.068	0.49	12.67	0.070	1.52	3.53	0.56	9.77	3.03	251	0.010	0.039	1.127	55
W3-34	M5	1.44	4.21	7.46	0.063	0.51	12.20	0.069	1.15	2.30	0.60	8.76	3.22	244	0.010	0.050	1.264	58
W3-35	M5	1.62	4.14	7.58	0.061	0.49	12.17	0.065	1.25	3.01	0.53	8.60	2.43	535	0.014	0.019	0.901	58
W3-36	M5	1.77	4.87	8.17	0.051	0.53	22.20	0.065	2.95	5.60	1.12	14.56	4.39	425	0.012	0.007	0.946	64
W3-37	M4	0.20	2.79	6.16	0.129	0.45	0.52	0.072	1.24	2.46	0.21	0.45	1.12	583	0.016	0.197	0.856	49
W3-38	M4	0.36	2.63	6.06	0.050	0.40	0.44	0.067	1.35	2.79	0.24	0.39	1.00	652	0.018	0.360	0.278	47
W3-39	M4	1.20	6.80	9.29	0.032	0.57	22.34	0.062	2.05	2.87	0.81	12.88	2.82	357	0.011	0.004	1.024	71
W3-40	M4	1.33	4.11	7.56	0.038	0.47	22.18	0.062	8.18	4.97	2.59	15.73	3.81	264	0.010	0.031	0.640	63
W3-41	M3	2.84	3.53	7.21	0.043	0.44	47.95	0.061	2.90	8.64	2.82	35.66	14.24	711	0.017	0.025	0.879	58
W3-42	M3	3.20	3.21	5.87	0.059	0.38	33.92	0.065	1.64	8.58	3.24	30.97	16.92	756	0.020	0.007	0.728	57
W3-43	M2	0.90	2.12	7.62	0.052	0.30	2.80	0.039	1.19	4.65	0.56	1.97	2.43	98	0.008	0.079	0.331	57
W3-44	M2	1.09	3.38	7.97	0.049	0.45	18.22	0.056	2.65	5.04	1.40	12.25	5.78	719	0.016	0.007	0.627	61
W3-45	M1	2.65	2.58	6.79	0.039	0.38	16.12	0.057	6.29	6.57	1.79	12.73	5.63	599	0.016	0.254	0.514	58
W3-46	M1	2.23	2.68	7.29	0.036	0.40	18.09	0.055	12.70	6.76	2.45	13.30	4.93	413	0.013	0.142	0.514	60
W3-47	M1	3.05	2.94	7.23	0.032	0.39	33.82	0.054	13.99	8.27	3.90	25.07	10.80	901	0.019	0.145	0.449	59

10.3389/feart.2025.1509332

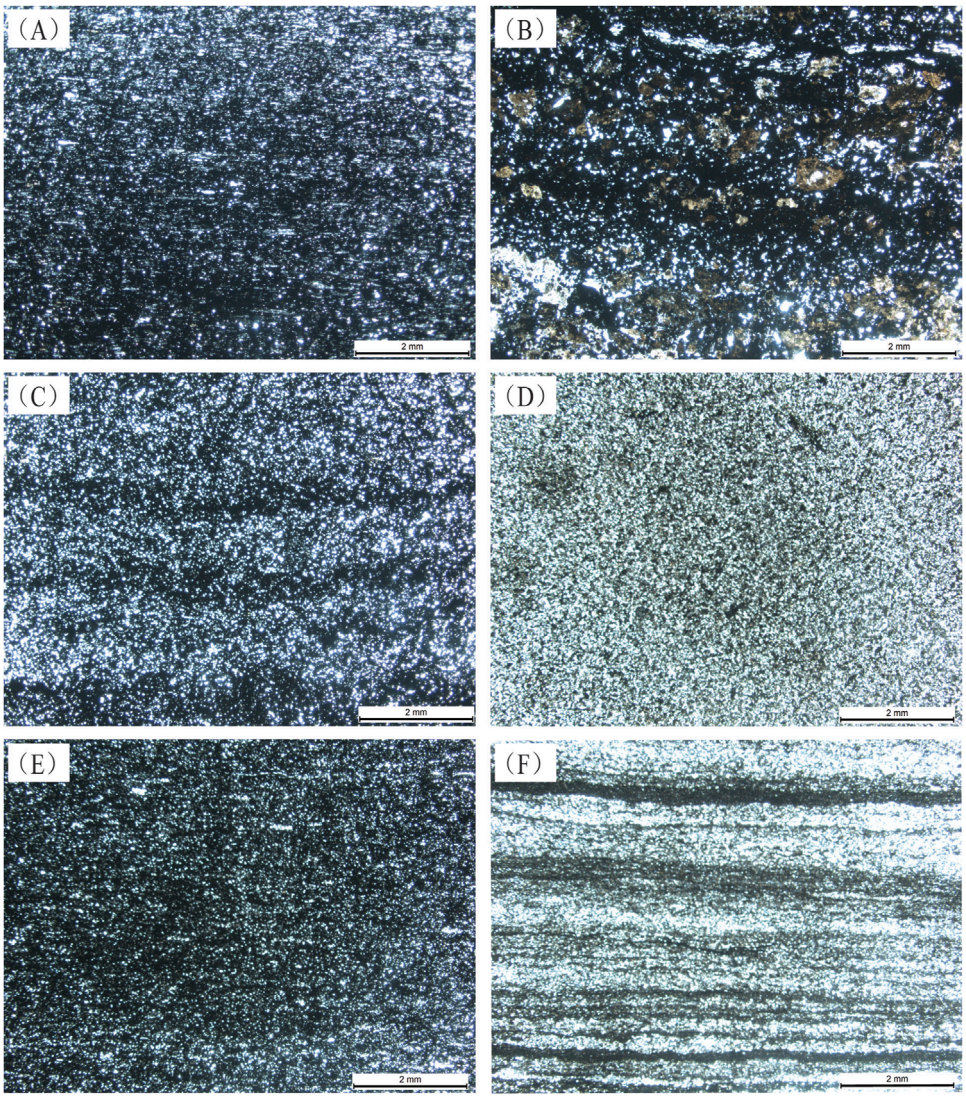

FIGURE 2
Thin sections from Well W1 showing shale lithofacies. **(A)** Weakly laminated black shale from Member 1. **(B)** Weakly laminated grey shale from Member 2. **(C)** Weakly laminated black shale from Member 3. **(D)** Homogeneous mudstone from Member 4. **(E)** Weakly laminated black shale from Member 5. **(F)** Laminated grey shale from Member 6.

4.2 Mineral compositions

Minerals in the studied samples consist of quartz, K-feldspar, plagioclase, calcite, dolomite, pyrite and clay minerals. Quartz, feldspar (K-feldspar + plagioclase) and clay minerals are the dominant components. There are clear distribution patterns of the shale mineral composition from Well W1 to W3 (Table 1). For example, the quartz content gradually decreases from W1 to W3, accounting for average of 54.79%, 38.83% and 37.31% of total mineral content, respectively (Table 1). Conversely, the clay minerals content gradually increases from W1 to W3, accounting for 14.85%, 15.40% and 24.47% of minerals on average, respectively (Table 1). These findings indicate that the water depth was gradually shallower from the interior of the faulted-sag to its exterior, resulting in the increase of terrigenous input, with a decrease in quartz content, and an increase in clay mineral content.

4.3 Total organic carbon contents

The total organic carbon (TOC) analysis results indicate significant lateral and vertical variations (Table 2). Laterally, the highest TOC content is observed in Well W1 located within the faulted-sag (average = 2.37%), followed by Well W2 on the slope of the faulted-sag (average = 1.55%), and Well W3, outside the faulted-sag, showing the lowest TOC content (average = 1.40%) (Table 2). These trends suggest a strong influence of the faulted-sag on organic matter deposition and preservation. The higher TOC content within the faulted-sag may reflect anoxic conditions and limited sediment dilution in this area. Within each well, the TOC content is notably higher in the black shale (M1, M3 and M5) compared to the grey shale (M2, M4 and M6) (Table 2). For instance, in Well W1, the average TOC values for M1, M3 and M5 are 4.45%, 3.27% and 2.26%, respectively, while M2, M4, M6 exhibit lower TOC averages of 2.95%, 0.22% and 1.09%, respectively. These findings suggest episodic variations in

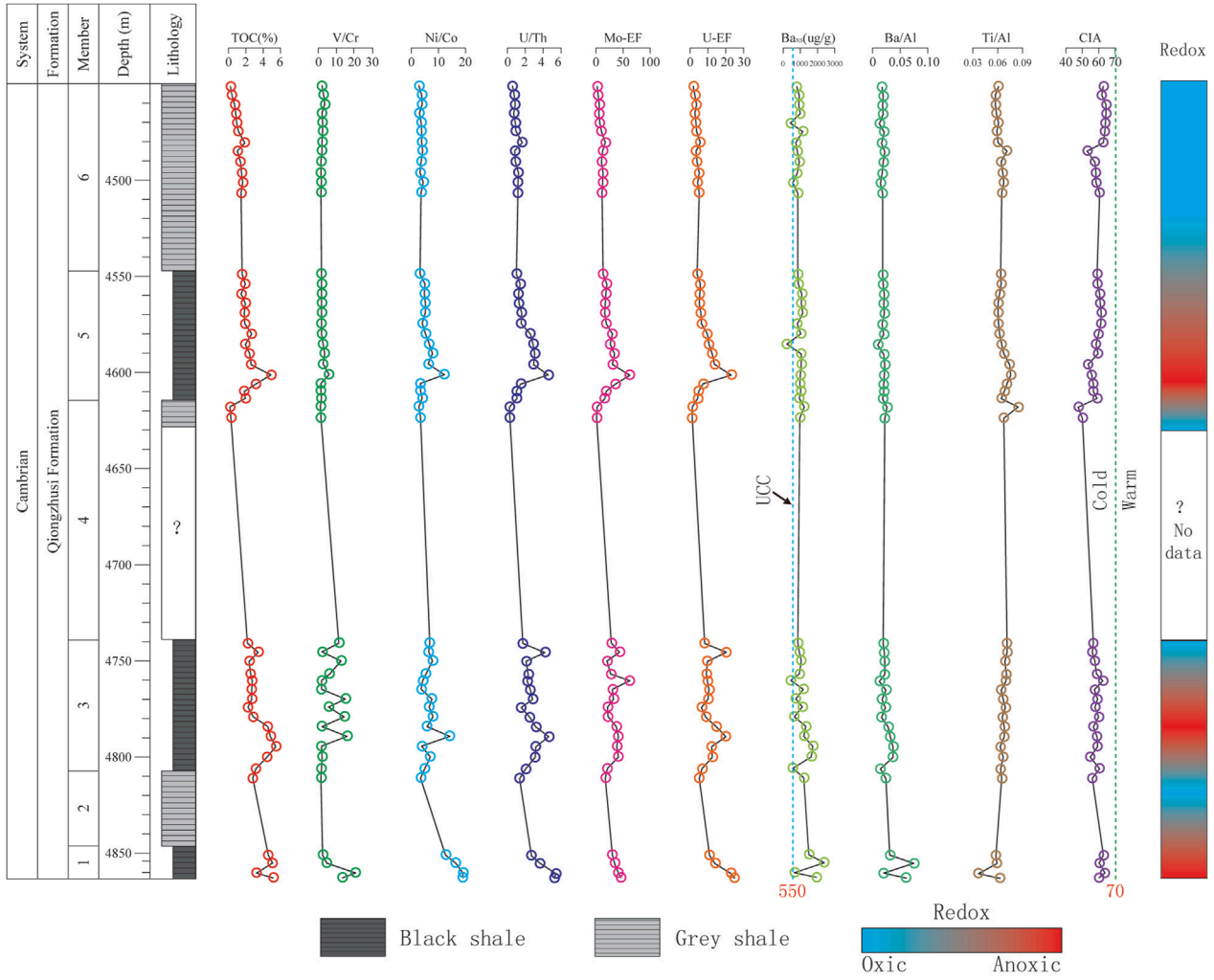

FIGURE 3
Vertical variations of TOC, V/Cr, Ni/Co, U/Th, Mo-EF, U-EF, Ba_{xs}, Ba/Al, Ti/Al and CIA of the Qiongzhusi Formation shale in the Lower Cambrian from the Well W1 in the Southern Sichuan Basin. Dashed blue line represents the upper continental crust (UCC) average. Dashed green line represents the boundary to separate cold from warm climate.

organic matter productivity and preservation conditions, with black shale likely corresponding to periods of enhanced organic productivity or restricted depositional environments.

4.4 Element variations

The analysis of major elements in the Qiongzhusi Formation shale indicates a dominance of SiO_2, TiO_2 and Fe_2O_3, with minimal variations across the studied wells (Table 2). In Well W1, the average contents of SiO_2, Al_2O_3 and Fe_2O_3 are 67.01%, 12.99% and 4.91%, respectively. In Well W2, SiO_2 content is slightly lower at 65.42%, while Al_2O_3 and Fe_2O_3 average 14.38% and 5.20%, respectively. Well W3 shows a further reduction in SiO_2 (60.45%) and slightly elevated levels of Al_2O_3 (13.65%) and Fe_2O_3 (5.17%). SiO_2 content exhibits a gradual decrease from the interior to the exterior of the faulted-sag. These trends indicate a progressive decrease in silica content from the faulted-sag interior to its exterior, likely linked to sediment input variations or diagenetic processes.

The trace element analysis reveals enrichment in several key elements, including Ba, V, Cr, Zn, Sr, and Rb, with Ba being particularly abundant (Table 2). Average Ba concentrations are highest in Well W1 (1,473 μg/g), followed by Well W3 (1,179 μg/g) and Well W2 (1,118 μg/g). All values significantly exceed the UCC average of 550 μg/g. Elements such as Mo, U, and V consistently exceed UCC levels across the wells, suggesting persistent anoxic conditions conducive to organic matter preservation. High Ba levels suggest high primary biogenic productivity, supporting the TOC trends observed in black shale.

5 Discussion

5.1 Paleo-redox conditions

Trace elements such as U, V, Cr, Th, Mo, Ni, Co along with ratios like U/Th, Ni/Co, V/Cr, V/Sc, V/(V + Ni) are widely used to infer redox conditions (Emerson and Huested, 1991; Jones

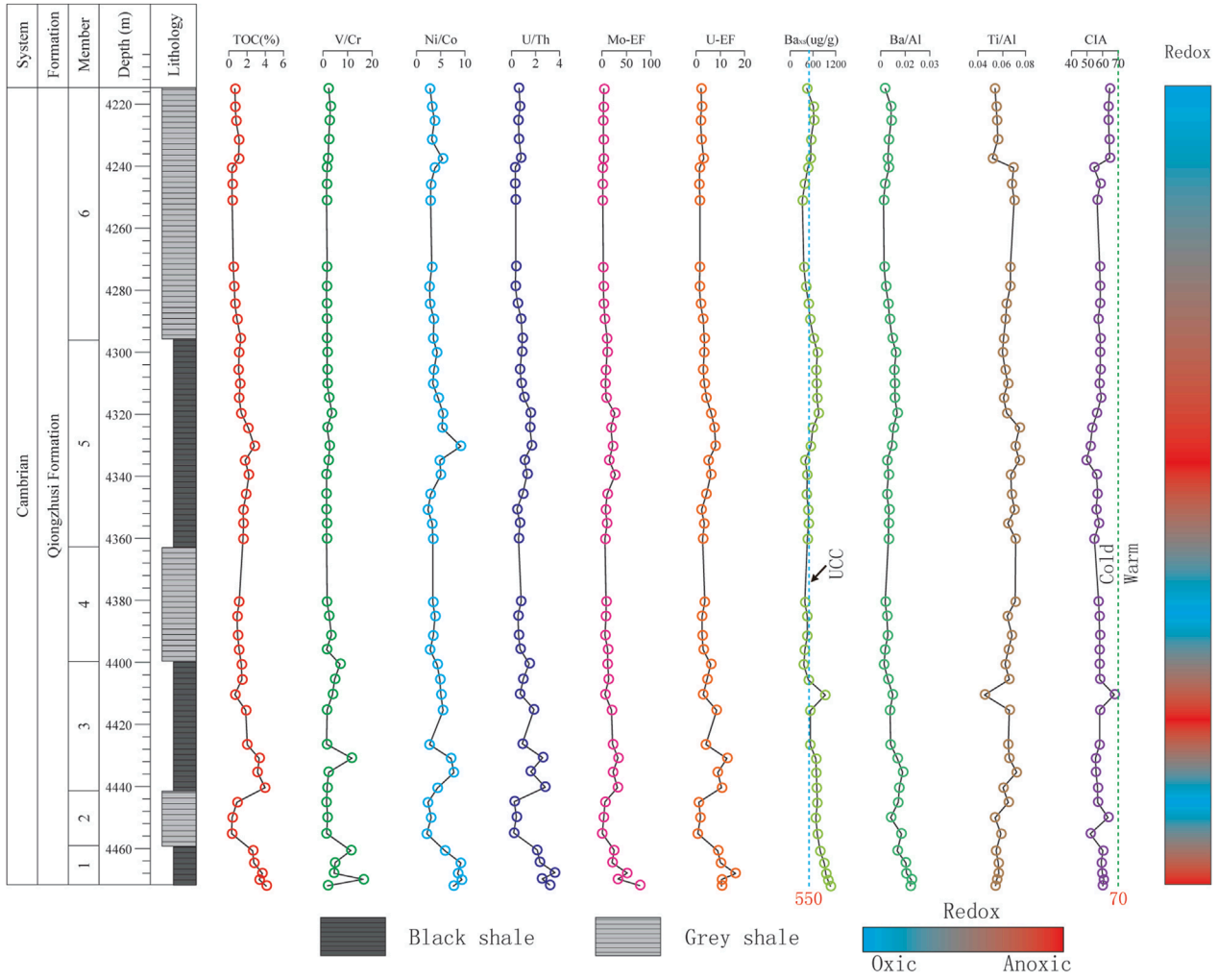

FIGURE 4
Vertical variations of TOC, V/Cr, Ni/Co, U/Th, Mo-EF, U-EF, Ba_{xs}, Ba/Al, Ti/Al and CIA of the Qiongzhusi Formation shale in the Lower Cambrian from the Well W2 in the Southern Sichuan Basin. Dashed blue line represents the upper continental crust (UCC) average. Dashed green line represents the boundary to separate cold from warm climate.

and Manning, 1994; Li et al., 2018; Liu et al., 2021; Pipe et al., 2025). Previous studies suggest that V/Cr < 2.00 indicates oxic conditions; 2.00 < V/Cr < 4.25 suggests suboxic conditions; and V/Cr > 4.25 indicates anoxic conditions (Jones and Manning, 1994). Similarly, Ni/Co < 5.00 indicates oxic conditions; 5.00 < Ni/Co < 7.00 suggests suboxic conditions; and Ni/Co > 7.00 indicates anoxic conditions (Jones and Manning, 1994). Besides, U/Th < 0.75 indicates oxic conditions; 0.75 < U/Th < 1.25 suggests suboxic conditions; and U/Th > 1.25 indicates anoxic conditions (Tonger Liu and Xu, 2004).

Based on the values of V/Cr, Ni/Co and U/Th, significant differences in redox conditions are observed among the Qiongzhusi Formation shale from the three wells (W1, W2 and W3) located in different tectonic settings. Overall, the black shale (M1, M3 and M5) exhibit a stronger reducing (anoxic-suboxic) conditions compared to the grey shale (M2, M4 and M6), which suggest a suboxic-oxic enviroment (Figures 3–5). Among the wells, Well W1, located inside the faulted-sag, exhibits the strongest reducing (anoxic) conditions (Table 2). Well W2 on the slope of the faulted-sag shows slightly lower values (e.g., for M1, average values of V/Cr, Ni/Co and U/Th are 7.69, 8.09 and 2.76, respectively) (Table 2). The Well W3, located outside the faulted-sag, reflects a moderate reducing environment (Table 2). Thus, the redox conditions were significantly influenced by the Mianyang-Changning configuration.

5.2 Water mass circulation

Trace elements such U and Mo are often used to study the degree of water mass restriction in modern and ancient marine environments. In oxic waters, both U and Mo exist in stable high-valence Species (U^{6+} and Mo^{6+}), while in anoxic environments, they are reduced to low-valence Species (U^{4+} and Mo^{4+}), leading to precipitation and enrichment in sediments (Algeo and Tribovillard, 2009; Tribovillard et al., 2012). However, the

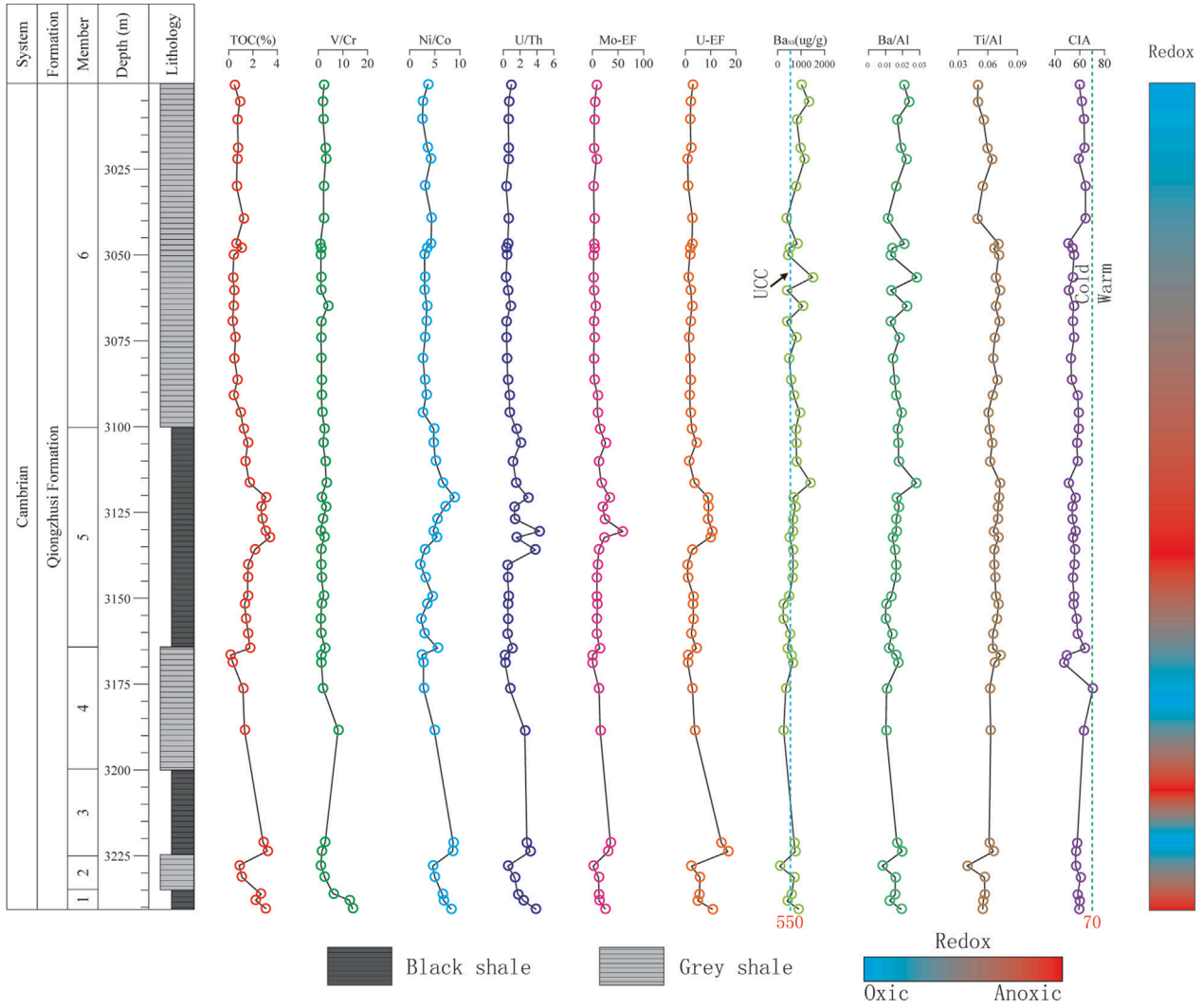

FIGURE 5
Vertical variations of TOC, V/Cr, Ni/Co, U/Th, Mo-EF, U-EF, Ba_{xs}, Ba/Al, Ti/Al and CIA of the Qiongzhusi Formation shale in the Lower Cambrian from the Well W3 in the Southern Sichuan Basin. Dashed blue line represents the upper continental crust (UCC) average. Dashed green line represents the boundary to separate cold from warm climate.

enrichment mechanisms of U and Mo are different. The uptake of U by sediments begins at the redox boundary between Fe (III) and Fe (II), whereas the uptake of Mo requires the presence of H_2S (Zheng et al., 2000). Therefore, U begins to accumulate at relatively shallow-water depths and under weaker reducing conditions, meaning the uptake of U by sediments occurs earlier than that of Mo (Algeo and Tribovillard, 2009). Secondly, Mn and Fe hydroxides can act as carriers to adsorb Mo from seawater, thereby facilitating its incorporation into sediments, while U remains unaffected (Algeo and Lyons, 2006; Algeo and Tribovillard, 2009). Previous studies have used the Mo/TOC ratio and the U-Mo covariation patterns to assess the degree of water mass restriction (Algeo and Lyons, 2006; Rowe et al., 2008; Algeo and Maynard, 2008; Algeo and Tribovillard, 2009; Tribovillard et al., 2012; Zou et al., 2015; Wu et al., 2017; Li et al., 2017). The uptake of authigenic Mo and U may be influlenced by benthic redox condition, particulate shuttles and changes in the aqueous Mo/U ratio (Algeo and Tribovillard, 2009). Consequently, the U-Mo covariation pattern can simultaneously indicate both water mass restriction and the redox conditions of marine basins (Algeo and Lyons, 2006; Algeo and Tribovillard, 2009). Studies of modern marine basins have established three types of U-Mo covariation patterns corresponding to non-restricted, weakly restricted and strongly restricted marine environments (Tribovillard et al., 2012).

The Mo vs TOC crossplot provides insight into environmental restriction levels. Both black and grey shale of the Qiongzhusi Formation indicate a moderate restriction environment, similar to Framvaren Fjord (Algeo and Lyons, 2006) (Figures 6A–C). The U-Mo covariation pattern also supports a moderately restricted environment (Figures 6D–F). Within this context, the grey shales have lower Mo-EF and U-EF values and were more oxygenated conditions than black shale, consistent with previous interpretations.

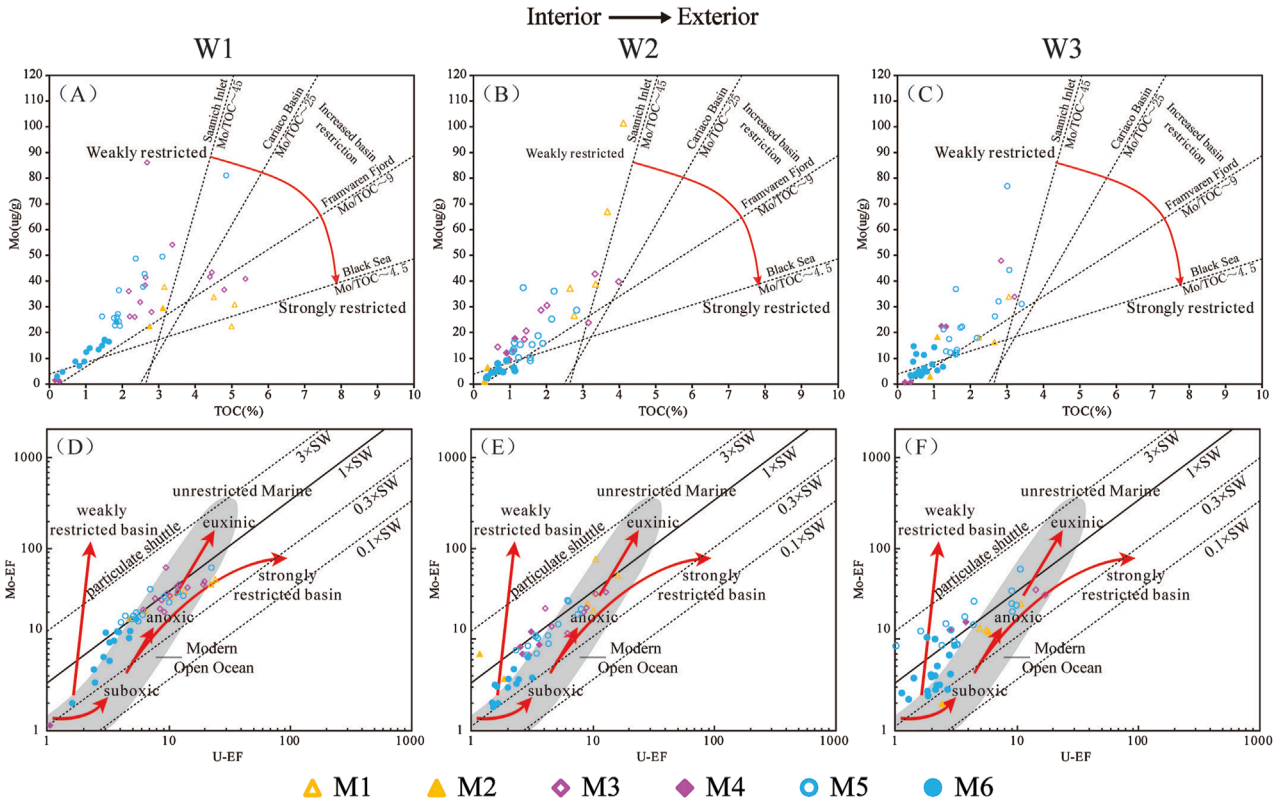

FIGURE 6
Crossplots of Mo concentration *versus* TOC for **(A)** Well W1; **(B)** Well W2; and **(C)** Well W3. Dashed lines represent the regression trends for four modern anoxic marine systems (Saanich Inlet, Cariaco Basin, Framvaren Fjord, and Black sea), indicating variable degrees of hydrographic restriction. Red arrows represent the restricted trends. Crossplots of Mo-EF *versus* U-EF for **(D)** Well W1; **(E)** Well W2; and **(F)** Well W3. Solid line shows Mo–U molar ratio equal to seawater value (1 × SW). Dashed lines indicate Mo–U molar ratios equal to fractions of seawater value (0.1 × SW, 0.3 × SW, 3 × SW). Grey field represents the "unrestricted marine" trend, characteristic of depositional systems with no limited trace metal renewal. Red arrows represent the restricted and reducing trends. M1, Member 1; M2, Member 2; M3, Member 3; M4, Member 4; M5, Member 5; M6, Member 6 (modified from Algeo and Lyons, 2006; Algeo and Tribovillard, 2009).

5.3 Paleoproductivity

The distribution of nutrient elements such as C, N, O, Si, P and Ba in the ocean is primarily regulated by biogeochemical metabolism processes. Typically, proxies such as P, Ba/Al and biogenic Ba (Ba_{xs}) are widely used to assess marine paleoproductivity (Dymond et al., 1992; Francois et al., 1995; Zhang et al., 2016; Wu et al., 2020; Qiu et al., 2022). Sedimentary Ba includes both biogenic Ba from biological sources and terristrial Ba conbined with silicate. Ba_{xs}, representing biogenic Ba in sediment, is calculated as total Ba in sediment minus terrigenous Ba, and serves a proxy for biological productivity in marine environments (Eagle et al., 2003).

Statistical analyses suggest that Ba_{xs} values exceeding 600 μg/g indicate high paleoproductivity, whereas values below 600 μg/g signify low productivity. Vertically, the Ba/Al and Ba_{xs} values in the Qiongzhusi Formation shale from the three Wells show a stable trend, with slightly higher values in the black shale intervals than in the grey shale ones (Figures 3–5). Laterally, the faulted-sag interior records higher paleoproductivity compared to that of the slope and the outside faulted-sag, which may be related to higher nutrient input from rifting activity in the northern South China block in the context of the Rodinia breakup (Wang et al., 2015) (Table 2).

5.4 Terrigenous input

It is generally believed that the major elements Al and Ti are very stable in seawater and can indicate the input of terrigenous debris. Al occurs only in clay minerals, while Ti occurs both in clay minerals and sand-sized or silt-sized minerals, The Ti/Al ratio is widely used as an indicator of terrigenous input and source provenance (Boström and Peterson, 1969; Adachi et al., 1986; Yamamoto, 1987; Murray, 1994; Murphy et al., 2000; Yeasmin et al., 2017; Liu et al., 2021).

The results of analysis suggest that the contents of Al and Ti and Ti/Al ratios in the Qiongzhusi Formation shale from study Wells show a stable trend, indicating relatively stable terrigenous input in the southern Sichuan Basin (Figures 3–5; Table 2). Vertically, the contents of Al from M2 to M6 are similar and slightly higher than that of M1. Laterally, the Al contents from Well W2 to W3 are similar and slightly higher than that of Well W1. In addition, the Ti contents from M2 to M6 are also similar and slightly higher than that of M1 and the Ti contents from Well W2 to W3 are similar and slightly higher than that of Well W1 too. The contents of Al and Ti indicate that there were relatively few terrigenous inputs in early Qiongzhusi Formation also in the faulted-sag. However, the Ti/Al ratios in the Qiongzhushi Formation shale from the three wells are similar and show a stable trend. For example, the averages of Ti/Al ratios are

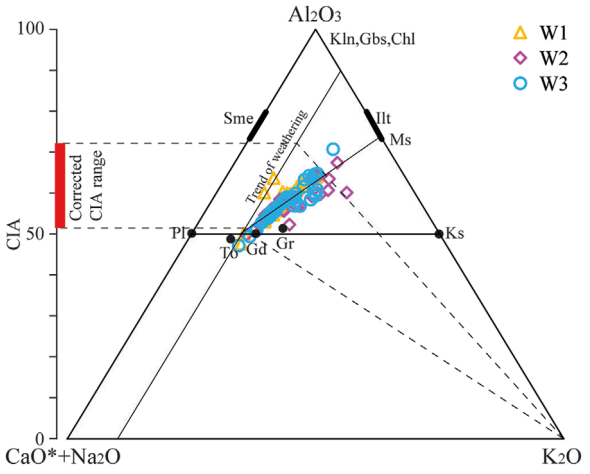

FIGURE 7
Ternary diagram of molecular proportions Al_2O_3–(CaO^*+ Na_2O)–K_2O of the Qiongzhusi Formation shale in the Lower Cambrian from W1 to W3 in the Southern Sichuan Basin. Data based on the method described by Nesbitt and Young (1982), (1984). Tonalite (To), granodiorite (Gd), and granite (Gr) data are from Condie (1993). Our Al_2O_3-CaO + Na_2O-K_2O ternary diagram shows a deviation from the weathering trend (Figure 7), reflecting a certain extent removal of K-bearing from parent rock. We correct the K contents and CIA based on the weathering trend which is parallel to A-CN line, forming another trend toward illite and muscovite. This suggests addition of K_2O to clays, i.e., K enrichment. A line from K apex through sample intersects the premetasomatized weathering trend at a point which represents its premetasomatized composition (Figure 7). A prematasomatized CIA value (i.e., CIAcorrected) can be read by extending a line from the point to the CIA apex, which is parallel to the CN-K line (Figure 7). Only two samples of Well W1 locate on the weathering line, indicating no K metasomatism (Figure 7). CIA–Chemical Index of Alteration, CaO^*–CaO incorporated in the silicate fraction of the sample, Pl–plagioclase, Kfs–K-feldspar, Sme–Smectite, Kln–kaolinite, Gbs–gibbsite, Chl–chlorite, Ms.–muscovite, and Ilt–Illite. The CIA*range mainly from 50 to 70, indicating that the Qiongzhushi Formation in the southern Sichuan Basin is predominantly experienced low weathering under a cold and arid climate.

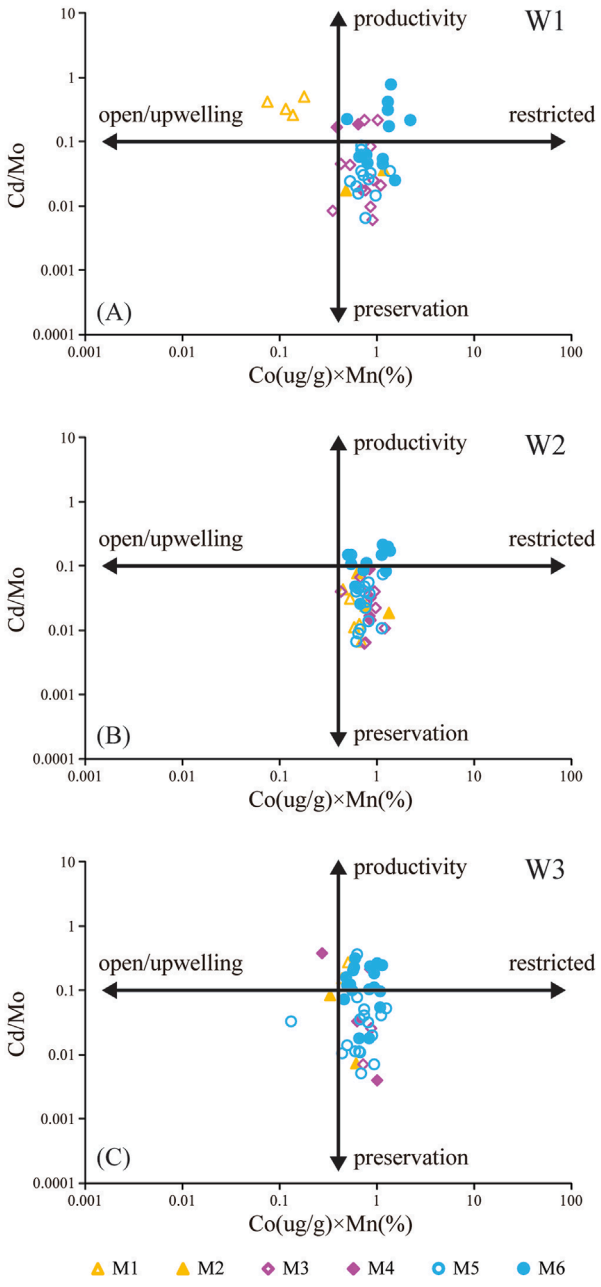

FIGURE 8
Crossplots of Cd/Mo against Co(ug/g) × Mn (%) of the Qiongzhusi Formation shale in the Lower Cambrian from W1 to W3 in the Southern Sichuan Basin **(A)** Well W1, **(B)** Well W2, **(C)** Well W3. M1, Member 1; M2, Member 2; M3, Member 3; M4, Member 4; M5, Member 5; M6, Member 6 (modified from Sweere et al., 2016)

0.065 for W1 located in the faulted-sag, 0.064 for W2 on the slope of the faulted-sag and 0.063 for W3 outside the faulted-sag, suggesting that terrigenous input in the Qiongzhushi Formation in the southern Sichuan Basin originated from a common source (Table 2).

5.5 Weathering

Nesbitt and Young (1982) proposed using the Chemical Index of Alteration (CIA) to assess the degree of chemical weathering of source rocks in the provenance area. The CIA can reflect the degree of weathering of sediment sources: when CIA is between 50 and 65, it indicates low weathering in a cold and arid climate; when CIA is between 65 and 85, it indicates moderate weathering in a warm climate; and when CIA is greater than 85, it indicates intense weathering in a hot and humid climate (Nesbitt and Young, 1982).

Our Al2O3-CaO+Na2O-K2O ternary diagram shows a deviation from the weathering trend (Figure 7), reflecting a certain extent removal of K-bearing from parent rock. We correct the K contents and CIA based on the weathering trend which is parallel to A-CN line, forming another trend toward illite and muscovite. This suggests addition of K2O to clays, i.e., K enrichment. A line from K apex through sample intersects the premetasomatized weathering trend at a point which represents its premetasomatized composition (Figure 7). A prematasomatized CIA value (i.e, CIAcorrected) can be read by extending a line from the point to the CIA apex, which is parallel to the CN-K line (Figure 7). Only two samples of Well W1 locate on the weathering line, indicating no K metasomatism (Figure 7). The CIA*values are similar to CIA (Figure 7), ranging mainly from 50 to 70, indicating that the Qiongzhushi Formation

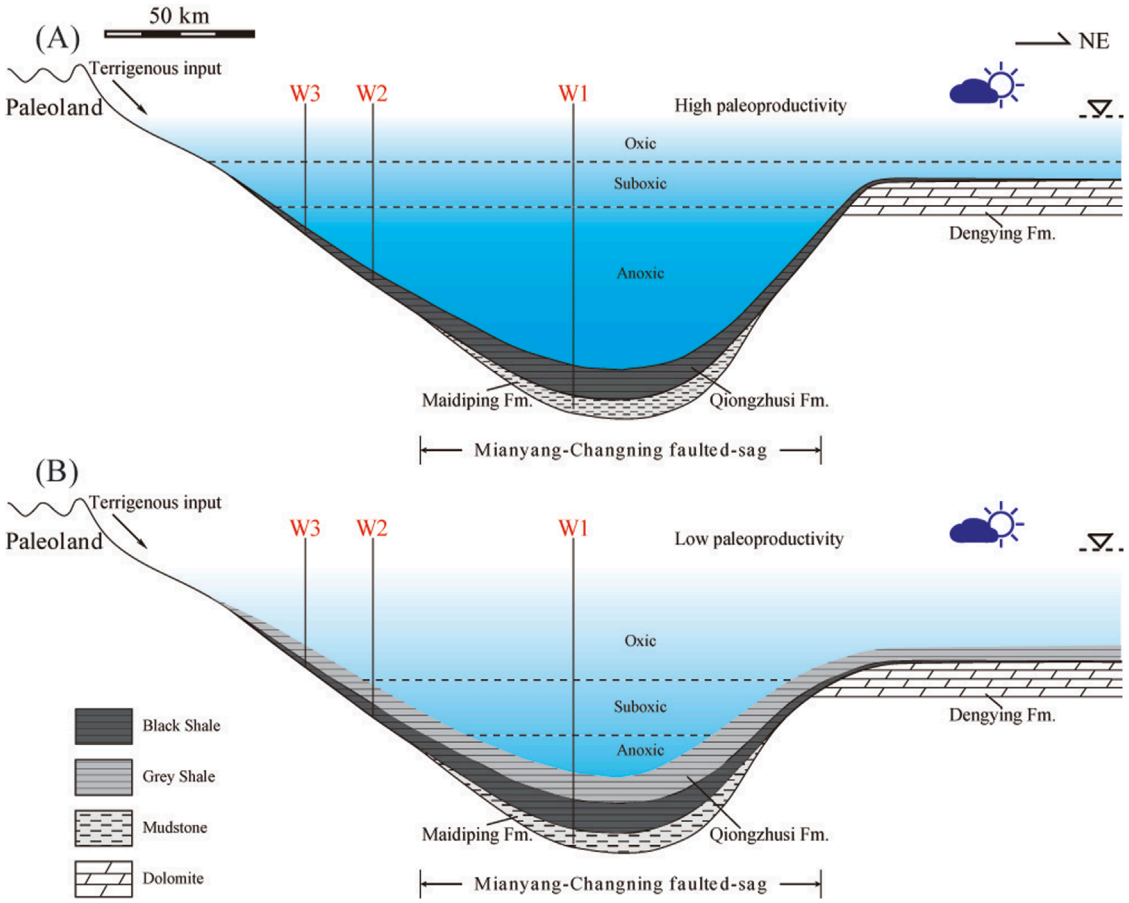

FIGURE 9
Organic matter accumulation model of the Qiongzhusi Formation shale in the Lower Cambrian from W1 to W3 in the Southern Sichuan Basin. **(A)** OM-enriched black shale, deposited under anoxic-suboxic conditions, experiencing a cold and arid climate and high paleoproductivity; **(B)** OM-lean grey shale, deposited under suboxic-oxic conditions, experiencing a cold and arid climate and low paleoproductivity

in the southern Sichuan Basin is predominantly experienced low weathering under a cold and arid climate. This conflicts with the tropical paleogeographic setting and the expected warm climate background. This deviation may be originated from provenance which is supported by variable Ti/Al ration in the study interval. Vertically, the CIA* values of the Qiongzhushi Formation shale from the three wells show minimal variation, with CIA* values mainly ranging from 50 to 70. This suggests that the weathering of the Qiongzhushi Formation shale in the southern Sichuan Basin is relatively stable and low intensity. Laterally, the shale from Well W1, located in the faulted-sag (average CIA* of 59), exhibits similar weathering intensity to Well W2 on the faulted-sag slope (average CIA* of 58) and Well W3 outside the faulted-sag (average CIA* of 57). This indicates a predominantly low degree of weathering and a cold and arid climate, likely influenced by the distance from the provenance (Table 2).

5.6 Upwelling events

Sweere et al. (2016) proposed using Cd/Mo ratios and Co (ug/g) × Mn (%) to assess the influence of upwelling events in marine deposits. Their research indicated that high Cd/Mo ratios are characteristic of sediments deposited in continental margin upwelling environments, whereas environments within restricted ocean basins show higher concentrations of Co and Mn (expressed as Co × Mn) (Sweere et al., 2016). Cd/Mo > 0.1 and Co (ug/g) × Mn (%) < 0.4 indicate a continental margin open ocean environment associated with upwelling currents (e.g., Namibian Margin). Cd/Mo < 0.1 and Co (ug/g) × Mn (%) > 0.4 indicate a restricted water column environment in marginal ocean basins (e.g., Black Sea) (Sweere et al., 2016). Currently, Cd/Mo and Co (ug/g) × Mn (%) are widely used to identify upwelling events in marine deposits (Zhang et al., 2018; Lu et al., 2019; McArthur, 2019; Qiu et al., 2023).

Based on the analyses of Cd/Mo and Co(ug/g) × Mn (%) of the Qiongzhusi Formation shale in the southern Sichuan Basin, the shale samples mainly indicate weak to moderate restricted water column conditions (Figures 8A–C), consistent with the interpretations mentioned above. The Cd/Mo values of the black shale (M1, M3 and M5) are predominantly less than 0.1, while those of the grey shale (M2, M4 and M6) are predominantly greater than 0.1 (Figures 8A–C). The Co (ug/g) × Mn (%) values both black and grey shale are predominantly above 0.4 (Figures 8A–C). The low Cd/Mo ratio indicates a deposition in a low oxygen or restricted environment, with minimal influence from upwelling currents (Sweere et al., 2016). This may be due to

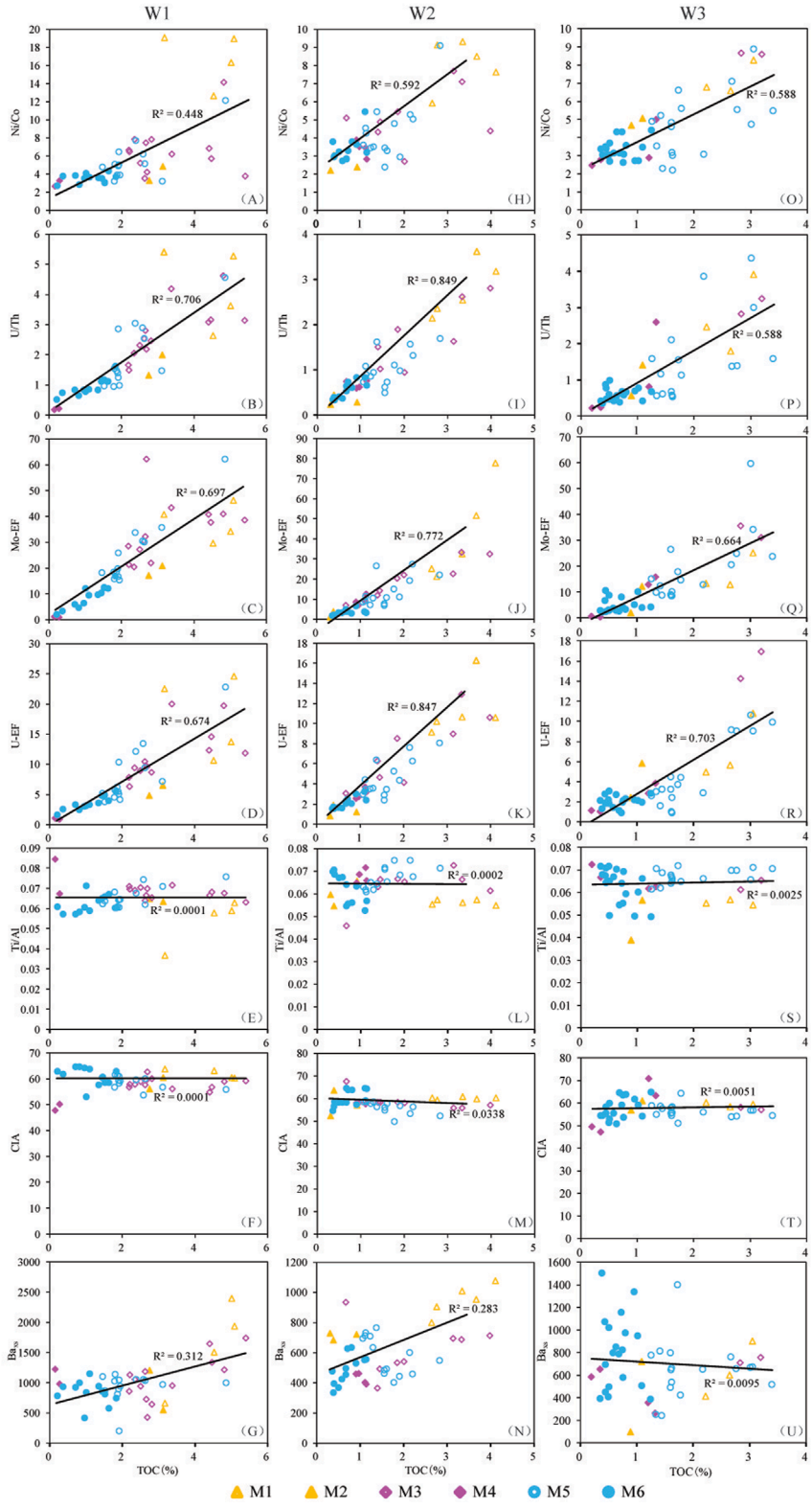

FIGURE 10
Crossplots of TOC against Ni/Co, U/Th, Mo-EF, U-EF, Ti/Al, CIA and Ba_{xs} for **(A-G)** Well W1; (H-N) Well W2; and **(O-U)** Well W3. M1, Member 1; M2, Member 2; M3, Member 3; M4, Member 4; M5, Member 5; M6, Member 6.

the palaeogeography location of the basin, which faced southwards to the ocean near to the northern margin of the Gondwana continent. Thus, it can be inferred that black shale was primarily deposited under oxygen-deficient or restricted conditions with limited upwelling influence, enhancing OM preservation, consistent with the conclusion mentioned above.

5.7 Mechanism of organic matter enrichment

Previous studies indicate the enrichment of organic matter in modern and ancient marine sediments is influenced by such as primary productivity, depositional environment, terrigenous sediment supply, microbial activity, *etc.* These studies have proposed two genetic models: the preservation mode and the productivity mode (Demaison and Moore, 1980; Calvert, 1987; Pedersen and Calvert, 1990; Arthur and Sageman, 1994; Murphy et al., 2000; Lash et al., 2014). Two sedimentation models are proposed for the black shale and grey shale of the Qiongzhusi Formation in the southern Sichuan Basin. OM-enriched black shales (M1, M3, M5) (Figure 9A) were deposited under anoxic-suboxic conditions, experienced a low degree of chemical weathering, under cold and arid climate with high paleoproductivity, responding to organic matter enrichment with high TOC content. In contrast, the OM-lean grey shales (M2, M4, M6) (Figure 9B) were deposited under suboxic-oxic conditions with a similarly low degree of weathering but lower paleoproductivity, suggesting that strong reducing conditions contributed OM enrichment. The alternating deposition of black shale and grey shale during the E-C transition in South China is tightly linked with transgressive events (Zhang et al., 2020). The redox proxies in study interval show positive correlation with TOC, while primary productivity proxies show weak or no correlation with TOC (Figure 10). This indicates a main-controlling factor of redox conditions on OM accumulation mechanism. The relationship between marine redox conditions, primary productivity, and nutrient input is the key for the discussion understanding the mechanisms of OM enrichment. High primary productivity in surface waters can lead to increased oxygen demand during OM decomposition on the sea floor, and thus resulting in low-oxygen, reducing or anoxic conditions (Wei et al., 2016). Restricted water-mass circulations in a silled basin usually yield low-oxygen conditions in bottom waters. Previous studies have generated conflicting interpretations about the OM accumulation mechanism of the Early Cambrian shale from Yangtze Platform. For example, some geologists proposed that climate played an important role in the OM enrichment (Yeasmin et al., 2017; Zhai et al., 2018; Wang et al., 2020), while others found that upwelling, hydrothermal activity, primary productivity and redox conditions were the main control factors for OM enrichment of black shale in the Yangtze Block during the Early Cambrian (Gao et al., 2016; Zhou et al., 2017; Ma et al., 2019; Wu et al., 2020; Liu et al., 2021). However, the influence of Mianyang-Changning faulted-sag on the OM enrichment was not considered in the previous studies.

By examining the relationships between these factors and TOC, the main controlling factors influencing organic matter enrichment of the Qiongzhusi Formation shale can be inferred. Geochemical indicators reflecting paleo-redox conditions (Ni/Co, U/Th, Mo-EF and U-EF) show a strong positive correlation with TOC (Figures 3–5, 10A–D,H–K, O, P, Q, R). Conversely, geochemical indicators of paleoproductivity (Ba_{xs}, Ba/Al), terrigenous input (Ti/Al) and weathering effects (CIA) show weak correlation with TOC (Figures 3–5, 10E–G, L, M, N, S, T, U). Therefore, these findings suggest that the organic matter enrichment in the Qiongzhusi Formation shale in the southern Sichuan Basin was primarily controlled by paleo-redox conditions. Water circulation conditions show low to moderate restriction, in contrast with high OM enrichment observed (Figure 6). In addition, no significant difference in water circulation conditions is observed between OM-rich black shale and OM-lean grey shale. This may indicated a weak or egligible correlation between OM enrichment and water circulation in the study area.

Within the same lithostratigraphic unit, the Well W1, located in the inner faulted-sag, exhibits the highest TOC content, followed by the Well W2 on the slope of the faulted-sag while the Well W3, located outside the faulted-sag, shows the lowest TOC content. Additionally, the OM-enriched black shale generally has higher TOC content compared to the OM-lean grey shale. These findings indicate the redox conditions decreased gradually from the inner faulted-sag to the outer faulted-sag and the black shale experienced more reducing conditions compared to the grey shale. In summary, organic matter enrichment in the Qiongzhushi Formation shale in the southern Sichuan Basin was controlled by the redox conditions, which were influenced by the Mianyang-Changning faulted-sag. The strongest reducing (anoxic) conditions in the inner faulted-sag were most conducive to the enrichment of organic matter.

6 Conclusion

The depositional environment of the Qiongzhusi Formation shale in the southern Sichuan Basin exhibits the following six key characteristics: (1) The black shale shows stronger reducing conditions compared to grey shale, with redox conditions being more intense in the faulted-sag interior than on the slope and outside faulted-sag; (2) The Qiongzhusi Formation shale were deposited under moderate restricted conditions; (3) The paleoproductivity of black shale was higher than that of grey shale, and the shale in the faulted-sag interior indicates higher paleoproductivity compared to that of the slope and outside faulted-sag; (4) A stable terrigenous input persisted throughout the entire depositional period of study interval; (5) The Qiongzhusi Formation shale experienced a low degree of chemical weathering, under a cold and arid climate; (6) The influence of upwelling currents was minimal, with black shale exhibiting higher degree of restriction compared to grey shale.

The organic matter enrichment of the Qiongzhusi Formation shale was primarily controlled by the redox conditions, which were influenced by the Mianyang-Changning faulted-sag. In particular, the reducing (anoxic) conditions in the inner faulted-sag were most conducive to the organic matter accumulation. Two sedimentary models have been established for the Qiongzhusi Formation shale: (1) OM-enriched black shale was deposited under anoxic-suboxic conditions and experienced a low degree of chemical weathering,

under a cold and arid climate and with high paleoproductivity; (2) OM-lean grey shale was deposited under suboxic-oxic conditions, and experienced a low degree of chemical weathering, a cold and arid climate and low paleoproductivity.

Data availability statement

The original contributions presented in the study are included in the article/supplementary material, further inquiries can be directed to the corresponding authors.

Author contributions

BL: Formal Analysis, Methodology, Writing–original draft. D-jH: Formal Analysis, Methodology, Writing–review and editing. C-nZ: Formal Analysis, Methodology, Writing–review and editing. X-zL: Data curation, Methodology, Writing–review and editing. R-sG: Data curation, Methodology, Writing–review and editing. H-yW: Methodology, Formal Analysis, Project administration, Writing–original draft, Writing–review and editing. ZQ: Data curation, Methodology, Writing–original draft.

Funding

The author(s) declare that financial support was received for the research and/or publication of this article. This work was supported by the National Natural Science Foundation of China (No. 42222209).

Acknowledgments

We thank Feng Liang, Qin Zhang, Xiang-yang Pei, Qi-min Guo, Long-yi Wang, Ji-chang Zhu, Yi-ze Huang and Nijun Qi for their assistance in the samples collection and geochemical analyses.

Conflict of interest

Authors BL, CZ, XL, RG, and ZQ were employed by China National Petroleum Corporation.

The remaining authors declare that the research was conducted in the absence of any commercial or financial relationships that could be construed as a potential conflict of interest.

Generative AI statement

The author(s) declare that no Generative AI was used in the creation of this manuscript.

Publisher's note

References

Adachi, M., Yamamoto, K., and Sugisaki, R. (1986). Hydrothermal chert and associated siliceous rocks from the northern Pacific their geological significance as indication od ocean ridge activity. *Sediment. Geol.* 47 (1-2), 125–148. doi:10.1016/0037-0738(86)90075-8

Algeo, T. J., and Lyons, T. W. (2006). Mo–total organic carbon covariation in modern anoxic marine environments: implications for analysis of paleoredox and paleohydrographic conditions. *Paleoceanography* 21 (1), 1016–1038. doi:10.1029/2004PA001112

Algeo, T. J., and Maynard, J. B. (2008). Trace metal covariation as a guide to water-mass conditions in ancient anoxic marine environments. *Geosphere* 4 (5), 872–887. doi:10.1130/ges00174.1

Algeo, T. J., and Tribovillard, N. (2009). Environmental analysis of paleoceanographic systems based on molybdenum-uranium covariation. *Chem. Geol.* 268 (3/4), 211–225. doi:10.1016/j.chemgeo.2009.09.001

Arthur, M. A., and Sageman, B. B. (1994). Marine Black Shales: depositional mechanisms and environments of ancient deposits. *Annu. Rev. Earth Pl. S. C.* 22 (1), 499–551. doi:10.1146/annurev.ea.22.050194.002435

Boström, K., and Peterson, M. N. A. (1969). The origin of aluminum-poor ferromanganoan sediments in areas of high heat flow on the East Pacific Rise. *Mar. Geol.* 7 (5), 427–447. doi:10.1016/0025-3227(69)90016-4

Calvert, S. E. (1987). Oceanographic controls on the accumulation of organic matter in marine sediments. *Geol. Soc. Lond. Spec. Publ.* 26 (1), 137–151. doi:10.1144/GSL.SP.1987.026.01.08

Canfield, D. E. (1994). Factors influencing organic carbon preservation in marine sediments. *Chem. Geol.* 114 (3-4), 315–329. doi:10.1016/0009-2541(94)90061-2

Chen, D., Wang, J., Qing, H., Yan, D., and Li, R. (2009). Hydrothermal venting activities in the Early Cambrian, South China: petrological, geochronological and stable isotopic constraints. *Chem. Geol.* 258 (3-4), 168–181. doi:10.1016/j.chemgeo.2008.10.016

Condie, K. C. (1993). Chemical composition and evolution of the upper continental crust: contrasting results from surface samples and shales. *Chem. Geol.* 104, 1–37. doi:10.1016/0009-2541(93)90140-E

Demaison, G. J., and Moore, G. T. (1980). Anoxic environments and oil source bed genesis. *Org. Geochem* 2 (1), 9–31. doi:10.1016/0146-6380(80)90017-0

Dong, Z. T., Tian, S. S., Xue, H. T., Lu, S. F., Liu, B., Erastova, V., et al. (2025). A novel method for automatic quantification of different pore types in shale based on SEM-EDS calibration. *Mar. Petrol Geol.* 173, 107278. doi:10.1016/j.marpetgeo.2024.107278

Dymond, J., Suess, E., and Lyle, M. (1992). Barium in deep-sea sediment: a geochemical proxy for paleoproductivity. *Paleoceanography* 7 (2), 163–181. doi:10.1029/92PA00181

Eagle, M., Paytan, A., Arrigo, K. R., Dijken, G. V., and Murray, R. W. (2003). A comparison between excess barium and barite as indicators of carbon export. *Paleoceanography* 18 (1), 2101–2113. doi:10.1029/2002PA000793

Emerson, S. R., and Huested, S. S. (1991). Ocean anoxia and the concentrations of molybdenum and vanadium in seawater. *Mar. Chem.* 34 (3), 177–196. doi:10.1016/0304-4203(91)90002-e

Fang, A. D. Q., Wu, L., Geng, A., and Deng, Q. (2019). Formation and evolution of the ediacaran to lower cambrian black shales in the Yangtze platform, south China. *Palaeogeogr. Palaeoclimatol. Palaeoecol.* 527, 87–102. doi:10.1016/j.palaeo.2019.04.025

Francois, R., Honjo, S., Manganini, S. J., and Ravizza, G. E. (1995). Biogenic barium fluxes to the deep sea: implications for paleoproductivity reconstruction. *Glob. Biogeochem. Cy* 9 (2), 289–303. doi:10.1029/95GB00021

Fu, Y., Zhou, W. X., Wang, H. J., Qiao, W. L., Ye, Y. T., Jiang, R., et al. (2021). The relationship between environment and geochemical characteristics of black rock series of Lower Cambrian in northern Guizhou. *Acta Geol. Sin.* 95 (2), 536–548. doi:10.19762/j.cnki.dizhixuebao.2021102

Gallego-Torres, D., Martínez-Ruiz, F., Paytan, A., Jiménez-Espejo, F. J., and Ortega-Huertas, M. (2007). Pliocene-Holocene evolution of depositional conditions in the eastern Mediterranean: role of anoxia vs. productivity at time of sapropel deposition. *Palaeogeogr. Palaeoclimatol. Palaeoecol.* 246 (2), 424–439. doi:10.1016/j.palaeo.2006.10.008

Gao, P., Liu, G. D., Jia, C., Young, A. L., Wang, Z. C., Wang, T. S., et al. (2016). Redox variations and organic matter accumulation on the Yangtze carbonate platform during Late Ediacaran-Early Cambrian: constraints from petrology and geochemistry. *Palaeogeogr. Palaeoclimatol. Palaeoecol.* 450, 91–110. doi:10.1016/j.palaeo.2016.02.058

Guo, Q. J., Shield, G. A., Liu, C. Q., Strauss, H., Zhu, M. Y., Pi, D., et al. (2007). Trace element chemostratigraphy of two Ediacaran-Cambrian successions in South China. Implications for organosedimentary metal ennchment and silic1Hcatlon in the early Cambnan. *Palaeogeogr Palaeoclimatol Palaeoecol*, 254, 194–216. doi:10.1016/j.palaeo.2007.03.016

He, X., Liang, F., Li, H., Zheng, M. J., Zhao, Q., Liu, Y., et al. (2024). Breakthrough and enrichment mode of marine shale gas in the Lower Cambrian Qiongzhusi Formation in high-yield wells in Sichuan Basin. *China Petrol Explor* 29 (1), 142–155. doi:10.3969/j.issn.1672-7703.2024.01.011

Hoffman, P. F., Kaufman, A. J., Halverson, G. P., and Schrag, D. P. (1998). A neoproterozoic snowball earth. *Science* 281 (5381), 1342–1346. doi:10.1126/science.281.5381.1342

Huang, J. L., Zou, C. N., Li, J. Z., Dong, D. Z., Wang, S. J., Wang, S. Q., et al. (2012). Shale gas generation and potential of the lower cambrian Qiongzhusi Formation in southern Sichuan Basin, China. *Petrol Explor Dev.* 39 (1), 69–75. doi:10.1016/S1876-3804(12)60017-2

Hyde, W. T., Crowley, T. J., Baum, S. K., and Peltier, W. R. (2000). Neoproterozoic "snowball Earth" simulations with a coupled climate/ice-sheet model. *Nature* 405 (6785), 425–429. doi:10.1038/35013005

Jin, C. S., Li, C., Algeo, T. J., Planaysky, N. J., Cui, H., Yang, X. L., et al. (2016). A highly redox-heterogeneous ocean in South China during the early Cambrian (~529-514Ma): implications for biota-environment co-evolution. *Earth Planet S. C. Lett.* 441, 38–51. doi:10.1016/j.epsl.2016.02.019

Jones, B., and Manning, D. A. C. (1994). Comparison of geochemical indices used for the interpretation of palaeoredox conditions in ancient mudstones. *Chem. Geol.* 111 (1-4), 111–129. doi:10.1016/0009-2541(94)90085-X

Kirschvink, Z., Ripperdan, R. L., and Evans, D. A. (1997). Evidence for a large-scale reorganization of early cambrian continental masses by inertial interchange true polar wander. *Science* 277, 541–545. doi:10.1126/science.277.5325.541

Knoll, A. H., and Walter, M. R. (1992). Latest proterozoic stratigraphy and earth history. *Nature* 356 (6371), 673–678. doi:10.1038/356673a0

Lash, G. G., and Blood, D. R. (2014). Organic matter accumulation, redox, and diagenetic history of the Marcellus Formation, southwestern Pennsylvania, Appalachian basin. *Mar. Petrol Geol.* 57, 244–263. doi:10.1016/j.marpetgeo.2014.06.001

Li, J., Tang, S. H., Zhang, S. H., Xi, Z., Yang, N., Yang, G. Q., et al. (2018). Paleo-environmental conditions of the Early Cambrian Niutitang Formation in the Fenggang area, the southwestern margin of the Yangtze Platform, southern China: evidence from major elements, trace elements and other proxies. *J. Asian Earth Sci.* 159, 81–97. doi:10.1016/j.jseaes.2018.03.013

Li, T. J., Zhao, S. X., Huang, Y. B., Zhang, L. H., Zhang, K., and Tang, H. M. (2013). The sedimentary micro-facies study of the lower cambrian Qiongzhusi Formation in southern Sichuan Basin. *Acta Geol. Sin.* 87 (8), 1136–1148. doi:10.3969/j.issn.0001-5717.2013.08.008

Li, X. H., Li, Z. X., Sinclair, J. A., Li, W. X., and Carter, G. (2006). Revisiting the "Yanbian Terrane": implications for neoproterozoic tectonic evolution of the western Yangtze block, south China. *Precambrian Res.* 151, 14–30. doi:10.1016/j.precamres.2006.07.009

Li, Y. F., Zhang, T. W., Ellis, G. S., and Shao, D. Y. (2017). Depositional environment and organic matter accumulation of upper ordovician-lower silurian marine shale in the upper Yangtze platform, south China. *Palaeogeogr. Palaeoclimatol. Palaeoecol.* 66 (15), 252–264. doi:10.1016/j.palaeo.2016.11.037

Liu, S. G., Deng, B., Li, Z. W., and Sun, W. (2011). The texture of sedimentary basin-orogenic belt system and its influence on oil/gas distribution: a case study from Sichuan basin. *Acta Petol Sin.* 27 (3), 621–635. doi:10.3724/SP.J.1011.2011.00415

Liu, Z. X., Yan, D. T., Du, X. B., and Li, S. J. (2021). Organic matter accumulation of the early Cambrian black shales on the flank of Micangshan-Hannan Uplift, northern upper Yangtze Block, South China. *J. Petrol Sci. Eng.* 200, 108378. doi:10.1016/j.petrol.2021.108378

Lu, Y. B., Jiang, S., Lu, Y. C., Xu, S., Shu, Y., and Wang, Y. X. (2019). Productivity or preservation? The factors controlling the organic matter accumulation in the late Katian through Hirnantian Wufeng organic-rich shale, South China. *Mar. Petrol Geol.* 109, 22–35. doi:10.1016/j.marpetgeo.2019.06.007

Ma, Y. Q., Lu, Y. C., Liu, X. F., Zhai, G. Y., Wang, Y. F., and Zhang, C. (2019). Depositional environment and organic matter enrichment of the lower Cambrian Niutitang shale in western Hubei Province, South China. *Mar. Petrol Geol.* 109, 381–393. doi:10.1016/j.marpetgeo.2019.06.039

Maruyama, S., and Santosh, M. (2008). Models on snowball earth and cambrian explosion: a synopsis. *Gondwana Res.* 14 (1-2), 22–32. doi:10.1016/j.gr.2008.01.004

Maruyama, S., Sawaki, Y., Ebisuzaki, T., Ikoma, M., Omori, S., and Tetsuya, K. (2014). Initiation of leaking Earth: an ultimate trigger of the Cambrian explosion. *Gondwana Res.* 25 (3), 910–944. doi:10.1016/j.gr.2013.03.012

McArthur, J. (2019). Early Toarcian black shales: a response to an oceanic anoxic event or anoxia in marginal basins? *Chem. Geol.* 522, 71–83. doi:10.1016/j.chemgeo.2019.05.028

Mclennan, S. M. (1993). Weathering and global denudation. *J. Geol.* 101 (2), 295–303. doi:10.1086/648222

McLennan, S. M. (2001). Relationships between the trace element composition of sedimentary rocks and upper continental crust. *Geochem Geophy Geosy.* 2 (4). doi:10.1029/2000GC000109

Murphy, A. E., Sageman, B. B., Hollander, D. J., Lyons, T. W., and Brett, C. E. (2000). Black shale deposition and faunal overturn in the Devonian Appalachian Basin: clastic starvation, seasonal water-column mixing, and efficient biolimiting nutrient recycling. *Paleoceanography* 15 (3), 280–291. doi:10.1029/1999PA000445

Murray, R. W. (1994). Chemical criteria to identify the depositional environment of chert: general principles and applications. *Sediment. Geol.* 90 (3-4), 213–232. doi:10.1016/0037-0738(94)90039-6

Nesbitt, H. W., and Young, G. M. (1982). Early Proterozoic climates and plate motions inferred from major element chemistry of lutites. *Nature* 299, 715–717. doi:10.1038/299715a0

Nesbitt, H. W., and Young, G. M. (1984). Prediction of some weathering trends of plutonic and volcanic rocks based on thermodynamic and kinetic considerations. *Geochim. Cosmochim. Ac* 48, 1523–1534. doi:10.1016/0016-7037(84)90408-3

Nesbitt, H. W., Young, G. M., McLennan, S. M., and Keays, R. R. (1996). Effects of chemical weathering and sorting on the petrogenesis of siliciclastic sediments, with implications for provenance studies. *J. Geol.* 104, 525–542. doi:10.1086/629850

Payne, J. L., Boyer, A. G., Brown, J. H., Finnegan, S., Kowalewski, M., Krause, R. A., et al. (2009). Two-phase increase in the maximum size of life over 3.5 billion years reflects biological innovation and environmental opportunity. *P Natl. Acad. Sci. U. S. A.* 106 (1), 24–27. doi:10.1073/pnas.0806314106

Pedersen, T. F., and Calvert, S. E. (1990). Anoxia vs. productivity: what controls the formation of organic-carbon-rich sediments and sedimentary rocks. *AAPG Bull.* 74 (4), 454–466. doi:10.1306/0C9B232B-1710-11D7-8645000102C1865D

Pipe, A. B., Leybourne, M. I., Johannesson, K. H., Hannigan, R. E., and Layton-Matthews, D. (2025). Trace and rare earth element geochemistry of black shales from the upper ordovician utica shale magnafacies. *Chem. Geol.* 672, 122507. doi:10.1016/j.chemgeo.2024.122507

Qiu, Z., Li, Y. F., Xiong, W., Fan, T. L., Zhao, Q., Zhang, Q., et al. (2023). Revisiting paleoenvironmental changes on the Upper Yangtze Block during the Ordovician-Silurian transition: new insights from elemental geochemistry. *Sediment. Geol.* 450, 106377. doi:10.1016/j.sedgeo.2023.106377

Qiu, Z., Zou, C. N., Mills, B. J. W., Xiong, Y. J., Tao, H. F., Lu, B., et al. (2022). A nutrient control on expanded anoxia and global cooling during the Late Ordovician mass extinction. *Commun. Earth Environ.* 3 (82), 82–89. doi:10.1038/s43247-022-00412-x

Rowe, H. D., Loucks, R. G., Ruppel, S. C., and Rimmer, S. M. (2008). Mississippian barnett formation, fort worth basin, Texas: bulk geochemical inferences and Mo-TOC constraints on the severity of hydrographic restriction. *Chem. Geol.* 257 (1/2), 16–25. doi:10.1016/j.chemgeo.2008.08.006

Schoepfer, S. D., Shen, J., Wei, H., Tyson, R. V., Ingall, E., and Algeo, T. J. (2015). Total organic carbon, organic phosphorus, and biogenic barium fluxes as proxies for paleomarine productivity. *Earth-Sci Rev.* 149, 23–52. doi:10.1016/j.earscirev.2014.08.017

Sweere, T., van den Boorn, S., Dickson, A. J., and Reichart, G. J. (2016). Definition of new tracemetal proxies for the controls on organic matter enrichment in marine sediments based on Mn, Co, Mo and Cd concentrations. *Chem. Geol.* 441, 235–245. doi:10.1016/j.chemgeo.2016.08.028

Tonger Liu, W. H., and Xu, Y. C. (2004). The discussion on anoxic environments and its geochemical identifying indices. *Acta Sedimentol. Sin.* 22 (2), 365–372. doi:10.3969/j.issn.1000-0550.2004.02.026

Tribovillard, N., Algeo, T. J., Baudin, F., and Riboulleau, A. (2012). Analysis of marine environmental condition based on molybdenum-uranium covariation-applications to Mesozoic paleoceanography. *Chem. Geol.* 324/325, 46–58. doi:10.1016/j.chemgeo.2011.09.009

Wang, J., and Li, Z. X. (2003). History of Neoproterozoic rift basins in South China: implications for Rodinia break-up. *Precambrian Res.* 122, 141–158. doi:10.1016/s0301-9268(02)00209-7

Wang, N., Li, M. J., Tian, X. W., Hong, H. T., Wen, L., and Wang, W. Z. (2020). Climate-ocean control on the depositional watermass conditions and organic matter enrichment in lower cambrian black shale in the upper Yangtze Platform. *Mar. Petrol Geol.* 120, 104570. doi:10.1016/j.marpetgeo.2020.104570

Wang, S. F., Zou, C. N., Dong, D. Z., Wang, Y. M., Li, X. J., Huang, J. L., et al. (2015). Multiple controls on the paleoenvironment of the Early Cambrian marine black shales

in the Sichuan Basin, SW China: geochemical and organic carbon isotopic evidence. *Mar. Petrol Geol.* 66, 660–672. doi:10.1016/j.marpetgeo.2015.07.009

Wang, T., Xiong, L., Xu, M., Dong, X. X., Zhou, R. Q., and Fu, X. N. (2016). Shale reservoir characteristics of the lower cambrian Qiongzhusi Formation in the southern Sichuan Basin. *Petrol Explor Dev.* 38 (2), 197–203. doi:10.11781/sysydz201602197

Wei, H. Y., Wei, X. M., Qiu, Z., Song, H. Y., and Shi, G. (2016). Redox conditions across the G-L boundary in South China: evidence from pyrite morphology and sulfur isotopic compositions. *Chem. Geol.* 440, 1–14. doi:10.1016/j.chemgeo.2016.07.009

Wu, C. J., Zhang, L. F., Zhang, T. W., Tuo, J. C., Song, D. J., Liu, Y., et al. (2020). Reconstruction of paleoceanic redox conditions of the lower Cambrian Niutitang shales in northern Guizhou, Upper Yangtze region. *Palaeogeogr. Palaeoclimatol. Palaeoecol.* 538, 109457. doi:10.1016/j.palaeo.2019.109457

Wu, Y., Fan, T., Jiang, S., and Yang, X. Q. (2017). Lithofacies and sedimentary sequence of the lower cambrian Niutitang shale in the upper Yangtze platform, south China. *J. Nat. Gas. Sci. Eng.* 43, 124–136. doi:10.1016/j.jngse.2017.04.002

Wu, Y. W., Tian, H., Gong, D. J., Li, T. F., and Zhou, Q. (2020). Paleo-environmental variation and its control on organic matter enrichment of black shales from shallow shelf to slope regions on the Upper Yangtze Platform during Cambrian Stage 3. *Palaeogeogr. Palaeoclimatol. Palaeoecol.* 545, 109653. doi:10.1016/j.palaeo.2020.109653

Yamamoto, K. (1987). Geochemical characteristics and depositional environments of cherts and associated rocks in the Franciscan and Shimanto Terranes. *Sediment. Geol.* 52 (1-2), 65–108. doi:10.1016/0037-0738(87)90017-0

Yeasmin, R., Chen, D. Z., Fu, Y., Wang, J., Guo, Z., and Guo, C. (2017). Climatic-oceanic forcing on the organic accumulation across the shelf during the early cambrian (age 2 through 3) in the mid-upper Yangtze block, NE guizhou, south China. *J. Asian Earth Sci.* 134, 365–386. doi:10.1016/j.jseaes.2016.08.019

Yin, L. M., Borjigin, T., Knoll, A. H., Bian, L. Z., Xie, X. M., Bao, F., et al. (2017). Sheet like microfossils from hydrothermally influenced basinal cherts of the lower cambrian (terreneuvian) Niutitang formation, guizhou, south China. *Palaeoworld* 26 (1), 1–11. doi:10.1016/j.palwor.2016.01.005

Zhai, L. N., Wu, C. D., Ye, Y. T., Zhang, S. C., and Wang, Y. Z. (2018). Fluctuations in chemical weathering on the Yangtze Block during the Ediacaran-Cambrian transition: implications for paleoclimatic conditions and the marine carbon cycle. *Palaeogeogr. Palaeoclimatol. Palaeoecol.* 490, 280–292. doi:10.1016/j.palaeo.2017.11.006

Zhang, B., Yao, S., Wignall, P. B., Hu, W., Ding, H., Liu, B., et al. (2018). Widespread coastal upwelling along the eastern paleo-tethys margin (south China) during the Middle permian (Guadalupian): implications for organic matter accumulation. *Mar. Petrol Geol.* 97, 113–126. doi:10.1016/j.marpetgeo.2018.06.025

Zhang, J. P., Fan, T. L., Algeo, T. J., Li, Y. F., and Zhang, J. C. (2016). Paleo-marine environments of the early cambrian Yangtze platform. *Palaeogeogr. Palaeoclimatol. Palaeoecol.* 443, 66–79. doi:10.1016/j.palaeo.2015.11.029

Zhang, X. L., Shu, D. G., Han, J., Zhang, Z. F., Liu, J. N., and Fu, D. J. (2014). Triggers for the cambrian explosion: hypotheses and problems. *Gondwana Res.* 25 (3), 896–909. doi:10.1016/j.gr.2013.06.001

Zhang, X. L., Zhou, X., and Hu, D. P. (2020). High-resolution paired carbon isotopic records from the Meishucun section in South China: implications for carbon cycling and environmental changes during the Ediacaran-Cambrian transition. *Precambrian Res.* 337, 105561. doi:10.1016/j.precamres.2019.105561

Zhao, K., Li, T. T., Zhu, G. Y., Zhang, Z. Y., Li, J. F., Wang, P. J., et al. (2020). Geochemical characteristics and formation mechanism of high-quality Lower Cambrian source rocks: a case study of the Tianzhushan profile in western Hubei. *Acta Petol Sin.* 41 (1), 13–26. doi:10.7623/syxb202001002

Zheng, Y., Anderson, R. F., Geen, A. V., and Kuwabara, J. (2000). Authigenic molybdenum formation in marine sediments: a link to pore water sulfide in the Santa Barbara Basin. *Geochim. Cosmochim. Ac* 64 (24), 4165–4178. doi:10.1016/S0016-7037(00)00495-6

Zhong, Y., Li, Y. L., Zhang, X. B., Liu, S. G., Liu, D. J., Deng, X. J., et al. (2013). Features of extensional structures in pre-Sinian to Cambrian strata, Scichuan Basin, China. *J Chengdu Univ Tech Sci. and Technol. Ed.* 40 (5), 498–510. doi:10.3969/j.issn.1671-9727.2013.05.02

Zhou, L., Kang, Z. H., Wang, Z. X., Peng, Y. Y., and Xiao, H. F. (2017). Sedimentary geochemical investigation for paleoenvironment of the lower cambrian Niutitang formation shales in the Yangtze platform. *J. Petrol Sci. Eng.* 159, 376–386. doi:10.1016/j.petrol.2017.09.047

Zou, C. N., Dong, D. Z., Wang, Y. M., Li, X. J., Huang, J. L., Wang, S. F., et al. (2015). Shale gas in China: characteristics, challenges and prospects (I). *Petrol Explor Dev.* 42 (6), 689–701. doi:10.11698/PED.2015.06.01

Zou, C. N., Zhao, Q., Cong, L. Z., Wang, H. Y., Shi, Z. S., Wu, J., et al. (2021). Development progress, potential and prospect of shale gas in China. *Nat. Gas. Ind.* 41 (1), 1–14. doi:10.3787/j.issn.1000-0976.2021.01.001

frontiers | Frontiers in Earth Science

TYPE Original Research
PUBLISHED 16 April 2025
DOI 10.3389/feart.2025.1502476

OPEN ACCESS

EDITED BY
George Kontakiotis,
National and Kapodistrian University of Athens, Greece

REVIEWED BY
Kunyue Ling,
Chinese Academy of Sciences (CAS), China
Ahmer Bilal,
Shandong University of Science and Technology, China

*CORRESPONDENCE
Zongxuan Zhang,
zzx199475@163.com
Zaixing Jiang,
jiangzx@cugb.edu.cn

RECEIVED 26 September 2024
ACCEPTED 03 February 2025
PUBLISHED 16 April 2025

CITATION
Zhang Z, Jiang Z and Yang Y (2025) Coevolution of minerals in lacustrine mudstone during diagenesis: a case study of the dongying depression in the Bohai Bay Basin.
Front. Earth Sci. 13:1502476.
doi: 10.3389/feart.2025.1502476

Coevolution of minerals in lacustrine mudstone during diagenesis: a case study of the dongying depression in the Bohai Bay Basin

Zongxuan Zhang[1,2]*, Zaixing Jiang[1,2]* and Yepeng Yang[1,2]

[1]School of Energy Resources, China University of Geosciences (Beijing), Beijing, China, [2]Key Laboratory of Marine Reservoir Evolution and Hydrocarbon Enrichment Mechanism, Ministry of Education, China University of Geosciences (Beijing), Beijing, China

In sedimentary basins, the lithologic characteristics of mudstone in different lithofacies differ, which is caused by the different types of diagenesis after sedimentation. An accurate understanding of the changes in and interactions among minerals in mudstone during diagenesis plays a key role in shale oil and gas exploration and development. In this work, the petrologic characteristics, XRD data, carbon and oxygen isotope data, main trace element data, and rock pyrolysis data of a total of 137 samples from 3 wells were used to divide the studied mudstone into 5 different types of lithofacies. For each rock phase and all kinds of primary minerals, the changes in secondary minerals and the relationships among them were studied. The five types of lithofacies belong to a relatively closed diagenetic system. The main development space of fibrous calcite/ankerite is laminar fractures formed during the sedimentary period. Ca^{2+}, Mg^{2+} and Fe^{2+} ions are provided by early carbonate and smectite–illite transformation. According to the temperature calculated from the $\delta^{18}O$ values, the formation time of fibrous calcite/ankerite is the same as that of organic acid production. A large amount of fine quartz is formed by the transformation of clay minerals, and SiO_2 precipitation is formed by the dissolution of terrigenous feldspar. The authigenic albite precipitates in carbonate dissolution pores when the production of organic acids is reduced. Authigenic carbonate affects the smectite-illite transformation process by influencing the ion concentration in the pore fluid. Pyrite transforms from colloidal pyrite formed by the action of BSR in the early stage of diagenesis and affects the concentration of Fe^{2+} ions in the early pore fluid. The contents and types of organic matter in different lithofacies differ, which directly leads to differences in pore fluid pressure and organic acid concentration during the thermal evolution stage of organic matter, thus affecting the diagenesis of different lithofacies.

KEYWORDS

mudstone, diagenesis, authigenic mineral, eocene, east China

1 Introduction

In recent years, shale oil and gas exploration has increased considerably in many countries, especially North America and China (U.S. Energy Information Administration, 2020). The shale oil and gas resources in North America are derived mainly from marine organic-rich shales such as the Barnett shale (Montgomery et al., 2005; Loucks et al., 2009), Marcellus shale (Milliken et al., 2013) and Haynesville shale. Continental organic-rich shale systems are widely distributed in China, such as the Cretaceous Qingshankou Formation in the Songliao Basin (Huang et al., 2013), the Triassic Yanchang Formation in the Ordos Basin (Cao et al., 2015; Wu et al., 2015), the Jurassic Ziliujing Formation in the Sichuan Basin (Nie et al., 2017), the Palaeogene Shahejie Formation (Li, 2015; Sun, 2017; Zhang et al., 2018) and the Kongdian Formation (Zhao et al., 2018) in the Bohai Bay Basin.

With the development of shale exploration and theoretical research, an increasing number of scholars are concerned with the change in shale porosity during diagenesis (Wu et al., 2017; Hu et al., 2019). The change in porosity is related mainly to the diagenetic evolution of minerals (Bilal et al., 2022a), the thermal evolution of organic matter (Chen and Xiao, 2014) and the development of fractures (Ma et al., 2020). Fibrous calcite (including beef veins and cone-in-cone structures) is a common mineral occurrence in mudstone; it is commonly found in black shale rich in organic matter and carbonate rock and has attracted extensive attention (Durney and Ramsay, 1973; Marshall, 1982; Cobbold et al., 2013; Weger et al., 2019; Song et al., 2020). Studies have shown that fibrous calcite formation is related to hydrocarbon generation overpressure (Zhang et al., 2016; Bilal et al., 2022b) and dissolution of carbonate formed during the sedimentary period (Luan et al., 2019). In the process of clay mineral transformation, large amounts of Si, Na, Ca, Mg, and Fe are discharged into the pore mixture and precipitate into quartz, feldspar, chlorite, and carbonate (Hower et al., 1976; Boles and Franks, 1979; Abercrombie et al., 1994; Bjørlykke, 1998), affecting the density and hardness of the reservoir (Yang et al., 2018; Xi et al., 2019). Strawberry pyrite may be converted from mackinaite formed by bacterial sulfate reduction (BSR) (Marin-Carbonne et al., 2014). Organic matter can form many organic acids and CO_2 during thermal evolution (Lundegard et al., 1984; Barth and Bjørlykke, 1993; Seewald, 2003), and the amount of organic acids and CO_2 production are closely related to the type of organic matter (Hu et al., 2020). When these fluids enter the pore fluid of mudstone, the diagenetic environment inside the mudstone changes.

This study investigates mudstone of the Es3x and Es4s submembers of the Dongying Depression, Bohai Bay Basin. The division of lithofacies and diagenesis of each lithofacies are investigated based on the petrology, mineral composition, stable isotope characteristics, major and trace element characteristics, and rock pyrolysis parameters of mudstone. The interactions between these minerals and minerals, between minerals and organic matter, and their secondary changes during burial constitute the so-called "coevolution of minerals." This evolution is crucial for the development of sweet spots. The main objectives of this study are (1) to explain the diagenesis types and diagenetic evolution of mudstone under lithofacies constraints and (2) to explore the evolution and relationships of primary and secondary minerals in each stage of petrogenesis. These works help to understand mineral development in mudstones and identify potential "sweet spots." This information is helpful for understanding how diagenesis changes the physical properties of mudstone, which is highly important for shale oil and gas exploration and development.

2 Geologic setting

The Dongying Depression is a typical lacustrine half-graben located in the Bohai Bay Basin in eastern China (Figure 1A). The Dongying Depression covers an area of approximately 5,000 km^2 and is adjacent to the Chenjiazhuang uplift to the north; the Luxi uplift and Guangrao uplift to the south; the Qingcheng uplift to the west; and the Qingtuozi uplift to the east (Figure 1B). It contains Palaeogene, Neogene and Quaternary strata, including the Shahejie (Es), Dongying (Ed), Guantao (Ng), Minghuazhen (Nm) and Pingyuan (Qp) formations, in ascending order. The Es Formation can be further divided into members Es4 (lower Es4x Submember and upper Es4s Submember) and Es3 (lower Es3x Submember, middle Es3z Submember, upper Es3s Submember) (Figures 1C, D). This depression hosts five secondary tectonic zones from south to north: the southern gentle slope zone, the southern zone (Niuzhuang Sag), the central anticline zone, the northern zone (Lijin Sag), and the northern steep slope zone (Figure 1D), with a central local thickness of approximately 5,000 m (Chen et al., 2007; Guo et al., 2010).

This study focuses on Es4s and Es3x. The Dongying Depression began to expand after the Mesozoic and reached its maximum diameter (>50 m) during this period, when a series of fan and braided deltas developed along the lake's edges, and the centre of the deep-water lake was filled with thick black shale (approximately 400 ms thick), which was the main source rock for the oil-bearing depression. These organic-rich laminated shales and massive mudstones have total organic contents (TOCs) ranging from 0.47 to 12.4 wt%. The organic matter is predominantly planktonic algae ditch whip algae, coccoliths, and Bohai algae. The shale is thermally mature, as supported by vitrinite reflectance (Ro) measurements (0.69%–1.21%) and Tmax values (435°C–460°C). The above data indicate that the shales of Es3x to Es4s in the Dongying Depression are in a stage of mesodiagenesis (Figure 1E).

3 Materials and methods

All the shale samples were taken from the cores of three wells (Figure 1B), and the total core length was 204.6 m. A total of 137 slices were impregnated with standard epoxy and partly stained with Alizarin Red S and K-ferricyanide for the differentiation of carbonate minerals. Optical photomicrographs were taken with plane-polarized light (PPL), cross-polarized light (XPL) and reflected light (RL) using an Axio Scope A2m Zeiss Polarizing Microscope. Fluorescence light (FL) photomicrographs were taken with a Leica Model DMRX HC polarization fluorescence microscope. Cathodoluminescence (CL) analyses were carried out with an Olympus microscope equipped with a CL8200-MK5 CL instrument with a beam voltage of 17 kV and a current of 600 μA. Backscattered electron (BSE) and scanning electron microscopy (SEM) observations were performed with a Nova Nano SEM 450.

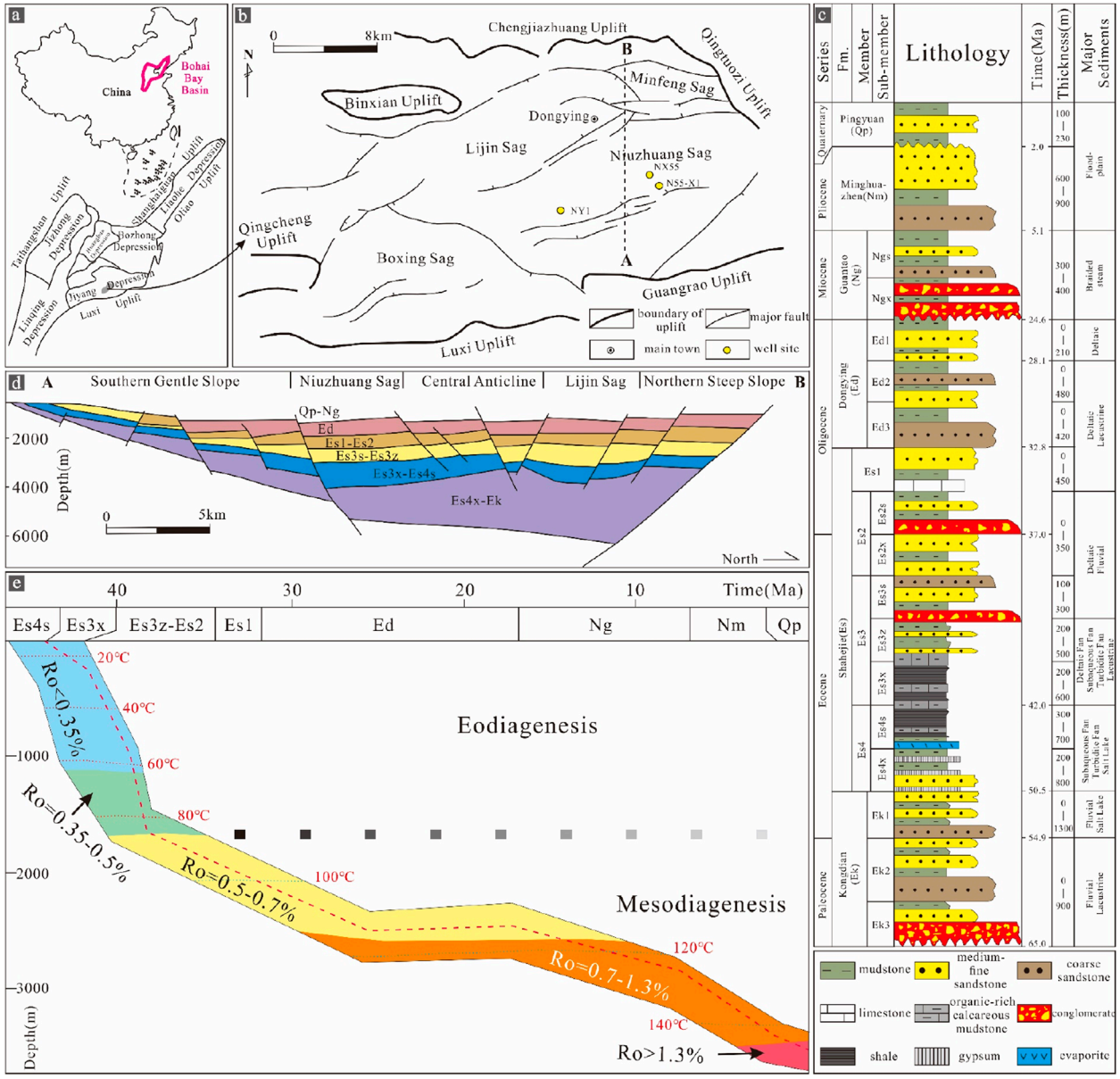

FIGURE 1
Basic information of the study area: **(A)** Location of the Bohai Bay Basin (Ma et al., 2021). **(B)** Structural features of the Dongying Depression and the sampling well locations in the study area. **(C)** Generalized Cenozoic–Quaternary stratigraphy of the Dongying Depression (Luan et al., 2019). **(D)** Cross-section AB showing the different tectonic–structural zones and key stratigraphic intervals (Guo et al., 2010). **(E)** Thermal and burial history of Es3x and Es4s and the general stages of diagenesis.

FSEM with a built-in Oxford X-Max 80 energy spectrometer. The voltage was 15 kV, the spot size was 5.5 nm, and the working distance was 5.0–6.5 mm. A portion of each sample was polished with argon ions to observe the mineral pore characteristics. A rock analyser (ROCK-EVAL. II) and a carbon and sulfur analyser (CS-230HC) were used for rock pyrolysis analysis and total organic carbon (TOC) analysis. The X-ray powder diffraction (XRD) analysis instrument used was a Phillips XPert PW3710 diffractometer with CuKα (λ = 1.54060 Å) radiation, a voltage of 40 kV and a tube current of 35 mA. Major and trace element contents were determined using an X-ray fluorescence (XRF) Phillips PW2400 spectrometer with Rh-Kα radiation and a power of 2400 W. In the carbon and oxygen isotope analysis, fibrous calcite, micritic lamellar calcite, and dispersed ankerite were sampled with a microscopically mounted drill assembly, whereas mudstone samples (without fibrous calcite) were powdery. The powder was reacted with ultrapure phosphoric acid at 25°C in an inert atmosphere. The extracted CO_2 was carried by helium gas through a column and transferred to a MAT251 isotope ratio mass spectrometer, where the gas was ionized and the isotope ratio was determined. All analyses are converted to VPDB.

10.3389/feart.2025.1502476

TABLE 1 Summary of organic geochemical parameters and mineral compositions of Es3x and Es4s from the Dongying Depression by XRD analysis.

Type of shale lithofacies	Mineral content (%)						Organic matter type	Organic volume (%)
	Carbonate	Qtz + Fs + Py	Clay					
	Min - Max		Tot	Mixed I/S	Ill		Min–Max (Average)	
laminated clay-rich carbonate mudstone (L1)	53.3–67.4	3.4–16.2	26.4–47.3	12.5–14.8	85.2–87.5	$I–II_1$	6.72–15.8 (10.36)	
laminated mixed mudstone (L2)	26.4–44.6	30.1–47.5	35.4–44.8	11.8–19.2	80.8–88.2	$I–II_1$	5.95–8.64 (7.43)	
laminated clay-rich siliceous mudstone (L3)	1.2–11.3	50.7–59.1	37.6–48.7	35.2–38.1	61.9–64.8	$II_2–III$	2.13–3.87 (3.13)	
massive argillaceous carbonate mudstone (L4)	25.2–39.5	11.3–17.7	35.1–49.7	31.0–37.6	62.4–69.0	$I–II_1$	4.32–7.13 (6.31)	
laminated argillaceous siliceous mudstone (L5)	7.3–18.4	26.4–42.6	36.3–47.2	41.4–46.3	53.7 53.7–58.6	$II_1–II_2$	3.21–5.93 (4.14)	

Tips: Qtz, quartz; Fs, feldspar; Py, pyrite; Ill, illite; I/S, illite/smectite; Organic volume (V_o) = $Wo*K*\rho_m/\rho_o$, **Wo:** TOC; **K:** organic matter conversion coefficient (Tian and Zhang, 2016); ρ_m: density of mudstone; ρ_o: density of organic matter.

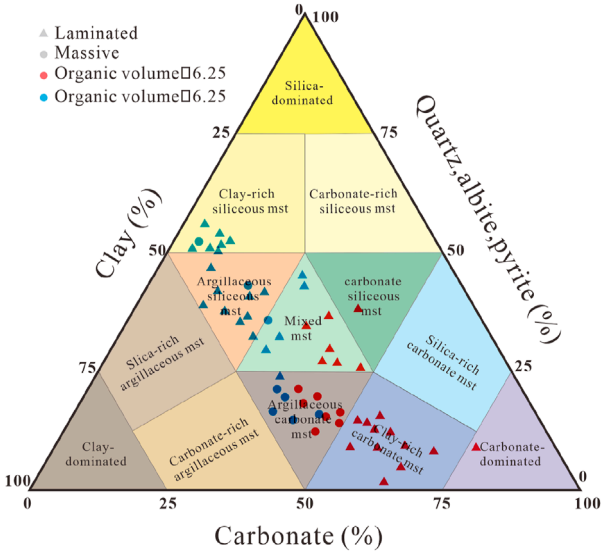

FIGURE 2
Three-end-member diagram of the mudstone mineral composition. The ternary diagram is simplified based on Diaz et al. (2013).

4 Results

4.1 Lithofacies descriptions

For convenience, the mineral composition, sedimentary structure characteristics and organic matter content of the mudstone were determined. The mineralogical data, such as the core and XRD data (Figure 2), were plotted on a ternary plot, and five lithologies were defined: laminated clay-rich carbonate mudstone (L1), laminated mixed mudstone (L2), laminated clay-rich siliceous mudstone (L3), massive argillaceous carbonate mudstone (L4), and laminated argillaceous siliceous mudstone (L5). Their respective characteristics are described in detail below.

Laminated clay-rich carbonate mudstone (L1) contains many fibrous calcite laminae, which are usually symbiotic with the micritic calcite laminae that formed during deposition. There are also abundant carbonate minerals in the noncalcite laminae. The organic matter content is high, and the organic matter type is mostly type I. This type of lithofacies is generally regarded as the "sweet spot" of mudstone reservoirs. Laminated mixed mudstone (L2) contains a certain amount of fibrous calcite, but this type of lamina is significantly less dense than that in L1. The content of clay minerals increased significantly, and a small amount of siliceous lamina was noted. This change is related to the change in the sedimentary environment during lithofacies formation. This type of lithofacies is omitted in the subsequent analysis because the lithofacies minerals are diverse and can be considered a transitional type between L1 and L3 or L5. Its characteristics are repeated with other types of lithofacies, so it will not be further described. Laminated clay-rich siliceous mudstone (L3) contains a large amount of siliceous lamina, in which quartz, feldspar and certain amounts of carbonate minerals are distributed. The organic matter type of the lithofacies is $II_2–III$,

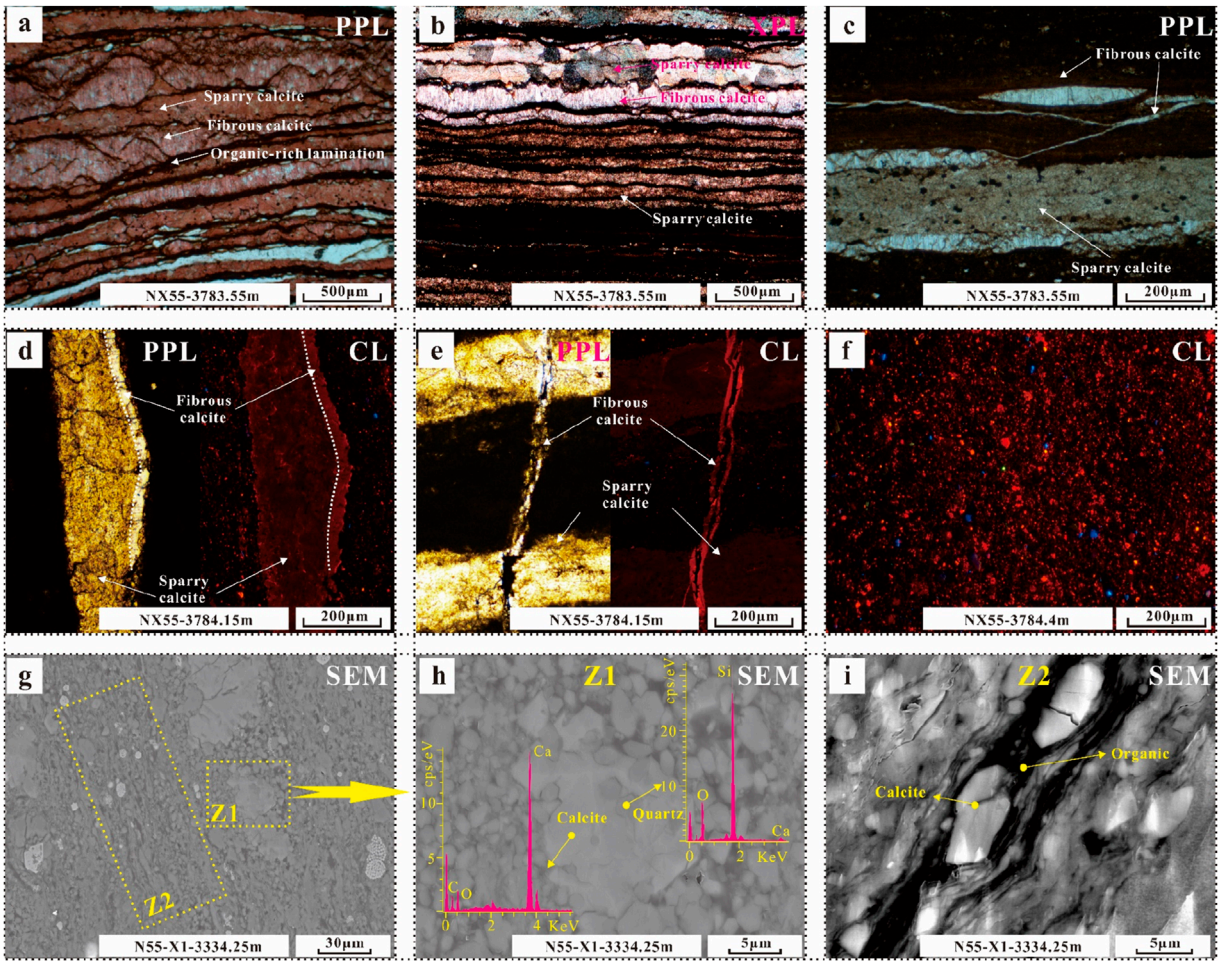

FIGURE 3
Photographs of the characteristics of calcite in different occurrences in various lithofacies. **(A)** Sparry calcite interbedded with fibrous calcite and occasionally exhibiting organic-rich laminae. **(B)** Some sparry calcite recrystallized to a high degree. **(C)** Fibrous calcite growing in cracks. **(D)** Contrast of CL between sparry calcite and fibrous calcite. **(E)** Sparry calcite in cracks. **(F)** Distribution of carbonate rocks in clay mineral beds. **(G–I)** Calcite of various occurrences and mineral associations in the clay mineral layers.

and the organic matter content is low. Massive argillaceous carbonate mudstone (L4) is characterized by a massive structure, in which the contents of clay and carbonate are high, mostly carbonate is distributed in clay minerals, the organic matter type is I_1–II_2, and the organic matter content is high. Laminated argillaceous siliceous mudstone (L5) also contains many siliceous laminae, but unlike those in L3, the siliceous laminae in this lithofacies are denser, the grains in the laminae are mainly quartz and clay minerals, the quartz particles are small, and the organic matter type is II1–II2 with moderate organic matter content.

4.2 Diagenetic minerals

4.2.1 Calcite

There are three main types of calcite: fibrous calcite, sparry calcite and micritic calcite. Sparry calcite is formed early by biological induction. The recrystallization of this calcite occurs during burial, and the degree of recrystallization is significantly greater in areas where fibrous calcite is densely developed (Figures 3A, B). Fibrous calcite occurs mainly in mud shales as fracture filler (Figures 3A, B). These fractures may be cracks in bedding, cracks caused by shrinkage during the diagenetic evolution of clay minerals, or structural fractures (Figure 3C). The CL characteristics of the two calcite types are significantly different, with fibrous calcite being brighter and showing a lower Fe content (Figures 3D, E). These two kinds of calcite are common in lithofacies L1 and L2.

Micritic calcite is distributed mainly in regions with undeveloped laminae, and its Cl characteristics are similar to those of fibrous calcite laminae (Figure 3F). It is dispersed in clay minerals and has two different forms (Figure 3G): in Zone 1, calcite particles are large and often symbiotic with fine quartz particles (Figure 3H); in Zone 2, there is also some fine calcite in the bedding clay mineral layer (Figure 3I). This calcite is common in lithofacies L1, L2, L4 and L5.

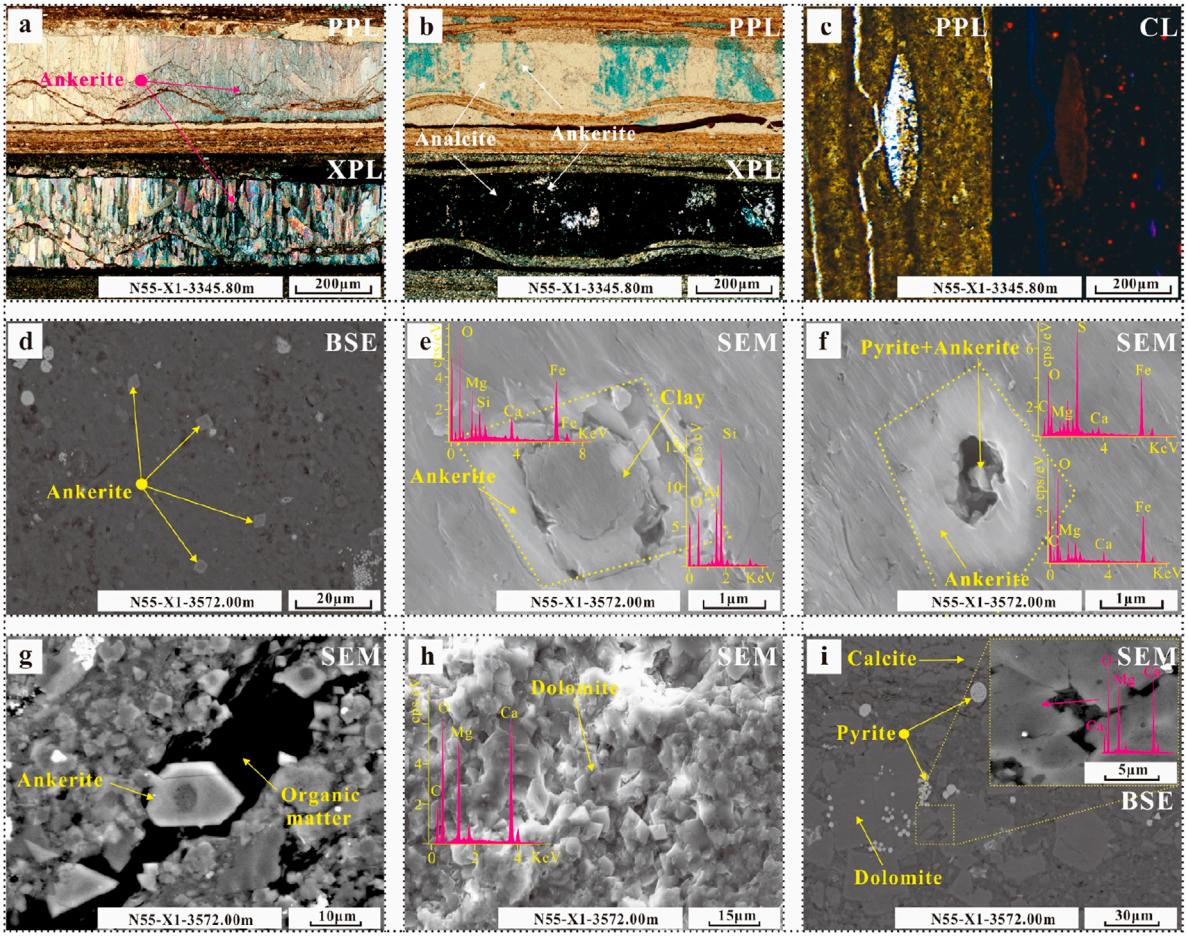

FIGURE 4
Photographs of the characteristics of dolomite–ankerite in different occurrences in various lithofacies. **(A)** Fibrous calcite metasomatized by ankerite. **(B)** The analogue was metasomatized by ankerite. **(C)** Characteristics of dolomite–ankerite under CL. **(D–G)** Distribution characteristics of ankerite with a foggy core/bright edge. **(H, I)** Dolomite distribution in the clay layers.

4.2.2 Dolomite–ankerite

Dolomite-ankerite is abundant in only one section of well N55-X1, the lithofacies type is not as comprehensive as that of the NX55 well, and only L1 and L4 are characterized in the core of this calibre. Fibrous ankerite is layered (Figure 3A), and ankerite cements are found in some of the dissolved pores in the analcime (Figure 4B). The CL characteristics are obviously dark, resulting in a high Fe content (Figure 4C). One of the most common characteristics is the widely distributed foggy core/bright edge ferrite in clay minerals (Figure 4D), which is shaped like a diamond; its core is usually clay minerals or pyrite, and its core is obviously dissolved (Figures 4E, F). This ferrite is sometimes associated with organic materials (Figure 4G). The dolomite content in this section is also high (Figure 4H), with abundant clay minerals in the form of clumps and aggregates (Figure 4I).

4.2.3 Quartz

There are two types of quartz: terrigenous quartz and authigenic quartz. Terrigenous clastic quartz is usually laminar and often contains water-escape structures formed by early undercompaction (Figures 5A, B). Some siliceous laminae contain organic matter (Figure 5C). Under CL, these laminae contain a certain amount of carbonate minerals (Figure 5D), the quartz includes blue and dark red high-temperature quartz, and there is no evidence of the luminescent diagenetic process of authigenic quartz (Figure 5E). This type of quartz is common in lithofacies L3 and L5.

SEM observations revealed that there are autogenic quartz types with different characteristics in different zones of lithofacies L1 (Figure 5F): those with sparry calcite dissolution pores, clay minerals, and a black line in fibrous calcite. In Zone 1, authigenic quartz half-fills the dissolution pores of micritic calcite in the form of cement (Figure 5G). In Zone 2, it fills the shrinkage crack of clay minerals in the form of cement (Figure 5H); in Zone 3, the quartz exists in gaps along the growth edges of fibrous calcite (Figure 5I).

4.2.4 Feldspar

Feldspars include terrigenous feldspar and authigenic feldspar. The distribution of terrigenous feldspar is similar to that of terrigenous quartz, but the dissolution degree is greater (Figure 6A). Pores at the grain margins and within the grains are developed (Figures 6B, C). Small amounts of anorthite are also found in different lithofacies (Figures 6D, E). Terrigenous feldspar is common in lithofacies L3 and L5. Authigenic feldspar is mostly found in lithofacies L1 and L2, mainly

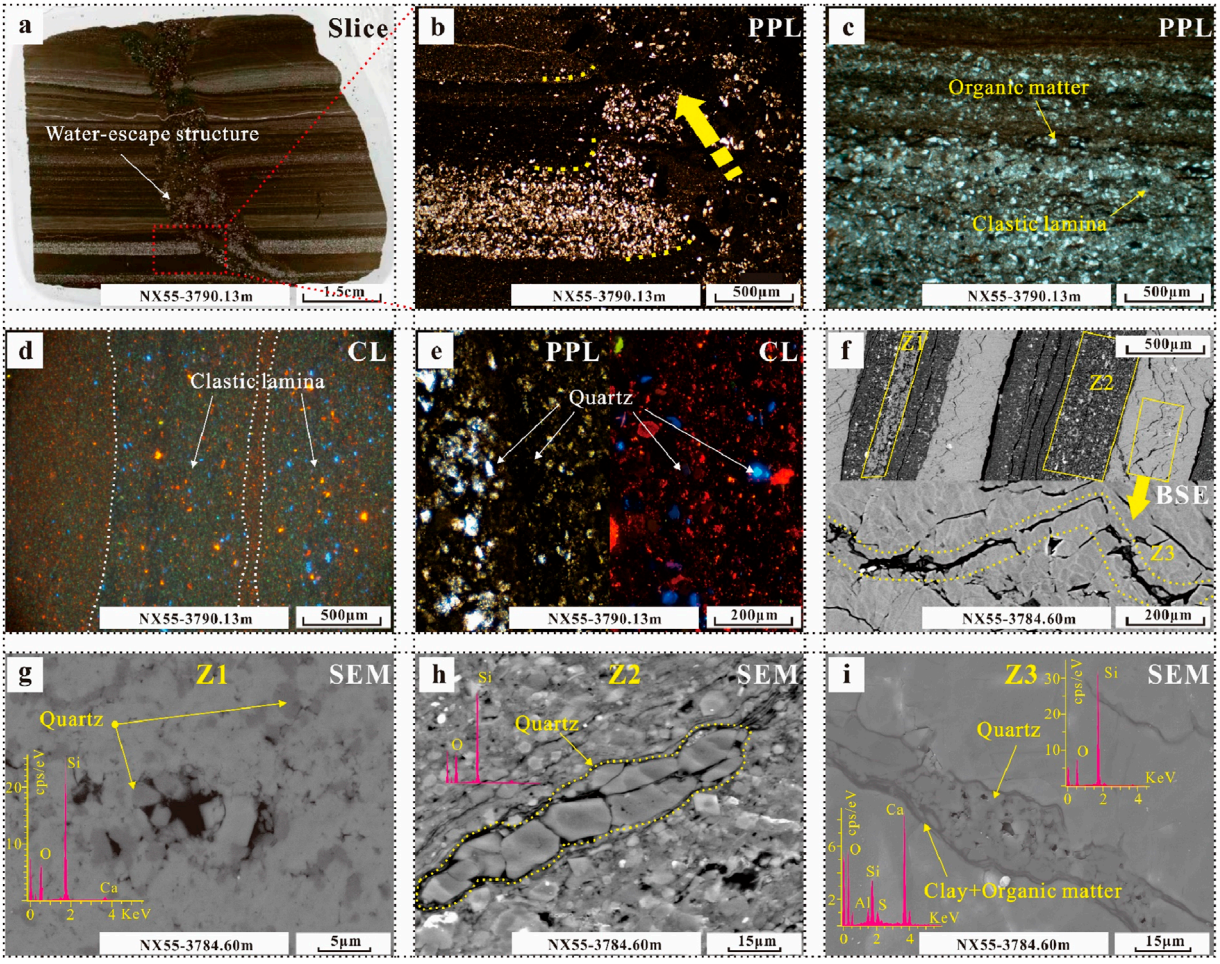

FIGURE 5
Photographs of the characteristics of different types of quartz in various lithofacies. **(A, B)** Quartz and a water-escape structure in a clastic lamina. **(C)** Distribution of quartz and organic matter in a lamina. **(D, E)** CL characteristics of quartz of different origins in the lamina. **(F–I)** Characteristics of quartz in different zones.

albite and orthoclase, which are distributed in the dissolution gap between calcite and ankerite (Figures 6F–I).

4.2.5 Clay

Clay minerals constitute an important part of mudstone. In addition to the clay layers, clay minerals mostly exist in the form of cement in the intergranular pores of minerals (Figures 7A–D). In the clay mineral layer, the main forms of clay minerals are illite and illite/smectite layers (Table 1). In laminar lithofacies (e.g., L1, L2, L4, and L5), clay minerals are layered, and minerals such as organic matter and pyrite are distributed between the laminar clay minerals (Figures 7E, F). In L4, clay minerals form massive aggregates with other minerals (Figure 7G). Most clay shapes are pilar and fibrous (Figure 7H). There is also a small amount of acicular chlorite in these rocks (Figure 7I).

4.2.6 Pyrite

Pyrite is widely distributed in this mudstone (Bilal et al., 2024), and there are two main types: strawberry pyrite in sparry calcite laminae (Figure 8A) and strawberry pyrite (Figures 8B, D), agglomerate pyrite (Figures 8B, C), or massive pyrite in clay minerals (Figure 8C). Intergranular pores are present in strawberry pyrite (Figure 8E), some of which contain organic matter (Figure 8F). The types of pyrite that form the cores of other minerals are described above.

4.2.7 Organic matter

Organic matter is widely distributed in various lithofacies. In L1, the fluorescence reaction is very strong. From clay minerals to fibrous calcite, the fluorescence colour changes from brown to blue to green, which indicates that the organic matter has a high degree of evolution (Figure 9A). In L3, although the organic matter content is very low, the thin section fluoresces green, indicating considerable organic matter evolution (Figure 9B). In L4, the overall luminous intensity is weak, with brown fluorescence and a low degree of organic matter evolution (Figure 9C). In L5, the organic matter is brown–green and has undergone moderate evolution (Figure 9D).

SEM observations reveal that organic matter sometimes appears with pyrite and that the pyrite is evenly distributed around the organic matter (Figure 9E). Organic matter develops different

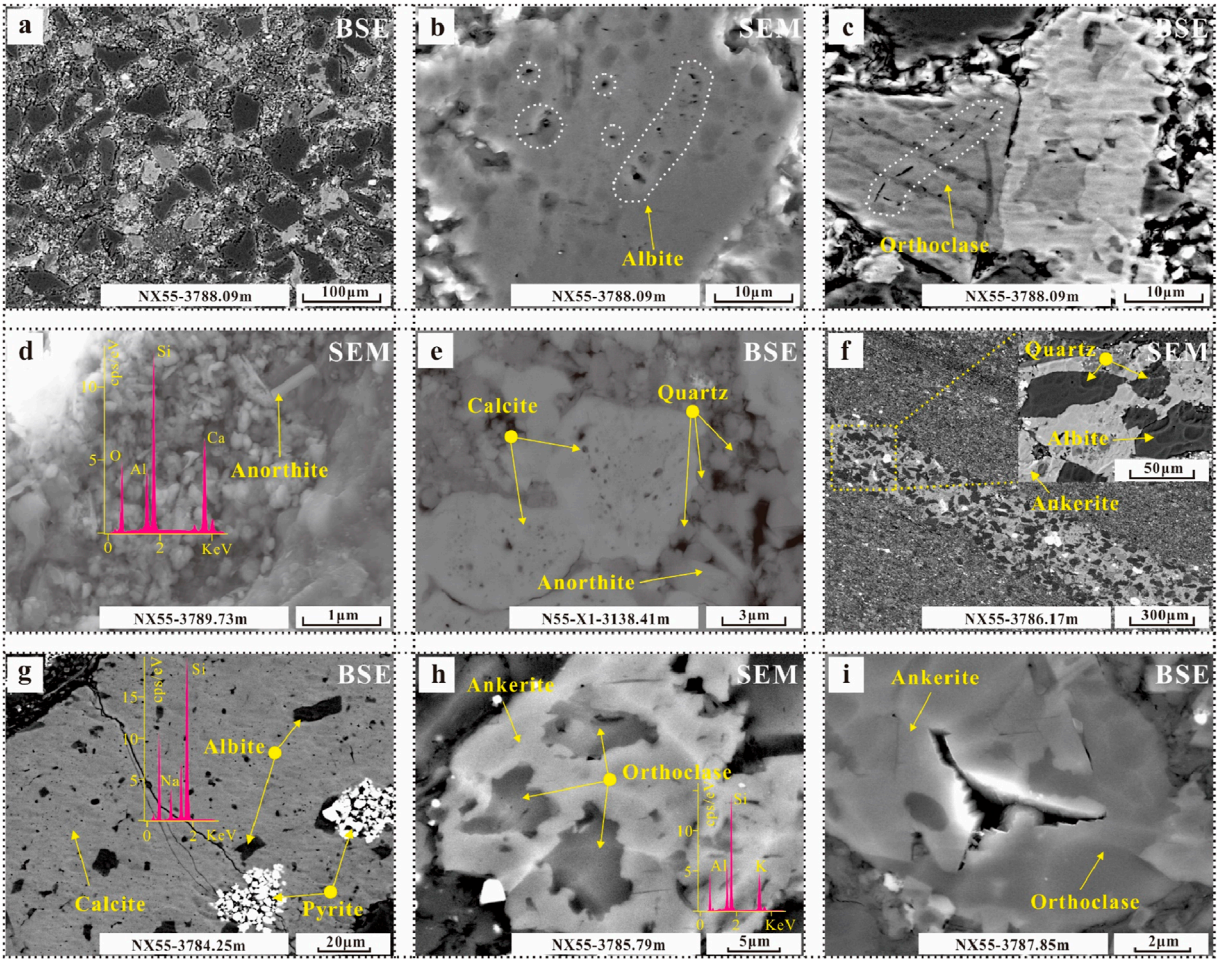

FIGURE 6
Photographs of the characteristics of feldspar in different occurrences in various lithofacies. **(A)** Distribution of terrigenous feldspar. **(B)** Dissolution on albite. **(C)** Dissolution on orthoclase. **(D)** Distribution of anorthite. **(E)** Mineral assemblage of calcite, quartz and anorthite. **(F–I)** Characteristics and distribution of authigenic feldspar.

pore types, which can be interpreted to determine the type of organic matter and its degree of evolution. Some highly evolved organic matter with well-developed internal and boundary pores is identified (Figure 9F). Some organic matter margins are associated with rock salt crystals (Figure 9G). Some organic matter has no pores but has developed small shrinkage cracks (Figure 9H) that grow through the organic matter as they develop (Figure 9I).

In this work, two methods were used to classify organic matter types: hydrogen index–oxygen index plots and hydrogen index-T_{max} plots. During the pyrolysis of type I organic matter, a large amount of pyrolytic hydrocarbon S_2 was released, whereas a small amount of type S_3 and type III organic matter produced only a small amount of pyrolysis S_2. The type of organic matter can be determined by placing the hydrogen and oxygen indices of mudstones on a map. The advantage of using the hydrogen index and T_{max} chart to classify organic matter is that the influence of the maturity index T_{max} on the hydrogen index is also considered. With increasing T_{max}, the hydrogen index of organic matter gradually decreases along the trajectory curve.

The calculation formulae of the hydrogen and oxygen indices shown in Figure 10 are given in Table 2. The drop points on the plot reflect the different types of organic matter in the different lithofacies (Figures 10A, B). The corresponding relationship between the lithofacies and depth of each well suggests that there is a correspondence between the lithofacies and organic matter types: L1 corresponds to I-II_1, L2 corresponds to I-II_1, L3 corresponds to II_2-III, L4 corresponds to I-II_1, and L5 corresponds to II_1-II_2 (Table 1).

5 Discussion

5.1 Sealing properties of diagenetic systems

Overpressure generally occurs in the Dongying Depression, and a large-scale overpressure system occurs in mainly the lower Es3 and upper Es4 members of the mudstone system (Liu and Xie, 2003; Zhang et al., 2010; Qiu, 2018). According to a large amount of drill stem test (DST) data, the depth of the abnormally high pressure in the Es3 and Es4 members is in the range of 2,200–4,400 m, the remaining pressure is in the range of 4–440 MP,

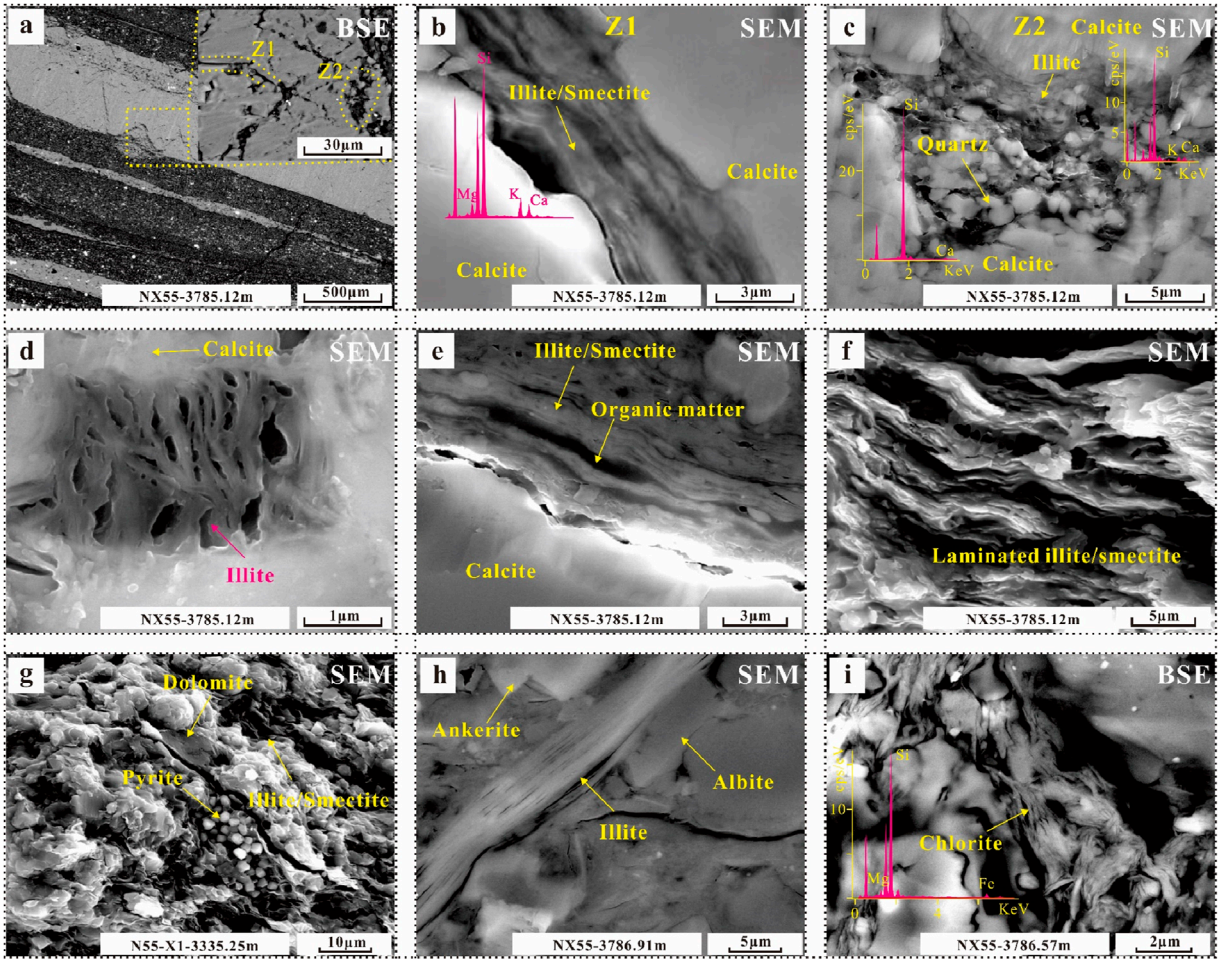

FIGURE 7
Photographs of the characteristics of clays in various lithofacies. **(A)** Characteristics of illite/smectite in different zones. **(B)** Clay minerals in a black line in fibrous calcite. **(C)** Clay minerals and authigenic quartz filling carbonate dissolution pores. **(D)** Illite filling carbonate dissolution pores. **(E–H)** Distribution, characteristics and associations of illite/smectite with other minerals. **(I)** Distribution and characteristics of chlorite.

and the pressure coefficient is in the range of 1.2–1.99 (He et al., 2012). Macroscopically, the pressure coefficient increases gradually from the edge to the interior of the depression. The occurrence of abnormal pressure is caused by the diagenesis and expulsion of hydrocarbons from organic matter.

In the absence of fracture development, the permeability of mudstone is generally less than 10^{-6} millidarcy (Jarvie, 2012), and the fluid in mudstone is difficult to transport. Eocene mudstone cores and thin beds in China are less fractured and have low permeability (Zhang et al., 2016). As a result, injecting external fluids into these mudstones is difficult.

The sealing property of mud shale can be used to analyse the openness of the diagenetic system. The Sr, Mn and Ca contents of each lithofacies in the NX55 well were calculated, and the Sr/Ca and Mn/Ca values were subsequently calculated (Figure 11). When the Sr/Ca value is high, the Mn/Ca value is low, and the diagenetic system tends to be closed. When the Sr/Ca value is low, the Mn/Ca value is high, and the diagenetic system tends to be open such that other fluids are involved in diagenesis (Tian and Zhang, 2016). Across the interval, the Sr/Ca values were high, and the Mn/Ca values were low. However, there are two sections with high Mn/Ca values in lithofacies L3 and L5. According to petrological evidence, the openness of the lithogenic system may be related to the following factors: terrigenous clastic grains are abundant, the porosity is high (L3), and early undercompaction leads to the development of drainage structures, which leads to the participation of other fluids in diagenesis (L5).

Based on the formation overpressure system, lithologic characteristics and elemental geochemistry data of Es3x and Es4s, the mudstone in this section corresponds to a relatively closed diagenetic system as a whole.

5.2 CO_2 and ion sources for authigenic carbonate

Stable carbon isotopes are highly stable in different deep-cycle carbon pools and can be used to indicate the carbon source of authigenic carbonate minerals during diagenesis (Siegel et al., 2004;

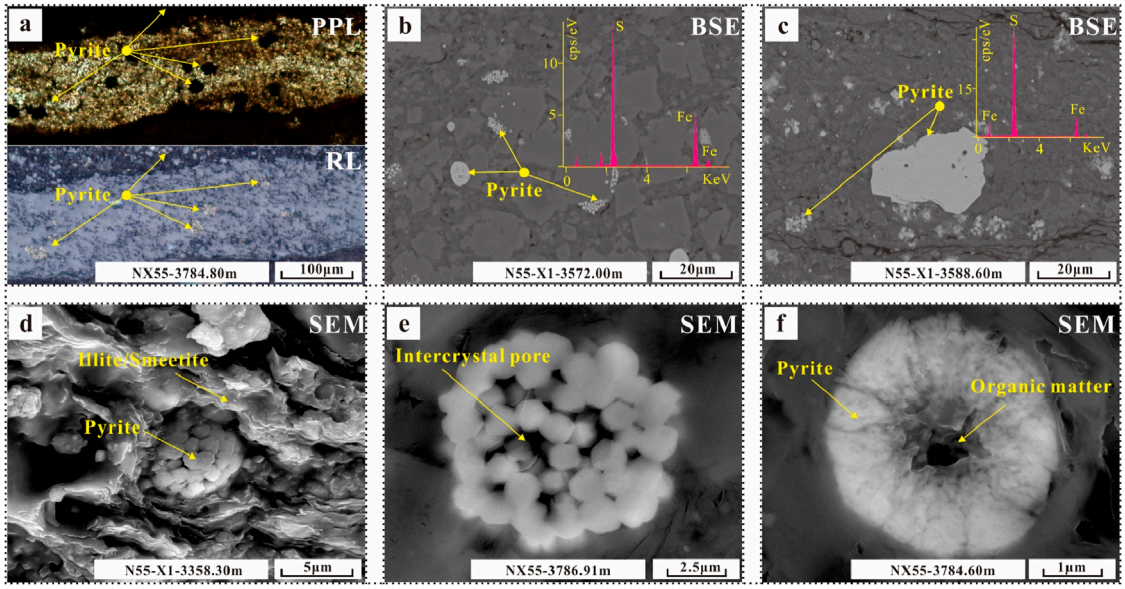

FIGURE 8
Photographs of the characteristics of pyrite in different occurrences in various lithofacies. **(A)** Distribution of pyrite in sparry calcite. **(B)** Distribution of strawberry and agglomerate pyrite. **(D)** Distribution of pyrite in clay minerals. **(E)** Pore characteristics of pyrite. **(F)** Organic matter in intergranular pores.

Cao et al., 2018). The $\delta^{13}C$ values range from 0.2 to 1.3 for sparry calcite, 3.2 to 6.4 for micritic calcite, 1.8 to 5.1 for fibrous calcite, 1.9 to 3.6 for ankerite, and 3.1 to 5.9 for micritic dolomite (Table 3). The $\delta^{13}C$ values of these five different types of carbonate vary greatly, which makes it possible to determine the source of dissolved CO_2 for authigenic carbonate minerals by analysing the distribution of $\delta^{13}C$ (Warren, 2000; Kordi et al., 2017). In terms of the overall carbon isotope characteristics, the carbon isotope characteristics of the main authigenic carbonate are similar to those of the lacustrine facies micritic carbonate and the early carbonate cements in the mudstone, indicating that the carbonate ions needed for authigenic carbonate mineral precipitation are derived mainly from this source (Figure 12). The decrease in the carbon isotope value may be related to the decomposition of organic matter by sulfate-reducing bacteria (Irwin et al., 1977; Jiang et al., 2013), the thermal decarboxylation of organic matter (Jansa and Urrea, 1990; Sensuła et al., 2006), and the influence of diagenesis on the isotopic composition of authigenic carbonate minerals (Fritz and Smith, 1970).

In the relatively closed environment of the diagenetic system, it is difficult for external fluid to enter the mudstone; therefore, the ions needed for the growth of authigenic carbonate minerals in the mudstone likely come from the mudstone itself. Petrological and geochemical findings indicate that fibrous carbonate rocks always exhibit laminar fractures, clay mineral shrinkage fractures and structural fractures in mudstones (Figure 3C). The $\delta^{18}O$ values of fibrous carbonate rocks are always lower than those of micritic carbonate and sparry calcite (Table 3), indicating that they formed relatively late in the diagenetic process (Irwin et al., 1977; Sass et al., 1991). The above analysis reveals that the carbonate ions needed for authigenic carbonate mineral precipitation mainly originate from lacustrine carbonate sediments. Therefore, the Ca^{2+} and Mg^{2+} ions needed to form authigenic carbonate rocks should also have originated from these lacustrine carbonate deposits. Montmorillonite-illite transformation also releases some Ca^{2+} and Mg^{2+} (Peltonen et al., 2009).

Due to the low porosity and permeability of mudstone, the Fe^{2+} supply in the pore water of this mudstone likely comes from montmorillonite-illite transformation (Figure 7) (Bjørlykke et al., 1992; Xi et al., 2015; Haile et al., 2019) and the dissolution of unstable minerals in pyroclastics (Figures 6A–C) (Boles and Franks, 1979; Morse and Wang, 1997). Petrological evidence shows that both types of Fe^{2+} are derived from terrigenous pyroclasts and that the transformation of montmorillonite-illite typically occurs in mudstones. No cyclic band of carbonate luminescence was found under cathodoluminescence, which indicates that the source and content of Fe^{2+} in pore water are stable in a closed diagenetic environment (Ma et al., 2021). Therefore, montmorillonite-illite transformation should be the main source of Fe^{2+} here.

5.3 Formation time and mechanism of authigenic carbonate

The fractionation coefficient of the oxygen isotopes is related to the temperature. The formation temperature of carbonate minerals can be calculated from the oxygen isotope values of the minerals and the oxygen isotope values of the palaeofluid. Similarly, the oxygen isotope values of palaeofluids can be obtained from the oxygen isotope values of carbonate minerals and precipitation temperatures (Zhang et al., 2021a). First, the oxygen isotope fractionation diagram of the calcite precipitation process and the oxygen isotope fractionation diagram of the dolomite precipitation process were drawn with the oxygen isotope fractionation formula presented by Friedman and O'Neil (1977), and the dolomite oxygen isotope fractionation formula presented by Land (1983), respectively. Thus,

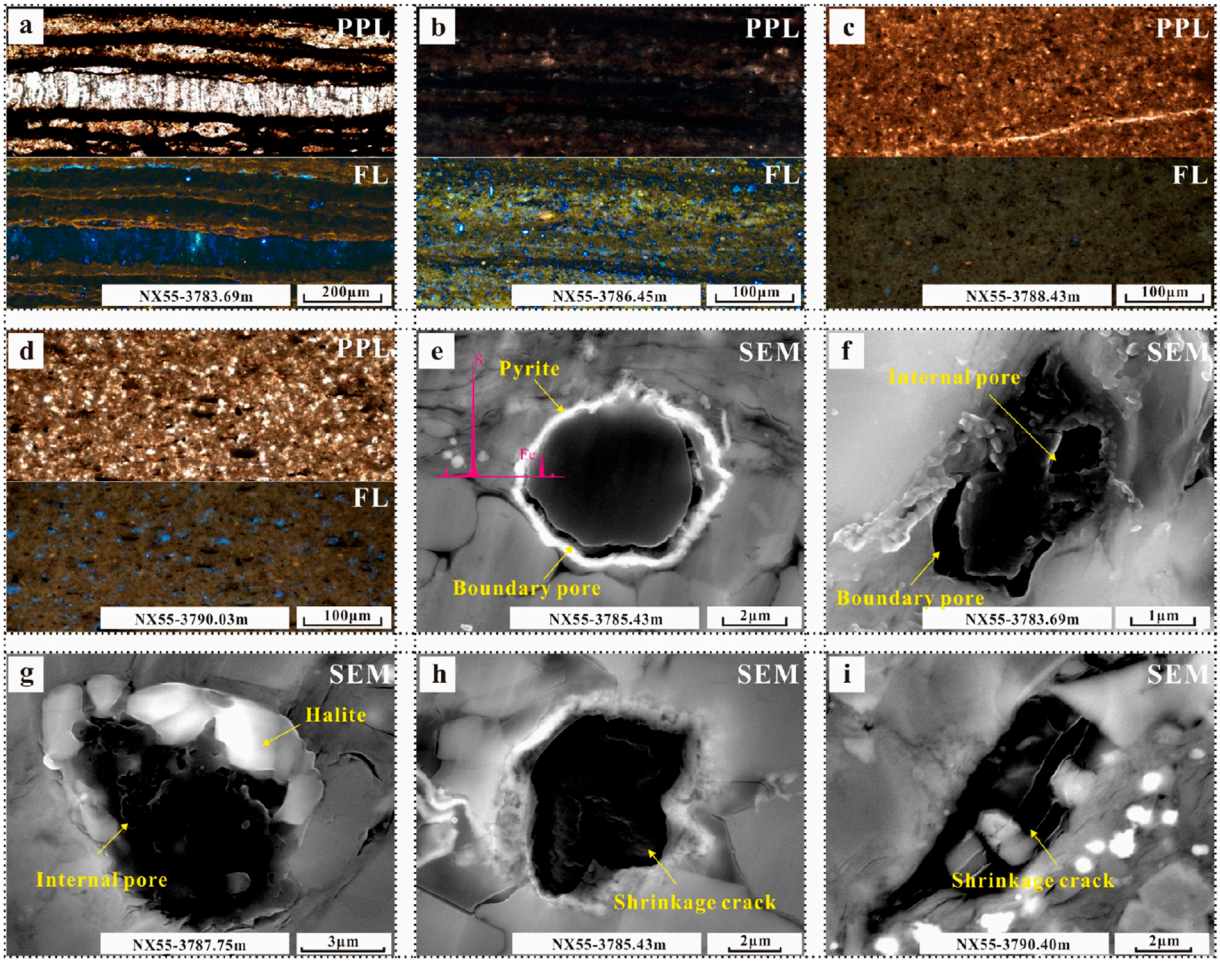

FIGURE 9
Photographs of the characteristics of organic matter in different occurrences in various lithofacies. **(A)** Distribution of organic matter in L1. **(B)** Distribution of organic matter in L3. **(C)** Distribution of organic matter in L4. **(D)** Distribution of organic matter in L5. **(E)** Pyrite is associated with the margin of organic matter. **(F)** Organic matter develops internal and boundary pores. **(G)** Organic development of irregular internal pores and margins associated with halite crystals. **(H)** Organic matter does not develop pores, but there are a few shrinkage cracks on its surface. **(I)** Shrinkage cracks throughout the organic matter.

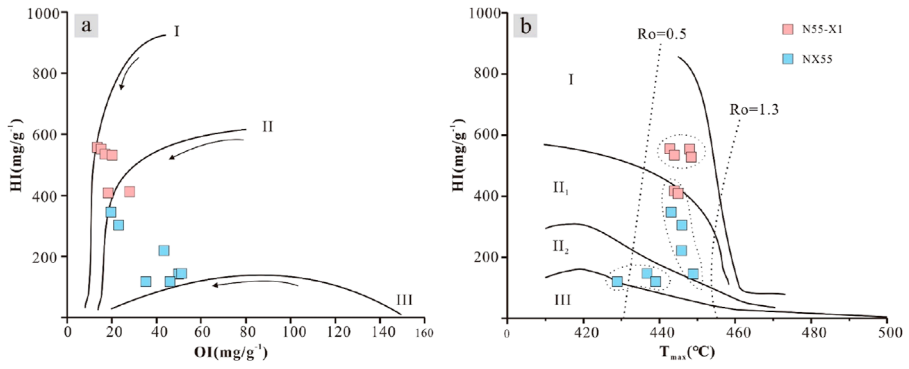

FIGURE 10
Determination of the organic matter type. **(A)** Hydrogen and oxygen indices of different mudstone samples. **(B)** Hydrogen indices and T_{max} values of different mudstone samples (Wu and Gu, 1986).

TABLE 2 Rock-Eval results, average TOCs, and hydrogen and oxygen indices of the samples from the N55–X1 and NX55 wells in the Dongying Depression.

No.	Well	Depth (m)	S_2 (mg/g)	S_3 (mg/g)	TOC (%)	Tmax (°C)	HI (mg/g TOC)	OI (mg/g TOC)
1	N55-X1	3427.70	16.64	0.52	3.11	444	535.05	16.72
2	N55-X1	3464.40	17.81	0.50	3.26	443	548.16	15.34
3	N55-X1	3540.40	13.86	0.52	2.60	448	533.08	20.15
4	N55-X1	3556.30	19.57	0.51	3.55	448	551.27	14.37
5	N55-X1	3587.00	8.74	0.59	2.12	444	412.26	27.83
6	N55-X1	3600.55	13.64	0.61	3.35	445	407.16	18.21
7	NX55	3783.69	9.83	0.57	2.83	443	347.35	20.14
8	NX55	3785.43	7.46	0.59	2.46	446	303.25	23.98
9	NX55	3785.79	1.70	0.34	0.90	439	118.89	37.78
10	NX55	3787.09	0.69	0.26	0.58	429	118.97	44.83
11	NX55	3787.85	0.74	0.25	0.52	449	142.31	48.08
12	NX55	3788.89	0.75	0.27	0.53	437	141.51	50.94
13	NX55	3790.40	1.88	0.37	0.87	446	216.10	42.53

Tips: HI, hydrogen index; OI, oxygen index.

the precipitation temperatures of various carbonate minerals were calculated. The temperature and $\delta^{18}O_{V\text{-}PDB}$ values were used to calculate the formation fluid temperatures of each carbonate mineral (Table 3).

Micritic carbonate and sparry calcite formed earlier, and their genesis was controlled by sedimentary factors (Liu et al., 2014). The $\delta^{18}O_{V\text{-}PDB}$ values of micritic calcite range from −10.3‰ to −7.4‰, those of micritic dolomite range from −10.4 to −8.0, and those of sparry calcite range from −9.6‰ to −7.6‰ (Table 3). The $\delta^{18}O_{V\text{-}SMOW}$ values of formation fluids during the formation of micritic calcite range from −9‰ to −2.5‰, those of micritic dolomite range from −9‰ to −2.7‰, and those of sparry dolomite range from −8.1‰ to −3.9‰ during the sedimentary period (Figure 13). The oxygen isotope values of dolomite that formed during the same period are approximately 2%–3% higher than those of calcite, on average (Zhang et al., 2021b). The results show that the fluid environment of the dolomite was essentially the same as that of the calcite formed during the same period, indicating that the difference in the oxygen isotope values was caused mainly by the difference in oxygen isotope fractionation. The $\delta^{18}O_{V\text{-}SMOW}$ values of the early pore fluids in Es3x and Es4s range from −9‰ to −2.5‰, which reflects the characteristics of continental fresh to brackish water and is consistent with the sedimentary environment of the continental lake basin (Jiang et al., 2013). In addition to the carbonate of sedimentary origin, some carbonate cements precipitated from the pore fluid in the early diagenetic stage. The range of $\delta^{18}O$ values for micritic calcite is wider than that for sparry calcite (Figure 13A), and the petrogenesis temperature should be higher.

The homogenization temperature of the fluid inclusions of the fibrous calcite in the upper submembers of Es3x and Es4s in the Dongying Depression is 86.4°C–117.4°C (Luan et al., 2019); this result is essentially the same as the precipitation temperature calculated by $\delta^{18}O$. Because the formation of fibrous calcite is related to hydrocarbon generation and expulsion, most of the inclusions that developed in the fibrous calcite are hydrocarbon inclusions, and the formation temperature of fibrous calcite should be slightly higher than this homogenization temperature. The $\delta^{18}O_{SMOW}$ values of formation fluids during the formation of fibrous calcite range from −2.1‰ to 3‰ (Figure 13A). Compared with those of fibrous calcite, the formation temperature and $\delta^{18}O_{SMOW}$ values of ankerite are greater, ranging from −5.8 to 3.1 (Figure 13B). The main occurrence of ankerite is laminated fibrous ankerite, cement or the "bright edge of the fog centre" (Figures 4A, B, D). From the petrological evidence, "fog heart bright side" ankerite or "fog heart centre" with clay minerals is given priority (Figures 4E, F), and its formation around the sedimentary clay minerals forms small clumps. The Fe ion needed for ankerite is provided by the transformation of the clay mineral; its formation time likely corresponds to the transformation of montmorillonite to illite or chlorite. Ankerite mainly exists in dissolution pores of carbonate minerals and silicoaluminate minerals (Figure 4B), and its formation is related to the discharge of organic acids caused by the maturation of organic matter. The laminated fibrous ankerite formation time should be equal to or after the laminated fibrous calcite formation time, as laminated fibrous ankerite does not require more diagenetic alteration (Figures 13A, B), which is not found in the mineral metasomatism mineral residue or mineral pseudomorphic changes

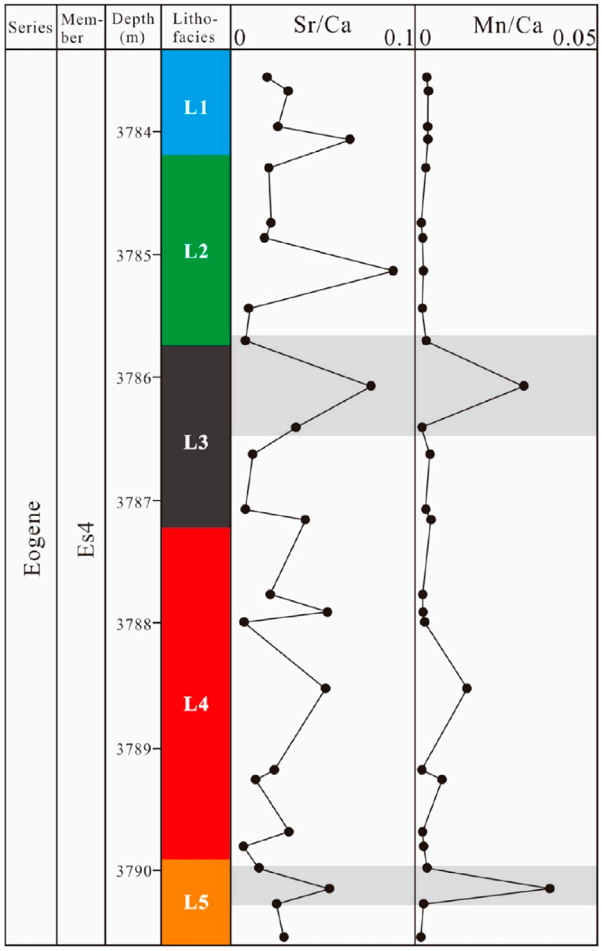

FIGURE 11
Lithofacies distribution and elemental geochemistry data of the NX55 well from 3,783.55 to 3,790.63 m.

under mineral cathodoluminescence, considering the different carbonate mineral generation types (Figures 4A, B). The formation of ankerite is likely due to the overpressure of fluid caused by the expulsion of hydrocarbons from organic matter (Zhang et al., 2016; Luan et al., 2019; Ma et al., 2020). The formation mechanism of ankerite is the same as that of fibrous calcite, and the difference in rock type is caused by the difference in the ionic environment.

5.4 Siliceous source and formation mechanism of authigenic silicates

The siliceous material in mudstone can be divided into terrigenous siliceous material and authigenic siliceous material formed during diagenesis, which can be distinguished by cathodoluminescence. Terrigenous quartz and feldspar usually have particle sizes larger than 5 μm and round, subround or angular shapes (Vos et al., 2014). Under cathodoluminescence, terrigenous quartz usually appears blue and dark red, terrigenous feldspar usually appears red, blue and green, and authigenic silica generally does not emit light. The cathodoluminescence observations of the samples reveal that there are small amounts of quartz and feldspar in all lithofacies, but most of them do not emit light, indicating that authigenic silicon is dominant in the silica content of the mudstone (Figures 3F, 5E). Zr and TiO_2 in rocks are usually associated with heavy minerals and can be used as evidence to characterize detrital input into mudstone. Among the 5 different lithofacies, the contents of TiO_2 in L3 and L5 are relatively high, and those of Zr in L3 and L4 are relatively high. The correlation coefficients are positive and negative but small (Figures 14C, D), indicating that terrigenous siliceous material accounts for a high proportion of these three lithofacies but is not the dominant source of siliceous material. In lithofacies L1 and L2, the contents of TiO_2 and Zr are very low (Figures 14C, D), indicating that these two lithofacies are mainly autogenic siliceous lithofacies.

Authigenic siliceous material mainly comes from terrigenous siliceous dissolution and precipitation, biogenic siliceous transformation, clay mineral transformation, and hydrothermal siliceous input (Guo et al., 2021). Al-Fe-Mn plots are commonly used to characterize the formation environments of siliceous minerals (Adachi et al., 1985). None of the test samples of the five types of lithofacies were located in the range of hydrothermal origin (Figure 14A), suggesting that there is no hydrothermal siliceous source. No siliceous microfossils were found in any lithofacies, and the corresponding relationship between quartz content and TOC showed discrete data and low correlation (Figure 14B). Therefore, it was speculated that no silica was generated by the biological action or dissolution of the siliceous microfossils. In the diagrams of SiO_2 and $K_2O + Na_2O$ and SiO_2 and Al_2O_3 (Figures 14E, F), L1 and L2 are highly positively correlated. Lithofacies L3, L4 and L5 have weak positive correlations, suggesting that the source of the authigenic siliceous material is related to the dissolution of feldspar and the transformation of clay minerals.

Based on the above evidence, three sources of siliceous materials are inferred: terrigenous direct input, reprecipitation of dissolved feldspar minerals, and siliceous release during the transformation of clay minerals. The cathodoluminescence and SEM images show that the three siliceous sources contribute to all the lithofacies. In L1 and L2, the siliceous materials formed by the transformation of clay minerals are dominant. In L3, terrigenous input siliceous materials are dominant. L4 and L5 are characterized by clay mineral transformation, terrigenous input and dissolution of feldspar minerals.

Clay mineral transformation is the main source of silica for authigenic quartz formation. Mudstone maturity is high in Es3x and Es4s in the Dongying Depression, and illite is the main component of clay. During the diagenetic process, the transformation of montmorillonite to illite results in silicon being released into the pore solution (Peltonen et al., 2009; Dowey and Taylor, 2020). Due to the low liquidity of the pore solution in the mudstone and the siliceous *in situ* precipitation crystallization of micron-scale silica particles, EDS reveals that this type of quartz contains a certain amount of Al (Figure 5H). This stage coincides with the beginning of the mass production of organic acids. Therefore, authigenic quartz precipitates in the dissolution pores of primary carbonate or early carbonate cements (Figures 3H, 5G). This phenomenon has occurred since the diagenetic evolution of mud shale entered the oil generation window, and the black line in the fibrous carbonate is actually the clay mineral boundary during the growth of such calcite (Figure 5F). The composition within the black line is mainly a

TABLE 3 Carbon and oxygen isotopic compositions of the sparry calcite, micritic calcite, fibrous calcite, ankerite and dolomite in the mudstone.

Minerals	n	$\delta^{13}C_{V\text{-}PDB}$(‰)	$\delta^{18}O_{V\text{-}PDB}$ (‰)	Precipitation temperature (°C)	
				[Min to max]	
				$\delta^{18}O_{V\text{-}SMOW}$ = −5‰	$\delta^{18}O_{V\text{-}SMOW}$ = 0‰
Sparry calcite	6	0.2 to 1.3	−9.6 to −7.6	21.4 to 33.6	—
Micritic calcite	10	3.2 to 6.4	−10.3 to −7.4	19.2 to 37.2	—
Fibrous calcite	9	1.8 to 5.1	−13.8 to −11.9	—	101.5 to 115.9
Ankerite	11	1.9 to 3.6	−12.4 to −10.1	—	76.5 to 129.2
Micritic dolomite	11	3.1 to 5.9	−10.4 to −8.0	47.2 to 65.7	—

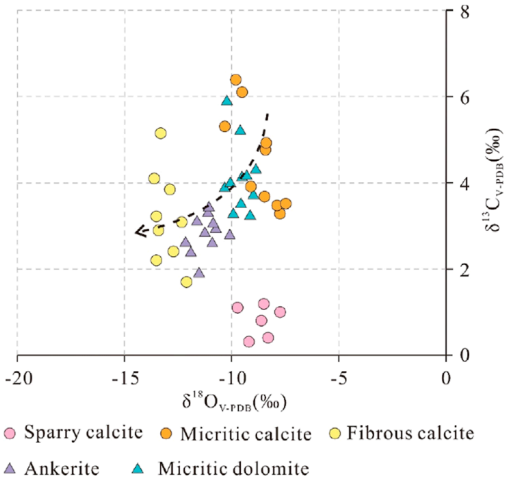

FIGURE 12
Cross plot of the carbon and oxygen isotopic compositions of carbonate minerals.

variety of clay types with authigenic micron-scale quartz, indicating this diagenetic process (Figure 5G).

The dissolution of feldspar requires an acidic fluid environment derived from atmospheric precipitation under shallow burial conditions (<1,000 m) or from the thermal evolution of organic matter (carboxylic acid or CO2) in mudstone during burial-related diagenesis (2,000–4,000 m) (Bjørlykke et al., 1989; Surdam et al., 1989). The intense dissolution of feldspar minerals requires a diagenetic environment in which inert Al is complexed and transported (Wilkinson et al., 2004). Mudstone in the widespread presence of clay minerals and its conversion from montmorillonite to illite during the process of diagenetic transformation provides this kind of environment because the conversion of montmorillonite to illite consumes Al, and the release of organic acid is greater in mudstone and organic acid in complex anions that complex with Al (Zhang et al., 2021a) to increase the solubility of Al and dissolve feldspar (Figures 6B, C, H, I). Through simulation experiments, Surdam and Crossey (1985) suggested that carboxylic acid anions can increase the solubility of Al by 3 orders of magnitude compared with that of inorganic acid at 100°C. In addition to the formation of Si and H_2O, many cations (Na, Ca, Mg and Fe) are released from the clay mineral transformation process. These cations must be consumed from the solution for montmorillonite–illite transformation to continue, which should be achieved by authigenic quartz and authigenic carbonate rocks (Hower et al., 1976; Boles and Franks, 1979; Abercrombie et al., 1994; Bjørlykke, 1998). According to petrological evidence, authigenic feldspar is mainly albite, which is produced in dissolution pores of carbonate rocks (Figures 6F, G). The dissolution and precipitation of these different minerals also reflect the change in ion concentration in the pore solution.

5.5 Clay transformation process

Clay minerals are the key factors affecting the structure and diagenetic evolution of mudstone (Bozkaya and Yalçın, 2005; Lu et al., 2011). With increasing burial depth, temperature and pressure, clay minerals continuously remove interlayer water and ions, which is one of the main sources of pore fluid generation in mud shale. On the one hand, the transformation of montmorillonite to illite or chlorite increases the order of the clay minerals (Ma et al., 2020), and the volume shrinks to produce shrinkage cracks in mudstone, which provides space for the growth of authigenic carbonate and siliceous materials. On the other hand, this diagenesis provides a rich ionic environment and absorbs some of the supersaturated ions in the pore fluid, thus promoting the continuous generation or dissolution of various minerals in the mudstone-confined environment during diagenetic evolution. The highest content of clay minerals in the Es3x and Es4s submembers of the Dongying Depression is illite (Table 1). According to petrologic and energy spectrum evidence, potassium feldspar is strongly dissolved (Figures 6B, C, H, I), and the K^+-rich environment needed for authigenic illite arises from the dissolution of potassium feldspar. Under certain temperature and pressure conditions, montmorillonite is converted into illite, and this process mainly begins at approximately 80°C (Peltonen et al., 2009).

Figure 15A shows that the clay mineral compositions of different lithofacies are different at the same burial depth and within the same area, indicating that the degree of smectite–illite transformation is

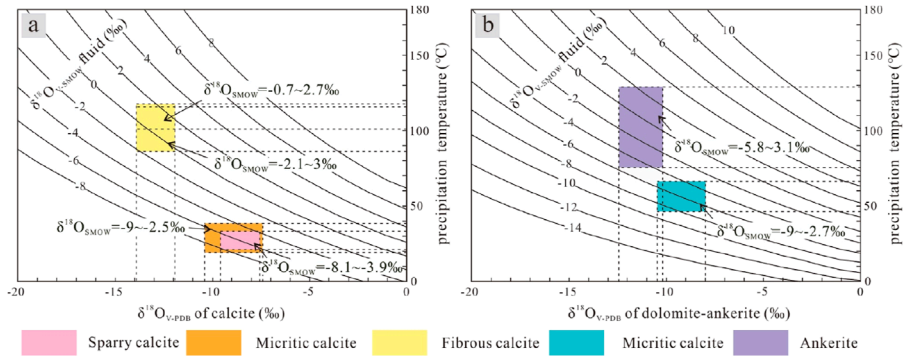

FIGURE 13
Oxygen isotope fractionation diagram of the carbonate mineral precipitation process in the Es3x and Es4s submembers in the Dongying Sag. **(A)** All kinds of calcite can be described with the following formula: $10^3 \ln\alpha = 2.78 \times 10^6 \times T^{-2} - 2.89$ (Friedman and O'Neil, 1977). **(B)** All kinds of dolomite-ankerite can be described with the formula $10^3 \ln\alpha = 3.2 \times 10^6 \times T^{-2} - 3.3$ (Land, 1983).

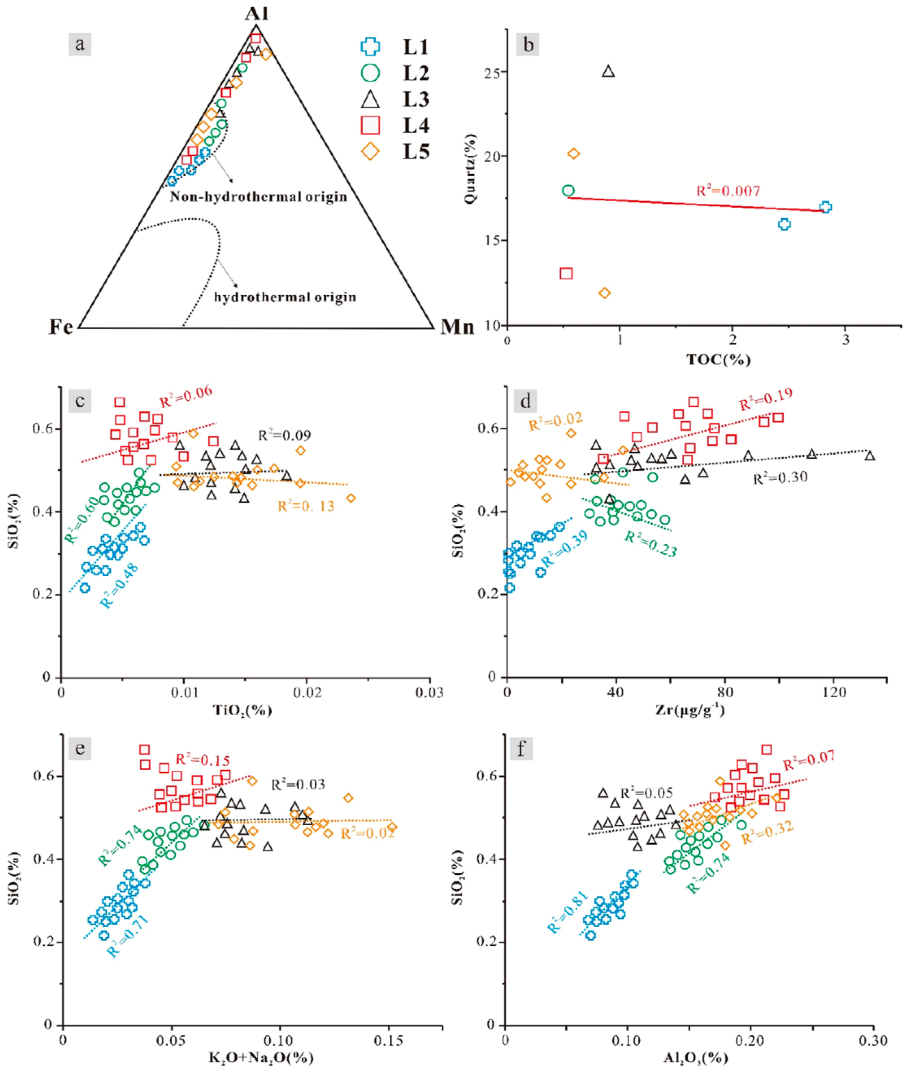

FIGURE 14
Explanation of the siliceous origins of various lithofacies. **(A)** Content diagram of Al, Fe, and Mn. **(B)** Relationship between the quartz content and TOC. Relationships between SiO_2 and **(C)** TiO_2, **(D)** Zr, **(E)** $K_2O + Na_2O$, and **(F)** Al_2O_3.

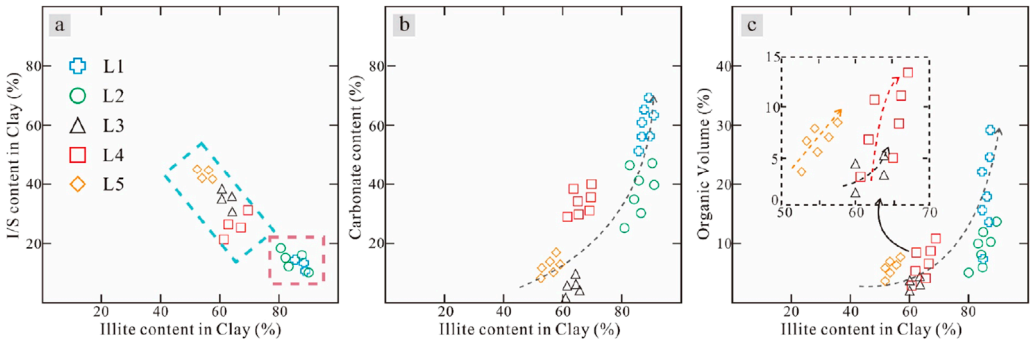

FIGURE 15
Relationships between illite content and **(A)** I/S content, **(B)** carbonate content, and **(C)** organic volume. Different lithofacies types are distinguished by different colours, which are the same as those in Figure 16.

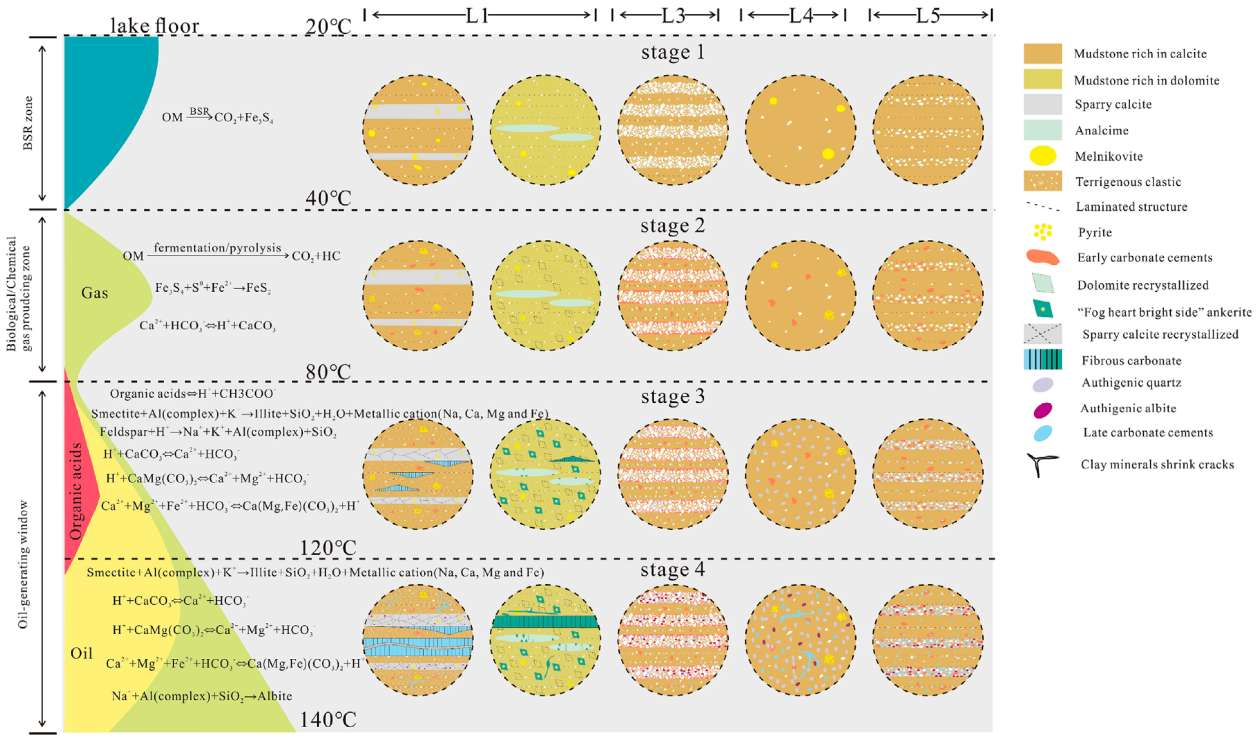

FIGURE 16
Model diagram of the organic matter evolution stage and various lithofacies evolution stages.

different in different lithofacies during the same diagenetic stage. The different characteristics of the five types of lithofacies mainly include their mineral compositions, sedimentary structures and organic matter contents (Table 1). According to the relationship between illite and I/S contents, L1 and L2 have the same clay mineral composition, whereas L3, L4 and L5 have the same clay mineral composition (Figure 15A). The illite content is positively correlated with the carbonate content (Figure 15b) and with the organic matter content (Figure 15C). Based on the above evidence, it can be inferred that smectite–illite transformation is controlled by organic matter content and sedimentary structure characteristics. First, the expulsion of hydrocarbons from the thermal evolution of organic matter can cause overpressure of the pore fluid, which can promote the diagenetic evolution of clay minerals. Second, the development of lamellar fibrous carbonate driven by organic acids (Zhang et al., 2016) consumes many cations (Ca and Mg) generated during the diagenetic transformation of clay minerals, which leads to a positive shift in the chemical balance of the transformation of clay minerals and ensures that the reaction can continue. In lithofacies L4, although the organic matter content is very high, because of its massive tectonic sedimentary characteristics, it does not have bedding, such as lithofacies L1 and L2; similarly, overpressure cannot

effectively occur after crack formation due to fluid pressure, and large authigenic carbonate grains are not produced. Thus, the ions in the pore fluid are unable to be consumed or are not greatly consumed, blocking smectite–illite transformation. Although facies L3 and L5 have bedding fractures, their organic matter content is low, and it is difficult to produce large-scale organic matter generation and expulsion of hydrocarbons and organic acids. Unlike clastic reservoirs with good porosity and permeability, such as sandstones, pore fluids can migrate under multiple dynamics. The diagenetic system of this mudstone is relatively closed, and the supersaturated pore fluid formed during the diagenetic process must reach a state of undersaturation through "internal consumption". In lithofacies L3, L4 and L5, although the degrees of transformation of smectite to illite are not as good as those of lithofacies L1 and L2, they also show positive correlations between the authentic illite content and the organic matter volume fraction and carbonate content (Figure 15C).

5.6 Evolution of pyrite and organic matter

The strawberry pyrite (Figures 8A, D–F) observed was converted from mackinaite formed by BSR during early precipitation (Marin-Carbonne et al., 2014). The combination of massive pyrite and dolomite–ankerite (Figure 8C) may indicate thermochemical sulfate reduction (TSR) (Radke and Mathis, 1980; Machel et al., 1995). Pyrite formed during diagenesis is also one of the consumption pathways of Fe^{2+}, which can also explain why Fe^{2+} does not enter the crystal lattice of dolomite during the rebonding process observed in petrology. The early precipitation of pyrite releases H^+ (Jiang et al., 2018), which leads to a decrease in the pH of the early pore water and the dissolution of carbonate rocks in the early diagenetic stage. During the process of organic matter thermal evolution, transition metals and sulfides have a good catalytic effect on organic matter evolution (Mango, 1992; Wang et al., 2014). Fe^{2+} can affect the electron cloud distribution of pyrolysed kerogen, reduce the activation energy required for the reaction, increase the degradation rate, and promote hydrocarbon generation in organic matter.

With increasing vitrinite reflectance, organic matter matures and is discharged into hydrocarbons, an increasing number of organic pores are generated in the residual organic matter, and the size of the pores is constantly changing (Figure 9). The organic matter types in the five lithofacies are different (Tables 1, 2), which is caused by changes in the depositional environment. Like the organic pores in the Barnett shale (Loucks et al., 2009; Slatt and O'Brien, 2011), the vast majority of organic matter observed in the studied mudstone had more internal pores than marginal pores (Figures 9F, G, I), and small shrinkage fractures were found in organic matter without significant pore development (Figure 9H). However, some organic matter is surrounded by inorganic minerals, and edge pores are highly developed in the absence of internal pores (Figure 9E), indicating the catalytic effect of inorganic minerals on the evolution of organic matter. Clay minerals, carbonate minerals, quartz and pyrite in inorganic minerals (Zhang and Zhang, 1996; Liu et al., 2009), inorganic salts such as $MgSO_4$ and $NaHCO_3$ in pore fluids (Li et al., 2002), and trace elements such as nickel and zinc (Chen and Zha, 2007) have catalytic effects on kerogen pyrolysis and hydrocarbon generation, which is beneficial for the formation of pores. Hu et al. (2020), through experiments at the same temperature and pressure and physical and chemical conditions, reported that, based on the relationship between the quantity of hydrocarbon expulsion and organic matter types (type I > type II > type III), the combination of the organic matter contents of different lithofacies can control the thermal evolution of organic matter under pore fluid overpressure: L1 > L2 > L4 > L5 > L3.

5.7 Model illustrating lithofacies control on mineral coevolution

The diagenesis of various lithofacies has different evolution characteristics because of the different sedimentary structures, types and contents of organic matter and mineral types and can be roughly divided into four stages (Figure 16). The two models of the L1 lithofacies differ in terms of the carbonate rock type. Although they belong to the same lithofacies, they have different diagenetic evolution characteristics. The diagenetic evolution is as follows:

Stage 1: This stage is the beginning of diagenesis, and the influence of compaction is not obvious. All lithofacies maintain their respective sedimentary characteristics. L1 and L4, which have high organic matter contents, form mackinaite under BSR due to the formation of a closed reducing environment (Marin-Carbonne et al., 2014).

Stage 2: In areas where organic matter is generated during the biochemical gas-generating stage, a large amount of pore water is discharged from the mudstone due to compaction. However, due to the lithologic characteristics of mudstone, pore fluid overpresses when pore water is not discharged. As the pressure of the overlying strata continues to increase, water-escape structures may form (Figure 5A). At this stage, mackinaite converts into pyrite by absorbing Fe^{2+} ions in the pore water (Sweeney and Kaplan, 1973), and Ca^{2+} ions in the pore water can form early carbonate cements with organic matter evolution or HCO_3^- ions in the pore water (Figures 3H, I). This phenomenon results in a decrease in the pH of the pore fluid. Moreover, the Ca^{2+} and Mg^{2+} ions in these pore waters also participate in the recrystallization of the original carbonate minerals in the mudstone, among which dolomite has a high degree of self-recrystallization (Figure 4I).

Stage 3: Due to acidification of stage 2 pore fluids, feldspar minerals from terrigenous clasts in the mudstones dissolve, and K^+ ions are released into the pore fluids. At this stage, due to the combined action of a K^+-rich environment and temperature and pressure, smectite–illite transformation takes place, releasing SiO_2, H_2O and metal cations (Na, Ca, Mg, and Fe) (Peltonen et al., 2009), and a large amount of SiO_2 precipitates as microquartz in the cracks formed by smectite–illite transformation (Figures 5G–I) (Towe, 1962). Some clay mineral masses release metal cations during diagenesis, causing carbonate rock to precipitate around these clay mineral masses, forming "the fog core bright side" ankerite (Figures 4D–F). Due to the organic acids formed by the thermal evolution of organic matter (Figure 16), the pH value of the pore fluid is further

reduced, the Al complex produced by feldspar dissolution is consumed during smectite–illite transformation, and feldspar and analcime dissolution is more intense (Figures 4B, 6I). SiO_2 from feldspar dissolution also contributes to the formation of microquartz (Figure 14E). Carbonate rocks that formed in the sedimentary and early diagenetic stages are dissolved by organic acids in the pore fluid. Recrystallization of the sparry calcite laminae occurs under the influence of overpressure. The transformation of clay mineral formation fluids that are rich in ions, fluid discharge from mineral recrystallization and organic matter thermal evolution form hydrocarbons and organic acids in the production of many "oil windows" within the shale formation with overpressure, and the fluid in the interior of the shale is prone to rupture via overpressure crack formation. These areas are usually laminated seams, exhibiting the transformation of clay minerals in terms of the formation of cracks, primary pores, and secondary pores produced during diagenesis. Due to the extremely high partial pressure of CO_2, Ca, Mg and Fe ions form in the pore fluid due to early carbonate dissolution and clay mineral transformation, and fibrous carbonate forms in these overpressure fractures, which mainly occur in laminated seams (Figures 3A, 4A). Due to insufficient organic matter content, L3 and L5 cannot form large-scale fluid overpressure at this stage and thus do not develop large-scale fibrous carbonate. Although L4 has a high organic matter content, there are no laminated seams suitable for the development of fibrous carbonate. L3, L4 and L5 are unable to form fibrous carbonate, resulting in a small consumption of metal cations formed during the transformation of clay minerals and a slower conversion rate of smectite to illite than that observed for L1 and L2.

Stage 4: The production of organic acids decreases but continues at the peak of hydrocarbon expulsion due to the thermal evolution of organic matter, and the fibrous carbonate in L1 and L2 gradually develops into laminae. Recrystallization of the sparry calcite lamina continues. In the clay mineral layer, the transformation of smectite to illite results in an increase in the overall order of the clay minerals, resulting in many shrinkage fractures, in which carbonate and quartz precipitate (Figure 3C). Due to the decrease in organic acid production and increase in the pH value of the pore fluid, the authigenic albitite precipitates in the secondary pores dissolve during diagenesis (Figures 6F, G).

6 Conclusion

In a closed diagenetic environment, the diagenetic characteristics of different lithofacies are controlled by the sedimentary structure, mineral types, and organic matter content and evolution. The coevolution of minerals is realized mainly through the ion exchange of different minerals during diagenesis. The main medium of ion exchange is pore fluid, and the change in ion concentration is driven by the transformation of clay minerals and organic acids generated during the thermal evolution of organic matter. The CO_2 needed for the formation of fibrous carbonate comes from carbonate of sedimentary origin in the mudstone and carbonate cement precipitated from pore fluid in the early diagenetic stage. The cations come from the dissolution of carbonate and the transformation of clay minerals in the early diagenetic stage, and fibrous carbonates form in laminar fractures formed during deposition. The transformation of smectite-illite requires a rich K^+ environment provided by the dissolution of orthoclase and feldspar in Al complexes by the consumption of clay minerals and the transformation and emission of large amounts of SiO_2 and metal cations. SiO_2 forms a large amount of microquartz and metal cations that participate in the formation of authigenic carbonate, quartz, albite, illite, and chlorite. Compared with L1, L4 lacks the lamellar structure required for fibrous carbonate formation. Due to the low organic matter contents in L3 and L5, it is difficult to form overpressure fractures and pore fluid environments rich in organic acids during the thermal evolution of organic matter in these lithofacies, resulting in different types of diagenetic phenomena among the various lithofacies.

Data availability statement

The original contributions presented in the study are included in the article/supplementary material, further inquiries can be directed to the corresponding authors.

Author contributions

ZZ: Conceptualization, Data curation, Formal Analysis, Investigation, Methodology, Software, Validation, Writing–original draft, Writing–review and editing. ZJ: Conceptualization, Funding acquisition, Project administration, Resources, Supervision, Writing–review and editing. YY: Formal Analysis, Methodology, Supervision, Writing–review and editing.

Funding

The author(s) declare that no financial support was received for the research, authorship, and/or publication of this article.

Conflict of interest

The authors declare that the research was conducted in the absence of any commercial or financial relationships that could be construed as a potential conflict of interest.

Generative AI statement

The author(s) declare that no Generative AI was used in the creation of this manuscript.

Publisher's note

References

Abercrombie, H. J., Hutcheon, I. E., Bloch, J. D., and de Caritat, P. (1994). Silica activity and the smectite–illite reaction. *J. Geol.* 22, 539–542. doi:10.1130/0091-7613(1994)022<0539:saatsi>2.3.co;2

Adachi, M., Yamamoto, K., and Sugisaki, R. (1985). Hydrothermal chert and associated siliceous rocks from the northern Pacific their geological significance as indication od ocean ridge activity. *J. Sediment. Geol.* 47, 125–148. doi:10.1016/0037-0738(86)90075-8

Barth, T., and Bjørlykke, K. (1993). Organic acids from source rock maturation: generation potentials, transport mechanisms and relevance for mineral diagenesis. *Appl. Geochem.* 8, 325–337. doi:10.1016/0883-2927(93)90002-X

Bilal, A., Yang, R., Fan, A., Mughal, M. S., Li, Y., Basharat, M., et al. (2022a). Petrofacies and diagenesis of thanetian lockhart limestone in the upper indus basin (Pakistan): implications for the ceno-tethys ocean. *J. Carbonates Evaporites* 37, 78. doi:10.1007/s13146-022-00823-z

Bilal, A., Yang, R., Li, Y., Zhang, J., and Janjuhah, H. T. (2024). Microfacies shift in the late paleocene-early eocene patala formation in the upper indus basin(Pakistan): implications for development of the ceno-tethys ocean. *Mar. Petroleum Geol.* 161, 106693. doi:10.1016/j.marpetgeo.2024.106693

Bilal, A., Yang, R., Mughal, M. S., Janjuhah, H. T., Zaheer, M., and Kontakiotis, G. (2022b). Sedimentology and diagenesis of the early–middle eocene carbonate deposits of the ceno-tethys ocean. *J. Mar. Sci. Eng.* 10 (11), 1794. doi:10.3390/jmse10111794

Bjørlykke, K. (1998). "Clay mineral diagenesis in sedimentary basins: a key to the prediction of rock properties: examples from the North Sea Basin," in *Clay minerals in the modern society. Mineralogical society* (London), 15–34. United King-dom. doi:10.1180/claymin.1998.033.1.03

Bjørlykke, K., Nedkvitne, T., Ramm, M., and Saigal, G. C. (1992). Diagenetic processes in the brent group (middle jurassic) reservoirs of the north sea: an overview. *J. Geol. Soc.* 61, 263–287. doi:10.1144/GSL.SP.1992.061.01.15

Bjørlykke, K., Ramm, M., and Saigal, G. C. (1989). Sandstone diagenesis and porosity modification during basin evolution. *J.Geologische Rundsch.* 78, 243–268. doi:10.1007/bf01988363

Boles, J. R., and Franks, S. G. (1979). "Clay diagenesis in Wilcox sandstones of Southwest Texas; implications of smectite diagenesis on sandstone cementation,"*J. J. Sediment. Res.*, 49. 55–70. doi:10.1130/0091-7613(1979)7<602:SERATM>2.0

Bozkaya, Ö., and Yalçın, H. (2005). Diagenesis and very low-grade metamorphism of the Antalya unit: mineralogical evidence of Triassic rifting, Alanya-Gazipas, A central Taurus belt, Turkey. *J. J. Asian Earth Sci.* 25, 109–119. doi:10.1016/j.jseaes.2004.02.001

Cao, Q., Zhou, W., Chen, W. L., Deng, H. C., Yan, C. H., and Deng, K. (2015). Analysis of pore types,sizes and genesis in continental shale gas reservoir of Chang 7 of Yanchagn Formation,Odros Basin. *J. J. Mineralogy Petrology.* 35, 90–97. doi:10.19719/j.cnki.1001-6872.2015.02.011

Cao, Z., Lin, C., Dong, C., Ren, L., Han, S., Dai, J., et al. (2018). Impact of sequence stratigraphy, depositional facies, diagenesis and CO_2 charge on reservoir quality of the lower cretaceous Quantou Formation. Southern Songliao Basin, China. *Mar. Petroleum Geol. J.* 93, 497–519. doi:10.1016/j.marpetgeo.2018.03.015

Chen, D. X., Pang, X. Q., Zhang, J., and Li, M. (2007). Application of quantitative grain fluorescence techniques to study subtle oil migration pathway of lithological reservoir. *J. Front. Earth Sci.* 1, 498–504. doi:10.1007/s11707-007-0061-y

Chen, J., and Xiao, X. M. (2014). Evolution of nanoporosity in organic-rich shales during thermal maturation. *J. Fuel* 129, 173–181. doi:10.1016/j.fuel.2014.03.058

Chen, Z. H., and Zha, M. (2007). Correlation between inorganic elements and abnormal vitrinite reflectance in lacustrine source rocks. *J. Geochim.* 36, 275–278. doi:10.1631/jzus.2007.A1858

Cobbold, P. R., Zanella, A., Rodrigues, N., and Løseth, H. (2013). Bedding-parallelfibrous veins (beef and cone-in-cone): worldwide occurrence and possible significance in terms of fluid overpressure, hydrocarbon generation and mineralization. *J. Mar. Petroleum Geol.* 43, 1–20. doi:10.1016/j.marpetgeo.2013.01.010

Diaz, H. G., Fuentes, C. C., Calvin, C., Yang, Y., MacPhail, K., and Lewis, R. (2013). *Evaluating the impact of mineralogy on reservoir quality and completion quality of organic shale plays*. Salt Lake City, Utah: AAPG Rocky Mountain Section Meeting, 22–24. Available at: https://www.mendeley.com/catalogue/8a34396f-2142-3633-8c82-4e52fc74c936/.

Dowey, P. J., and Taylor, K. G. (2020). Diagenetic mineral development within the upper jurassic haynesville-bossier shale, USA. *J. Sedimentol.* 67, 47–77. doi:10.1111/sed.12624

Durney, D. W., and Ramsay, J. G. (1973). "Incremental strains measured by syntectonic crystal growths," in *Gravity and tectonics*. Editors K. A. De Jong, and K. Scholten (New York: Wiley), 67–96.

Friedman, I., and O'Neil, J. R. (1977). *Data of geochemistry: compilation of stable isotope fractionation factors of geochemical interest*, 440. Washington, DC: US Government Printing Office. Available at: https://refhub.elsevier.com/S0264-8172(19)30010-8/sref24.

Fritz, P., and Smith, D. G. W. (1970). The isotopic composition of secondary dolomites. *J. Geochimica Cosmochimica Acta* 34, 1161–1173. doi:10.1016/0016-7037(70)90056-6

Guo, W., Dong, D. Z., Li, M., Sun, S. S., Quan, G. Z., and Zhang, S. R. (2021). Quartz genesis in organic-rich shale and its indicative significance to reservoir quality: a case study on the first sub-member of the first Member of Lower Silurian Longmaxi Formation in the southeastern Sichuan Basin and its periphery. *J. Nat. Gas. Ind.* 41, 65–74. doi:10.3787/j.issn.1000-0976.2021.02.008

Guo, X. W., He, S., Liu, K. Y., Song, G. Q., Wang, X. J., and Shi, Z. H. (2010). Oil generation as the dominant overpressure mechanism in the cenozoic dongying depression, Bohai Bay Basin, China. *J. AAPG Bull.* 94, 1859–1881. doi:10.1306/05191009179

Haile, B., Czarniecka, U., Xi, K., Smyrak-Solpra, A., Jahren, J., Braathen, A., et al. (2019). Hydrothermally induced diagenesis: evidence from shallow marine-deltaic sediments, Wilhelmøya, Svalbard. *J. Geosci. Front.* 10, 629–649. doi:10.1016/j.gsf.2018.02.015

He, S., Song, G. Q., Wang, Y. S., Hao, X. F., Wang, B. J., Li, N., et al. (2012). Distribution and major control factors of the present-day large-scale overpressured system in Dongying depression. *J. Earth Science—Journal China Univ. Geosciences* 37, 1029–1042. doi:10.3799/dqkx.2012.110

Hower, J., Eslinger, E. V., Hower, M. E., and Perry, E. A. (1976). Mechanism of burial meta-morphism of argillaceous sediment: 1. Mineralogical and chemical evidence. *J. Geol. Soc. Am. Bull.* 87, 725–737. doi:10.1130/0016-7606(1976)87<725:mobmoa>2.0.co;2

Hu, J. J., Tang, Y. J., He, D. X., Bo, N., and Li, M. J. (2020). Comparison and exploration of hydrocarbon expulsion patterns of different types of source rocks. *J. J. Geomechanics* 26, 941–951. doi:10.12090/j.issn.1006-6616.2020.26.06.075

Hu, W. X., Yao, S. P., Lu, X. C., Wu, H. G., Sun, F. N., and Qin, X. (2019). Effects of organic matter evolution on oil reservoir property during diagenesis of typical continental shale sequences. *J. Oil and Gas Geol.* 40, 947–956. doi:10.11743/ogg20190501

Huang, Z. K., Chen, J. P., Wang, Y. J., Xue, H. T., Deng, C. P., and Wang, M. (2013). Characteristics of micropores in mudstones of the cretaceous Qingshankou Formation,Songliao Basin. *J. Acta Pet. Sin.* 34, 30–36. doi:10.7623/syxb201301004

Irwin, H., Curtis, C., and Coleman, M. (1977). Isotopic evidence for source of diagenetic carbonates formed during burial of organic-rich sediments. *J. Nat.* 269, 209–213. doi:10.1038/269209a0

Jansa, L. F., and Urrea, V. H. N. (1990). Geology and diagenetic history of overpressured sand-stone reservoirs, venture gas field, offshore Nova scotia. Canada (1). *J. AAPG Bull.* 74, 1640–1658. doi:10.1306/0C9B2551-1710-11D7-8645000102C1865D

Jarvie, D. M. (2012). "Shale resource systems for oil and gas: part 1-shale-gas resource systems,". *Shale reservoirs-giant resources for the 21st century*. Editor J. A. Breyer (Washington, DC: AAPG Memoir), 97, 69–88. doi:10.1306/13321446M973489

Jiang, L., Worden, R. H., and Yang, C. B. (2018). Thermochemical sulphate reduction can improve carbonate petroleum reservoir quality. *J. Geochim. Cosmochim. Acta.* 223, 127–140. doi:10.1016/j.gca.2017.11.032

Jiang, Z. X., Liang, C., Wu, J., Zhang, J. G., Zhang, W. Z., Wang, Y. S., et al. (2013). Several issues in sedimentological studies on hydrocarbon-bearing fine-grained sedimentary rocks. *J. Acta Pet. Sin.* 34, 1031–1039. doi:10.7623/syxb201306001

Kordi, M., Morad, S., Turner, B., and Salem, A. M. (2017). Sequence stratigraphic controls on formation of dolomite: insights from the carboniferous um bogma formation, SinaiEgypt. *J. Pet. Sci. Eng.* 149, 531–539. doi:10.1016/j.petrol.2016.10.067

Land, L. S. (1983). The application of stable isotopes to studies of the origin of dolomite and to problems of diagenesis of clastic sediments. *J. SEPM Short. Course (SC10)* 4, 1–22. doi:10.2110/scn.83.01.0000

Li, J. Y. (2015). Pore characteristics and their evolution in paleogene mud shales, dongying sag, Bohai Bay Basin. *J. Petroleum Geol. Exp.* 37, 566–574. doi:10.11781/sysydz201505566

Li, S. Y., Lin, S. J., Guo, S. H., and Liu, L. F. (2002). Effects of inorganic salts on the hydrocarbon generation from kerogens. *J. Geochim.* 31, 15–20. doi:10.1080/12265080208422884

Liu, H. P., Zhang, Z. L., Ji, Z. K., and Li, B. (2009). Effects of inorganic is salts on the hydrocarbon generation of mixed ester catalyzed by natural minerals at low temperature. *J. Acta Sedimentol. Sin.* 26, 886–890. doi:10.14027/j.cnki.cjxb.2008.05.010

Liu, S. B., Huang, S. J., Shen, Z. M., Lv, Z. X., and Song, R. C. (2014). Diagenetic fluid evolution and water-rock interaction model of carbonate cements in sandstone: an example from the reservoir sandstone of the Fourth Member of the Xujiahe Formation of the Xiaoquan-Fenggu area, Sichuan Province, China. *J. Sci. China Earth Sci.* 57, 1077–1092. doi:10.1007/s11430-014-4851-2

Liu, X. F., and Xie, X. N. (2003). Study on fluid pressure system in Dongying depression. *J. Earth Sci. J. China Univ. Geosciences* 28, 78–86.

Loucks, R. G., Reed, R. M., Ruppel, S. C., and Jarvie, D. M. (2009). Morphology, genesis, and distribution of nanometer-scale pores in siliceous mudstones of the Mississippian Barnett Shale. *J. J. Sediment. Res.* 79, 848–861. doi:10.2110/jsr.2009.092

Lu, J., Milliken, K. L., Reed, R. M., and Hovorka, S. (2011). Diagenesis and sealing capacity of the middle Tuscaloosa mudstone at the Cranfield carbon dioxide injection site, Mississippi, USA. *J. Environ. Geosci.* 18, 35–53. doi:10.1306/eg.09091010015

Luan, G. Q., Dong, C. M., Karem, A., Lin, C. Y., Ma, C. F., Ren, L. H., et al. (2019). Origin of bedding-parallelfibrous calcite veins in lacustrine black shale: a case study from Dongying Depression, Bohai Bay Basin. *J. Mar. Petroleum Geol.* 102, 873–885. doi:10.1016/j.marpetgeo.2019.01.010

Lundegard, P. D., Land, L. S., and Galloway, W. E. (1984). Problem of secondary porosity: frio formation (oligocene), Texas gulf coast. *Tex. Gulf Coast J. Geol.* 12, 399. doi:10.1130/0091-7613(1984)12<399:pospff>2.0.co;2

Ma, C. F., Dong, C. M., Derek, E., Wang, Q., Huang, Z., Liu, H. L., et al. (2020). Insights from electron backscatter diffraction into the origin offibrous calcite veins in organic-rich shale from lower Es3 to upper Es4, Jiyang Depression, China. *Mar. Petroleum Geol.* 113, 104131. doi:10.1016/j.marpetgeo.2019.104131

Ma, P. J., Lin, C. Y., Jens, J., Dong, C. M., Ren, L. H., and Helge, H. (2021). Cyclic zoning in authigenic saddle dolomite-ankerite: indications of a complex interplay between fault-rupturing and diagenetic alteration. *J. Chem. Geol.* 599 (2021), 119831. doi:10.1016/j.chemgeo.2020.119831

Machel, H. G., Krouse, H. R., and Sassen, R. (1995). Products and distinguishing criteria of bacterial and thermochemical sulfate reduction. *J. Geol. Soc. Spec. Publ.* 10, 373–389. doi:10.1016/0883-2927(95)00008-8

Mango, F. D. (1992). Transition metal catalysis in the generation of petroleum and natural gas. *J. Geochimica Cosmochimica Acta* 56, 553–555. doi:10.1016/0016-7037(92)90153-A

Marin-Carbonne, J., Rollion-Bard, C., Bekker, A., Rouxel, O., Agangi, A., Cavalazzi, B., et al. (2014). Coupled Fe and S isotope variations in pyrite nodules from Archean shale. *J. Sci. Lett.* 392, 67–79. doi:10.1016/j.epsl.2014.02.009

Marshall, J. D. (1982). Isotopic composition of displacive fibrous calcite veins: reversals in pore-water composition trends during burial diagenesis. *J. Sediment. Res.* 52, 615–630. doi:10.1306/212F7FB3-2B24-11D7-8648000102C1865D

Milliken, K. L., Rudnicki, M., Awwiller, D. N., and Zhang, T. (2013). Organic matter–hosted pore system, marcellus formation (devonian), Pennsylvania. *J. Aapg Bull.* 97, 177–200. doi:10.1306/07231212048

Montgomery, S. L., Jarvie, D. M., Bowker, K. A., and Pollastro, R. M. (2005). Mississippian Barnett shale, Fort Worth Basin, north-central Texas: gas-shale play with multi-trillion cubic foot potential. *J. AAPG Bull.* 89, 155–175. doi:10.1306/09170404042

Morse, J. W., and Wang, Q. (1997). Pyrite formation under conditions approximating those in anoxic sediments: II. Influence of precursor iron minerals and organic matter. *J. Mar. Chem.* 57, 187–193. doi:10.1016/S0304-4203(97)00050-9

Nie, H. K., Ma, X., Yu, C., Ye, X., Bian, R. K., and Liu, Z. B. (2017). Shale gas reservoir characteristics and its exploration potential-Analysis on the Lower Jurassic shale in the eastern Sichuan Basin. *J. Oil Gas Geol.* 38, 438–447. doi:10.11743/ogg20170303

Peltonen, C., Marcussen, Ø., Bjørlykke, K., and Jahren, J. (2009). Clay mineral diagenesis and quartz cementation in mudstones: the effects of smectite to illite reaction on rock properties. *Mar. Petroleum Geol.* 26, 887–898. doi:10.1016/j.marpetgeo.2008.01.021

Qiu, Y. B. (2018). Overpressure structure in Dongying sag and its controlling factors. *J. China Pet. Explor.* 23, 28–34. doi:10.3969/j.issn.1672-7703.2018.03.004

Radke, B. M., and Mathis, R. L. (1980). On the formation and occurrence of saddle dolomite. *J. Sediment. Res.* 50, 1149–1168. doi:10.1306/212F7B9E-2B24-11D7-8648000102C1865D

Ross, D. J. K., and Bustin, R. M. (2009). Investigating the use of sedimentary geochemical proxies for paleoenvironment interpretation of thermally mature organic-rich strata: examples from the Devonian–Mississippian shales, Western Canadian Sedimentary Basin. *J. Chem. Geol.* 260, 1–19. doi:10.1016/j.chemgeo.2008.10.027

Sass, E., Bein, A., and Almogi-Labin, A. (1991). Oxygen-isotope composition of diagenetic calcite in organic-rich rocks: evidence for18O depletion in marine anaerobic pore water. *J. Geol.* 19, 839–842. doi:10.1130/0091-7613(1991)019<0839:oicodc>2.3.co;2

Seewald, J. S. (2003). Organic-inorganic interactions in petroleum-producing sedimentary basins. *J. Nat.* 426, 327–333. doi:10.1038/nature02132

Sensuła, B., Bottger, T., Pazdur, A., Piotrowska, N., and Wagner, R. (2006). Carbon and oxygen isotope composition of organic matter and carbonates in recent lacustrine sediments. *J. Geochronometria.* 25, 77–94. doi:10.1016/j.geobios.2004.10.004

Siegel, D. I., Lesniak, K. A., Stute, M., and Frape, S. (2004). Isotopic geochemistry of the Saratoga springs: implications for the origin of solutes and source of carbon dioxide. *J. Geol.* 32, 257–260. doi:10.1130/G20094.1

Slatt, R. M., and O'Brien, N. R. (2011). Pore types in the Barnett and Woodford gas shales: contribution to understanding gas storage and migration pathways in fine-grained rocks. *J. AAPG Bull.* 95, 2017–2030. doi:10.1306/03301110145

Song, M., Liu, H., Wang, Y., and Liu, Y. (2020). Enrichment rules and exploration practices of paleogene shale oil in jiyang depression, Bohai basin, China. *Petroleum Explor. Dev.* 47, 225–235. doi:10.1016/S1876-3804(20)60043-X

Sun, H. Q. (2017). Exploration practice and cognitions of shale oil in Jiyang Depression. *J. China Pet. Explor.* 22, 1–14. doi:10.3969/j.issn.1672-7703.2017.04.001

Surdam, R. C., and Crossey, L. J. (1985). Organic-inorganic reactions during progressive burial: key to porosity and permeability enhancement and preservation. *J. Philosophical Trans. R. Soc.*, 315, 135–156. doi:10.1016/0198-0254(86)91076-9

Surdam, R. C., Crossey, L. J., Hagen, E. S., and Heasler, H. P. (1989). Organic-inorganic interactions and sandstone diagenesis. *J. Am. Assoc. Petroleum Geol. Bull.* 73. doi:10.1306/703c9ad7-1707-11d7-8645000102c1865d

Sweeney, R. E., and Kaplan, I. R. (1973). Pyrite framboid formation; laboratory synthesis and marine sediments. *J. Econ. Geol.* 68, 618–634. doi:10.2113/gsecongeo.68.5.618

Tian, J. C., and Zhang, X. (2016). *Sedimentary geochemistry (in chinses)*. Beijing: Geological Publishing House.

Towe, K. M. (1962). Clay mineral diagenesis as a possible source of silica cement in sedimentary rocks. *J. J. Sediment. Petrology* 32, 26–28. doi:10.1306/74d70c3b-2b21-11d7-8648000102c1865d

U.S. Energy Information Administration (2020). International energy outlook. (Accessed 25 November 2020). Available at: https://www.eia.gov/outlooks/ieo/.

Vos, K., Vandenberghe, N., and Elsen, J. (2014). Surface textural analysis of quartz grains by scanning electron microscopy (SEM): from sample preparation to environmental interpretation. *J. Earth-Science Rev.* 128, 93–104. doi:10.1016/j.earscirev.2013.10.013

Wang, Q. T., Lu, H., Shen, C. C., Liu, J. Z., Peng, P., and Hsu, C. S. (2014). Impact of inorganically bound sulfur on late shale gas generation. *J. Energy and Fuels* 28, 785–793. doi:10.1021/ef401468w

Warren, J. (2000). Dolomite: occurrence, evolution and economically important associations. *J. Earth Sci. Rev.* 52, 1–81. doi:10.1016/S0012-8252(00)00022-2

Weger, R., Murray, S., McNeill, D., Swart, P. K., Eberli, G. P., Blanco, L. R., et al. (2019). Paleothermometry and distribution of calcite beef in the vaca muerta formation, neuquén basin, Argentina. *J. AAPG Bull.* 103, 931–950. doi:10.1306/10021817384

Wilkinson, M., Haszeldine, R. S., and Milliken, K. L. (2004). "Cross-formational flux of aluminium and potassium in gulf coast (USA) sediments,". *Clay mineral cements in sandstones*. Editors R. Worden, and S. Morad (Washington, DC: J. International Association of Sedimentologists Special Publication), 34, 147–160. doi:10.1002/9781444304336.ch7

Wu, H. G., Hu, W. X., Tang, Y., Cao, J., Wang, X. L., Wang, Y. C., et al. (2017). The impact of organic fluids on the carbon isotopic compositions of carbonate-rich reservoirs: case study of the Lucaogou Formation in the Jimusaer Sag, Junggar Basin, NW China. *J. Mar. Petroleum Geol.* 85, 136–150. doi:10.1016/j.marpetgeo.2017.05.003

Wu, L. Y., and Gu, X. Z. (1986). The application of pyrolysis Technique in source rock research. *J. Acta Pet. Sin. J.* 7, 13–19. doi:10.7623/syxb198602003

Wu, S. T., Zhu, R. K., Cui, J. G., Cui, J. W., Bai, B., Zhang, X. X., et al. (2015). Characteristics of lacustrine shale porosity evolution, triassic chang 7 member, Ordos Basin,NW China. *J. Petroleum Explor. Dev.* 42, 185–195. doi:10.1016/S1876-3804(15)30005-7

Xi, K. L., Cao, Y. C., Jahren, J., Zhu, R., Bjørlykke, K., Haile, B. G., et al. (2015). Diagenesis and reservoir quality of the lower cretaceous quantou formation tight sandstones in the southern Songliao Basin, China. *J. Sediment. Geol.* 330, 90–107. doi:10.1016/j.sedgeo.2015.10.007

Xi, Z. D., Tang, S. H., Zhang, S. H., Yi, Y. X., Dang, F., and Ye, Y. P. (2019). Characterization of quartz in the Wufeng Formation in northwest Hunan Province, south China and its implications for reservoir quality. *J. Petroleum Sci. Eng.* 179, 979–996. doi:10.1016/j.petrol.2019.04.051

Yang, X. R., Yan, D. T., W, X. S., Zhang, L. W., Zhang, B., Xu, H. W., et al. (2018). Different formation mechanism of quartz in siliceous and argillaceous shales: a case study of Longmaxi Formation in South China. *J. Mar. Petroleum Geol.* 94, 80–94. doi:10.1016/j.marpetgeo.2018.03.036

Zhang, J. G., Jiang, Z. X., Jiang, X. L., Wang, S. Q., Liang, C., and Wu, M. H. (2016). Oil generation induces sparry calcite formation in lacustrine mudrock, Eocene of east China. *J. Mar. Petroleum Geol.* 71, 344–359. doi:10.1016/j.marpetgeo.2016.01.007

Zhang, J. L., and Zhang, P. Z. (1996). A Discussion of pyrite catalysis on the hydrocarbon generation process. *Adv. Earth Sci.* 11, 282–287.

Zhang, S., Liu, H. M., Wang, M., Fu, A. B., Bao, S. Y., Wang, W. Q., et al. (2018). Pore evolution of shale oil reservoirs in Dongying Sag. *J. Acta Pet. Sin.* 9, 754–766. doi:10.7623/syxb201807003

Zhang, S. C., Zhang, H. L., Zha, M., Zhu, R. F., and Liu, Q. (2010). Control of pressure system development on reservoir formation in the Dongying sag. *J. Petroleum Explor. Dev.* 37, 289–296.

Zhang, Y. W., Jang, S. B., and Li, F. (2021a). Influence of sandstone – shale contact on feldspar diagenesis in the sandstone reservoir of the Shahejie Formation in the Dongying depression, Bohai Bay basin. *J. Acta Geol. Sin.* 95, 883–894. doi:10.19762/j.cnki.dizhixuebao.2021126

Zhang, Z., Pang, J., Yang, Y. T., Cao, Y. H., Qi, M. H., Zhang, Y. Y., et al. (2021b). Carbon and oxygen isotope characteristics and genesis of carbonate in sandstone of the 4th Member if Xujiahe Formation in the central western Sichuan depression, Sichuan basin, China. *J. Acta Geol. Sin.* 95. doi:10.19762/j.cnki.dizhixuebao.2022260

Zhao, X. Z., Zhou, L. H., Pu, X. G., Jin, M. F., Han, Z. W., Xiao, G. T., et al. (2018). Geological characteristics of shale rock system and shale oil exploration breakthrough in a lacustrine basin: a case study from the Paleogene 1st sub-member of Kong 2 Member in Cangdong sag,Bohai Bay Basin, China. *J. Petroleum Explor. Dev.* 45, 377–388. doi:10.1016/S1876-3804(18)30043-0

frontiers | Frontiers in Earth Science

TYPE Original Research
PUBLISHED 22 July 2025
DOI 10.3389/feart.2025.1507500

OPEN ACCESS

EDITED BY
Yifan Li,
China University of Geosciences, China

REVIEWED BY
Youwei Wang,
University of Virginia, United States
Yibo Yang,
Chinese Academy of Sciences (CAS), China
Shun Li,
Shanghai Jiao Tong University, China

*CORRESPONDENCE
Min Gao,
zhennigao89@gmail.com

†PRESENT ADDRESS
Domenico Chiarella,
Biological, Geological and Environmental Sciences Department, Alma Mater Studiorum University of Bologna, Bologna, Italy

RECEIVED 08 October 2024
ACCEPTED 06 March 2025
PUBLISHED 22 July 2025

CITATION
Gao M, Fan M, Zhuang G and Chiarella D (2025) Continental hydroclimate during the late Paleocene-early Eocene in the central Rockies: insights from sedimentological and geochemical records preserved in the greater Green River Basin, southwestern Wyoming, U.S.A..
Front. Earth Sci. 13:1507500.
doi: 10.3389/feart.2025.1507500

Continental hydroclimate during the late Paleocene-early Eocene in the central Rockies: insights from sedimentological and geochemical records preserved in the greater Green River Basin, southwestern Wyoming, U.S.A.

Min Gao[1,2,3]*, Majie Fan[2], Guangsheng Zhuang[4] and Domenico Chiarella[3†]

[1]Research Institute of Petroleum Exploration and Development, PetroChina, Beijing, China, [2]Department of Earth and Environmental Sciences, The University of Texas at Arlington, Arlington, TX, United States, [3]Department of Earth Sciences, Royal Holloway, University of London, Egham, United Kingdom, [4]Department of Geology and Geophysics, Louisiana State University, Baton Rouge, LA, United States

The late Paleocene to early Eocene (LPEE, ~59–50 Ma) greenhouse condition is the most recent geologic analogue for future climate change induced by increased atmospheric CO_2 partial pressure (pCO_2). Recognition of the hyperthermals and reconstruction of the continental hydroclimate and atmospheric pCO_2 during this warm period are fundamental to the understanding of Earth's surface responses to high atmospheric pCO_2. Here we study paleosol morphology, bulk organic matter $\delta^{13}C_{org}$, leaf wax n-alkanes $\delta^{13}C_{n\text{-}alk}$ and $\delta D_{n\text{-}alk}$, and reconstruct mean annual precipitation (MAP) and atmospheric pCO_2 from the fine-grained floodplain deposits in the greater Green River Basin, western U.S.A., to examine the hydroclimate evolution in the continental interior during the LPEE. The Paleocene-Eocene Thermal Maximum (PETM) was identified as a ~4‰–5‰ negative carbon isotope excursion (CIE) in the bulk organic $\delta^{13}C_{org}$ record and leaf wax n-alkanes $\delta^{13}C_{n\text{-}alk}$ record, and a 30‰–50‰ increase in leaf wax n-alkanes $\delta D_{n\text{-}alk}$ record. Well drained green paleosols and water-logged histosols dominated the floodplain deposition during the LPEE, and poorly drained red paleosols and carbonate-rich calcisols characterized the hyperthermal. Our reconstructed MAP is generally high (800–1,500 mm) during the LPEE and does not show significant change during the PETM. Our estimated atmospheric pCO_2, by integrating bulk organic $\delta^{13}C_{org}$ and paleosol carbonate $\delta^{13}C_c$ values, is generally in the range of 600–900 ppm during the early Eocene, 1–2 times higher than the preindustrial level. These records suggest that the continental hydroclimate was generally humid and warm during the LPEE, and transient drying likely happened during the PETM.

KEYWORDS

carbon isotope, leaf wax n-alkanes, paleosol, precipitation, pCO_2, Paleocene-Eocene Thermal Maximum

Highlights

- PETM was recognized as a ~4‰–5‰ negative carbon isotope excursion in the greater Green River Basin
- Continental climate was generally humid and warm during the late Paleocene-early Eocene based on proxy data
- Transient drying likely happened during the PETM based on an $\delta D_{n\text{-}alk}$ increase and soil morphology change.

1 Introduction

Continental hydroclimate and environment during the late Paleocene-early Eocene (LPEE, 59–50 Ma) greenhouse state are fundamental to the understanding of Earth's surface responses to future global warming (e.g., McInerney and Wing, 2011). The warm climate during the LPEE culminated at the Early Eocene Climatic Optimum (EECO) during 52–50 Ma (Zachos et al., 2001), and the LPEE consists of several short-term hyperthermal events, including the most prominent Paleocene-Eocene Thermal Maximum (PETM) occurred at ~55.5 Ma (Zachos et al., 2001), and smaller Eocene Thermal Maximum 2 and 3 (ETM-2, ETM-3) at ~53.5 Ma and ~52.8 Ma, respectively (e.g., Zachos et al., 2001; Lourens et al., 2005; Sluijs et al., 2009; Abels et al., 2012; Schneider-Mor and Bowen, 2013). During the LPEE greenhouse state, benthic foraminifera $\delta^{18}O_c$ values decreased by at least 1.0‰, representing ~4°C increase in ocean bottom temperature, and the $\delta^{13}C_c$ values decreased ~2.0‰ (Zachos et al., 2001). It has been suggested that the warm global climate during the LPEE was associated with injection of a very large mass of ^{13}C-depleted carbon into the atmosphere or ocean (e.g., Zachos et al., 2008). Possible sources of the carbon include: 1) deeply buried rocks that were liberated as methane and CO_2 by intrusive volcanisms (Svensen et al., 2004); 2) high methane fluxes from large marine gas hydrate capacitors as a result of increasing deep-sea temperature (e.g., Dickens, 2003); 3) metamorphic decarbonation of carbonate-rich pelagic sediments and release of CO_2 when the Tethyan oceanic crust was subducted during the India and Eurasia collision (e.g., Caldeira, 1992; Kent and Muttoni, 2008; Guo et al., 2021); or 4) repeated, large-scale releases of dissolved organic carbon from the ocean by ventilation of the ocean interior (e.g., Sexton et al., 2011).

The responses of continental climate and environment to future global warming can be predicted from detailed continental hydroclimate records during the LPEE. Sedimentary basins at different global sites provide a rich archive of continental hydroclimate for this warm period, and many studies have been conducted to examine the contemporaneous climatic and ecological responses based on paleopedology, stable isotope analysis, and climate modeling (e.g., Koch et al., 1995; Bowen et al., 2001; Sewall and Sloan, 2006; Hren et al., 2010; Hyland et al., 2013; Snell et al., 2013; Carmichael et al., 2017; 2018; Hollis et al., 2019; Rush et al., 2021; Cramwinckel et al., 2023). However, most of these studies focus only on a short period of the early Paleogene, such as the PETM and EECO (e.g., Bowen et al., 2001; Bowen and Beerling, 2004; McInerney and Wing, 2011; Hyland et al., 2013). Up to now, long and continuous terrestrial climate records covering the entire early Paleogene are rare.

The hyperthermal events occurred during the LPEE have been well documented in marine isotope record and continental isotope record in the Bighorn Basin in the western U.S.A. The PETM is characterized by a more than 1.0‰ negative excursion of deep-sea carbonate $\delta^{18}O_c$ values and ~4°C–8°C increase of deep-sea temperature over a duration of ~100 kyr (e.g., Kennett and Stott, 1991; Röhl et al., 2000; Zachos et al., 2003; Tripati and Elderfield, 2005; Röhl et al., 2007). The PETM is also expressed as a ~3‰–8‰ negative CIE in the marine and terrestrial carbon isotope records (e.g., Kennett and Stott, 1991; Zachos et al., 2001; Koch et al., 2003; Pagani et al., 2006; Baczynski et al., 2016). In the Bighorn Basin, the PETM and ETM-2 have been characterized by negative CIEs in isotope records of soil carbonate and organic matter (e.g., Koch et al., 1995; Stott et al., 1996; Wing et al., 2005; Hyland et al., 2013; Baczynski et al., 2016; Abels et al., 2016).

The paleoenvironmental condition in continental mid-latitude during the extreme hyperthermal events and the atmospheric pCO_2 during the LPEE have been debated. A global increase in wetland deposits during the PETM was used to suggest intensified precipitation (Sloan et al., 1992; 1999), which was supported by clay mineral assemblages that suggest wetter conditions (e.g., Robert and Kennett, 1994), and climate modeling that suggests wetter subtropical environment (e.g., Rind, 1998). However, other sedimentological studies and precipitation reconstructions suggest dry conditions in Europe (Schmitz and Andreasson, 2001; Schmitz and Pujalte, 2003), and in the Bighorn Basin in the western U.S.A. (Kraus et al., 2013). Based on paleosol carbon isotope records, Sinha and Stott (1994) proposed that the atmospheric pCO_2 during the LPEE was generally between 300 and 700 ppm. Paleosol carbon isotope studies in the Wind River Basin in the western U.S.A. suggest that the atmospheric pCO_2 ranged from 350 to 1,265 ppm during the EECO (Fan et al., 2011; Hyland et al., 2013). The most recent, The Cenozoic CO_2 Proxy Integration Project (CenCO2PIP) Consortium (2023) assessed a comprehensive collection of proxy reconstructions and suggested that pCO_2 during the LPEE ranged between ~400 and ~1700 ppm, and the highest was at ~51 Ma.

To improve our understanding of mid-latitude terrestrial responses to the global climate changes during the LPEE, we conducted a multi-method study on the early Paleogene floodplain deposits in the greater Green River Basin in southwest Wyoming. Specifically, this study constructs a high-resolution, continuous bulk organic $\delta^{13}C_{org}$ record that is assisted by leaf-wax *n*-alkanes $\delta^{13}C_{n\text{-}alk}$ trend to identify the PETM; uses paleosol morphology, leaf-wax *n*-alkanes $\delta D_{n\text{-}alk}$ and the chemical index of alteration without potassium (CIA-K) of bulk sediments in paleosol B-horizons to reconstruct paleoclimate; and reconstructs pCO_2 using paleosol carbonate $\delta^{13}C_c$ and bulk organic $\delta^{13}C_{org}$ values.

2 Geological background

The greater Green River Basin was in the Sevier foreland during the Late Cretaceous and evolved into an isolated intermontane basin during the latest Cretaceous-early Eocene Laramide orogeny (Dickinson et al., 1988; DeCelles, 2004; Gao et al., 2016). The basin is bounded by the Sevier thrust belt to the west, the Wind River Range and Granite Mountains to the north, the Rawlins uplift and Sierra Madre Mountains to the east, and the Uinta Mountains to

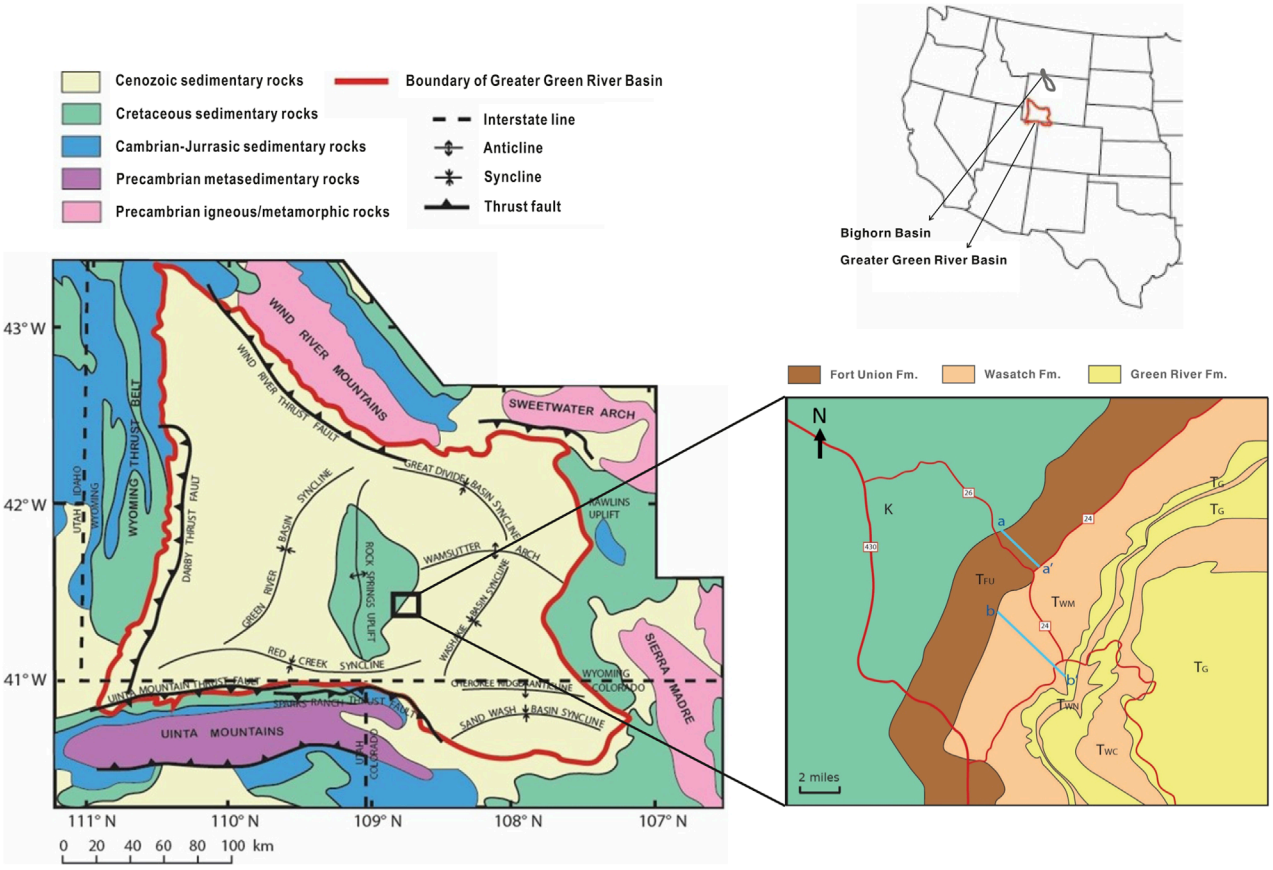

FIGURE 1
Location of the study area and major structural features in the greater Green River Basin [based on Roehler (1992) and geologic map courtesy of USGS]. The black box represents the study area. a-a' represents the measured section of the Fort Union Formation, b-b' represents the measured section of the Wasatch Formation.

the south (Figure 1). The samples used for analysis in this study were collected along a ~1430-m-thick measured section of the lower Paleogene strata in the southern part of the basin, to the southeast of the Rock Springs Uplift (Figure 1). The section consists of two segments: the Fort Union Formation with a thickness of about 780 m, and the Wasatch Formation with a thickness of about 650 m. Detailed description and in-depth sedimentological study of this section have been conducted and published in our earlier work (Gao and Fan, 2018).

The Paleogene strata in the greater Green River Basin consist of three formations: the Paleocene Fort Union Formation and the lower Eocene Wasatch Formation, both deposited in predominantly fluvial systems, and the overlying lower Eocene Green River Formation deposited in fluvial and lacustrine environments (e.g., Dickinson and others, 1988; Shuster and Steidtmann, 1988; Roehler, 1992; Pietras and others, 2003; Gao and Fan, 2018). This study focuses on the Fort Union and the Wasatch formations, to investigate the recorded signals of the continental hydroclimate during the Paleocene-early Eocene. On the sampled section of this study, the Fort Union Formation is characterized by multiple fining-upward sequences, with lithofacies changes from very fine-to medium-grained, horizontally bedded (S_h), laminated (S_l), and massive (S_m) sandstone to massive (F_m) and laminated (F_l) mudstone, paleosol (F_p), and coal (C) in each sequence, typical of a distal floodplain environment (Figure 2); the Wasatch Formation conformably overlies the Fort Union Formation, and is featured by stacked, thick or thin lenticular sandstone units with erosional bases and trough-cross stratifications (S_t), ripples (S_r), or other sedimentary structures (S_h, S_l, S_m), nested in fine-grained lithofacies (F_m, F_l, F_p), interpreted to be frequently migrating river channels over the floodplain in a braided river system (Figure 2) (Gao and Fan, 2018). The fine-grained deposits of these two formations along the sampled section contain large amount of paleosols, providing the opportunity to build long isotope and element records for the interpretation of early Paleogene continental climate.

The chronology of the greater Green River Basin relies mainly on land mammal fossil assemblages and pollen biostratigraphy (e.g., Roehler and Martin, 1987; 1992; Honey, 1988; Woodburne, 2004); paleomagnetostratigraphy and radiometric dating of volcanic ash beds were only conducted to some intervals of the Eocene strata stratigraphically above our section (e.g., Mauger, 1977; Machlus et al., 2004). North America Land Mammal ages have been calibrated to absolute geologic time scale based on paleomagnetostratigraphy and radiometric dating of ash beds in other basins in Wyoming (e.g., Clyde et al., 1997). Mammal fossils of *Diacodon*, *Gelastops*, *Mixodectes*, *Paleotomus*, *Promioclaenus*,

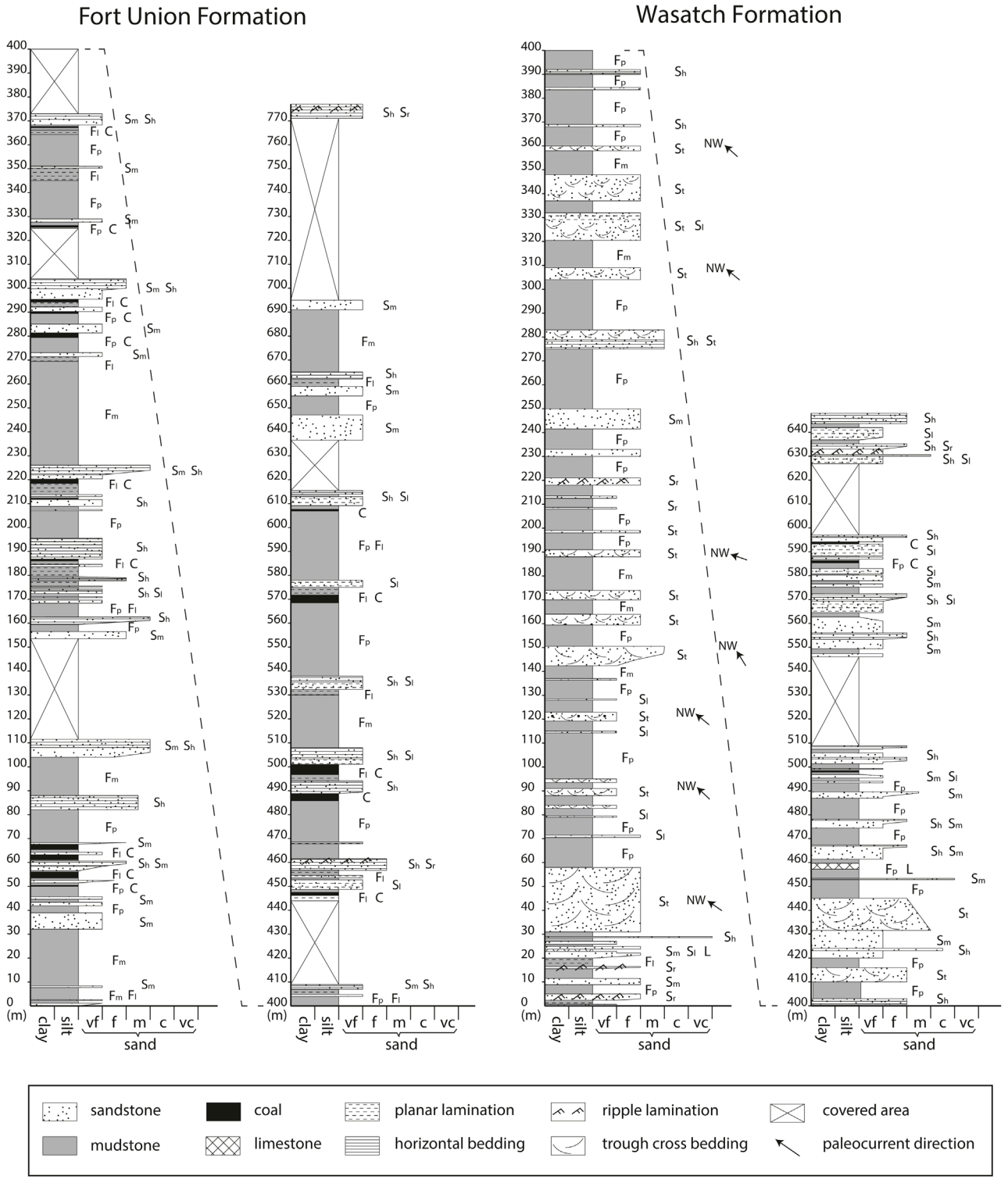

FIGURE 2
Measured stratigraphic sections of the Paleocene Fort Union Formation and the lowermost Eocene Wasatch Formation (Gao and Fan, 2018, © Yale University-AJS, used with permission). Section locations are shown in Figure 1.

etc., typical to the early Torrejonian land mammal stage (To_2, ~61.3–62.3 Ma), were found in the Fort Union Formation, ~8 km south of our studied locality (Rigby, 1980). Age-diagnostic fossils were previously documented at several stratigraphic levels in other measured sections of the Wasatch Formation near our studied section (Roehler, 1992). These stratigraphic levels can be correlated

to our section based on lithostratigraphic correlations. The presence of *Hyracotherium, Hyopsodus, Haplomylus, and Diacodexis,* in the main body of the Wasatch Formation in several localities places the deposition to the early Wasatchian stage (Wa_0-Wa_5, ~55.0–53.4 Ma). The top of the main body of the Wasatch Formation is determined to be older than ~53 Ma because the presence of *Heptodon, Lambdotherium, and Meniscotherium* in the Niland Tongue Member of the Wasatch Formation (e.g., Roehler, 1992; Tauxe et al., 1994), stratigraphically above our studied interval, places the Member to middle or late Wasatchian stage (Wa_6-Wa_7, ~52.9–52.6 Ma).

3 Methods

Four types of data were collected to reconstruct the continental hydroclimate during the LPEE in the greater Green River Basin, including paleosol morphology observations documenting changes in paleosol type; high-resolution bulk organic $\delta^{13}C_{org}$ and low-resolution leaf wax *n*-alkanes $\delta^{13}C_{n\text{-}alk}$ and $\delta D_{n\text{-}alk}$ values for the identification of PETM; coupled paleosol carbonate $\delta^{13}C_c$ and bulk organic $\delta^{13}C_{org}$ values to reconstruct pCO_2; and CIA-K of paleosol B-horizons for the reconstruction of MAP.

3.1 Paleosol classification

The paleosol description and classification in this study are mainly based on the field observations of soil texture and structure, mottled color and mineral accretions. The B-horizon in the soil profile is the key interest of this study, for its important role in reflecting the drainage condition and assisting the pCO_2 reconstruction. Several key features were used to identify the B-horizons during our field examination of paleosols: 1) B-horizons often display reddish, yellowish, or brownish colors due to the accumulation of iron oxides or clay minerals; 2) B-horizons usually exhibit distinctive ped structures, such as wedge-shaped peds or slickensides; and 3) accumulated materials are often present in B-horizons as evidence of illuviation, such as the shiny clay films that form along the wedge-shaped peds or slickensides, the iron oxide coatings, the pedogenic carbonate nodules, etc. (e.g., Mack et al., 1993; Retallack, 1997; 2001; Kraus, 1999; Daniels and Haering, 2006; Kraus et al., 2013).

3.2 Carbon and hydrogen isotope analysis

Carbon isotope analysis in this study includes analysis of bulk organic matter $\delta^{13}C_{org}$, paleosol carbonate $\delta^{13}C_c$, and leaf wax *n*-alkanes $\delta^{13}C_{n\text{-}alk}$. Bulk paleosol and mudstone samples were collected every 0.5–1.0 m from the floodplain facies throughout the measured sections, and pedogenic carbonate nodules were collected where available. Fresh bulk paleosol and mudstone samples were collected after removing the surface layers to avoid any possible contamination from recent organic material. Pedogenic carbonate nodules were collected at a depth greater than 30 cm below the paleosol surface in order to reduce the influence of atmospheric CO_2 on $\delta^{13}C_c$. Petrographic analysis and X-ray diffraction analysis have been done to these pedogenic carbonate nodules in our earlier study (Gao and Fan, 2018), and the results show that these paleosol carbonates are dominated by low-magnesium calcite, predominantly micritic, suggesting minimal diagenetic influence.

For $\delta^{13}C_{org}$ analysis, the samples were examined under a microscope and any obvious modern organic matter was removed by hand picking. Samples were then powdered using a ceramic mortar and pestle and weighted into open silver capsules. Carbonate in the powdered samples was removed using hydrogen chloride fumigation method. Samples were loaded into silver capsules and wetted by adding one drop of deionized water. Open silver capsules were placed in a sealed desiccator containing a beaker of 12 N fuming HCl for at least 4 days, then dried in oven at 75°C for at least 12 h. Each silver capsule was then carefully placed in a tin capsule and tightly packed and loaded into a Costech ECS 4010 Analyzer, which was connected to a Delta V Advantage Mass Spectrometer via ConFlo IV, at the University of Texas at Arlington. The isotope ratios were calibrated using USGS 40, USGS 41, and the precision of $\delta^{13}C_{org}$ is better than ±0.2‰ (1σ) based on repeated analysis of standards. The $\delta^{13}C_{org}$ values are reported relative to Vienna Pee Dee Belemnite (VPDB).

For $\delta^{13}C_c$ analysis, the carbonate samples were powdered using a ceramic mortar and pestle. Powdered samples were weighed and loaded into sample vials. After flushing the vials using ultrapure helium, dehydrated phosphoric acid was injected into the vials to react with the samples at 70°C. The $\delta^{13}C$ values of the resulted CO_2 were analyzed using a Gasbench II and a Delta V Advantage Mass Spectrometer at the University of Texas at Arlington. The isotope ratios were calibrated using NBS-19, NBS-18, and the precision of $\delta^{13}C$ values is better than ±0.2‰ (1σ) based on repeated analysis of standards. All the isotope values of carbonate were reported relative to VPDB.

Based on the trend of $\delta^{13}C_{org}$ data and potential PETM, six paleosol samples were selected to analyze $\delta^{13}C_{n\text{-}alk}$ and $\delta D_{n\text{-}alk}$ at the Louisiana State University to verify the presence of PETM in our record. These six samples include four within and two outside of the interpreted PETM. Lipids were extracted from 30 to 60 g of powdered rock samples using Soxhlet extractors with a solvent mixture of dichloromethane (DCM) and methanol (MeOH) 2:1 (v/v) for over 48 h. Total lipid extracs (TLE) were evaporated using a TurboVap II evaporator under a stream of purified nitrogen. TLE was separated into compound classes using ~4.0 g of pre-extracted, activated (@200°C for 2 h) silica gel. Organic compounds in TLE were separated into apolar, intermediate, and polar fractions by using 4 mL hexane, 4 mL DCM, and 4 ml methanol, respectively. *n*-Alkanes abundances were determined using a Thermal Trace 1,310 Ga Chromatography (GC)-flame ionization detector (FID) fitted with a programmable temperature vaporization (PTV) injector and a fused silica, TG-1MS column (60 m long, 0.25 mm i. d., 0.25 μm film thickness). Samples were carried by helium at a rate of 2 mL/min. GC oven temperature was ramped from 60°C (holding for 1 min) to 320°C at 15°C/min (holding for 20 min).

Measurements of compound-specific $\delta^{13}C_{n\text{-}alk}$ values were performed using a Thermal Trace 1,310 Ga Chromatography (GC) coupled to a Thermo Delta V Advantage isotope ratio mass spectrometer (IRMS) interfaced with a Thermo Isolink interface. The GC column and carrier flow conditions were identical to above. Compounds were separated on the GC with a temperature program

TABLE 1 Leaf wax $\delta^{13}C_{n\text{-}alk}$ and $\delta D_{n\text{-}alk}$ values of the six samples in this study.

Formation	Meter level(m)	Relative to PETM	$\delta^{13}C_{org}$ (‰)		$\delta^{13}C_{n\text{-}alk}$ (‰)								$\delta D_{n\text{-}alk}$ (‰)							
			Avg.	S.D.	C_{27} Avg.	C_{27} S.D.	C_{29} Avg.	C_{29} S.D.	C_{31} Avg.	C_{31} S.D.	C_{33} Aye,	C_{33} S.D.	H_{27} Avg.	H_{27} S.D.	H_{29} Avg.	H_{29} S.D.	H_{31} Avg.	H_{31} S.D.	H_{33} Avg.	H_{33} S.D.
Fort Union	573.0	before	−26.5	<0.2	−28.1	0.2	−28.3	0.4	−28.7	0.5	−28.5	0.7	−205.0	–	−214.7	–	−200.6	–	−181.5	–
Wasatch	80.5	PETM	−26.0	<0.2	−31.8	0.3	−30.7	0.6	−31.0	0.4	−30.9	0.2	−199.6	2.0	−199.0	6.3	−203.8	4.2	−184.6	1.4
Wasatch	81.0	PETM	−28.3	<0.2	−32.0	0.4	−31.3	0.4	−31.0	0.3	−30.4	0.4	−210.8	11.5	−194.5	8.5	−194.3	12.2	−187.2	10.0
Wasatch	137.8	PETM	−28.7	<0.2	−32.1	0.6	−32.4	0.3	−32.1	0.4	−32.1	0.6	−162.4	1.5	−179.7	4.8	−174.0	2.7	−132.1	5.4
Wasatch	172.0	PETM	−27.8	<0.2	−33.1	0.8	−31.1	0.4	−31.6	0.1	−30.2	0.9	−179.9	6.4	−201.5	5.2	−176.4	1.8	−153.9	9.5
Wasatch	336.0	after	−25.9	<0.2	−29.6	0.6	−29.2	0.2	−29.9	0.3	−28.8	0.7	−212.3	7.6	−196.6	4.4	−195.0	7.8	−184.0	12.5

Avg.—average value of multiple measurements.
S.D.—standard deviation

from 60°C (held for 1 min) to 170°C at 14°C/min, to 300°C at 3°C/min, and then to 325 at 14°C/min with an isothermal holding of 10 min. Carbon isotope ratio values were determined relative to a reference, calibrated against Mix A6 (n-C_{16} to n-C_{30}; Arndt Schimmelmann, Indiana University), and reported relative to VPDB and with two standard deviations.

Measurements of compound-specific $\delta D_{n\text{-alk}}$ values were performed using a Thermo Trace 1310 GC coupled to a Delta V Advantage isotope ratio mass spectrometer (IRMS) interfaced with an Isolink interface. The GC column and carrier flow conditions were identical to carbon isotope analysis. Compounds were separated on the GC with a temperature program from 60°C (held for 2 min) to 170°C at 14°C/min, to 300°C at 3°C/min, and then to 325°C at 14°C/min with an isothermal holding of 10 min. The H_3^+ factor (Sessions, 2001) was monitored daily prior to δD analysis and was less than eight for the measurement periods. The drift of the instrument was routinely monitored, and individual n-alkane isotope ratios were corrected to n-alkane reference materials (Mix A3, A. Schimmelmann, Indiana University, Bloomington). $\delta D_{n\text{-alk}}$ values are reported relative to Vienna Standard Mean Ocean Water (VSMOW) and with two standard deviations (Table 1).

3.3 pCO_2 reconstruction

We followed Equation 1 that was presented in Cerling and Harris, (1999) for atmospheric pCO_2 reconstruction.

$$pCO_2(ppmv) = S(z)\frac{\delta^{13}C_s - 1.0044 * \delta^{13}C_r - 4.4}{\delta^{13}C_a - \delta^{13}C_s} \quad (1)$$

In the equation, pCO_2 is the concentration of atmospheric CO_2, S(z) is the concentration of soil-respired CO_2, $\delta^{13}C_s$ is the carbon isotope composition of soil CO_2, $\delta^{13}C_r$ is the carbon isotope composition of soil-respired CO_2, $\delta^{13}C_a$ is the carbon isotope composition of atmospheric CO_2. $\delta^{13}C_s$ is determined from the paleosol carbonate $\delta^{13}C_c$ and paleosol carbonate precipitation temperature using the temperature-sensitive equilibrium isotope fractionation factor between calcite and CO_2 Equation 2 (Romanek et al., 1992):

$$\delta^{13}C_s = \frac{\delta^{13}C_{cc} + 1000}{\frac{(11.98-0.12T)}{1000} + 1} - 1000 \quad (2)$$

$\delta^{13}C_r$ was traditionally represented by paleosol $\delta^{13}C_{org}$ values (e.g., Cerling, 1992; Retallack, 2009). However, several studies have shown that bulk $\delta^{13}C_{org}$ values in modern soils are comparable to those found in surface litter, but they tend to increase with soil depth (e.g., Torn et al., 2002; Wynn et al., 2005; Wynn and Bird, 2007). Therefore, organic carbon in soil B-horizons, which are typically sampled when working with paleosol carbonate, have $\delta^{13}C_{org}$ values higher than the average biomass, and the $\delta^{13}C_r$ in Equation 1 can be approximated by measured $\delta^{13}C_{org}$ values minus 1‰ (Bowen and Beerling, 2004; Breecker, 2013). $\delta^{13}C_a$ was −6.1‰ during the early Eocene (Tipple et al., 2010). S(z) is commonly assumed as summer minimum soil-respired CO_2 in this equation because soil carbonates are likely to precipitate preferentially during warm seasons (Breecker et al., 2009; Passey et al., 2010; Quade et al., 2013; Hough et al., 2014). We use the value of 2,500 ppm for S(z) as it is commonly used for the subhumid temperature and tropical climates (Breecker et al., 2010).

3.4 MAP reconstruction

Bulk paleosol samples from the B-horizons were analyzed for major element concentrations using a Shimadzu EDX-7000 X-ray fluorescence (XRF) spectrometer at the University of Texas at Arlington. The reported weight percentages were calibrated using three USGS standards: SDO-1 (Devonian Ohio Shale), SBC-1 (Brush Creek Shale), and SGR-1 (Green River Shale) (Supplementary Table S2). The weight percentages were then recalculated to molar ratios, following Sheldon et al. (2002). Since the intensity of chemical weathering of paleosols depends in part on precipitation, Sheldon et al. (2002) developed an empirical relationship (Equation (3)) relating the mean annual precipitation (MAP) to the chemical index of alteration without potassium (CIA-K). The error associated with the regression analysis is ±181 mm (Sheldon et al., 2002; Sheldon and Tabor, 2009).

$$\mathrm{MAP(millimeters/year)} = 221e^{0.0197*\mathrm{CIA\text{-}K}};\ r^2 = 0.72 \quad (3)$$

$$\mathrm{CIA\text{-}K} = \left[Al_2O_3/\left(Al_2O_3 + CaO^* + Na_2O\right)\right] \times 100 \quad (4)$$

The chemical index CIA-K, which excludes potassium (K), is derived from Equation 4. K is excluded in calculation because diagenesis can yield elevated K concentrations in paleosols (McLennan, 1993). CIA-K is calculated based on the molar ratio of Al_2O_3, to the sum of Al_2O_3, CaO^*, and Na_2O. CaO^* is the smaller value between CaO and Na_2O to account for CaO derived from the silicate fraction, excluding the carbonate fraction (McLennan, 1993).

4 Results

4.1 Paleosol classification

4.1.1 Fort Union Formation

The floodplain facies in this formation contains many coal beds. Figure 3a shows a typical succession that contains a coal bed in the Fort Union Formation. Below each coal bed a sequence of mudstone with color changes from light grey to dark grey toward the coal is commonly observed, representing upward increase of organic matter content. Above each coal bed is usually a short sequence of tan or greyish mudstone, which gradually changes upward into very fine- to fine-grained and laminated sandstone. Beds with the presence of coals in this formation are classified as histosols according to the definition that each coal originated as a water-logged surface horizon containing a high concentration of plant debris, called histic epipedon (Soil Survey Staff, 1975; Buol et al., 1980; Mack et al., 1993).

4.1.2. Main body of the Wasatch Formation

Three types of paleosols are observed in this formation: the calcic paleosol (Figure 3b), the green paleosol (Figures 3c–e), and the red paleosol (Figures 3f–g). The calcic paleosols were mostly found at about 80–100 m above the base of the Wasatch Formation, coincident with the ~4‰ negative CIE on $\delta^{13}C_{org}$ record (Figures 3, 4). The B-horizons of these calcic paleosols typically have tan color with small, white and hard carbonate nodules, and lack peds or slickenside structures, suggesting low precipitation and poor drainage. The green paleosols and the red paleosols contain high clay content and vertic features including wedge-shaped peds, hummock and swale structure, and slickensides. The green paleosols are the most prevalent in the main body of the Wasatch Formation, while the red paleosols are mostly present in two segments of the section: one is at 80–180 m above the formation base, and the other is in the upper part of the section within about 100 m below the early Eocene lacustrine facies. Carbonate accumulations can be found in the B-horizons of both the green paleosols and red paleosols, while more common and developed as nodules in the red paleosols.

The calcic paleosols found in this formation are classified as calcisols based on their combined features of soil structure and the presence of carbonate nodules. Since calcisols are commonly formed in semi-arid to arid climate (e.g., Badía-Villas and del Moral, 2016; Elidrissi et al., 2018), the accumulation of calcisols here might indicate a transient drying during the PETM. The green paleosols and the red paleosols were classified to be ancient analogs to vertisols, based on their mottled colors and vertic features (e.g., Mack et al., 1993; Nettleton et al., 2000; Driese et al., 2005).

4.2 Isotope record, reconstructed MAP, and atmospheric pCO_2

The $\delta^{13}C_{org}$ values of the organic-rich pedogenic mudstone that is usually accompanied with coal beds in the Paleocene Fort Union Formation vary between −23.2‰ and −26.5‰, with an average of −25.0‰ (Supplementary Table S1; Figure 4b). The $\delta^{13}C_{org}$ values of the paleosol B-horizons in the main body of the lower Eocene Wasatch Formation vary between −24.0‰ and −29.4‰, with an average of −26.3‰ (Supplementary Table S1; Figure 4b).

The $\delta^{13}C_{org}$ values of the non-pedogenic mudstone samples have similar variations as the $\delta^{13}C_{org}$ values of paleosols. In the Fort Union Formation, the $\delta^{13}C_{org}$ values of non-pedogenic mudstone samples vary between −22.8‰ and −26.1‰, with an average of −24.5‰ (Supplementary Table S1; Figure 4b). In the main body of the Wasatch Formation, these $\delta^{13}C_{org}$ values vary between −22.5‰ and −27.2‰, with an average value of −25.7‰ (Supplementary Table S1; Figure 4b).

At ~70 m above the base of the Wasatch Formation, the $\delta^{13}C_{org}$ values show a transient drop of ~4‰, and the CIE spans ~70 m on the record (Figure 4b). The $\delta^{13}C_{n-alk}$ values in this interval show a negative excursion on the order of ~4‰–5‰ on long–chain *n*–alkanes with 27, 29, 31, and 33 carbon atoms (Table 1; Figure 5), δD_{n-alk} values in this interval show increases of 30‰–50‰ (Table 1; Figure 6). Another CIE of ~2‰ is documented in the $\delta^{13}C_{org}$ record after the Paleocene–Eocene boundary, at the 490–590 m level above the base of Wasatch Formation, and is older than ~53 Ma based on the biostratigraphic age constraint of our studied strata (Figure 4b).

Based on the well calibrated major element data (Table 2; Supplementary Table S2), the reconstructed MAP throughout the Paleocene and the earliest Eocene is generally high, in the range of 800–1,500 mm (Table 2; Figure 4b). An extremely low value of 408 mm occurs at 168.8 m of Wasatch Formation, however, this estimate is not accurate due to its high Na_2O content (5.1 wt%) compared to the other samples (<2.8 wt%). The elevated Na_2O is likely due to diagenetic salt, rather than a contribution from silicate.

10.3389/feart.2025.1507500

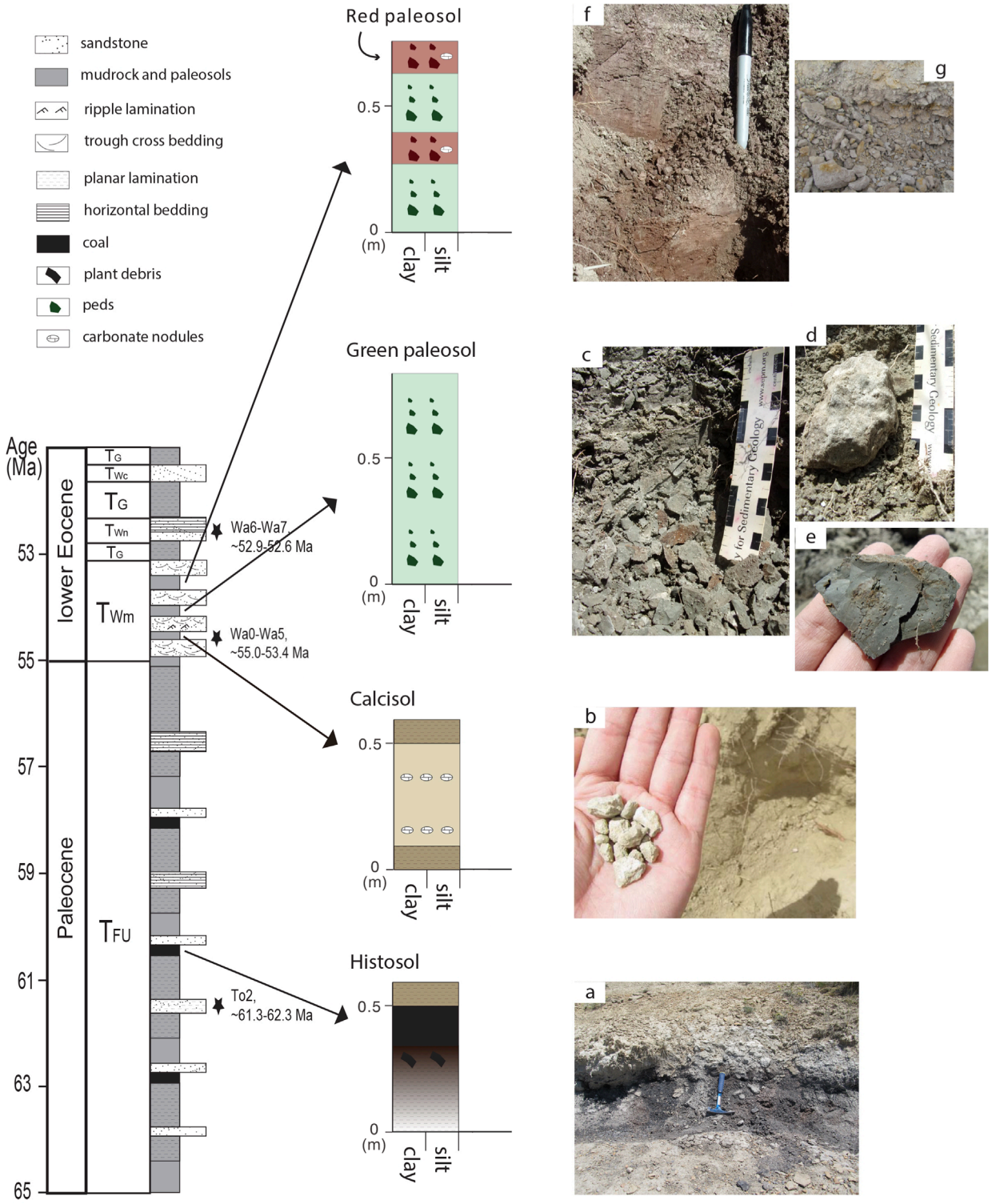

FIGURE 3
Field pictures and conceptual sketch of the four types of paleosol in this study. The simplified stratigraphic column of the studied strata is based on Figure 2, and stars represent stratigraphic levels of the age constraints summarized in the text. **(a)** field picture of a histosol; **(b)** field picture of a calcisol with soil carbonate nodules; **(c)** field picture of a green paleosol with **(d)** carbonate nodules and **(e)** peds structure; and **(f)** field pictures of a red paleosol with **(g)** carbonate horizon. T_{FU}: Fort Union Formation; T_{Wm}: main body of the Wasatch Formation; T_{Wn}, Niland Tongue of the Wasatch Formation; T_{Wc}, Cathedral Bluffs Tongue of the Wasatch Formation; T_G, Green River Formation. Field pictures **(a,b)** are from Gao and Fan (2018), © Yale University-AJS, used with permission.

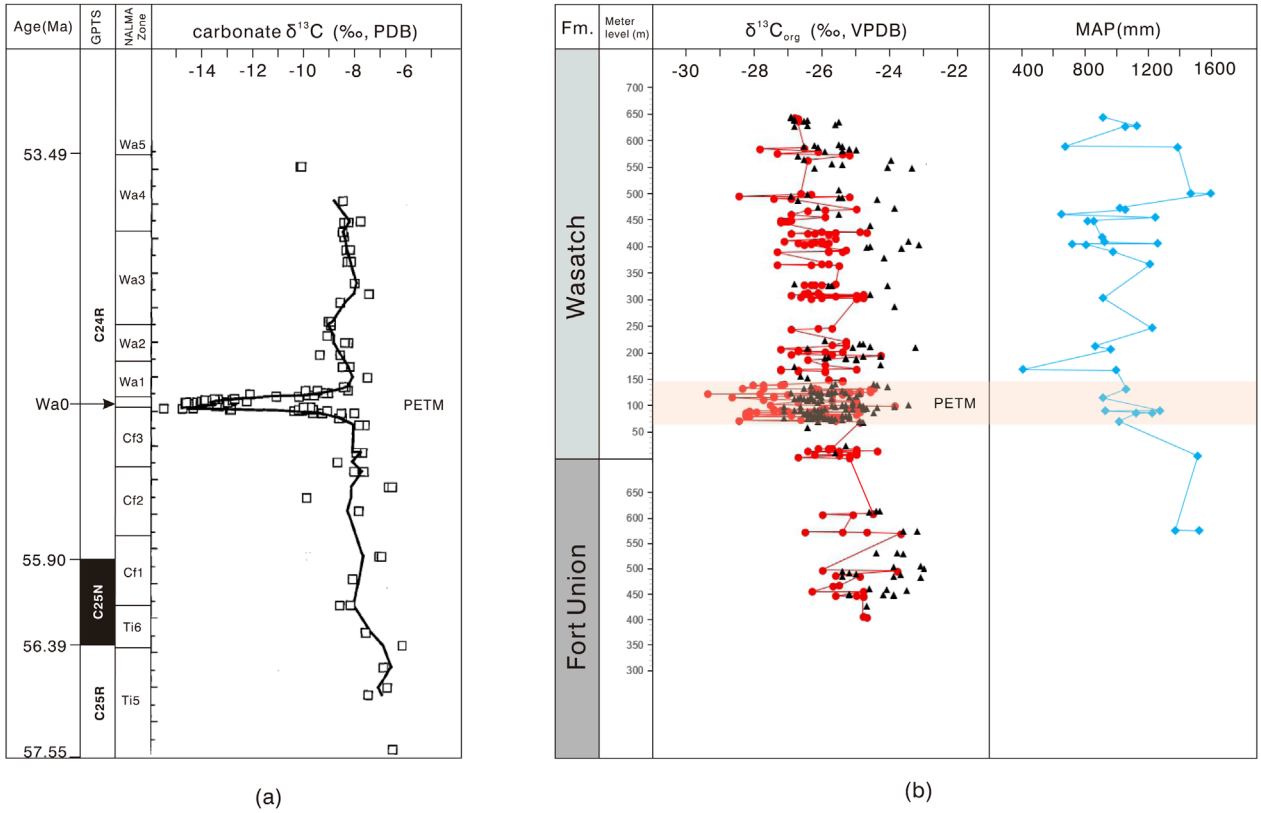

FIGURE 4
Carbon isotope record and MAP estimates for the late Paleocene-early Eocene hydroclimate. **(a)** Carbon isotope record from paleosol carbonates in the Bighorn Basin (Koch et al., 2003, © The Geological Society of America, used with permission); **(b)** $\delta^{13}C_{org}$ record and MAP estimates (this study). Red dots represent the $\delta^{13}C_{org}$ values of paleosol samples, and black triangles represent the $\delta^{13}C_{org}$ values of non-pedogenic mudstone samples. Please note that the low MAP at 168.8 m of Wasatch Formation is due to elevated Na_2O level, likely originating from diagenetic salt, and is therefore not accurate.

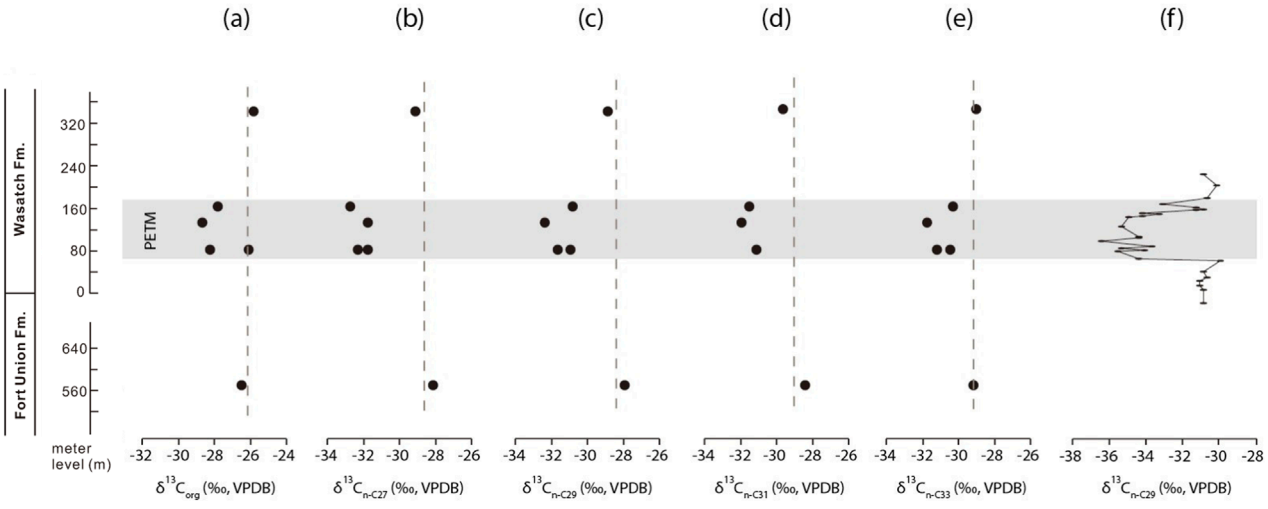

FIGURE 5
Bulk organic $\delta^{13}C_{org}$ values **(a)** and compound-specific leaf wax $\delta^{13}C_{n-alk}$ values **(b–e)** of the six selected samples in this study are compared to a record **(f)** in the Bighorn Basin (Baczynski et al., 2016).

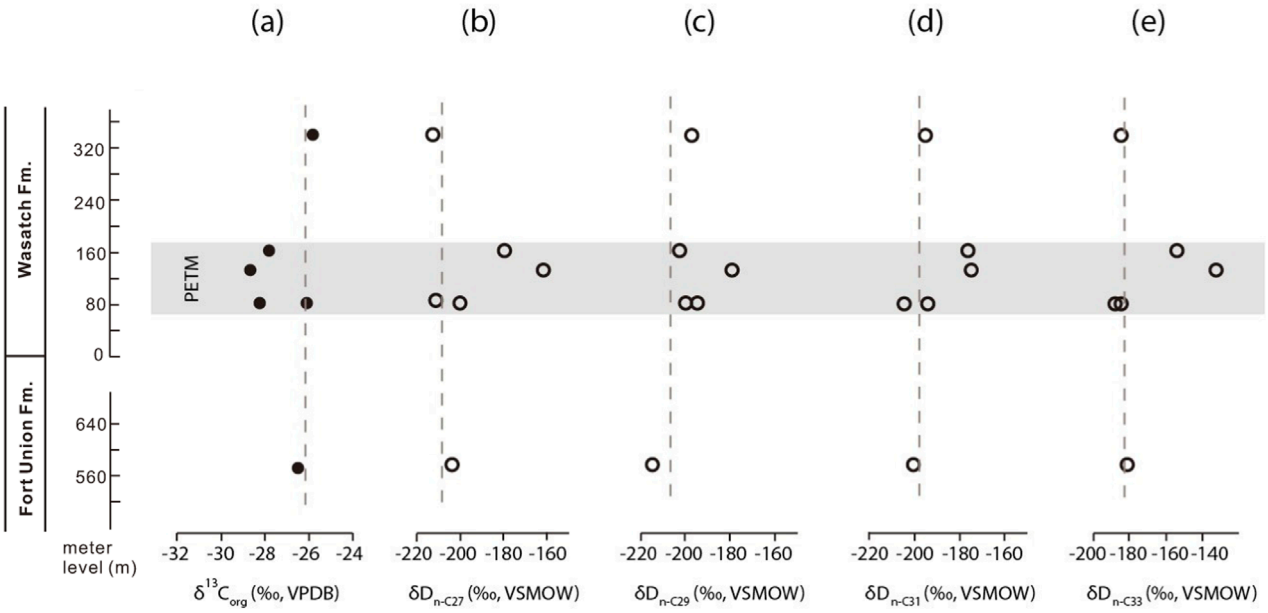

FIGURE 6
Compound–specific leaf wax δD_{n-alk} values **(b–e)** in our study. Bulk organic $\delta^{13}C_{org}$ values of the samples are also shown **(a)**.

The other two samples at 405 m and 588 m of Wasatch Formation, where Na_2O content is greater than 2.0 wt%, also show low MAP estimates. The atmospheric pCO_2 during the early Eocene was estimated to be in the range of 600–900 ppm from the six selected paleosol samples in the Wasatch Formation (Table 3).

5 Discussion

5.1 Recognition of PETM

We identify CIEs in both the $\delta^{13}C_{n-alk}$ and $\delta^{13}C_{org}$ records near the Paleocene–Eocene boundary in the greater Green River Basin (Figures 4b, 5). The magnitude is on the order of 4–5‰, which is consistent with, or smaller than those of CIEs of the PETM in marine and other continental records. In marine benthic foraminifera $\delta^{13}C_c$ record, the PETM is expressed as a ~3‰ CIE (e.g., Zachos et al., 2001). Continental records show that the CIE during the PETM has variable magnitude, depending on the type of samples studied. Such CIE records include a ~6‰ drop based on studies of bulk organic $\delta^{13}C_{org}$ in the Paris Basin, France (Magioncalda et al., 2001), a ~6‰–8‰ drop based on studies of paleosol carbonates $\delta^{13}C_c$ in the Bighorn Basin (Bowen et al., 2001; Koch et al., 2003; Abels et al., 2016), a ~5‰ drop based on a study of mammalian tooth enamel $\delta^{13}C$ in the Bighorn Basin (Secord et al., 2012), and a 4‰–5‰ drop based on studies of bulk organic $\delta^{13}C_{org}$ and leaf wax $\delta^{13}C_{n-alk}$ in the Bighorn Basin (Baczynski et al., 2013; 2016). The depositional duration of the ~4–5‰ CIE in our record seems also to match the duration of PETM in the Bighorn Basin. Our CIE spans ~70 m, aligning with the stratigraphic interval of PETM in the Bighorn Basin, which varies between 40 m and 100 m depending on the specific study location (Bowen et al., 2001; Koch et al., 2003; Secord et al., 2012; Baczynski et al., 2013; 2016). Therefore, we suggest that the ~4–5‰ CIE in our record is the PETM. The variations in CIE magnitude in different locations could reflect differences in soil properties, the type of C_3 vegetation (e.g., Cerling and Quade, 1993), the mixing of carbon from different sources (e.g., autochthonous or allochthonous), and different degrees of organic matter degradation (Baczynski et al., 2013; 2016).

The second CIE on our $\delta^{13}C_{org}$ record, with a magnitude of ~2‰, occurred after the PETM but before ~53 Ma (Figure 4b). This CIE most likely represents the ETM–2 hypothermal event. The ETM–2 is the most pronounced early Eocene hyperthermal event and is expressed as a ~1‰ negative CIE in marine bulk sediment records (Zachos et al., 2010). In the continental environment, ETM–2 has been documented as a ~3‰ drop in paleosol carbonate $\delta^{13}C_c$ in the Bighorn Basin (Abels et al., 2016). Although our $\delta^{13}C_{org}$ record does not show an ideal CIE that could precisely represent the ETM–2, the timing and magnitude of this excursion resemble those of the ETM–2, or a combination of ETM–2 and other smaller hyperthermals that happened within the next ~500 kyr of the ETM–2 (e.g., Cramer et al., 2003; Lourens et al., 2005).

5.2 Humid LPEE and transient drying during the PETM

Kraus et al. (2013) reconstructed the MAP in the Bighorn Basin based on a ~70 m thick interval of paleosols covering the PETM, their results show that the MAP values in the pre– and post–PETM intervals are generally high, in the range of 1,100–1,500 mm, and the values dropped to 800–1,100 mm during the main phase of PETM. However, our estimated MAP remains relatively stable, ranging between 800–1,500 mm during the entire LPEE (Figure 4b). The absence of a decrease in MAP during the PETM in this studied section contrasts with records from other basins and the transient

TABLE 2 Major elements weight percentages and calculated CIA–K and MAP.

Formation	Meter level	MgO	Al_2O_3	SiO_2	K_2O	CaO	TiO_2	Fe_2O_3	Na_2O	CaO*	CIA–K	MAP
	(m)	wt%	wt%	wt%	wt%	wt%	wt%	wt%	wt%	wt%		(mm)
Fort Union	573.0	1.5	14.0	46.0	1.4	6.7	0.4	2.6	0.1	0.1	98	1,519
Fort Union	573.5	2.5	16.5	70.6	3.3	0.4	0.6	3.1	0.4	0.4	92	1,367
Wasatch	7.0	1.7	12.1	57.4	2.2	4.6	0.4	4.7	0.1	0.1	97	1,508
Wasatch	72.0	3.0	11.6	68.0	3.0	3.5	0.4	4.5	1.0	1.0	77	1,012
Wasatch	87.0	3.1	14.4	60.3	4.6	1.1	0.6	7.8	0.9	0.9	82	1,121
Wasatch	87.3	2.6	13.5	58.8	4.3	1.0	0.6	6.1	0.6	0.6	87	1,224
Wasatch	91.3	3.1	10.1	63.3	2.1	5.7	0.4	3.4	1.1	1.1	73	928
Wasatch	92.0	2.4	13.3	76.6	3.4	0.9	0.5	3.3	0.5	0.5	88	1,269
Wasatch	115.4	1.7	7.0	40.3	1.6	10.3	0.2	1.3	0.8	0.8	72	911
Wasatch	132.5	3.1	14.5	62.1	4.0	1.0	0.5	5.8	1.2	1.0	79	1,058
Wasatch	168.0	2.8	11.1	69.5	2.4	1.8	0.5	3.7	1.0	1.0	76	997
Wasatch	168.8	9.2	7.9	45.2	1.8	8.1	0.3	2.5	5.1	5.1	31	408
Wasatch	207.0	3.4	14.0	73.3	4.0	1.3	0.5	4.2	1.5	1.3	74	960
Wasatch	212.8	3.7	11.5	64.3	2.7	4.0	0.5	4.2	1.5	1.5	69	862
Wasatch	246.8	2.4	11.1	74.0	1.8	1.0	0.4	2.7	0.5	0.5	86	1,221
Wasatch	303.3	3.4	12.3	66.7	2.7	2.1	0.5	3.3	1.4	1.4	72	912
Wasatch	366.5	2.7	12.8	69.4	3.0	1.2	0.5	4.7	0.6	0.6	86	1,209
Wasatch	390.5	3.3	12.5	62.6	2.8	3.2	0.5	4.3	1.2	1.2	75	974
Wasatch	403.5	4.1	11.8	55.0	3.1	6.8	0.4	4.9	1.8	1.8	65	806
Wasatch	405.0	4.3	10.2	53.5	2.5	7.1	0.4	4.3	2.0	2.0	60	718
Wasatch	406.0	2.3	12.7	70.4	2.9	0.7	0.5	4.6	0.5	0.5	88	1,257
Wasatch	408.5	3.6	11.8	71.3	2.6	2.3	0.5	3.1	1.3	1.3	72	924
Wasatch	417.0	3.7	12.1	54.2	3.2	6.4	0.5	5.1	1.4	1.4	71	906
Wasatch	448.0	3.2	9.7	59.2	1.3	6.5	0.4	2.3	1.3	1.3	68	853
Wasatch	448.5	3.0	8.1	49.5	1.2	9.7	0.3	1.8	1.2	1.2	66	816
Wasatch	454.5	2.3	14.3	54.6	2.1	2.8	0.6	6.9	0.6	0.6	87	1,240
Wasatch	460.5	1.2	2.8	56.2	2.1	3.6	0.5	3.3	1.2	0.2	54	650
Wasatch	469.5	2.8	11.8	65.4	2.0	5.7	0.4	3.1	0.9	0.9	79	1,055
Wasatch	472.5	2.7	11.8	58.7	2.3	6.9	0.4	3.4	1.0	1.0	77	1,018
Wasatch	499.5	1.1	11.5	65.7	1.8	0.3	0.6	8.3	0.0	0.0	100	1,593
Wasatch	500.0	2.0	16.0	73.7	3.4	0.6	0.6	2.5	0.2	0.2	96	1,467

(Continued on the following page)

TABLE 2 (*Continued*) Major elements weight percentages and calculated CIA–K and MAP.

Formation	Meter level	MgO	Al_2O_3	SiO_2	K_2O	CaO	TiO_2	Fe_2O_3	Na_2O	CaO*	CIA–K	MAP
	(m)	wt%	wt%	wt%	wt%	wt%	wt%	wt%	wt%	wt%		(mm)
Wasatch	586.5	1.9	13.6	70.4	3.1	0.4	0.6	6.4	0.3	0.3	93	1,385
Wasatch	588.0	5.9	12.6	54.1	2.9	5.1	0.4	3.7	2.8	2.8	56	676
Wasatch	625.5	2.6	10.4	56.1	1.1	5.7	0.4	4.2	0.8	0.8	79	1,052
Wasatch	626.2	3.2	14.5	58.3	2.3	1.1	0.7	6.9	0.9	0.9	82	1,124
Wasatch	643.2	3.6	12.3	64.7	1.6	3.4	0.5	3.9	1.4	1.4	72	912

TABLE 3 Reconstructed atmospheric pCO_2 based on isotopic analysis of paleosols.

Sample ID	Meter level	$\delta^{13}C_c$	$\delta^{13}C_r$	$\delta^{13}C_s$	$\delta^{13}C_a$	S(z)	pCO_2
	(m)	(‰)	(‰)	(‰)	(‰)	(ppm)	(ppm)
WMB–n1	76.0	−9.2	−25.9	−17.4	−6.1	2,500	922
WMB–n2	80.0	−9.8	−25.4	−18.0	−6.1	2,500	646
WMB–n3	96.5	−9.4	−24.9	−17.6	−6.1	2,500	645
WMB–n4	102.0	−9.7	−25.5	−17.9	−6.1	2,500	694
WMB–n5	380.0	−8.1	−24.3	−16.3	−6.1	2,500	894
WMB–n6	425.0	−9.6	−26.3	−17.8	−6.1	2,500	892

drying observed in leaf wax δD_{n-alk} and changes in paleosol morphology in this study. For example, a dry PETM was also suggested from a sedimentology study in the Axehandle Basin in central Utah (Bowen and Bowen, 2008) and a leaf physiognomy study in the Bighorn Basin (Wing et al., 2005). Several studies have questioned the accuracy of MAP estimates based on CIA–K, particularly for thinner paleosols (B horizon less than 1 m thick), as they had less time for weathering and may not have a cation distribution representative of precipitation (e.g., Adams et al., 2011). The possibility that the low sampling resolution in our record is responsible for the absence of decreasing MAP cannot be completely ruled out.

The 30‰–50‰ increase in leaf wax δD_{n-alk} values in our record show transient drying during the PETM (Figure 6). Studies of terrestrial plants and soils have suggested that leaf waxes are refractory, and their δD_{n-alk} values primarily reflect meteoric water δD values (e.g., Sauer et al., 2001; Smith and Freeman, 2006). The increase in δD_{n-alk} values during the PETM most likely reflects a combination of increasing meteoric water δD due to decreasing precipitation amount, increasing soil evaporation, and reducing hydrogen isotope fractionation between water and leaf wax during climate drying. It has been suggested that soil evaporation enriches deuterium in soil water and decrease the apparent fractionation factor, especially in arid climate (e.g., Smith and Freeman, 2006). The development of different types of paleosols throughout our measured section further supports the inferred transient drying. During the Paleocene, the floodplains were generally water–logged and had histosols (coal beds) developed, indicating that the climate was wet. During the early Eocene, paleosol types within the PETM are different compared to those in the rest of the section. Within the PETM, poorly drained red paleosols and calcisols developed, indicating dry environment. Outside of the hyperthermal, the floodplain deposition was dominated by well drained green paleosols, indicating wet climate. Soil type representing wet paleoclimate changed from histosols during the Paleocene to green paleosols during the early Eocene, possibly reflecting a change in ecosystem when climate became very hot during the early Eocene.

The transient drying during the PETM may be explained by the mid–latitude bypass mechanism, which was proposed to explain the elevated runoff and deuterium–enriched precipitation in the Arctic during the PETM (Pagani et al., 2006). Decreased meridional temperature gradients during the PETM might have reduced rainout of water vapor by synoptic eddies in the mid–latitudes, and increased moisture delivery to the high latitudes, because a decreased temperature gradient provides a smaller energy supply for synoptic eddies (Pierrehumbert, 2002; Pagani et al., 2006). This mechanism predicts temporally drier conditions during the PETM than other times during the early Paleogene in the mid–latitudes, and spatially drier conditions in the southerly sites than in the northerly sites in Wyoming during the PETM (Bowen and Bowen, 2008). Bowen and Bowen (2008) found that the CIE in central Utah was ~2‰ smaller than the ~6‰–8‰ drop in the Bighorn Basin during the PETM, both determined from paleosol carbonates

$\delta^{13}C_c$, and suggested that the smaller CIE could have been caused by drier conditions. The speculative correlation of the PETM with a ~15–m–thick evaporite sequence deposited in the Flagstaff lake system in central Utah also supports a significant increase in regional aridity during the PETM at this location compared to the Bighorn Basin (Bowen and Bowen, 2008). The CIE magnitude in the greater Green River Basin is consistent with that based on leaf wax $\delta^{13}C_{n-alk}$ in the Bighorn Basin (Baczynski et al., 2013; 2016), indicating no evidence of southward aridification.

The general wet climate during the LPEE is consistent with climate model predictions. However, the model also predicts that the PETM, with higher *p*CO2 levels compared to the rest of the LPEE, should be wetter. By using the Community Climate System Model (CCSM3) with atmospheric CO_2 concentrations of 4×, 8×, and 16× the preindustrial value, Winguth et al. (2010) demonstrated that precipitation during the PETM slightly increases, and evaporation minus precipitation slightly decreases in mid to high latitudes with increased surface temperatures, and attributed the changes to responses to CO_2 radiative forcing (also seen in Sloan and Rea, 1996; Shellito et al., 2003). This prediction is not supported by the observed transient drying. The discrepancy between model predictions and proxy data could arise from several uncertainties. These include, but are not limited to, that model simulations may overestimate CO_2 radiative forcing, as our records show that the pCO_2 levels during the PETM were only 1–2 times higher, not at least 4 times higher, than preindustrial levels; model simulations may not fully account for the topography development in the western U.S.A. during the early Paleogene; and seasonal distribution of precipitation and potential biases in leaf wax records towards growing season precipitation.

6 Conclusion

This study presents an extensive record of continental hydroclimate responses to the warm late Paleocene–early Eocene global climate, including the extremely hot PETM. At our site in the greater Green River Basin, the reconstructed MAP during the entire LPEE is 800–1,500 mm, which is wetter than present conditions. The reconstructed atmospheric pCO_2 during the early Eocene is 600–900 ppm. The PETM is marked by a ~4‰ negative CIE in our bulk organic $\delta^{13}C_{org}$ record and a ~4‰–5‰ negative CIE in our leaf wax n-alkanes $\delta^{13}C_{n-alk}$ record. During the PETM, the leaf wax n-alkanes δD_{n-alk} increased by 30‰–50‰, indicating a phase of transient drying. Overall, our records show that the continental hydroclimate in the greater Green River Basin during the LPEE was generally warm and humid, but transient drying occurred during the PETM. The humid LPEE climate promoted formation of well drained green paleosols and water–logged histosols. In contrast, transient drying during the PETM resulted in the development of poorly drained red paleosols and carbonate–rich calcisols. This study contributes to the growing body of knowledge in understanding the continental hydroclimate responses to the global warming during the LPEE.

Data availability statement

The original contributions presented in the study are included in the article/Supplementary Material, further inquiries can be directed to the corresponding author. All the data supporting the conclusions can be found in the article/Supplementary Material and the cited references.

Author contributions

MG: Investigation, Formal analysis, Writing – original draft, Writing – review and editing. MF: Conceptualization, Supervision, Writing – review and editing. GZ: Formal analysis, Writing – review and editing. DC: Writing – review and editing.

Funding

The author(s) declare that financial support was received for the research, and/or publication of this article. This study is funded by American Chemical Society Petroleum Research Fund (grant number: PRF–54673–DNI8) to M. Fan, and is partially supported by a GSA graduate student research grant to M. Gao.

Acknowledgments

Acknowledgments are made to the donors of the American Chemical Society Petroleum Research Fund (grant number: PRF–54673–DNI8) awarded to M. Fan and the GSA graduate student research grant awarded to M. Gao. We are grateful to the journal editors and reviewers for their comments and suggestions that improved the earlier version of this manuscript.

Conflict of interest

Author MG was employed by PetroChina.

The remaining authors declare that the research was conducted in the absence of any commercial or financial relationships that could be construed as a potential conflict of interest.

Generative AI statement

The author(s) declare that no Generative AI was used in the creation of this manuscript.

Publisher's note

All claims expressed in this article are solely those of the authors and do not necessarily represent those of

their affiliated organizations, or those of the publisher, the editors and the reviewers. Any product that may be evaluated in this article, or claim that may be made by its manufacturer, is not guaranteed or endorsed by the publisher.

Supplementary material

The Supplementary Material for this article can be found online at: https://www.frontiersin.org/articles/10.3389/feart.2025.1507500/full#supplementary-material

References

Abels, H. A., Clyde, W. C., Gingerich, P. D., Hilgen, F. J., Fricke, H. C., Bowen, G. J., et al. (2012). Terrestrial carbon isotope excursions and biotic change during Palaeogene hyperthermals. *Nat. Geosci.* 5, 326–329. doi:10.1038/ngeo1427

Abels, H. A., van Yperen, A. E., Zachos, J. C., Lourens, L. J., Gingerich, P. D., Bowen, G. J., et al. (2016). Environmental impact and magnitude of paleosol carbonate carbon isotope excursions marking five early Eocene hyperthermals in the Bighorn Basin, Wyoming. *Clim. Past* 12, 1151–1163. doi:10.5194/cp–12–1151–2016

Adams, J. S., Kraus, M. J., and Wing, S. L. (2011). Evaluating the use of weathering indices for determining mean annual precipitation in the ancient stratigraphic record. *Palaeogeogr. Palaeoclimatol. Palaeoecol.* 309, 358–366. doi:10.1016/j.palaeo.2011.07.004

Baczynski, A. A., McInerney, F. A., Wing, S. L., Kraus, M. J., Bloch, J. I., Boyer, D. M., et al. (2013). Chemostratigraphic implications of spatial variation in the paleocene-eocene thermal maximum carbon isotope excursion, SE Bighorn Basin, Wyoming. *Geochem. Geophys. Geosystems* 14 (10), 4133–4152. doi:10.1002/ggge.20265

Baczynski, A. A., McInerney, F. A., Wing, S. L., Kraus, M. J., Morse, P. E., Bloch, J. I., et al. (2016). Distortion of carbon isotope excursion in bulk soil organic matter during the Paleocene–Eocene thermal maximum. *Geol. Soc. Am. Bull.* 128, 1352–1366. doi:10.1130/b31389.1

Badía–Villas, D., and del Moral, F. (2016). Soils of the arid areas. *Soils Spain*, 145–161. doi:10.1007/978–3–319–20541–0_4

Bowen, G. J., and Beerling, D. J. (2004). An integrated model for soil organic carbon and CO_2: implications for paleosol carbonate pCO_2 paleobarometry. *Glob. Biogeochem. Cycles* 18. doi:10.1029/2003gb002117

Bowen, G. J., and Bowen, B. B. (2008). Mechanisms of PETM global change constrained by a new record from central Utah. *Geology* 36, 379–382. doi:10.1130/g24597a.1

Bowen, G. J., Koch, P. L., Gingerich, P. D., Norris, R. D., Bains, S., and Corfield, R. M. (2001). *Refined isotope stratigraphy across the continental paleocene–eocene boundary on polecat bench in the northern Bighorn Basin: paleocene–eocene stratigraphy and biotic change in the Bighorn and clarks fork basins*, 33. Wyoming: University of Michigan Papers on Paleontology, 73–88.

Breecker, D. (2013). Quantifying and understanding the uncertainty of atmospheric CO_2 concentrations determined from calcic paleosols. *Geochem. Geophys. Geosystems* 14, 3210–3220. doi:10.1002/ggge.20189

Breecker, D., Sharp, Z., and McFadden, L. D. (2009). Seasonal bias in the formation and stable isotopic composition of pedogenic carbonate in modern soils from central New Mexico, USA. *Geol. Soc. Am. Bull.* 121, 630–640. doi:10.1130/b26413.1

Breecker, D. O., Sharp, Z. D., and McFadden, L. D. (2010). Atmospheric CO^2 concentrations during ancient greenhouse climates were similar to those predicted for AD 2100. *Proc. Natl. Acad. Sci.* 107 (2), 576–580. doi:10.1073/pnas.0902323106

Buol, S., Hole, F., and McCracken, R. (1980). Soil genesis and classification: ames.

Caldeira, K. (1992). Enhanced Cenozoic chemical weathering and the subduction of pelagic carbonate. *Nature* 357 (6379), 578–581. doi:10.1038/357578a0

Carmichael, M. J., Inglis, G. N., Badger, M. P., Naafs, B. D. A., Behrooz, L., Remmelzwaal, S., et al. (2017). Hydrological and associated biogeochemical consequences of rapid global warming during the Paleocene–Eocene Thermal Maximum. *Glob. Planet. Change* 157, 114–138. doi:10.1016/j.gloplacha.2017.07.014

Carmichael, M. J., Pancost, R. D., and Lunt, D. J. (2018). Changes in the occurrence of extreme precipitation events at the Paleocene–Eocene thermal maximum. *Earth Planet. Sci. Lett.* 501, 24–36. doi:10.1016/j.epsl.2018.08.005

Cerling, T. E. (1992). Use of carbon isotopes in paleosols as an indicator of the P (CO_2) of the paleoatmosphere. *Glob. Biogeochem. Cycles* 6, 307–314. doi:10.1029/92gb01102

Cerling, T. E., and Harris, J. M. (1999). Carbon isotope fractionation between diet and bioapatite in ungulate mammals and implications for ecological and paleoecological studies. *Oecologia* 120, 347–363. doi:10.1007/s004420050868

Cerling, T. E., and Quade, J. (1993). Stable carbon and oxygen isotopes in soil carbonates. *Clim. Change Cont. Isotopic Rec.*, 217–231. doi:10.1029/gm078p0217

Clyde, W. C., Zonneveld, J., Stamatakos, J., Gunnell, G. F., and Bartels, W. S. (1997). Magnetostratigraphy across the Wasatchian/Bridgerian NALMA boundary (early to middle Eocene) in the western Green River basin, Wyoming. *J. Geol.* 105, 657–670. doi:10.1086/515970

Cramer, B. S., Wright, J. D., Kent, D. V., and Aubry, M. (2003). Orbital climate forcing of $\delta^{13}C$ excursions in the late Paleocene–early Eocene (chrons C24n–C25n). *Paleoceanography* 18. doi:10.1029/2003pa000909

Cramwinckel, M. J., Burls, N. J., Fahad, A. A., Knapp, S., West, C. K., Reichgelt, T., et al. (2023). Global and zonal-mean hydrological response to early Eocene warmth. *Paleoceanogr. Paleoclimatology* 38 (6), e2022PA004542. doi:10.1029/2022pa004542

Daniels, W. L., and Haering, K. C. (2006). *Concepts of basic soil science. The MidAtlantic nutrient management handbook*, 31.

DeCelles, P. G. (2004). Late Jurassic to Eocene evolution of the Cordilleran thrust belt and foreland basin system, western USA. *Am. J. Sci.* 304, 105–168. doi:10.2475/ajs.304.2.105

Dickens, G. R. (2003). A methane trigger for rapid warming? *Science* 299, 10171017. doi:10.1126/science.1080789

Dickinson, W. R., Klute, M. A., Hayes, M. J., Janecke, S. U., Lundin, E. R., McKITTRICK, M. A., et al. (1988). Paleogeographic and paleotectonic setting of Laramide sedimentary basins in the central Rocky Mountain region. *Geol. Soc. Am. Bull.* 100, 1023–1039. doi:10.1130/0016–7606(1988)100<1023:papsol>2.3.co;2

Driese, S. G., Nordt, L. C., Lynn, W. C., Stiles, C. A., Mora, C. I., and Wilding, L. P. (2005). Distinguishing climate in the soil record using chemical trends in a Vertisol climosequence from the Texas Coast Prairie, and application to interpreting Paleozoic paleosols in the Appalachian Basin, USA. *J. Sediment. Res.* 75, 339–349. doi:10.2110/jsr.2005.027

Elidrissi, S., Daoudi, L., and Fagel, N. (2018). Palygorskite occurrences and genesis in calcisol and groundwater carbonates of the Tensift Al Haouz area, Central Morocco. *Geoderma* 316, 78–88. doi:10.1016/j.geoderma.2017.12.013

Fan, M., DeCelles, P. G., Gehrels, G. E., Dettman, D. L., Quade, J., and Peyton, S. L. (2011). Sedimentology, detrital zircon geochronology, and stable isotope geochemistry of the lower Eocene strata in the Wind River Basin, central Wyoming. *Geol. Soc. Am. Bull.* 123, 979–996. doi:10.1130/b30235.1

Gao, M., and Fan, M. (2018). Depositional environment, sediment provenance and oxygen isotope paleoaltimetry of the early Paleogene greater Green River Basin, southwestern Wyoming, USA. *Am. J. Sci.* 318 (10), 1018–1055. doi:10.2475/10.2018.02

Gao, M., Fan, M., and Moucha, R. (2016). Southwestward weakening of Wyoming lithosphere during the Laramide orogeny. *J. Geophys. Res. Solid Earth* 121, 6219–6234. doi:10.1002/2016jb013130

Guo, Z., Wilson, M., Dingwell, D. B., and Liu, J. (2021). India–Asia collision as a driver of atmospheric CO_2 in the Cenozoic. *Nat. Commun.* 12 (1), 3891. doi:10.1038/s41467–021–23772–y

Hollis, C. J., Dunkley Jones, T., Anagnostou, E., Bijl, P. K., Cramwinckel, M. J., Cui, Y., et al. (2019). The DeepMIP contribution to PMIP4: methodologies for selection, compilation and analysis of latest Paleocene and early Eocene climate proxy data, incorporating version 0.1 of the DeepMIP database. *Geosci. Model Dev.* 12 (7), 3149–3206. doi:10.5194/gmd–12–3149–2019

Honey, J. (1988). *A mammalian fauna from the base of the Eocene cathedral Bluffs Tongue of the Wasatch Formation: cottonwood Creek area, southeast Wasatch basin*, 1669. Wyoming: US Geological Survey Bulletin C, 1–13.

Hough, B. G., Fan, M., and Passey, B. H. (2014). Calibration of the clumped isotope geothermometer in soil carbonate in Wyoming and Nebraska, USA: implications for paleoelevation and paleoclimate reconstruction. *Earth Planet. Sci. Lett.* 391, 110–120. doi:10.1016/j.epsl.2014.01.008

Hren, M. T., Pagani, M., Erwin, D. M., and Brandon, M. (2010). Biomarker reconstruction of the early Eocene paleotopography and paleoclimate of the northern Sierra Nevada. *Geology* 38, 7–10. doi:10.1130/g30215.1

Hyland, E., Sheldon, N. D., and Fan, M. (2013). Terrestrial paleoenvironmental reconstructions indicate transient peak warming during the early Eocene climatic optimum. *Geol. Soc. Am. Bull.* 125, 1338–1348. doi:10.1130/b30761.1

Kennett, J., and Stott, L. (1991). Abrupt deep sea warming, paleoceanographic changes and benthic extinctions at the end of the Paleocene.

Kent, D. V., and Muttoni, G. (2008). Equatorial convergence of India and early Cenozoic climate trends. *Proc. Natl. Acad. Sci. U. S. A.* 105, 16065–16070. doi:10.1073/pnas.0805382105

Koch, P. L., Clyde, W. C., Hepple, R. P., Fogel, M. L., Wing, S. L., and Zachos, J. C. (2003). "Carbon and oxygen isotope records from paleosols spanning the

Paleocene–Eocene boundary, Bighorn Basin, Wyoming," in *Causes and Consequences of Globally Warm Climates in the Early Paleogene*. Editor S. L. Wing, P. D. Gingerich, B. Schmitz, and E. Thomas (Boulder, Colorado: Geological Society of America Special Paper), 49–64. doi:10.1130/0-8137-2369-8.49

Koch, P. L., Zachos, J. C., and Dettman, D. L. (1995). Stable isotope stratigraphy and paleoclimatology of the Paleogene Bighorn Basin (Wyoming, USA). *Palaeogeogr. Palaeoclimatol. Palaeoecol.* 115, 61–89. doi:10.1016/0031–0182(94)00107–j

Kraus, M. J. (1999). Paleosols in clastic sedimentary rocks: their geologic applications. *Earth–Science Rev.* 47 (1–2), 41–70. doi:10.1016/s0012–8252(99)00026–4

Kraus, M. J., McInerney, F. A., Wing, S. L., Secord, R., Baczynski, A. A., and Bloch, J. I. (2013). Paleohydrologic response to continental warming during the paleocene–eocene thermal maximum, Bighorn Basin, Wyoming. *Palaeogeogr. Palaeoclimatol. Palaeoecol.* 370, 196–208. doi:10.1016/j.palaeo.2012.12.008

Lourens, L. J., Sluijs, A., Kroon, D., Zachos, J. C., Thomas, E., Röhl, U., et al. (2005). Astronomical pacing of late Palaeocene to early Eocene global warming events. *Nature* 435, 1083–1087. doi:10.1038/nature03814

Machlus, M., Hemming, S. R., Olsen, P. E., and Christie–Blick, N. (2004). Eocene calibration of geomagnetic polarity time scale reevaluated: evidence from the Green River Formation of Wyoming. *Geology* 32, 137–140. doi:10.1130/g20091.1

Mack, G. H., James, W. C., and Monger, H. C. (1993). Classification of paleosols. *Geol. Soc. Am. Bull.* 105, 129–136. doi:10.1130/0016–7606(1993)105<0129:cop>2.3.co;2

Magioncalda, R., Dupuis, C., Blamart, D., Fairon–Demaret, M., Perreau, M., Renard, M., et al. (2001). L'excursion isotopique du carbone organique (delta $^{13}C_{org}$) dans les paleoenvironnements continentaux de l'intervalle Paleocene/Eocene de Varangeville (Haute–Normandie). *Bull. Société géologique Fr.* 172 (3), 349–358. doi:10.2113/172.3.349

Mauger, R. L. (1977). K–Ar ages of biotites from tuffs in Eocene rocks of the Green River, Washakie, and Uinta basins, Utah, Wyoming, and Colorado. *Rocky Mt. Geol.* 15, 17–41.

McInerney, F. A., and Wing, S. L. (2011). The Paleocene–Eocene Thermal Maximum: a perturbation of carbon cycle, climate, and biosphere with implications for the future. *Annu. Rev. Earth Planet. Sci.* 39, 489–516. doi:10.1146/annurev–earth–040610–133431

McLennan, S. M. (1993). Weathering and global denudation. *J. Geol.* 101 (2), 295–303. doi:10.1086/648222

Nettleton, W., Olson, C., and Wysocki, D. A. (2000). Paleosol classification: problems and solutions. *Catena* 41, 61–92. doi:10.1016/s0341–8162(00)00109–0

Pagani, M., Caldeira, K., Archer, D., and Zachos, J. C. (2006). An ancient carbon mystery. *Science–New York then Washingt–.* 314, 1556–1557. doi:10.1126/science.1136110

Passey, B. H., Levin, N. E., Cerling, T. E., Brown, F. H., and Eiler, J. M. (2010). Hightemperature environments of human evolution in East Africa based on bond ordering in paleosol carbonates. *Proc. Natl. Acad. Sci. U. S. A.* 107, 11245–11249. doi:10.1073/pnas.1001824107

Pierrehumbert, R. T. (2002). The hydrologic cycle in deep–time climate problems. *Nature* 419 (6903), 191–198. doi:10.1038/nature01088

Quade, J., Eiler, J., Daeron, M., and Achyuthan, H. (2013). The clumped isotope geothermometer in soil and paleosol carbonate. *Geochimica Cosmochimica Acta* 105, 92–107. doi:10.1016/j.gca.2012.11.031

Retallack, G. J. (1997). *Colour guide to paleosols*, xi+–175.

Retallack, G. J. (2009). Greenhouse crises of the past 300 million years. *Geol. Soc. Am. Bull.* 121, 1441–1455. doi:10.1130/b26341.1

Rigby, J. K. (1980). *Swain quarry of the Fort Union Formation, middle Paleocene (torrejonian), carbon county, Wyoming, geologic setting and mammalian fauna*. Evolutionary Monographs, University of Chicago.

Rind, D. (1998). Latitudinal temperature gradients and climate change. *J. Geophys. Res. Atmos.* 103, 5943–5971. doi:10.1029/97jd03649

Robert, C., and Kennett, J. P. (1994). Antarctic subtropical humid episode at the Paleocene–Eocene boundary: clay–mineral evidence. *Geology* 22, 211. doi:10.1130/0091–7613(1994)022<0211:asheat>2.3.co;2

Roehler, H. W. (1992). in *Greater Green River Basin, Wyoming, Utah, and Colorado.Correlation, composition, areal distribution, and thickness of Eocene stratigraphic units*.

Roehler, H. W., and Martin, P. (1987). *Geological investigations of the vermillion Creek coal bed in the Eocene Niland Tongue of the Wasatch Formation*. Wyoming: Sweetwater County.

Röhl, U., Bralower, T., Norris, R., and Wefer, G. (2000). New chronology for the late Paleocene thermal maximum and its environmental implications. *Geology* 28, 927–930. doi:10.1130/0091–7613(2000)28<927:ncftlp>2.0.co;2

Röhl, U., Westerhold, T., Bralower, T. J., and Zachos, J. C. (2007). On the duration of the Paleocene–Eocene thermal maximum (PETM). *Geochem. Geophys. Geosystems* 8. doi:10.1029/2007gc001784

Romanek, C. S., Grossman, E. L., and Morse, J. W. (1992). Carbon isotopic fractionation in synthetic aragonite and calcite: effects of temperature and precipitation rate. *Geochimica Cosmochimica Acta* 56, 419–430. doi:10.1016/0016–7037(92)90142–6

Rush, W. D., Kiehl, J. T., Shields, C. A., and Zachos, J. C. (2021). Increased frequency of extreme precipitation events in the North Atlantic during the PETM: observations and theory. *Palaeogeogr. Palaeoclimatol. Palaeoecol.* 568, 110289. doi:10.1016/j.palaeo.2021.110289

Sauer, P. E., Eglington, T. I., Hayes, J. M., Schimmelman, A., and Sessions, A. L. (2001). Compound–specific D/H ratios of lipid biomarkers from sediments as a proxy for environmental and climatic conditions. *Geochimica Cosmochimica Acta* 65 (2), 213–222. doi:10.1016/s0016–7037(00)00520–2

Schmitz, B., and Andreasson, F. P. (2001). Air humidity and lake $\delta^{18}O$ during the latest Paleocene–earliest Eocene in France from recent and fossil fresh–water and marine gastropod $\delta^{18}O$, $\delta^{13}C$, and $^{87}Sr/^{86}Sr$. *Geol. Soc. Am. Bull.* 113, 774–789. doi:10.1130/0016–7606(2001)113<0774:ahalod>2.0.co;2

Schmitz, B., and Pujalte, V. (2003). Sea–level, humidity, and land–erosion records across the initial Eocene thermal maximum from a continental–marine transect in northern Spain. *Geology* 31, 689–692. doi:10.1130/g19527.1

Schneider–Mor, A., and Bowen, G. J. (2013). Coupled and decoupled responses of continental and marine organic–sedimentary systems through the PaleoceneEocene thermal maximum, New Jersey margin, USA. *Paleoceanography* 28, 105–115. doi:10.1002/palo.20016

Secord, R., Bloch, J. I., Chester, S. G., Boyer, D. M., Wood, A. R., Wing, S. L., et al. (2012). Evolution of the earliest horses driven by climate change in the Paleocene–Eocene Thermal Maximum. *Sci. (New York, N.Y.)* 335, 959–962. doi:10.1126/science.1213859

Sessions, A. L. (2001). "Hydrogen isotope ratios of individual organic compounds," in *(Doctoal dissertation)* (Bloomington, IN: Indiana University), 149.

Sewall, J. O., and Sloan, L. C. (2006). Come a little bit closer: a high–resolution climate study of the early Paleogene Laramide foreland. *Geology* 34, 81–84. doi:10.1130/g22177.1

Sexton, P. F., Norris, R. D., Wilson, P. A., Pälike, H., Westerhold, T., Röhl, U., et al. (2011). Eocene global warming events driven by ventilation of oceanic dissolved organic carbon. *Nature* 471, 349–352. doi:10.1038/nature09826

Sheldon, N. D., Retallack, G. J., and Tanaka, S. (2002). Geochemical climofunctions from North American soils and application to paleosols across the Eocene Oligocene boundary in Oregon. *J. Geol.* 110, 687–696. doi:10.1086/342865

Sheldon, N. D., and Tabor, N. J. (2009). Quantitative paleoenvironmental and paleoclimatic reconstruction using paleosols. *Earth–Science Rev.* 95, 1–52. doi:10.1016/j.earscirev.2009.03.004

Shellito, C. J., Sloan, L. C., and Huber, M. (2003). Climate model sensitivity to atmospheric CO_2 levels in the Early–Middle Paleogene. *Palaeogeogr. Palaeoclimatol. Palaeoecol.* 193 (1), 113–123. doi:10.1016/s0031–0182(02)00718–6

Shuster, M. W., and Steidtmann, J. R. (1988). Tectonic and sedimentary evolution of the northern Green River basin, western Wyoming. *Geol. Soc. Am. Memoirs* 171, 515–530. doi:10.1130/mem171–p515

Sinha, A., and Stott, L. D. (1994). New atmospheric pCO_2 estimates from palesols during the late Paleocene/early Eocene global warming interval. *Glob. Planet. Change* 9, 297–307. doi:10.1016/0921–8181(94)00010–7

Sloan, L. C., Huber, M., and Ewing, A. (1999). "Polar stratospheric cloud forcing in a greenhouse world," in *Reconstructing Ocean history* (Springer), 273–293.

Sloan, L. C., and Rea, D. K. (1996). Atmospheric carbon dioxide and early Eocene climate: a general circulation modeling sensitivity study. *Palaeogeogr. Palaeoclimatol. Palaeoecol.* 119 (3–4), 275–292. doi:10.1016/0031–0182(95)00012–7

Sloan, L. C., Walker, J. C., Moore, T., Rea, D. K., and Zachos, J. C. (1992). Possible methane–induced polar warming in the early Eocene. *Nature* 357, 320–322. doi:10.1038/357320a0

Sluijs, A., Schouten, S., Donders, T. H., Schoon, P. L., Röhl, U., Reichart, G., et al. (2009). Warm and wet conditions in the arctic region during Eocene thermal maximum 2. *Nat. Geosci.* 2, 777–780. doi:10.1038/ngeo668

Smith, F. A., and Freeman, K. H. (2006). Influence of physiology and climate on δD of leaf wax n–alkanes from C3 and C4 grasses. *Geochimica Cosmochimica Acta* 70, 1172–1187. doi:10.1016/j.gca.2005.11.006

Snell, K. E., Thrasher, B. L., Eiler, J. M., Koch, P. L., Sloan, L. C., and Tabor, N. J. (2013). Hot summers in the Bighorn Basin during the early Paleogene. *Geology* 41, 55–58. doi:10.1130/g33567.1

Soil Survey Staff (1975). *Soil taxonomy: a basic system of soil classification for making and interpreting soil surveys*. Washington, D.C: U.S. Department of Agriculture, Soil Conservation Service.

Stott, L. D., Sinha, A., Thiry, M., Aubry, M. P., and Berggren, W. A. (1996). Global $\delta^{13}C$ changes across the Paleocene–Eocene boundary: criteria for terrestrial–marine correlations. *Geol. Soc.* 101 (1), 381–399. doi:10.1144/gsl.sp.1996.101.01.19

Svensen, H., Planke, S., Malthe–Sørenssen, A., Jamtveit, B., Myklebust, R., Eidem, T. R., et al. (2004). Release of methane from a volcanic basin as a mechanism for initial Eocene global warming. *Nature* 429, 542–545. doi:10.1038/nature02566

Tauxe, L., Gee, J., Gallet, Y., Pick, T., and Bowen, T. (1994). Magnetostratigraphy of the willwood formation, Bighorn Basin, Wyoming: new constraints on the location of paleocene/eocene boundary. *Earth Planet. Sci. Lett.* 125, 159–172. doi:10.1016/0012–821x(94)90213–5

The Cenozoic CO_2 Proxy Integration Project (CenCO2PIP) Consortium, Hönisch, B., Royer, D. L., Breecker, D. O., Polissar, P. J., Bowen, G. J., Henehan, M. J., et al. (2023). Toward a Cenozoic history of atmospheric CO_2. *Science* 382, eadi5177. doi:10.1126/science.adi5177

Tipple, B. J., Meyers, S. R., and Pagani, M. (2010). Carbon isotope ratio of Cenozoic CO_2: a comparative evaluation of available geochemical proxies. *Paleoceanography* 25. doi:10.1029/2009pa001851

Torn, M. S., Lapenis, A. G., Timofeev, A., Fischer, M. L., Babikov, B. V., and Harden, J. W. (2002). Organic carbon and carbon isotopes in modern and 100–year–oldsoil archives of the Russian steppe. *Glob. Change Biol.* 8, 941–953. doi:10.1046/j.1365–2486.2002.00477.x

Tripati, A., and Elderfield, H. (2005). Deep–sea temperature and circulation changes at the paleocene–eocene thermal maximum. *Sci. (New York, N.Y.)* 308, 1894–1898. doi:10.1126/science.1109202

Wing, S. L., Harrington, G. J., Smith, F. A., Bloch, J. I., Boyer, D. M., and Freeman, K. H. (2005). Transient floral change and rapid global warming at the Paleocene–Eocene boundary. *Science* 310 (5750), 993–996. doi:10.1126/science.1116913

Winguth, A., Shellito, C., Shields, C., and Winguth, C. (2010). Climate response at the paleocene–eocene thermal maximum to greenhouse gas forcing—a model study with CCSM3. *J. Clim.* 23, 2562–2584. doi:10.1175/2009jcli3113.1

Woodburne, M. O. (2004). *Late cretaceous and cenozoic mammals of north America: biostratigraphy and geochronology*. Columbia University Press.

Wynn, J. G., and Bird, M. I. (2007). C4–derived soil organic carbon decomposes faster than its C3 counterpart in mixed C3/C4 soils. *Glob. Change Biol.* 13, 2206–2217. doi:10.1111/j.1365–2486.2007.01435.x

Wynn, J. G., Bird, M. I., and Wong, V. N. (2005). Rayleigh distillation and the depth profile of $^{13}C/^{12}C$ ratios of soil organic carbon from soils of disparate texture in Iron Range National Park, Far North Queensland, Australia. *Geochimica Cosmochimica Acta* 69, 1961–1973. doi:10.1016/j.gca.2004.09.003

Zachos, J., Pagani, M., Sloan, L., Thomas, E., and Billups, K. (2001). Trends, rhythms, and aberrations in global climate 65 Ma to present. *Sci. (New York, N.Y.)* 292, 686–693. doi:10.1126/science.1059412

Zachos, J. C., Dickens, G. R., and Zeebe, R. E. (2008). An early Cenozoic perspective on greenhouse warming and carbon–cycle dynamics. *Nature* 451, 279–283. doi:10.1038/nature06588

Zachos, J. C., McCarren, H., Murphy, B., Röhl, U., and Westerhold, T. (2010). Tempo and scale of late Paleocene and early Eocene carbon isotope cycles: implications for the origin of hyperthermals. *Earth Planet. Sci. Lett.* 299, 242–249. doi:10.1016/j.epsl.2010.09.004

Zachos, J. C., Wara, M. W., Bohaty, S., Delaney, M. L., Petrizzo, M. R., Brill, A., et al. (2003). A transient rise in tropical sea surface temperature during the Paleocene–Eocene thermal maximum. *Sci. (New York, N.Y.)* 302, 1551–1554. doi:10.1126/science.1090110

Frontiers in Earth Science

Investigates the processes operating within the major spheres of our planet

Advances our understanding across the earth sciences, providing a theoretical background for better use of our planet's resources and equipping us to face major environmental challenges.

Discover the latest Research Topics

See more →

Frontiers

Avenue du Tribunal-Fédéral 34
1005 Lausanne, Switzerland
frontiersin.org

Contact us

+41 (0)21 510 17 00
frontiersin.org/about/contact